Modélisation de l'entraînement d'air dans l'eau avec la méthode SPH

Thomas Fonty

UNIVERSITÉ PARIS-EST

École Doctorale SIE

Laboratoire d'Hydraulique Saint-Venant

Thèse

Présentée pour l'obtention du grade de

DOCTEUR DE L'UNIVERSITE PARIS-EST

par

Thomas Fonty

Modélisation de l'entraînement d'air dans l'eau avec la méthode SPH

Spécialité : Mécanique des Fluides

Soutenue le 24 Octobre 2019 devant un jury composé de :

Rapporteur	**Prof. Stefano Sibilla**	(Università di Pavia)
Rapporteure	**Prof. Véronique Roig**	(IMFT)
Président du jury	**Prof. Olivier Simonin**	(IMFT)
Examinateur	**Prof. Jean-Philippe Matas**	(LMFA)
Examinateur	**Dr. Jean-Christophe Marongiu**	(Andritz AG)
Directeur de thèse	**Dr. Damien Violeau**	(EDF R&D & LHSV)
Co-encadrant de thèse	**M. Martin Ferrand**	(EDF R&D & CEREA)
Invitée	**Dr. Agnès Leroy**	(EDF R&D & LHSV)
Invité	**M. Grégory Guyot**	(EDF EN CIH)

Thèse effectuée au sein du **Laboratoire d'Hydraulique Saint-Venant**

de l'Université Paris-Est

6, quai Watier

BP 49

78401 Chatou cedex

France

Financements : ANR (bourse CIFRE # 2016-0362) et EDF R&D

Résumé

Les écoulements au sein d'ouvrages hydrauliques – déversement au-dessus d'un barrage, déferlement d'une vague sur une digue, etc. – sont le siège de forts mélanges d'eau et d'air qui se traduisent visuellement par la formation d'eaux blanches à la dynamique complexe. Représenter fidèlement le phénomène d'entraînement/capture des bulles d'air dans l'eau revêt donc un aspect stratégique important pour le dimensionnement de ces ouvrages. La modélisation tant physique que numérique de tels cas s'avère délicate à cause du fort rapport de densité entre les phases et de la nature multi-échelle de ces écoulements impliquant des effets de turbulence et de tension de surface. La méthode numérique SPH (*Smoothed Particle Hydrodynamics*), approche totalement lagrangienne qui représente l'écoulement comme un ensemble de particules en mouvement sans recours à un maillage, est particulièrement adaptée à la simulation de tels écoulements fortement déformés. Néanmoins, les limites actuelles de puissance de calcul empêchent encore de simuler finement des cas d'application industriels à large emprise en hydraulique. On se propose donc dans cette thèse de modéliser ces écoulements de manière macroscopique via un modèle de mélange qui consiste à voir chaque particule SPH comme un volume de mélange d'eau et d'air en mouvement. On détaille d'abord la dérivation des équations continues de ce modèle de mélange, puis on présente un état de l'art des simulations multiphasiques SPH. A partir du modèle continu et des outils actuels de discrétisation, un modèle de mélange diphasique SPH est ensuite mis en place en vue de son implémentation sur GPU (*Graphics Processing Unit*). Un accent tout particulier est mis sur les éléments originaux de discrétisation développés, notamment la dérivation d'un schéma aux bonnes propriétés numériques pour le suivi de l'évolution des volumes par phase et l'écriture d'un formalisme de frontières ouvertes pour un mélange. La turbulence, centrale dans le phénomène d'entraînement d'air, est modélisée via un modèle $k - \epsilon$ incluant un terme de flottabilité. Ce modèle de mélange est validé sur des cas académiques bidimensionnels de complexité croissante tels que la séparation d'un mélange eau-huile, un écoulement de Poiseuille diphasique, l'instabilité de Rayleigh–Taylor et un lâché de sédiments, illustrant sa polyvalence. La phénoménologie de l'entraînement d'air est ensuite décrite, et le modèle appliqué à des structures communément rencontrées en hydraulique, comme des jets plongeants et des coursiers en marches d'escalier, en introduisant une fermeture spécifique de la vitesse relative entre les phases. Enfin, on présente un premier cas d'application industriel à la géométrie et dynamique complexes.

Mots-clé:

SPH, entraînement d'air, turbulence, ouvrages d'eau, diphasique.

Modeling air entrainment in water with the SPH method

Abstract

Flows over hydraulic works – a nappe falling over a spillway, a wave breaking on a dike, etc. – undergo strong mixtures of air and water that lead to the appearance of white waters with complex dynamics. Faithfully capturing the phenomenon of air bubbles entrainment/entrapment in the flowing water is therefore pivotal for the design of those works. Both experimental and numerical modeling prove to be complex due to the high density ratio between phases and the multiscale nature of those flows involving turbulence and surface tension effects. The SPH (Smoothed Particle Hydrodynamics) method, a fully Lagrangian approach that models the flow as a set of moving particles without any mesh, is particularly well-suited to simulate such highly-distorted flows. Nevertheless, the current computational limits still prevent one from finely simulating industrial application cases with large domains in hydraulics. In this work, we aim at simulating macroscopically those flows with a mixture model in which each SPH particle stands for a moving volume of air and water. The derivation of the continuous equations of this mixture model is first detailed, then a state of the art of multiphase simulations in SPH is presented. Equipped with this continuous model and the existing discretization tools, a two-phase SPH mixture model is then derived and implemented on GPU (Graphics Processing Unit). A focus is made on original elements developed in the discretization, especially the derivation of a scheme with good numerical properties to follow the phase volume variations and the writing of an open boundary framework for mixtures. Turbulence, prominent for the air entrainment phenomenon, is modeled with a $k-\epsilon$ model including a buoyancy term. This model is validated against bidimensional academic test cases of increasing complexity, namely an oil-water separation, a two-phase Poiseuille flow, the Rayleigh-Taylor instability and a sand dumping case, proving its versatility. The air entrainment phenomenology is then described and the model is applied to common structures in hydraulics such as plunging jets and stepped spillways by introducing a specific closure for the relative velocity between phases. Finally, a first industrial application case with complex geometry and dynamics is presented.

Keywords:

SPH, air entrainment, turbulence, hydraulic works, two-phase flows.

Remerciements

Trois ans déjà que cela passe vite trois ans[1] *!* Tant de riches rencontres !

L'équipe SPH a été l'artisan majeur du bon déroulement de cette thèse. Je tiens à remercier en premier lieu mon directeur de thèse Damien Violeau. Merci pour ton encadrement, ta pédagogie, ta disponibilité pour réfléchir aux différents questionnements scientifiques qui se sont posés. Merci pour tes relectures attentives, précises et rigoureuses (dans des temps défiant toute concurrence !) qui ont renforcé ma confiance en la qualité des travaux produits. Merci aussi pour ton optimisme moteur tout au long de cette thèse. Merci Agnès et Martin pour votre temps, pour votre aide précieuse tant pour réfléchir sur des questions physiques que pour lever les soucis informatiques rencontrés, pour ce foisonnement d'idées qui a alimenté l'avancée de cette thèse. Votre parcours a été inspirant pour moi ! Merci à Antoine qui m'a accompagné dans mes premières simulations SPH. Merci à Alex et Rémi pour leurs remarques toujours opportunes et leur aide bienvenue dès mes premiers pas en thèse dans la découverte du monde de Sphynx. Merci à Athanasios, Elie et Vito que la sphère SPH m'a permis de rencontrer au détour de conférences d'abord et avec qui j'ai continûment échangé ensuite. Merci aux stagiaires qui ont participé à la vie de l'équipe durant ces trois années.

J'adresse des remerciements tout particuliers à Olivier Simonin qui a suivi avec attention ces travaux et donné de précieux avis, explications et conseils sur les écoulements diphasiques tout au long de la thèse.

Je remercie mes rapporteurs Stefano Sibilla et Véronique Roig ainsi que mes examinateurs Jean-Philippe Matas et Jean-Christophe Marongiu pour avoir accepté de faire partie de mon jury de thèse. Merci pour l'intérêt que vous avez accordé à ce travail et pour votre relecture attentive de ce manuscrit.

J'adresse également mes remerciements à EDF R&D et l'ANRT qui ont financé la thèse dans le cadre de la convention CIFRE #2016-0362, et au Laboratoire d'Hydraulique Saint-Venant qui a accueilli cette thèse.

Merci à Sandrine Dyèvre pour son animation de la communauté des doctorants, sa gentillesse et le temps passé à réaliser les exercices de communication sur la formation de docteur et le pitch de thèse. L'expérience a été enrichissante et laisse de sympathiques supports de communication. Merci aussi à l'équipe de l'Innovation Hub, Aurélie Renard et Christine Derouet.

Merci à l'équipe scientifique de la conférence SPHERIC que j'ai eu plaisir à retrouver trois années de suite. Merci pour votre intérêt pour mes travaux.

[1] Pastiche du poème *Strophes pour se souvenir* de Louis Aragon.

Merci aux membres de mon comité de suivi de thèse que je n'ai pas encore cités, Namane Mechitoua et Stéphane Mimouni, pour leur disponibilité et leurs conseils avisés. Ces échanges ont été importants dans l'avancée de mes recherches.

Une pensée toute particulière pour les équipes du CIH au Bourget du Lac, notamment Grégory Guyot pour m'avoir encadré il y a cinq ans déjà dans mes premiers pas avec SPH. Merci pour ton intérêt et ton enthousiasme pour mes travaux de thèse.

Merci aux ingénieurs et chercheurs du laboratoire avec qui j'ai eu tant plaisir à échanger : Marissa et Christophe en premier lieu car ils sont à l'origine de mon arrivée à EDF ! Ainsi que Nicole, Charles, Ludovic, Sébastien, Kim-Dan, Vincent, Riadh, Pablo, Jeffrey, Yvan. Merci à Sergina pour sa gentillesse et sa disponibilité pour résoudre les petits tracas.

Les équipes du MFEE également : Jean-Marc, Jean-Pierre, et Olivier d'abord qui ont eu plusieurs fois la gentillesse de m'accorder leur temps pour réfléchir sur les modèles diphasiques, mais aussi Sofiane, Dominique, Marie-Charlotte, Solène, Bertrand et l'ancienne équipée de stagiaires, docteurs en devenir tout prochainement, Gaëtan, Clément, Vladimir, Thibault.

Merci à mes professeurs qui ont su développer mon goût pour les sciences, notamment Alain Ehrlacher qui m'a si bien guidé dans le département de Génie Mécanique de l'Ecole des Ponts et a gardé un intérêt toujours renouvelé pour les travaux des anciens de l'école, mais aussi mes professeurs de classes préparatoires Vincent Bayle, Alain Soyeur, Jean-Pierre Migeon et Philippe Gaillard ainsi que mes professeurs du secondaire François, Jean, Valérie, Isabelle, Hélène, Catherine et Bertrand. Vous avez été les premiers artisans de ce que je suis aujourd'hui.

Un grand merci à tous les doctorants, post-doctorants et stagiaires du laboratoire qui ont entretenu une ambiance de groupe très agréable durant ces trois années : les compagnons du deuxième étage d'abord mon co-bureau Konstantin et nos voisins Sofiane et Adrien, la team italienne formée par Roberto et Daniel (organisateur fameux du maintenant rituel gâteau du Jeudi !), Marina, Florent, Florian, Pierrick, Sophia, Rémi, Ismail, Steven, Wei, Cécile, Paul, Teddy, Lydia, Hanna, Rajaé, Camille, Sébastien, Romain, Dena, Max, Marie, Eki.

Une pensée amicale à ceux qui m'ont soutenu de près, mon colocataire Pierre-Loïk d'abord, passé par les mêmes moments que moi durant ces trois années, sa famille, et le très cher cercle d'amis formé par Pierre, Laurent, Maud, Auréliane, Pierre-Adrien, Laure, Louis, Robert, Jean, Nicolas, Paul et Louise avec qui j'ai passé de riches journées de vacances, des parties de jeu de société endiablées et des joyeux repas !

Merci aussi à ma chorale Inside Voices Paris qui m'a été d'un grand soutien pour souffler un peu toutes les semaines. Dédicace toute spéciale à Boubakar, Raphaël, Marie, Hélène, Marianne et bien sûr la solaire Sheilah. Dans ce monde de sphères musicales, une pensée amicale également à Anne-Cécile, Kenny, Marie et Tiago !

Merci aux amis de la famille qui ont suivi de près mon évolution depuis 27 années : Micheline et Michèle, Catherine, Franck et Véronique, Mireille, Jacques et Claudie, Maria et François. Vous

comptez beaucoup et c'est un vrai plaisir de vous retrouver quand je retourne dans ma terre natale ! Une pensée émue pour Jack qui, passionné de sciences, échangeait volontiers avec moi sur mes travaux.

Merci à mes oncles, tantes et cousins pour leur soutien.

Évidemment – les mots s'avéreront bien pauvres – merci à ceux qui m'ont apporté depuis toujours leur soutien inconditionnel, dans les moments de doute comme ceux de réussite, qui ont fait preuve d'une patience et d'une capacité d'écoute infinie, qui m'ont porté durant ces longues années d'études et m'ont permis de grandir et de m'épanouir, mes parents.

Une pensée affectueuse enfin pour ma Kléeia, partie trop tôt.

Contents

List of Figures

List of Tables

Nomenclature

Superscripts

n	Current time step
α	Dispersed phase index
β	Continuous phase index
k	Phase index denoting either α or β
$'$	Fluctuating part with respect to the Reynolds average
$''$	Fluctuating part with respect to the Favre average

Subscripts

a	Current SPH particle
b	Neighboring SPH particle
ext	External state
i	Interface
int	Internal state
ℓ	Left state
n	Normal component
r	Right state
s	Boundary segment
$\star$	Dimensionless quantity
τ	Tangential component
v	Vertex particle

Abbreviations

ALE	Arbitrary Lagrangian-Eulerian
CFD	Computational Fluid Dynamics
CFL	Courant Friedrichs Levy
CIH	Hydraulic Engineering Center
CPU	Central Processing Unit
CUDA	Compute Unified Device Architecture
DEM	Discrete Element Method
DES	Detached Eddy Simulation
DNS	Direct Numerical Simulation
EARSM	Explicit Algebraic Reynolds Stress Model
EDF	Électricité de France
FV	Finite Volumes
GPU	Graphics Processing Unit
GSPH	Godunov Smoothed Particle Hydrodynamics
ISPH	Incompressible Smoothed Particle Hydrodynamics
LES	Large Eddy Simulation
MUSCL	Monotonic Upwind Scheme for Conservation Laws
PBE	Population Balance Equation
RANS	Reynolds-Averaged Navier–Stokes
SPHERIC	SPH rEsearch and engineeRing International Community
SPH	Smoothed Particle Hydrodynamics
USAW	Unified Semi-Analytical Wall
VLES	Very Large Eddy Simulation
VoF	Volume of Fluid
WCSPH	Weakly Compressible Smoothed Particle Hydrodynamics

Roman symbols

$\boldsymbol{a}$	Acceleration	(m/s^2)
$\boldsymbol{a}^n_{ab}$	Acceleration term for the quasi-buoyancy correction	(m/s^2)
$\boldsymbol{A}^{ij}$	Surface metric tensor	(m^2)
A^k	Interfacial density area	(m^{-1})
A^p	Cross-section of a bubble/grain	(m^2)
a_R	Coefficient of the Reynolds number function f	(–)
a_ρ	Coefficient for the Van der Waals cohesive pressure	(–)
$\mathcal{A}_s$	Area of an interface subjected to air entrainment	(m^2)
$\boldsymbol{B}$	Matrix for the non conservative formulation of the Euler system	
b_R	Coefficient of the Reynolds number function f	(–)
C	Measure of SPH particle concentration for shifting	(–)
c	Sound speed	(m/s)
c_0	Sound speed at $\rho = \rho_0$	(m/s)
c_0^k	Phase sound speed at $\rho^\alpha = \rho_0^\alpha$	(m/s)
C_1, C_2	Constants of the Poiseuille velocity profile	(–)
c^k	Phase sound speed	(m/s)
c_{ab}	Weighting coefficient for pressure balancing	(–)
C_{air}	Coefficient quantifying the part of the raised disturbance volume occupied by air	(–)
C_{ent}	Calibration coefficient for air entrainment	(–)
C_{ϵ_i}	Constants of the $k-\epsilon$ model, $i \in \{1, .., 5\}$	(–)
$C^Y_{\epsilon_2}$	C_{ϵ_2} constant of the $k-\epsilon$ model modified by the Yap correction	(–)
c_g	Chanteperdrix sound speed	(m/s)
C_i	Coefficient related to the bubble shapes and sizes for mean curvature computation	(m)
c_i	Van der Waals constants with $i \in \{1, 2\}$	(–)
C_{mean}	Mean concentration of air over Y_{90}	(–)

C_μ	Prandtl-Kolmogorov constant	(–)
C_ν	Constant of the $k-\epsilon$ model	(–)
c_p	Correction coefficient for SPH neighbor pressure of Zhou	(–)
C_i^q	Coefficient for q_t relation, $i \in \{1,2\}$	(m/s)
c_R	Coefficient of the Reynolds number function f	(–)
C_s	Smagorinsky constant	(–)
c_w	Wood sound speed	(m/s)
$\boldsymbol{D}$	Diagonal matrix of eigenvalues	
D	Bottle diameter	(m)
d_1	Plunging jet thickness at the impact	(m)
$\boldsymbol{d}_{ab}$	Distance vector to the interface along $\boldsymbol{r}_{ab}$	(m)
$\mathcal{D}_a^n$	Volume diffusion term	(m)
d_c	Critical depth	(m)
Δp	Pressure difference	(kg/m/s^2)
d_{ent}	Depth of the entrainment layer	(m)
d_H	Hinze scale	(m)
d_h	Bottle neck height	(m)
d_i	Distance to the interface	(m)
d	Geometrical dimension of the domain (=2 or 3)	(–)
D_a	SPH divergence operator	(m^{-1})
D_a^γ	SPH divergence operator normalized by γ	(m^{-1})
$D_a^{-,k}$	SPH symmetric divergence operator	(m^{-1})
$D_a^{+,k}$	SPH antisymmetric divergence operator	(m^{-1})
$\mathbb{D}^k$	Interfacial extra deformation tensor	(s^{-1})
d^k	Dispersed phase local diameter	(m)
$d_{\max}$	Maximum bubble size	(m)

d_n	Bottle neck diameter ..... (m)
dS	Infinitesimal surface ..... (m^2)
$\mathcal{D}_a^s$	Diffusion coefficient for particle shifting ..... (m^2/s)
D_{Sm}	Bubble Sauter mean diameter ..... (m)
$D_T^{\alpha\beta}$	Turbulent dispersion coefficient ..... (s^{-1})
dV	Infinitesimal volume ..... (m^3)
d_w	Clear-water depth ..... (m)
e	Characteristic width ..... (m)
e	Half-height of the domain ..... (m)
$\boldsymbol{e}_{ab}$	Direction vector between SPH particles from b to a ..... (–)
E_c	SPH integration error
E_d	SPH discretization error
$\boldsymbol{e}_g$	Unit vector oriented along the gravity vector ..... (–)
ϵ_I	Coefficient for the pressure gradient additional force of Grenier ..... (–)
$\boldsymbol{e}_i$	Unit vector of the basis, $i \in \{x, y, z\}$ ..... (–)
$\boldsymbol{F}$	Longitudinal force for the Poiseuille flow ..... ($kg.m/s^2$)
$\boldsymbol{F}_{\beta\to\alpha}$	Numerical force resulting from the SPH interpolation process for pressure gradient ($kg.m/s^2$)
f_c	Hindering drag function ..... (–)
$\boldsymbol{F}_{QB}$	Qausi-buoyancy pressure gradient correction ..... ($kg.m/s^2$)
$\boldsymbol{F}_R$	Repulsive force of Grenier ..... ($kg.m/s^2$)
$\boldsymbol{f}_r$	Function for the conservative formulation of the Euler system ..... (–)
f_R	Reynolds number function ..... (–)
$\boldsymbol{F}_V$	Viscous force ..... ($kg.m/s^2$)
f_w	Dimensionless Wendland kernel ..... (–)
f'_w	First derivative of the dimensionless Wendland kernel ..... (–)

$\mathbb{G}$	Buoyancy term in the $k-\epsilon$ equations	(m^2/s^3)
$\boldsymbol{g}$	Gravity vector	(m/s^2)
g	Norm of the gravity vector	(m/s^2)
$\boldsymbol{G}_a$	SPH gradient operator	(m^{-1})
$\boldsymbol{G}_a^{\gamma}$	SPH gradient operator normalized by γ	(m^{-1})
$\boldsymbol{G}_a^{-,k}$	SPH symmetric gradient operator with $k \in \mathbb{Z}$	(m^{-1})
$\boldsymbol{G}_a^{+,k}$	SPH antisymmetric gradient operator with $k \in \mathbb{Z}$	(m^{-1})
$\boldsymbol{G}_a^{R}$	SPH renormalized gradient operator	(m^{-1})
H	Height of the domain	(m)
h	Smoothing length	(m)
H_0	Initial height of the sand cloud	(m)
$H_{\beta\alpha}$	Mean curvature	(m^{-1})
H_d	Outlet height of the stepped spillway	(m)
h_s	Free surface height	(m)
h_{st}	Step height	(m)
h_{up}	Variable upstream water height for the stepped spillway	(m)
$\boldsymbol{J}$	Eulerian fluid velocity	(m/s)
$\boldsymbol{j}^k$	Phase drift velocity	(m/s)
$\boldsymbol{j}$	Mixture velocity with respect to the volume center or volumetric flux	(m/s)
$\boldsymbol{j}^{\star}$	Mixture velocity at a first intermediate time step	(m/s)
$\boldsymbol{j}^{\star\star}$	Mixture velocity at a second intermediate time step	(m/s)
j_n	Normal component of the mixture velocity at an open boundary	(m/s)
j_τ	Tangential component of the mixture velocity at an open boundary	(m/s)
$j_{\star,th}$	Analytical solution for dimensionless mixture velocity	(–)
j_x	Longitudinal component of the mixture velocity	(m/s)
K	Constant diffusion coefficient for the relative velocity	(m^2/s)

k	Turbulent kinetic energy	(m^2/s^2)
$\hat{k}$	Favre-averaged turbulent kinetic energy	(m^2/s^2)
k_b	Boltzmann constant	(–)
K_h	Calibration constant of Hirt model	(–)
K_i	Integration constants for volume fraction profiles on stepped spillways, $i \in \{1, .., 4\}$	(–)
K_i^d	Empirical coefficients for the hindering drag function, $i \in \{1, 2\}$	(–)
k^k	Phase turbulent kinetic energy	(m^2/s^2)
K^p	Drag coefficient of Brethour	(kg/s)
k_s	Roughness size	(m)
$k^\star$	Turbulent kinetic energy at an intermediate time step	(m^2/s^2)
$K_\star$	Constant equal to $\operatorname{argtanh}\left(\sqrt{0.1}\right)$	(–)
K_T	Turbulent diffusivity	(m^2/s)
K_V	Coefficient for the velocity profile of a plunging jet	(–)
L	Length of the domain	(m)
L_0	Reference length for the sand cloud	(m)
λ_c	Taylor length scale	(m)
L_a	SPH Laplacian operator	(m^{-1})
$\boldsymbol{L}_a^{bound}$	Boundary term of the SPH Laplacian operator	(m^{-1})
L_a^γ	SPH Laplacian operator normalized by γ	(m^{-1})
L	Characteristic length scale of the flow	(m)
L_M	Characteristic length of the model	(m)
L_P	Characteristic length of the real-world prototype	(m)
L_T	Characteristic size of the eddies	(m)
$\boldsymbol{M}$	Interfacial momentum source	($kg/m^2/s^2$)
m	Mixture mass	(kg)

$\boldsymbol{M}_a$	SPH renormalization matrix	(–)
$\boldsymbol{M}_{ab}$	Symmetrized renormalization matrix for SPH–ALE	(–)
$\dot{m}$	Mass flux	(kg/s)
$\boldsymbol{M}^k$	Phase interfacial momentum source	($kg/m^2/s^2$)
m^k	Phase mass	(kg)
$\boldsymbol{M'}$	Fluctuations of interfacial momentum source	($kg/m^2/s^2$)
$\boldsymbol{n}$	Unit vector normal to a surface	(–)
n	Hindering power	(–)
$\boldsymbol{n}^k$	Unit vector normal to an interface	(–)
n_r	Dimension of the Riemann system	(–)
n_v	Power for velocity profile fitting on the stepped spillway case	(–)
$\mathbb{P}$	Production of turbulent kinetic energy	(m^2/s^3)
$\boldsymbol{P}$	Matrix of eigenvectors	
P	Mixture pressure including turbulent kinetic energy	($kg/m/s^2$)
p	Mixture pressure	($kg/m/s^2$)
p_{ab}^E	Upwind solution of the moving Riemann problem for pressure in SPH–ALE	($kg/m/s^2$)
$p_{ab}^\star$	Riemann pressure	($kg/m/s^2$)
$\tilde{p}_{ab}$	Inter-particle pressure	($kg/m/s^2$)
p_B	Background pressure	($kg/m/s^2$)
p_B^k	Phase background pressure	($kg/m/s^2$)
$p_{b,new}$	Corrected SPH neighbor pressure of Zhou	($kg/m/s^2$)
p^d	Dynamic component of the pressure	($kg/m/s^2$)
P_D	Volumic disturbance kinetic energy	($kg/m/s^2$)
p_I	Pressure at the interface of the hydrostatic case	($kg/m/s^2$)
p_i	Interface pressure	($kg/m/s^2$)
$\mathbb{P}^j$	Production of turbulent kinetic energy relying on the volumetric flux	(m^2/s^3)

p^k	Partial pressure of the phase k	(kg/m/s^2)
p_i^k	Interfacial partial pressure	(kg/m/s^2)
$\mathcal{P}_p$	Perimeter of an interface disturbance	(m)
P_T	Volumic turbulent kinetic energy	(kg/m/s^2)
p_{th}	Analytical solution for pressure	(kg/m/s^2)
q	Dimensionless distance to kernel center	(–)
Q^k	Volume flow rate of phase k	(m^3/s)
q^k	Volume flow rate of phase k per unit width	(m^2/s)
QS^k	Phase quasi-buoyancy contribution	(m/s^2)
q_t	Turbulent velocity	(m/s)
$\boldsymbol{r}$	Position vector	(m)
R	Viscosity ratio	(–)
r_{ab}	Distance between SPH particles a and b	(m)
R_c	Critical radius of deformation of an interface	(m)
$\boldsymbol{R}_d$	Non linear resistance force	(kg.m/s^2)
$\boldsymbol{r}_i$	Mid-point position vector between particles a and b	(m)
$\boldsymbol{R}^k$	Phase Reynolds stress tensor	(m^2/s^2)
R_k	Riemann invariant, $k \in \{-1, +1\}$	
R_m	Acceptable radius of deformation of an interface	(m)
R_μ	Dynamic relative viscosity ratio for the Poiseuille flow	(–)
R_ν	Kinematic relative viscosity ratio for the Poiseuille flow	(–)
$\boldsymbol{r}'$	Neighbor position vector	(m)
R_ρ	Relative density ratio for the Poiseuille flow	(–)
R_s	Radius of curvature of a surface disturbance	(m)
$\boldsymbol{r}_k$	Eigen vector, $k \in \{-1, 0, +1\}$	
$\boldsymbol{r}_{ab}$	Relative position vector between SPH particles a and b	(m)

$\boldsymbol{s}$	Strain rate tensor	(s^{-1})
$\boldsymbol{s}^j$	Strain rate tensor relying on the volumetric flux	(s^{-1})
S	Scalar mean rate-of-strain	(s^{-1})
S_m	Material surface	(m^2)
S_c	Shock speed	(m/s)
S^j	Scalar mean rate-of-strain relying on the volumetric flux	(s^{-1})
$\boldsymbol{s}^k$	Phase strain rate tensor	(s^{-1})
$\mathcal{S}_p$	Area of an interface disturbance	(m^2)
S_s	Segment surface	(m^2)
$\mathbb{T}$	Shear stress tensor	$(kg/m/s^2)$
$\boldsymbol{\tau}$	Unit vector tangent to a surface	(–)
T	Temperature	(K)
t	Time	(s)
t_0	Reference time for the falling sand cloud	(s)
$\boldsymbol{t}_{as}$	Wall tangential vector	(–)
θ_s	Slope of a chute	(°)
$\boldsymbol{t}_i$	Hybrid vector	(–)
$\mathbb{T}_i^k$	Interfacial phase shear stress tensor	$(kg/m/s^2)$
$\mathbb{T}^j$	Average viscous stress tensor with reference velocity $\boldsymbol{j}$	$(kg/m/s^2)$
$\mathbb{T}_D^j$	Diffusion stress tensor with reference velocity $\boldsymbol{j}$	$(kg/m/s^2)$
$\mathbb{T}_+^j$	Additional terms to the viscous tensor	$(kg/m/s^2)$
$\mathbb{T}_T^j$	Turbulent stress tensor with reference velocity $\boldsymbol{j}$	$(kg/m/s^2)$
$\mathbb{T}^k$	Phase shear stress tensor	$(kg/m/s^2)$
$\mathbb{T}_T^k$	Turbulent phase shear stress tensor	$(kg/m/s^2)$
$\mathbb{T}^\star$	Shear stress tensor at an intermediate time step	$(kg/m/s^2)$
$\mathbb{T}^v$	Average viscous stress tensor with reference velocity $\boldsymbol{v}$	$(kg/m/s^2)$

$\mathbb{T}_D^v$	Diffusion stress tensor with reference velocity $\boldsymbol{v}$	(kg/m/s^2)
$\mathbb{T}_T^v$	Turbulent stress tensor with reference velocity $\boldsymbol{v}$	(kg/m/s^2)
$\mathbb{T}_w$	Wall shear stress tensor	(kg/m/s^2)
$\boldsymbol{u}$	Single-fluid velocity	(m/s)
U	Reference velocity	(m/s)
u_0	Reference velocity for the falling sand cloud	(m/s)
$\boldsymbol{u}^k$	Phase diffusion velocity	(m/s)
U_{m0}	Discharge of the single-phase Poiseuille flow	(m/s)
U_m	Discharge of the two-phase Poiseuille mixture flow	(m/s)
u_n	Normal component of the velocity at an open boundary	(m/s)
$u_\star$	Friction velocity	(m/s)
u_τ	Tangential component of the velocity at an open boundary	(m/s)
U_W	Clear-water flow velocity	(m/s)
V	Volume	(m^3)
V_m	Material volume	(m^3)
$\boldsymbol{v}^0$	Velocity of the moving frame of reference for SPH-ALE	(m/s)
$\boldsymbol{v}_0$	Pressure gradient/gravity part of the relative velocity	(m/s)
V_0	Reference volume	(m^3)
$v_{0,\text{eff}}$	Effective relative velocity	(m/s)
V_1	Impact velocity of the jet	(m/s)
v_1'	Characteristic turbulent velocity of the impinging jet	(m/s)
V_{90}	Longitudinal interfacial velocity at Y_{90}	(m/s)
$\boldsymbol{v}_{ab}^E$	Upwind solution of the moving Riemann problem for velocity in SPH–ALE	(m/s)
$\boldsymbol{v}_{ab}^\star$	Riemann velocity	(m/s)
$\tilde{\boldsymbol{v}}_{ab}$	Transport velocity for SPH–ALE	(m/s)
$\bar{V}$	Reference volume	(m^3)

V_c	Critical velocity	(m/s)
$\boldsymbol{V}^d$	Mean drift velocity	(m/s)
$\boldsymbol{v}_d$	Barycentric velocity defined by Price	(m/s)
V_e	Onset velocity for air entrainment	(m/s)
$\boldsymbol{v}^k$	Phase velocity	(m/s)
v_{ent}	Entrainment velocity limit	(m/s)
$\boldsymbol{v}_i$	Interfacial air-water velocity	(m/s)
V^k	Phase volume	(m^3)
$V_a^{k,\star}$	Phase volume before application of the volume diffusion	(m^3)
$V_{\max}$	Maximal velocity magnitude	(m/s)
$\boldsymbol{v}$	Mixture velocity with respect to the mass center	(m/s)
V_n	Velocity the nozzle	(m/s)
v_n	Inward component of the average liquid velocity on the interface	(m/s)
v'	Characteristic turbulent velocity	(m/s)
V^p	Volume of a bubble/grain	(m^3)
v_i'	Velocity fluctuation according to the i coordinate, $i \in \{x, y\}$	(m/s)
$\boldsymbol{V}^r$	Mean relative velocity	(m/s)
$\boldsymbol{v}^r$	Relative mean velocity	(m/s)
$\boldsymbol{v}^r_{\text{eff}}$	Effective relative velocity	(m/s)
v_n^r	Normal component of the relative velocity at an open boundary	(m/s)
v_τ^r	Tangential component of the relative velocity at an open boundary	(m/s)
$V_a^\star$	Total volume before application of the volume diffusion	(m^3)
v_τ	Wall tangential velocity	(m/s)
$\boldsymbol{v}_w$	Wall velocity	(m/s)
V_x	Longitudinal interfacial air-water velocity	(m/s)
$V_{x\max}$	Maximal longitudinal velocity	(m/s)

W	Width of the sand cloud	(m)
w	Kernel function	(m^{-d})
W_0	Initial width of the sand cloud	(m)
w_{ab}	Kernel function applied to r_{ab}	(m^{-d})
$w^\star_{ab}$	Normalized kernel function	(m^{-d})
w_c	Falling sand cloud frontal velocity	(m/s)
w_r	Riemann invariant	
W_s	Width of the channel	(m)
$\boldsymbol{W}$	State vector	
(x, y, z)	Coordinates of the position vector in the space basis	(m)
x_1	Distance to the nozzle	(m)
Y_{90}	Vertical position of the point with 90% of air	(m)
$Y_{\alpha_{\max}}$	Transverse location of the maximum volume fraction	(m)
Y^k	Mass fraction of the phase k	(–)
Y''^k	Fluctuation of the mass fraction of the phase k	(–)
y^+	Dimensionless distance to a wall in turbulent regime	(–)
Y_{V50}	Transverse location at which $V_x = V_{x\,\max}/2$	(m)
Z	Depth of the sand cloud front	(m)
z_w	Fluctuations of the free surface elevation	(m)

Greek symbols

α	Volume fraction of the liquid phase	(–)
α_0	Initial uniform volume fraction	(–)
α_1	Volume fraction factor for the two-phase Poiseuille flow	(–)
α_f	Tuning coefficient for artificial viscosity	(–)
$\alpha_{\max}$	Maximum volume fraction	(–)
α_{mp}	Maximum packing	(–)

α_n, β_n	Tuning parameters for shifting	(–)
α_s	Tuning coefficient for δ–SPH	(–)
α_t	Dust fraction defined by Price	(–)
α_{th}	Analytical solution for volume fraction	(–)
$\alpha_{w,d}$	Normalized constant of the Wendland kernel in geometrical dimension d	(–)
β	Volume fraction of the gas phase	(–)
χ^k	Phase characteristic function	(–)
Δ	Brezzi diffusion term	(kg/m^3/s)
δ	Dirac distribution	(m^{-d})
$\Delta\alpha$	Variation of volume fraction	(–)
$\delta\gamma_a^{i/o}$	Part of the inlet/outlet contribution in the continuity equation	(s^{-1})
$\Delta p_\star$	Variation of dimensionless pressure	(kg/m/s^2)
δr	Particle diameter	(m)
δr_{as}	Normal distance to the wall	(m)
$\delta r_{aa'}$	SPH particle shift	(m)
$\delta r^{i/o}$	Virtual displacement at inlet/outlet	(m)
Δ_s	Size of the LES spatial filter	(m)
δ_s	Tuning coefficient for δ–SPH	(–)
$\delta\sigma_a^{i/o}$	Part of the inlet/outlet contribution in the continuity equation	(m^{-3})
δt	Time step	(s)
δV	Volume of air entrained per unit time	(m^3/s)
ΔV_x	Variation of interfacial velocity	(m/s)
$\Delta z_\star$	Variation of dimensionless vertical position	(m)
ϵ	Dissipation rate of the turbulent kinetic energy	(m^2/s^3)
$\hat{\epsilon}$	Favre-averaged dissipation rate of the turbulent kinetic energy	(m^2/s^3)
$\epsilon^\star$	Dissipation rate of the turbulent kinetic energy at an intermediate time step	(m^2/s^3)

η_a	Weighting factor for artificial viscosity	(kg/m^3)
η_α	Fitting coefficient for the phase volume positivity condition	(–)
γ	Coefficient for the drag force computation	(kg/m^3/s)
$\gamma(\boldsymbol{r})$	Kernel wall renormalization function at position $\boldsymbol{r}$	(–)
Γ_a	Shepard renormalization factor	(–)
γ_a	Kernel wall renormalization factor	(–)
Γ_a^k	Phase Shepard renormalization factor	(–)
κ	Von Kármán constant	(–)
Λ	Brezzi diffusion coefficient	(–)
λ	Scale factor	(–)
λ_{ab}	$\lambda(\boldsymbol{r}_a, \boldsymbol{r}_b)$	(–)
λ^k	Phase second viscosity or volume viscosity	(kg/m/s)
λ_k	Eigenvalues of the Riemann problem $k \in \{-1, 0, +1\}$	(m/s)
λ_T	Turbulent thermal diffusivity	(m^2/s)
μ	Dynamic viscosity	(kg/m/s)
μ_0	Reference dynamic viscosity	(kg/m/s)
μ^k	Phase dynamic viscosity	(kg/m/s)
μ_T	Dynamic eddy viscosity	(kg/m/s)
μ_T^k	Phase dynamic eddy viscosity	(kg/m/s)
ν	Kinematic viscosity	(m^2/s)
ν_{art}	Artificial kinematic viscosity	(m^2/s)
ν^k	Phase kinematic viscosity	(m^2/s)
ν_T	Kinematic eddy viscosity	(kg/m/s)
ν_T^k	Phase kinematic eddy viscosity	(m^2/s)
$\nu_{T,\max}$	Maximum kinematic eddy viscosity	(m^2/s)
$\nu_T^\star$	Kinematic eddy viscosity at an intermediate time step	(m^2/s)

ϕ_r	Part of the Riemann invariant for the mixture model related to α variations
π_{ab}	Individual term of the SPH viscous operator ..... (m^2/s^2)
$\boldsymbol{\pi}_{ab}$	Individual term of the continuity δ–SPH diffusion operator ..... (kg/m^4)
ψ_e	Intermediate function for the analytical volume fraction profile computation .... (–)
ψ_r	Part of the Riemann invariant for the classical or mixture model related to ρ or σ variations respectively
ρ	Mixture density ..... (kg/m^3)
ρ_0	Reference density ..... (kg/m^3)
ρ_{ab}^E	Upwind solution of the moving Riemann problem for density in SPH–ALE . (kg/m^3)
ρ^k	Phase density ..... (kg/m^3)
$\rho_\star^k$	Dimensionless phase density ..... (kg/m^3)
ρ_0^k	Reference phase density ..... (kg/m^3)
ρ_m	Density of the surrounding fluid ..... (kg/m^3)
ρ_t	Total density defined by Price ..... (kg/m^3)
σ	Inverse of the mixture volume ..... (m^{-3})
$\boldsymbol{\Sigma}$	Cauchy stress tensor ..... ($kg/m/s^2$)
σ_0	Inverse of the reference mixture volume ..... (m^{-3})
σ_e	Kernel standard deviation ..... (m)
σ_ϵ	Constant of the $k-\epsilon$ model
σ_k	Constant of the $k-\epsilon$ model
$\boldsymbol{\Sigma}^k$	Phase Cauchy stress tensor ..... ($kg/m/s^2$)
σ_S	Surface tension ..... (kg/s^2)
θ	Ratio of the SPH particle mass with respect to the reference mass ..... (–)
ξ_α	Fitting coefficient for the phase volume positivity condition ..... (–)
ξ^k	Phase polytropic index ..... (–)
ζ	Power of Richardson and Zaki's correlation ..... (–)

ζ^k	Bulk viscosity	(kg/m/s)

Differential Symbols

$\frac{\partial}{\partial \boldsymbol{n}}$	Derivative with respect to the normal to the interface considered	(m^{-1})
$\frac{\partial}{\partial \boldsymbol{\tau}}$	Derivative with respect to the tangent to the interface considered	(m^{-1})
$\boldsymbol{\nabla}\gamma_a$	Gradient of the wall renormalization factor	(m^{-1})
$d\Gamma'$	Surface element	(m^2)
$\boldsymbol{\nabla}\gamma_{as}$	Contribution of the segment s to the gradient of γ_a	(m^{-1})
$\boldsymbol{\nabla}w_{ab}$	Kernel gradient	(m^{-d-1})
$\frac{D}{Dt}$	Material derivative with respect to $\boldsymbol{v}$	(s^{-1})
$\frac{d}{dt}$	Material derivative with respect to $\boldsymbol{j}$	(s^{-1})
$\frac{d_k}{dt}$	Material derivative with respect to $\boldsymbol{v}^k$	(s^{-1})

Sets

$\mathcal{C}^k$	Set of functions with continuous k first derivatives
$\partial\Omega$	Boundary of the computational domain
$\partial\Omega_i$	Interface between fluids
$\partial\Omega_o$	Inflow/outflow boundary of the computational domain
$\partial\Omega_w$	Wall boundary of the computational domain
$\mathcal{F}$	Set of free particles
N	Neighborhood in $\mathbb{R}^{n_r}$
Ω	Computational domain
Ω^k	Computational domain occupied by phase k
$\Omega_{\boldsymbol{r}}$	Support of the kernel function centered on $\boldsymbol{r}$
$\mathcal{P}$	Set of fluid particles
$\mathcal{S}$	Set of boundary segments
$\mathcal{S}^{I/O}$	Set of inlet/outlet boundary segments
$\mathcal{V}$	Set of vertex particles

$\mathcal{V}^{I/O}$	Set of inlet/outlet vertex particles

Dimensionless numbers

A	Atwood number
C_α	α limitation for time step
C_{CFL}	CFL number
C_D	Drag coefficient
$C_{D,eff}$	Drag coefficient including a hindering term
C_γ	γ limitation for time step
C_P	Pressure coefficient
C_{visc}	Viscous limitation for time step
Eo	Eötvös number
Eu	Euler number
Fr	Froude number
Ma	Mach number
Mo	Morton number
Pe_0	Reference Péclet number
Pe	Péclet number
Pe_σ	Numerical Péclet number
Re	Reynolds number
Re^k	Particle Reynolds number
Sc_T	Turbulent Schmidt number
Tu	Turbulent intensity
We	Weber number
We_c	Critical Weber number

Mathematical Symbols

$\overline{x}$	General average operator

$[x]_c$	Continuous SPH interpolation
$\overline{x}^{\chi}$	Component-weighted average
$\mathrm{adj}(\boldsymbol{x})$	Adjugate matrix
$[x]_c^{\gamma}$	Renormalized continuous SPH interpolation
$[x]_d$	Discrete SPH interpolation
$\det(\boldsymbol{x})$	Determinant
$[x]_d^{\gamma}$	Renormalized discrete SPH interpolation
$\mathbb{F}[x]$	Fourier transform
$\overline{x}^{\chi\rho}$	Favre average
$\mathbb{I}$	Identity tensor
$[x]_{\partial\Omega_i}$	Jump at the interface $\partial\Omega_i$
Li_2	Dilogarithm function
ϕ^l	Limiter function
${}^t x$	Transpose operation
$x_{,j}$	Covariant derivative
W_0	Principal branch of the Lambert function
$[x]_a$	$x(\boldsymbol{r}_a)$
$[x]^-$	Negative part
$[x]^+$	Positive part

Introduction

Un torrent dévalant les pentes alpines, une vague cassant sur les rives cariocas... les eaux blanches résultant du mélange eau-air sont un phénomène commun, tant dans les écoulements environnementaux que dans le domaine industriel, avec des effets parfois positifs, parfois délétères. Le caractère diphasique de l'écoulement modifie de manière importante sa dynamique. La compréhension de l'entraînement d'air – la capture de bulles d'air par le flot d'eau – revêt un intérêt majeur pour la sécurité et le bon fonctionnement des ouvrages hydrauliques. La turbulence est centrale dans les mécanismes physiques mis en jeu et renforce l'aspect multi-échelles de l'écoulement. La modélisation physique, et plus récemment numérique, de ce phénomène a fait l'objet de nombreux travaux, mais l'enjeu reste de taille pour comprendre l'ensemble des mécanismes physiques générateurs et pour les simuler dans des temps raisonnables. Des modèles diphasiques moyennés ont notamment été développés, les plus simples d'entre eux prenant la forme de modèles de mélange. De récents travaux ont soulevé l'intérêt de tenter ce type d'approches dans la méthode Lagrangienne Smoothed Particle Hydrodynamics *(SPH), bien adaptée à la simulation d'écoulements fortement déformés tels que ceux rencontrés sur les structures hydrauliques. L'objectif de cette thèse est de développer et d'implémenter dans un environnement GPU un modèle de mélange SPH diphasique et de l'appliquer à la simulation d'écoulements aérés communément rencontrés dans les écoulements environnementaux et configurations industrielles. Les équations continues de ce modèle font l'objet du Chapitre 1. Le Chapitre 2 présente ensuite un état de l'art des simulations multiphasiques dans la méthode SPH. Dans le Chapitre 3, la discrétisation SPH du modèle retenu est exposée et validée sur des cas académiques simples. La physique de l'entraînement d'air est ensuite détaillée au Chapitre 4 et le modèle est appliqué à des cas réalistes.*

A torrent swirling and hurtling the slopes of the Alps along a hiking path, a wave breaking and hunting the surfers at a spot of Rio de Janeiro, the Falls of the Rhine captured by the brush of W. Turner… *white waters* resulting from the air-water intense mixing are permanently occurring on the Earth's surface as illustrated on Figure 1, despite the *large density ratio* that tends to generate well separated configurations. Its aesthetic has been inspirational for artists, as exemplified on Figure 2, and its visual effect leveraged in structures. The entrapment of air bubbles of the surrounding atmosphere into the flowing water, called *air entrainment* or *aeration*, has not only natural but also artificial occurrences: structuring the design of fountains as in Figure 3, it is also of prominent significance for industrial applications, from the chemical industry to hydraulic and nuclear facilities. Its presence might be desirable or not depending on the situation as detailed by Bińi [24]: while it proves to be useful to increase the *interfacial area* and hence the gas-liquid transfers in chemical mixing, wastewater treatment process or water oxygenation during stressful periods for fish farming, it can also lead to harmful effects in industrial processes for molten glass, metals, plastics, etc. or in defense applications for surface ships due to propeller cavitation or detrimental underwater noise and wakes generated by the air entrained by waves along the hull [271].

Those air-water mixtures fall within the scope of the wide and complex field of *two-component* gas-liquid flows. The presence of two components strongly modifies the dynamics of the flow, especially due to the interactions with *turbulence*, the vertical momentum introduced together with the changes in bulk fluid in terms of density, viscosity and compressibility. Those interactions are still the object of active research because of their complexity. An accurate modeling of the phenomenon is of prime importance for the design, good performance and safe operation of hydraulic works – dams and adjacent structures – as illustrated by Falvey [122] and Kobus [189] for *free surface* and *confined* flows.

Turbulence is often at the core of the entrainment phenomenon and makes it a full *multi-scale* problem as characteristic lengths go from the several meters of a *separated flow* to the millimeter size of a *dispersed flow* of bubbles and drops. It deforms the air-water interface and the consequent irregularities can then trap air bubbles. The downwards vertical velocity generated by the turbulence, if strong enough to exceed the resisting forces of *gravity* and *surface tension* maintaining a continuous interface, leads to diffusion of air in the bulk of the liquid.

Regarding the role of surface tension and turbulence in bubble entrainment dynamics, it is all but impossible representing with perfect *similarity* these flows in *physical scale models* of a laboratory. However, they still give prominent insights for the considered flows as highlighted by Chanson [62] and a wide literature is available. Conversely, *numerical modeling* appears as an enticing, cheap and versatile tool, even though the accurate prediction of the air-entrainment process in a wide variety of air-water turbulent flows remains a computationally challenging problem under current investigation. Following Lopes et al. [224], "an ideal numerical model needs to be accurate and fast in the definition of a macroscopic interface and simultaneously precise enough to take into account the formation of bubbles through the free surface, their

(a) Water jet (Briançon, France)

(b) Torrent (Briançon, France)

(c) Waterfall (Tijuca Park, Rio, Brazil)

(d) Wave breaking (Barra de Tijuca, Rio, Brazil)

(e) Rooster tail (Camaret-Sur-Mer, France)

Figure 1: Air entrainment in environmental flows.

(a) The Falls of the Rhine at Schaffhausen, 1841 (b) Upper Falls of the Reichenbach, 1802

Figure 2: Paintings of William Turner, The Courtauld Gallery.

(a) Fontaine aux Lions, Paris, France (b) Fontaine Saint-Sulpice, Paris, France

Figure 3: Fountains.

transport and their natural interactions". One needs to define what are the practical quantities of interest for the engineering applications considered and design a numerical model accordingly. Among the possible questions are the following: how much air is entrained locally and globally? What is the air bubble size distribution? What is the relative velocity between air and water? How does the air presence modify the flow dynamics? How does it affect the water quality? [188]

Complete resolution of air-water flows over an hydraulic structure being beyond numerical capabilities, a variety of averaged multiphase models were designed and implemented in CFD codes, generally in an Eulerian framework, to handle such cases in reasonable times. Two-fluid model as built by Ishii [176] and further studied by Rusche [316] is a very common approach that proves to give good results as soon as interfacial interactions are correctly modeled. A further simplification consists in *mixture models* as extensively presented by Ishii [176], Manninen and Taivassalo [239] for which an algebraic relation on the relative velocity between phases can be given, substituting to one of the phase momentum equations. Such models implemented in *Eulerian* codes gave some promising results on air-water flows [281]. At the same time, as highly deformed flows are considered, *Lagrangian* approaches such as the *Smoothed Particle Hydrodynamics* (SPH) method can be an asset thanks to the mesh-free feature. Without any tracking of the interface, recent developments of the numerical framework have allowed to model some air-water flows [86, 150, 170, 171, 307]. However the accurate description of air entrainment would still require some very refined simulations. Mixture models were introduced in the SPH approach [90, 149, 297, 305] but never applied to air-water flows to the author's knowledge. If such models lose the sharp interface property when diffusion of phases occur, it is still of interest to see what can be their performances in a mesh-free Lagrangian approach that does not trigger numerical diffusion due to advection modeling and can handle complex geometries as found in practical industrial applications without the need to build a mesh. Moreover, their use can bring some interesting insights for other types of flows such as sediment flows (for which the air phase modeling is not required) and one can indeed see some active research in this field today [330].

The aim of this thesis is to build an SPH model for industrial applications able to:

- Model 3D free surface or confined aerated flows;
- Predict the air concentration and velocity profiles altered by the air presence together with pressure forces applied to the structures;
- Handle different types of components from moderate (water-sediment) to high density ratios (air-water).

The main achievements of this work are:

- The development of a Weakly Compressible SPH (WCSPH) mixture model with relative velocity between phases;

- Its adaptation to the semi-analytical (USAW) wall boundary conditions;
- The extension of an open boundaries formulation to handle mixtures;
- The application of this model to schematic bidimensional and industrial three-dimensional cases.

The numerical developments were implemented into the EDF in-house research SPH code Sphynx, a fork from the open-source software GPUSPH [1]. It was written in the Cuda programming language for GPU.

This thesis consists of four chapters:

- Chapter 1 outlines the derivation of a volume-based two-component mixture model from the Navier-Stokes equations in a weakly compressible framework together with its boundary conditions. It sketches the assumptions underlying the mixture approach.
- Chapter 2 is a literature review of the existing SPH formulations for two-component flows, from the usual multifluid approach to recently developed mixture approaches. It shall give the necessary numerical tools to discretize the two-component mixture model.
- Chapter 3 describes the two-component SPH mixture model developed in this work and validates it on academic cases. Special focus is made on the derivation of a numerical scheme with good numerical properties to follow the interface motions. Moreover, the SPH open boundary formulation for mixture is comprehensively detailed.
- Chapter 4 first focuses on the physics of the air entrainment phenomenon to propose an adequate formulation in the mixture model, especially regarding the relative velocity expression. The present SPH model is then applied to experimental test cases. Finally, preliminary results on a three-dimensional industrial application of air-water flows are presented.

Chapter 1

Governing equations and modeling choices

Ce chapitre s'attache à présenter les équations continues du modèle de mélange régissant l'évolution des écoulements diphasiques considérés. On présente la dérivation du modèle de mélange à partir des équations de Navier–Stokes diphasiques. On détaille les choix adoptés pour la modélisation de la turbulence, via un modèle $k - \epsilon$, ainsi que les modèles de fermeture retenus pour la vitesse relative entre les phases. Les hypothèses et approximations faites lors des choix de modélisation sont exposées. A l'issue de ce chapitre, nous nous trouvons munis du système d'équations continues qu'il faudra résoudre numériquement.

This chapter aims at introducing the notations used, together with the derivation of the two-component mixture model implemented and tested in Chapters 3 and 4. It does not claim to be an exhaustive review of the literature about two-phase flow modeling that one can find in [114, 177] but rather, it shall stress the underlying set of hypotheses and modeling choices to draw the scope of this model. Due to the proximity of the mixture model with single-fluid formulation, the latter will first be introduced before highlighting the additional terms brought by the former.

1.1 From the local instant formulation to the mixture model

1.1.1 Diversity and complexity of multicomponent flows

Multiphase flows are encountered in a wide variety of situations from power (boiler, pump) to process (fluidized beds, chemical reactor, porous media) systems, from transport (pipeline, hydrofoil) to lubrication facilities, from environmental (sedimentation, cloud, dune, landslide) to biological (blood, breathing) domains [176]. While the same set of transport laws rule those different flows, it leads to a large range of flow behaviors that can be classified with respect to the nature of the phases (solid, liquid, gas, plasmas), their miscibility and the flow topology generated (three main classes: separated, mixed/transitional and dispersed flows). In the following, we will consider an *isothermal* flow consisting of two *immiscible* weakly compressible viscous fluids denoted α and β *without phase changes*.

1.1.2 Local instant formulation

The analysis of multicomponent flows can be performed with the standard approach of continuum mechanics: the domain of interest Ω is divided into single-phase regions with moving boundaries. The multiphase flow problem therefore corresponds to a set of standard differential balance equations in each region complemented by jump conditions between phases and boundary conditions: this problem is the *local instant formulation*, being expressed as a function of local instant variables. The application of mathematical tools detailed hereafter relies on a sufficient regularity of the variables. The practical use of this formulation remains limited to the study of separated flows or single/small number of bubbles or droplets [45, 48]. The complexity stems from the multiple deformable and moving interfaces, the fluctuations due to turbulence and interface motion, the large discontinuities of fluid properties at interfaces. It proves to be hard to tackle and prevents many mathematical developments or direct computational application. However, this formulation is the breeding ground of the *macroscopic two-phase flow models* generated by proper averaging processes detailed in this chapter.

1.1.2.1 Single-phase balance equation

Let us introduce the phase density ρ^α, the flux $\mathbb{J}^\alpha$, the body source ϕ^α and a quantity per unit mass ψ^α. The general integral balance states that the temporal variation of $\rho^\alpha\psi^\alpha$ in a material volume V_m depends on the flux through its material boundary S_m and the body source [177]:

$$\frac{d}{dt}\int_{V_m}\rho^\alpha\psi^\alpha dV = -\oint_{S_m}\boldsymbol{n}^\alpha\cdot\mathbb{J}^\alpha dS + \int_{V_m}\rho^\alpha\phi^\alpha dV \tag{1.1}$$

where t is the time and $\boldsymbol{n}^\alpha$ is the outward-pointing unit normal vector. Some mathematical relations will be of practical use in the following. Let us consider an arbitrary $\mathcal{C}^1$ field F.

Theorem 1.1.1 (Leibniz's rule) *For an arbitrary control volume $V(t)$ bounded by the surface $S(t)$ of displacement velocity $\boldsymbol{v}\cdot\boldsymbol{n}$*

$$\frac{d}{dt}\int_{V(t)}FdV = \int_{V(t)}\frac{\partial F}{\partial t}dV + \oint_{S(t)}F\boldsymbol{v}\cdot\boldsymbol{n}dS \tag{1.2}$$

Theorem 1.1.2 (Reynolds transport theorem) *Applying the Leibniz's rule 1.1.1 to the material volume V_m delimited by the material surface S_m*

$$\frac{d}{dt}\int_{V_m}FdV = \int_{V_m}\frac{\partial F}{\partial t}dV + \oint_{S_m}F\boldsymbol{v}^\alpha\cdot\boldsymbol{n}dS \tag{1.3}$$

where $\boldsymbol{v}^\alpha$ denotes the velocity of a fluid material point.

Theorem 1.1.3 (Green theorem)

$$\int_V\boldsymbol{\nabla}\cdot\boldsymbol{F} = \oint_S\boldsymbol{F}\cdot\boldsymbol{n}dS \tag{1.4}$$

Applying these theorems to the relation (1.1) leads to the differential balance:

$$\frac{\partial\rho^\alpha\psi^\alpha}{\partial t} + \boldsymbol{\nabla}\cdot(\rho^\alpha\boldsymbol{v}^\alpha\psi^\alpha) = -\boldsymbol{\nabla}\cdot\mathbb{J}^\alpha + \rho^\alpha\phi^\alpha \tag{1.5}$$

One can then deduce the conservation equations:

- Mass conservation ($\psi^\alpha = 1$, $\phi^\alpha = 0$, $\mathbb{J}^\alpha = 0$)

$$\frac{\partial\rho^\alpha}{\partial t} + \boldsymbol{\nabla}\cdot(\rho^\alpha\boldsymbol{v}^\alpha) = 0 \tag{1.6}$$

- Momentum conservation ($\psi^\alpha = \boldsymbol{v}^\alpha$, $\phi^\alpha = \boldsymbol{g}$, $\mathbb{J}^\alpha = -\boldsymbol{\Sigma}^\alpha$)

$$\frac{\partial\rho^\alpha\boldsymbol{v}^\alpha}{\partial t} + \boldsymbol{\nabla}\cdot(\rho^\alpha\boldsymbol{v}^\alpha\otimes\boldsymbol{v}^\alpha) = -\boldsymbol{\nabla}p^\alpha + \boldsymbol{\nabla}\cdot\mathbb{T}^\alpha + \rho^\alpha\boldsymbol{g} \tag{1.7}$$

where $\mathbf{\Sigma}^\alpha = -p^\alpha \mathbb{I} + \mathbb{T}^\alpha$ is the Cauchy stress tensor depending on the phase pressure p^α, $\mathbb{T}^\alpha$ is the shear stress tensor and $\boldsymbol{g}$ is a body force, generally the standard gravity.

Constitutive relations We now need a proper set of constitutive equations that forms a mathematical model for the response and behavior of certain groups of fluids. For the stress tensor, a mechanical constitutive equation is required. We will work in the framework of Newtonian fluids as the fluids considered in this work are generally air and water, so that the shear stress tensor $\mathbb{T}^\alpha$ is linearly linked to the strain rate tensor $\boldsymbol{s}^\alpha$ through:

$$\mathbb{T}^\alpha = \lambda^\alpha \boldsymbol{\nabla} \cdot \boldsymbol{v}^\alpha \mathbb{I} + 2\mu^\alpha \boldsymbol{s}^\alpha \tag{1.8}$$

where μ^α is the dynamic molecular viscosity, $\lambda^\alpha = \zeta^\alpha - \frac{2}{3}\mu^\alpha$ is the second/volume viscosity with ζ^α the bulk viscosity and $\boldsymbol{s}^\alpha$ is defined as:

$$\boldsymbol{s}^\alpha = \frac{1}{2}\left(\boldsymbol{\nabla}\boldsymbol{v}^\alpha + {}^t\boldsymbol{\nabla}\boldsymbol{v}^\alpha\right) \tag{1.9}$$

where the superscript ^{t} denotes the transpose operation. Under the Stokes hypothesis, we will neglect the second viscosity contribution [87].

The second constitutive equation is the state law. In the standard WCSPH (Weakly Compressible SPH) approach, the flow is considered as barotropic and the pressure is calculated based on the density values, using the Tait equation of state (adiabatic form of the stiffened equation of state for liquids) as reported in [88] and commonly used in SPH [266]:

$$p^\alpha = \frac{\rho_0^\alpha (c_0^\alpha)^2}{\xi^\alpha}\left[\left(\frac{\rho^\alpha}{\rho_0^\alpha}\right)^{\xi^\alpha} - 1\right] + p_B^\alpha \tag{1.10}$$

where ρ_0^α is a reference density (1000 kg/m^3 for the water and 1.23 kg/m^3 for the air), ξ^α is the polytropic index (generally taken to 7 for water and 1.4 for air), c_0^α is the speed of sound at $\rho^\alpha = \rho_0^\alpha$ (physical values are 1480 m/s for the water and 340 m/s for the air) and p_B^α is a background pressure (numerical parameter to avoid the occurrence of spurious negative pressures and voids). One can then deduce the local speed of sound c^α:

$$c^\alpha = \sqrt{\frac{\partial p^\alpha}{\partial \rho^\alpha}} = c_0^\alpha \sqrt{\left(\frac{\rho^\alpha}{\rho_0^\alpha}\right)^{\xi^\alpha - 1}} \tag{1.11}$$

This speed is chosen so that only slight variations of the density, below 1%, are allowed. Introducing the material derivative:

$$\frac{d_\alpha}{dt} = \frac{\partial}{\partial t} + \boldsymbol{v}^\alpha \cdot \boldsymbol{\nabla} \tag{1.12}$$

The momentum equation (1.7) writes:

$$\frac{d_\alpha \boldsymbol{v}^\alpha}{dt} = -\frac{1}{\rho^\alpha}\boldsymbol{\nabla} p^\alpha + \frac{1}{\rho^\alpha}\boldsymbol{\nabla}\cdot\mathbb{T}^\alpha + \boldsymbol{g} \tag{1.13}$$

Dimensionless numbers By introducing reference quantities f_0 for each variable f and non-dimensionalizing them under the form $f_\star = f \cdot f_0$, this relation becomes:

$$\frac{d_\alpha \boldsymbol{v}^\alpha_\star}{dt} = -\frac{1}{\rho^\alpha_\star}\boldsymbol{\nabla} p^\alpha_\star + \frac{1}{\mathsf{Re}}\frac{1}{\rho^\alpha_\star}\boldsymbol{\nabla}\cdot\mathbb{T}^\alpha_\star + \frac{1}{\mathsf{Fr}^2}\boldsymbol{e}_g \tag{1.14}$$

where $\mathsf{Re} = \rho_0 L_0 U_0/\mu_0$ is the Reynolds number (ratio of inertial to viscous forces), $\mathsf{Fr} = \sqrt{U_0^2/(L_0 g)}$ is the Froude number (whose square is the ratio of kinetic energy to gravitational potential energy) with $g = |\boldsymbol{g}|$, $\boldsymbol{e}_g = \boldsymbol{g}/g$ and we have assumed $p_0 = \rho_0 U_0^2$ (*i.e.* Euler number $\mathsf{Eu} = p_0/\left(\rho_0 U_0^2\right)$ equal to 1) and:

$$p^\alpha_\star = \frac{1}{\mathsf{Ma}^2 \xi^\alpha}\left[(\rho^\alpha_\star)^{\xi^\alpha} - 1\right] \tag{1.15}$$

where $\mathsf{Ma} = U_0/c_0$ is the Mach number (whose square is the ratio of inertial to compressibility forces).

1.1.2.2 Interfacial balance

Sharp changes of variables across interfaces between phases require writing specific balance equations to rule the exchanges of mass and momentum. Let us underline that a wall forms a special case of interface. For the sake of legibility, we do not detail the reasoning to write those conditions, that consists in deriving a balance equation on a control volume encompassing the interface. As we do not consider phase changes, there is no mass transfers across interfaces so that the interfacial mass balance is not used. For the interfacial momentum balance, in absence of mass transfers, it writes:

$$\sum_{k\in\{\alpha,\beta\}} \boldsymbol{n}^k\cdot\boldsymbol{\Sigma}^k = 2H_{\beta\alpha}\sigma_S\boldsymbol{n} + \boldsymbol{t}_i\boldsymbol{A}^{ij}\left(\sigma_S\right)_{,j} \tag{1.16}$$

where the right-hand side accounts for surface tension σ_S effects through the normal force due to the mean curvature $H_{\beta\alpha}$ (positive if the interface is convex with respect to phase α), the local normal $\boldsymbol{n}$ pointing from α to β, and the tangential force generated by the surface tension gradient in a surface curved coordinates (with the hybrid vector $\boldsymbol{t}_i$, the surface metric tensor A^{ij} and the covariant surface derivative $()_{,j}$, see [12, 177] for more details). If one neglects the surface tension and projects the relation along the local normal $\boldsymbol{n}$ and the tangent $\boldsymbol{\tau}$ vectors to the interface, one gets:

$$\left(p^\alpha - p^\beta\right)\boldsymbol{n} - \boldsymbol{n}\cdot\left(\mathbb{T}^\alpha - \mathbb{T}^\beta\right) = 0 \tag{1.17}$$

$$\boldsymbol{\tau} \cdot \left(\mathbb{T}^{\alpha} - \mathbb{T}^{\beta} \right) = 0 \tag{1.18}$$

1.1.3 Multifluid models

The complexity of multiphase flows was highlighted in the preceding section. However, the prediction of small-scale interfaces might not be either possible or desirable, *e.g.* in sedimentation tanks, cyclone separators, heat exchangers [98]... Multifluid approaches were developed to model them [159]. To avoid postulating macroscopic equations without references to the microscopic behaviour, an averaging process is required [111]. Temporal or spatial averages can be interpreted as a low-pass filtering getting rid of local instant fluctuations originating from turbulence and deforming interfaces while an ensemble average considers a two-phase flow as a particular sample of a random process [105]. Statistical information on the fluctuations will nevertheless be required to model the macroscopic behavior conveniently. Indeed, the interfacial structure will deeply influence the macroscopic flows, *e.g.* the wave dynamics in a separated flow, the bubble coalescence, collapse, nucleation in a dispersed flow. We will focus here on an Eulerian average, naturally consistent with observation and instrumentation, with time and space considered as independent variables. The averaging has a fundamental consequence: the two-phase medium turns into two continua coexisting simultaneously at each point, the interface being no longer explicitly tracked.

The averaging operation This process consists in introducing the averaging operator, denoted by an overlining $x \rightarrow \overline{x}$, a characteristic function $\chi^{\alpha}(\boldsymbol{x}, t)$ that will identify the presence of component α at position $\boldsymbol{x}$ and time t (equal to 1 if the phase α is present, 0 otherwise), and writing conveniently the Leibniz (1.1.1) and Green (1.1.3) rules in this new framework to formally switch averaging and differential operators. The average operation applied to the characteristic function will precisely give what is usually referred to as *volume fraction* α:

$$\alpha = \overline{\chi^{\alpha}} \tag{1.19}$$

Let us underline that the choice of average (temporal as in [176], spatial as in [383], combinations of them as in [112] or ensemble as in [114]; in an Eulerian, Lagrangian or Boltzmann statistical framework) influences the definition of the averaged quantities that are used. The temporal or spatial dimension of averaging is considered large enough to smooth the local fluctuations of the properties and small enough compared to the scale of variability of the macroscopic flow (spatially the size of the flow domain, temporally the scale of unsteadiness). Assumptions behind each of those approaches, regarding the stationarity, homogeneity or statistic uniformity of the flows to which they are applied, shall condition their area of applications and the interpretation of the variables, *e.g.* the particular nature of the local time fraction (for a temporal average), volume fraction (for a volume average) or the expected value of the ratio of the volume of component α to the total volume (for an ensemble average). Drew and Passman [114] highlighted links between

the usual averaging approaches under assumptions of ergodicity or homogeneity of the flow. A convenient consequence of those averaging processes is nevertheless their leading to formally equivalent sets of equations of motion, so that we will not give further details and refer the reader to the extensive treatment of this question in the cited literature. An important property that will be useful in the following is the *saturation* condition:

$$\sum_{\alpha} \alpha = 1 \tag{1.20}$$

which states that the domain is fully occupied by the different present components. Another variable of interest to describe the topological structure of the interfaces is the *interfacial area density* of component α:

$$A^{\alpha} = -\overline{\boldsymbol{n}^{\alpha} \cdot \boldsymbol{\nabla} \chi^{\alpha}} \tag{1.21}$$

It refers to the expected value of the ratio of interfacial area in a small volume to the volume itself, and thus has the dimension of the inverse of length.

Component and mass weighted averages From a general field F associated with the two components, considered to be continuously differentiable everywhere but in the interfacial regions, we define the associated field of α-phase $F^{\alpha} = \chi^{\alpha} F$. From the averaging process, one can define:

- The component-weighted average:

$$\overline{F^{\alpha}}^{\chi} = \frac{\overline{\chi^{\alpha} F}}{\overline{\chi^{\alpha}}} \tag{1.22}$$

- The mass-weighted (or Favre) average [124]:

$$\overline{F^{\alpha}}^{\chi\rho} = \frac{\overline{\chi^{\alpha} \rho F}}{\overline{\chi^{\alpha} \rho}} \quad \text{and} \quad \overline{F}^{\chi\rho} = \frac{\overline{\rho F}}{\overline{\rho}} \tag{1.23}$$

As a result of the average properties, one can write:

$$\overline{F} = \sum_{\alpha} \overline{F^{\alpha}} = \sum_{\alpha} \alpha \overline{F^{\alpha}}^{\chi} \tag{1.24}$$

Assuming the smoothness of mean values, the average operator is idempotent. Fluctuations of the variables resulting from turbulence or component motions due to deformation of the interfaces are defined with respect to the mean field through:

$$F'' = F - \overline{F}^{\chi\rho} \tag{1.25}$$

Let us define mixture quantities, component-weighted or mass-weighted depending on their na-

ture:

- The mixture density:
$$\overline{\rho} = \sum_{\alpha} \overline{\rho^{\alpha}} = \sum_{\alpha} \alpha \overline{\rho^{\alpha}}^{\chi} \tag{1.26}$$

- The *mass fraction*:
$$Y^{\alpha} = \frac{\overline{\rho^{\alpha}}}{\overline{\rho}} \tag{1.27}$$
that accounts for the prominence of α-phase mass with respect to the mixture mass.

- The *mixture velocity* with respect to the center of mass:
$$\overline{\boldsymbol{v}}^{\chi\rho} = \frac{\overline{\rho \boldsymbol{v}}}{\overline{\rho}} = \frac{1}{\overline{\rho}} \sum_{\alpha} \overline{\rho^{\alpha} \boldsymbol{v}^{\alpha}} = \frac{1}{\overline{\rho}} \sum_{\alpha} \overline{\rho^{\alpha}}\, \overline{\boldsymbol{v}^{\alpha}}^{\chi\rho} = \sum_{\alpha} Y^{\alpha} \overline{\boldsymbol{v}^{\alpha}}^{\chi\rho} \tag{1.28}$$

- The mixture velocity with respect to the center of volume, or mixture *volumetric flux*:
$$\boldsymbol{j} = \sum_{\alpha} \alpha \overline{\boldsymbol{v}^{\alpha}}^{\chi\rho} \tag{1.29}$$

- The mixture flux:
$$\overline{\mathbb{J}} = \sum_{\alpha} \alpha \overline{\mathbb{J}^{\alpha}}^{\chi} \tag{1.30}$$

- The mixture source term:
$$\overline{\phi} = \sum_{\alpha} Y^{\alpha} \overline{\phi^{\alpha}}^{\chi\rho} \tag{1.31}$$

To study the behavior of the two-phase flow, several velocity fields can prove to be useful:

- The *relative mean velocity*:
$$\boldsymbol{v}^{r} = \overline{\boldsymbol{v}^{\alpha}}^{\chi\rho} - \overline{\boldsymbol{v}^{\beta}}^{\chi\rho} \tag{1.32}$$

- The relative velocity with respect to the mass center or *diffusion velocity*:
$$\boldsymbol{u}^{\alpha} = \overline{\boldsymbol{v}^{\alpha}}^{\chi\rho} - \overline{\boldsymbol{v}}^{\chi\rho} \tag{1.33}$$

- The relative velocity with respect to the volume center or *drift velocity*:
$$\boldsymbol{j}^{\alpha} = \overline{\boldsymbol{v}^{\alpha}}^{\chi\rho} - \boldsymbol{j} \tag{1.34}$$

These quantities can be linked through relations detailed in Appendix E. Within this framework,

the average convective flux of a mixture for a scalar quantity ψ writes:

$$\begin{aligned}\overline{\mathbb{J}} = \overline{\rho\psi\boldsymbol{v}} &= \sum_\alpha \alpha\overline{\rho^\alpha\psi^\alpha\boldsymbol{v}^\alpha}^\chi = \sum_\alpha \alpha\overline{\rho^\alpha}^\chi\overline{\psi^\alpha}^{\chi\rho}\overline{\boldsymbol{v}^\alpha}^{\chi\rho} + \sum_\alpha \alpha\overline{\rho^\alpha\psi''^\alpha\boldsymbol{v}''^\alpha}^\chi \\ &= \overline{\rho}\,\overline{\psi}^{\chi\rho}\overline{\boldsymbol{v}}^{\chi\rho} + \sum_\alpha \alpha\overline{\rho^\alpha}^\chi\overline{\psi^\alpha}^{\chi\rho}\overline{\boldsymbol{u}^\alpha}^{\chi\rho} + \sum_\alpha \alpha\mathbb{J}_T^\alpha\end{aligned} \tag{1.35}$$

Where $\mathbb{J}_T^\alpha = \overline{\rho^\alpha\psi''^\alpha\boldsymbol{v}''^\alpha}^\chi$ correspond to the covariance of the turbulent flux. One can identify three transport mechanisms: the first due to mixture properties, the second due to the macroscopic phase diffusion and the last due to statistical two-phase effects and turbulent fluctuations. Equipped with these variables and the adequate theorems of interchange of the derivation and average operators (dependent on the averaging operator) that generate interfacial terms, one can write the mixture general balance:

$$\frac{\partial\overline{\rho}\,\overline{\psi}^{\chi\rho}}{\partial t} + \boldsymbol{\nabla}\cdot\left(\overline{\rho}\,\overline{\psi}^{\chi\rho}\overline{\boldsymbol{v}}^{\chi\rho}\right) = \boldsymbol{\nabla}\cdot\overline{\mathbb{J}} + \overline{\rho\phi}^{\chi\rho} + \boldsymbol{I} \tag{1.36}$$

and the balance equation for the α-phase writes:

$$\frac{\partial\alpha\overline{\rho^\alpha}^\chi\,\overline{\psi^\alpha}^{\chi\rho}}{\partial t} + \boldsymbol{\nabla}\cdot\left(\alpha\overline{\rho^\alpha}^\chi\,\overline{\psi^\alpha}^{\chi\rho}\overline{\boldsymbol{v}^\alpha}^{\chi\rho}\right) = \boldsymbol{\nabla}\cdot\left[\alpha\left(\overline{\mathbb{J}^\alpha}^\chi + \mathbb{J}_T^\alpha\right)\right] + \alpha\overline{\rho^\alpha}^\chi\overline{\rho\phi}^{\chi\rho} + \boldsymbol{I}^\alpha \tag{1.37}$$

where $\boldsymbol{I}$ and $\boldsymbol{I}^\alpha$, interfacial sources for the mixture and the α-phase respectively, are related through $\boldsymbol{I} = \sum_\alpha \boldsymbol{I}^\alpha$ and will be addressed in the Section 1.1.5. The two-fluid model and the mixture model can now be derived from these balance equations. For the sake of legibility, we will now drop the averaging overlining. One can refer to the present paragraph to check the kind of averaging applied to each mean field. We will work throughout this work with averaged fields.

1.1.4 Two-component models

Two different kinds of models can be derived from these balance equations:

- *Two-fluid models.* Each phase is described by a continuity and a momentum equations. Interfacial interactions introduce additional terms in these equations. They are closed by constitutive laws, depending on the flow regime, but their determination can prove to be tedious;

- *Mixture models.* The flow is seen as a single-fluid flow with one continuity and one momentum equations that rule the evolution of mixture quantities complemented by an additional equation for the mass conservation of one phase. Additional terms linked to the relative velocity between phases, computed through a closure law depending on the flow regime, appear in these equations. In the absence of relative velocity, one gets a so-called homogeneous formulation.

These models are of common use when one phase is dispersed in another phase considered as continuous. In such a configuration, some specific simplifications and closures can be made.

1.1.4.1 Two-fluid field equations

The balance equation (1.37) can be applied for each phase:

- Mass conservation ($\psi^\alpha = 1$, $\phi^\alpha = 0$, $\mathbb{J}^\alpha = \mathbf{0}$, $\mathbb{J}_T^\alpha = \mathbf{0}$, $\boldsymbol{I}^\alpha = \mathbf{0}$)

$$\frac{\partial \alpha\rho^\alpha}{\partial t} + \boldsymbol{\nabla}\cdot(\alpha\rho^\alpha \boldsymbol{v}^\alpha) = 0 \tag{1.38}$$

  There is no interfacial source term due to the absence of phase change in the present work.

- Momentum conservation ($\psi^\alpha = \boldsymbol{v}^\alpha$, $\phi^\alpha = \boldsymbol{g}$, $\mathbb{J}^\alpha = -\boldsymbol{\Sigma}^\alpha$, $\mathbb{J}_T^\alpha = \mathbb{T}_T^\alpha$, $\boldsymbol{I}^\alpha = \boldsymbol{M}^\alpha$)

$$\frac{\partial \alpha\rho^\alpha \boldsymbol{v}^\alpha}{\partial t} + \boldsymbol{\nabla}\cdot(\alpha\rho^\alpha \boldsymbol{v}^\alpha \otimes \boldsymbol{v}^\alpha) = -\boldsymbol{\nabla}(\alpha p^\alpha) + \boldsymbol{\nabla}\cdot[\alpha(\mathbb{T}^\alpha + \mathbb{T}_T^\alpha)] + \alpha\rho^\alpha \boldsymbol{g} + \boldsymbol{M}^\alpha \tag{1.39}$$

  $\boldsymbol{M}^\alpha$ denotes the α-phase interfacial momentum transfer. Under the assumption of Newtonian fluids and considering that densities and viscosities are constant over the averaging domain, the viscous tensor writes [177]:

$$\mathbb{T}^\alpha = \mu^\alpha\left(\boldsymbol{\nabla}\boldsymbol{v}^\alpha + {}^t\boldsymbol{\nabla}\boldsymbol{v}^\alpha + 2\mathbb{D}^\alpha\right) \tag{1.40}$$

  where $\mathbb{D}^\alpha$ stands for an interfacial extra deformation tensor resulting from the fluctuating component of the phase velocity (the average operator applied to (1.8) generates an interfacial term linked to the deformations of the interface). In absence of phase changes, for sufficiently regular interface motions in a dispersed regime, one can write [177]:

$$\mathbb{D}^\alpha = \mathbf{0} \tag{1.41}$$

$$\mathbb{D}^\beta = -\frac{1}{2\beta}\left(\boldsymbol{\nabla}\beta \otimes \boldsymbol{v}^r + \boldsymbol{v}^r \otimes \boldsymbol{\nabla}\beta\right) \tag{1.42}$$

  where α is the dispersed phase. Regarding the turbulent viscous contribution, we have:

$$\mathbb{T}_T^\alpha = -\overline{\rho^\alpha \boldsymbol{v}''^\alpha \otimes \boldsymbol{v}''^\alpha}^\chi = -\overline{\rho^\alpha}\,\overline{\boldsymbol{v}''^\alpha \otimes \boldsymbol{v}''^\alpha}^{\chi\rho} = -\overline{\rho^\alpha}\boldsymbol{R}^\alpha \tag{1.43}$$

  where $\boldsymbol{R}^\alpha = \overline{\boldsymbol{v}''^\alpha \otimes \boldsymbol{v}''^\alpha}^{\chi\rho}$ is the Reynolds stress tensor that needs to be modeled: the turbulence closure is addressed in the Section 1.2.

1.1.4.2 Mixture field equations

The mixture is now considered as a whole. One can apply the mixture balance equation (1.36) for continuity and momentum equations, and complement it by a diffusion equation to track

concentration changes:

- Continuity ($\psi = 1$, $\phi = 0$, $\mathbb{J} = \mathbf{0}$)

$$\frac{\partial \rho}{\partial t} + \boldsymbol{\nabla} \cdot (\rho \boldsymbol{v}) = 0 \tag{1.44}$$

- Mass conservation for one phase stemming from (1.38):

$$\frac{\partial \alpha \rho^\alpha}{\partial t} + \boldsymbol{\nabla} \cdot (\alpha \rho^\alpha \boldsymbol{v}) = -\boldsymbol{\nabla} \cdot (\alpha \rho^\alpha \boldsymbol{u}^\alpha) \tag{1.45}$$

- Momentum conservation ($\psi = \boldsymbol{v}$, $\phi = \boldsymbol{g}$, $\mathbb{J} = -\boldsymbol{\Sigma}$ where $\boldsymbol{\Sigma} = \mathbb{T}^v + \mathbb{T}^v_D + \mathbb{T}^v_T$, $\boldsymbol{I} = \boldsymbol{M}$):

$$\frac{\partial \rho \boldsymbol{v}}{\partial t} + \boldsymbol{\nabla} \cdot (\rho \boldsymbol{v} \otimes \boldsymbol{v}) = -\boldsymbol{\nabla} p + \boldsymbol{\nabla} \cdot (\mathbb{T}^v + \mathbb{T}^v_D + \mathbb{T}^v_T) + \rho \boldsymbol{g} + \boldsymbol{M} \tag{1.46}$$

  where $\boldsymbol{M}$ denotes the mixture interfacial momentum transfer and cancels out if surface tension is neglected as highlighted in Section 1.1.5 so that no interfacial term appears in this mixture momentum equation. The other quantities are the mixture pressure $p = \sum_\alpha \alpha p^\alpha$, the average viscous stress $\mathbb{T}^v = \sum_\alpha \alpha \mathbb{T}^\alpha$, the diffusion stress $\mathbb{T}^v_D = -\sum_\alpha \alpha \rho^\alpha \boldsymbol{u}^\alpha \otimes \boldsymbol{u}^\alpha$ and the turbulent stress $\mathbb{T}^v_T = -\sum_\alpha \alpha \overline{\rho^\alpha \boldsymbol{v}''^\alpha \otimes \boldsymbol{v}''^\alpha}$.

The mixture model can be deduced from the two-fluid model by summing the mass and momentum equations respectively: summing (1.38) for both phases leads to (1.44) while summing (1.39) gives (1.46).

1.1.5 Interfacial momentum transfer

Molecular fluxes at the interface form source terms for mass and momentum equations. Without phase changes, only the interfacial momentum source resulting from stresses acting on the interface remains. It is defined as [114]:

$$\boldsymbol{M}^\alpha = -\overline{\boldsymbol{\Sigma} \cdot \boldsymbol{\nabla} \chi^\alpha} \tag{1.47}$$

Let us introduce the interfacial pressure p_i^α and viscous stresses $\mathbb{T}_i^\alpha$ to separate the mean field from local effects in the interfacial force associated to the interface i of interfacial area density A^α:

$$p_i^\alpha = \frac{\overline{p \boldsymbol{n}^\alpha \cdot \boldsymbol{\nabla} \chi^\alpha}}{A^\alpha} \quad \text{and} \quad \mathbb{T}_i^\alpha = \frac{\overline{\mathbb{T}^\alpha \boldsymbol{n}^\alpha \cdot \boldsymbol{\nabla} \chi^\alpha}}{A^\alpha} \tag{1.48}$$

The interfacial momentum source becomes:

$$\boldsymbol{M}^\alpha = p_i^\alpha \boldsymbol{\nabla} \alpha - \mathbb{T}_i^\alpha \cdot \boldsymbol{\nabla} \alpha + \boldsymbol{M}''^\alpha \tag{1.49}$$

where the interfacial extra momentum source $\boldsymbol{M}''^{\alpha}$ accounts for local surface forces resulting from pressure and shear stress deviations from interfacial average values: it includes drag, lift, virtual mass and transient effects. It is usually assumed that this term can be approximated as a linear combination of the constitutive relations for each individual effect [113]. In the following, we will only consider the drag contribution. For a two-phase flow with a dispersed phase α in a continuous phase β with constant surface tension, common assumptions are [112]:

$$p_i^{\alpha} = p^{\alpha} \quad \text{and} \quad p_i^{\beta} = p_i^{\alpha} - 2H_{\beta\alpha}\sigma_S \tag{1.50}$$

$$\mathbb{T}_i^{\alpha} = \mathbb{T}^{\alpha} \quad \text{and} \quad \mathbb{T}_i^{\alpha} = \mathbb{T}_i^{\beta} \tag{1.51}$$

Within this framework, if $\boldsymbol{M}''^{\alpha} = -\boldsymbol{M}''^{\beta}$, given the relation (1.20), one gets:

$$\boldsymbol{M} = \boldsymbol{M}^{\alpha} + \boldsymbol{M}^{\beta} = -2H_{\beta\alpha}\sigma_S \tag{1.52}$$

so that the sum of interfacial momentum sources cancels out in absence of surface tension. Before going any further, we shall write an appropriate closure for the tensor linked to velocity fluctuations $\mathbb{T}_T^v$.

1.2 Turbulence modeling

For high Reynolds numbers, as one can encounter on hydraulic structures, Navier–Stokes equations exhibit a chaotic behavior, unsteady and of complex structure, that corresponds to the turbulence. The turbulent structures cover a wide range of sizes that makes the system a full multiscale problem complex to solve. As detailed in Chapter 4, air entrainment and turbulence are deeply linked. It is therefore of prime importance to include turbulent effects in the model. The Direct Numerical Simulation (DNS) solves all these structures, at the price of very small spatial and temporal steps and hence prohibitively high computational cost, not admissible for industrial applications. Therefore, turbulence modeling is required. However, writing constitutive relations for turbulent fluxes is a hard task, even for single-phase flows. Motion of the interface and induced turbulence form part of an increased complexity in two-phase flows. Large-Eddy Simulation (LES) models were developed, representing the turbulent eddies down to a given scale and employing a sub-grid model to take into account the effects of smaller eddies. This intermediate approach remains computationally expensive on large domains. Once the Navier–Stokes equations are treated by a low-pass filter, one can define a turbulent viscosity thanks to a sub-grid scale model first introduced by Smagorinsky [334]:

$$\nu_T^{\alpha} = (C_s\Delta_s)^2 \sqrt{2\boldsymbol{s}^{\alpha} : \boldsymbol{s}^{\alpha}} \tag{1.53}$$

where C_s is a constant usually taken around 0.1 and Δ_s is the size of the spatial filter. The LES approach is more and more used, allowing modelers to deal with more complex flows, but remains

too expensive for the hydraulic applications considered here. A common practice in turbulence modeling is to work with Reynolds-averaged models: the averaging process indeed generates a Reynolds stress tensor (1.43) that requires modeling. The compressible two-phase flow framework led us to work with the Favre average instead of the Reynolds average of common use in single-phase incompressible flows: it has some modeling consequences that will be highlighted. Two modeling approaches exist: either propose a phenomenological closure as illustrated by the mixing length approach of Prandtl or solve additional dynamical equations describing the turbulent transport through higher moments of the momentum equation. Heuristic closure is though still needed as non-closed one-order-higher moments always appear.

1.2.1 Eddy viscosity models

Eddy viscosity model consists in a first-order closure that accounts for the turbulent contribution through diffusion due to the turbulent eddy viscosity ν_T^α prefigured in [33] and an additional pressure induced by the flow through the turbulent kinetic energy defined as:

$$k^\alpha = \frac{1}{2} tr\left(\boldsymbol{R}^\alpha\right) = \frac{1}{2}\overline{\boldsymbol{v}''^\alpha \cdot \boldsymbol{v}''^\alpha}^{\chi\rho} \tag{1.54}$$

This model reads:

$$\boldsymbol{R}^\alpha = -2\nu_T^\alpha \boldsymbol{s}^\alpha + \frac{2}{3}\nu_T^\alpha \left(\boldsymbol{\nabla}\cdot\boldsymbol{v}^\alpha\right)\boldsymbol{I} + \frac{2}{3}k^\alpha \boldsymbol{I} \tag{1.55}$$

The turbulent kinetic energy and the eddy viscosity shall be modeled as well. The turbulent kinetic energy transport equation can be deduced by taking the trace of the Reynolds transport equation deduced from the higher moment of the momentum equation.

1.2.2 The $k-\epsilon$ approach

In this work, we use a two-equation turbulence model: the $k-\epsilon$ model developed by Launder and Spalding [206] with the model constants presented in Table 1.1. The average operators will appear in this section for the sake of precision.

1.2.2.1 The incompressible formulation

For an incompressible single-phase flow (we drop locally the α superscripts), it writes:

$$\frac{\partial k}{\partial t} + \overline{\boldsymbol{v}}\cdot\boldsymbol{\nabla}k = -\frac{1}{\rho}\boldsymbol{\nabla}\cdot\left(\frac{1}{2}\rho\overline{(\boldsymbol{v}'\cdot\boldsymbol{v}')\,\boldsymbol{v}'} + \overline{p'\boldsymbol{v}'} - \overline{\mathbb{T}\cdot\boldsymbol{v}'}\right) - \overline{\boldsymbol{v}'\otimes\boldsymbol{v}'} : \overline{\boldsymbol{s}} - \frac{1}{\rho}\overline{\mathbb{T}:\boldsymbol{\nabla}\boldsymbol{v}'} \tag{1.56}$$

where the mean strain rate tensor is denoted $\overline{\boldsymbol{s}}$ and the single prime notation refers to the fluctuation with respect to the Reynolds average. One can identify three different contributions in the right-hand side of this relation:

- The first term corresponds to the turbulent transport of kinetic and potential energy and the molecular diffusion. It is modeled through a diffusion term:

$$-\frac{1}{\rho}\boldsymbol{\nabla}\cdot\left(\frac{1}{2}\rho\overline{(\boldsymbol{v}'\cdot\boldsymbol{v}')\,\boldsymbol{v}'}+\overline{p'\boldsymbol{v}'}-\overline{\mathbb{T}\cdot\boldsymbol{v}'}\right)=\frac{1}{\rho}\boldsymbol{\nabla}\cdot\left[\left(\mu+\frac{\mu_T}{\sigma_k}\right)\boldsymbol{\nabla}k\right] \tag{1.57}$$

- The second term is a production term defined as $\mathbb{P}=-\boldsymbol{R}:\overline{\boldsymbol{s}}$ and can be approximated by using the eddy viscosity model (1.55) and neglecting the divergence contributions:

$$\mathbb{P}=\nu_T S^2 \tag{1.58}$$

  where the scalar mean rate-of-strain is defined as $S=\sqrt{2\overline{\boldsymbol{s}}:\overline{\boldsymbol{s}}}$.

- The last term refers to the dissipation of turbulent kinetic energy and will be denoted ϵ defined as:

$$\epsilon=\frac{1}{\rho}\overline{\mathbb{T}:\boldsymbol{\nabla}\boldsymbol{v}'} \tag{1.59}$$

The relation (1.56) becomes:

$$\frac{\partial k}{\partial t}+\overline{\boldsymbol{v}}\cdot\boldsymbol{\nabla}k=\frac{1}{\rho}\boldsymbol{\nabla}\cdot\left[\left(\mu+\frac{\mu_T}{\sigma_k}\right)\boldsymbol{\nabla}k\right]+\mathbb{P}-\epsilon \tag{1.60}$$

In the $k-\epsilon$ model, the dissipation is computed thanks to a transport equation homogeneous to the turbulent kinetic energy counterpart:

$$\frac{\partial \epsilon}{\partial t}+\overline{\boldsymbol{v}}\cdot\boldsymbol{\nabla}\epsilon=\frac{1}{\rho}\boldsymbol{\nabla}\cdot\left[\left(\mu+\frac{\mu_T}{\sigma_\epsilon}\right)\boldsymbol{\nabla}\epsilon\right]+\frac{\epsilon}{k}\left(C_{\epsilon_1}\mathbb{P}-C_{\epsilon_2}\epsilon\right) \tag{1.61}$$

Let us underline that this relation is not theoretically derived and relies on empirical determination of the constants. According to the Kolmogorov dimensional analysis [191], the eddy viscosity depends on k and ϵ. The dependence is achieved following the relation:

$$\nu_T=C_\mu\frac{k^2}{\epsilon} \tag{1.62}$$

where C_μ is the Prandtl-Kolmogorov constant. Due to over-estimations of the turbulent kinetic energy for high values of the strain rate, the production term is limited at high strain rate following Guimet and Laurence [154]:

$$\mathbb{P}=\min\left(\sqrt{C_\mu}kS,\nu_T S^2\right) \tag{1.63}$$

Table 1.1: Constants of the $k-\epsilon$ model.

C_ν	C_μ	σ_k	σ_ϵ	$C_{\epsilon 1}$	$C_{\epsilon 2}$	κ
5.2	0.09	1.0	1.3	1.44	1.92	0.41

Moreover in this model, eddies can be arbitrarily large, so that an increase of the dissipation of turbulent kinetic energy is introduced following Yap [394] by modifying the C_{ϵ_2} coefficient:

$$C_{\epsilon_2}^Y = \max\left(C_{\epsilon_2} - \max\left[0, 0.83\left(\frac{L_T}{L_c}-1\right)\left(\frac{L_T}{L_c}\right)^2\right], 0\right) \tag{1.64}$$

where L_c is a characteristic size of the flow and $L_T = C_\mu^{\frac{3}{4}} k^{3/2}/\epsilon$ is a measure of the size of the large eddies. In this work, the density can undergo significant changes due to the mixture presence. One should therefore rather consider the compressible version of the $k-\epsilon$ model.

1.2.2.2 The compressible formulation

In the compressible framework, a Favre-averaged formulation ($\hat{k} = \frac{1}{2}\overline{\boldsymbol{v}''\cdot\boldsymbol{v}''}^{\chi\rho}$ and $\hat{\epsilon} = \frac{1}{\rho}\overline{\mathbb{T}:\boldsymbol{\nabla}\boldsymbol{v}''}$) in place of a Reynolds-averaged formulation ($k = \frac{1}{2}\overline{\boldsymbol{v}'\cdot\boldsymbol{v}'}$ and $\epsilon = \frac{1}{\rho}\overline{\mathbb{T}:\boldsymbol{\nabla}\boldsymbol{v}'}$ resulting from a statistical average). The turbulent energy equation [76] is modified accordingly:

$$\begin{aligned}\frac{\partial\hat{k}}{\partial t} + \overline{\boldsymbol{v}}^{\chi\rho}\cdot\boldsymbol{\nabla}\hat{k} \;=\; & -\frac{1}{\overline{\rho}}\boldsymbol{\nabla}\cdot\left(\frac{1}{2}\overline{\rho(\boldsymbol{v}''\cdot\boldsymbol{v}'')\,\boldsymbol{v}''}^{\chi\rho} + \overline{p'\boldsymbol{v}''} - \overline{\mathbb{T}\cdot\boldsymbol{v}''}\right) - \overline{\boldsymbol{v}''\otimes\boldsymbol{v}''}^{\chi\rho} : \boldsymbol{\nabla}\overline{\boldsymbol{s}}^{\chi\rho} \\ & - \frac{1}{\overline{\rho}}\overline{\mathbb{T}:\boldsymbol{\nabla}\boldsymbol{v}''} - \frac{1}{\overline{\rho}}\overline{\boldsymbol{v}''}\cdot\boldsymbol{\nabla}\overline{p} + \frac{1}{\overline{\rho}}\overline{p'\boldsymbol{\nabla}\cdot\boldsymbol{v}''}\end{aligned} \tag{1.65}$$

Please note $p' = p - \overline{p}$ is defined in a Reynolds-average sense whereas $\boldsymbol{v}'' = \boldsymbol{v} - \overline{\boldsymbol{v}}^{\chi\rho}$ is defined with respect to the Favre average (1.25) (and therefore $\overline{\boldsymbol{v}''} \neq \boldsymbol{0}$). If we put aside the discrepancy of averaging, compared to the relation (1.56), one can notice the appearance of the last two terms in the second line that correspond to the mean pressure work and the pressure dilatation correlation generated by non solenoidal velocity fluctuations. Moreover, another difference is the dissipation term that comprises of a solenoidal and dilatation parts. Following Vallet et al. [358], in their framework of mixture model for two-phase flow, one can compute:

$$\overline{\boldsymbol{v}''} = \overline{\rho}\overline{\boldsymbol{v}''Y^{\beta\prime\prime}}^{\chi\rho}\left(\frac{1}{\rho^\beta} - \frac{1}{\rho^\alpha}\right) \tag{1.66}$$

where $\overline{\boldsymbol{v}''Y^{\beta''}}^{\chi\rho}$ also appears as the dispersion term in transport equation of the mass fraction and is modeled through a gradient law:

$$\overline{\rho}\overline{\boldsymbol{v}''Y^{\beta''}}^{\chi\rho} = -\frac{\mu_T}{\mathrm{Sc}_T}\boldsymbol{\nabla}\overline{Y^{\beta}}^{\chi\rho} \tag{1.67}$$

Similarly to the incompressible case, one can write on the same model an equation on the dissipation:

$$\begin{aligned}\frac{\partial\hat{\epsilon}}{\partial t} + \overline{\boldsymbol{v}}^{\chi\rho}\cdot\boldsymbol{\nabla}\hat{\epsilon} \;=\; & -\frac{1}{\overline{\rho}}\boldsymbol{\nabla}\cdot\left[\left(\mu+\frac{\mu_T}{\sigma_\epsilon}\right)\boldsymbol{\nabla}\hat{\epsilon}\right] - C_{\epsilon_1}\frac{\hat{\epsilon}}{\hat{k}}\overline{\boldsymbol{v}''\otimes\boldsymbol{v}''}^{\chi\rho} : \boldsymbol{\nabla}\overline{\boldsymbol{s}}^{\chi\rho} \\ & - C_{\epsilon_2}\frac{\hat{\epsilon}^2}{\hat{k}} - C_{\epsilon_3}\frac{\hat{\epsilon}}{\hat{k}}\frac{1}{\overline{\rho}}\overline{\boldsymbol{v}''}\cdot\boldsymbol{\nabla}\overline{p} + C_{\epsilon_4}\frac{\hat{\epsilon}}{\hat{k}}\frac{1}{\overline{\rho}}\overline{p'\boldsymbol{\nabla}\cdot\boldsymbol{v}''}\end{aligned} \tag{1.68}$$

where it has been assumed that the non solenoidal part of the dissipation was negligible.

1.2.2.3 A two-phase $k-\epsilon$ model

Another part of the complexity arise from the two-phase nature of the considered flow. Some literature is devoted to the development and test of $k-\epsilon$ models for two-phase flows following Elghobashi and Abou-Arab [118]. Politano et al. [295] used a classical $k-\epsilon$ model with mixture quantities and added production and suppression terms due to modeled bubble-induced turbulence following the model developed by Kataoka et al. [184] for dilute bubbly flows in pipes: those terms proved to have significant impact on the bubbly spillway surface jet they studied. Bertodano et al. [22] presented a two-phase $k-\epsilon$ model for bubbly flows assuming linear superposition of shear-induced and bubble-induced turbulence, further used by Lahey Jr. [201]. Troshko and Hassan [350] proposed a two-phase $k-\epsilon$ model for bubbly flows deriving from the exact turbulent kinetic energy equation of a two-phase mixture and included wall functions (logarithmic law with constants depending on the flow parameters) accounting for the two-phase nature of the flow. Those models assumed a dilute bubbly phase and got reasonable agreements in bubbly pipe flows. As noted in [350], when gravity dominates in a bubbly flow, the instant relative velocity is primarily aligned with the gravity so that the fluctuations of bubble motions will enhance the component of the liquid velocity fluctuation aligned with gravity: this anisotropy is not taken into account by such eddy viscosity models. However to avoid to increase the complexity of the modeling with an unsure gain in accuracy due to fundamental weaknesses of these closures, it appears safer as a first approach to use the $k-\epsilon$ model directly for the mixture and avoid to combine phase quantities. This approach may miss some coupling terms: buoyancy effects are nevertheless included through the term $\mathbb{G} = -\overline{\boldsymbol{v}''}\cdot\boldsymbol{\nabla}\overline{p}$ completed by the relations (1.66) and (1.67). Consistently with this approach, following Simonin [332], Viollet and Simonin [370], this term derived from the instantaneous fluid momentum equations is related to the relative velocity

expression and, anticipating with the notations introduced in the following section, writes:

$$\mathbb{G} = \alpha\gamma \boldsymbol{V}^r \cdot \boldsymbol{V}^d \tag{1.69}$$

where $\boldsymbol{V}^r$ is the average relative velocity (1.94) (to distinguish from the relative mean velocity introduced in (1.32)) and $\boldsymbol{V}^d$ is a mean drift velocity (1.97). In the following, as in [50], we will neglect the pressure-dilatation correlation, last term of (1.65) and make an additional approximation: the volumetric flux $\boldsymbol{j}$ will replace the mixture velocity $\boldsymbol{v}$ involved in the advection and strain rate terms, neglecting the relative velocity contribution detailed in the relation (E.5). Omitting from now on the hat symbols, the system becomes:

$$\frac{\partial k}{\partial t} + \boldsymbol{j} \cdot \boldsymbol{\nabla} k = \frac{1}{\rho} \boldsymbol{\nabla} \cdot \left[\left(\mu + \frac{\mu_T}{\sigma_k} \right) \boldsymbol{\nabla} k \right] + \mathbb{P}^j + \mathbb{G} - \epsilon \tag{1.70}$$

$$\frac{\partial \epsilon}{\partial t} + \boldsymbol{j} \cdot \boldsymbol{\nabla} \epsilon = \frac{1}{\rho} \boldsymbol{\nabla} \cdot \left[\left(\mu + \frac{\mu_T}{\sigma_\epsilon} \right) \boldsymbol{\nabla} \epsilon \right] + \frac{\epsilon}{k} \left(C_{\epsilon_1} \mathbb{P}^j + C_{\epsilon_5} \mathbb{G} - C_{\epsilon_2} \epsilon \right) \tag{1.71}$$

The C_{ϵ_5} term weakens turbulence in case of stable stratification. We will take it equal to 1 if $\mathbb{G} < 0$ and 0 otherwise. The production term $\mathbb{P}^j$ is computed following (1.63):

$$\mathbb{P}^j = \min \left(\sqrt{C_\mu} k S^j, \nu_T \left(S^j \right)^2 \right) \tag{1.72}$$

but the strain rates depend on the volumetric flux $\boldsymbol{j}$ rather than the mixture velocity $\boldsymbol{v}$, neglecting the relative velocity contribution:

$$S^j = \sqrt{2 \boldsymbol{s}^j : \boldsymbol{s}^j} \quad \text{with} \quad \boldsymbol{s}^j = \frac{1}{2} \left(\boldsymbol{\nabla} \boldsymbol{j} + {}^t \boldsymbol{\nabla} \boldsymbol{j} \right) \tag{1.73}$$

1.2.2.4 $k - \epsilon$ model boundary conditions

Due to the presence of walls denoted $\partial\Omega_w$, the turbulence becomes anisotropic and shearing effects resulting from the high velocity gradient to fit the wall no-slip condition increase the production of turbulence. The development of boundary layers is pivotal in many air entrainment industrial applications so that the near-wall turbulence must be properly modeled. To avoid the need of a refined discretization near the wall, semi-empirical relations can be used to introduce wall functions: in the Lagrangian framework, an Eulerian mean velocity with non-zero tangential value is set at the wall to get the adequate wall shear stress and used for the rate-of-strain and viscous force computations. Let us introduce y^+ the dimensionless distance to a wall defined as:

$$y^+ = \frac{y u_\star}{\nu} \tag{1.74}$$

where y is the wall normal coordinate, ν a mixture kinematic viscosity to be defined (as we considered the mixture as a whole, but this is also an approximation as the usual wall law considers

a single fluid) and $u_\star$ the friction velocity defined as:

$$u_\star^2 = \nu \left. \frac{dj_\tau}{dy} \right|_{\partial\Omega_w} \tag{1.75}$$

with j_τ the wall tangential velocity. The shear stress at the wall follows:

$$\mathbb{T}_w = -\rho u_\star^2 \frac{\boldsymbol{j}}{|\boldsymbol{j}|} \tag{1.76}$$

and the friction velocity is assumed to satisfy the logarithmic law for a smooth velocity profile:

$$\frac{j_\tau}{u_\star} = \frac{1}{\kappa} \ln\left(y_+\right) + C_\nu \tag{1.77}$$

where κ is the Von Kármán constant. Following the work of Leroy [212], Neumann conditions derived from the equilibrium $\mathbb{P} = \epsilon$ in the logarithmic zone for fully developed turbulence are used in the second order differential operator computation close to the walls (small y):

$$\begin{cases} \boldsymbol{\nabla} k \cdot \boldsymbol{n}|_{\partial\Omega_w} = 0 \\ \boldsymbol{\nabla} \epsilon \cdot \boldsymbol{n}|_{\partial\Omega_w} = -\dfrac{u_\star^3}{\kappa y^2} \end{cases} \tag{1.78}$$

At an imposed velocity boundary, the turbulent kinetic energy and its dissipation are imposed whereas at an imposed pressure boundary they are computed through an homogeneous Neumann condition. Finally, on free surfaces, we will consider in this work that an homogeneous Neumann condition is fulfilled for both fields: while legitimate for the turbulent kinetic energy due to the absence of energy flux, the free surface condition for the dissipation is questionable.

1.2.2.5 Limits of the $k-\epsilon$ model and possible variations

In addition to the limits already detailed with respect to the compressibility and two-phase behavior inherent to the chosen implementation in this work, the $k-\epsilon$ model finds its limitations for non-inertial flows or in case of streamline curvature effects. However it is of wide use for industrial applications since it deals with enriched physics compared to a mixing length model and appears as a good starting point for the integration of turbulence. Higher order models can be used, with transport equations on the Reynolds stresses, as done for liquid jet atomization through an air-water mixture model in Carrasco [50], Luca et al. [229]: such modifications will be left to further work if the numerical results clearly highlight some deficiency. Many variations are available in the literature. Several references [214, 281] dealing with air entrainment cases considered the realizable $k-\epsilon$ model developed by Shih et al. [329] in combination with the mixture model approach. Nikseresht et al. [281] highlighted that among the $k-\epsilon$ models, the Re-Normalisation Group (RNG) approach following [389] performed better in the cases they considered. Behzadi et al. [19] developed a mixture $k-\epsilon$ model able to work at all volume fractions

of the dispersed phase. Even though numerical results might benefit from these modifications of the standard model (*e.g.* regarding the backward facing flows appearing in the stepped spillway treated in Chapter 4), the additional modeling effort required to include such approaches in the SPH model (adapt boundary terms, include variable density effects) led us to firstly use the standard approach given by equations (1.70) and (1.71).

1.3 Volume-weighted mixture model

1.3.1 Choice of variables

As seen before, several choices of variables can be made for the phase weighting coefficient (volume fraction or mass fraction), mixture velocity and relative velocity. This choice can be driven by two main aspects: a natural way of writing the equations or expressing a closure arising for a certain definition of the variables (mixture viscous efforts in terms of volumetric flux as at the end of Appendix E, closure on the drift velocity [177]) and a friendly writing of the equations in view of their numerical discretization. A common approach is to retain the previous system with the variables $(\alpha, \boldsymbol{v}, \boldsymbol{u}^\alpha)$, now written in Lagrangian form where the material derivative refers to:

$$\frac{D}{Dt} = \frac{\partial}{\partial t} + \boldsymbol{v} \cdot \boldsymbol{\nabla} \tag{1.79}$$

The system becomes:

$$\frac{D\rho}{Dt} = -\rho \boldsymbol{\nabla} \cdot \boldsymbol{v} \tag{1.80}$$

$$\frac{D\alpha\rho^\alpha}{Dt} = -\alpha\rho^\alpha \boldsymbol{\nabla} \cdot \boldsymbol{v} - \boldsymbol{\nabla} \cdot (\alpha\rho^\alpha \boldsymbol{u}^\alpha) \tag{1.81}$$

$$\frac{D\boldsymbol{v}}{Dt} = -\frac{1}{\rho}\boldsymbol{\nabla} p + \frac{1}{\rho}\boldsymbol{\nabla} \cdot (\mathbb{T}^v + \mathbb{T}^v_D + \mathbb{T}^v_T) + \boldsymbol{g} + \frac{1}{\rho}\boldsymbol{M} \tag{1.82}$$

Another common practice is to write the system using the mass fraction $(Y^\alpha, \boldsymbol{v}, \boldsymbol{u}^\alpha)$, that changes the phase mass conservation equation into:

$$\frac{DY^\alpha}{Dt} = -\frac{1}{\rho}\boldsymbol{\nabla} \cdot (\rho Y^\alpha \boldsymbol{u}^\alpha) \tag{1.83}$$

Even though this relation appears simpler at first sight, the numerical treatment of the right-hand side of this relation proved to trigger some conservation issues at high density ratios, due to the lack of symmetry between phases combined with the weighting by the density that significantly differs in both fluids. To have a symmetric writing of the equations and get rid of the density weight in the phase mass conservation, the choice of variables $(\alpha, \boldsymbol{j}, \boldsymbol{v}^r)$ is enticing. However, deriving the consequent system from the two-phase equations without adding too much complexity to the system (temporal and spatial derivatives) requires an additional assumption: we will consider constant phase densities as in the Volume of Fluid (VoF) approach [165]. Let us

underline that the material derivative is denoted:

$$\frac{d}{dt} = \frac{\partial}{\partial t} + \boldsymbol{j} \cdot \boldsymbol{\nabla} \tag{1.84}$$

The derivation is made in Appendix E and leads to the following system:

$$\boldsymbol{\nabla} \cdot \boldsymbol{j} = 0 \tag{1.85}$$

$$\frac{d\alpha}{dt} = -\boldsymbol{\nabla} \cdot (\alpha\beta \boldsymbol{v}^r) \tag{1.86}$$

$$\begin{aligned} \frac{d\boldsymbol{j}}{dt} = &-\frac{1}{\rho}\boldsymbol{\nabla} p + \frac{1}{\rho}\boldsymbol{\nabla} \cdot \left(\mathbb{T}^j + \mathbb{T}^j_D + \mathbb{T}^j_T \right) + \boldsymbol{g} + \frac{1}{\rho}\boldsymbol{M} \\ &+ \alpha\beta \frac{\rho^\alpha - \rho^\beta}{\rho} \left(\frac{\partial \boldsymbol{v}^r}{\partial t} + \boldsymbol{v}^\alpha \cdot \boldsymbol{\nabla}\boldsymbol{v}^\alpha - \boldsymbol{v}^\beta \cdot \boldsymbol{\nabla}\boldsymbol{v}^\beta \right) \end{aligned} \tag{1.87}$$

where:

$$\begin{aligned} \mathbb{T}^j &= \mu \left(\boldsymbol{\nabla}\boldsymbol{j} +^t \boldsymbol{\nabla}\boldsymbol{j} \right) + \alpha\mu^\alpha \left(\boldsymbol{\nabla} (\beta \boldsymbol{v}^r) +^t \boldsymbol{\nabla} (\beta \boldsymbol{v}^r) \right) - \beta\mu^\beta \left(\boldsymbol{\nabla} (\alpha \boldsymbol{v}^r) +^t \boldsymbol{\nabla} (\alpha \boldsymbol{v}^r) \right) \\ &\quad +2 \left(\alpha\mu^\alpha \mathbb{D}^\alpha + \beta\mu^\beta \mathbb{D}^\beta \right) \\ \mathbb{T}^j_T &= \mu_T \left(\boldsymbol{\nabla}\boldsymbol{j} +^t \boldsymbol{\nabla}\boldsymbol{j} \right) - \tfrac{2}{3}\rho k \boldsymbol{I} \\ &\quad + \alpha\mu^\alpha_T \left(\boldsymbol{\nabla} (\beta \boldsymbol{v}^r) +^t \boldsymbol{\nabla} (\beta \boldsymbol{v}^r) \right) - \beta\mu^\beta_T \left(\boldsymbol{\nabla} (\alpha \boldsymbol{v}^r) +^t \boldsymbol{\nabla} (\alpha \boldsymbol{v}^r) \right) \\ \mathbb{T}^j_D &= -\boldsymbol{\nabla} \cdot (\alpha\beta \boldsymbol{v}^r \otimes \boldsymbol{v}^r) \end{aligned} \tag{1.88}$$

where we defined the viscosity:

$$\mu = \alpha\mu^\alpha + \beta\mu^\beta \tag{1.89}$$

A mixture viscosity The definition (1.89) shall not be seen as the expression of a mixture viscosity, as some additional viscous terms appear. In the literature of mixture models, it is a common use to introduce apparent mixture viscosity [239]. Moreover, instead of introducing the combination of dynamic viscosities, one could make a similar combination of the kinematic ones, but Chanteperdrix [75] does not find a final conclusion on this point. Let us note that the chosen definition here is somewhat natural in the derivations.

The volume fraction equation The relation (1.86), if we except the relative velocity term, is somewhat similar to the Volume of Fluid approach proposed by Hirt and Nichols [165] or the topological equation introduced in 7-equations models for two-phase flows as detailed by Baer and Nunziato [16], neglecting compressibility and thermodynamical effects. A volume fraction equation has been proposed by Chanteperdrix [75] and includes additional terms due to compressibility effects that might be considered in further studies.

Volume-weighted models in the literature Early works with volume-weighted mixture models with relative/drift velocity were performed with monodimensional[1] [373] or bidimensional [404] two-phase mixture models at imposed kinematics (or drift-flux models) to study pipe flows [105]. They were used more recently for example [280] for buoyant mixture flows to take advantage of the divergence-free condition of the volumetric flux – interest already underlined by [176] – or [77] to handle dry granular materials in which one constituent (in that case the voids) has a significantly lower density than the other. Brethour and Hirt [38] implemented a mixture model in the commercial software FLOW-3D® with a relative velocity depending on the pressure gradient and switching of dispersed phase definition depending on the volume fraction. They gave the example of an oil-water dispersion. Solid-liquid-gas flows were studied with that kind of approach by Bohorquez [30].

At this point, compared to the mass-weighted formulation, the only additional approximation is that phase densities are constant. Due to the choice of variables, we see that an additional term arose in the fourth line of (1.87). We are now going to further simplify this relation in view of the physics considered and in order to have a practical way of solving this equation.

1.3.2 Mixture model for a two-phase dispersed flow at high density ratio

We consider a dispersed two-phase flow. Following Ishii and Hibiki [177], Manninen and Taivassalo [239], several common assumptions are made:

- The phase α is dispersed within the continuous phase β, so that one can use the closures (1.41) and (1.42);
- A local equilibrium of phases is reached over short spatial length scales so that we consider that the last term of (1.87) is negligible;
- Surface tension effects are neglected, hence one can approximate $\boldsymbol{M} = \mathbf{0}$;
- There is a mechanical equilibrium of partial pressures, giving $p = p^\alpha = p^\beta$, as the pressure relaxation time is generally small compared to the other characteristic times of the flow, as illustrated in [200] in case of bubbly flows.

For the turbulent contribution, we make the additional assumption that the velocity fluctuations are equal in both phases, yielding $k = k^\alpha = k^\beta$. Under this set of hypotheses, and defining a new pressure including turbulent fluctuations:

$$P = p + \frac{2}{3}\rho k \tag{1.90}$$

[1] Let us underline that a monodimensional flow cannot exhibit mixed phases as shown by Landau and Lifshitz [202]. We are here talking of monodimensional mixture models.

The momentum equation finally becomes:

$$\frac{d\boldsymbol{j}}{dt} = -\frac{1}{\rho}\boldsymbol{\nabla}P + \frac{1}{\rho}\boldsymbol{\nabla}\cdot\left(\mathbb{T}^j + \mathbb{T}^j_D + \mathbb{T}^j_T\right) + \boldsymbol{g} \tag{1.91}$$

where

$$\begin{aligned}
\mathbb{T}^j &= \mu\left(\boldsymbol{\nabla}\boldsymbol{j} +^t \boldsymbol{\nabla}\boldsymbol{j}\right) + \tfrac{1}{\rho}\boldsymbol{\nabla}\cdot\left(\alpha\left(\mu^\alpha - \mu^\beta\right)\left[\boldsymbol{\nabla}\left(\beta\boldsymbol{v}^r\right) +^t \boldsymbol{\nabla}\left(\beta\boldsymbol{v}^r\right)\right]\right) \\
\mathbb{T}^j_T &= \mu_T\left(\boldsymbol{\nabla}\boldsymbol{j} +^t \boldsymbol{\nabla}\boldsymbol{j}\right) \\
&\quad + \alpha\mu^\alpha_T\left(\boldsymbol{\nabla}\left(\beta\boldsymbol{v}^r\right) +^t \boldsymbol{\nabla}\left(\beta\boldsymbol{v}^r\right)\right) - \beta\mu^\beta_T\left(\boldsymbol{\nabla}\left(\alpha\boldsymbol{v}^r\right) +^t \boldsymbol{\nabla}\left(\alpha\boldsymbol{v}^r\right)\right) \\
\mathbb{T}^j_D &= -\boldsymbol{\nabla}\cdot\left(\alpha\beta\boldsymbol{v}^r\otimes\boldsymbol{v}^r\right)
\end{aligned} \tag{1.92}$$

To work in a Lagrangian framework, we introduce an equation of advection accounting for the resolution at moving points:

$$\frac{d\boldsymbol{r}}{dt} = \boldsymbol{j} \tag{1.93}$$

where $\boldsymbol{r}$ is the position vector.

1.3.3 Relative velocity closure

To close the system, an algebraic relation substituting to one of the momentum equations (1.39) of the two-fluid model and allowing us to compute the relative velocity is required. In this prospect, we shall write a model of the interfacial momentum transfer term and deduce a relation on the relative velocity. It is a common practice in two-phase flows to close this interfacial term with a drag force [332]. Neglecting the fluctuations of the drag coefficient and averaging, one can write:

$$\boldsymbol{M}^\alpha = -\alpha\gamma\boldsymbol{V}^r \tag{1.94}$$

where $\boldsymbol{V}^r$ stands for the averaged value of the local relative velocity and, considering monodisperse spherical inclusions of diameter d^α, the coefficient γ writes:

$$\gamma = \frac{3\mathrm{C_D}|\boldsymbol{V}^r|\rho^\beta}{4d^\alpha\beta^{n-1}} \tag{1.95}$$

where n is a hindering coefficient and $\mathrm{C_D}$ is a drag coefficient generally expressed as a function of the dispersed phase Reynolds number:

$$\mathrm{Re}^\alpha = \frac{|\boldsymbol{V}^r|d^\alpha}{\nu^\beta} \tag{1.96}$$

More details will be given when applying the model to physical cases in Chapters 3 and 4. The averaged value of the local relative velocity $\boldsymbol{V}^r$ can be expressed as the sum of the relative mean velocity previously introduced $\boldsymbol{v}^r$ and a mean drift velocity $\boldsymbol{V}^d$ due to the correlation between

the instant distribution of the dispersed phase and the large scale turbulent fluid motion. In the limiting case of a null dispersed phase diameter, it can be shown according to Simonin [332] that this dispersion term takes the form:

$$\boldsymbol{V}^d = -D_T^{\alpha\beta}\left(\frac{\boldsymbol{\nabla}\alpha}{\alpha} - \frac{\boldsymbol{\nabla}\beta}{\beta}\right) = -D_T^{\alpha\beta}\frac{\boldsymbol{\nabla}\alpha}{\alpha\beta} \tag{1.97}$$

with a diffusive coefficient $D_T^{\alpha\beta}$ that we will address below. Ishii [176] suggests to handle with care such a constitutive law, analogy of Newton's law of viscosity or Fourier's law of heat conduction. Indeed in those latter cases, they are applied to molecular transport phenomena, hence microscopic diffusion, whereas in the suggested closure, the diffusion of phases is macroscopic. The interfacial momentum transfer term then writes:

$$\boldsymbol{M}^\alpha = -\alpha\gamma\boldsymbol{v}^r - \gamma D_T^{\alpha\beta}\frac{\boldsymbol{\nabla}\alpha}{\beta} \tag{1.98}$$

To get an expression for the relative velocity, we can equate this relation with the derived formulation on this interfacial term given in Appendix E (equation E.26) simplified by the above-mentioned assumptions:

$$\begin{aligned}\boldsymbol{M}^\alpha = {}& \alpha\beta\frac{\rho^\beta - \rho^\alpha}{\rho}\boldsymbol{\nabla}P - P\boldsymbol{\nabla}\alpha \\ & - Y^\beta\boldsymbol{\nabla}\cdot\left[\alpha\left(\mu^\alpha + \mu_T^\alpha\right)\left(\boldsymbol{\nabla}\boldsymbol{v}^\alpha + {}^t\boldsymbol{\nabla}\boldsymbol{v}^\alpha\right)\right] + Y^\alpha\boldsymbol{\nabla}\cdot\left[\beta\left(\mu^\beta + \mu_T^\beta\right)\left(\boldsymbol{\nabla}\boldsymbol{v}^\beta + {}^t\boldsymbol{\nabla}\boldsymbol{v}^\beta\right)\right] \\ & - Y^\beta\boldsymbol{\nabla}\cdot\left(2\alpha\mu^\alpha\mathbb{D}^\alpha\right) + Y^\alpha\boldsymbol{\nabla}\cdot\left(2\beta\mu^\beta\mathbb{D}^\beta\right) + \frac{2}{3}\alpha\beta\left[\left(\rho^\alpha - \rho^\beta\right)\boldsymbol{\nabla}k + \left(\rho^\alpha + \rho^\beta\right)k\frac{\boldsymbol{\nabla}\alpha}{\alpha\beta}\right]\end{aligned} \tag{1.99}$$

For the non fluctuating contributions, following [239], we consider that the pressure gradient contribution is the leading term. Moreover, regarding the fluctuation part, following [46], we will consider that it can be gathered in the dispersion term with a coefficient of the form $\nu_T^\beta/\mathrm{Sc}_T$ where Sc_T is a turbulent Schmidt number taken equal to 1. Simonin [332] suggested that under a specific set of assumptions, it could indeed be identified by such a form. The resulting relative velocity writes:

$$\boldsymbol{v}^r = \beta\frac{\rho^\alpha - \rho^\beta}{\gamma\rho}\boldsymbol{\nabla}P - \frac{\nu_T^\beta}{\mathrm{Sc}_T}\frac{\boldsymbol{\nabla}\alpha}{\alpha\beta} \tag{1.100}$$

If we add a hydrostatic hypothesis and neglect the turbulent contribution distinguishing p and P, the relation becomes:

$$\boldsymbol{v}^r = \beta\frac{\rho^\alpha - \rho^\beta}{\gamma}\boldsymbol{g} - \frac{\nu_T^\beta}{\mathrm{Sc}_T}\frac{\boldsymbol{\nabla}\alpha}{\alpha\beta} \tag{1.101}$$

We shall use this relation as a first approach due to numerical issues that will be underlined in Chapter 3. Introducing this closure in the buoyant term of the $k-\epsilon$ model (1.69) and approxi-

mating the diffusivity of the drift velocity part by the eddy viscosity only, one can write:

$$\mathbb{G} = \frac{\rho^\beta - \rho^\alpha}{\rho} \frac{\nu_T^\beta}{\mathrm{Sc}_T} \boldsymbol{\nabla} P \cdot \boldsymbol{\nabla} \alpha \tag{1.102}$$

1.3.4 Mixture state equation

For numerical reasons detailed in Chapter 2, a weakly compressible framework is considered. In this prospect, the divergence free condition (1.85) is relaxed and a conservation equation on the inverse volume σ derived from the study of the deformation of an infinitesimal volume [364] is written:

$$\frac{d\sigma}{dt} = -\sigma \boldsymbol{\nabla} \cdot \boldsymbol{j} \tag{1.103}$$

To close the system, another constitutive relation, the equation of state, is therefore needed to compute the pressure field of the medium. The relation of common use in multifluid SPH (1.10) was previously presented. For two-phase mixtures, Wood [385] derived a formulation of sound speed valid for gas bubbles in a fluid at thermodynamic equilibrium [344] of the form:

$$\rho c_w^2 = \left(\frac{\alpha}{\rho^\alpha \left(c^\alpha\right)^2} + \frac{\beta}{\rho^\beta \left(c^\beta\right)^2} \right)^{-1} \tag{1.104}$$

where c^α and c^β are the sound speeds in the fluids forming the mixture. Due to strong volume deformations around the dispersed phase, the sound speed undergoes a severe damping as displayed on Figure 1.1. Chanteperdrix [75] developed a two-phase mixture model in which he showed that the sound speed should write:

$$\rho c_g^2 = \alpha \rho^\alpha \left(c^\alpha\right)^2 + \beta \rho^\beta (c^\beta)^2 \tag{1.105}$$

to ensure the hyperbolicity of the system. The corresponding sound speed is also plotted on Figure 1.1 so that one can notice the significant discrepancy between both formulations (computed assuming constant phase densities). Let us underline that under the condition $\rho^\alpha \left(c^\alpha\right)^2 = \rho^\beta \left(c^\beta\right)^2$ that will appear in Chapter 2 in the case of a unit polytropic index as a practical hypothesis suggested by [86], we find $c_w = c_g$. This remark is of importance as in the numerical implementation, the sound speed is used as a numerical nature as we do not resolve the acoustics, and therefore becomes a parameter that the user should adequately define, allowing this equality of sound speeds to be possibly fulfilled. We adapted the state equation to a two-phase mixture with a unit polytropic index and a sound speed c computed with Chanteperdrix [75] approach as the significant decrease of sound speed of Wood [385] formula at intermediate volume fractions triggered numerical instability due to a too high compressibility. The unit poplytropic index, that amounts to a linearization of the state law, is a common assumption, as in [242] for example. Within the mixture framework, it allows for a proper derivation of the mixture state law

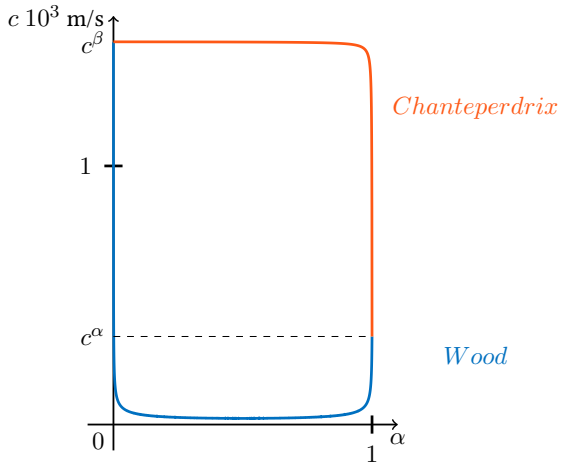

Figure 1.1: Comparison of the sound velocities following [385] and [75].

from phase state laws (1.10) for equal phase sound speeds (this equality being respected in the applications made in this work). We linked the pressure to a ratio of volumes instead of densities:

$$p = \rho c^2 \left(\frac{\sigma}{\sigma_0} - 1 \right) + p_B \tag{1.106}$$

where σ_0 is the reference volume equal to δr^{-d}, δr being the particle discretization length and d the space dimension. This formula reduces to a one-phase formulation for null or unit volume fraction: in single-phase SPH, when particle masses are constant, the ratio of densities ρ/ρ_0 can be identified to the ratio of volumes σ/σ_0. In the following, if not specified, we assume that the background pressure p_B is null (motivations for its choice will be given in Chapter 2) and sound speeds are chosen so as to ensure that $c^k > 10 \max\left(V_{\max}, \sqrt{g h_s}\right)$ where $V_{\max}$ is the maximum mixture velocity and h_s is the maximum height of the flow under gravity. As in classical WCSPH, this ensures the compressibility effect is purely numerical: the Mach number Ma remains below 0.1, and the relative density fluctuations proportional to Ma^2 stay within 1% variations, as explained by Monaghan [262]. The local speed of sound at constant volume fraction will be written:

$$c = \sqrt{\frac{\sigma_0}{\rho_0} \frac{\partial p}{\partial \sigma}} \tag{1.107}$$

where $\rho_0 = \alpha \rho^\alpha + \beta \rho^\beta$.

1.3.5 Geometry of the interface

Important approximations regarding the topological structure of the interface have been made when expressing the relative velocity between phases in Section 1.3.3. Two given volumes of the same size can have the same volume fraction but a completely different interface structure as highlighted on Figure 1.2. The dispersed phase was assumed to consist in monodisperse spher-

(a) Highly dispersed flow (b) Dispersed flow (c) Separated flow

Figure 1.2: Two-phase flow configurations with the same volume fraction.

ical bubbles or drops: such a choice highlights that the model cannot be able to capture regime transition as observed in pipe flows for example. In the cases considered in Chapter 3, we also considered separation cases for which physically, both phases can be dispersed. We therefore operate a switch of dispersed phase definition at $\alpha = 0.5$, but this is a severe choice, as α does not provide sufficient information to decide whether a phase is dispersed. In [253], switches between intermediate and dispersed phase models were made at $\alpha = 0.3$ and $\alpha = 0.7$. A useful quantity has been previously introduced in (1.21) to get further insights into the local topology of the flow: the interfacial area density. This interfacial area density can be followed with an additional transport equation as suggested by Ishii [176]:

$$\frac{\partial A^\alpha}{\partial t} + \boldsymbol{\nabla} \cdot (A^\alpha \boldsymbol{v}_i) = \text{source term (bubble expansion, collapse, coalescence...)} \tag{1.108}$$

that requires additional closures for the interface velocity $\boldsymbol{v}_i$ and the sources terms generated by the interface deformation, or may be closed through an algebraic relation:

$$A^\alpha = A^\alpha \left(\boldsymbol{v}^r, \rho^\alpha, \mu^\alpha, \alpha, |\boldsymbol{\nabla}\alpha|, \sigma_S, g\right) \tag{1.109}$$

For a dispersed flow of spherical bubbles, one can link it to the volume fraction thanks to the bubble Sauter mean diameter:

$$D_{Sm} = \frac{6\alpha}{A^\alpha} \tag{1.110}$$

that can be dynamically used for the relative velocity computation (recall A^α has an inverse length dimension). Introducing a factor C_i accounting for the shape and size of the dispersed phase (equal to 1 for uniform droplets or particles), one can write the mean curvature:

$$H_c = \frac{A^\alpha}{3C_i\alpha} \tag{1.111}$$

Other approaches, under the assumption of spherical dispersed phase, would be to introduce a size distribution, and solve an evolution equation on the number density of spheres [114], or introduce several classes of bubble/drop sizes, and possibly solve Population Balance Equations

(PBE) to follow the evolution of the radii, due to coalescence, fragmentation... In the framework of air-water flows, one can refer to the work of Carrasco [50], Luca et al. [229], Vallet et al. [358] that focus on the atomization of a water jet and used a mixture model complemented by an equation on the interfacial area density. In the present work, this degree of complexity was not added and is left for further work.

1.4 Boundary value problem

To close the boundary value problem of the two-phase mixture flow, initial and boundary conditions are needed.

1.4.1 Initial conditions

The imposition of initial conditions is generally quite natural, though it must be carefully made numerically to avoid perturbing the computations, especially in presence of open boundaries. We will mostly consider fluid initially at rest, except if the fluid velocity is easily known. For the pressure field in a separated case, we can impose the hydrostatic profile, phase α being above phase β with respect to the gravity:

$$p\left(z\right) = p_B + \begin{cases} \rho^\alpha (c^\alpha)^2 \left(\exp\left[\frac{g}{(c^\alpha)^2}(H-z) \right] - 1 \right) & \text{if } z \geq h_s \\ p_I \exp\left[\frac{g}{(c^\beta)^2}(h_s - z) \right] + \rho^\beta (c^\beta)^2 \left(\exp\left[\frac{g}{(c^\beta)^2}(h_s - z) \right] - 1 \right) & \text{otherwise} \end{cases} \tag{1.112}$$

with the pressure at the interface:

$$p_I = \rho^\alpha \left(c^\alpha\right)^2 \left(\exp\left[\frac{g}{\left(c^\alpha\right)^2}(H - h_s) \right] - 1 \right) \tag{1.113}$$

where h_s the free surface height and H the container height. However the compressible correction did not introduce significant discrepancies as the sound speeds are high (as testified by Figure A.1), so that a linearization is a good approximation of the previous system. We therefore settle for the incompressible profile:

$$p(z) = p_B + \begin{cases} \rho^\alpha g(H - z) & \text{if } z \geq h_s \\ \rho^\alpha g(H - h_s) + \rho^\beta g(H - z) & \text{otherwise} \end{cases} \tag{1.114}$$

where z denotes the vertical position of the considered point.

1.4.2 Boundary conditions

Boundary conditions are of complex prescription in numerical models, especially in the SPH approach as it will be illustrated in Chapters 2 and 3. A boundary condition corresponds to the imposition of values of the field (*Dirichlet* condition), its gradient (*Neumann* condition) or a combination of both (*Robin* condition). Different conditions shall be considered whether we consider a wall boundary $\partial\Omega_w$, an interface between fluids $\partial\Omega_i$ or an open boundary $\partial\Omega_o$.

1.4.2.1 Fluid-wall interfaces

We will not consider surface tension in this work, so that we do not detail considerations for contact lines. For an impermeable wall (*i.e.* no mass transfer), the normal component of the velocity is continuous:

$$\boldsymbol{j} \cdot \boldsymbol{n}|_{\partial\Omega} = \boldsymbol{v}_w \cdot \boldsymbol{n} \tag{1.115}$$

where $\boldsymbol{v}_w$ denotes the wall velocity. Furthermore, for a viscous fluid, a no-slip condition is applied due to friction so that the tangential velocity is equal to the tangential velocity of the wall:

$$(\boldsymbol{j} - \boldsymbol{j} \cdot \boldsymbol{n})|_{\partial\Omega} = \boldsymbol{v}_w - \boldsymbol{v}_w \cdot \boldsymbol{n} \tag{1.116}$$

Those conditions combine to give a Dirichlet condition on the fluid velocity:

$$\boldsymbol{j}|_{\partial\Omega} = \boldsymbol{v}_w \tag{1.117}$$

from which one can write an approximate condition on the dynamic pressure at walls following Violeau [364] through an homogeneous Neumann condition:

$$\left.\frac{\partial p^d}{\partial n}\right|_{\partial\Omega} = 0 \tag{1.118}$$

where $p^d = p - \rho \boldsymbol{g} \cdot \boldsymbol{r}$.

1.4.2.2 Fluid-fluid interfaces

The continuity of the stress across the interface leads to the continuity of pressure and shear stress:

$$[p]_{\partial\Omega_i} = 0 \tag{1.119}$$

$$[\mathbb{T}_w \cdot \boldsymbol{n}]_{\partial\Omega_i} = \boldsymbol{0} \tag{1.120}$$

where the brackets denotes the jump across the discontinuity. For immiscible viscous fluids, the kinematic condition states the continuity of velocities across the interface:

$$[\boldsymbol{j}]_{\partial\Omega_i} = \mathbf{0} \tag{1.121}$$

Let us underline that given the mixture model retained, the interface shall be treated implicitly.

1.4.2.3 Open boundaries

Thorough discussion for open boundaries is made in the corresponding parts in Chapters 2 and 3. One may want to impose a velocity or pressure profile through a Dirichlet condition. In case of outlets, a Neumann condition on pressure can also be considered.

1.5 Summary

1.5.1 Choice of a mixture model

With appropriate constitutive laws, two-fluid models, as they use two velocities, might give more precise insights in the study of two-phase flows. Indeed, in the mixture model, further assumptions are required to close the relative velocity, by neglecting advective and temporal variations. The mixture model takes advantage of the ease of its formulation, as an extension of a single-flow configuration with an additional equation and an algebraic closure that can be adapted depending on the regime and phases considered, giving it versatility. It also appears as a first step before getting to more complex two-fluid models. The counterpart of this simplicity is a restrictive framework of legitimate application, namely dispersed flows with a strong coupling between phases, in the scope of this work. Moreover, important approximations have been made with respect to the turbulence modeling. Warning will be made in the following chapters whenever we would reach the limits of this model.

1.5.2 Set of equations

One should keep in mind that we refer here to mean fields due to the averaging process. The system of equations to be solved (we dropped all the averaging signs) reads:

$$\begin{cases} \dfrac{d\sigma}{dt} = -\sigma \boldsymbol{\nabla} \cdot \boldsymbol{j} \\ \dfrac{d\alpha}{dt} = -\boldsymbol{\nabla} \cdot (\alpha\beta \boldsymbol{v}^r) \\ \dfrac{d\boldsymbol{j}}{dt} = -\dfrac{1}{\rho}\boldsymbol{\nabla} P + \dfrac{1}{\rho}\boldsymbol{\nabla} \cdot \left(\mathbb{T}^j + \mathbb{T}^j_D + \mathbb{T}^j_T \right) + \boldsymbol{g} \\ \dfrac{d\boldsymbol{r}}{dt} = \boldsymbol{j} \\ \dfrac{dk}{dt} = \dfrac{1}{\rho}\boldsymbol{\nabla} \cdot \left[\left(\mu + \dfrac{\mu_T}{\sigma_k} \right) \boldsymbol{\nabla} k \right] + \mathbb{P}^j + \mathbb{G} - \epsilon \\ \dfrac{d\epsilon}{dt} = \dfrac{1}{\rho}\boldsymbol{\nabla} \cdot \left[\left(\mu + \dfrac{\mu_T}{\sigma_\epsilon} \right) \boldsymbol{\nabla} \epsilon \right] + \dfrac{\epsilon}{k} \left(C_{\epsilon_1} \mathbb{P}^j + C_{\epsilon_5} \mathbb{G} - C_{\epsilon_2} \epsilon \right) \end{cases} \tag{1.122}$$

with

$$\begin{cases} \boldsymbol{v}^r = \beta \frac{\rho^\alpha - \rho^\beta}{\gamma \rho} \boldsymbol{\nabla} P - \frac{\nu_T^\beta}{\mathrm{Sc}_T} \frac{\boldsymbol{\nabla}\alpha}{\alpha\beta} \\ p = \rho c^2 \left(\frac{\sigma}{\sigma_0} - 1 \right) + p_B \\ \mu = \alpha \mu^\alpha + \beta \mu^\beta \\ \mu_T = C_\mu \frac{k^2}{\rho\epsilon} \\ \mathbb{T}^j = \mu \left(\boldsymbol{\nabla} \boldsymbol{j} +^t \boldsymbol{\nabla} \boldsymbol{j} \right) + \frac{1}{\rho} \boldsymbol{\nabla} \cdot \left(\alpha \left(\mu^\alpha - \mu^\beta \right) \left[\boldsymbol{\nabla} (\beta \boldsymbol{v}^r) +^t \boldsymbol{\nabla} (\beta \boldsymbol{v}^r) \right] \right) \\ \mathbb{T}^j_T = \mu_T \left(\boldsymbol{\nabla} \boldsymbol{j} +^t \boldsymbol{\nabla} \boldsymbol{j} \right) \\ \quad + \alpha \mu_T^\alpha \left(\boldsymbol{\nabla} (\beta \boldsymbol{v}^r) +^t \boldsymbol{\nabla} (\beta \boldsymbol{v}^r) \right) - \beta \mu_T^\beta \left(\boldsymbol{\nabla} (\alpha \boldsymbol{v}^r) +^t \boldsymbol{\nabla} (\alpha \boldsymbol{v}^r) \right) \\ \mathbb{T}^j_D = -\boldsymbol{\nabla} \cdot (\alpha\beta \boldsymbol{v}^r \otimes \boldsymbol{v}^r) \\ \mathbb{P}^j = \min \left(\sqrt{C_\mu} k S^j, \nu_T \left(S^j \right)^2 \right) \\ \mathbb{G} = \frac{\rho^\beta - \rho^\alpha}{\rho} \frac{\nu_T^\beta}{\mathrm{Sc}_T} \boldsymbol{\nabla} P \cdot \boldsymbol{\nabla} \alpha \end{cases} \tag{1.123}$$

This system reduces to the single-fluid formulation for a null relative velocity with a unit or null volume fraction. This important property shall also be enforced in the numerical discretization process that will be detailed in Chapters 2 and 3. In the following, we will denote the pressure including the turbulent kinetic energy contribution as p instead of P.

Chapter 2

SPH and multiphase flows

Après une description introductive du formalisme Smoothed Particle Hydrodynamics *(SPH), ce chapitre se concentre sur la présentation de l'état de l'art de la simulation des écoulements multiphasiques dans la méthode SPH, tout particulièrement dans le cas de forts rapports de densités, au regard des systèmes d'équations présentés dans le Chapitre 1. Discrétisations spatiales et temporelles sont abordées. Un accent est mis sur le traitement des conditions aux limites.*

Continuous media can be described through two main approaches: while, in an *Eulerian* description, attention is focused on the properties of the medium at a given point in space as a function of time, the *Lagrangian* viewpoint tracks material parts of the considered domain and monitors their property changes throughout the computations. The mesh-free numerical method Smoothed Particle Hydrodynamics (SPH) lies within the Lagrangian formalism without the use of a mesh: the domain of interest is discretized with a set of material points, referred hereafter to as particles, that correspond to interpolation points that convey all physical properties (volume, mass, velocity, pressure, etc.). The evolutions of these variables are ruled by a set of discrete differential equations derived from the continuous governing equations presented in Chapter 1 and solved with a time-marching scheme and space-discretized differential operators. At each time step, the computed velocity, used to move particles, leads to a new distribution of the interpolation points and convects the physical quantities. In this chapter, a quick overview of the SPH formalism is done to introduce the notations and tools. Then a special focus is done on the SPH modeling of multiphase flows and especially mixture models. This state-of-the-art shall give the appropriate tools and highlight the missing ingredients to develop our SPH mixture model in Chapter 3.

2.1 Fundamentals of SPH

After a brief description of the genesis of SPH, that sheds light on extant applications of models of interest in this work, the basics of SPH are quickly addressed following Monaghan [265] and Violeau [364] to prepare the derivations of the SPH two-phase mixture model adopted in this thesis.

2.1.1 A brief history of SPH

Let us start with a jump into time. The SPH method was first developed in the 1970's for astrophysical applications by Lucy [230] and, independently, by Gingold and Monaghan [146]. The simulation of non-axisymmetric phenomena took advantage of the assets of SPH: the mesh-free nature allowed one to model only the material parts in an unbounded domain composed of large void regions and to deal with highly distorted configurations and large density variations for which classical Eulerian methods were not adapted. The ease to implement an SPH model with complex physics made it quite enticing to deal with violent phenomena with non linear behaviors. SPH was further applied in solid mechanics for large deformation, impact and fractures of materials [182, 216]. It was then applied in fluid mechanics, especially for free surface flows [262], but also to multicomponent flows as it will be further illustrated in Section 2.2 with air-water flows, sediment-laden flows, etc.

2.1.2 The SPH interpolation process

The SPH method relies on a double interpolation process detailed hereafter.

2.1.2.1 Double interpolation

Let us consider a scalar field A (equivalent reasoning can be made for vector or tensor fields) in a domain $\Omega \in \mathbb{R}^d$ equipped with an orthonormal basis $(\boldsymbol{e}_x, \boldsymbol{e}_y, \boldsymbol{e}_z)$ for the space dimension $d = 3$ (we may also work in dimension $d = 2$). For the sake of legibility, the temporal dependence is omitted. The position vector denoted $\boldsymbol{r}$ is defined as:

$$\boldsymbol{r} = x\boldsymbol{e}_x + y\boldsymbol{e}_y + z\boldsymbol{e}_z \tag{2.1}$$

where (x, y, z) are the coordinates of the position in the space basis. The interpolation process is two-fold and can be read at the light of Figure 2.1. The starting point consists in writing the field value at position $\boldsymbol{r}$ as the spatial convolution product with the Dirac δ distribution:

$$A(\boldsymbol{r}) = \int_{\Omega} A(\boldsymbol{r}')\, \delta(\boldsymbol{r} - \boldsymbol{r}')\, d\boldsymbol{r}' \tag{2.2}$$

where $\delta(\boldsymbol{r}) = \delta(x)\delta(y)\delta(z)$, the Dirac δ distribution being zero everywhere except at the origin, where it is infinite, and satisfying:

$$\int_{-\infty}^{+\infty} \delta(x)\, dx = 1 \tag{2.3}$$

Continuous interpolation: the smoothing step. As the Dirac δ distribution cannot be estimated numerically, it is generally approximated with a radial bell-shaped interpolation function w, herein called *kernel*, with a support of non-null measure: the value of the scalar field is computed with a continuous interpolation involving its values in a d-ball $\Omega_{\boldsymbol{r}}$ parametrized by the *smoothing length* h around the position of interest $\boldsymbol{r}$. It reads:

$$[A]_c(\boldsymbol{r}) = \int_{\Omega_{\boldsymbol{r}}} A(\boldsymbol{r}')\, w(\boldsymbol{r} - \boldsymbol{r}')\, d\boldsymbol{r}' \tag{2.4}$$

The properties and choice of the kernel function are detailed in Section 2.1.2.2. The number of particles within the kernel support is conditioned by the ratio of the smoothing length h over the particle diameter δr.

Discrete interpolation: the sampling step. The continuous medium is sampled into a set $\mathcal{F}$ of material points, hereafter called 'particles', with physical properties of mass, volume, velocity, pressure, etc. They form interpolation points for the previously-written continuous interpolation. The discrete interpolation resulting from the approximation of the integral (2.4) by a discrete

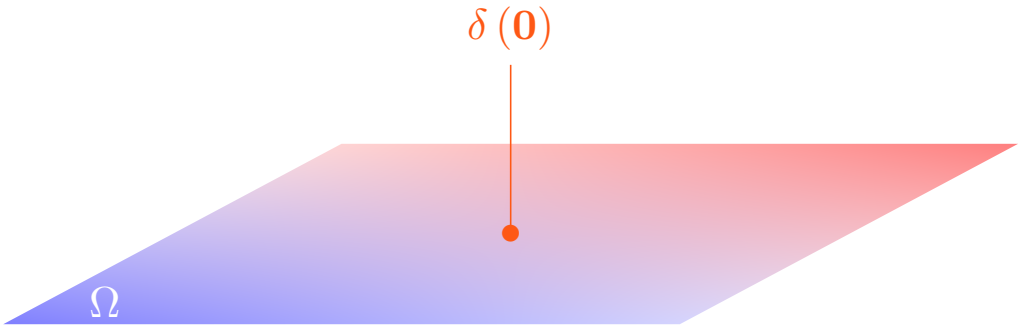

(a) Dirac convolution

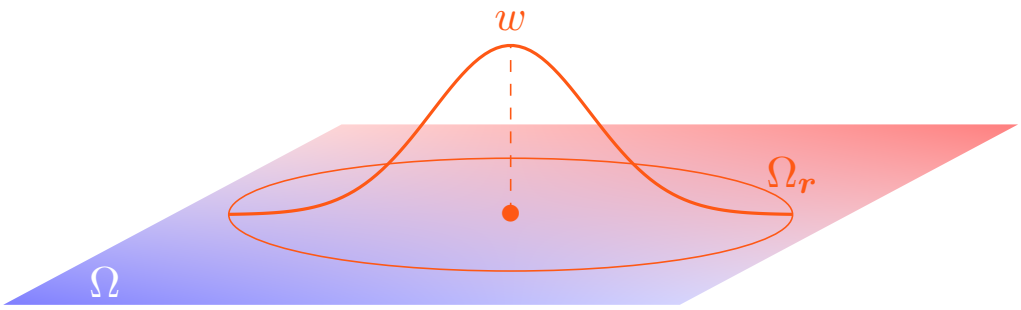

(b) Continuous interpolation

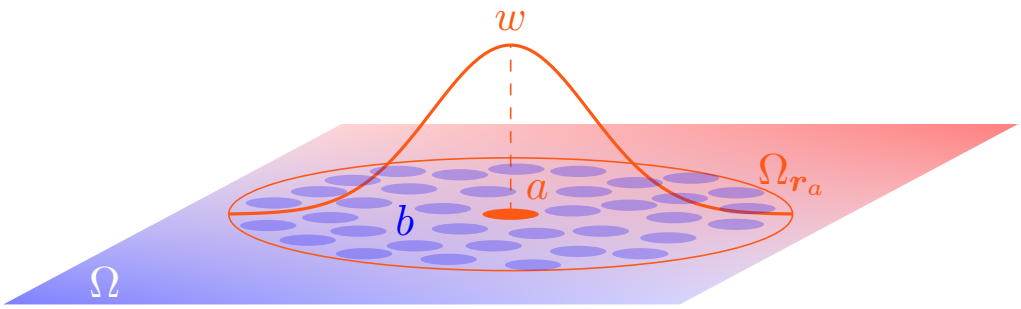

(c) Discrete interpolation

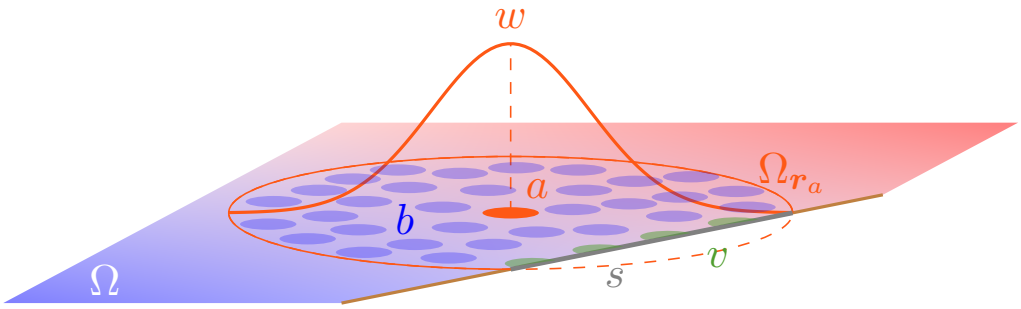

(d) Wall intersecting particle support

Figure 2.1: SPH interpolation process (case $d = 2$).

sum over the neighboring particles b within the support of the particle a at position $\boldsymbol{r}_a$ reads:

$$[A]_d(\boldsymbol{r}_a) = \sum_{b \in \mathcal{F}} V(\boldsymbol{r}_b) A(\boldsymbol{r}_b) w(\boldsymbol{r}_a - \boldsymbol{r}_b) \tag{2.5}$$

where $V(\boldsymbol{r}_b)$ is the volume of the particle b. To simplify the notations, from now on, the subscripts a, b will refer to the particles so that for any field $A_b = A(\boldsymbol{r}_b)$. With this notation, the discrete interpolation will finally write:

$$A_a = \sum_{b \in \mathcal{F}} V_b A_b w_{ab} \tag{2.6}$$

where $w_{ab} = w(\boldsymbol{r}_a - \boldsymbol{r}_b)$. In the present work, SPH particles are initially distributed on a Cartesian grid with an inter-particle distance δr over the computational domain and are assigned a reference volume $V_0 = \delta r^d$ (recall d is the space dimension). Due to the weakly-compressible SPH (WCSPH) framework used in this work, volumes may slightly vary with the compressibility, so that the actual particle volume can differ from the reference one and can be linked to the particle mass m_b and density ρ_b through $V_b = m_b/\rho_b$.

2.1.2.2 Kernel function

Let us highlight some of the properties of the kernel:

- Convergence towards the Dirac δ distribution in the sense of distributions when the support size tends to zero;
- First order consistency of the continuous interpolation (2.4), for which two conditions on zeroth and first moments of the kernel should be verified:

$$\int_{\Omega_{\boldsymbol{r}}} w(\boldsymbol{r} - \boldsymbol{r}')\, d\boldsymbol{r}' = 1 \tag{2.7}$$

$$\int_{\Omega_{\boldsymbol{r}}} w(\boldsymbol{r} - \boldsymbol{r}') \quad (\boldsymbol{r} - \boldsymbol{r}')\, d\boldsymbol{r}' = \boldsymbol{0} \tag{2.8}$$

- Positive definiteness to satisfy stability conditions (avoid pairing instability) [367]. This means that the kernel Fourier transform should be positive.

Piecewise compactly-supported polynomials were built to satisfy the above properties. The 5th-order Wendland $\mathcal{C}^2$ kernel described in [382] is used in this work. Let us introduce the dimensionless radius:

$$q = \frac{|\boldsymbol{r} - \boldsymbol{r}'|}{h} \tag{2.9}$$

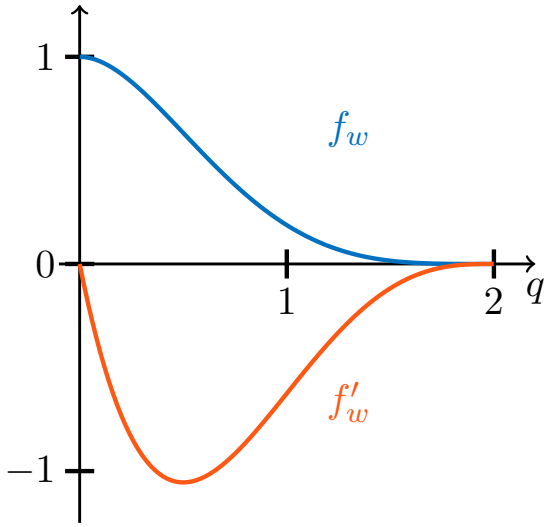

Figure 2.2: Wendland $\mathcal{C}^2$ kernel and its derivative.

A general kernel expression therefore writes:

$$w(\boldsymbol{r}-\boldsymbol{r}') = \frac{\alpha_{w,d}}{h^d} f_w(q) \tag{2.10}$$

The 5th-order Wendland kernel is defined as:

$$f_w(q) = \begin{cases} \left(1-\frac{q}{2}\right)^4 (1+2q) & 0 \le q \le 2 \\ 0 & 2 < q \end{cases} \tag{2.11}$$

The first derivative writes:

$$f'_w(q) = \begin{cases} -5q\left(1-\frac{q}{2}\right)^3 & 0 \le q \le 2 \\ 0 & 2 < q \end{cases} \tag{2.12}$$

The normalization constants used to satisfy (2.7) are:

$$\alpha_{w,2} = \frac{7}{4\pi}, \quad \alpha_{w,3} = \frac{21}{16\pi} \tag{2.13}$$

The kernel and its derivative are displayed on Figure 2.2. Following [128, 213], the ratio $h/\delta r$ is taken to 2.0 in 2D and 1.3 in 3D, what corresponds to around 50 and 270 particles respectively.

2.1.2.3 Accuracy of the interpolation

The double-step process of SPH interpolation introduces errors with respect to the continuous representation, namely an integration error E_c and a discretization error E_d defined as:

$$E_c = [A]_c(\boldsymbol{r}) - \int_{\Omega_{\boldsymbol{r}}} A(\boldsymbol{r}')\,\delta(\boldsymbol{r}-\boldsymbol{r}')\,d\boldsymbol{r}' \tag{2.14}$$

$$E_d = [A]_d(\boldsymbol{r}) - [A]_c(\boldsymbol{r}) \tag{2.15}$$

Dehnen and Aly [104] underlined the interest to consider the kernel standard deviation σ_e:

$$\sigma_e^2 = \frac{1}{d}\int_{\mathbb{R}^d} r^2 w(r)\,d\boldsymbol{r} \tag{2.16}$$

to measure the SPH smoothing distance. The integration error was computed for common SPH first and second order operators by Violeau and Fonty [365] and expanded in terms of σ_e and the derivatives of the interpolated field A. The first term of the error expansion is independent of the considered kernel and is proportional to $\frac{1}{2}\sigma_e^2$ as long as the kernel fulfills the first order consistency condition (2.8). The discretization error is practically more complex to assess as the particle arrangement is varying and generally disordered. Violeau [364] computed the error for particles on a Cartesian grid in an unbounded domain:

$$E_d = dA(\boldsymbol{r})\,\mathbb{F}[w]\left(\frac{2\sigma_e\pi}{\delta r}\right) - \frac{1}{2}\boldsymbol{\nabla}^2 A(\boldsymbol{r})\,\sigma_e^2\mathbb{F}''[w]\left(\frac{2\sigma_e\pi}{\delta r}\right) + \mathcal{O}\left(\sigma_e^3\right) \tag{2.17}$$

where $\mathbb{F}$ is the Fourier transform. For this particle arrangement, the discrete error therefore varies as σ_e^2 and reaches a lower bound equal to the first term of the right-hand side. Quinlan et al. [301] and then Amicarelli et al. [9] highlighted that a disordered arrangement of particles led to a higher numerical error.

2.1.2.4 First order differential operators

The approximation (2.4) can be applied to the gradient of an arbitrary $\mathcal{C}^1$ field A:

$$[\boldsymbol{\nabla}A]_c(\boldsymbol{r}) = \int_{\Omega\cap\Omega_{\boldsymbol{r}}} \boldsymbol{\nabla}_{\boldsymbol{r}'}A(\boldsymbol{r}')\,w(\boldsymbol{r}-\boldsymbol{r}')\,d\boldsymbol{r}' \tag{2.18}$$

where $\boldsymbol{\nabla}_{\boldsymbol{r}'}A(\boldsymbol{r}') = \dfrac{\partial A(\boldsymbol{r}')}{\partial \boldsymbol{r}'}$. The integration by part yields:

$$[\boldsymbol{\nabla}A]_c(\boldsymbol{r}) = -\int_{\Omega\cap\Omega_{\boldsymbol{r}}} A(\boldsymbol{r}')\,\boldsymbol{\nabla}_{\boldsymbol{r}'}w(\boldsymbol{r}-\boldsymbol{r}')\,d\boldsymbol{r}' - \oint_{\partial\Omega\cap\Omega_{\boldsymbol{r}}} A(\boldsymbol{r}')\,w(\boldsymbol{r}-\boldsymbol{r}')\,\boldsymbol{n}(\boldsymbol{r}')\,d\Gamma' \tag{2.19}$$

where $\boldsymbol{n}(\boldsymbol{r}')$ is the inward unit vector normal to the surface element $d\Gamma'$ of the domain boundary $\partial\Omega$. If the interpolation point $\boldsymbol{r}$ is sufficiently far from the boundaries so that $\partial\Omega\cap\Omega_{\boldsymbol{r}} = \varnothing$, due

to the compact support property of the kernel, the boundary term disappears. As the kernel is radial, its gradient is antisymmetric and one finally gets:

$$[\boldsymbol{\nabla} A]_c(\boldsymbol{r}) = \int_{\Omega_{\boldsymbol{r}}} A(\boldsymbol{r}')\, \boldsymbol{\nabla}_{\boldsymbol{r}} w(\boldsymbol{r} - \boldsymbol{r}')\, d\boldsymbol{r}' \tag{2.20}$$

A first attempt of the discrete SPH gradient therefore writes:

$$\boldsymbol{G}_a\{A_b\} = \sum_{b\in\mathcal{F}} V_b A_b \boldsymbol{\nabla} w_{ab} \tag{2.21}$$

where the discrete kernel gradient $\boldsymbol{\nabla}_{\boldsymbol{r}_a} w_{ab}$ has been denoted $\boldsymbol{\nabla} w_{ab}$ for the sake of legibility. The relation (2.21) is a possible discrete SPH approximation of the continuous gradient, among others. One can see that the gradient of a constant field is not null. To circumvent this issue, one can use the following identity:

$$\boldsymbol{\nabla} A = \frac{1}{B^k}\left[\boldsymbol{\nabla}\left(B^k A\right) - A\boldsymbol{\nabla} B^k\right] \tag{2.22}$$

to get the following symmetric (with respect to the particles indices) expression of the SPH gradient as detailed in Appendix A:

$$\boldsymbol{G}_a^{-,k}\{A_b\} = -\frac{1}{\rho_a^{2k}} \sum_{b\in\mathcal{F}} V_b \left(\rho_a\rho_b\right)^k (A_a - A_b)\, \boldsymbol{\nabla} w_{ab} \tag{2.23}$$

With $B = \rho$ and $k = 1$, the latter formula yields:

$$\boldsymbol{G}_a^{-,1}\{A_b\} = -\frac{1}{\rho_a} \sum_{b\in\mathcal{F}} m_b (A_a - A_b)\, \boldsymbol{\nabla} w_{ab} \tag{2.24}$$

The zero-order consistency is then guaranteed and hinders spurious kinetic energy production when applied to the velocity field. However, an important feature for the momentum equation is to enforce linear momentum conservation. In this prospect, an antisymmetric formulation of the SPH gradient is required to fulfill the action-reaction principle. Using the relation:

$$\boldsymbol{\nabla} A = B^k \boldsymbol{\nabla}\left(\frac{A}{B^k}\right) + \frac{A}{B^k}\boldsymbol{\nabla} B^k \tag{2.25}$$

the resulting SPH gradient writes:

$$\boldsymbol{G}_a^{+,k}\{A_b\} = \sum_{b\in\mathcal{F}} V_b \frac{\rho_b^{2k} A_a + \rho_a^{2k} A_b}{\left(\rho_a\rho_b\right)^k} \boldsymbol{\nabla} w_{ab} \tag{2.26}$$

With $B = \rho$ and $k = 1$, the latter formula writes:

$$\boldsymbol{G}_a^{+,1}\{A_b\} = \rho_a \sum_{b\in\mathcal{F}} m_b \left(\frac{A_a}{\rho_a^2} + \frac{A_b}{\rho_b^2}\right) \boldsymbol{\nabla} w_{ab} \tag{2.27}$$

The total momentum time evolution, in presence of the pressure gradient only and for constant particle masses, writes:

$$\frac{d}{dt}\sum_{a\in\mathcal{F}} m_a \boldsymbol{v}_a = m_a \sum_{a\in\mathcal{F}} \frac{d\boldsymbol{v}_a}{dt} = -\sum_{a\in\mathcal{F}}\sum_{b\in\mathcal{F}} m_a m_b \left(\frac{A_a}{\rho_a^2} + \frac{A_b}{\rho_b^2}\right) \boldsymbol{\nabla} w_{ab} = 0 \tag{2.28}$$

Similarly the total angular momentum is preserved [296]. Using different values of k, one can see that an infinity of SPH gradient operators can be derived. The choice is driven by the prominent feature searched, often as a trade-off between accuracy and conservation properties [296]. This question shall be further investigated in Section 2.2. The same reasoning can be developed for the divergence operator and one gets the following possible discrete operators:

$$D_a\{\boldsymbol{A}_b\} = \sum_{b\in\mathcal{F}} V_b \boldsymbol{A}_b \cdot \boldsymbol{\nabla} w_{ab} \tag{2.29}$$

$$D_a^{-,1}\{A_b\} = -\frac{1}{\rho_a}\sum_{b\in\mathcal{F}} m_b \left(\boldsymbol{A}_a - \boldsymbol{A}_b\right) \cdot \boldsymbol{\nabla} w_{ab} \tag{2.30}$$

$$D_a^{+,1}\{A_b\} = \rho_a \sum_{b\in\mathcal{F}} m_b \left(\frac{\boldsymbol{A}_a}{\rho_a^2} + \frac{\boldsymbol{A}_b}{\rho_b^2}\right) \cdot \boldsymbol{\nabla} w_{ab} \tag{2.31}$$

An interesting property of the operators $\boldsymbol{G}_a^+$ and D_a^- is their skew-adjointness [364] that yields energy conservation as long as time is treated as a continuous variable [296].

If a precise first-order consistent operator is needed, an option is to use renormalized operators [32] by introducing the renormalization matrix:

$$\boldsymbol{M}_a = \left[t \left(\sum_{b\in\mathcal{F}} V_b \boldsymbol{r}_{ab} \otimes \boldsymbol{\nabla} w_{ab} \right) \right]^{-1} \tag{2.32}$$

The resulting modified gradient writes:

$$\boldsymbol{G}_a^R\{A_b\} = -\sum_{b\in\mathcal{F}} V_b \left(A_a - A_b\right) \boldsymbol{M}_a \cdot \boldsymbol{\nabla} w_{ab} \tag{2.33}$$

2.1.2.5 Second order differential operators

The momentum equation, together with the k and ϵ diffusion terms in the system (1.122), require SPH forms of the second order derivative operators. Let us first focus on the Laplacian $\boldsymbol{\nabla}^2$. If we

proceed as in the preceding section, we get:

$$L_a\{A_b\} = \sum_{b\in\mathcal{F}} A_b \boldsymbol{\nabla}^2 w_{ab} \tag{2.34}$$

However, this formula is reported to be really sensitive to the particle disorder [265] and is not antisymmetric, thus breaking momentum conservation. Cummins and Rudman [94] suggested to write the Laplacian as:

$$L_a\{A_b\} = D_a\{\boldsymbol{G}_b\{A_c\}\} \tag{2.35}$$

so that it is consistent with the first order formulation of differential operators. However this approach is both computationally expensive and subject to checker-board instability development due to the collocated nature of SPH [94]. Let us consider the general expression of a diffusion term applied to the $\mathcal{C}^2$ field A with a diffusion coefficient B possibly variable in space $\mathcal{C}^1$. Morris et al. [274] followed the decomposition (2.35) but with a finite difference approximation of the gradient. The second order operator is made symmetric using the equality:

$$\boldsymbol{\nabla}\cdot(B\boldsymbol{\nabla}A) = B\boldsymbol{\nabla}A\cdot\boldsymbol{\nabla}1 + \boldsymbol{\nabla}\cdot(B\boldsymbol{\nabla}A) \tag{2.36}$$

The continuous integration writes:

$$\begin{aligned}\left[\boldsymbol{\nabla}\cdot(B\boldsymbol{\nabla}A)\right]_c(\boldsymbol{r}) = &\int_{\Omega\cap\Omega_{\boldsymbol{r}}} \left[B(\boldsymbol{r})\,\boldsymbol{\nabla}_{\boldsymbol{r}}A(\boldsymbol{r}) + B(\boldsymbol{r}')\,\boldsymbol{\nabla}_{\boldsymbol{r}'}A(\boldsymbol{r}')\right]\cdot\boldsymbol{\nabla}_{\boldsymbol{r}}w(\boldsymbol{r}-\boldsymbol{r}')\,d\boldsymbol{r}' \\ &- \oint_{\partial\Omega\cap\Omega_{\boldsymbol{r}}} \left[B(\boldsymbol{r})\,\boldsymbol{\nabla}_{\boldsymbol{r}}A(\boldsymbol{r}) + B(\boldsymbol{r}')\,\boldsymbol{\nabla}_{\boldsymbol{r}'}A(\boldsymbol{r}')\right]\cdot\boldsymbol{n}(\boldsymbol{r}')\,w(\boldsymbol{r}-\boldsymbol{r}')\,d\Gamma'\end{aligned} \tag{2.37}$$

The finite difference approximation of the gradient writes:

$$B(\boldsymbol{r})\,\boldsymbol{\nabla}A(\boldsymbol{r})\cdot(\boldsymbol{r}-\boldsymbol{r}') \approx \overline{B}(\boldsymbol{r},\boldsymbol{r}')\left[A(\boldsymbol{r})-A(\boldsymbol{r}')\right] \approx -B(\boldsymbol{r}')\,\boldsymbol{\nabla}A(\boldsymbol{r}')\cdot(\boldsymbol{r}-\boldsymbol{r}') \tag{2.38}$$

where $\overline{B}$ stands for a mean diffusion coefficient that can be computed with an arithmetic mean:

$$\overline{B}(\boldsymbol{r},\boldsymbol{r}') = \frac{1}{2}\left(B(\boldsymbol{r}) + B(\boldsymbol{r}')\right) \tag{2.39}$$

or a harmonic mean:

$$\overline{B}(\boldsymbol{r},\boldsymbol{r}') = \frac{2B(\boldsymbol{r})\,B(\boldsymbol{r}')}{B(\boldsymbol{r}) + B(\boldsymbol{r}')} \tag{2.40}$$

The harmonic mean proved to give better results than the arithmetic mean for shear stress continuity across interfaces [170] that is particularly important for multifluid flows with different viscosities. Let us now consider that we are far form boundaries. Substituting (2.38) in (2.37), the second order operator then writes:

$$\left[\boldsymbol{\nabla}\cdot(B\boldsymbol{\nabla}A)\right]_c(\boldsymbol{r}) = 2\int_{\Omega\cap\Omega_{\boldsymbol{r}}} \overline{B}(\boldsymbol{r},\boldsymbol{r}')\,\frac{A(\boldsymbol{r})-A(\boldsymbol{r}')}{(\boldsymbol{r}-\boldsymbol{r}')^2}\,(\boldsymbol{r}-\boldsymbol{r}')\cdot\boldsymbol{\nabla}_{\boldsymbol{r}}w(\boldsymbol{r}-\boldsymbol{r}')\,d\boldsymbol{r}' \tag{2.41}$$

The associated discrete SPH second order operator is then:

$$L_a\{B_b, A_b\} = 2\sum_{b\in\mathcal{F}} V_b \overline{B}_{ab} \frac{A_a - A_b}{r_{ab}^2} \boldsymbol{r}_{ab} \cdot \boldsymbol{\nabla} w_{ab} \tag{2.42}$$

where $\boldsymbol{r}_{ab} = \boldsymbol{r}_a - \boldsymbol{r}_b$ and $r_{ab} = |\boldsymbol{r}_{ab}|$. This operator was reported to be inconsistent near the free surface [87]. Another approach is developed by Español and Revenga [121] and Violeau [363] to derive a second operator in case of a non-constant diffusion coefficient, that occurs especially in multiphase flows, turbulent flows with a RANS model or non-isothermal flows, of the form $\boldsymbol{\nabla} \cdot \left[B \left(\boldsymbol{\nabla} \boldsymbol{A} +^t \boldsymbol{\nabla} \boldsymbol{A}\right)\right]$:

$$L_a\{B_b, \boldsymbol{A}_b\} = \sum_{b\in\mathcal{F}} V_b \overline{B}_{ab} \left[(d+2)\left((\boldsymbol{A}_a - \boldsymbol{A}_b)\cdot \boldsymbol{e}_{ab}\right)\boldsymbol{e}_{ab} + (\boldsymbol{A}_a - \boldsymbol{A}_b)\right] \frac{\boldsymbol{r}_{ab}\cdot\boldsymbol{\nabla} w_{ab}}{r_{ab}^2} \tag{2.43}$$

where $\boldsymbol{e}_{ab} = \boldsymbol{r}_{ab}/r_{ab}$.

2.1.3 Density

Following Price [296], a pivotal question rises:

> How does one compute the density from an arbitrary distribution of point mass particles?

Once this computation defined, the SPH formulation for the equations of motion can be self-consistently derived. Let us have a look to the possible computations. Correction terms developed in the literature to tackle flows in hydrodynamics will be introduced in the Section 2.1.6. The density can be computed using the SPH interpolation (2.5) of density:

$$\rho_a = \sum_{b\in\mathcal{F}} m_b w_{ab} \tag{2.44}$$

However this computation is not adapted for free surface flows due to the truncated kernel support close to the interface. One can also chose to solve directly the continuity equation (1.6) thanks to an SPH divergence operator:

$$\frac{d\rho_a}{dt} = -\rho_a D_a\{\boldsymbol{u}_b\} \tag{2.45}$$

The latter form is tantamount to (2.44) as long as time is considered as a continuous variable, and with an appropriate choice of the SPH divergence [360]. However, Ferrand et al. [128] showed that the interpolation and discretization errors could lead to an inconsistency between the velocity and the density fields. A middle way was offered by Vila [360], differentiating (2.44) and

deriving it with respect to time:

$$\frac{d\rho_a}{dt} = \frac{d}{dt}\left(\sum_{b\in\mathcal{F}} m_b w_{ab}\right) \tag{2.46}$$

that can be integrated explicitly when particle masses are constant, avoiding integration errors, to get:

$$\rho_a^{n+1} = \rho_a^n + \sum_{b\in\mathcal{F}} m_b \left(w_{ab}^{n+1} - w_{ab}^n\right) \tag{2.47}$$

where n denotes the current time step index. The density now depends on the particle positions only.

2.1.4 Momentum equation

The momentum equation (1.13) is usually discretized with the operators defined in Sections 2.1.2.4 and 2.1.2.5 as:

$$\frac{d\boldsymbol{v}_a}{dt} = -\frac{1}{\rho_a}\boldsymbol{G}_a^{+,1}\{p_b\} + \frac{1}{\rho_a}\boldsymbol{L}_a\{\mu_b, \boldsymbol{v}_a\} + \boldsymbol{g} \tag{2.48}$$

2.1.5 Wall boundary conditions

Imposing the adequate conditions at the limits of the domain within a Lagrangian framework remains one of the Grand Challenges for the SPH rEsearch and engineeRing International Community (SPHERIC) [2], especially for open boundaries often required in practical engineering applications and for coupling with other numerical models. After a short review of the available approaches in the literature, we will give more details on the retained technique.

2.1.5.1 Classical approaches

Close to the domain boundaries, the SPH kernel happens to be truncated so that the interpolation becomes inconsistent. The boundary integral of the integration by parts used for differential operators no longer cancels. Several approaches were developed in the SPH literature. They consist in modifying the discretization, either by adding interpolation points inside the wall or by completing the stencil of the particles getting close to the boundaries.

Mirror particle approach In the approach presented by Libersky et al. [217], each fluid particle has a mirror particle across the boundary. Neumann conditions are easily enforced by giving the same value to twin particles. However, some linear extrapolations are required to impose Dirichlet conditions. It proves difficult to extend this approach to complex geometries.

Repulsive force boundary conditions As described by Monaghan [262] and refined in [267], the wall frontier is discretized with particles that allow one to impose repulsive forces to the fluid particles through a Lennard-Jones potential. While being computationally cheap, easy to implement and ensuring the wall impermeability, this method does not address the consistency of the SPH operators, which leads to inaccuracies. Spurious particle distributions and pressure profiles appear near boundaries as highlighted by Ferrand et al. [128]. It is not possible to enforce explicitly Neumann nor Dirichlet boundary conditions.

Dummy particle approach Many forms of dummy (or fictitious) particle techniques were developed in the literature. The walls are discretized with several layers of particles outside the boundary to complete the kernel support of fluid particles approaching the boundary. However, the main task relies in assigning the correct fields to these boundary particles. In the dynamic particle approach presented by Dalrymple and Knio [96], the continuity and state equations are solved for boundary particles while their velocity is set to the wall velocity. The arrangement of the layers of dummy particles is a challenge which triggers some issues for complex geometries [4].

None of these approaches allows the user to enforce proper arbitrary boundary conditions for complex boundary geometries. Ferrand et al. [128] in the WCSPH framework, followed by Leroy et al. [213] in the Incompressible SPH (ISPH) framework, suggested another option that will be used in this work: the Unified Semi-Analytical Wall boundary condition framework (USAW), developed in the next section.

2.1.5.2 The Unified Semi-Analytical Wall boundary conditions

In a bounded domain, kernel support truncation can occur: as suggested by Kulasegaram et al. [194], to restore the normalizing property of the kernel close to the walls (2.7) and (2.8), a wall renormalization factor is introduced:

$$\gamma\left(\boldsymbol{r}\right) = \int_{\Omega\cap\Omega_{\boldsymbol{r}}} w\left(\boldsymbol{r}-\boldsymbol{r}'\right) d\boldsymbol{r}' \tag{2.49}$$

with its spatial derivative:

$$\boldsymbol{\nabla}\gamma\left(\boldsymbol{r}\right) = \oint_{\partial\Omega\cap\Omega_{\boldsymbol{r}}} w\left(\boldsymbol{r}-\boldsymbol{r}'\right)\boldsymbol{n}\left(\boldsymbol{r}'\right) d\Gamma' \tag{2.50}$$

so that the continuous interpolation (2.5) becomes:

$$\left[A\right]_c^{\gamma}\left(\boldsymbol{r}\right) = \frac{1}{\gamma\left(\boldsymbol{r}\right)}\int_{\Omega\cap\Omega_{\boldsymbol{r}}} A\left(\boldsymbol{r}'\right) w\left(\boldsymbol{r}-\boldsymbol{r}'\right) d\boldsymbol{r}' \tag{2.51}$$

The corresponding discrete interpolation writes:

$$[A]_d^\gamma(\boldsymbol{r}_a) = \frac{1}{\gamma_a}\sum_{b\in\mathcal{F}} V_b A_b w_{ab} \tag{2.52}$$

Kulasegaram et al. [194] and de Leffe et al. [102] developed approximate formulation to compute γ. Feldman and Bonet [127] described the first analytical computation in simple cases. Ferrand et al. [128] and Violeau et al. [369] proposed an analytical method to compute γ in 2D and 3D respectively. A semi-analytical approach was also described by Monaco et al. [259] with non-renormalized differential operators. Using a partial Riemann solver as described by Dubois [115], Marongiu [240], Marongiu et al. [241] (employing boundary terms without γ) and de Leffe et al. [102] carried out a full discretization of the wall into a set of segments interacting with the fluid particles. This type of boundary conditions is still the object of research and improvements were done in [81, 82].

As shown by Kulasegaram et al. [194], the SPH differential operators are modified by this newly defined SPH interpolation. Ferrand et al. [128] proposed a different formulation of these operators addressing issues of [194]. Considering the new interpolation, the continuous interpolation of the gradient resulting from an integration by parts now writes:

$$\begin{aligned}[\boldsymbol{\nabla}A]_c^\gamma(\boldsymbol{r}) \quad = \quad & -\frac{1}{\gamma(\boldsymbol{r})}\int_{\Omega\cap\Omega_{\boldsymbol{r}}} A(\boldsymbol{r}')\,\boldsymbol{\nabla}_{\boldsymbol{r}'}w(\boldsymbol{r}-\boldsymbol{r}')\,d\boldsymbol{r}' \\ & -\frac{1}{\gamma(\boldsymbol{r})}\oint_{\partial\Omega\cap\Omega_{\boldsymbol{r}}} A(\boldsymbol{r}')\,w(\boldsymbol{r}-\boldsymbol{r}')\,\boldsymbol{n}(\boldsymbol{r}')\,d\Gamma'\end{aligned} \tag{2.53}$$

The boundary integral terms appearing due to the intersection of the SPH kernel support with the boundaries of the domain were computed to get consistent operators. To do so, the SPH boundary is formed of a set of boundary particles called hereafter *segments* $s \in \mathcal{S}$ used for the computation of the boundary integral, and *vertex* particles $v \in \mathcal{V}$, that are fluid particles placed at the boundary that increase the accuracy of the modified SPH operators, as displayed on Figure 2.1d. Dirichlet conditions are imposed through the vertices and Neumann conditions through the segments. The discrete counterpart of (2.53) then writes:

$$\boldsymbol{G}_a^\gamma\{A_b\} = \frac{1}{\gamma_a V_a}\sum_{b\in\mathcal{P}}\left(V_a^2A_a + V_b^2A_b\right)\boldsymbol{\nabla}w_{ab} - \frac{1}{\gamma_a V_a}\sum_{s\in\mathcal{S}}\frac{1}{V_s}\left(V_a^2A_a + V_s^2A_s\right)\boldsymbol{\nabla}\gamma_{as} \tag{2.54}$$

where $\mathcal{P} = \mathcal{F}\cup\mathcal{V}$ denotes the set of all the fluid particles, free to move $\mathcal{F}$ or moving at the wall velocity $\mathcal{V}$ and $\boldsymbol{\nabla}\gamma_{as}$ is defined as:

$$\boldsymbol{\nabla}\gamma_{as} = \int_{\partial\Omega_s\cap\Omega_{\boldsymbol{r}_a}} w(\boldsymbol{r}_a-\boldsymbol{r}')\,\boldsymbol{n}(\boldsymbol{r}')\,d\Gamma' \tag{2.55}$$

with $\partial\Omega_s$ the part of the boundary corresponding to segment s. Let us underline that vertices are truncated particles, so that their mass m shall be computed consequently, as a fraction θ of a

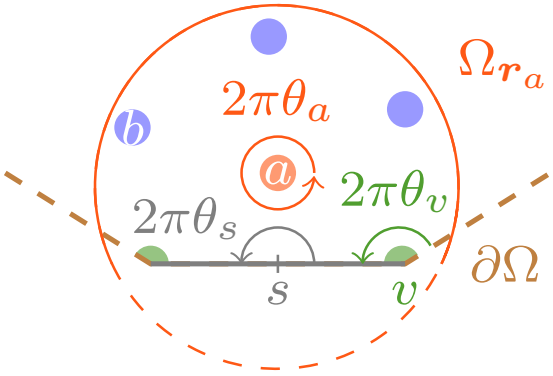

Figure 2.3: θ values for the different types of SPH particles.

reference mass $\overline{m}$. θ is computed as the ratio of the solid angle between the segments connected to the vertex and the solid angle of the d-unit ball (*i.e.* 2π for $d = 2$ and 4π for $d = 3$). Hence $\theta_v \in]0;1[$ as presented in Ghaïtanellis [143]. We define $\theta_a = 1$ for fluid particles and $\theta_s = 1/2$ for segments. An illustration is given on Figure 2.3. Following Ferrand et al. [128], $\boldsymbol{\nabla}\gamma_{as}$ is computed analytically whereas the wall renormalization γ_a is computed with the dynamic governing equation:

$$\frac{d\gamma_a}{dt} = \boldsymbol{\nabla}\gamma_a \cdot (\boldsymbol{v}_a - \boldsymbol{v}_w) \tag{2.56}$$

where $\boldsymbol{v}_w$ is the wall velocity and $\boldsymbol{\nabla}\gamma_a$ is computed analytically from:

$$\boldsymbol{\nabla}\gamma_a = \sum_{s\in\mathcal{S}} \boldsymbol{\nabla}\gamma_{as} \tag{2.57}$$

We can make a similar reasoning for the second order operator, taking into account the boundary term:

$$\begin{aligned}\left[\boldsymbol{\nabla}\cdot(B\boldsymbol{\nabla}A)\right]_c(\boldsymbol{r}) = \frac{2}{\gamma(\boldsymbol{r})}(\boldsymbol{r})\int_{\Omega\cap\Omega_{\boldsymbol{r}}} \overline{B}(\boldsymbol{r},\boldsymbol{r}')\frac{A(\boldsymbol{r})-A(\boldsymbol{r}')}{(\boldsymbol{r}-\boldsymbol{r}')^2}(\boldsymbol{r}-\boldsymbol{r}')\cdot\boldsymbol{\nabla}_{\boldsymbol{r}}w(\boldsymbol{r}-\boldsymbol{r}')\,d\boldsymbol{r}' \\ -\frac{1}{\gamma(\boldsymbol{r})}\oint_{\partial\Omega\cap\Omega_{\boldsymbol{r}}}\left[B(\boldsymbol{r})\boldsymbol{\nabla}_{\boldsymbol{r}}A(\boldsymbol{r})+B(\boldsymbol{r}')\boldsymbol{\nabla}_{\boldsymbol{r}'}A(\boldsymbol{r}')\right]\cdot\boldsymbol{n}(\boldsymbol{r}')\,w(\boldsymbol{r}-\boldsymbol{r}')\,d\Gamma'\end{aligned} \tag{2.58}$$

The associated discrete SPH second order operator is then:

$$L_a^{\gamma}\{B_b,A_b\} = \frac{2}{\gamma_a}\sum_{b\in\mathcal{P}} V_b\overline{B}_{ab}\frac{A_a-A_b}{r_{ab}^2}\boldsymbol{r}_{ab}\cdot\boldsymbol{\nabla}w_{ab} - \frac{1}{\gamma_a}\sum_{s\in\mathcal{S}}(B_a\boldsymbol{\nabla}A_a + B_s\boldsymbol{\nabla}A_s)\cdot\boldsymbol{\nabla}\gamma_{as} \tag{2.59}$$

The renormalization also modifies the density computation. From (2.52), the interpolated density (2.44) now writes:

$$\rho_a = \frac{1}{\gamma_a}\sum_{b\in\mathcal{P}} m_b w_{ab} \tag{2.60}$$

The evolution equation of the density (2.46) becomes:

$$\frac{d\gamma_a\rho_a}{dt} = \frac{d}{dt}\left(\sum_{b\in\mathcal{P}} m_b w_{ab}\right) \tag{2.61}$$

So that the exact time integration (2.46) becomes:

$$\rho_a^{n+1} = \frac{1}{\gamma_a^{n+1}}\left[\gamma_a^n\rho_a^n + \sum_{b\in\mathcal{P}} m_b\left(w_{ab}^{n+1} - w_{ab}^n\right)\right] \tag{2.62}$$

2.1.5.3 Practical enforcement of boundary conditions

Free surface Near the free surface, if the air phase is not discretized, the truncation of the kernel support makes the density tend to zero so that the pressure also tends to zero through the equation of state. The Dirichlet condition of zero pressure at the free surface is therefore automatically fulfilled. The kinematic condition of a free surface is naturally respected due to the Lagrangian framework. The absence of neighbors at the free surface also ensures the fulfillment of the dynamic condition of homogeneous Neumann for the shear stress. Therefore, the other Neumann conditions on k and ϵ do not require any special treatment.

Wall condition on pressure Following Ferrand et al. [128], the Neumann condition on pressure is computed at segments and vertices through an interpolation of the dynamic pressure:

$$p_a = \frac{\sum_{b\in\mathcal{F}} V_b\left[p_b + (\boldsymbol{r}_a - \boldsymbol{r}_b)\cdot\boldsymbol{g}\right] w_{ab}}{\sum_{b\in\mathcal{F}} V_b w_{ab}} \tag{2.63}$$

Wall condition on velocity The Dirichlet condition on velocities is imposed by giving to vertices the wall velocity. Care must be taken to write properly the boundary term of the second order operator (2.59) used for the viscous stresses $\boldsymbol{L}_a^{bound}\{\nu_b, \boldsymbol{v}_b\}$. As tested by Leroy [212] in ISPH and Ferrand et al. [128] in WCSPH, the boundary term was approximated as:

$$\boldsymbol{L}_a^{bound}\{\nu_b, \boldsymbol{v}_b\} = \frac{2}{\gamma_a}\sum_{s\in\mathcal{S}} \nu_i \left(\frac{\partial \boldsymbol{v}}{\partial \boldsymbol{n}}\right)_i |\boldsymbol{\nabla}\gamma_{as}| \tag{2.64}$$

where i is a fictitious point defined as:

$$\boldsymbol{r}_i = \frac{\boldsymbol{r}_a + \boldsymbol{r}_b}{2} \tag{2.65}$$

and, under the assumption of linear and tangential velocity, the normal derivative writing:

$$\left(\frac{\partial \boldsymbol{v}}{\partial \boldsymbol{n}}\right)_i = \frac{(\boldsymbol{v}_a - \boldsymbol{v}_s)\cdot\boldsymbol{t}_{as}}{\delta r_{as}}\boldsymbol{t}_{as} \tag{2.66}$$

with the wall tangential vector:

$$\boldsymbol{t}_{as} = \frac{(\boldsymbol{v}_a - \boldsymbol{v}_s) - [(\boldsymbol{v}_a - \boldsymbol{v}_s) \cdot \boldsymbol{n}_s]\, \boldsymbol{n}_s}{|\,(\boldsymbol{v}_a - \boldsymbol{v}_s) - [(\boldsymbol{v}_a - \boldsymbol{v}_s) \cdot \boldsymbol{n}_s]\, \boldsymbol{n}_s|} \tag{2.67}$$

and:

$$\delta r_{as} = \max\left[(\boldsymbol{r}_a - \boldsymbol{r}_s) \cdot \boldsymbol{n}_s, \delta r\right] \tag{2.68}$$

2.1.5.4 Open boundaries

If periodic conditions, as used for plane Poiseuille or Couette flows, cannot handle the desired problem, open boundaries in SPH are usually modeled thanks to buffer layers. This approach has been addressed with variations by several authors, sometimes using Riemann invariants [205, 353] in the WCSPH [8, 149, 283, 340], or in the ISPH framework [163, 167, 196]. Most recent works can handle inlets and outlets in a unified framework [269, 340]. Buffer layers consist in the addition of several layers of particles beyond the open boundaries to complete the kernels of fluid particles getting close to the inlet or outlet. In the buffer zone, physical fields are either assigned or extrapolated from the fluid domain: at the inlet, the velocity field and water depth are frequently imposed while the density is extrapolated from the bulk of the fluid domain. A particle leaving the inlet buffer layer becomes a free particle whose physical fields are left to evolve according to the governing equations, whereas when a particle enters the outlet buffer layer, it becomes a buffer particle with prescribed features before it completely exits the numerical domain.

Many variations were made on the particle feature assignment and the creation/deletion of fluid particles, especially to tackle the issue of reflecting waves by open boundaries or shocks due to sudden change of particle nature [13], as in Alvarado-Rodríguez et al. [8] that developed an outlet condition solving a wave equation for outgoing particles. Following Kunz et al. [196], Monteleone et al. [269] used mirror particles near open boundaries to set pressure boundary conditions and applied this model on a multi-domain case of blood vessels to allow different discretizations depending on the region considered.

The approach retained here follows the work of Ferrand et al. [129] and its generalization of USAW conditions with the resolution of a 1D Riemann problem at open boundaries. Open boundaries are discretized with vertex particles of varying masses and segments. The mass of vertex particles is left to evolve according to the ingoing/outgoing mass fluxes through the connected open boundary segments. If this mass exceeds an upper or lower threshold, the corresponding vertex is released in the flow as a new fluid particle, or deleted. At the inlet, the mass of the vertex increases according to the imposed flux until the critical size is reached as illustrated on Figure 2.4. At the outlet, the mass of the fluid particles crossing the segments is distributed over the vertex particles connected to the segment with an adequate weighting. This continuous management of the mass variations within the domain limits the possible perturbations of

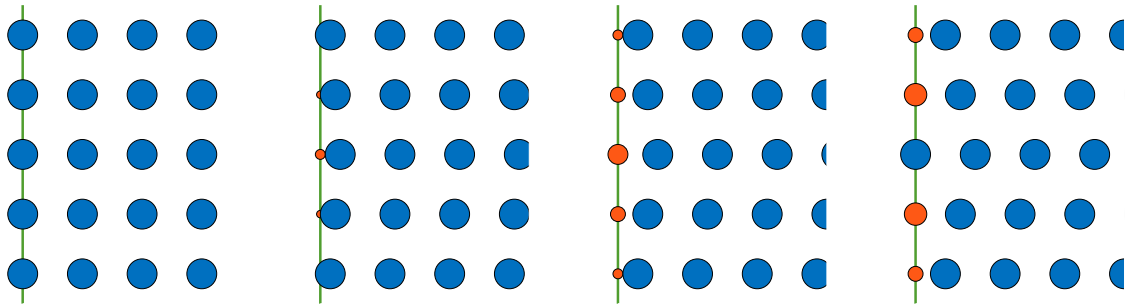

Figure 2.4: Particle creation at an inlet boundary with a parabolic profile.

the numerical resolution within the bulk of the fluid. It also leads to a correct distribution of particles near boundaries. A correction is needed in the continuity equation resolution to avoid perturbation of the density field. Though time consuming, this approach allows one to impose precisely the desired velocity or pressure profiles and deduces the missing quantities through a rigorous framework inspired from finite volume developments of Blondel et al. [26]. The practical implementation of open boundaries, adapted to the model developed in this work, will be further addressed in Section 2.2.3.

2.1.6 Numerical SPH corrections for stability

Numerical operations are often done to smooth the pressure field and get an homogeneous arrangement of the SPH particles, either by introducing additional terms in the continuity and momentum equation or by acting directly on particle positions. The common corrections used in Section 2.2 and their motivations are described.

2.1.6.1 Density diffusion

As identified by Ferrari et al. [130], and further studied by Fatehi and Manzari [123], due to the collocated nature of SPH (*i.e.* all variables are located at the same position, on SPH particles), checker-board effects appear as in grid-based methods: zero-energy modes of pressure oscillations can develop as a numerical (but not physical) solution of the discrete SPH equations and jeopardize the computations. Ferrari et al. [130] described a diffusion term to add in the continuity equation. Antuono et al. [11] presented the δ–SPH formulation, detailed in 2.1.6.6, which includes diffusion terms in the continuity and momentum equations. In grid-based methods, one of the answers was to work with staggered grids to avoid the collocation of variables. It was tested in SPH by Dyka and Ingel [116] for 1D SPH simulation of elastic bar with stresses computed at different points than SPH nodes, with an increase in computational time that is predicted to be important for multidimensional problems. Most of the literature focused on col-

located solutions. In this work, we used the correction suggested by Brezzi and Pitkäranta [39]. To stabilize the steady incompressible Navier–Stokes equations, a diffusive term was introduced in the continuity equation at the correction step of a projection method, with some similarity with the work carried out by Ferrari et al. [130] in a weakly compressible framework. Let us consider the spatially discretized continuity equation with continuous time:

$$\frac{d\rho_a}{dt} = -\rho_a D_a\{\boldsymbol{v}_b\} \tag{2.69}$$

Following the time integration scheme (2.62), one can then write:

$$\frac{\rho_a^{n+1} - \rho_a^n}{\delta t} = -\rho_a^n D_a\{\boldsymbol{v}_b^{n+1}\} \tag{2.70}$$

Neglecting the viscous contribution in the momentum equation (2.48), it can be written as:

$$\frac{\rho_a^{n+1} - \rho_a^n}{\delta t} = -\rho_a^n D_a\{\boldsymbol{v}_b^n - \frac{\delta t}{\rho_b^n}\boldsymbol{G}_b\{p_c^n\} + \delta t\boldsymbol{g}\} \tag{2.71}$$

$$\frac{\rho_a^{n+1} - \rho_a^n}{\delta t} = -\rho_a^n \left(D_a\{\boldsymbol{v}_b^n\} - D_a\{\frac{\delta t}{\rho_b^n}\boldsymbol{G}_b\{p_c^n\}\} + D_a\{\delta t\boldsymbol{G}_b\{\boldsymbol{g}\cdot\boldsymbol{r}_b^n\}\}\right) \tag{2.72}$$

We therefore introduce the diffusion term Δ:

$$\Delta^n = \rho_a^n \left(L_a\{\frac{\delta t}{\rho_b^n}, p_c^n\} - L_a\{\delta t, \boldsymbol{g}\cdot\boldsymbol{r}_b^n\}\right) \tag{2.73}$$

The diffusion only occurs between fluid particles so that no boundary term appears in the SPH Laplacian. As the Laplacian and the divergence of a gradient are slightly different due to the SPH discretization, this diffusion term is not exactly equal to the second part of the right-hand side of (2.72). Let us remark that [308] suggested to exploit this discrepancy between two approximations of the Laplacian to reduce the pressure oscillations, leading to a finite volume scheme whose SPH counterpart is close to the δ–SPH briefly addressed in Section 2.1.6.6. With our choice, the discrete continuity equation (2.62) is then modified:

$$\rho_a^{n+1} = \frac{1}{\gamma_a^{n+1}}\left[\gamma_a^n\rho_a^n + \sum_{b\in\mathcal{P}} m_b\left(w_{ab}^{n+1} - w_{ab}^n\right)\right] + \Lambda\Delta^n \tag{2.74}$$

The numerical experiments lead to chose $\Lambda = 0.1$.

2.1.6.2 Density re-initialization

As SPH particles are free to move, the total volume in the support domain of a particle can vary when solving the above evolution equation for the density, so that an inconsistency can appear between the mass, density and the region occupied by the particle [261, 274]. The normalization

of the kernel function is therefore affected and density oscillations can appear (with consequent pressure instabilities through the state equation). Density re-initialization is therefore periodically performed by some authors [77, 86] to improve the pressure field with a careful attention on the interpolation operator used:

$$\rho_a = \sum_{b\in\mathcal{F}} m_b w^\star_{ab} \tag{2.75}$$

where $w^\star$ is a kernel modified to gain better accuracy, either by a Shepard renormalization as in Shepard [324] or a Moving Least Square method as in [86]. The Shepard renormalization can indeed be used to correct the kernel in case of truncation, near boundaries or free surface and writes:

$$\Gamma_a = \sum_{b\in\mathcal{F}} V_b w_{ab} \tag{2.76}$$

We will not use these methods here.

2.1.6.3 Background pressure

A background pressure is usually added to the equation of state (1.10) to prevent the appearance of unphysical voids. From the continuous point of view, the pressure is only involved through its gradient so that it shall not modify the solution. However, numerically, as the gradient of a constant field is not zero and particles happen to be disordered, it has some effect and helps stabilizing the computations, fighting against the particle clumping known as tensile instability [264] and filling the spurious voids that can appear near the walls of a rigid body. This pressure can be related to $\rho_0 c_0^2$ even though no universal factor has been found from our experience. A too large value tends to destabilize the computations and decrease the accuracy [367]. In case of confined flows, the background pressure is usually required to ensure the stability of simulations. However, it cannot be used for free surface flows since it would break the Dirichlet pressure condition at the surface.

2.1.6.4 Particle shifting

SPH particles often reorganize in uneven distributions as they stick to streamlines as exemplified by simulations of Taylor-Green vortices [388] and voids may appear [255]. These distributions tend to decrease the accuracy of the method [9] and trigger some noise in the pressure field. Adding a background pressure as described in 2.1.6.3 allows one to prevent the appearance of voids but is generally not sufficient to get an even arrangement of particles. Shifting algorithms were developed to circumvent this issue. Monaghan [260] introduced the XSPH correction in the

equation (1.93) preserving linear and angular momenta conservation:

$$\frac{d\boldsymbol{r}_a}{dt} = \boldsymbol{v}_a - \sum_{b\in\mathcal{F}} \frac{2m_b}{\rho_a + \rho_b} \left(\boldsymbol{v}_a - \boldsymbol{v}_b\right) w_{ab} \tag{2.77}$$

In the ISPH formulations (shortly addressed in Section 2.1.7), a shifting algorithm was first introduced by Xu et al. [388] and further improved by Lind et al. [218] to handle free surfaces, particles being moved from high to low concentration zones by Fick's law of diffusion to avoid highly anisotropic distributions:

$$\delta\boldsymbol{r}_{aa'} = -\delta t \mathcal{D}_a^s \boldsymbol{G}_a\{C_b\} \tag{2.78}$$

with the index a' of the particle at the new position, a diffusion coefficient $\mathcal{D}_a^s = 2h|\boldsymbol{v}_a|$ suggested by Skillen et al. [333] and C a measure of the concentration of particles. Special treatment is made at particles identified as free surface particles to limit diffusion in the normal direction:

$$\delta\boldsymbol{r}_{aa'} = -\delta t \mathcal{D}_a^s \left[\frac{\partial C_a}{\partial \boldsymbol{\tau}}\boldsymbol{\tau} + \alpha_n \left(\frac{\partial C_a}{\partial \boldsymbol{n}} - \beta_n\right)\boldsymbol{n}\right] \tag{2.79}$$

where (α_n, β_n) are tuning parameters. The hydrodynamic variables are then corrected thanks to a Taylor series expansions:

$$A_{a'} = A_a + \left[\boldsymbol{\nabla} A\right]_a \cdot \delta\boldsymbol{r}_{aa'} + O\left(\delta\boldsymbol{r}_{aa'}^2\right) \tag{2.80}$$

but it proved to lead to negligible corrections for velocity and density [255]. However the computational cost is increased by this operation. Similar ideas were then successfully extended to WCSPH [322] and in particular to the δ–SPH approach presented in Section 2.1.6.6 by Sun et al. [337]. Variations of the technique were suggested, as Adami et al. [6] that modified the advection velocity by a background pressure term while introducing a correction term in the resolution of the momentum equation.

2.1.6.5 Artificial viscosity

Artificial viscosity was introduced in the early SPH simulations [261] with different variations to stabilize the simulations, avoid nonphysical aggregation (activated when particles are getting closer) and simulate shocks. It is defined as:

$$\pi_{ab} = -\nu_{art} \frac{\left(\boldsymbol{v}_a - \boldsymbol{v}_b\right)\cdot\boldsymbol{r}_{ab}}{r_{ab}^2 + 0.01h^2} \text{ if } \boldsymbol{v}_{ab}\cdot\boldsymbol{r}_{ab} < 0 \tag{2.81}$$

with $\nu_{art} = \frac{\alpha_f h(c_a+c_b)}{\rho_a+\rho_b}$ and the α_f parameter tuning the intensity of the diffusion. It is inserted as a force in the momentum equation (2.48):

$$\frac{d\boldsymbol{v}_a}{dt} = -\sum_{b\in\mathcal{F}} m_b \pi_{ab} \boldsymbol{\nabla} w_{ab} + \text{ other terms} \tag{2.82}$$

The choice of the tuning parameter is critical as it may cause too large numerical diffusion and large errors if it is too high. The main difference between this kind of viscous term and the physical viscous force appearing in (2.48) is that here the viscosity is purely numerical since it is decreased when refining the discretization.

2.1.6.6 δ–SPH

Molteni and Colagrossi [258] introduced the δ–SPH scheme in the WCSPH framework, further improved to handle free surfaces by Antuono et al. [11] and thoroughly investigated by Marrone et al. [242] to study violent 2D and 3D dam break flows. In the lineage of density diffusion and artificial viscosity previously detailed, it consists in the introduction of diffusive terms within the continuity and momentum equations:

$$\begin{cases} \dfrac{d\rho_a}{dt} = -\rho_a \boldsymbol{G}_a^{-,1}\{\boldsymbol{v}_b\} + \delta_s h c_0 \displaystyle\sum_{b\in\mathcal{F}} V_b \boldsymbol{\psi}_{ab} \cdot \boldsymbol{\nabla} w_{ab} \\ \dfrac{d\boldsymbol{v}_a}{dt} = -\dfrac{1}{\rho_a}\boldsymbol{G}_a^{+,0}\{p_b\} + \boldsymbol{g} + \alpha_s h c_0 \dfrac{\rho_0}{\rho_a} \displaystyle\sum_{b\in\mathcal{F}} V_b \pi_{ab} \boldsymbol{\nabla} w_{ab} \end{cases} \tag{2.83}$$

where

$$\begin{cases} \boldsymbol{\psi}_{ab} = 2\left(\rho_a - \rho_b\right) \dfrac{\boldsymbol{r}_a - \boldsymbol{r}_b}{r_{ab}^2} - \left(\boldsymbol{G}_a^R\{\rho_c\} + \boldsymbol{G}_b^R\{\rho_c\}\right) \\ \pi_{ab} = \dfrac{(\boldsymbol{v}_a - \boldsymbol{v}_b)\cdot \boldsymbol{r}_{ab}}{r_{ab}^2} \end{cases} \tag{2.84}$$

and the parameters are usually chosen as $\delta_s = 0.1$ and $\alpha_s = 0.02$. These diffusive terms decrease as the numerical accuracy increases so that one recovers the consistency of the discrete equations. The smoothing of the pressure field is effective. Compared to density diffusion approaches previously described, this correction is of first order and shall help the computations to stay in a configuration for which physics can be accurately solved. Sun et al. [338] presented a consistent shifting, however not momentum-preserving, called δ^+–SPH However, this promising approach was not retained here.

2.1.6.7 Godunov–SPH and SPH–ALE

The use of Godunov schemes, initially introduced in SPH by [175, 257, 263, 287] to handle shocks and avoid using artificial viscosity, received increased interest in the past two decades and proved

to improve the stability and generate less noisy pressure fields. The Euler conservation equations (*i.e.* no physical viscosity) are considered so as to write a one-dimensional Riemann problem between each pair (a, b) of interacting SPH particles: the resolution of this problem gives the Riemann pressure $p^\star_{ab}$ and velocity $\boldsymbol{v}^\star_{ab}$ that are then injected into the following possible set of discretized equations:

$$\begin{cases} \dfrac{d\rho_a}{dt} = 2\rho_a \displaystyle\sum_{b\in\mathcal{F}} \frac{V_b}{h} \left(\boldsymbol{v}^\star_{ab} - \boldsymbol{v}_a\right) \cdot \boldsymbol{\nabla} w_{ab} \\ \dfrac{d\boldsymbol{v}_a}{dt} = -\dfrac{2}{\rho_a} \displaystyle\sum_{b\in\mathcal{F}} \frac{V_b}{h} p^\star_{ab} \boldsymbol{\nabla} w_{ab} + \boldsymbol{g} \end{cases} \tag{2.85}$$

Some details about the Riemann problem resolution can be found in Appendix B where a partial Riemann problem is solved at a boundary to derive an open boundary formulation. More general details can be found in [287, 302] for example. Vila [360] followed by Jang et al. [179] and Leduc et al. [209] proposed an ALE (Arbitrary Lagrangian-Eulerian) framework for SPH making use of these Riemann solvers:

$$\begin{cases} \dfrac{d\boldsymbol{r}_a}{dt} = \boldsymbol{v}^0_a \\ \dfrac{dV_a}{dt} = V_a \displaystyle\sum_{b\in\mathcal{F}} V_b \left(\boldsymbol{v}^0_a - \boldsymbol{v}^0_b\right) \boldsymbol{M}_{ab} \cdot \boldsymbol{\nabla} w_{ab} \\ \dfrac{dV_a\rho_a}{dt} + 2V_a \displaystyle\sum_{b\in\mathcal{F}} V_b \rho^E_{ab} \left(\boldsymbol{v}^E_{ab} - \boldsymbol{v}^0_{ab}\right) \boldsymbol{M}_{ab} \cdot \boldsymbol{\nabla} w_{ab} = 0 \\ \dfrac{dV_a\rho_a\boldsymbol{v}_a}{dt} + 2V_a \displaystyle\sum_{b\in\mathcal{F}} V_b \left[\rho^E_{ab}\boldsymbol{v}^E_{ab} \otimes \left(\boldsymbol{v}^E_{ab} - \boldsymbol{v}^0_{ab}\right) + p^E_{ab}\right] \boldsymbol{M}_{ab} \cdot \boldsymbol{\nabla} w_{ab} = V_a\rho_a\boldsymbol{g} \end{cases} \tag{2.86}$$

where $\boldsymbol{v}^0$ is the velocity of the moving frame of reference, $\boldsymbol{M}_{ab} = \frac{1}{2}\left(\boldsymbol{M}_a + \boldsymbol{M}_b\right)$ is the symmetrized renormalization matrix of (2.32) and $\left(\rho^E_{ab}, \boldsymbol{v}^E_{ab}\right)$ is the upwind solution of the moving Riemann problem [209]. This model can benefit from the similarity with the Finite Volumes approach. To mitigate the strong dissipation introduced by such approach as a well-known effect of upwind formulations, a second order scheme like the MUSCL (Monotonic Upwind Scheme for Conservation Laws) scheme [210] including slope limiters can enhance the stability of the computations and help to handle more easily boundary conditions due to their Eulerian nature. Total mass is conserved but the masses of particles are no longer constant. As shown in (2.86), an additional equation is introduced to follow explicitly the geometrical deformation of points that shall now be considered as moving control volumes.

2.1.7 Weakly Compressible *vs.* Incompressible SPH

The modeling of incompressible flows is usually done through the weakly compressible approach in the SPH community [265], pressure being linked to the density through a state equation, usu-

ally of the form (1.10) and weak compressibility being enforced by a low Mach number. However, this approach is known to generate some very noisy pressure fields. As illustrated in Section 2.1.6, many tools were developed to tackle this issue.

However a change of formulation can help to address this question. Cummins and Rudman [94] first introduced a projection scheme from Chorin [83] in SPH to handle incompressible flows, giving birth to Incompressible SPH (ISPH). The pressure becomes a numerical result of this scheme, generally computed by solving a pressure Poisson equation that is the object of extensive research. For regular particle distributions, pressure predictions are then accurate and noise-free [213]. One drawback of the ISPH models is to require the explicit detection of the free surface to assign the dynamic boundary condition that is naturally fulfilled in the WCSPH framework.

2.1.8 Turbulence modeling

While DNS remains generally computationally too expensive (Mayrhofer et al. [246] simulated a 3D turbulent channel for a friction Reynolds number around 200), turbulence modeling can be practically achieved through Large Eddy Simulations (LES) or Reynolds-Averaged Navier–Stokes (RANS) approaches as long as wall functions can be imposed with the SPH boundary conditions. As highlighted in Chapter 1, Neumann conditions are required for the velocity, turbulent kinetic energy and dissipation rate but were not available in numerous boundary approaches, what did not prevent the developments of such turbulence models that will be addressed only shortly here.

LES Work has been done to model turbulent flows with an LES approach in SPH. A LES-based sub particle scale turbulence model using the Smagorinsky eddy viscosity was developed to study the coherent turbulent structures during the wave breaking in 2D by Lo and Shao [223] and in 2D and 3D by Rogers and Dalrymple [313]. Issa et al. [178] tested a 3D LES model to simulate non-linear water waves. It was used even for multiphase flows such as water-sediment mixtures in [327]. However the computations still remain very expensive for practical cases. Moreover, Mascio et al. [243] proved that the δ–SPH variant can be understood as a kind of LES in SPH resulting in the δ–LES–SPH model. The parameters (α_s, δ_s) were then dynamically computed for each particle based on the velocity gradients in Meringolo et al. [252].

RANS A wide variety of averaged turbulent models were implemented by Violeau and Issa [366] and applied to open channel flow and dam break cases. The study gave satisfactory results, even though the $k-\epsilon$ model proved to require some improvements to handle free surface flows correctly. Thanks to the developments of Ferrand et al. [128], Leroy [212], Leroy et al. [213] in the USAW framework, the $k-\epsilon$ model implemented in SPH provides results with similar accuracy to grid-based approaches. As highlighted in Chapter 1, this model has limits but it is simple, of wide use in the industry and gives good results in many configurations. Following Leroy [212],

the discrete SPH $k-\epsilon$ equations including buoyancy effects write:

$$\frac{dk_a}{dt} = \mathbb{P}_a + \mathbb{G}_a - \epsilon_a + \frac{1}{\rho_a} L_a\{\mu_{k,b}, k_b\} \tag{2.87}$$

$$\frac{d\epsilon_a}{dt} = \frac{\epsilon_a^n}{k_a^n}\left(C_{\epsilon_1}\mathbb{P}_a + C_{\epsilon_5}\mathbb{G}_a - C_{\epsilon_2}\epsilon_a\right) + \frac{1}{\rho_a} L_a\{\mu_{\epsilon,b}, \epsilon_b\} \tag{2.88}$$

The production term $\mathbb{P}_a$ is computed as:

$$\mathbb{P}_a = \nu_{T,a} S_a^2 \tag{2.89}$$

where the scalar mean rate of strain is defined as $S_a = \sqrt{2\boldsymbol{s}_a : \boldsymbol{s}_a}$ with:

$$\boldsymbol{s}_a = \frac{1}{2}\left[\boldsymbol{G}_a\{\boldsymbol{v}_b\} + {}^t\boldsymbol{G}_a\{\boldsymbol{v}_b\}\right] \tag{2.90}$$

and the buoyancy term write:

$$\mathbb{G}_a = -\frac{1}{\rho}\left.\frac{\partial \rho}{\partial T}\right|_p \lambda_T \boldsymbol{G}_a\{T_b\} \cdot \boldsymbol{g} \tag{2.91}$$

where T is the temperature, λ_T is the turbulent thermal diffusivity and the partial density derivative is derived at constant pressure.

2.1.9 Time integration

The time-stepping in WCSPH knows different implementations, from modified Euler to fourth order Runge-Kutta schemes. Together with the question of time integration goes the aspects of numerical stability that were extensively discussed by Violeau and Leroy [367] for WCSPH.

2.1.9.1 Explicit integration scheme

In this work, time integration is performed with the full explicit symplectic scheme detailed by Ferrand et al. [128] for conservation motivations:

1. Velocity update by operator splitting of the momentum equation:

   - Potential force step:

   $$\boldsymbol{v}_a^* = \boldsymbol{v}_a^n + \delta t\left[-\frac{1}{\rho_a^n}\boldsymbol{G}\{p_b^n\} + \boldsymbol{g}\right] \tag{2.92}$$

   - Viscous force step:

   $$\boldsymbol{v}_a^{n+1} = \boldsymbol{v}_a^* + \delta t \frac{1}{\rho_a^n}\boldsymbol{L}_a\{\nu_b + \nu_{T,b}^n, \boldsymbol{v}_b^*\} \tag{2.93}$$

2. Particle position update:

$$\boldsymbol{r}_a^{n+1} = \boldsymbol{r}_a^n + \delta t \boldsymbol{v}_a^{n+1} \tag{2.94}$$

3. Wall renormalization factor update

$$\gamma_a^{n+1} = \gamma_a^n + \delta t \left(\boldsymbol{\nabla}\gamma_a\right)^{n+1} \cdot \left(\boldsymbol{v}_a^{n+1} - \boldsymbol{v}_w^{n+1}\right) \tag{2.95}$$

4. Density computation with the continuity equation:

$$\rho_a^{n+1} = \frac{1}{\gamma_a^{n+1}} \left[\gamma_a^n \rho_a^n + \sum_{b\in\mathcal{P}} m_b \left(w_{ab}^{n+1} - w_{ab}^n\right)\right] + \Lambda\Delta^n \tag{2.96}$$

5. Pressure computation using state equation:

$$p_a^{n+1} = \frac{\rho_0 c_0^2}{\xi}\left[\left(\frac{\rho_a^n}{\rho_0}\right)^{\xi} - 1\right] + p_B \tag{2.97}$$

6. $k-\epsilon$ model resolution:

$$\frac{k_a^{n+1} - k_a^n}{\delta t} = \mathbb{P}_a^n + \mathbb{G}_a^n - \epsilon_a^n \frac{k_a^{n+1}}{k_a^n} + \frac{1}{\rho_a^n} L_a\{\mu_{k,b}^n, k_b^n\} \tag{2.98}$$

$$\frac{\epsilon_a^{n+1} - \epsilon_a^n}{\delta t} = \frac{\epsilon_a^n}{k_a^n}\left(C_{\epsilon_1}\mathbb{P}_a^n + C_{\epsilon_5}\mathbb{G}_a^n - C_{\epsilon_2}^n \epsilon_a^{n+1}\right) + \frac{1}{\rho_a^n} L_a\{\mu_{\epsilon,b}^n, \epsilon_b^n\} \tag{2.99}$$

leading to the turbulent viscosity:

$$\nu_{T,a}^{n+1} = C_\mu \frac{\left(k_a^{n+1}\right)^2}{\epsilon_a^{n+1}} \tag{2.100}$$

2.1.9.2 Numerical stability

The maximum step size for numerical stability, studied in detail in Violeau and Leroy [367], is constrained by several numbers:

- The Courant-Friedrichs-Levy (CFL) defined as:

$$\mathrm{C}_{\mathrm{CFL}} = \frac{c_0 \delta t}{\sigma_e} \tag{2.101}$$

- The viscous limitation:

$$\mathrm{C}_{\mathrm{visc}} = \frac{\nu \delta t}{\sigma_e^2} \tag{2.102}$$

- According to Ferrand et al. [128], the governing equation on γ (2.56) leads to the following

condition:

$$\mathrm{C}_\gamma = \delta t \max_{a\in\mathcal{P}} \left(|\boldsymbol{\nabla}\gamma_{as}\cdot\boldsymbol{v}_{as}|\right) \tag{2.103}$$

Hence, numerical stability is ensured for:

$$\delta t \leq \min\left(\mathrm{C}_{\mathrm{CFL}}\frac{\sigma_e}{c_0}, \mathrm{C}_{\mathrm{visc}}\frac{\sigma_e^2}{\nu}, \mathrm{C}_\gamma\frac{1}{\max_{a\in\mathcal{P}}\left(|\boldsymbol{\nabla}\gamma_{as}\cdot\boldsymbol{v}_{as}|\right)}\right) \tag{2.104}$$

One has typically $(\mathrm{C}_{\mathrm{CFL}}, \mathrm{C}_{\mathrm{visc}}, \mathrm{C}_\gamma) = (0.76, 0.45, 0.004)$ in 2D and $(0.76, 0.45, 0.001)$ in 3D.

2.2 General multiphase flow modeling in SPH

The aim of this work is to model flows involving several immiscible fluids that we shall refer to as multiphase flows. Multicomponent flows with high density ratios play a prominent role in many engineering applications and imply complex strong flow dynamics. The SPH method therefore appears as a natural way to deal with such cases, due to its ability to model highly deformed flows without specific interface tracking. If the effect of the air on the water, generally restricted to its thermodynamic pressure, can be neglected, the air phase does not need to be modeled and SPH can therefore handle free surface flows easily. However if these effects comes to be significant (when the air cavity of the dam-break is formed [86], when the water slams an offshore structure with air cushioning effect [219], even though the aerated water can be simulated as a single-phase flow with adapted physical parameters as in [321]), each phase is then modeled with a different set of particles and the interface does not have to be followed, being between particles belonging to different phases. Multifluid SPH models have been extensively studied and particular attention was paid to high density ratio cases applied to classical air-water flows at different scales from mesoscopic flows usually involving surface tension effects with droplet deformation or bubble rising into different media [5, 150, 170, 171, 192, 268, 306, 341, 396, 400], to 2D or 3D macroscopic cases such as gravity currents, Rayleigh–Taylor instability, sloshing tanks and dam breaks [78, 86, 150, 255, 268, 400]. Engineering applications were also considered: Lind et al. [219] studied the air-water wave slamming, Gong et al. [147] made an in-depth study of a wedge entry in water, Wan et al. [374] focused on the air-water turbulent mixing in hydraulic jump or over dam spillways. The graphics SPH community also considered air-water flows [174] but with the objective of realistic simulations without quantitative validation and some questionable numerical operations.

Accurately modeling multifluid phenomena including mixing with the usual SPH approach in the air-water case requires choosing a particle discretization of less than the size of an air bubble or water drop, which leads to prohibitive computational cost at the scale of practical interest for engineering applications. Another approach, less considered in the SPH literature but getting stronger interest [90, 149, 297, 305, 327], is to work with the averaged models described in Chapter 1 in which SPH particles carry the different phases with their respective volume fractions.

Whereas in multifluid SPH the particles have a once and for all assigned phase, the particles can now exchange the different phases in the mixture model. Due to the averaging process, the interface between phases may no longer be explicitly tracked when a mixture occurs. These models are of particular interest for modeling flows with small-scale interfaces (*e.g.* dispersed air phase in a water flow) and are usually implemented using the finite volume approach as in [99]. A prominent point consists in solving the volume fraction evolution properly as underlined by [316]. Nevertheless, all the methods developed in the SPH literature for multiphase computations will be of interest for the implementation of such models. In what follows, we will therefore detail the challenges of the multiphase flow modeling in SPH, give some details about how these questions are addressed by the multiphase models developed in the literature before focusing on mixture models and their specific challenges.

2.2.1 Challenges of a multifluid formulation

Multiphase flow modeling in basic SPH consists in using a set of particles for each phase without any specific treatment at the interface: kernel supports of particles near interfaces therefore encompass particles of both phases and consequent interpolations imply continuity of pressure and shear stresses. The set of discretized equations and operators presented in the Section 2.1 are applied to the different fluids. From low to moderate density ratios, this approach does not trigger significant issues [368]. However some issues appear at high density ratios: a nonphysical gap is generated near the interfaces where the pressure field gets very noisy [86]. The main challenge in the simulation of multiphase flows therefore lies in the treatment of discontinuities across the interface between fluids. As highlighted in the Section 2.1, the derivations assumed that the considered fields were $\mathcal{C}^1$. As we are no longer in this framework, densities being discontinuous, some care must be taken with the operators used. Several challenges need to be addressed.

2.2.1.1 The density computation

The approaches described in the Section 2.1.3 lead to inconsistencies due to the use of particles with significantly different densities in the computation of the interpolation or divergence operator. The density is therefore smoothed over the interface.

2.2.1.2 Continuous interpolation of the pressure gradient

The pressure gradient is generally discontinuous across the interface. Its discretization is known to cause numerical instabilities, especially as the density ratio increases as noted by Colagrossi and Landrini [86]. This issue originates from the SPH continuous interpolation process described in Section 2.1.2. The continuous interpolation for the pressure force writes:

$$\left[\frac{\boldsymbol{\nabla} p}{\rho}\right](\boldsymbol{r}) = \frac{1}{\rho(\boldsymbol{r})} \int_{\Omega_{\boldsymbol{r}}} \boldsymbol{\nabla}_{\boldsymbol{r}} p(\boldsymbol{r}')\, w(\boldsymbol{r}-\boldsymbol{r}')\, dV' \tag{2.105}$$

For a given particle a in the α phase whose kernel support $\Omega_{\boldsymbol{r}}$ is shared between Ω^α (phase α) and Ω^β (phase β), after splitting the integral between the phases and assuming an incompressible hydrostatic configuration (*i.e.* $\boldsymbol{\nabla} p = \rho^\alpha \boldsymbol{g}$ in the α phase and $\rho^\beta \boldsymbol{g}$ in the β phase), one gets:

$$\left[\frac{\boldsymbol{\nabla} p}{\rho}\right](\boldsymbol{r}) = \boldsymbol{g} + \boldsymbol{F}_{\beta\to\alpha}(\boldsymbol{r}) \text{ with } \boldsymbol{F}_{\beta\to\alpha}(\boldsymbol{r}) = \left(\frac{\rho^\beta}{\rho^\alpha} - 1\right)\boldsymbol{g}\int_{\Omega_{\boldsymbol{r}}\cap\Omega^\beta} w\left(\boldsymbol{r}-\boldsymbol{r}'\right) dV' \quad (2.106)$$

One can see that due to the density discontinuity, an additional force $\boldsymbol{F}_{\beta\to\alpha}$ appears. It cancels out if $\rho^\alpha = \rho^\beta$ (no density discontinuity) or if $\Omega_{\boldsymbol{r}} \cap \Omega^\beta = \varnothing$ (the kernel support of a particle of one phase does not overlap the other phase). This spurious force is proportional to the density ratio so that when $\rho^\beta \gg \rho^\alpha$, a large force is generated in the lighter phase and a small one in the water phase (exchange the superscripts α and β). This discrepancy leads to a gap configuration as an equilibrium position – the particles of the lighter phase reduce the overlapping of the kernel support with the heavier phase – and significant unrest in the lighter phase. Further details on this issue can be found in Appendix A.

2.2.1.3 Mixtures

The accuracy of the SPH method relies on the existence of a sufficient number of particles within the kernel support to compute the SPH interpolations. In multiphase configurations, if one does not consider separated flows, mixing is likely to happen and triggers some isolated particles of one phase in the other if the discretization is not refined enough. This situation was for example noticed for the long-time behavior of the Rayleigh–Taylor instability with an incomplete separation of phases: the pressure gradient was probably wrongly computed for isolated particles.

2.2.2 Classical multiphase SPH formulations

In case of air-water flows, classical examples include macroscopic cases such as dam break and sloshing, but also mesoscopic applications of air bubble deformation and rising that may require surface tension modeling. As we are interested in modeling flow at scales in which surface tension effects are negligible, we do not focus on this aspect in the following. Let us just underline that intrinsic surface tension, potentially larger than the physical one, can originate of the numerical implementation [166].

2.2.2.1 The state equation

The Tait equation (1.10) is of wide use for linking the pressure to the density in water. For gases, a classical link is the ideal gas law involving thermal energy that should therefore be solved thanks to an energy equation. However, one can think in including physical behavior within the state equation by adopting a specific writing. Tartakovsky et al. [342] used the Van der Waals equation of state in function of the inverse of the volume or specific volume σ to study bubbly and layered

flows in channels:

$$p = \frac{\sigma k_b T}{1 - c_1 \sigma} - c_2 \sigma^2 \tag{2.107}$$

where k_b is the Boltzman constant, T the temperature (assumed constant in their work) and c_k are Van der Waals constants. Combined with the momentum equation, it proves to be a powerful tool to include multicomponent physics (surface tension, contact line) but requires some calibrations. Nevertheless, most of the SPH literature on air-water flows considers the same state equation for both phases and avoid solving an energy equation. Colagrossi and Landrini [86] underline that, while being classical for ensuring the weak compressibility of the water phase, the choice of the Tait equation with the polytropic coefficient of 1.4 for the air phase can be seen as an adiabatic evolution for a truly compressible gas, and this coefficient should be lessened for air-water mixtures of dispersed small bubbles at 1 for an isothermal evolution. In their work, in order to keep the interface sharp, the state equation for the lighter fluid was modified by a Van der Waals cohesive pressure already used in an early work on air bubbles in water in SPH by Nugent and Posch [282]:

$$p\left(\rho\right) = p_0 \left[\left(\frac{\rho}{\rho_0} \right)^{\xi} - 1 \right] + p_B - a_\rho \rho^2 \tag{2.108}$$

where $a_\rho = 1.5 g \rho_0^\beta / \rho_0^\alpha L_c$ with L_c a characteristic length of the problem. This force shall be negligible in the bulk of the fluids and act mostly at the interface.

2.2.2.2 The simulation of interfacial flows

Colagrossi and Landrini [86] made pioneering work in the study of air-water flows at realistic density ratios. Facing the instabilities of the classical SPH method at high density ratios, a panel of numerical choices and corrections were introduced and their effects were separately investigated. The set of their discrete equations was derived following Bonet and Lok [32], leading to differential operators expressed in terms of volume rather than density $\boldsymbol{G}_a^{+,0}\{p_b\}$ in the momentum equation and $D_a^{-,1}\{\boldsymbol{v}_b\}$ in the continuity equation treated in a non-conservative way. Density re-initialization was periodically performed thanks to a first order accurate SPH interpolation of the density with a Moving-Least-Square kernel every 20 time steps. A modified version of the artificial viscosity of Monaghan [261] was also introduced, now weighted by the factor $\frac{1}{2}\left(\eta_a + \eta_b\right)$ where:

$$\eta_a = \frac{|D_a\{\boldsymbol{v}_b\}|}{|D_a\{\boldsymbol{v}_b\}| + \sqrt{\boldsymbol{s}_a : \boldsymbol{s}_a} + 10^{-4} c_a / h} \tag{2.109}$$

A key ingredient, which is also a drawback of the model, is the choice of sound speeds that should follow the following relation:

$$\frac{\rho_0^\alpha \left(c^\alpha\right)^2}{\xi^\alpha} = \frac{\rho_0^\beta (c^\beta)^2}{\xi^\beta} \tag{2.110}$$

in order for both fluids to operate in the same pressure range (required by the dynamic condition at the interface). For air-water flows, it triggers a sound speed ratio around 13 with usual values of densities and polytropic indices indicated in Chapter 1, which leads to small time steps in the air phase due to the CFL condition (2.101). Moreover the sound speed is then higher in air than in water: physics indicate the reverse behavior as the sound speed is around 343 m/s in air and 1481 m/s in water at $20°C$ with a 4.3 ratio. Let us however recall that in SPH the numerical sound speed is seen as a tool to enforce weak compressibility. If one uses unit polytropic indices in case of a linearized state equation, the ratio between numerical sound speeds becomes 28.5, decreasing even more the time step.

Coming back to Colagrossi and Landrini's work, fragmentation of the interface was noticed when modeling air bubbles. The correction of the state equation detailed in the previous section was employed. The XSPH correction described in Section 2.1.6.4 was used to prevent particles interpenetration and to regularize the computation, without taking into account the influence of the other medium in the corresponding interpolations. The effects of these corrections are thoroughly studied on dam break simulations and the results agree well with Level-Set approach computations. If they brought some significant improvements in the accuracy, they also trigger an increase in computational time.

In this prospect Mokos et al. [254] made an in-depth work on GPU acceleration and applied this model to simulate a 3D dry-bed dam break over an obstacle, showing an improvement compared to single-phase computations. Mokos et al. [255] however identified some issues at fine resolutions with the occurrence of non physical voids and phase separation on a 2D dam break. The shifting algorithm developed by Lind et al. [218], Skillen et al. [333], Xu et al. [388] is adapted by switching off the free surface correction in the air phase to allow its expansion. The correction is validated on 2D and 3D dam breaks, and a 2D sloshing case.

Colagrossi and Landrini [86] approach was also used by Gong et al. [147] to model sloshing, dam break and to carry out an in-depth study of a wedge entry with focus on the bubble formation, showing the interest of the two-phase modeling.

2.2.2.3 The specific volume formulation

The density computation introduced in Section 2.1.3 is suitable as long as masses do not vary during the computations. However the mixture model further detailed does not preserve the mass of particles. Moreover, this classical density definition leads to a smoothing at the interfaces [170]. Another way shall be considered.

Español and Revenga [121] presented a scheme in which the particle volumes were computed thanks to an SPH interpolation. Distinct from the geometrical ones, they referred to thermodynamical volumes. Tartakovsky and Meakin [341] wrote the set of equations for single-phase flow with varying masses due to a solute concentration with particle number density assimilated to

the specific volume σ, including an expression of the pressure force of the form:

$$\frac{dm_a \boldsymbol{v}_a}{dt} = -\sum_{b\in\mathcal{F}} \left(\frac{p_a}{\sigma_a^2} + \frac{p_b}{\sigma_b^2}\right) \boldsymbol{\nabla} w_{ab} + \text{ other terms} \tag{2.111}$$

This was further used by Hu and Adams [170] to develop another multifluid SPH model in view of mesoscopic and macroscopic flows. They rewrote the SPH equations in terms of particle specific volume that becomes a main variable of the model and allows one to handle density discontinuity across interfaces. The neighboring particles indeed no longer contribute through their density but their specific volume. Instead of interpolating the densities as in the relation (2.44), the specific volume is interpolated to get:

$$\rho_a = m_a \sigma_a = m_a \sum_{b\in\mathcal{F}} w_{ab} \tag{2.112}$$

that allows density discontinuities and exact conservation of the mass. A good computation of the positions is therefore required to have a good estimation of densities. Written in the USAW framework, it becomes:

$$\gamma_a \sigma_a = \sum_{b\in\mathcal{F}} w_{ab} \tag{2.113}$$

Following a reasoning similar to the one developed by Vila [360], the differentiation leads to:

$$\frac{d\gamma_a \sigma_a}{dt} = \frac{d}{dt}\left(\sum_{b\in\mathcal{F}} w_{ab}\right) \tag{2.114}$$

And finally, the temporal explicit integration making this formulation suitable for free surface flows writes:

$$\sigma_a^{n+1} = \frac{1}{\gamma_a^{n+1}} \left[\gamma_a^n \sigma_a^n + \sum_{b\in\mathcal{F}} \left(w_{ab}^{n+1} - w_{ab}^n\right)\right] \tag{2.115}$$

Back to Hu and Adams' work, the pressure gradient now writes:

$$\boldsymbol{G}_a\{p_b\} = \sigma_a \sum_{b\in\mathcal{F}} \left(\frac{p_a}{\sigma_a^2} + \frac{p_b}{\sigma_b^2}\right) \boldsymbol{\nabla} w_{ab} \tag{2.116}$$

A new viscous term, analogous to Español and Revenga's one, is formulated to handle viscosity discontinuities and guarantees the continuity of shear stress across the interface thanks to a harmonic mean of the viscosities, but does not preserve angular momentum:

$$\boldsymbol{F}_V = \frac{1}{m_a} \sum_{b\in\mathcal{F}} \frac{2\mu_a\mu_b}{\mu_a + \mu_b} \left(\frac{1}{\sigma_a^2} + \frac{1}{\sigma_b^2}\right) \left[\left(\boldsymbol{e}_{ab} \cdot \boldsymbol{v}_{ab}\right) \boldsymbol{e}_{ab} + \boldsymbol{v}_{ab}\right] \frac{\boldsymbol{r}_{ab} \cdot \boldsymbol{\nabla} w_{ab}}{r_{ab}^2} \tag{2.117}$$

Some mesoscopic developments regarding surface tension and interface slip are also developed. Droplet oscillation, three-phase interaction with contact line and mesoscopic flows in channels

are considered (droplet deformation, moving contact line). Ghaïtanellis et al. [145] extended this formulation to the USAW framework by renormalizing the operators thanks to the coefficient (2.49). Further details will be given in Chapter 3 as this formulation will be the ground of our mixture model. Further developments were made in the ISPH framework by Hu and Adams [171, 172] and are presented in the dedicated Section 2.2.2.6. Their model was recently modified by Krimi et al. [192] by using the renormalization matrix (2.32) to get first order consistency of the surface tension model so as to improve the interface stability. To smooth the initial transients of gravitational flow simulations, a particle redistribution approach smoothing the velocity and particle distribution was described: the gravity is gradually applied considering that all particles belong to the heavier phase to handle multiphase flows initialization. The model is then successfully applied to droplet deformation, two-phase hydrostatic pressure case up to a 100 density ratio, Rayleigh–Taylor instability and rising bubbles. These works were nevertheless not applicable for free surface flows.

2.2.2.4 Kernel renormalization and repulsive force

In a formulation with similarities with Hu and Adams [170] by using the specific volumes and Colagrossi and Landrini [86] with respect to the choices of sound speeds and differential operators, Grenier [149] and Grenier et al. [150] derived from Lagrangian variational principles a multifluid SPH model that was further applied in Grenier et al. [151] to model viscous and surface tension effects as in a viscous bubbly flow in an oil-water separator. In particular, free surface flows can be treated thanks to a kernel renormalization by the Shepard filter (2.76) with consequent modifications of the discrete differential operators. The density is computed thanks to an interpolation involving particles of the same phase:

$$\rho_a = \frac{1}{\Gamma_a^\alpha} \sum_{b\in\alpha} m_b w_{ab} \quad \text{with} \quad \Gamma_a^\alpha = \sum_{b\in\alpha} V_b w_{ab} \tag{2.118}$$

Volume distribution therefore needs to be known to compute the density and is followed thanks to a continuity equation on volumes. The direct relation between mass, density and volume is relaxed through this process. The differential operators then writes:

$$D_a\{\boldsymbol{v}_b\} = -\frac{1}{\Gamma_a^\alpha} \sum_{b\in\mathcal{F}} V_b \left(\boldsymbol{v}_a - \boldsymbol{v}_b\right) \cdot \boldsymbol{\nabla} w_{ab} \tag{2.119}$$

$$\boldsymbol{G}_a\{p_b\} = -\sum_{b\in\mathcal{F}} V_b \left(\frac{p_a}{\Gamma_a^\alpha} + \frac{p_b}{\Gamma_b^\alpha}\right) \cdot \boldsymbol{\nabla} w_{ab} \tag{2.120}$$

The viscous force is modified:

$$\boldsymbol{F}_V = \sum_{b\in\mathcal{F}} V_b \frac{8\mu_a\mu_b}{\mu_a+\mu_b} \left(\frac{1}{\Gamma_a^\alpha} + \frac{1}{\Gamma_b^\alpha}\right) \frac{\boldsymbol{r}_{ab}\cdot\boldsymbol{\nabla} w_{ab}}{r_{ab}^2} \tag{2.121}$$

The resulting system preserves linear and angular momentum. Surface tension was modeled but when it happened to be negligible, spurious fragmentation could occur. An empirical repulsive force bearing some similarities with that of Monaghan [264] was therefore added to the pressure gradient by summing on particles belonging to the other phase:

$$\boldsymbol{F}_R = \epsilon_I V_b \sum_{b\in\beta} \left(\left| \frac{p_a}{\Gamma_a^\alpha} \right| + \left| \frac{p_b}{\Gamma_b^\alpha} \right| \right) \boldsymbol{\nabla} w_{ab} \tag{2.122}$$

with ϵ_I between 0.01 and 0.1. This model was successfully applied to an air bubble rising in water, the Rayleigh–Taylor instability and gravity currents, and the ability of the model to deal with a free surface was illustrated. However, density ratios considered were lower than 2.

Monaghan and Rafiee [268] detailed an SPH multiphase flow modeling at high density ratios. It includes a repulsion term between the phases similar to the one of Grenier et al. [150] lower than 8% of the pressure force for high density ratios. The sound speed ratio required is around three times smaller than the one required from [86] although no general relation is found. Surface tension effects are neglected. The pressure gradient (2.27) is used. An artificial viscosity similar to (2.81) is employed with a modified $\nu_{art} = \frac{\nu_a \nu_b (\rho_a + \rho_b)}{\rho_a \nu_a + \rho_b \nu_b}$ in case of high viscosity ratios. An initial damping phase is applied to reduce the potential perturbations, considering if necessary the lighter phase as a rigid body. This model is applied to elliptical region deformation, interfacial waves up to a density ratio of 100, the Rayleigh–Taylor instability and gravity currents with density ratios from 1.33 to 20. These results prove to be in good agreement with numerical and experimental data from the literature.

2.2.2.5 Adverse phase ghost particles

Chen et al. [78] described an SPH model for multiphase flow with large density differences. Artificial viscosity is employed. For a given particle, all the neighbors belonging to another phase in the support of the kernel are considered as interpolation points of the same phase, *i.e.* fluid particles of a different phase are treated as ghost particles for which only information continuous across the interface is retained. Density re-initialization adapted to this assumption by using the inverse state equation for particles of the other phase is employed. A cut-off value is given to the particle density to avoid negative pressures. Pressure gradient was computed as a basic SPH gradient (2.21). Same sound speeds were taken in both fluids, ensuring a weak compressibility of the water phase, and background pressure was used. This model was tested on the Rayleigh–Taylor instability, a gravity current and a dam break. The model indeed results in a smooth pressure field even close to the interface and reasonable agreement with the positions of the developing flows and the pressure evolution in the dam break problem. The continuity of the pressure force is however not ensured, which may cause numerical instabilities in the long term. Significant diffusion is present, with consequent delays in dynamic behaviors, so that further modifications were performed by Zheng and Chen [400] as described in Section 2.2.2.8.

Zhou et al. [401] incremented on the model of Chen et al. [78] by introducing a pressure correction derived from a small interface deformation assumption and tuned by a case-dependent parameter c_p (that depends on the interface deformation). The pressure contributions of the dense phase in the light phase computation are then computed as:

$$p_{b,new} = p_b - c_p \left(\frac{\rho_{0,a}}{\rho_{0,b}} - \rho_{0,b} \right) (p_a - p_b) \tag{2.123}$$

This corrected pressure is used in the density re-initialization step to avoid nonphysical pressure transfers from the dense to the light fluids. Numerical applications of air-water flows are then considered. A two-phase hydrostatic pressure case was successfully simulated without instabilities developing. The model was then applied to sloshing and dam break, and got a reasonable agreement with experimental data with some improvements. Finally a water entry test case was considered and no significant discrepancy was noticed with the correction.

Following Chen et al. [78], Zhu et al. [402] used the renormalization matrix (2.32) for kernel gradients used in all differential operators. A repulsive interface force is introduced like in Grenier et al. [150] but with the basic SPH gradient (2.21). A good agreement with the two-phase dam break time history of the pressure is obtained. The Rayleigh–Taylor instability growth is satisfactorily reproduced but interface fragmentation occurs. Good results are obtained for the shape of an air bubble rising in water.

2.2.2.6 Incompressible multifluid SPH

Few works have been performed in ISPH to model multiphase flows: we will focus hereafter on recent attempts. Hu and Adams [171] developed a multiphase ISPH model ensuring zero variation of the density through a fractional time-step integration algorithm within the framework of specific volume formulation presented in the Section 2.2.2.3. To ensure the continuity of the pressure force across the interface, an inter-particle averaged reasoning is introduced and suggests the following form for the gradient operator:

$$\boldsymbol{G}_a\{p_b\} = \frac{1}{m_a} \sigma_a \sum_{b \in \mathcal{F}} \left(\frac{1}{\sigma_a^2} + \frac{1}{\sigma_b^2} \right) \frac{\rho_a p_b + \rho_b p_a}{\rho_a + \rho_b} \boldsymbol{\nabla} w_{ab} \tag{2.124}$$

Chen et al. [78] considered that the inter-particle pressure of Hu and Adams [171] reduces the interaction of phases to the action of air particles on the water phase and not the reverse way: for a pair of particles with $a \in \alpha$ and $b \in \beta$

$$\tilde{p}_{ab} = \frac{\rho_a p_b + \rho_b p_a}{\rho_a + \rho_b} \approx \frac{\rho_b}{\rho_a + \rho_b} p_a \approx p_a \tag{2.125}$$

This reasoning is approximate and depends on the discretization retained: it indeed considers that p_b is not too large compared to p_a which is not true for coarse discretizations. The two-way

coupling is still present. Taylor–Green flow, capillary waves and Rayleigh–Taylor instability are considered by Hu and Adams [170] for validation and highlight good agreement with theory and references in the literature. This work is extended by the same authors [172] with a correction in the fractional time-step algorithm that allows one to deal with high density ratio flows, again applied to droplet deformation and Rayleigh–Taylor instability. The specific volume formulation combined with the above pressure gradient is further applied to 2D and 3D droplet deformations at high density ratios by Adami et al. [5] with a new surface tension formulation. The viscous force is modeled through:

$$\boldsymbol{F}_V = \frac{1}{m_a} \sum_b \frac{2\mu_a \mu_b}{\mu_a + \mu_b} \left(\frac{1}{\sigma_a^2} + \frac{1}{\sigma_b^2} \right) \boldsymbol{v}_{ab} \frac{\boldsymbol{r}_{ab} \cdot \boldsymbol{\nabla} w_{ab}}{r_{ab}^2} \tag{2.126}$$

Shao [323] presented two ISPH models applied to low density ratio flows: a coupled one applying standard single-fluid ISPH techniques irrespective of the phases without any interface treatment and an uncoupled one for which each phase is treated independently before coupling through pressure and shear stress continuities. These models were tested on a gravitational underflow in a flume and an horizontal lock exchange flow. The decoupled model performed well on the whole range of density ratios while the coupled model failed at modeling the highest density ratios equal to 1.3. Some work was required to handle the resolution of the PPE at high density ratios. Zainali et al. [396] developed a 2D ISPH model with an improved interface treatment applied to high density (1000) and viscosity (100) ratios: a different kernel was used for the surface tension force eliminating the interphase penetration and a renormalized pressure gradient (2.33) was employed. Transport parameters of constituents across the interface were smoothed when required in the computations to prevent numerical instabilities. This model was successfully applied to the simulation of single vortex flow, bubble or droplet deformation and bubble rising, as a very good agreement is obtained on the shapes of the structures studied with references of the literature. In the following, Rezavand et al. [306] modeled high density ratio flows with ISPH but introducing repulsive forces of Monaghan and Rafiee [268] between the phases to maintain the interface sharpness. Two-phase Poiseuille flow, Rayleigh–Taylor instability, droplet oscillation and rising bubbles were considered and compared well with the analytical solutions and reference results of the literature. King and Lind [187] developed a partitioned approach for high density ratio flows in ISPH by separately modeling liquid and gas and coupling the phases with momenta-conserving interfacial boundary conditions: the liquid drives the kinematics of the gas phase at the interface while the gas gives an interfacial stress to the liquid. Contrary to Zainali et al. [396] and Rezavand et al. [306], the density and viscosity were not smoothed across the interface. An accurate pressure field was obtained on a two-phase hydrostatic pressure case. Liquid drop impact was also studied with observations more consistent with experiments than Rezavand et al.'s results. A smaller quantity of air was however entrained by the impact and these particles were then disregarded by the model. These results are promising for the use of ISPH solvers for high density ratio flows, even though the question of dispersed phase remains to be tackled, due

to the necessity to follow the interface and apply appropriate conditions on it.

2.2.2.7 Incompressible-compressible multifluid SPH

Previous works described in the WCSPH framework required to use nonphysical sound speeds to handle high density ratios. Lind et al. [220] have developed a two-phase incompressible-compressible SPH method handling a discontinuous high density ratio at the interface between air and water: the compressible air phase gave a surface pressure to the incompressible water phase and reversely the incompressible phase gave a surface velocity to the compressible one. A Fickian shifting was employed in the water phase to avoid particle clustering due to particle moving along streamlines and shift particles in a somewhat equispaced distribution. In the air phase, a conservative uncorrected gradient operator was used for pressure and a linearized state equation was employed. The density field was regularly filtered by a Shepard filter (2.76) and artificial viscosity was introduced in the momentum equation for numerical stability. This model was validated with a two-layer elliptical drop deformation, standing waves, Kelvin–Helmotz instability and a two-phase dam break. The compressibility of air being of interest for coastal and offshore engineering (wave breaking, impact and sloshing…), this work was also applied to air-water wave slam by Lind et al. [219]. Similar conclusions to the previous paragraph can however be drawn regarding this kind of approach.

2.2.2.8 Multiphase δ–SPH

Hammani et al. [158] adapted δ–SPH to the multifluid framework, replacing the continuity equation by the volumetric strain rate equation and adapting consequently the diffusion terms of the model that are computed by summing on particles of the same phase. Density is then computed thanks to an SPH interpolation. Background pressure is included. This model is successfully applied to a two-phase hydrostatic test case which proves to be stable in the long-time simulation, an oscillating drop and a dam break flow for which a smooth pressure field and a good agreement with the single phase flow is obtained until air-cushioning effects of the generated cavity are involved. Sound speeds are however still chosen according to Colagrossi and Landrini [86] work, resulting in large sound speeds in the light phase. Zheng and Chen [400] made several modifications to Chen et al. [78] model to reduce numerical diffusion. Inspired from the δ–SPH approach, a density correction is introduced to replace the density re-initialization. Compared to δ–SPH, the correction is computed with the density increment $\left(\rho^k - \rho_0^k\right)$ instead of the density thanks to the inverse state law, which should be more suitable for multiphase flows. Regarding the artificial viscosity term, a switch function is used to activate viscosity only in regions with large pressure gradient and velocities based on a threshold value for the quantity $\boldsymbol{\nabla} P \cdot \boldsymbol{v}$. The Rayleigh–Taylor instability and a solitary wave propagation along an oil–water interface were accurately modeled. Then a bubble rising compared well with Level-Set results. Air bubble oscillations highlighted the lower diffusion of the present model compared to [78]. Dam break

computations triggered a relatively smooth pressure field but interface fragmentation occurred.

2.2.2.9 Multifluid SPH–ALE and Riemann solvers

Leduc et al. [208] followed by Marongiu et al. [241] and Leduc et al. [209] extended the Riemann solvers to multiphase SPH and included surface tension. Solving Riemann problem for multiphase flows requires special care: the ALE property is used so that the velocity obtained with the Riemann solver is given to the interface velocity. Sharp interfaces can therefore be preserved and followed in a fully Lagrangian manner. Moreover high density ratio flows can be modeled in a stable way. Rafiee et al. [303] used this approach due to its ability to work with physical sound speeds, which is usually not possible in WCSPH, to model compressible inviscid two-phase flows such as wave impact on a rigid wall described in [303]. Rezavand et al. [307] extended to two-phase flows the low-dissipation Riemann solver of Zhang et al. [398] and introduced a transport velocity formulation in the light phase detailed below to compute violent 2D and 3D air-water flows (dam break, sloshing). The first point aimed at stabilizing the interface while the second allowed them to get rid of voids and spurious fragmentations: the heavy phase is then seen as a moving wall boundary by the light phase while it undergoes a variable free surface pressure. The same sound speed was used in both phases. No artificial repulsive pressure force nor density re-initialization scheme were needed. In the light phase, the density is computed thanks to the SPH interpolation of [170] and transport velocity formulation writes:

$$\tilde{\boldsymbol{v}}_a\left(t+\delta t\right)=\boldsymbol{v}_a\left(t\right)+\delta t\left(\frac{d\boldsymbol{v}_a}{dt}-p_B\frac{2}{\rho_a}\sum_{b\in\mathcal{F}}V_b\boldsymbol{\nabla}w_{ab}\right) \tag{2.127}$$

The momentum equation is then computed as:

$$\frac{d\boldsymbol{v}_a}{dt}=-\frac{2}{\rho_a}\sum_{b\in\mathcal{F}}V_b p^{\star}_{ab}\boldsymbol{\nabla}w_{ab}+\frac{1}{\rho_a}\sum_{b\in\mathcal{F}}V_b\left[\rho_a\boldsymbol{v}_a\left(\tilde{\boldsymbol{v}}_a-\boldsymbol{v}_a\right)+\rho_b\boldsymbol{v}_b\left(\tilde{\boldsymbol{v}}_b-\boldsymbol{v}_b\right)\right]\boldsymbol{\nabla}w_{ab} \tag{2.128}$$

2.2.2.10 An interface pressure gradient correction

Kruisbrink et al. [193] assimilated the spurious upward force between phases near an interface $\boldsymbol{F}_{\beta\rightarrow\alpha}$ (see equation (2.106)) to a buoyancy effect:

$$\boldsymbol{F}_{\beta\rightarrow\alpha,a}=-\left(\rho_m-\rho_a\right)V_a\boldsymbol{g} \tag{2.129}$$

where ρ_m is the density of the surrounding fluid. A quasi-buoyancy (QB) pressure gradient correction is therefore suggested:

$$\boldsymbol{F}_{QB}=\sum_{b\in\Omega_{\boldsymbol{r}}\cap\Omega^{\beta}}\left(\rho_b-\rho_a\right)V_aV_b\left(\boldsymbol{g}-\boldsymbol{a}_b\right)w_{ab} \tag{2.130}$$

where $\boldsymbol{a}_b = \boldsymbol{a}(\boldsymbol{r}_b)$ is the acceleration of the neighboring particle. A measure of the quasi-submergence of the considered particle within the other phase is computed to introduce a criterion so that true buoyancy can be taken into account and avoid to be canceled out by the above correction. The full correction writes:

$$\boldsymbol{F}_{QB} = \sum_{b \in \Omega_{\boldsymbol{r}} \cap \Omega^{\beta}} \sqrt{QS_a^{\alpha} QS_b^{\beta}} m_a m_b \left(\frac{1}{\rho_a} - \frac{1}{\rho_b} \right) (\boldsymbol{g} - \boldsymbol{a}_{ab}) \, w_{ab} \tag{2.131}$$

where

$$\boldsymbol{a}_{ab}^{n} = \frac{m_a \boldsymbol{a}_a^{n-1} + m_b \boldsymbol{a}_b^{n-1}}{m_a + m_b} \tag{2.132}$$

$$QS_a^{\alpha} = \frac{\sum_{b \in \Omega_{\boldsymbol{r}} \cap \Omega^{\beta}} \operatorname{sign}\left[(\boldsymbol{g} - \boldsymbol{a}_a) \cdot \boldsymbol{r}_{ab} \right] V_b w_{ab}}{\sum_{b \in \Omega_{\boldsymbol{r}} \cap \Omega^{\beta}} V_b w_{ab}} \tag{2.133}$$

This approach allowed them to deal with high density ratio flows and physical sound speed ratios. A stagnant air-water flow in a tank kept stable, contrary to the other approaches tested, and results on Rayleigh–Taylor instability and rising air bubble were reproduced with satisfactory accuracy. The pressure gradient, if we exclude the above-described correction, is computed following Colagrossi and Landrini [86].

2.2.3 Multifluid open boundaries in the literature

Few references of the literature addressed the question of multifluid open boundaries. Once again the challenge is two-fold: have different fluid entering or leaving the domain, possibly in contact at the inlet/outlet, and deal with high density ratios. Let us first underline that an option for inlets can be to make separate inlets for each fluid, but this assumes that there is not any mixture at the entrance. For the outlet it would imply to make sure that the fluid reaches the boundary without any mixture, for example thanks to a "decantation" reservoir. This approach requires adaptation to each geometry and is therefore not general. As described in section 2.1.5.4, the most common approach consists in using buffer layers. Grenier [149] and Grenier et al. [151], following Oger [283], introduced oil bubbles at the inlet of a water tank thanks to a buffer layer in which some bubbles are created and advected with an imposed velocity without SPH interpolation. Both velocity and pressure (compressible hydrostatic profile) are imposed at the inlet and only velocity at the outlet with a boundary pressure equal to the pressure of nearest particles. Some instabilities and wave generation issues are pointed out.

In ISPH, Kunz et al. [196], following the idea of Hirschler et al. [163] to use mirrored particles at open boundaries with a linear projection method to impose true Dirichlet boundary conditions, wrote an algorithm able to handle inflow and outflow at the same boundary and that proved to handle back-flowing water at a gas injection nozzle forming bubbles. Douillet-Grellier et al. [110]

adapted the idea of Tafuni et al. [340] to simulate the variability of two-phase flow regimes in pipes, from moderate to high density (up to 427) and viscosity (up to 32) ratios, in the multiphase framework presented by Hu and Adams [170] but had to make a separated flow enter the domain before seeing the specific pipe regime development. To keep a clean interface, the interface stress was also computed in the buffer layer. If they succeeded in reproducing different two-phase flow behaviors with respect to classical flow regime maps, they underlined that their results could be improved by a more accurate (and more complex) approach such as semi-analytical boundaries.

In the present work, we choose to extend the work of Ferrand et al. [129] to the mixture model presented before. This model has to be able to handle either separated flows or mixtures and is presented in Chapter 3.

2.3 Averaged models in SPH

Two-phase averaged models as derived in Section 1.1.4 have received a limited interest in the SPH literature. The usual averaging process indeed corresponds to an Eulerian point of view, so that the use in a Lagrangian approach triggers some specific issues, *e.g.* the loss of the intrinsic tracking of the interface due to the possible diffuse interface. However, it is not an insuperable obstacle: zones in which the interfaces are separated can be preserved if the physics and numerical implementation allow it. Moreover, if the considered phases are water and sediments, one can take advantage of the intrinsic free surface treatment to avoid modeling the air phase and still follow the deformations of the interface. As detailed further, the few references in the SPH literature addressed some significantly different kinds of flows with averaged models. Among the averaged models, mixture models are of particular interest. Thanks to the unique velocity field for the motion of SPH particles, they are close to the usual single-fluid set of equations and can therefore be implemented with limited effort. The reduced number of equations to solve is expected to limit the computations compared to two-fluid approaches with a different set of particles for each phase.

2.3.1 Overlapping frames of particles

Early work on multiphase flow modeling and first occurrence of volume fraction representation in SPH were achieved in an astrophysical framework to study gas/dust mixtures by Monaghan and Kocharyan [266] and Monaghan [263] in view of pyroclastic flows or fluidized beds, further applied by Maddison [238] and Barrière-Fouchet et al. [18] to dust distribution in protoplanetary disks, by Xiong et al. [387] to fluidization systems and by Kwon and Monaghan [198, 199] to sedimentation. The dusty fluid is modeled by two interpenetrating domains with pressure and drag interactions. Each phase is assigned a set of particles, one frame overlapping the other, and corresponding continuity, momentum and energy equations are solved: this is a two-velocity

single-pressure model. The volume fraction is computed as:

$$\alpha_a = 1 - \frac{1}{\rho^\beta} \sum_{b \in \mathcal{F}} m_b w_{ab} \tag{2.134}$$

where β refers to the dust phase. This relation is also used in the further references. Computations were carried out for high density ratio flows (2400). With a similar idea of two frames of particles, Rice et al. [310] used massless gas particles interacting with dust particles for astrophysical applications.

Porous media are a particular application of such approach and received a significant interest. This approach was applied to water-soil interactions by Wang et al. [377] including the effects of volume fractions on the mixture dynamics. Bui and Nguyen [43] simulated fluid flow in deformable porous media with a two-phase theory and an elastoplastic solid phase, each phase being discretized by a different set of particles. The pore fluid was modeled as an incompressible fluid, solved with ISPH, while the soil skeleton remained fixed. The solid volume fraction, considered to be always much less than 1, was solved with an evolution equation and was then interpolated to deduce the fluid volume fraction through (2.134). It was successfully validated on seepage flow and failure response of porous medium. Peng et al. [289] developed a WCSPH mixture model to simulate flows through saturated porous media based on the theory of Drew [111]. While water is modeled with the WCSPH δ–SPH formulation, the solid phase is represented by fixed particles with porosity. Only the motion of the fluid phase is computed. The porous medium applies a non linear resistance force $\boldsymbol{R}_d$ (basically issued from a Darcy's law that can take more complex expressions) in the momentum equation, giving the following set of evolution equations:

$$\frac{d\rho}{dt} = -\rho \boldsymbol{\nabla} \cdot \boldsymbol{v} - \frac{\rho}{\alpha} \frac{d\alpha}{dt} \tag{2.135}$$

$$\frac{d\boldsymbol{v}}{dt} = -\frac{1}{\rho} \boldsymbol{\nabla} p + \frac{1}{\alpha\rho} \boldsymbol{\nabla} \cdot (\alpha \mathbb{T}) + \boldsymbol{g} - \frac{1}{\rho} \boldsymbol{R}_d \tag{2.136}$$

Let us underline that the variables are not mixture quantities but refer to the fluid phase, so that the notion of mixture model given in these papers will differ from the one adopted in this manuscript. Satisfactory agreement is obtained with analytical and experimental results on seepage, water flows in rockfill and wave interaction with porous structures. Similarly to Peng et al. [289], Khayyer et al. [185] developed an enhanced ISPH two-phase model for application to media of variable porosity and applied it on a wide array of tests, from flow in U-tube, to seepage flows and solitary wave attenuation over a porous bed and interaction with a submerged porous structure that compared satisfactorily with analytical, numerical and experimental results. Shimizu et al. [330] introduced in this model a former volume increase concept inside the porous medium to handle unsaturated flows. The volume of fluid particles is then computed through $V = V_0/\alpha$ where α is assumed to remain sufficiently close to 1. Such approaches have the cost to model two different sets of particles, even though this cost is significantly reduced when one of these

sets remained fixed.

2.3.2 Lagrangian/Lagrangian approach

The SPH framework offers a straightforward coupling with other Lagrangian methods describing the dispersed phase: the Discrete Element Model (DEM) received attention from the SPH community, especially to model the solid phase for sedimentation processes as it allows one to compute the motions and effects of numerous small particles: while the liquid is modeled with a continuous approach, the dispersed phase is modeled with a set of particles that are followed independently and interact with the continuous medium. Gao and Herbst [141] introduced a two-way coupling between SPH and the Discrete Element Model (DEM) modifying the multiphase model detailed by Monaghan and Kocharyan [266]. Interaction between fluid and solid phase in view of dense particulate flows in a grinding mill through three contributions are taken into account through volume fraction, pressure and drag force. Robinson and Ramaioli [312] used the locally averaged Navier–Stokes equations of Anderson and Jackson [10] and coupled them with a Discrete Element Model (DEM) model to create a simulation tool for one or two-way coupled fluid-particle systems. They applied this approach to the sedimentation of single or multiple particles. Breinlinger et al. [37] included additional forces in such models for granular material transport and powder processes. Solid-liquid flows with free surface were successfully simulated by Sun et al. [339] with DEM–SPH approach. For bubble flows, Torti and Sibilla [348] described in their work a Lagrangian approach coupling an SPH representation of the continuous liquid phase with a direct solution of the Newton's law for the trajectories of computational particles standing for sets of gas bubbles. The bubble motions generate a force in the liquid momentum equation while the bubble trajectories are modified by the force generated by the liquid phase within a local equilibrium assumption neglecting the transients. They successfully applied this approach to a bubble column and a gas-liquid jet. Works are still carried out in this field, *e.g.* He et al. [160] developed a GPU-based coupled DEM–SPH to study particle-fluid flows including free surfaces in multiphase chemical processes (agitated tubular reactor, rotating drum).

2.3.3 Two-velocity single-pressure averaged model

Recent developments have been made in the SPH method to implement two-phase models with two velocities but only one set of particles compared to the methods described in the previous sections. Obviously, a choice has to be made for the velocity moving the particles.

2.3.3.1 A two-fluid approach

Shi and Yu [326], Shi et al. [327, 328] developed a two-phase SPH model to study solid-liquid mixtures. The single set of SPH particles is moved with the water velocity. Turbulence effects are included thanks to LES through a Smagorinsky model with parameters used as tuning values.

The momentum equations are coupled with a drag force $\pm\gamma\alpha\boldsymbol{v}^r$ including an hindering factor accounting for the surrounding sediment concentration and an interphase momentum transfer due to subscale turbulence $\gamma/\beta\overline{\alpha'\boldsymbol{v}'}$ modeled with a gradient transport law following [247] in the framework of dilute sediment flows. The test cases include free surface, taking advantage of the feature of SPH to avoid modeling the air phase, and compare well with the experimental values.

2.3.3.2 Miscible flows approaches

Tartakovsky and Meakin [341] modeled miscible flow fluid particles with variable masses depending linearly on the solute concentration. The solute concentration was computed thanks to an advection-diffusion equation. The model was applied to the Rayleigh–Taylor instability development of salty water above fresh water and miscible flows in fractures. It focused on solute-solvent flows with identical solvent. Kwon [197] developed a one-fluid SPH description to model miscible gaseous mixtures: a momentum equation is solved for each component, these equations being coupled by a drag force, and particles are moved by the barycentric velocity $\boldsymbol{v}$. Volume fractions of SPH particles evolve for each component due to three mechanisms, namely the Maxwell–Stefan diffusion, the inter-particle advective flux due to the drift velocities and the particle-transport-related advection linked to the compressibility of the flow. Stratification by gravity of initially homogeneous mixtures are tackled with good agreement with an Eulerian two-phase model.

2.3.4 Single-velocity single-pressure averaged model

2.3.4.1 Cueille and Grenier's formulations

A mixture model with a volume fraction formulation and a diffusion of phases between particles following a Fick law has been implemented and tested on gravity currents in Cueille [90], extending to the Lagrangian framework the Eulerian model proposed by Chanteperdrix [75] and derived from a thermodynamical reasoning. The SPH particle is formed of two components in pressure equilibrium $p^\alpha = p^\beta$. Solving mass conservation equation on $\alpha\rho^\alpha$ and using the linearized state equations for partial pressures $p^\alpha = (c^\alpha)^2(\rho^\alpha - \rho_0^\alpha)$ where ρ_0^α is the reference density for the α phase as the phase densities are left to vary, an equilibrium volume fraction can be computed. This work highlighted the importance of the choice of solver in the resolution, especially the interest of using Riemann solvers, solving separately the hyperbolic part of the equations, to obtain good results for gravity currents. Following Cueille [90], a mixture model with a volume fraction formulation without phase exchanges between particles was implemented and compared to a multifluid formulation by Grenier [149] with an SPH–ALE approach as described in Section 2.1.6.7, especially on shock tubes, wave sloshing and Rayleigh–Taylor instability cases. It highlighted the diffusion of the interfaces triggered by the mixture model. To improve the precision, the MUSCL (Monotonic Upwind Scheme for Conservation Laws) with limiters was introduced

but required some corrections for the gradient computations for realizability issues. However the results were adversely affected by this correction. The mixture model results remain generally satisfying but the multifluid formulation of SPH described in Section 2.2.2.4 proved to perform better on the cases tested.

2.3.4.2 Mixture models in the graphics community

SPH mixture models were developed recently in the graphics community to simulate multifluid phenomena that are not adequately simulated with single-fluid approaches such as mixing, diffusion processes, chemical reactions, etc. The aim of these works is to provide simulations of realistic appearance. No quantitative validation is done. The volume fraction representation was introduced by Liu et al. [222] for simulating visually realistic mixing phenomena. Mixture models were implemented to capture a wide range of physical phenomena for liquid mixtures by Ren et al. [305] further extended to deal with fluid-solid interactions by Yan et al. [391]. This work included a closure for diffusion velocities. Yang et al. [393] introduced user-adjusted Helmholtz free energy functions, the fluid evolving from high-energy states to low-energy states, to model various mixing and unmixing processes. The Cahn-Hilliard equation describing the process of phase separation was employed.

2.3.4.3 Mixture models in astrophysics

To simulate dust settling in protoplanetary discs, Price and Laibe [297, 298] proposed a mixture model preserving conservation properties by rewriting the two-phase equations through the introduction of new variables, combinations of phase variables, to overcome some issues inherent to the two-fluid approach (overdamping at high drag that requires small temporal and spatial discretizations, artificial trapping of dust particles below the gas resolution). The original two-phase system of equations from which the mixture model is derived only include gravity and a drag coupling $\pm\gamma \boldsymbol{v}^r$ between momentum equations, plus an energy equation. The new set of variables comprises the total density $\rho_t = \rho^\alpha + \rho^\beta$, the dust fraction $\alpha_t = \rho^\alpha/\rho$, the barycentric velocity defined as $\boldsymbol{v}_d = \left(\rho^\alpha \boldsymbol{v}^\alpha + \rho^\beta \boldsymbol{v}^\beta\right)/\rho_t$ and the relative velocity $\boldsymbol{v}^r$. A system similar to the mass fraction formulation described in Section 1.3.1 was obtained. A classical antisymmetric discretization of the diffusion term of the dust fraction is made. For strong drag, the system was simplified under the terminal velocity approximation, similarly to what is done in the present work for the relative velocity equation to get:

$$\boldsymbol{v}^r \approx \frac{\rho^\alpha}{\rho_t \gamma} \boldsymbol{\nabla} p \tag{2.137}$$

The relative velocity equation become a purely diffusive relation for which a second order operator of the form (2.42) is used. The results compared well with the analytical model developed in previous works.

2.3.4.4 Mixture models for sediments

Bertevas et al. [20, 21], Tran-Duc et al. [349] developed a two-phase mixture model for simulating ocean sediment transport. The sediment concentration is followed though an advection-diffusion equation including turbulent diffusion with an anisotropic coefficient resulting from a mixing length turbulence model in its vertical component. Antisymmetric operators are used for conservation. The settling velocity follows the Stokes law with the hindering coefficient of Richardson and Zaki [311]. Particles with variable masses are therefore used. A mixture velocity adapted to particle suspensions is employed. The model is verified on analytical solutions and then applied to an oceanic case without comparisons to get insights in the sediment transport and deposition.

2.4 Summary

Among the prominent challenges of multiphase flow numerical modeling, one can refer to the density and viscosity jumps across the interface, the possibly highly distorted moving interface and the topological transition at these interfaces. While the last two issues are naturally addressed by the usual WCSPH multifluid formulation, the first proves to be tricky to handle. Before presenting a summary of the approaches available in SPH literature, let us have a quick look at how the Eulerian methods tackle those three questions.

2.4.1 A parallel with Eulerian approaches

We do not aim here at discussing extensively the common numerical Eulerian approaches but rather give a few hints to make the links with what is done in the SPH framework. Furthermore, these approaches can be used for comparison in the numerical results sections. In the Eulerian framework, two main principles with different possible implementations were developed to compute the interfaces:

- The interface tracking methods. Those methods are used for configurations for which capturing the interface is pivotal, with potential effects of surface tension, adhesion… *e.g.* bubble formation, nozzles, free-surface problems. In the widely used Volume of Fluid (VoF) approach as introduced by Hirt and Nichols [165], an advection equation is used to follow the interface that is diffused over a few cells. The Level-Set method first developed by Osher and Sethian [285] and front tracking approach described by Unverdi and Tryggvason [352] that keeps a sharp interface are other options.

- The interface modeling approach: two-phase and mixtures models as presented in Chapter 1 belong to this category.

The DNS approaches involving interface tracking methods were for example applied to single bubble rising at large Reynolds number [48] or to dispersed bubbly flows with a few hundreds bubbles moving at Reynolds number of a few tens [45] but due to computational cost, the domain of applications still remains limited. So called Euler–Euler simulations corresponding to the second item have a wider range of applicability, but at the price of modeling with regime-specific closures the interfacial terms arising from the model and given in the literature, see *e.g.* [113, 177]. Some work was done recently to couple these approaches [98, 99, 291, 351] to take advantage of their relative assets depending on the scale of the interfaces considered. Another option is to increase the number of phases in the two-phase approach by introducing dispersed and continuous gas fields and a continuous liquid field, namely a three-field model, as done for example by Denèfle et al. [107] and Mimouni et al. [253]. In the multifluid SPH approach as described in Section 2.2, the interface is not tracked and is defined as the surface in-between particles belonging to different fluids. This a significant asset for the SPH approach. The introduction of a multiphase approach as described in Section 2.3 following the second item triggers diffuse interface, so that this important asset is at least partially lost.

2.4.2 Challenges for the present formulation

Multiphase flows with high density ratios are handled more easily with volume-based SPH formulation of operators and this is the choice made in the following chapter, consistently with the volume-weighted formulation developed in Chapter 1 and the work of Hu and Adams [170] and Ghaïtanellis et al. [145]. The operators can be derived from a Lagrangian variational principle of virtual works as shown by Grenier et al. [150]. The literature displays a wide variety of two-phase averaged models that rely heavily on the kind of flows considered, going from an SPH–DEM approach for a dispersed flow of bubbles to a full rewriting of the equations for gas-dust astronomical flows. Numerical ingredients of varying complexity – missing sometimes of physical grounds – were introduced in the density and momentum equations with their share of advantages and drawbacks, at the core of which is a too strong diffusion, however required to stabilize the computations (Riemann solvers, density re-initialization, artificial viscosity). Few works really addressed the intrinsic issue relative to the continuous interpolations step leading to a wrong interfacial pressure force at high density ratios. Large speeds of sound are of common use but result in long computational times. Repulsive forces, though artificial, appeared to be necessary to avoid fragmentation of the interfaces. As far as mixture models are concerned, main assets are their versatility and simplicity for a first implementation of averaged equations. This literature review highlights that some challenges should be tackled with respect to the precision, the handling of high density ratios and some partially missing features such as open boundaries or turbulence modeling. While ISPH can be enticing to enforce the divergence-free volumetric flux condition, the difficulties linked to the interface management prevent a safe application to the mixture model with diffuse interface. A change of formulation by implementing the δ–SPH

approach or Riemann solvers in an SPH-ALE framework, while enticing and promising for the mixture model formulation (some similarities can arise due to the split of the phase velocities into the mixture velocity and relative velocity contribution parts), will be left to further work.

Chapter 3

The SPH two-component mixture model

On s'emploie ici à la description du modèle de mélange développé dans le cadre de cette thèse et à sa validation sur des cas bidimensionnels de complexité croissante. Un accent tout particulier est mis sur la résolution de l'équation régissant l'évolution des volumes de chaque phase avec de bonnes propriétés numériques. On décrit le schéma de diffusion de volume pour empêcher le développement d'ondes de pression artificielles. On détaille également l'extension du formalisme des conditions d'entrées/sorties SPH au modèle de mélange. Les limites du formalisme retenu, notamment pour l'écriture du gradient de pression, sont soulignées. Au terme de ce chapitre, nous sommes équipés du schéma numérique discret pour résoudre les équations du premier chapitre. On vérifie le respect des bonnes propriétés numériques du schéma proposé. Lorsque cela est possible on compare le modèle à d'autres modèles SPH, volumes finis ou Volume of Fluid.

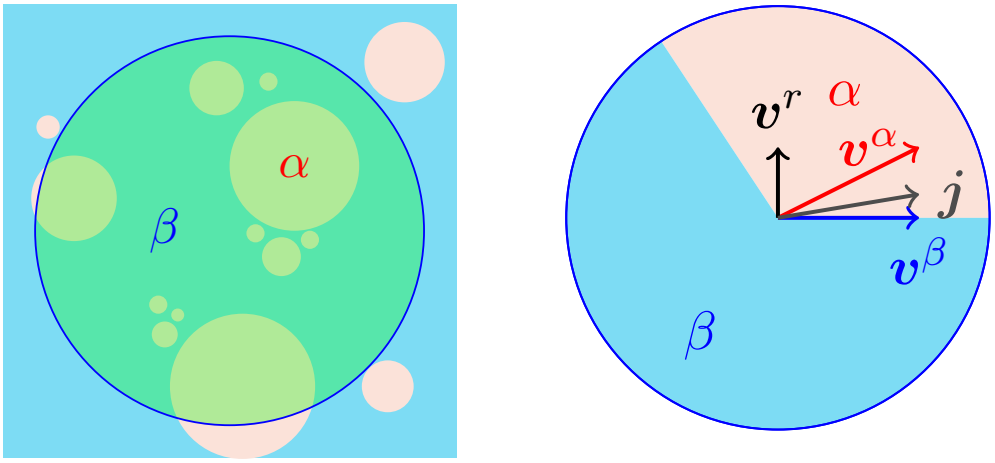

(a) Schematic view (b) Velocities

Figure 3.1: Control volume in a two-component flow (gas phase in red, liquid phase in blue), the corresponding volume fractions and velocity fields.

Chapter 1 has provided the continuous framework of the two-phase model and Chapter 2 described the state of the art of the tools in the SPH literature available to discretize this set of equations. The aim of this chapter is to present the specific SPH two-component model developed in this work, supported by those tools, but also introducing original ones. Two main contributions will be stressed: the derivation of an SPH upwind numerical scheme to follow phase volumes with good properties [135, 136] and the construction of SPH open boundaries for mixtures [138]. Analogies with the Finite Volumes (FV) approaches will be central in this prospect. In order to make the following developments as general as possible, we consider, in addition to air/water mixtures, the case of water/sediment mixtures.

3.1 Notations

Let us consider a two-phase flow (*e.g.* air bubbles rising or sediments falling within water). This section aims at detailing the notations and the mixture equations adopted to model such a flow. We consider the control volume[1] presented in Figure 3.1a. The presence of phases is taken into account through volume fractions, as schematically illustrated in Figure 3.1b. The two phases are denoted by α and β.

For the sake of clarity, the phase quantities are listed in Table 3.1. They are used to compute the mixture quantities presented in Table 3.2. Several choices are possible for the phase quantities to be considered: in view of achieving the conservation of phase quantities at high density ratios, a volume formulation has been retained here for the phase description (volume fraction[2])

[1] The control volume models an SPH particle that will be introduced in the next section.
[2] We denote α and β the volume fractions as well as the phase names, without any risk of confusion.

Table 3.1: Phase quantities ($k = \alpha$ or β).

Volume	V^k
Mass	m^k
Density	$\rho^k = m^k/V^k$
Kinematic viscosity	ν^k
Dynamic viscosity	μ^k
Velocity	$\boldsymbol{v}^k$
Pressure	p^k

Table 3.2: Mixture quantities.

Volume	$V = V^\alpha + V^\beta$
Mass	$m = m^\alpha + m^\beta$
Density	$\rho = m/V = \alpha\rho^\alpha + \beta\rho^\beta$
Volume fractions	$\alpha = V^\alpha/V$ and $\beta = V^\beta/V$
Mass fractions	$Y^\alpha = \alpha\rho^\alpha/\rho$ and $Y^\beta = \beta\rho^\beta/\rho$
Mixture velocity w.r.t. the volume center	$\boldsymbol{j} = \alpha\boldsymbol{v}^\alpha + \beta\boldsymbol{v}^\beta$
Mixture velocity w.r.t. the mass center	$\boldsymbol{u} = Y^\alpha\boldsymbol{v}^\alpha + Y^\beta\boldsymbol{v}^\beta$
Relative velocity	$\boldsymbol{v}^r = \boldsymbol{v}^\alpha - \boldsymbol{v}^\beta$
Drift velocity	$\boldsymbol{j}^\alpha = \boldsymbol{v}^\alpha - \boldsymbol{j}$
Diffusion velocity	$\boldsymbol{u}^\alpha = \boldsymbol{v}^\alpha - \boldsymbol{u}$
Mixture pressure	p

and mixture velocity. The mixture velocity is indeed defined here with respect to the volume center, and is also called volumetric flux, due to weighting by volume fractions. A weighting by mass fractions would correspond to a definition with respect to the mass center. A mass formulation using mass fractions would lead to a simpler set of mixture equations but has proved during our investigations to trigger numerical issues for high density ratio flows: as indicated in Section 1.3.1, the mass fraction equation, due to its weighting be mixture density, could not be discretized in a conservative way with respect to the relative velocity contribution. To preserve the symmetry of the system necessary to ensure conservation, we choose to work with relative velocities instead of drift/diffusion velocities.

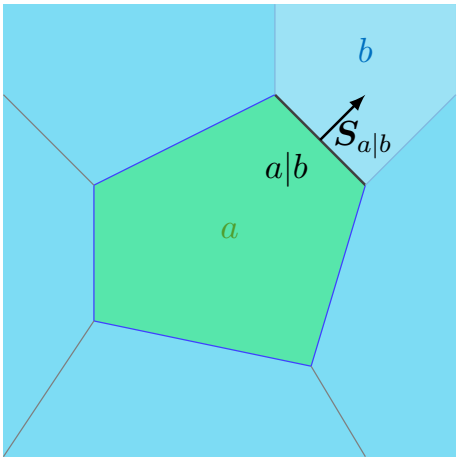

Figure 3.2: Voronoi diagram.

3.2 Numerical implementation of phase exchanges

The usual SPH discretization with a symmetric or antisymmetric divergence for the right-hand side of the volume fraction equation (1.86) triggers conservation and realizability issues (i.e. volume fractions may take non-physical values). We intend to derive a realizable phase volume equation, conservative with respect to the relative velocity contribution, through a FV-like approach. In this prospect, we will consider a Voronoi tessellation that discretizes the fluid, as illustrated in Figure 3.2. The cells in this figure are a schematic representation of the SPH particles [3], used to derive the subsequent equations. During a simulation, the exact shape of the particles is never actually known (nor used). $a|b$ stands for the interface[4] index between the cells a and b, the outwards-oriented surface vector associated to this interface being denoted $\boldsymbol{S}_{a|b}$. For the sake of clarity, we first apply this approach to a single phase medium to see how one can recover the WCSPH volume conservation equation:

$$\frac{dV}{dt} = V \boldsymbol{\nabla} \cdot \boldsymbol{j} \tag{3.1}$$

After this, a similar reasoning will be applied to the two-phase case. To start with, we only consider particles that do not interact with the boundaries of the domain.

[3] This is done in analogy with FV, though a partition of unity is not reached in classical SPH.

[4] In SPH, contrary to FV, two particles may have a common "interface" even if they are not connected through a line segment like in Figure 3.2.

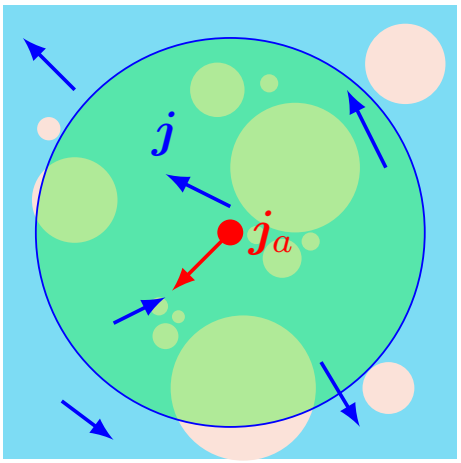

Figure 3.3: Mixture velocity field $\boldsymbol{j}$. $\boldsymbol{j}_a$ is the mixture velocity of the particle a, constant within the volume of the particle.

3.2.1 Integral balance for a single-phase flow

3.2.1.1 Leibniz's rule

Let us apply the Leibniz's rule 1.1.1 for a scalar field A on a particle a seen as a material volume Ω_a moved and deformed by the fluid velocity $\boldsymbol{j}$:

$$\frac{d}{dt}\int_{\Omega_a(t)} A dV = \int_{\Omega_a(t)} \frac{\partial A}{\partial t} dV + \int_{\partial\Omega_a(t)} A\boldsymbol{j}\cdot\boldsymbol{dS} \tag{3.2}$$

For $A = 1$, equation (3.2) gives:

$$\frac{dV_a}{dt} = \int_{\partial\Omega_a(t)} \boldsymbol{j}\cdot\boldsymbol{dS} \tag{3.3}$$

We therefore recognize an integral form of equation (3.1). For a closed surface:

$$\int_{\partial\Omega_a(t)} \boldsymbol{dS} = 0 \tag{3.4}$$

Subtracting $\boldsymbol{j}_a \cdot$ (3.4), one gets:

$$\frac{dV_a}{dt} = \int_{\partial\Omega_a(t)} (\boldsymbol{j} - \boldsymbol{j}_a)\cdot\boldsymbol{dS} \tag{3.5}$$

In the above equation, $\boldsymbol{j}$ is the velocity at the continuous level, while $\boldsymbol{j}_a$ is the velocity of the particle a, which is a discrete field, constant over the support of the particle (see Figure 3.3).

3.2.1.2 Discrete SPH approximation

Let us proceed with a finite volume formulation of the integrals in equation (3.5). For each neighboring cell, one has:

$$\int_{a|b} \boldsymbol{dS} = \boldsymbol{S}_{a|b} \tag{3.6}$$

$$\int_{a|b} \boldsymbol{j} \cdot \boldsymbol{dS} \equiv \boldsymbol{j}_{a|b} \cdot \boldsymbol{S}_{a|b} \tag{3.7}$$

Equation (3.6) is exact while equation (3.7) should be understood as a definition of the interface mixture velocity $\boldsymbol{j}_{a|b}$. By summing over all neighbors (*i.e.* all the $a|b$ interfaces), one gets:

$$\frac{dV_a}{dt} = \sum_{a|b} \left(\boldsymbol{j}_{a|b} - \boldsymbol{j}_a\right) \cdot \boldsymbol{S}_{a|b} \tag{3.8}$$

The similarity between SPH-ALE and Finite Volume (FV) approaches has been underlined in [278], among others. In the SPH formalism, this analogy is based on the following relation:

$$\boldsymbol{S}_{a|b} = 2V_aV_b\boldsymbol{\nabla}w_{ab} \tag{3.9}$$

to determine the virtual surface vector of the interface between particles. As highlighted by Neuhauser [278], an important difference between FV and SPH, is the definition of a neighbor in each method: only cells that share (part of) a face with the considered cell in FV are considered as neighbors, whereas all SPH particles within the kernel support are considered as neighbors (their number thus depends on the ratio smoothing length/particle size). This difference of neighbor definition requires an adequate handling of the weighting of the neighboring SPH particle contribution, which is done through the presence of the kernel gradient in equation (3.9). A limit of this approach is that the property $\sum_{a|b} \boldsymbol{S}_{a|b} = \boldsymbol{0}$, that is true in FV, does not hold in SPH (as zeroth consistency is not fulfilled, which is equivalent to the lack of partition of unity). Choosing a centered value to approximate $\boldsymbol{j}_{a|b}$, (3.8) becomes:

$$\frac{dV_a}{dt} = -V_a \sum_{b\in\mathcal{F}} V_b \left(\boldsymbol{j}_a - \boldsymbol{j}_b\right) \cdot \boldsymbol{\nabla}w_{ab} \tag{3.10}$$

We recognize a discrete SPH approximation of (3.1), the right-hand side being an SPH discrete divergence operator as described in [364].

3.2.2 Integral balance for a two-phase flow

One can now make a similar reasoning in the case of a two-phase flow. Due to the mixture model we have adopted, we can consider that we have a single fluid, but whose characteristics will vary depending on the local volume fraction α.

3.2.2.1 Leibniz's rule

For $A = \alpha$, equation (3.2) becomes:

$$\frac{d}{dt}\int_{\Omega_a(t)} \alpha dV = \int_{\Omega_a(t)} \frac{\partial \alpha}{\partial t} dV + \int_{\partial\Omega_a(t)} \alpha \boldsymbol{j} \cdot \boldsymbol{dS} \tag{3.11}$$

Using (1.86) to compute the right-hand side volume integral and using Gauss' theorem, one gets:

$$\frac{dV_a^\alpha}{dt} = \int_{\Omega_a(t)} \left[\alpha \boldsymbol{\nabla} \cdot \boldsymbol{j} - \boldsymbol{\nabla} \cdot (\alpha\beta \boldsymbol{v}^r)\right] dV \tag{3.12}$$

Expanding α at the zeroth order, we make the following approximation:

$$\int_{\Omega_a(t)} \alpha \boldsymbol{\nabla} \cdot \boldsymbol{j} dV = \alpha_a \int_{\Omega_a(t)} \boldsymbol{\nabla} \cdot \boldsymbol{j} dV \tag{3.13}$$

Subtracting $\alpha_a \boldsymbol{j}_a \cdot$ (3.4) leads to:

$$\frac{dV_a^\alpha}{dt} = \alpha_a \int_{\partial\Omega_a(t)} (\boldsymbol{j} - \boldsymbol{j}_a) \cdot \boldsymbol{dS} - \int_{\partial\Omega_a(t)} \alpha\beta \boldsymbol{v}^r \cdot \boldsymbol{dS} \tag{3.14}$$

3.2.2.2 Discrete SPH approximation

The FV-like approximation of the integrals in (3.14) leads to:

$$\frac{dV_a^\alpha}{dt} = \alpha_a \sum_{a|b} \left(\boldsymbol{j}_{a|b} - \boldsymbol{j}_a\right) \cdot \boldsymbol{S}_{a|b} - \sum_{a|b} \left(\alpha\beta \boldsymbol{v}^r\right)_{a|b} \cdot \boldsymbol{S}_{a|b} \tag{3.15}$$

where we identify two contributions: the first term corresponds to a divergence of the mixture velocity field $\alpha \boldsymbol{\nabla} \cdot \boldsymbol{j}$ and the second to a contribution from the relative displacements of phases $\boldsymbol{\nabla} \cdot (\alpha\beta \boldsymbol{v}^r)$.

Numerical properties The interface $a|b$ quantities still need to be defined in equation (3.15). Four principles guide our choice in this prospect:

- Conservation: the fluxes must be symmetrical with respect to the particle labels (a, b);
- Realizability: phase volumes V^α and V^β should remain positive;
- Reduction to single phase model: for $\alpha = 1$ and $\boldsymbol{v}^r = \boldsymbol{0}$, we want to recover single-fluid WCSPH equations;
- Symmetry with respect to phases: we can interchange α and β without modifying the equations.

A classical choice is to consider a centered approach for the interface quantities:

$$\boldsymbol{j}_{a|b} = \frac{1}{2}\left(\boldsymbol{j}_a + \boldsymbol{j}_b\right) \quad \text{and} \quad \left(\alpha\beta\boldsymbol{v}^r\right)_{a|b} = \frac{1}{2}\left(\alpha_a\beta_a\boldsymbol{v}^r_a + \alpha_b\beta_b\boldsymbol{v}^r_b\right) \tag{3.16}$$

that leads to the phase volume equation:

$$\frac{dV^\alpha_a}{dt} = -\frac{1}{2}\alpha_a\sum_{b\in\mathcal{F}}\left(\boldsymbol{j}_a - \boldsymbol{j}_b\right)\cdot\boldsymbol{S}_{ab} - \frac{1}{2}\sum_{b\in\mathcal{F}}\left(\alpha_a\beta_a\boldsymbol{v}^r_a + \alpha_b\beta_b\boldsymbol{v}^r_b\right)\cdot\boldsymbol{S}_{a|b} \tag{3.17}$$

One can recognize the first term of the right-hand side using (3.10). However, in our numerical tests, this formulation did not allow us to enforce the realizability property. In analogy with the FV approach, we therefore write:

$$\left(\alpha\beta\boldsymbol{v}^r\right)_{a|b} = \alpha_a\beta_b\left[\boldsymbol{v}^r_{a|b}\cdot\boldsymbol{S}_{ab}\right]^+ + \alpha_b\beta_a\left[\boldsymbol{v}^r_{a|b}\cdot\boldsymbol{S}_{ab}\right]^- \tag{3.18}$$

where $[x]^+ = \max(x,0)$, $[x]^- = \min(x,0)$ and a centered approach is retained for the relative velocity:

$$\boldsymbol{v}^r_{a|b} = \frac{1}{2}\left(\boldsymbol{v}^r_a + \boldsymbol{v}^r_b\right) \tag{3.19}$$

We finally have the following relation on the phase volume:

$$\frac{dV^\alpha_a}{dt} = \alpha_a\frac{dV_a}{dt} - 2V_a\sum_{b\in\mathcal{F}}V_b\left(\alpha_a\beta_b\left[\boldsymbol{v}^r_{a|b}\cdot\boldsymbol{\nabla}w_{ab}\right]^+ + \alpha_b\beta_a\left[\boldsymbol{v}^r_{a|b}\cdot\boldsymbol{\nabla}w_{ab}\right]^-\right) \tag{3.20}$$

The equation for the other phase volume can be obtained from (3.20) by changing α into β, since these relations are symmetric (this switch changes the sign of the relative velocity), or by using the mixture volume definition together with the mixture continuity equation (3.10):

$$\frac{dV^\beta_a}{dt} = \beta_a\frac{dV_a}{dt} + 2V_a\sum_{b\in\mathcal{F}}V_b\left(\alpha_a\beta_b\left[\boldsymbol{v}^r_{a|b}\cdot\boldsymbol{\nabla}w_{ab}\right]^+ + \alpha_b\beta_a\left[\boldsymbol{v}^r_{a|b}\cdot\boldsymbol{\nabla}w_{ab}\right]^-\right) \tag{3.21}$$

Highlights on the choices made Let us detail the important choices for the derivation of equation (3.20) from equation (3.15):

- The first term of the right-hand side of equation (3.15) can be identified as the first term of equation (3.20) using the relation (3.8). The computation of the temporal derivative of the total volume relies on the use of an exact time integration scheme, following what is suggested by Ferrand et al. [128], applied to the relation (1.103). It proves to be better at simulating the mixture at rest (the usual continuity equation resolution with antisymmetric divergence led to spurious convection cells which appeared to be linked to the accumula-

tion of numerical errors). Starting from the SPH volume interpolation:

$$\frac{\gamma_a}{V_a} = \sum_{b \in (\mathcal{F} \cup \mathcal{V})} \theta_b w_{ab} \tag{3.22}$$

one can update the total volume through:

$$\frac{\gamma_a^{n+1}}{V_a^{n+1}} - \frac{\gamma_a^n}{V_a^n} = \sum_{b \in (\mathcal{F} \cup \mathcal{V})} \left(\theta_b^{n+1} w_{ab}^{n+1} - \theta_b^n w_{ab}^n \right) \tag{3.23}$$

- The second term of the right-hand side of equation (3.15) is computed through an upwind formulation, symmetric with respect to phases, that ensures the realizability of the scheme (under a condition detailed in Section 3.2.6). The flux $\boldsymbol{v}_{a|b}^r \cdot \boldsymbol{S}_{a|b}$ at the midpoint of the pair of particles (a, b) is split into its positive and negative parts. The factor $\alpha\beta$ then takes a different form depending on the sign of the flux: in $\alpha_a \beta_b$, α is upwinded with respect to $\boldsymbol{v}^r$ and β is convected by $(-\boldsymbol{v}^r)$. The choice of alternate indices a and b for the volume fractions ensures the symmetry with respect to the phases and the conservation of the total quantity of each phase.

Similar formulations A similar formulation was written by Shi et al. [327] that details a two-phase model for sediment laden flows with an asymmetric treatment of the liquid and solid phases. The volume fraction of sediment is updated with an equation looking like (3.20) but with β taken to 1 and a usual SPH divergence of the fluid velocity field to compute the total volume variation. Instead of a β equation, an equation on $\beta\rho^\beta$ is solved. Our approach has the advantage to keep a symmetrical treatment of both phases and to be conservative with respect to the relative velocity contribution. The model can therefore handle only water or air phase within a particle when the approach detailed in [327] assumes constant water mass in particles, as classically done in two-phase models for sediments [330], which may trigger some significant volume variations. Besides, we are only solving three equations instead of four, which decreases the computational cost of the approach. On the other hand, a mixed upwind/downwind operator in a finite volume framework is proposed by Larreteguy et al. [204] to solve a volume fraction equation with drift velocities and a mass-weighted mixture velocity (α is upwinded whereas the drift velocity encompassing β and $\boldsymbol{v}^r$ is downwinded). Such a distinction between upwind and downwind, due to a stencil limited to a pair of particles in SPH, does not seem possible to implement if we restrict ourselves to the given set of SPH particles. Some approaches were developed to deal with higher order schemes for SPH by building larger stencils, for example in [15, 359].

Conservation The total volume is not conserved due to the weak compressibility of the formulation (like in the traditional, one-phase WCSPH approach). However, the antisymmetry of

the discrete terms concerning the relative velocity ensures that the relative phase motion does not affect the total volume. Introducing the wall renormalization factor γ of equation (2.49), the phase volume equation (3.20) becomes:

$$\frac{dV_a^\alpha}{dt} = \alpha_a \frac{dV_a}{dt} - 2\frac{V_a}{\gamma_a}\sum_{b\in\mathcal{F}} V_b \left(\alpha_a\beta_b \left[\boldsymbol{v}^r_{a|b} \cdot \boldsymbol{\nabla} w_{ab} \right]^+ + \alpha_b\beta_a \left[\boldsymbol{v}^r_{a|b} \cdot \boldsymbol{\nabla} w_{ab} \right]^- \right) \tag{3.24}$$

the temporal variation of V_a being computed from (3.23). The symmetry of the relative velocity term is somewhat broken by this factor γ near the boundaries, as always with the USAW technique, but it did not prove to introduce significant discrepancies. Regarding a boundary term for this operator, we first tried to derive a term consistent with the relative velocity closure that may comprise an advection and a diffusion term as it will be shown in Section 3.2.5. By considering a no-flux condition it was then possible to compute the Laplacian boundary term arising from the diffusion term of the relative velocity by replacing the normal derivative by its value for a null relative velocity. However, it proved not to be conservative on a two-phase mixture Poiseuille flow similar to the case presented in Section 3.5.2. The final solution was to consider no boundary term nor vertices contribution so as to ensure a no-flux condition at the boundaries. Moreover, in the numerical implementation, phase volumes have been nondimensionalized by the reference volume V_0 to avoid the accumulation of numerical errors that triggered some spurious pressure profiles (due to the values of the numerical sound speed, small errors in the volumes resulted in large errors in the pressure field).

Realizability The respect of physical boundaries was enforced by the construction of the single numerical scheme for phase volumes. However, in the literature, Rusche [316] and Gastaldo et al. [142] indicate that this realizability property should be ensured by the discretization of the system of equations as a whole (*i.e.* continuity, volume fraction and momentum equations). Let us underline that for sediment flows, as studied in Section 3.5.4, the volume fraction can have an upper limit lower than 1 due to the maximum packing α_{mp}. This limit cannot be ensured by the present model and shall be respected in the resolution of the whole system. If not, a change in the relative velocity closure or in the numerical discretization of the model should be considered. A different approach could allow to write an appropriate scheme:

$$\boldsymbol{\nabla} \cdot [\alpha\beta\boldsymbol{v}^r] = \boldsymbol{\nabla} \cdot [\alpha\,(\alpha_{mp} - \alpha)\,\boldsymbol{v}^r] + (1 - \alpha_{mp})\,\boldsymbol{\nabla} \cdot (\alpha\boldsymbol{v}^r) \tag{3.25}$$

By replacing $\beta = 1 - \alpha$ by $(\alpha_{mp} - \alpha)$ in the numerical scheme, it is expected that the boundaries $\alpha \in [0, \alpha_{mp}]$ will be respected. However, such a choice corresponds to neglecting the last term of the right-hand side of (3.25). Such an approach was not needed in the application cases considered in the present work but might be addressed in other cases. Indeed, the risk with a non-realizable scheme is to make the time step tend to zero as the viscosities for sediment flows are usually getting higher and higher when α gets closer to its maximum packing value.

3.2.3 Volume diffusion

Checker-board effects appear in simulations as a consequence of the collocated nature of SPH. Analogously to the density diffusion presented in the Section 2.1.6.1, a possible way to circumvent this issue is to introduce volume diffusion when phase volumes are updated. The derivation of this additional term is detailed in Appendix C.1 and takes the form:

$$V_a^{\alpha,n+1} = V_a^{\alpha,\star} + \frac{\delta t}{\gamma_a} \Lambda \alpha_a^n \mathcal{D}_a^n \tag{3.26}$$

where $V_a^{\alpha,\star}$ is the phase volume before its modification by the diffusion term that writes:

$$\mathcal{D}_a^n = 2V_a \delta t \sum_{b \in \mathcal{F}} V_b \frac{1}{r_{ab}} \left(\frac{2}{\rho_a + \rho_b} (p_a - p_b) - \boldsymbol{g} \cdot \boldsymbol{r}_{ab} \right) \boldsymbol{\nabla} w_{ab} \tag{3.27}$$

The weighting coefficient Λ of this volume diffusion is equal to 0.1 unless otherwise specified. One can note that the diffusion term is the density diffusion term dimensionalized to become a volume diffusion term. Volume diffusion has also been addressed in a similar manner, by using the density diffusion term, in multifluid δ–SPH by Hammani et al. [158], the diffusion being made on particles belonging to the same phase. It was noted that an "intuitive" way to develop volume diffusion may consist in switching from density to volume variable in the diffusion term. It was also argued that the volume spatial distribution did not have a linear hydrostatic component. However such an approach proved to be unsuccessful. As shown in the appendix, the writing of the diffusion term arises from the momentum discretization that involves densities and not volumes: that could be the origin of this issue. Moreover in our approach the volume does have a hydrostatic component, due to the computation of the particle characteristics detailed hereafter.

3.2.4 Particle characteristics

Once phase volumes are computed, one can assess the other particle quantities according to their definitions (particle labels a are dropped in this subsection for the sake of simplicity):

$$m = (\alpha \rho^\alpha + \beta \rho^\beta) V_0 \tag{3.28}$$

$$\rho = \frac{m}{V} \tag{3.29}$$

$$\alpha = \frac{V^\alpha}{V} \tag{3.30}$$

where ρ_0 is the density accounting for the volume fraction variations but not the compressibility:

$$\rho_0 = \alpha \rho^\alpha + \beta \rho^\beta \tag{3.31}$$

Special attention shall be paid to the particle mass computation. Particle masses are usually constant in single-fluid SPH, if we except ALE approaches such as in [360] and the two-phase models described in Chapter 3, so that they do not vary due to compressibility effects; only the density and volume do. To recover this behaviour, we introduce the reference volume V_0 to compute particle masses, so that they only vary due the volume fraction variations. With this choice, we indeed have a varying density due to the fluid (weak) compressibility. This way of calculating the particle quantities constitutes a discrete approximation of the continuous equations (E.10) and (1.86). To check that, one can deduce from (3.20) the discrete governing equations of the mixture density and volume fraction:

$$\frac{d\rho}{dt} = -\frac{\rho_a}{V_a}\frac{dV_a}{dt} - \left(\rho^\alpha - \rho^\beta\right)\frac{V_0}{V_a^2}\sum_b \left(\alpha_a\beta_b\left[\boldsymbol{v}^r_{a|b}\cdot\boldsymbol{S}_{a|b}\right]^+ + \alpha_b\beta_a\left[\boldsymbol{v}^r_{a|b}\cdot\boldsymbol{S}_{a|b}\right]^-\right) \tag{3.32}$$

$$\frac{d\alpha}{dt} = -\frac{1}{V_a}\sum_b \left(\alpha_a\beta_b\left[\boldsymbol{v}^r_{a|b}\cdot\boldsymbol{S}_{a|b}\right]^+ + \alpha_b\beta_a\left[\boldsymbol{v}^r_{a|b}\cdot\boldsymbol{S}_{a|b}\right]^-\right) \tag{3.33}$$

The sum on the right-hand side of those equations is an SPH approximation of $\boldsymbol{\nabla}\cdot(\alpha\beta\boldsymbol{v}^r)$, as previously explained. From these definitions, we can write a useful relation. As mass in (3.28) varies only due to volume fraction variations under the constant phase density hypothesis, one gets, from (3.29) and (3.31) (recall $\sigma = 1/V$):

$$m = \frac{\rho}{\sigma} = \frac{\rho_0}{\sigma_0} \tag{3.34}$$

And therefore:

$$\frac{\rho}{\rho_0} = \frac{\sigma}{\sigma_0} \tag{3.35}$$

3.2.5 Closure law for the relative velocity

The closure law for the relative velocity is flow-dependent and one can refer to the extensive literature, for example [177], to find adequate closures depending on the two-phase flow regime. The relations used in this work assume constant size of bubbles or sediment grains d^α. As detailed in Section 1.3.5, more complex models solving transport equations for bubbles/grains diameters exist but we will focus on the simple closures described hereafter in view of the validation cases of the SPH two-phase mixture model. Specific closure for air-water cases will be addressed in Section 4.3.2.2. Let us note $\boldsymbol{v}_0$ the terminal rising/settling velocity of a single, small spherical bubble/grain of diameter d^α within an infinite viscous medium at rest under gravity. According to Stokes' law, for very small Reynolds numbers $\mathrm{Re}^\alpha = d^\alpha|\boldsymbol{V}^r|/\nu^\beta$, the balance between weight, buoyancy and drag gives:

$$\boldsymbol{v}_0 = \frac{\left(\rho^\alpha - \rho^\beta\right)\left(d^\alpha\right)^2}{18\mu^\beta}\boldsymbol{g} \tag{3.36}$$

According to [239], under the assumption that a local equilibrium can be reached over a short spatial length scale, one can write an algebraic expression of the relative velocity. Several cases are presented in this chapter:

- A constant relative velocity:

$$\boldsymbol{v}^r = \boldsymbol{v}_0 \tag{3.37}$$

- In the mixture model developed by Brethour and Hirt [38], the relative velocity is variable and linked to the pressure gradient through:

$$\boldsymbol{v}^r = \frac{V^p}{K^p}\frac{\beta\left(\rho^\alpha - \rho^\beta\right)}{\rho}\boldsymbol{\nabla} p \tag{3.38}$$

where the coefficient K_p is computed as:

$$K^p = \frac{1}{2}A^p\rho^\beta|\boldsymbol{v}^r|\left(\mathrm{C_D} + \frac{24}{\mathrm{Re}^\alpha}\right) \tag{3.39}$$

with $A^p = \frac{1}{4}\pi\left(d^\alpha\right)^2$ and $V^p = \frac{1}{6}\pi\left(d^\alpha\right)^3$ the cross sections and volumes of the bubbles/grains. One can note that this formulation gives the Stokes' formula when setting the turbulent drag coefficient $\mathrm{C_D}$ to zero and when the pressure gradient is in equilibrium with $\rho\boldsymbol{g}$. The default value of the turbulent drag coefficient is set to $\mathrm{C_D} = 0.7$ (Grégory Guyot personal communication). To account for the particle-particle interactions (hindered rising/settling), the Richardson and Zaki's correlation [311] can be employed to compute the effective relative velocity [5]:

$$\boldsymbol{v}^r_{\mathrm{eff}} = \beta^\zeta \boldsymbol{v}^r \tag{3.40}$$

where ζ is computed using the Reynolds number as:

$$\begin{cases} \mathrm{Re}^\alpha < 1 & \zeta = 4.35/\left(\mathrm{Re}^\alpha\right)^{0.03} \\ 1 < \mathrm{Re}^\alpha < 500 & \zeta = 4.45/\left(\mathrm{Re}^\alpha\right)^{0.1} \\ 500 < \mathrm{Re}^\alpha & \zeta = 2.39 \end{cases} \tag{3.41}$$

To close (3.38), we use here $\boldsymbol{\nabla} p = \rho\boldsymbol{g}$ in the separation case 3.5.1.1, assuming hydrostatic equilibrium. A variant of this model appropriate to air-water mixtures will be presented in Section 4.3.2.2.

- Finally, we propose a formulation for the relative velocity including a volume fraction gradient:

$$\boldsymbol{v}^r = \boldsymbol{v}_0 - K\frac{\boldsymbol{\nabla}\alpha}{\alpha} \tag{3.42}$$

[5] Brethour and Hirt [38] referred wrongly to it as the dispersed volume fraction factor.

where the coefficient $K > 0$ accounts for turbulent-like diffusion effects. This form can be related to the expression (1.101) assuming α is small enough to take $\beta = 1$ and considering a constant turbulent diffusion coefficient. The presence of a gradient requires some numerical precautions: to avoid double summation that can lead to instabilities as discussed in Section 2.1.2.5, a second order SPH operator using a single sum is used. Substituting (3.42) in (3.15), one gets:

$$\frac{dV_a^\alpha}{dt} = \alpha_a \frac{dV_a}{dt} - \sum_{b\in\mathcal{F}} (\alpha\beta \boldsymbol{v}_0)_{a|b} \cdot \boldsymbol{S}_{a|b} + K \sum_{b\in\mathcal{F}} (\beta \boldsymbol{\nabla}\alpha)_{a|b} \cdot \boldsymbol{S}_{a|b} \tag{3.43}$$

The relative velocity contribution in the phase volume equation is divided in two parts: the $\boldsymbol{v}_0$ part is treated as in (3.20) whereas the diffusion term in K is discretized separately as a usual SPH Laplacian of the form (2.59) introduced by Morris et al. [274]:

$$\begin{aligned} \frac{dV_a^\alpha}{dt} &= \alpha_a \frac{dV_a}{dt} - \sum_{b\in\mathcal{F}} \left(\alpha_a\beta_b \left[\boldsymbol{v}_{0,a|b} \cdot \boldsymbol{S}_{a|b}\right]^+ + \alpha_b\beta_a \left[\boldsymbol{v}_{0,a|b} \cdot \boldsymbol{S}_{ab}\right]^- \right) \\ &+ K \sum_{b\in\mathcal{F}} \frac{\beta_a + \beta_b}{2} \frac{\alpha_a - \alpha_b}{r_{ab}} \frac{\boldsymbol{r}_{ab} \cdot \boldsymbol{S}_{a|b}}{r_{ab}} \end{aligned} \tag{3.44}$$

3.2.5.1 Required modeling of the lighter phase

Modeling explicitly the light phase in this framework, at least with several particle layers so that kernels of the heavy phase are not truncated in case of free surface flows, appeared to be necessary to preserve the quantities of each phase, so that particles can effectively exchange volumes of each phase. In the case of air/water mixtures, for example, this means that a sufficiently thick air layer should be initially set above the water surface. This is an issue for the model as it is numerically more expensive. However, no satisfying solution has been found yet to address this problem. One could think about modeling only the water phase and, given an entrainment criterion, incorporate air within particles near the free surface: that would however trigger an increase in the volume of the surface particles. One should then consider splitting too large particles. As long as compressibility effects of the air phase are not involved, one should consider to avoid modeling too many air particles by putting only a few air particle layers or reducing the domain size.

3.2.6 Phase volume positivity condition

The resolution of the phase volume equation (3.20) introduces a condition on the time step for positivity of the phase volume (*i.e.* realizability of the numerical scheme). Let us consider the relative velocity of general form (3.42). It is associated to the numerical Péclet number

$$\mathrm{Pe}_\sigma = \frac{v_{0\,\max}\sigma_e}{K} \tag{3.45}$$

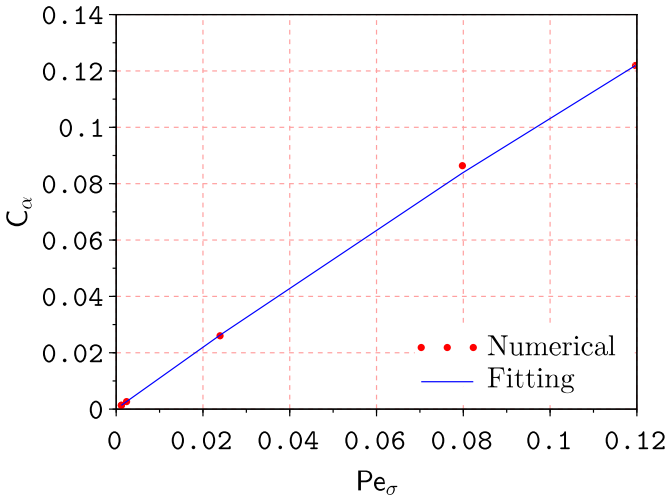

Figure 3.4: Advection-diffusion: limit of stability of the volume fraction profile (stability region below the curve).

where $v_{0\,\max} = \max_{a\in\mathcal{F}}(|\boldsymbol{v}_{0,a}|)$ and σ_e is the kernel standard deviation described in [367]. Appendix C.2 details the derivation of the sufficient condition that guarantees the positivity of $V_a^{\alpha,n+1}$ given the positivity of $V_a^{\alpha,n}$, $V_a^{\beta,n}$:

$$\mathrm{C}_\alpha = \frac{v_{0\,\max}\delta t}{\sigma} \leq \xi_\alpha \left(\eta_\alpha + \frac{1}{\mathrm{Pe}_\sigma}\right)^{-1} \tag{3.46}$$

The non-positivity of V^α can trigger some instabilities so that this sufficient condition of positivity is interpreted as a condition of numerical stability. For an advection-diffusion of the volume fraction α along the vertical axis, we got numerically $\xi_\alpha \approx 1.1$ and $\eta_\alpha \approx 0.8$ for $\mathrm{Pe}_\sigma \in [0.0012, 0.12]$ (optimized with respect to the $\mathcal{L}_1$ norm of the relative error). The fitting curve is displayed in Figure 3.4. In the numerical implementation, we solve an equation for V^α and an equation for V so that V^β is then deduced from and therefore does not introduce an additional constraint. We multiplied C_α by a factor of 0.5 to avoid to be at the limit of the condition for positiveness.

3.3 Discretization of the whole system

We now address the spatial and temporal discretization of the whole system, supported by the literature review of the Chapter 2 and the previous developments of the present chapter.

3.3.1 Mixture momentum equation

Compared to the single-fluid formulation, the mixture momentum equation requires to take into account its specificity as mixture variables are employed and additional terms linked to the rel-

ative velocity appear.

3.3.1.1 Pressure gradient operator

As underlined in Section 2.2.1.2, the discontinuity of the pressure gradient across the interface can cause numerical instabilities. Colagrossi and Landrini [86] suggested to chose sound speeds following the relation (2.110): with the state equation (1.10) and the air-water characteristics detailed below it, the ratio of numerical sound speeds is equal to 13. Here, we work with the linearized state equation (1.106) so that we have to take $\xi^\alpha = \xi^\beta = 1$ in (2.110): the ratio of sound speeds then reaches 28.5. It leads to prohibitively expensive computational times. Moreover it is a nonphysical sound speed ratio: Kruisbrink et al. [193] highlighted the instabilities developing for air water flows using the models of Colagrossi and Landrini [86] or Hu and Adams [171] in case of physical sound speed ratio. Thus, it appeared necessary to investigate a possible different formulation of the pressure gradient as done for single and two-phase flows in Appendix A. The multiple tests made with different formulations suggested in the literature [170, 171, 193] did not allow us to identify a completely satisfactory discrete expression. The specific volume formulation presented in Section 2.2.2.3 following [170] and used in the beginning of this chapter is known to improve the behaviour. However for high density ratio flows, it does not appear to be sufficient. Ghaïtanellis et al. [144] employed this formulation and applied it to a dam break, modeling both the air and water phases: a background pressure was introduced to prevent the development of a too large nonphysical gap between the phases. Air-water interface destabilization still appeared in our implementation of the operators suggested by [171, 193]. We finally retained the multifluid operator of Ghaïtanellis et al. [145], that originates from the specific volume formulation of [170], together with a small background pressure that shall remain limited to avoid decreasing the accuracy: the background pressure introduced is generally large with respect to the air phase and triggers some spurious motion (for a box at rest with an air phase above the water phase with periodic lateral conditions, significant motion of the air phase was observed). We generally used the same sound speeds in both fluids. The present model proved not to be robust, especially near walls or open boundaries, due to the unrest of particles near the interface. Riemann solvers as recently used for air-water flow computations by Rezavand et al. [307] might be helpful to handle high density ratio flows.

3.3.1.2 Viscous stress operator

As a first step, to avoid increasing the complexity of our numerical model, we chose to neglect the additional viscous stress tensors depending on the relative velocity in (1.87). In the framework of the mixture model, the viscosity ν varies in space due to its dependence on the volume fraction. We used in the second operator of Morris et al. [274] presented in the relation (2.42). However, while it allows to take variable viscosity effects into account, it misses the transpose part of the viscous stresses. Español and Revenga [121] and Violeau [363] detailed the operator (2.43) taking

this part into account.

3.3.1.3 Convective transfer term

With respect to the single-phase formulation, one can note two main differences with the mixture model: mixture quantities are used for the variables and an additional term linked to the relative velocity appears in (1.87) as particles are moved with the mixture velocity. It corresponds to the third term of (1.88). In view of momentum conservation, an antisymmetric formulation is retained without boundary term:

$$\boldsymbol{D}_a^\gamma\{\alpha_b\beta_b\boldsymbol{v}_b^r\otimes\boldsymbol{v}_b^r\}=\frac{1}{\gamma_a V_a}\sum_{b\in\mathcal{F}}\left[V_a^2\alpha_a\beta_a\boldsymbol{v}_a^r\left(\boldsymbol{v}_a^r\cdot\boldsymbol{\nabla}w_{ab}\right)+V_b^2\alpha_b\beta_b\boldsymbol{v}_b^r\left(\boldsymbol{v}_b^r\cdot\boldsymbol{\nabla}w_{ab}\right)\right] \tag{3.47}$$

This term proved to generate spurious behaviors along the air-water interface, generating artificial mixing, so that, if not specified, it was neglected in the application cases detailed hereafter. Similarly to the treatment of the term $\boldsymbol{\nabla}\cdot(\alpha\beta\boldsymbol{v}^r)$ in the phase volume equation (3.20), one could consider an upwind formulation of this convective transfer term: this is left for future investigations.

3.3.1.4 Summary

Using the relations (2.54), (2.59) and (3.47), the momentum equation solved writes:

$$\frac{d\boldsymbol{j}_a}{dt}=-\frac{1}{\rho_a}\boldsymbol{G}_a^\gamma\{p_b\}+\frac{1}{\rho_a}\boldsymbol{L}_a^\gamma\{\nu_b,\boldsymbol{j}_b\}+\boldsymbol{g}-\boldsymbol{D}_a^\gamma\{\alpha_b\beta_b\boldsymbol{v}_b^r\otimes\boldsymbol{v}_b^r\} \tag{3.48}$$

the last term being considered only when specified.

3.3.2 Time marching scheme

The detailed resolution of our system is as follows (particle labels are dropped here and the notation $f_i, i\in\{1,4\}$ indicates the dependence on the model variables):

1. Relative velocity update using a closure of Sections 3.2.5 or 4.3.2.2:

$$\boldsymbol{v}^{r,n}=f_1\left(\rho^n,\alpha^n\right) \tag{3.49}$$

2. Operator splitting for the momentum equation: velocity update

   - Potential force step:

$$\boldsymbol{j}^\star=\boldsymbol{j}^n+\delta t\left[-\frac{1}{\rho^n}\boldsymbol{\nabla}p^n+\boldsymbol{g}\right] \tag{3.50}$$

- Convective transfer step (if taken into account):

$$\boldsymbol{j}^{\star\star} = \boldsymbol{j}^{\star} - \delta t \left[\boldsymbol{\nabla} \cdot (\alpha^n \beta^n \boldsymbol{v}_r^n \otimes \boldsymbol{v}_r^n)\right] \tag{3.51}$$

- $k - \epsilon$ update with (1.70) and (1.71) to compute the turbulent viscosity (if taken into account):

$$\nu_T^{\star} = f_2\left(k^{\star}, \epsilon^{\star}\right) \tag{3.52}$$

- Viscous force step:

$$\boldsymbol{j}^{n+1} = \boldsymbol{j}^{\star\star} + \delta t \left[\frac{1}{\rho^n} \boldsymbol{\nabla} \cdot \mathbb{T}^{\star}\right] \text{ with } \mathbb{T}^{\star} = \rho^n \left(\nu^n + \nu_T^{\star}\right) \left(\boldsymbol{\nabla} \boldsymbol{j}^{\star\star} +^t \boldsymbol{\nabla} \boldsymbol{j}^{\star\star}\right) \tag{3.53}$$

3. Particle position update:

$$\boldsymbol{r}^{n+1} = \boldsymbol{r}^n + \delta t \boldsymbol{j}^{n+1} \tag{3.54}$$

4. Total volume update using (3.23):

$$V^{n+1} = f_3(V^n, \boldsymbol{r}^n, \boldsymbol{r}^{n+1}) \tag{3.55}$$

5. Phase volume computations with (3.20):

$$V^{\alpha,n+1} = V^{\alpha,n} + \alpha^n \left(V^{n+1} - V^n\right) - \delta t V^n \boldsymbol{\nabla} \cdot (\alpha^n \beta^n \boldsymbol{v}^{r,n}) \tag{3.56}$$

6. Computation of other flow features using the expressions of the Section 3.2.4:

$$m^{n+1},\ \rho^{n+1},\ \alpha^{n+1} \tag{3.57}$$

7. Pressure computation using state equation (1.10):

$$p^{n+1} = f_4\left(\alpha^{n+1}, \rho^{n+1}\right) \tag{3.58}$$

To comply with the saturation condition (1.20), we deduce $\beta = 1 - \alpha$ when needed in the implementation.

3.3.3 Numerical stability

The conditions detailed in the Section 2.1.9.2 are used, complemented by the condition for positiveness of phase volumes (3.46). The convective transfer term (3.47) comprises an advective and a diffusion components and therefore requires a condition too. Nevertheless, as it was not included in most of the applications further detailed, we have not made the appropriate derivation. As long as the relative velocity stays small compared to the maximum velocity of the flow and the diffusion coefficient remains of the order of the (possibly turbulent) viscosity of the fluid, it seems reasonable to consider that this term will not introduce an additional stability condition.

3.4 Boundary conditions

3.4.1 Wall boundary conditions

The USAW boundary conditions presented in Section 2.1.5.2, with a safety factor of 0.5 to 0.75 in front of the C_{CFL} coefficient, together with the tools defined in Section 2.1.5.3 are used. A slight modification compared to previous works is that the density, instead of being interpolated from the values in the bulk of the fluid, is now computed through the inverse state law applied to the interpolated pressure. This allows to have consistent fields at the boundaries and take into account the pressure increment due to gravity.

Let us address the boundary conditions for volume fractions introduced in this chapter.

Neumann boundary condition In what follows, except in Section 3.5.2, the volume fractions at boundaries are computed with a Neumann condition using the following approximation:

$$\alpha_v = \sum_{b \in \mathcal{F}} V_b^\alpha w_{ab} \tag{3.59}$$

This value of the volume fraction of vertex particles (and segments) is employed in the inverse state law to compute the density and mass of vertex particles from the interpolated pressure: indeed, densities and masses are used to compute the volumes involved in the boundary term of the SPH pressure gradient (2.54).

Robin boundary condition In the Section 3.5.2, a Robin boundary condition is needed. Several formulations were developed to model Robin boundary conditions in SPH. A possible approach is described by Mayrhofer et al. [245]. Sikarudi and Nikseresht [331] claim an improved accuracy in two dimensions with a method less sensitive to particle disorder. An alternative way is to modify the governing equations. Pan et al. [286] used the Continuous Boundary Force (CBF) method: a homogeneous Neumann boundary condition and a volumetric force term added to the momentum conservation equation replace the Robin boundary condition. Ryan et al. [317] employed the Continuum Surface Reaction (CSR) model: the interface is then considered as as a diffuse region over which the flux boundary condition is applied. The approach of Mayrhofer et al. [245] is considered here and detailed in the Section 3.5.2.

3.4.2 Open boundaries

The mixture open boundaries developed in this work lie within the framework of Ferrand et al. [129] and its generalization of USAW conditions with the resolution of a one-dimensional Riemann problem at open boundaries. Though time consuming, it allows one to impose precisely the desired velocity or pressure profiles and deduce the missing quantities through a rigorous

framework inspired from finite volume developments. The extension to the mixture model detailed here requires taking into account the additional volume fraction equation and the possible presence of mixtures at open boundaries. In the derivation, we will consider that there is no relative velocity at the boundary: the resolution of the consequent homogeneous system, where the volume (or mass) fraction is a transported quantity, was already studied in the finite volume approach, see for example Blondel et al. [26]. Compared to those studies, we work here in a simplified framework of barotropic and subsonic flow: fewer configurations of the Riemann problem have to be considered. For the sake of legibility, the theoretical developments made are presented in Appendix B where the method is first recalled for the single-fluid framework in Appendix B.2 and then extended to the mixture model in Appendix B.3. The prominent features of this extension of the formulation of Ferrand et al. [129] to the mixture model are the switch from density to specific volume as main variable and the inclusion of the volume fraction equation in the Riemann problem resolution. This formulation allows one to treat indifferently inlets and outlets, even on the same boundary, in a way variable in space and time.

Correction in the single-fluid formulation In Appendix B.2, a correction of the formalism was made compared to the method presented in [129]: indeed, in this work, for a shock wave, the relations were derived as if the shock wave velocity was null. We derive here the relations without any approximation on the shock speed. Moreover it was considered that the equality of left and right states of the tangential velocity was an assumption. It is shown here that it is a consequence of the Riemann formulation. The test cases developed in [129] were run with these improvements and compared to the original formulation, namely the non-orthogonal flux on inlet/outlet in a square, a rapidly expanding pipe, 2D periodic free-surface water wave and a 2D solitary wave. Similar behaviors as in Ferrand et al. [129] were obtained: the computed solutions of the Riemann problems at boundaries in case of shock wave (the only different configuration) are close. Nevertheless, it is an improvement as seen on the 2D periodic free-surface water wave test case for which we get more regular fields near the open boundaries.

Time integration of the continuity equation The open boundaries modify the resolution of the continuity equation (3.23). Some terms are added to avoid spurious density variations close to the open boundaries. This formulation now relying on specific volumes instead of densities is detailed in Appendix B.1.

Update of vertex particles features Vertices have variable masses and volumes. Masses are computed similarly to Ferrand et al. [129] except that the mass flux on a vertex v surrounded by segments s is now assessed using:

$$\dot{m}_v = \frac{1}{2}\sum_b \frac{\alpha_v\rho^\alpha + \beta_v\rho^\beta}{\alpha_s\rho^\alpha + \beta_s\rho^\beta}\rho_s S_s \left(\boldsymbol{J}_s - \boldsymbol{j}_s\right)\cdot\boldsymbol{n}_s \tag{3.60}$$

where S_s is the segment surface and where a factor, function of volume fractions, has been added in the sum to prevent one fluid to disrupt the mass flux computation of the other near the interface. Here $\boldsymbol{J}$ denotes the Eulerian velocity field while $\boldsymbol{j}$ is the Lagrangian velocity field, these fields being distinct only at open boundaries.

Pressure and velocity at open boundaries A one-dimensional Riemann problem is solved at open boundaries to compute compatible pressure and velocity fields (*i.e.* deduce a velocity field from an imposed pressure profile, or conversely). Characteristic waves allow one to make the link between the exterior state (the boundary condition we impose) and the interior state (interpolated from the fluid values) and finally deduce the state at the boundary. Notations and derivations are presented in Appendix B.3. The relation between pressure and velocity fields will depend on the type of discontinuity – expansion or shock – of the characteristic wave propagating in the domain. Due to the linearized state equation used, the case distinction between expansion and shock waves was simplified to a comparison between interior and exterior states for velocities or pressures respectively, depending on whether the velocity or pressure is imposed by the user.

Disclaimer An error was only lately identified in the open boundary framework: the term denoted ϕ_r in the Appendix B.3 was not considered in the computations exposed here. It can normally only be neglected under the Colagrossi and Landrini's choice of sound speeds (2.110) but it was not the choice of parameters retained in the considered cases. One will see that the inlets and outlets of mixed flows work properly on a simple test case without gravity. It was checked on the more complex cases including gravity of Chapter 4 that the flow enters and leaves the domain correctly, without disturbances for the region of interest for the study. The choice of working with equal phase sound speeds with a formulation that reduces to the single-fluid formulation in absence of ϕ_r may explain the correct behaviour obtained for the air entrainment test cases.

3.5 Numerical verification and validation

Verification and validation [6] are now carried out. All the verification/validation cases are two-dimensional with particles initially arranged on a Cartesian lattice.

3.5.1 Separation

The separation of liquid dispersions or the sedimentation in a settling tank are common industrial separation problems. In this section, we investigate two applications of this separation

[6] *"Solving the equations right" vs. "solving the right equations"* following Blottner [27].

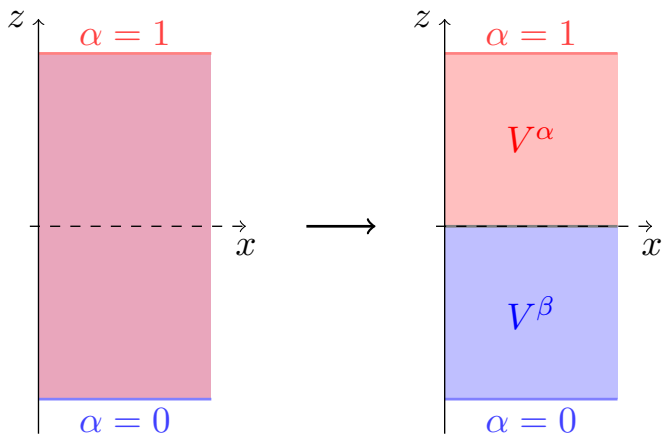

Figure 3.5: Separation case: initial and final states.

phenomenon illustrated in Figure 3.5. This validation test case is of particular interest to check the realizability and conservativity of the numerical scheme.

3.5.1.1 Separation of an oil-water dispersion

Description A vertical rectangular column of dimensions $L \times H$ contains a mixture of oil and demineralized water, with an initial uniform volume fraction of oil $\alpha_0 = 0.3$. The physical and numerical parameters are detailed in Table 3.3. A relatively fine discretization (183 particles over the fluid column) is used to track the interface position accurately.

Table 3.3: Parameters for the separation of an oil-water dispersion.

L	0.24	m	H	0.915	m
ρ^α	837	kg/m^3	ρ^β	996	kg/m^3
ν^α	1.5 10^{-6}	m^2/s	ν^β	10^{-6}	m^2/s
c^α	45	m/s	c^β	45	m/s
d^α	1.2	mm	d^β	1.2	mm
δr	5	mm	p_B	0	Pa

In the momentum equation, in order to stabilize the flow and as our focus is on the volume fraction resolution, we used higher viscosities, equal for both fluids $\nu^\alpha = \nu^\beta = 0.03$ m^2/s. As the mixture is assumed to remain in hydrostatic equilibrium, this should not influence the result very much: particles have negligible motions and the separation is driven by the phase volume equation that triggers phase exchanges between particles.

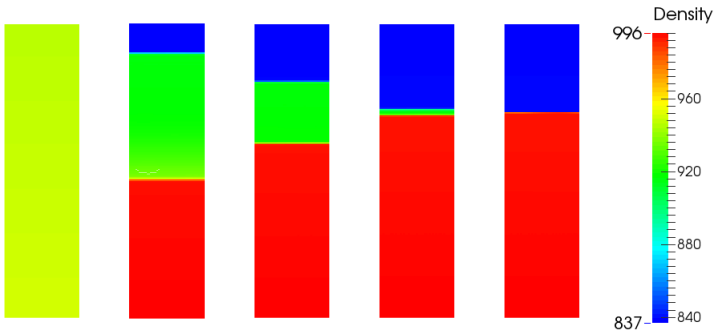

(a) t=0 s (b) t=50 s (c) t=100 s (d) t=150 s (e) t=200 s

Figure 3.6: Separation of an oil-water dispersion: density evolution through the decantation process.

Reference data Experimental and numerical validation (FLOW-3D® software) are provided in Jeelani and Hartland [180] and Brethour and Hirt [38], respectively. FLOW-3D® is a finite difference code based on structured meshes as described in [139]. It uses a semi-implicit resolution of the continuity/momentum equation with a first order convergence. For dispersed two-phase flow, it provides a mixture model similar to the one exhibited in the present work with a volume-based formulation using a volume-weighted mixture velocity (to automatically enforce incompressibility). This model is described in [38] and the relative velocity closure is as in (3.38). A switch of the definition of the dispersed phase is done at the threshold $\alpha = 0.5$, so that continuous and dispersed phase are exchanged in the relative velocity definition.

Results The temporal evolution of the separation is displayed in Figure 3.6. We can observe the generation and motion of two clear interfaces until complete separation of oil and water phases. Figure 3.7 shows the evolution of the positions of these interfaces through the separation process, and shows good agreement with FLOW-3D® and experimental results. Convergence in time is illustrated by the final interface position, located at 30% to the top wall (which confirms that phase conservation is fulfilled). The slowdown of the interface progression velocity around 50 s is reproduced, and appeared to be linked to the switch of definitions of dispersed and continuous phases made at $\alpha = 0.5$ for the computation of the relative velocity. Let us recall that d^α and d^β are the only calibration parameters of this model.

3.5.1.2 Separation of an air-water mixture

Description A vertical rectangular column of dimensions $L \times H$ contains a mixture of air and water with an initial volume fraction of air $\alpha_0 = 0.5$. The physical and numerical parameters are presented in Table 3.4. As a first step, high kinematic viscosities are taken. The constant relative velocity used is equal to 0.45 m/s. Compared to the previous one, this validation case aims at challenging conservation for high density ratios; we are mainly interested in the final state.

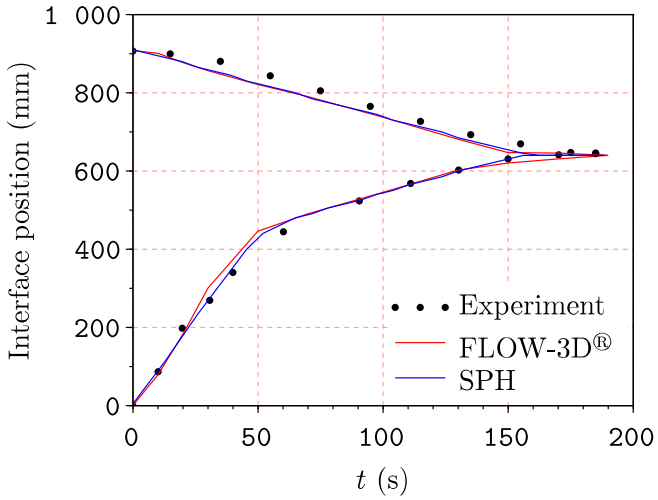

Figure 3.7: Separation of an oil-water dispersion: evolution of the upper and lower interface positions. Comparison of experimental data of [180] and numerical results of the present model and [38].

Table 3.4: Parameters for the separation of an air-water mixture.

L	1	m	H	2	m
ρ^α	1.23	kg/m^3	ρ^β	1000	kg/m^3
ν^α	0.03	m/s^2	ν^β	0.03	m/s^2
c^α	45	m/s	c^β	45	m/s
d^α	1.2	mm	d^β	1.2	mm
δr	10	mm	p_B	0	Pa

Results Figure 3.8a shows that at convergence, both fluids are separated, and volume is conserved (the interface appears in the middle of the domain). Note that the upwind integration scheme (3.20) that we introduced was essential to obtain such a result. Once the separation is established, we observe some instabilities developing near the interface, due to the pressure gradient computation, as highlighted in Figure 3.8b. The pressure gradient discontinuity is however well computed at convergence, as shown in Figure 3.9a. One can see in Figure 3.9b that there is a non negligible error at the interface, but also near the upper boundary as pressure values are quite small (for the relative error computation, the minimum pressure in the domain has been subtracted, as a constant pressure offset was present throughout the domain). In the bulk of the fluid domain, the error is close to 1%, as expected in WCSPH.

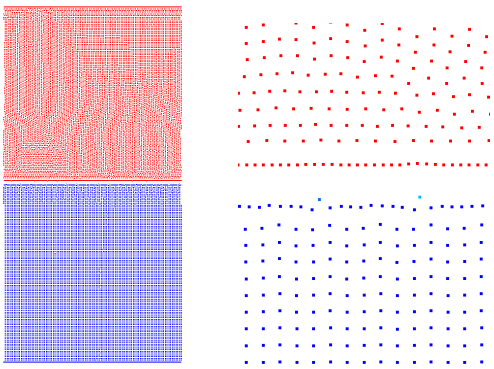

(a) Global view. (b) Focus on the interface.

Figure 3.8: Separation of an air-water mixture: separated state.

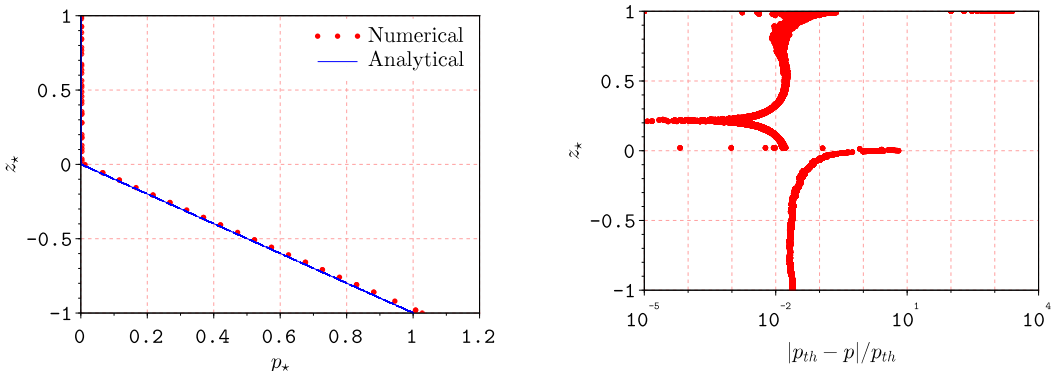

(a) Pressure profile (reduced number of particles displayed). (b) Relative error.

Figure 3.9: Separation of an air-water mixture: pressure field of the separated state.

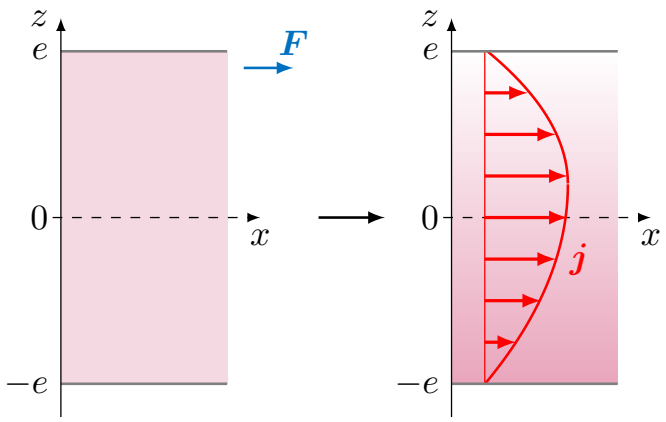

Figure 3.10: Two-phase mixture Poiseuille flow: initial and final states.

3.5.2 Two-phase mixture Poiseuille flow

Description In this verification case, the computational domain is a rectangle of dimensions $e \times 2e$ periodic along the x direction as illustrated in Figure 3.10. The fluid is submitted to a longitudinal force $\rho \boldsymbol{F}$ mimicking a pressure gradient as in a pipe Poiseuille flow. However, no gravity is introduced as it proved to trigger some small instabilities in the velocities and pressure profiles (the gravity effect is all included in the closure of the relative velocity). Starting from a homogeneous mixture $\alpha_0 = 0.05$ at rest, the flow should converge towards the analytical dimensionless steady state detailed in Appendix D, obtained with a relative velocity given by (3.42) at constant mixture kinematic viscosity $\nu^\alpha = \nu^\beta$ and under an incompressibility hypothesis. Note that our first model developed and presented in [136] used a mixture kinematic viscosity instead of a dynamic viscosity. The convergence studies are therefore carried out with a mixture kinematic viscosity. We checked when we switched to mixture dynamic viscosity that the solution still got to the corresponding analytical solution also derived in Appendix D. The values of bubble diameter and diffusivity are chosen arbitrarily to exhibit a steep volume fraction gradient. The corresponding Péclet number equals $\mathrm{Pe} = 7.26$.

This flow is analogous to a Rouse flow described in Rouse [314] but with a rising instead of settling velocity and constant turbulent coefficient K. More complex semi-analytical approaches have been developed, including variable turbulence, for sediment flows as done by Hsu et al. [169]. A background pressure is set to avoid particle disorder near boundaries that usually appears in WCSPH Poiseuille flows. The physical and numerical parameters are presented in Table 3.5.

Robin boundary condition The volume fraction at vertices v of normal $\boldsymbol{n}_v$ is computed thanks to a second order approximation method for Robin boundary condition as detailed in Mayrhofer et al. [245]. The no-flux condition at the boundary:

$$\boldsymbol{v}^r = \boldsymbol{0} \quad \longleftrightarrow \quad \alpha \left(\boldsymbol{v}_0 \cdot \boldsymbol{n} \right) - K \frac{\partial \alpha}{\partial \boldsymbol{n}} = 0 \tag{3.61}$$

Table 3.5: Parameters for the two-phase mixture Poiseuille flow.

e	1	m	K	0.02	m^2/s
ρ^α	1.23	kg/m^3	ρ^β	1000	kg/m^3
ν^α	0.03	m^2/s	ν^β	0.03	m^2/s
c^α	1	m/s	c^β	1	m/s
d^α	200	mm	d^β	200	mm
δr	10	mm	p_B	250	Pa
$\lvert \boldsymbol{F} \rvert$	0.02	m/s^2	g	0	m/s^2

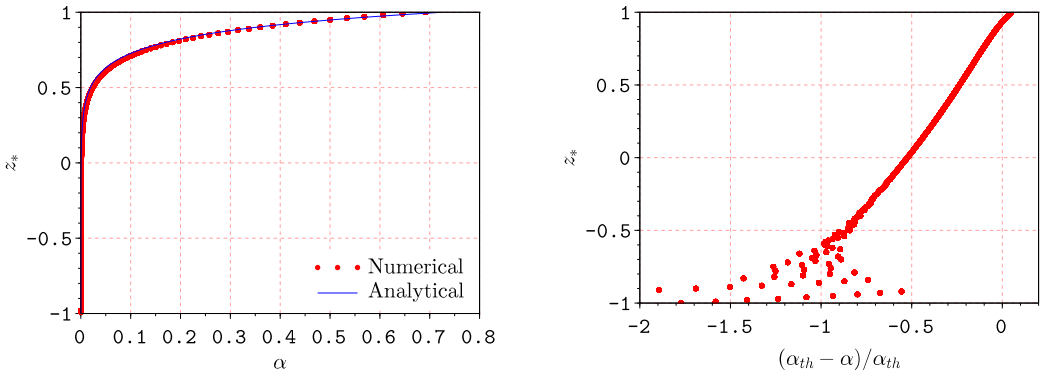

(a) Volume fraction profile

(b) Relative error

Figure 3.11: Two-phase mixture Poiseuille flow with constant kinematic viscosity: volume fraction at steady-state.

where $\boldsymbol{n}$ is the normal to the wall is approximated using:

$$\alpha_v = \sum_{b\in\mathcal{F}} \frac{V_b^\alpha}{\Sigma_v} \left(Y_v \left(1 - (\boldsymbol{v}_0 \cdot \boldsymbol{n}_v)(\boldsymbol{r}_{vb} \cdot \boldsymbol{n}_v)/K\right) - Z_v (\boldsymbol{r}_{vb} \cdot \boldsymbol{n}_v)^2 \right) w_{vb} \tag{3.62}$$

$$\Sigma_v = X_v Y_v - Z_v^2 \tag{3.63}$$

$$X_v = \sum_{b\in\mathcal{F}} V_b \left(1 - (\boldsymbol{v}_0 \cdot \boldsymbol{n}_v)(\boldsymbol{r}_{vb} \cdot \boldsymbol{n}_v)/K\right)^2 w_{vb} \tag{3.64}$$

$$Y_v = \sum_{b\in\mathcal{F}} V_b (\boldsymbol{r}_{vb} \cdot \boldsymbol{n}_v)^4 w_{vb} \tag{3.65}$$

$$Z_v = \sum_{b\in\mathcal{F}} V_b \left(1 - (\boldsymbol{v}_0 \cdot \boldsymbol{n}_v)(\boldsymbol{r}_{vb} \cdot \boldsymbol{n}_v)/K\right) (\boldsymbol{r}_{vb} \cdot \boldsymbol{n}_v)^2 w_{vb} \tag{3.66}$$

Results The resulting volume fraction and longitudinal velocity profiles at convergence are displayed in Figures 3.11 and 3.12. There is a very good agreement between analytical and numerical solutions. Let us underline that the highest relative errors are obtained in zones where the volume fraction or the mixture velocity are very small.

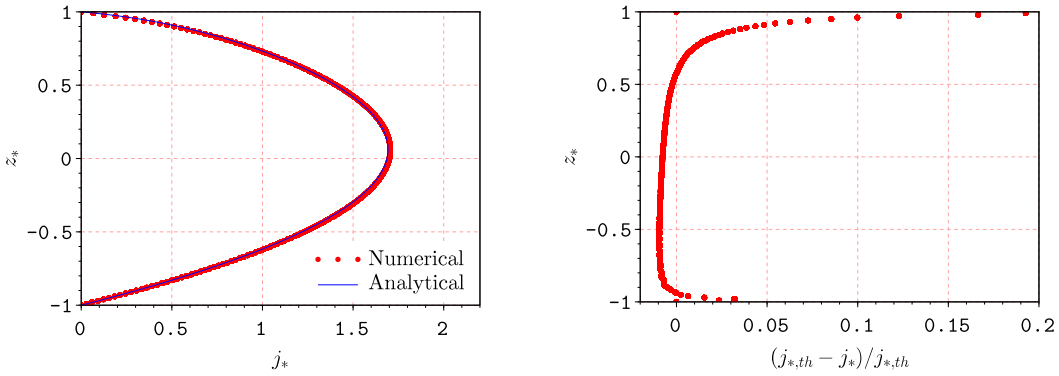

(a) Longitudinal velocity profile.

(b) Relative error.

Figure 3.12: Two-phase mixture Poiseuille flow with constant kinematic viscosity: longitudinal velocity at steady-state. Note that the theoretical solution (see Appendix D) is not a parabola.

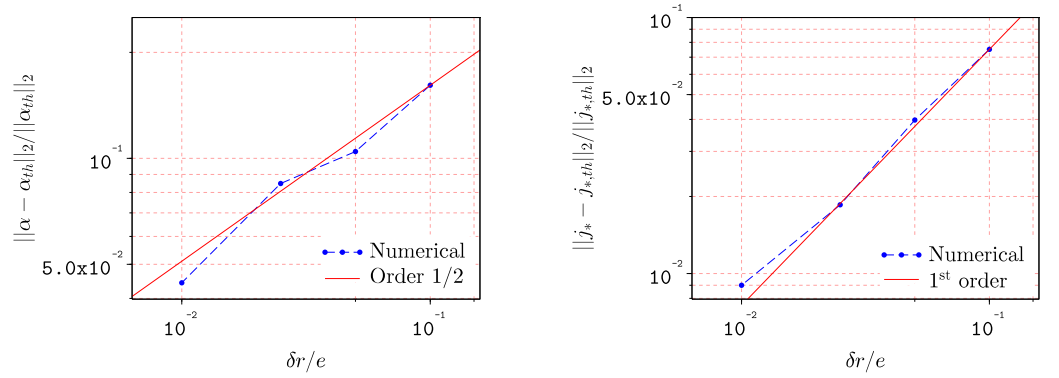

(a) Volume fraction.

(b) Longitudinal velocity.

Figure 3.13: Two-phase mixture Poiseuille flow: convergence studies.

Convergence curves are displayed for the volume fraction and longitudinal velocity profiles in Figures 3.13a and 3.13b respectively, plotting the instantaneous $\mathcal{L}^2$ relative error for the steady-state field as a function of the dimensionless particle size $\delta r/e$. This relative error for a field A compared to the analytical profile A_{th} is computed as:

$$\frac{||A - A_{th}||_2}{||A_{th}||_2} = \sqrt{\frac{\sum_{b\in\mathcal{F}} \left(A_b - A_{th}\left(z_b\right)\right)^2}{\sum_{b\in\mathcal{F}} A_{th}\left(z_b\right)^2}} \tag{3.67}$$

The convergence slope is approximately of order 1/2 for the volume fraction and 1 for the longitudinal velocity. The upwind low-order formulation of the phase volume equation might explain this weak order of convergence for the volume fraction.

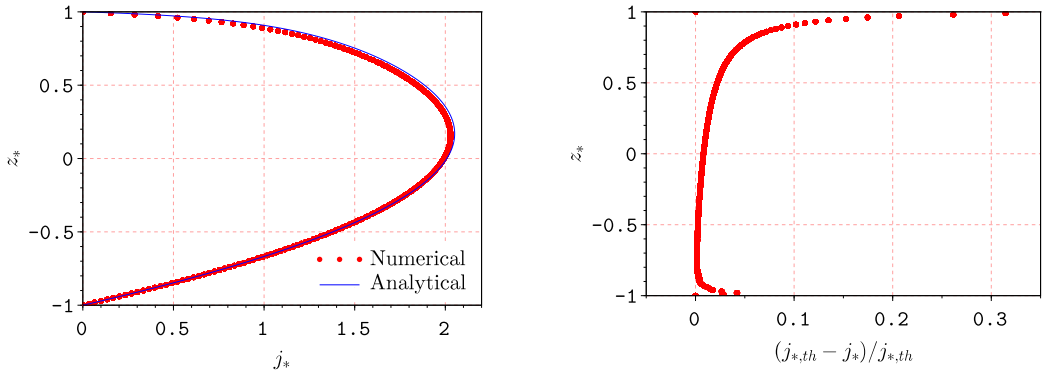

(a) Longitudinal velocity profile.

(b) Relative error.

Figure 3.14: Two-phase mixture Poiseuille flow with varying kinematic viscosity: longitudinal velocity profile at steady-state.

As a second step, one can consider a case with a varying mixture kinematic viscosity. Only the longitudinal velocity profile is modified: its expression is detailed in Appendix D. All parameters remain unchanged compared to previous configuration, except the viscosity $\nu^\alpha = 0.001$ m^2/s. We get, after convergence, the longitudinal velocity profile displayed in Figure 3.14 (the volume fraction profile is unchanged). Again, analytical and numerical solutions agree very well, even though, due to slight discrepancies on the volume fraction profiles, one can notice that the velocities are a bit smaller than expected in the upper part of the flow (the kinematic viscosity also varies with the volume fraction in this case, and the largest absolute errors on the volume fraction are made in the upper part of the flow, therefore influencing the shear stress, and consequently the quality of the velocity profile).

Switch of dispersed in the relative velocity A similar study was carried out in the case we use a relative velocity with a switch of dispersed phase as further detailed in Section 4.3.2.2 and adequate parameters that allow for the derivation of an analytical solution. One can refer to Fonty et al. [138] for further details.

3.5.3 Rayleigh–Taylor instability

Description The computational domain of this validation case is a rectangle of dimensions $e \times 2e$ bounded by walls. As illustrated in Figure 3.15, the fluid domain initially consists of a heavy phase over a light phase with an interface defined by $z = 1 - 0.15\sin(2\pi x)$. The homogeneous model is solved, *i.e.* without relative velocities. The physical and numerical parameters are presented in Table 3.6 and chosen to be consistent with Grenier et al. [150].

Table 3.6: Parameters for the Rayleigh–Taylor instability.

e	1	m	g	1	m/s^2
ρ^α	1000	kg/m^3	ρ^β	1800	kg/m^3
ν^α	$2.381\ 10^{-3}$	m^2/s	ν^β	$2.381\ 10^{-3}$	m^2/s
c^α	14	m/s	c^β	10	m/s
ξ	7		p_B	3.6	Pa

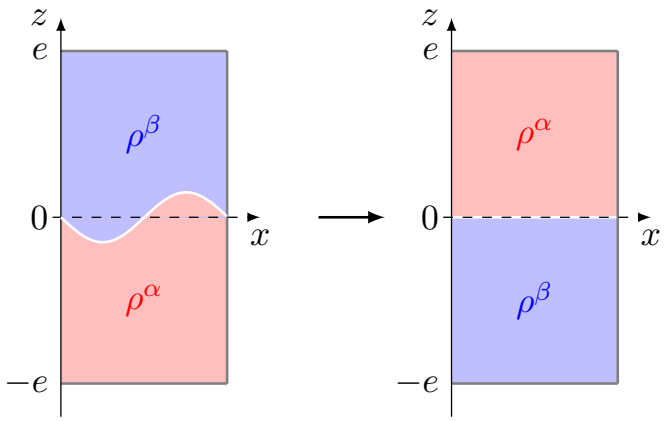

Figure 3.15: Rayleigh–Taylor instability: initial and final states.

Pressure To compare with the results from [150], the state equation takes the form:

$$p = \frac{\left(\alpha\rho^\alpha (c^\alpha)^2 + \beta\rho^\beta (c^\beta)^2\right)}{\xi}\left[\left(\frac{\rho}{\alpha\rho^\alpha + \beta\rho^\beta}\right)^\xi - 1\right] + p_B \tag{3.68}$$

Sound speeds are chosen following (2.110). As spurious fragmentation occurs at the interface between fluids, a small repulsive force was added in the pressure gradient, following [150]. This force consists of an additional term in the pressure gradient when the neighboring particle belongs to another phase. Its expression was extended to the mixture model (without boundary term):

$$\begin{aligned} \boldsymbol{G}_a^\gamma\{p_b\} &= \frac{1}{\gamma_a V_a}\sum_{b\in\mathcal{F}}\left(V_a^2 p_a + V_b^2 p_b\right)\boldsymbol{\nabla} w_{ab} \\ &+\epsilon_I \frac{1}{\gamma_a V_a}\sum_{b\in\mathcal{F}}\left(\alpha_a\beta_b + \alpha_b\beta_a\right)\left(V_a^2|p_a| + V_b^2|p_b|\right)\boldsymbol{\nabla} w_{ab} \end{aligned} \tag{3.69}$$

where the factor $(\alpha_a\beta_b + \alpha_b\beta_a)$ is equal to 1 when a and b belong to distinct phases, and 0 otherwise as long as phases remain separated, as in this Rayleigh–Taylor case without relative velocity. The relevance of this term for intermediate volume fractions is questionable. As suggested by [150], ϵ is taken equal to 0.01.

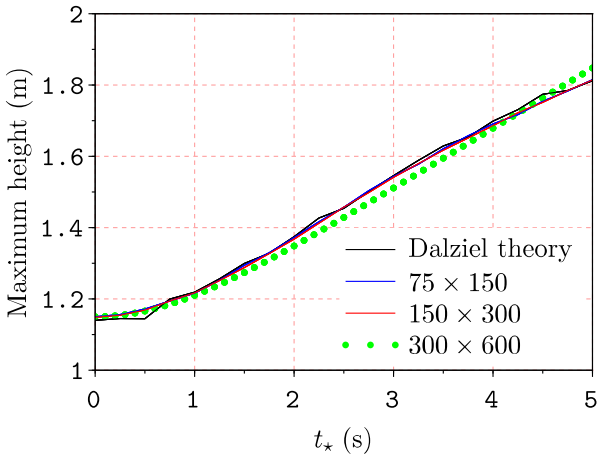

Figure 3.16: Rayleigh–Taylor instability: time variation of the vertical position of the highest point of the low-density fluid for the three discretizations considered with the Layzer's theory (though obtained for a periodic domain) as simplified by Dalziel [97].

Results This test case aims at checking the numerical behaviour for separated phases: the multifluid behaviour should be recovered. Figure 3.17 shows the temporal evolution of the phases with the finest resolution (300 particles per unit length). Figure 3.18a displays a convergence study of the shape of the interface at the dimensionless time $t_\star = t\sqrt{g/e} = 5$ in which one can see the convergence of the interface shape. Figure 3.18b compares the finest discretization interface with the one obtained in [150] with SPH and a Level-Set model at equivalent discretizations, showing a good agreement. Some discrepancies can be observed in the curling-up region of the mushroom-shaped heads. We compare on Figure 3.16, the time variation of the vertical position of the highest point of the low-density fluid for the three discretizations considered with the Layzer's theory (though obtained for a periodic domain) as simplified by Dalziel [97]. One can observe that the three numerical curves are superimposed and agree well with the theory.

Introducing a constant relative velocity (3.37) chosen arbitrarily with $d^\alpha = 0.07$ m, phases first diffuse and rapidly converge towards a separated state as in section 3.5.1. Simulations without and with relative velocity are displayed in Figure 3.19. One can see that without relative velocity (*i.e.* configuration equivalent to the multifluid model), phases are not fully separated as some drops remain in both phases and are under-resolved because of the size of SPH particles (a steady state is not reached even at $t_\star = 500$ even though phases are then more clearly separated). An inaccurate pressure gradient computation for those small size structures might explain this behavior, making our mixture approach useful in such circumstances.

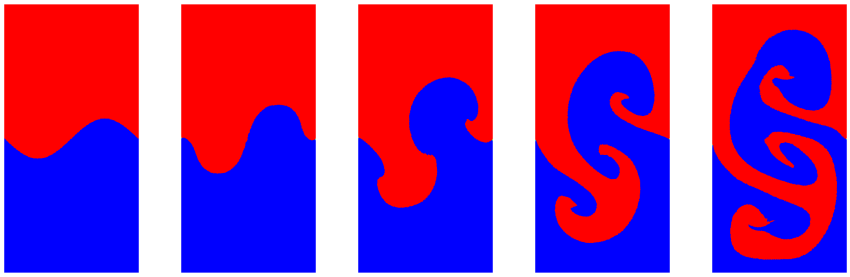

(a) $t_\star = 0$ (b) $t_\star = 1.25$ (c) $t_\star = 2.5$ (d) $t_\star = 3.75$ (e) $t_\star = 5$

Figure 3.17: Rayleigh–Taylor instability: light (blue) and heavy (red) phases evolution for a discretization of 300 particles per unit length.

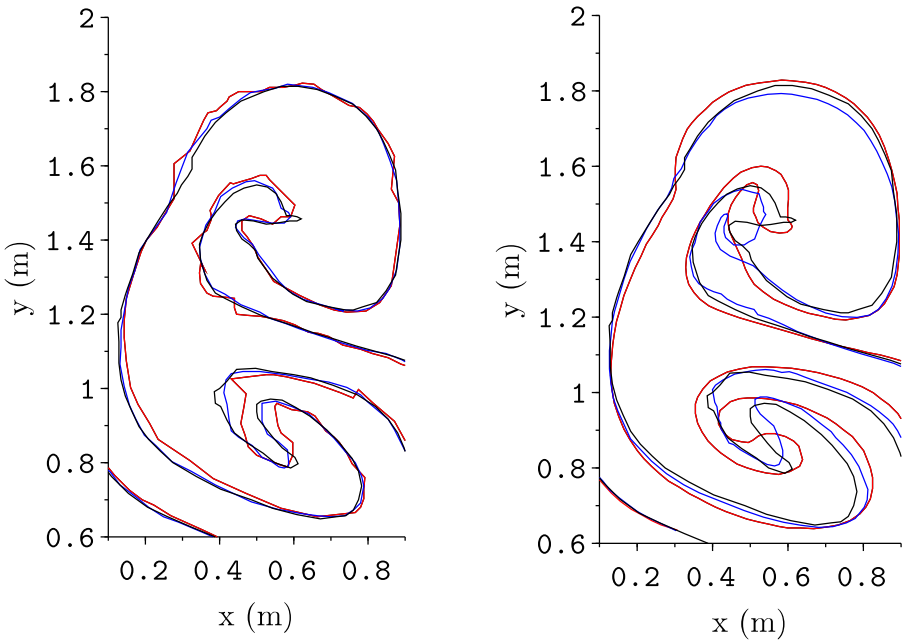

(a) Convergence study. (b) Comparison with [150].

Figure 3.18: Comparison of the interfaces for the Rayleigh–Taylor instability case at $t_\star = 5$. On the left, a convergence study is displayed for 75 (red line), 150 (blue line) and 300 (black line) particles per unit length. On the right, a comparison is made between Level-Set (red line) and SPH (blue line) results of [150] and the present SPH model (black line) for the same resolution.

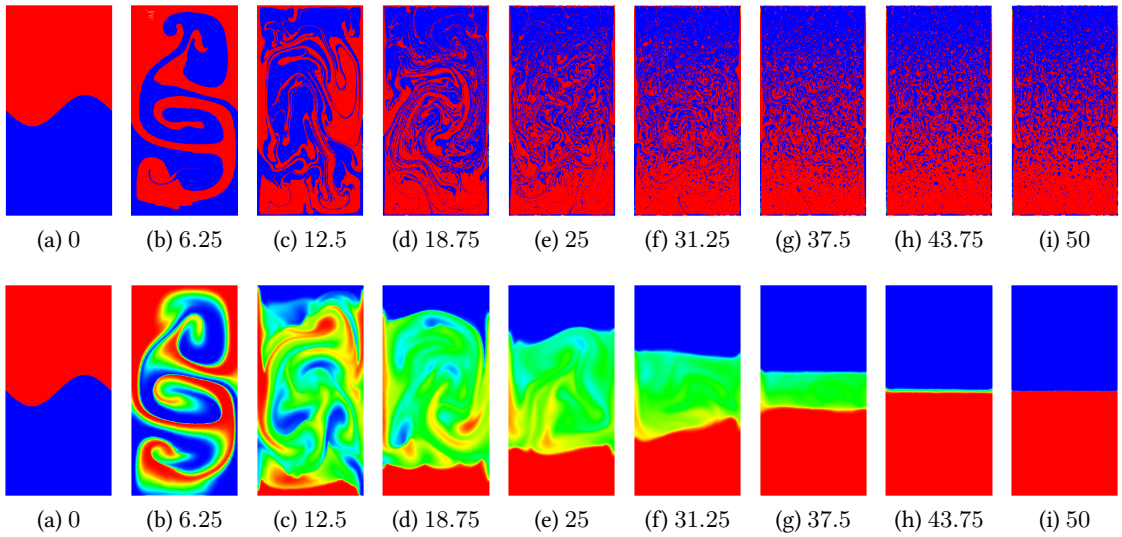

Figure 3.19: Rayleigh–Taylor instability: evolution of the volume fractions with $t_\star$ from the light (blue) to heavy (red) phases without (upper series) and with (lower series) relative velocity for a discretization of 300 particles per unit length.

3.5.4 Limits of the mixture model: a sand dumping case

In this section, the performances of the presented mixture model are assessed on a case of sand dumping described by Shi et al. [327]. Shi et al.'s two-velocity model was described in Section 2.3.3.1. Several test cases were considered in their work: among them, the settling of natural sand in still water (corresponding to the advection of a cosine function of volume fraction) and the sand dumping case. We quickly addressed the former and saw that our numerical scheme proved to be more diffusive for the volume fractions, the maximum volume fraction decreasing faster. We focus in the following on the latter case. It implies enriched physics compared to the previous cases described in the present chapter, with the presence of a free surface and a physically-based relative velocity closure. α denotes the sediment phase and β the water phase.

Description The configuration of this validation case is a square water tank of dimension L with a free surface as described in Figure 3.20. In the middle of the domain, just under the free surface, a sand block is initially released with a volume fraction α_0 equal to the maximum sediment packing α_{mp}. Many different configurations were considered in [327] but we will focus on the tests for which experimental results are available. The sand cloud is initially $W_0 = 2$ or 4 cm wide and $H_0 = 2.5$ cm high. The three sizes of sediment d^α considered are 0.8 mm, 1.3 mm and 5 mm that correspond to settling velocities of 12.60 cm/s, 19.61 cm/s and 49.52 cm/s, respectively. The physical and numerical parameters are detailed in Table 3.7.

Table 3.7: Parameters for the sand dumping case.

L	1	m	g	9.81	m/s^2
ρ^α	2650	kg/m^3	ρ^β	1000	kg/m^3
ν^α		varies	ν^β	10^{-6}	m^2/s
c^α	32	m/s	c^β	32	m/s
δr	5	mm	p_B	0	Pa

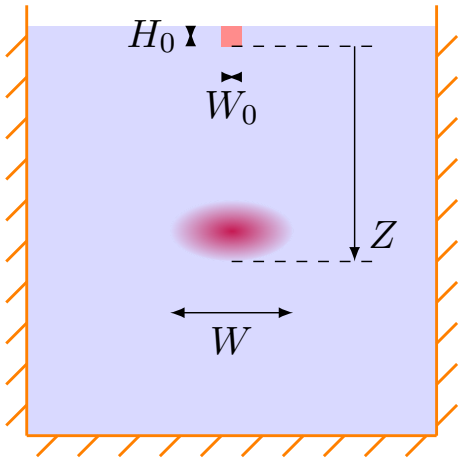

Figure 3.20: Sand dumping: sand cloud features.

Modeling choices In order to have a fair comparison with the two-fluid approach developed in [327], several changes were introduced to deal with the complete physics of this case:

- Computation of the sediment phase viscosity following Alihan and Sleath's formula [7]:

$$\nu^\alpha = 1.2\frac{\rho^\beta}{\rho^\alpha}\left[\left(\frac{\alpha_{mp}}{\alpha}\right)^{\frac{1}{3}} - 1\right]^{-2}\nu^\beta \tag{3.70}$$

  where the maximum sediment volumetric concentration α_{mp} was set to 0.607 in our computations (instead of 0.606 in [327]) to avoid singularity of the viscosity at the initialization (indeed the sediment cloud starts with this concentration).

- Computation of a turbulent viscosity, added to the physical one, following a Smagorinsky model[7]:

$$\nu_T = (C_s\delta r)^2\, S^j \left(1 - \frac{\alpha}{\alpha_{mp}}\right)^{n_s} \tag{3.71}$$

  where $C_s = 0.1$ and $n_s = 5$. Please note that we are using here the mixture rate-of-strain tensor defined by (1.73) that differs from the phase rate-of-strain tensors used for distinct

[7]Some prefer using the smoothing length h in place of δr. It is a matter of convenience about the definition of C_s. However, we emphasize that, following Dehnen and Aly [104], h is meaningless and should be replaced by the kernel standard deviation.

phase turbulent viscosities computations in [327]. Moreover, a sensitivity analysis has been conducted in [327] to optimize the results with adequate choice of the Smagorinsky coefficients and power law, choices that might not be optimal in the framework of our mixture model.

- A relative velocity closure is deduced from [327] continuous equations. It includes the drag effect, an hindering factor computed with Richardson and Zaki's formula [311] and a turbulent diffusion of volume fraction based on a gradient transport law:

$$\boldsymbol{v}^r = \frac{4}{3}\frac{\beta^{2.65}\left(\rho^\alpha - \rho^\beta\right) d^\alpha}{\rho^\beta \mathsf{C_D}|\boldsymbol{v}^r|}\frac{\boldsymbol{\nabla} p}{\rho} - \frac{\nu_T}{\mathsf{Sc}_T}\frac{\boldsymbol{\nabla}\alpha}{\alpha\beta} \tag{3.72}$$

  where the drag coefficient is computed according to the Reynolds number following the Schiller and Naumann's formula [85, 320]:

$$\mathsf{C_D} = \begin{cases} \frac{24}{\mathsf{Re}^\alpha}\left(1 + 0.15\left(\mathsf{Re}^\alpha\right)^{0.687}\right) & \text{if } \mathsf{Re}^\alpha < 1000 \\ 0.44 & \text{if } \mathsf{Re}^\alpha \geq 1000 \end{cases} \tag{3.73}$$

  Iterations are made to converge to a well-defined value of the relative velocity, due to the implicit relation implied by the drag. The turbulent Schmidt number Sc_T is taken equal to 1.

- The convective transfer $\boldsymbol{\nabla}\cdot\left(\alpha\beta\boldsymbol{v}^r\otimes\boldsymbol{v}^r\right)$ term was included in the momentum equations and proved to be necessary to reproduce the topology of the cloud, as a consequence of the dynamics of the flow. A correction has been made in the pressure gradient factor compared to the formulation detailed in Fonty et al. [136] as the interfacial momentum transfer term was not closed correctly compared to what is done in Chapter 1. The second order operator (2.43) is considered. Negligible difference was obtained with (2.42) on this test case.

A different state equation is used in [327] but the tests made did not highlight any significant modification of the following results. One can follow temporally the evolution of the cloud, defined as the particles with a sediment volume fraction α equal to at least 5% of the maximum value in the domain at the considered instant, through its vertical position Z, its width W and its frontal velocity w_c. Moreover, one can follow the free surface fluctuations at the release point z_w: this must be handled with care however, as the fluctuations after the initial jump are of the order of the particle size. The nondimensionalization coefficients used in the graphs are:

$$L_0 = \sqrt{W_0 H_0} \quad \text{and} \quad u_0 = \sqrt{\frac{\alpha_0\rho^\alpha + (1-\alpha_0)\rho^\beta}{\rho^\beta} g L_0} \tag{3.74}$$

Results Computations used 40000 particles and last for one hour for 6 seconds of physical time. These computational times are comparable with the one of [327] that has an additional

equation to solve but the code used here as not been optimized yet. Numerical results of the mixture model are compared with SPH results of Shi et al. [327] and experimental results of Nakasuji et al. [276] for the frontal velocity of the cloud in Figures 3.21a and 3.21b, for the vertical position of the cloud in 3.22 and for the cloud width in Figures 3.23a and 3.23b. The frontal velocity is overestimated in the late time of the simulation, once the initial transient is passed, even though there is an overall good trend. The cloud falls more rapidly than in [327], especially for large sediments (*i.e.* large relative velocities). According to Bühler and Papantoniou [42], the fall can be separated in two regimes, the distinction being made when the frontal velocity of the cloud goes down to the terminal velocity of the sediments: the thermal stage during which the fluid moves together with the sediments and a swarm stage for which sediments fall within a fluid nearly at rest. Figure 3.22 highlights that we reproduce correctly the first phase but miss the change of regime occurring, the cloud falling faster than expected, consistently with the frontal velocity computations. According to Nguyen et al. [279], vorticity is largely underestimated with a single-velocity model: the absence of recirculations slowing down the fall within the lower part of the cloud could explain that the cloud falls more rapidly with the mixture model. However it corresponds to the swarm state in which the fluid should remain close to rest. The cloud width is correctly reproduced for small sediments in the first moments of the fall, until $Z = 4L_0$, then the model fails at reproducing the change of slope with an increase of the cloud width growth. Figure 3.24 shows the good reproduction of the free surface fluctuations. Regarding the cloud distribution, the two-phase model of [327] predicts a double-peak turbidity distribution (two symmetrical cores) of the sediment cloud (no experimental evidence found). The mixture model fails at reproducing this topology if the convective transfer is not included in the model: only one turbidity core is detected, at least at low resolution, as shown on Figure 3.25, the double-peak configuration appearing if one refines the discretization. However the introduction of the convective transfer term modifies the dynamics and allows one to get this configuration. A comparison of the resulting sediment cloud is displayed in Figure 3.26. If following Nguyen et al. [279], vorticity is underestimated, it can explain the discrepancy in the distribution of volume fraction as [327] underlined the importance of this field in the modification of the cloud. The peaks of volume fractions are indeed underestimated. Refining the discretization leads to a significant loss of symmetry of the sediment cloud as shown on Figure 3.27 and a modification of its topology due to its initial agitation when it is close to the free surface during the first iterations. In Shi et al. [327], change of discretization were not performed and the absence of experimental evidence prevents a proper quantitative comparison of the cloud topology.

3.5.5 Open boundaries

In this section, we aim at validating the open boundary formulation for mixtures. To this end we consider two-phase separated and mixture Poiseuille flows.

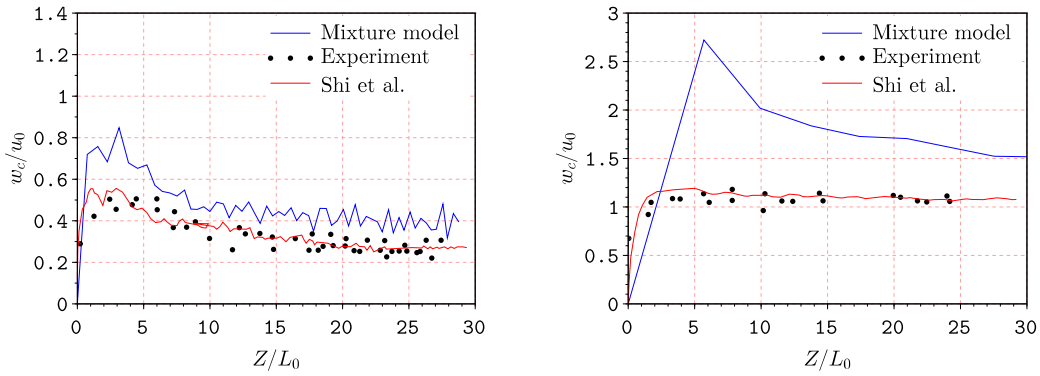

(a) $d^\alpha = 0.8$ mm and $W_0 = 2$ cm. (b) $d^\alpha = 5$ mm and $W_0 = 2$ cm.

Figure 3.21: Comparison of the cloud frontal velocity for the present mixture model, Shi et al.'s numerical results and Nakasuji et al.'s experimental results.

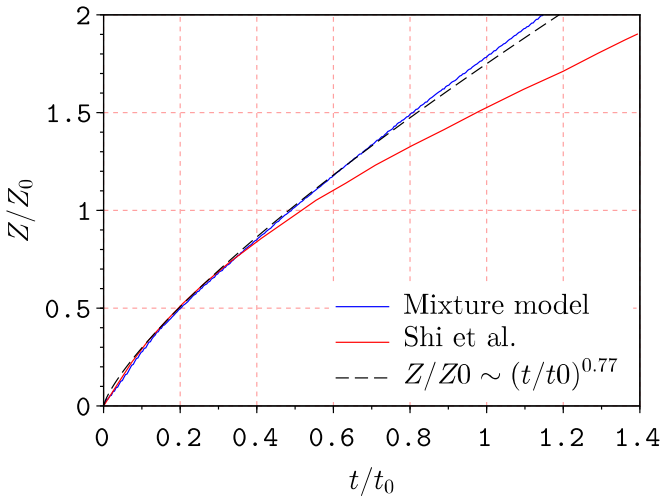

Figure 3.22: Comparison of the frontal position of the cloud for the present mixture model, numerical results and scale law in [327].

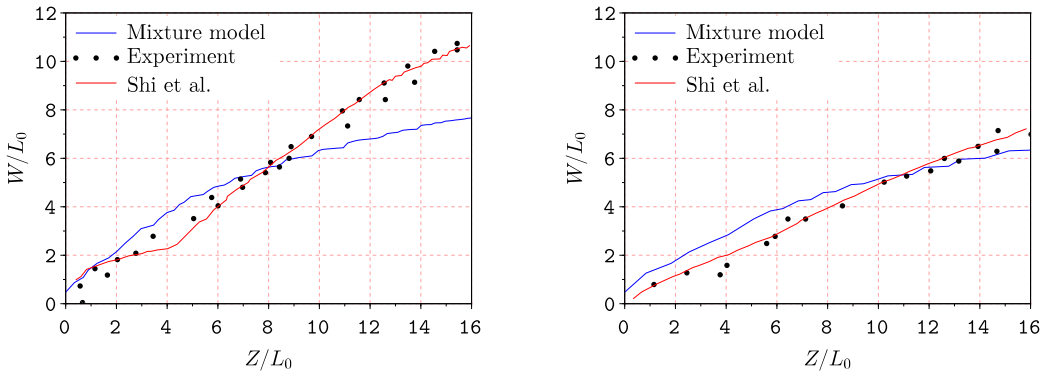

(a) $d^\alpha = 1.3$ mm and $W_0 = 4$ cm. (b) $d^\alpha = 5$ mm and $W_0 = 4$ cm.

Figure 3.23: Comparison of the cloud width for the present mixture model, Shi et al.'s numerical results and Nakasuji et al.'s experimental results for $d^\alpha = 0.8$ mm and $W_0 = 2$ cm.

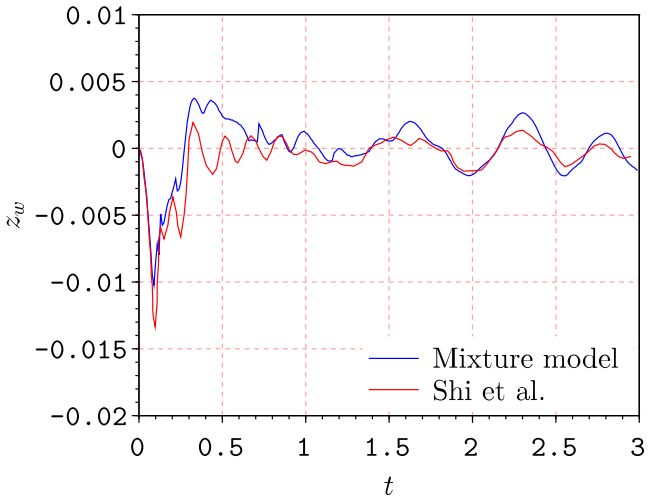

Figure 3.24: Comparison of the fluctuations of the free surface for the present mixture model and Shi et al.'s numerical results for $d^{\alpha} = 0.8$ mm and $W_0 = 2$ cm.

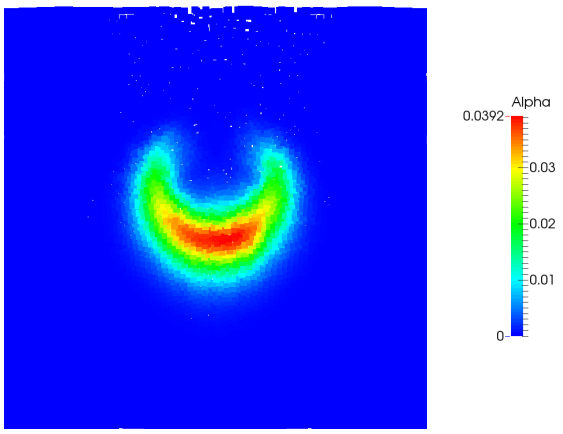

Figure 3.25: Sediment cloud at $t = 1$ s in the region $x \in [0.3; 0.7]$ and $z \in [0.6; 1.0]$ for $d^{\alpha} = 0.8$ mm and $W_0 = 2$ cm without convective transfer term.

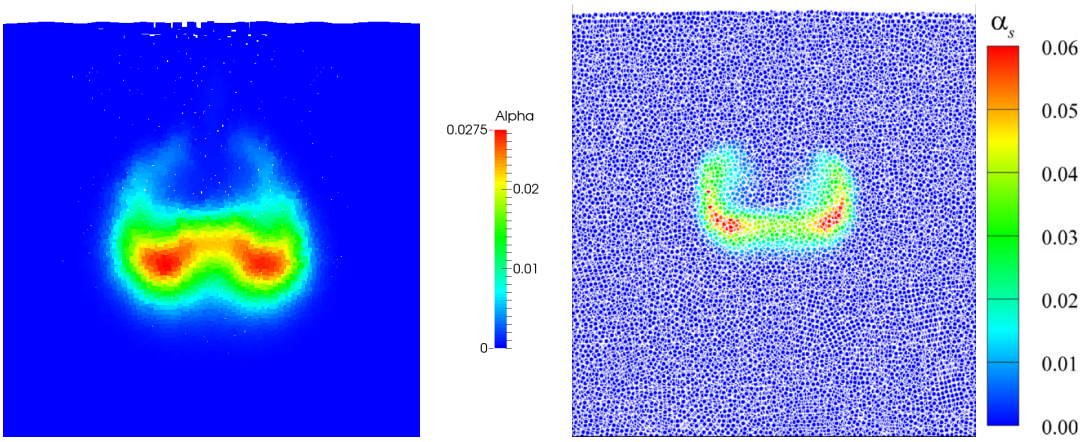

(a) Mixture model. (b) Shi et al. [327].

Figure 3.26: Comparison of the sediment clouds at $t = 1$ s with convective transfer term for $d^{\alpha} = 0.8$ mm and $W_0 = 2$ cm in the region $x \in [0.3; 0.7]$ and $z \in [0.6; 1.0]$. Left: present mixture model. Right: Shi et al.'s two-velocity SPH model.

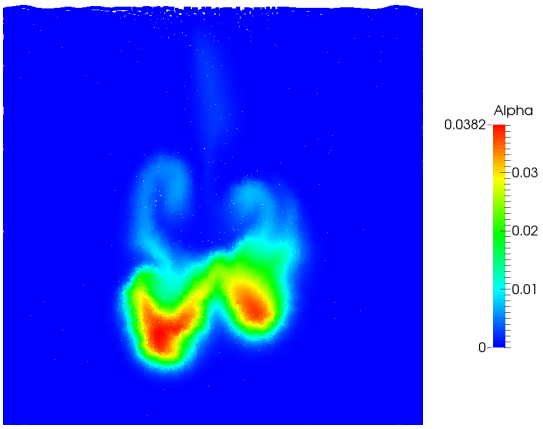

Figure 3.27: Sediment cloud at $t = 1$ s with the present mixture model in the region $x \in [0.3; 0.7]$ and $z \in [0.6; 1.0]$ for $d^{\alpha} = 0.8$ mm and $W_0 = 2$ cm with a discretization divided by two.

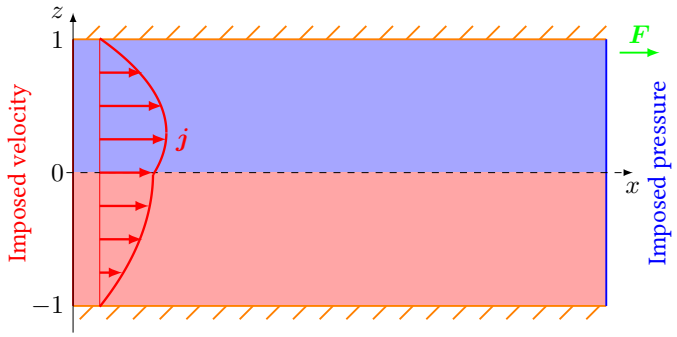

Figure 3.28: Two-phase separated Poiseuille flow with open boundaries: geometry.

3.5.5.1 Two-phase separated Poiseuille flow

Description The computational domain of this verification case is a rectangle of dimensions $L \times 2e$ bounded by walls. The lower part is filled with a fluid denoted β while the upper part is filled with a lighter fluid denoted α as illustrated on Figure 3.28. At the inlet, a velocity profile is imposed following the work of Ghaïtanellis et al. [144]. At the outlet, a hydrostatic pressure profile is imposed. The Reynolds number is $\mathrm{Re} = 20$. A longitudinal force $\rho\boldsymbol{F}$ of 4.10^{-7} N maintains the flow within the domain (in absence of this force compatible with the two-phase Poiseuille velocity profile imposed at the inlet, some instabilities develop within the domain): this point requires further investigation on the inlet/outlet formalism as with the chosen conditions at open boundaries, this force should not be used. The physical and numerical parameters are listed in Table 3.8.

Table 3.8: Parameters for the two-phase separated Poiseuille flow with inlet/outlet with low and high density ratios.

L	10	m	e	1	m
ρ^α	1000 or 10	kg/m^3	ρ^β	4000 or 1000	kg/m^3
ν^α	0.0001	m^2/s	ν^β	0.0004	m^2/s
c^α	0.02	m/s	c^β	0.02	m/s
δr	25	mm	p_B	0.0001	Pa

Results Without gravity, and considering low to high density ratios, the flow exhibits the expected behaviour as testified by the preserved volume fraction and longitudinal dimensionless velocity fields (nondimensionalized by $|\boldsymbol{F}|e^2/(2\nu^\alpha)$) plotted on Figures 3.30 for a density ratio of 4 and 3.32 for a density ratio of 100. However, for the highest density ratio, one can notice some peak pressures near the interface crossing the inlet, and a slow flapping of the velocity profile near the outlet. When reaching the air-water density ratio, these instabilities tend to increase and destabilize the computations. Two remedies can be considered: increasing the volume diffusion

(a) Inlet. (b) Outlet.

Figure 3.29: Two-phase separated Poiseuille flow with open boundaries: focus on the volume fraction field at inlet and outlet at $t = 3000$ s for a density ratio of 4.

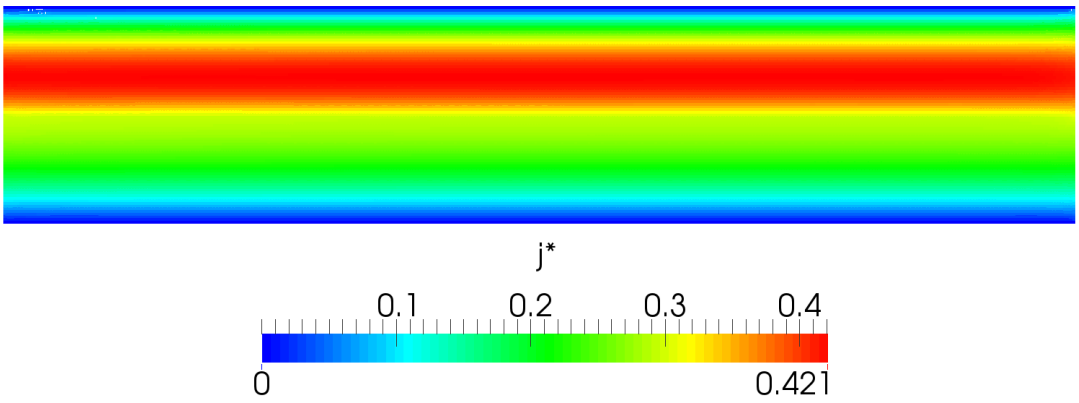

Figure 3.30: Two-phase separated Poiseuille flow with open boundaries: longitudinal velocity field at $t = 3000$ s for a density ratio of 4.

tends to smooth the pressure peaks while introducing one or several layers of intermediate volume fraction at the interface stabilizes the computations. In the very long term, some instabilities develop near the walls but do not appear to be directly linked to the inlet or outlet. Introducing a vertical body force analogous to gravity also tends to destabilize the computations.

3.5.5.2 Two-phase mixture Poiseuille flow

Description We consider the same geometry as in the previous section. The physical and numerical parameters are listed in Table 3.9. Following the solution described in Appendix D, a two-phase mixture is imposed with the analytical profile at the inlet while the background pressure is imposed at the outlet. The volume fraction is imposed at both open boundaries and the variables are initialized with the analytical solution within the domain. There is no body

(a) Inlet. (b) Outlet.

Figure 3.31: Two-phase separated Poiseuille flow with open boundaries: focus on the volume fraction field at inlet and outlet at $t = 2800$ s for a density ratio of 100.

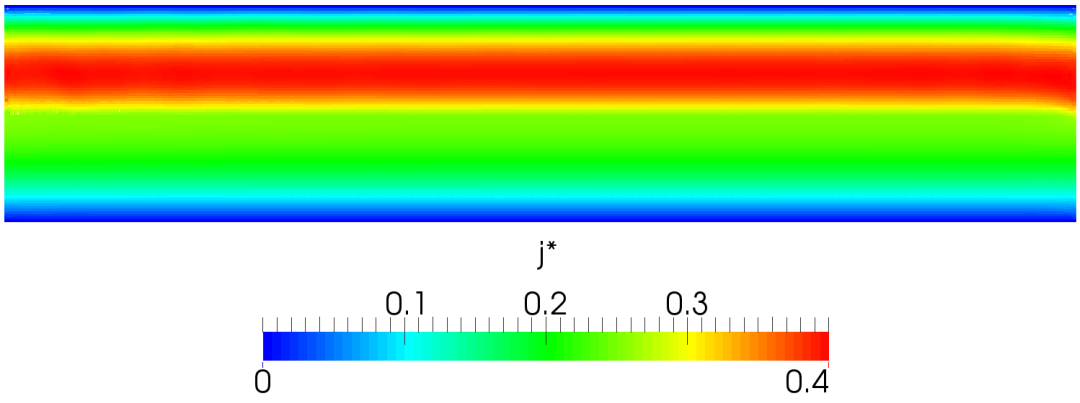

Figure 3.32: Two-phase separated Poiseuille flow with open boundaries: longitudinal velocity field at $t = 480$ s for a density ratio of 100.

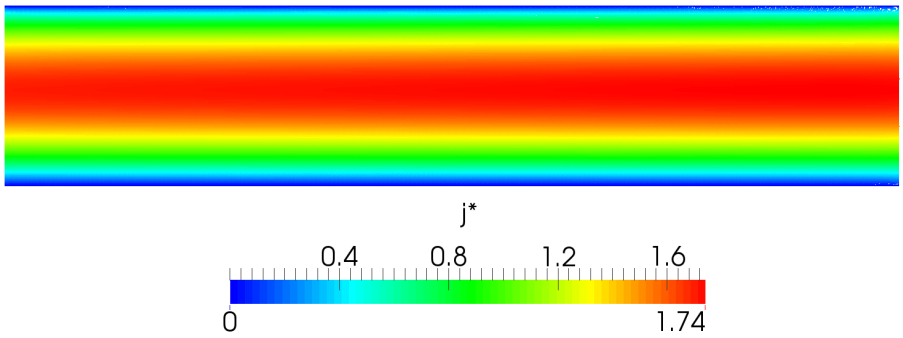

Figure 3.33: Two-phase mixture Poiseuille flow with open boundaries: longitudinal velocity field at $t = 50$ s.

force, but the gravity is used to compute the relative velocity.

Table 3.9: Parameters for the two-phase mixture Poiseuille flow with inlet/outlet.

L	10	m	e	1	m
ρ^α	1.23	kg/m^3	ρ^β	1000	kg/m^3
ν^α	0.03	m^2/s	ν^β	0.03	m^2/s
c^α	3.3	m/s	c^β	3.3	m/s
d^α	0.2	m	K	0.1	m^2/s
δr	0.01	mm	p_B	1	Pa

Results While the previous test case showed the ability of the model to handle separated flows entering the domain, this test case highlighted the capability to do the same with mixtures. Figure 3.33 highlights a smooth velocity field that is not altered near the open boundaries. One can check on Figures 3.34a and 3.34b that the volume fraction and velocity profiles fit well with the analytical solutions.

3.6 Summary

3.6.1 Model and limits

We have developed in this chapter an SPH two-phase mixture model for high density ratio flows: we have focused on a convenient spatial and temporal SPH discretization of the continuous model derived in the first chapter to have good numerical properties, namely the respect of physical boundaries on volume fractions, the conservation of the overall mass of each phase and the reduction to single-fluid formulation in absence of relative velocity. A mixture open boundary

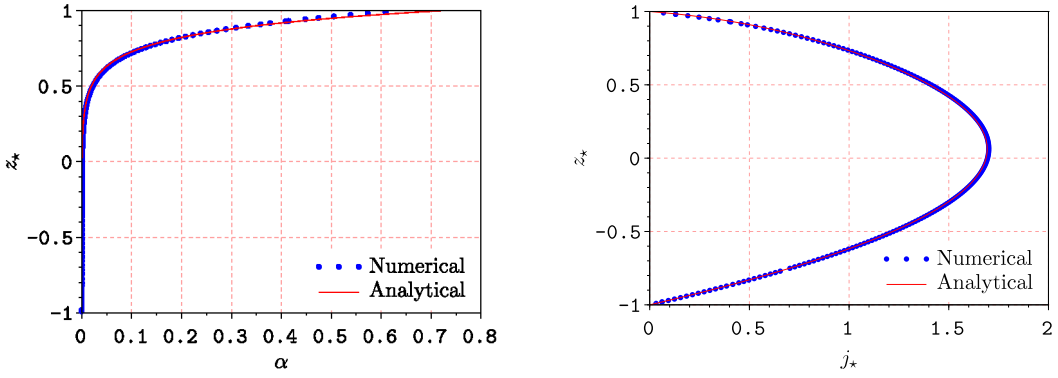

(a) Inlet.

(b) Outlet.

Figure 3.34: Two-phase mixture Poiseuille flow with open boundaries: comparison of the analytical and numerical profiles at $t = 50$ s at a section in the middle of the domain.

formalism was also developed but still require further investigations. The correct implementation of the mixture model has been checked on several test cases. Some limits have been stressed regarding the pressure gradient computation at high density ratios and the order of accuracy of the volume fraction resolution. A validation case of sediment-water mixture highlighted some limits in the reproduction of the dynamics of two-phase flows, but also illustrated the ability to handle a two-phase flow in presence of a free surface. The model can now be applied, with adequate relative velocity closure, to the air entrainment modeling. One could ask for the interest of having developed such a two-phase model in the SPH framework while they have been thoroughly developed within the finite volume approach: while no particular gain was expected from changing the numerical framework regarding the modeling of multiphase flows, the motivation was mainly to meet industrial needs for such models within a Lagrangian approach that is usually well-suited to model free surface flows as shown in Chapter 2, to deal either with air-water or sediment-water flows.

3.6.2 Further insights

The Lagrangian framework gives an interesting property to this model: for a separated flow, as long as the diffusion in the relative velocity remains null, no phase exchange occurs and the interface stays sharp without numerical diffusion. A diffuse interface appears only when diffusion effects are activated by the user or the physics. In this prospect, if the relative velocity expression is physically grounded (with respect to the flow considered, to the choice of spatial discretization compared to the dispersed phase diameter, etc.) and boundary conditions are appropriately chosen, one can reproduce the regions where phases remain separated or mixed. However, we will see in the following chapter that these conditions are not always fulfilled.

In recent works, Damián [98] and Damián and Nigro [99] coupled a mixture model and the

Volume of Fluid method (that they derived from the mixture model) to handle flows with small and long interfaces in the finite volume method. A switching criterion depending on the local topology of the flow allowed them to alternate between a mixture model similar to developments of Chapter 1 and the VoF approach where the relative velocity became an interface-compression term and relative velocity terms disappeared in the momentum equation, replaced by a surface tension term.

To some extent, with the artificial surface tension generated by SPH operators at high density ratio (as highlighted in Section 2.2.1.2) and in the absence of numerical diffusion of phases, the mixture model developed in the present work has intrinsically a similar feature with the advantage of keeping a sharp interface without special treatment. Let us underline at once that in partially mixed zone this similarity is not that clear. A surface tension term was introduced during this work but still requires investigations so that it is not presented in this manuscript. By introducing a criterion as suggested in Damián and Nigro [99] following Černe et al. [351], one could activate this surface tension term only when large interfaces are detected.

Chapter 4

Air entrainment modeling in the SPH method

On s'emploie dans ce chapitre à décrire la physique de l'entraînement d'air, à proposer en conséquence les lois de fermeture adéquates et à utiliser le modèle de mélange développé dans le Chapitre 3 sur des cas schématiques communs d'entraînement d'air dans les structures hydrauliques : le déversoir en escalier et le jet plongeant. Les résultats numériques sont confrontés à des expériences physiques. Le modèle est enfin appliqué à un cas industriel tridimensionnel de jets plongeants multiples générant un nuage du bulles modifiant significativement la dynamique dans le bassin de réception.

"La schiuma dell'acqua si dimostrerà di minor bianchezza,
la quale sarà piú remota dalla superficie dell'acqua."
— Leonardo Da Vinci, *Trattato della Pittura*

The air entrainment is defined by Chanson [59] as

> "the entrainment or entrapment of un-dissolved air bubbles and air pockets that are carried away within the flowing fluid. The resulting air-water mixture consists of both air packets within water and water droplets surrounded by air. It includes also spray, foam and complex air-water structures."

Air entrainment generates a two-phase flow of complex topology appearing visually as white waters – the *bianchezza* of the above-mentioned epigraph [361] – one can experience in daily life in the swirls of a torrent, the breaking of a wave, the flow of a waterfall, the bubble swarm in a sink. They also appear on many hydraulic structures as early described by Leonardo Da Vinci [362]… even though white waters can occur without air entrainment. The reason lies within our perception of the phenomenon. When air bubbles are entrained, their large amount triggers numerous reflections of the light that the eye is not able to respond to in sufficiently short a time: the flow turns into a blurred field, as testified by high speed cameras. A rough water surface flowing at high velocity can also have this white feature without entrained air [122].

In this chapter, we detail the stakes of air entrainment for hydraulic structures, then describe its phenomenology before introducing an appropriate modeling in the volume-weighted SPH mixture model presented in the Chapter 3. We apply it to schematic air entrainment test cases: the stepped spillway and the plunging jet. Finally, results for a three-dimensional industrial test case are presented. While general remarks will be drawn in the sections dedicated to the phenomenology description of the air entrainment, case-specific information will be detailed in the application parts.

4.1 Hydraulic structures at stake

Air entrainment modeling is a strategic challenge for the dimensioning, performance and safe operation of hydraulic works (dams and adjacent structures) as illustrated by Falvey [122] and Kobus [189] for free surface as well as confined flows. This last distinction between open and confined waters is of importance as the controlling conditions for local air entrainment, detailed in the next sections, may change between those configurations. Air-water interactions involve a wide range of temporal and space scales. Spatially it ranges from the prototype scale (*e.g.* typically several meters) to the scale of bubble coalescence (down to 0.01 μm for film break-up process) [53]. Temporally, it goes from the fastest processes (*e.g.* film break-up in 20 ms for bubbles of 4 mm in [309], fragmentation of bubbles in tens of milliseconds in [211]) to long term mechanisms for oceanic applications (tides, oceanic mass transfers) [62]. Due to the two-phase

nature of the flow, bulk properties of the mixture can differ significantly from the fluid features in terms of density, viscosity and compressibility. The air bubbles modify the turbulence and the vertical momentum introduced by the buoyancy can strongly alter the flow dynamics. Air entrainment occurrence can therefore be beneficial or detrimental depending on the case considered among the wide variety of existing hydraulic structures (channels, spillways, weirs, gates, shafts, siphons…):

- Fast flowing waters in open channels can entrain large amounts of air bubbles that lead to an increase of the water depth known as flow bulking [28]. Structures such as ski jumps [273], morning-glory or stepped spillways shall therefore be able to convey the design flood and the entrained air that enhances dissipation, mitigates cavitation (around 8% of air is sufficient to prevent damage [293]) and may trigger drag reduction [61];
- Adequate ventilation is often needed to read correctly measuring weirs and prevent cavitation hazards so that aerators are sometimes introduced in the structures [54, 122, 214];
- Free surface vortices at intake regions [256] or plunging jets in reservoirs [190] can generate air entrainment, propagating bubbles in the pipes that can hinder proper work of hydraulic machinery: pumps in hydraulic structures can experience water hammer effects and a loss of priming that will decrease their efficiency [152, 256];
- Long pipelines require air release zones as some air pockets can appear and result in stationary effects such as hydraulic capacity reduction or increased corrosion of ferrous pipelines and in unsteady flow behaviors like pressure fluctuations and flow instabilities such as blow-out or blow-back [152, 256];
- Pressure waves associated to hydraulic transient can be damped thanks to the increased compressibility of the mixture [122];
- Aeration of falling liquid jets results in their atomization, with a reduction of their break-up length, and significant changes at jet impact on a structure or in a plunge pool: while the mean pressure tends to decrease, one can notice higher fluctuations compared to a non-aerated falling jet [120, 244, 292];
- Entrainment by plunging solid, liquid or gaseous jets through a free liquid surface is commonplace in hydraulic structures as in drop structures along waterways, power plant cooling system, plunging breaker, waterfall [91];
- Water jets as described by Carrasco [50] in view of agriculture applications are also of use for fire-fighting (for which air entrained shall be prevented) or industrial jet cutting;
- Weirs and stepped spillways are very effective in air-water mass transfers of atmospheric gases, such as oxygen (or degassing methane resulting from vegetation decomposition) and

therefore in improving poor quality water that impacts the downstream river life [119, 347]. However, a strong air-water mixing can trigger supersaturation of gas like nitrogen in the flow, leading to stress or mortality of affected fishes [295, 315].

We mainly focused here on aerated flows on hydraulic structures, but they are also at the core of many other industrial applications, from chemical reactors [14] to wastewater treatment [25, 390] or naval propulsion [53, 195, 271]. Let us also underline that bubble entrainment also occurs for other gas/liquid systems as impurities captured during metal processes [399] or gas entrained in liquid sodium in fast breeder reactors [237, 288].

4.2 The air entrainment phenomenon

The air entrainment process can be split into three stages: an air volume is first entrapped at the surface, it then breaks up in a set of bubbles that are finally carried away by the flow. This entrapment happens through different possible processes: capture by a low pressure region such as in a vortex core or a trailing edge, collapse of a cavity formed by an air film, a plunging breaker or a falling drop [53, 284]. Many physical phenomena are at stake and act at different scales: turbulence, shear, buoyancy and surface tension govern bubble interactions, involving break-up and coalescence that lead to a generally wide bubble size distribution comprised between the Kolmogorov microscale and the turbulent macroscale [59], with sizes ranging from 20 μm to 1 cm. The air entrainment is an illustration of the significant influence of small-scale processes over large-scale phenomena [159]. The aim of this section is to describe those important features.

4.2.1 Dimensional analysis and similarity

Experiments are usually carried out at reduced scale. *Scale effects* are likely to appear, as the change of dimension can trigger some significant discrepancies in the physical mechanisms at stake, and increase with the scale factor [161]:

$$\lambda = \frac{L_P}{L_M} \tag{4.1}$$

where L_P is a characteristic length of the real-world prototype and L_M the corresponding model length. The reduced scale will be denoted $1 : \lambda$. The mechanical similarity between the two configurations relies on three criteria [161]:

- The *geometric* similarity: all spatial dimensions are λ times shorter in the model.
- The *kinematic* similarity: it encompasses the geometric similarity and adds the similarity of motions, keeping the ratios of time, velocity, acceleration and discharge constant.
- The *dynamic* similarity: all force ratios are identical.

Identifying the important parameters of the system is pivotal to preserve the consistency between the physical model and its corresponding full scale one. Several approaches exist for model–prototype similitude as described by Heller [161]: among them, the dimensional analysis is detailed hereafter.

4.2.1.1 π theorem

The Vaschy–Buckingham π theorem [41] is an essential tool in this prospect. Kobus [188] considered a configuration described by a reference length L of the geometry, a reference velocity U and a turbulent intensity Tu of the approaching flow and a pressure difference ΔP of the air supply system. With the fluid characteristics and gravity, one can then define and relate the dimensionless parameters:

$$f\left(\text{geom. ratios}, \mathsf{Tu}, \mathsf{C_P} = \frac{\Delta P}{\frac{1}{2}\rho^\beta U^2}, \mathsf{Fr} = \frac{U}{\sqrt{gL}}, \mathsf{Re} = \frac{UL}{\nu^\beta}, \mathsf{We} = \frac{\rho^\beta U^2 L}{\sigma_S}\right) = 0 \tag{4.2}$$

Let us recall that σ_S is the surface tension. Following Chanson [63], air density and viscosity are ignored as the air-water mixture features can be expressed with water properties and air concentration only. One can refer to Chanson [62] for dimensional analysis of classical air entrainment configurations. Some are detailed for the present work application in the Section 4.4. Another number of practical use for bubbles is the Eötvös or Bond number that reads:

$$\mathsf{Eo} = \frac{g\left(\rho^\beta - \rho^\alpha\right)\left(d^\alpha\right)^2}{\sigma_S} \tag{4.3}$$

The Weber number We might be replaced by the Morton number Mo defined as:

$$\mathsf{Mo} = \frac{g\left(\mu^\beta\right)^4\left(\rho^\beta - \rho^\alpha\right)}{\left(\rho^\beta\right)^2\sigma_S^3} \tag{4.4}$$

that depends only on the gas and liquid characteristics. The quality of the water, with a possible presence of surfactants or bio-chemicals, can affect the air entrainment and was not included in the above analysis. Chanson et al. [74] discussed this question for breaking wave and plunging jets with fresh water, seawater and artificial salt water and highlighted less entrained air and finer bubbles in the two latter cases.

4.2.1.2 Application to the bubble slip velocity

Let us consider the classical behavior of a spherical single bubble of small diameter d^α rising in stagnant water. The previous dimensional analysis leads to the following dependence for the

drag coefficient:

$$\mathsf{C_D} = f\left(\mathsf{Re}^\alpha = \frac{U d^\alpha}{\nu^\beta}, \mathsf{Eo}\right) \tag{4.5}$$

Figure 4.1 displays the dependence on the Reynolds number. The value of the terminal velocity of air bubbles depending on their volume equivalent diameter is plotted on Figure 4.2. As bubbles get larger, they deform and the volume equivalent diameter is the diameter of the sphere with the same volume than the considered bubble. One can note the significant effect of surfactants for intermediate Reynolds, as the interfaces are rapidly saturated by contaminants [316], even though Tomiyama et al. [346] pointed the initial shape deformation as the primal origin of the observed scatter, surfactants damping the oscillations.

The conventional approach for drag coefficient relations is to distinguish different regimes with an associated experimental fit when the theoretical developments are not possible. For a liquid sphere free of contaminants in the Stokes regime, Hadamard [157] and Rybczynski [318] derived the drag coefficient:

$$\mathsf{C_D} = \frac{24}{\mathsf{Re}^\alpha}\frac{2+3R}{3+3R} \tag{4.6}$$

where $R = \mu^\alpha/\mu^\beta \sim 0.020$ for air-water. Therefore, for a small air bubble in water within the Stokes regime, one has $\mathsf{C_D} = 16/\mathsf{Re}^\alpha$. For intermediate Reynolds numbers, other analytical developments have been made [270]. However, when bubbles get larger, the inertial effects become significant, the shape tends to be an ellipsoid, the motion of the bubble gets deeply affected and empirical relations are then computed [85, 189]. Very large bubbles take a spherical cap shape following a straight rising: consistently with Davies and Taylor [101], Joseph [183] found a constant value of $\mathsf{C_D} = 6$ based on the sphere diameter of the cap and made the link with the volume equivalent diameter for which $\mathsf{C_D} = 2.67$ as on Figure 4.1. At large Reynolds numbers, the surface tension becomes prominent and the dependence is ensured by the Eötvös number. Tomiyama et al. [345] gathered different correlations and compared successfully their relation for a large data set:

$$\mathsf{C_D} = \max\left(\min\left(\frac{24}{\mathsf{Re}^\alpha}\left(1+0.15\left(\mathsf{Re}^\alpha\right)^{0.687}\right), \frac{72}{\mathsf{Re}^\alpha}\right), \frac{8}{3}\frac{\mathsf{Eo}}{\mathsf{Eo}+4}\right) \tag{4.7}$$

where it has been assumed that the dispersed phase could take non-spherical shapes and the water was slightly contaminated. For contaminated systems, the second term of the minimum function is removed. For more details, one can refer to the detailed review made by Clift et al. [85], Rusche [316], Tomiyama et al. [345] for drag computations for particles, droplets and bubbles.

The above results focused on a single bubble in stagnant water. However, in practice, the bubble is surrounded by other bubbles that can interact in a turbulent environment. Rusche [316] made a review of the modifications of the drag coefficient at high phase fractions, sometimes combined with the definition of a mixture viscosity appearing in the Reynolds number. The general idea is

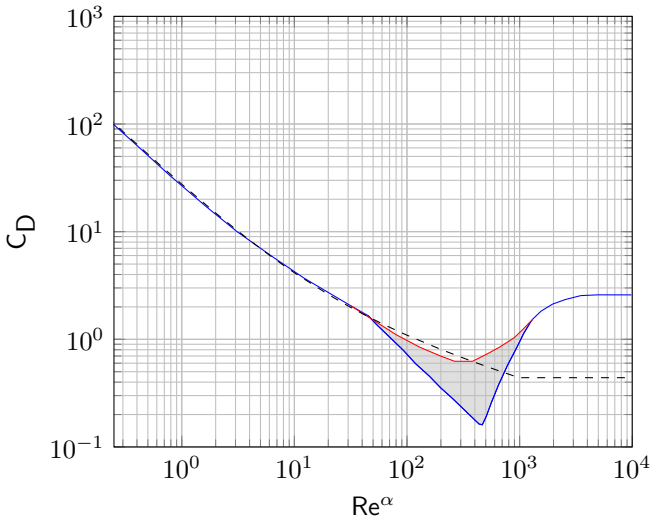

Figure 4.1: Drag coefficient of an air bubble in filtered water depending on the Reynolds number based on the volume equivalent diameter. Blue line refers to filtered water and red line to tap water. The darker region in-between corresponds to partially contaminated water. Data extracted from [156].

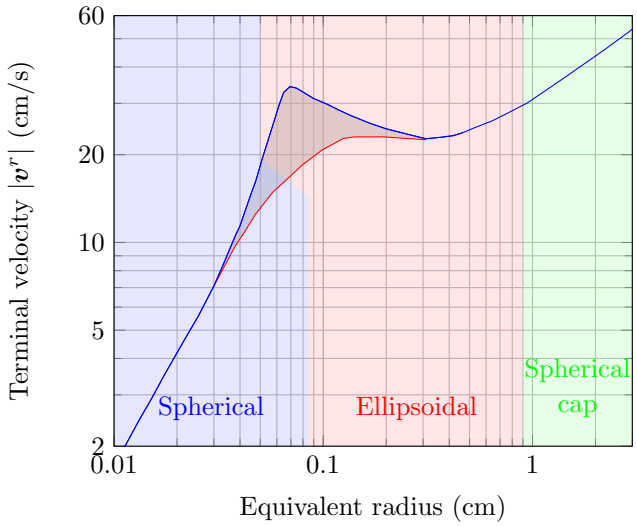

Figure 4.2: Terminal bubble rise velocity of a single air bubble in an extended body of water at rest. Blue line refers to filtered water and red line to tap water. The darker region in-between corresponds to partially contaminated water. Data extracted from [156]. Associated regimes for the bubble shapes [189].

to introduce a hindering term of the form:

$$\mathsf{C}_{\mathsf{D,eff}} = f_c\left(\alpha\right)\mathsf{C}_{\mathsf{D}} \tag{4.8}$$

The function f_c usually takes the form $f_c\left(\alpha\right) = \left(1-\alpha\right)^{3-2n}$ where n is a hindering coefficient, Rusche [316] reported values between 1.5 and 2 depending on the regimes but no value is available for the most critical regime in our study. Rusche [316] suggested an empirical form adapted for some data set:

$$f_c\left(\alpha\right) = \exp\left(K_1^d\alpha\right) + \alpha^{K_2^d} \tag{4.9}$$

with $K_1^d = 3.64$ and $K_2^d = 0.864$ for bubbles. The scatter of the bubble data, larger than for solid particles or droplets, uncertainties being especially related to turbulence effects, requires to take these closures with caution.

Other elements can significantly affect the previously presented dependencies. The pressure gradient, if not hydrostatic, can modify the bubble motion as underlined by Kobus [189] (*e.g.* sub-atmospheric pressure below a falling nappe over a stepped spillway). The turbulence, either carried by the flow (from wall or free shear layer) or generated by the bubble motions (bubble-induced turbulence) can also have a prominent action on break-up, coalescence and transport of bubbles Kobus [189]: if water flow turbulence is the leading contribution in high-speed flows (flow speed *vs.* rising bubble speed), the bubble-induced turbulence can be significant in slowly moving or stagnant water due to the buoyancy force of the bubbles, as exemplified by a bubble swarm rising from the injection at the bottom of a tank initially at rest.

4.2.1.3 Similarity

As highlighted in the relation (4.2), the local air-water turbulent flow properties are therefore dependent on the geometrical ratios, the Froude and the Reynolds numbers and the upcoming turbulent intensity. A true dynamic similarity is achieved if each dimensionless number is preserved from prototype to model. However, in a geometrically scaled model, despite the importance of gravity and viscous effects in air-water flows, full dynamic similarity cannot be achieved [62, 188]. The most relevant force ratio shall be preserved and care must be taken for the scale effects resulting for the discrepancies on the other ratios to be negligible [161]. Let us underline that the instrumentation is not scaled in most works of the literature.

Similitudes Air and water are generally used in the physical model so that the Morton number is an invariant. In free surface flows, the Froude similarity is generally retained by tuning the approach velocity, leading to smaller Reynolds numbers [62]: scale effects can therefore occur. Let us underline that the geometric (bubble size) and dynamic (bubble rising velocity) similarities for air bubbles may be violated at the scale model [188], so that some experimental works are directly performed at (nearly) prototype scale depending on the quantities of interest (for

example for mass transfer studies as in Chanson et al. [72], Erpicum et al. [119], Toombes and Chanson [347]). Kobus [189] argued that a large enough Reynolds number is a requirement for a scale model as the turbulence features become independent of this number for fully turbulent flows. Boes and Hager [28] suggested $Re > 10^5$ and $We > 10^2$ to avoid scale effects on stepped spillways together with a scale factor below 15 for the considered geometry.

Felder and Chanson [125] made a comparative study on stepped spillways for the Froude and Reynolds similitudes. The Froude similitude did not prove to be satisfied at a 1:2 geometric scaling, fewer bubbles with larger sizes being entrained at reduced scale. Turbulence was also lower so that energy dissipation may be underestimated. The Reynolds similitude proved to be invalid for such flow. Chanson and Carosi [67] made a comparative study at Froude similitude on a hydraulic jump case and highlighted also significant scale effects. Chanson [62] summed up by underlining the underestimation of turbulence levels, entrained bubble sizes, interfacial areas and mass transfer rates according to the Froude similitude, even for large models.

For impact of water waves, Peregrine and Thais [290] recalled a common issue of scaling experimental data from laboratory to prototype scales. The Froude similarity is usually retained for surface gravity waves but leads to nonphysical large prototype forces. The compressibility is indeed a key parameter due to the high pressures, the short elapsed time for the phenomenon and the air-water mixing.

Self-similarity An important tool in fluid mechanics to study turbulence and air-water flows is self-similarity. Chanson [59, 62], Chanson and Carosi [67] highlighted relations with scaling symmetry for the air concentration and velocity profiles for common air entrainment applications such as stepped spillways, plunging jets and hydraulic jumps at a macroscopic level. Self-similar behaviors were also described at the microscopic level for the distribution of bubble chords. Such results can therefore be used on prototype structures. They will be detailed for the application cases of the Section 4.4.

4.2.2 Controlling parameters

The air entrainment phenomenon is driven by different controlling conditions sorted out by Kobus [188]. They will be described in the four coming sections as a gateway to understand air entrainment, highlighting the different physical processes at stake and the wide variety of criteria that were developed.

4.2.2.1 Entrainment limit

Air entrainment occurs at a discontinuity of the flow: the approaching flow shall give the conditions for the generation of this discontinuity. The Froude number is the prominent parameter in this prospect: an hydraulic jump requires a super-critical flow determined by $Fr > 1$ to appear,

the flow regime of a stepped spillway – and therefore the air entrainment process – is also dependent on the Froude number. Chanson [59] distinguished two kinds of air entrainment depending on the nature of the discontinuity:

- *Local aeration* occurs at a flow singularity: the impingement point or line forms a source of bubbles and vorticity at the toe of the surface of the roller of a hydraulic jump as in Figure 4.3a, at the intersection of the plunging jets and the water surface of the pool as in Figure 4.3b;
- *Interfacial* or *self aeration* happens along the whole air-water interface as in an open channel as for a stepped spillway displayed on Figure 4.3c, along a chute or a developed water jet as in Figure 4.3d.

Both regimes can occur in some flow configurations as for the hydraulic jump where air can also be entrained at the interface of the surface roller.

4.2.2.2 Inception limit

Once the discontinuity is generated, air bubbles can be entrapped and turbulent stresses appear as the main factor of mixing: the turbulent shear stresses overcome the resisting forces formed by the buoyancy and the surface tension. Once this general statement made, the wide variety of physical processes at stake requires to further specify the considered problem. A breaking wave can entrap an air cavity that is then broken up into a set of bubbles [103, 108], falling drops can capture air bubbles when impinging a free surface [299, 304], free surface deformations due to turbulence can entrap air [40]... To get a general – though probably not comprehensive – overview, we now go back to the distinction between local and interfacial aeration introduced in the previous section.

Interfacial aeration The interactions between turbulence and free surface have been the subject of in-depths studies. Using the idea of turbulent stresses exceeding the stabilizing forces of gravity and surface tension, Brocchini and Peregrine [40] estimated critical values of Froude and Weber numbers based on an energetic reasoning. Considering L_T a typical length scale, a reasonable choice being the most energetic turbulent scale, and q_T a turbulent velocity linked to the turbulent kinetic energy density through $k = q_T^2/2$, they estimated an equation for a transition zone in a (L_T, q_T)–plane between non-aerated and aerated regions:

$$q_T^2 = C_1^q g L_T + C_2^q \frac{\sigma_S}{\rho^\beta L_T} \tag{4.10}$$

where the coefficients C_i^q depend on the assumptions regarding the free surface deformation geometry. Four regions were identified as displayed on Figure 4.4 and allow one to distinguish the different free surface behaviors depending on the turbulence features. Air entrainment mainly

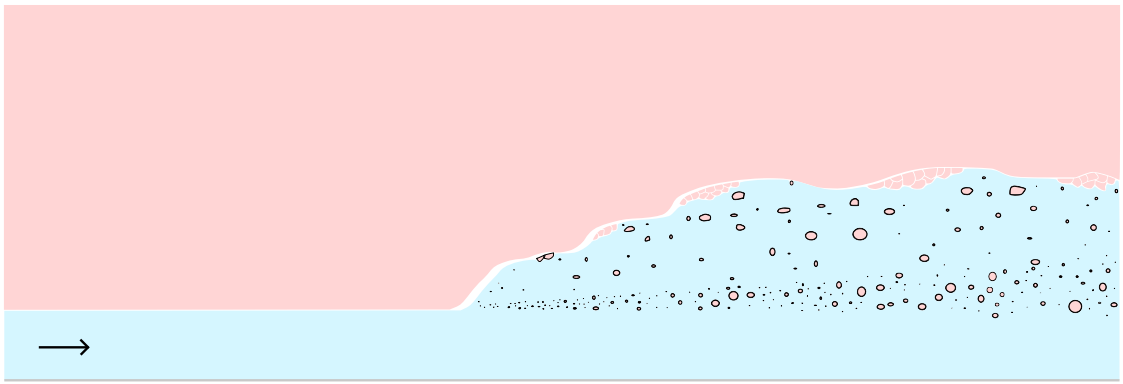

(a) Hydraulic jump

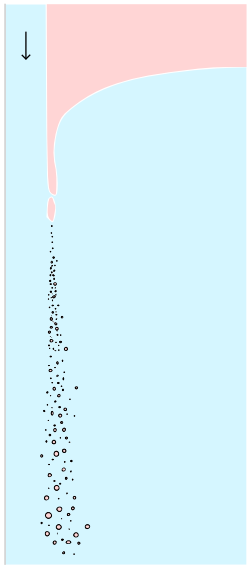

(b) Plunging jet

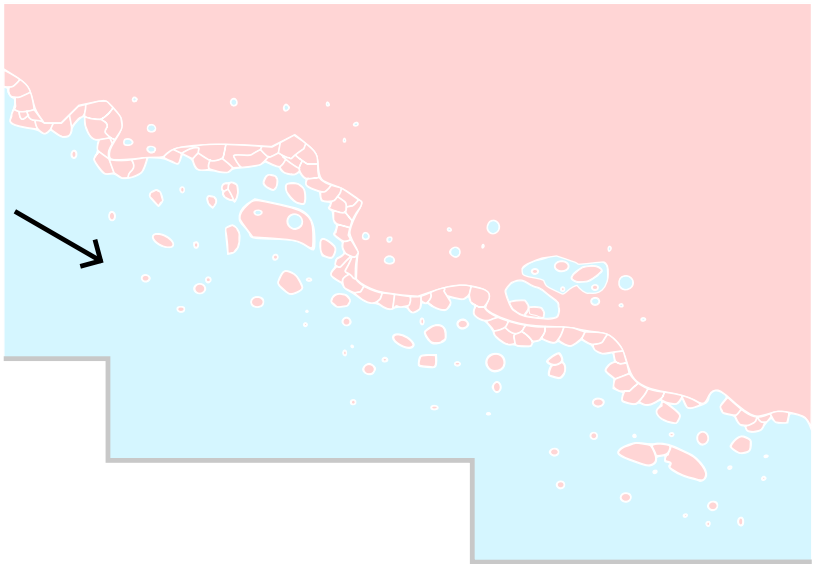

(c) Stepped spillway

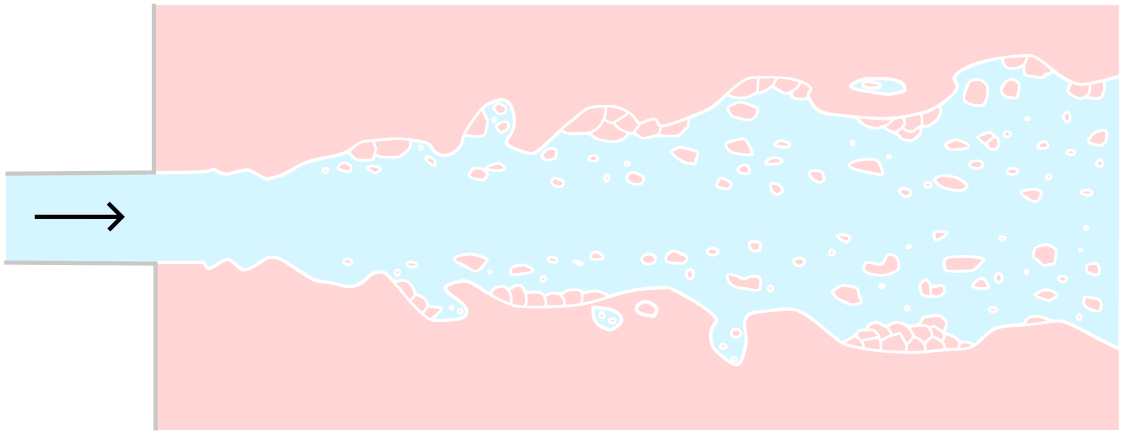

(d) Water jet

Figure 4.3: Classical air entrainment configurations (adapted from [62]).

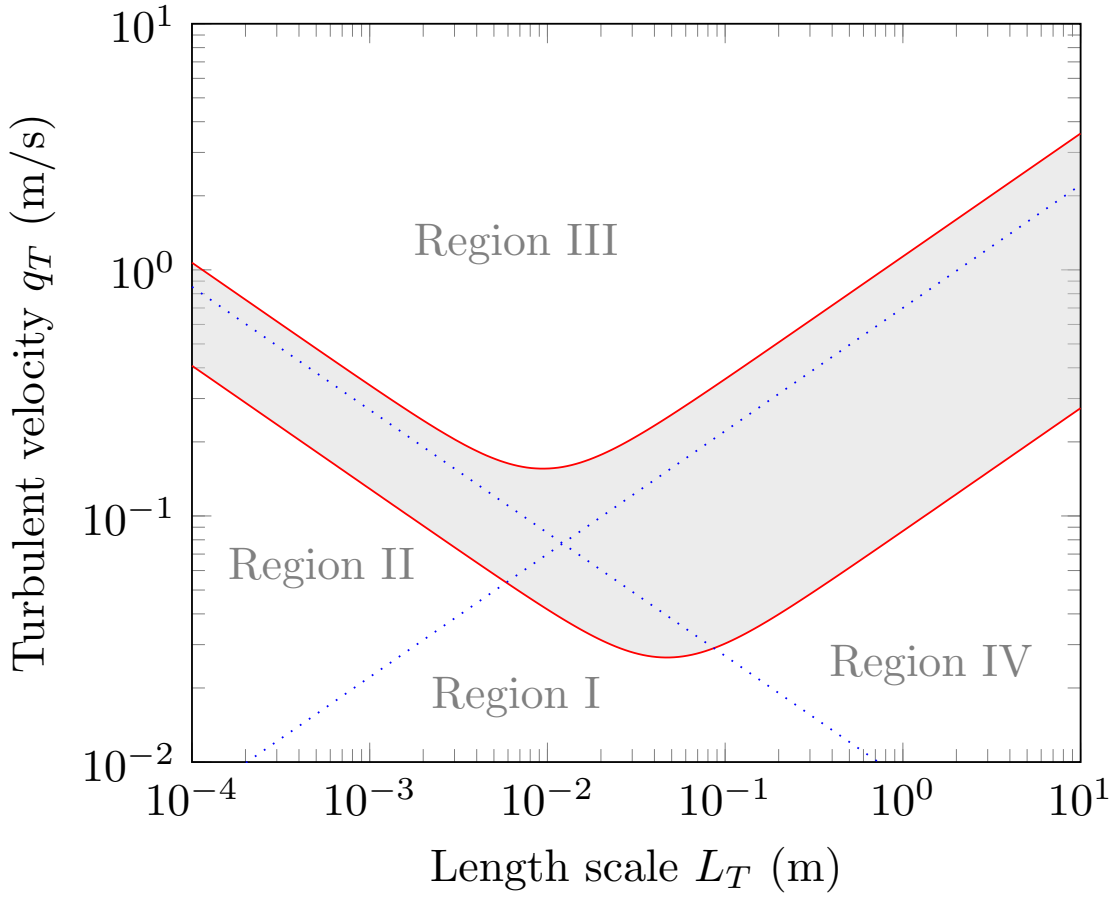

Figure 4.4: Water (L_T, q_T)–plane described by Brocchini and Peregrine [40]. Dotted lines correspond to critical Froude and Weber numbers defined through $q_T^2 = 2\mathsf{Fr}_c g L_T$ and $q_T^2 = 2\mathsf{We}_c \sigma_S/(\rho^\beta L_T)$ and taken arbitrarily in the derived bounds $\mathsf{Fr}_c = 0.025$ and $\mathsf{We}_c = 0.5$. The shaded area is a transitional zone between non-aerated (below) and aerated (above) flows and is related to the variety of free surface deformation assumptions used in the energetic reasoning.

occurs in the Region III where neither the surface tension nor the gravity can maintain the cohesion of the free surface due to strong turbulence. This plane can be seen as a practical tool to study flows: their evolution can be understood as a trajectory from one region to another, depending on the evolution of the turbulent structures in the flow.

Interactions between turbulence and free surfaces are complex and some literature was devoted to their study, generally in simplified cases. Hunt and Graham [173] focused on the modification of the turbulent features close to a moving boundary. Their work was extended to flat free surfaces by Teixera and Belcher [343] and checked numerically with DNS computations by Flores et al. [131]. A two-layer region was described. The source layer, related to the kinematic blocking effect of the interface boundary, brings the normal component of the fluid velocity to zero at the interface while the thin viscous layer along the interface allows for the tangential fluctuations to adjust to the shear-free boundary condition. Normal velocity fluctuations are constrained near the free surface and the energy spreads in the tangential components. However, when turbulence effects are strong enough in the sense explained previously following Brocchini and Peregrine [40], the free surface will deform [356].

Spillways form a particular and extensively studied case of interfacial aeration. Early studies related the inception of air entrainment to time-averaged velocities: Ehrenberger [117] is usually referred to as giving the first explanation for air entrainment on spillways, as a direct consequence of the high velocity of the flow. Such criterion disregards the complex two-phase anisotropic turbulent features of the flow. Further works considered the self-aeration over hydraulic structures as a consequence of the boundary layer developing from the wall reaching the free surface [203] and this criterion was generally adopted in the hydraulic community [59] even though it was highlighted that entrainment could occur earlier: Valero and Bung [355] indicated that several references in the literature locate air entrainment at the position where the boundary layer thickness is approximately 80% of the mean free surface level. A characteristic roughening, wavy flow is noticed before the inception. The inception point determination have been the object of many further works in the literature, trying to identify a convenient criterion as done by Meireles et al. [248], as its position is likely to vary due to the unsteadiness of turbulence of the free surface and the boundary layer. Some considered a mean air concentration of 20% as a criterion [44]. Others referred to the bottom inception point with a concentration above 1% [294]. The distinction was sometimes made between the entrapment of air, between wave crests, and the entrainment of these bubbles, captured and carried by the flow. Assuming a thin viscous layer and a blockage/source layer of Hunt and Graham [173] of the size of the eddies that induces disturbances of the free surface with the same size, Valero and Bung [356] studied free surface perturbation dynamics and derived a break-up criterion for the free surface disturbance steepness before entrainment. Most unstable length scale were found to relate to the

Taylor length scale derived from the inviscid Kelvin–Helmoltz instability:

$$\lambda_c = 2\pi\sqrt{\frac{\sigma_S}{g\left(\rho^\beta - \rho^\alpha\right)}} \sim 1.7 \text{ cm for air-water} \tag{4.11}$$

In the case of a viscous formulation as studied by Funada and Joseph [140], values can decrease around 1.5 cm. For wavelength sufficiently larger, surface tension can be neglected. The normal fluctuations do not vanish outside the boundary layer thickness: combined with the air drag effect, it can explain the occurrence of aeration before the intersection of the boundary layer with the free surface. Characteristic free surface roughness observable upstream of the inception point were described by this model, with a wide range of wavelengths that can explain the range of scales observed after the entrainment inception.

Regarding the importance of turbulence in self-aerating flows, a characteristic level of normal Reynolds stresses became a classical criterion in the literature. In the following, x is aligned with the flow and y refers to the normal component to the mean free surface. Studying falling jets, Ervine and Falvey [120] suggested that the lateral kinetic energy should exceed the restraining surface tension pressure, leading to the criterion:

$$v'_y \geq \sqrt{\frac{4\sigma_S}{\rho^\beta R_s}} \tag{4.12}$$

where R_s is the radius of curvature of the surface disturbance. Under further assumptions on the turbulence and dissipation, it was converted in a jet velocity at the onset of aeration:

$$V_e = \frac{0.275}{\mathsf{Tu}} \tag{4.13}$$

In the case of chutes, an additional condition was introduced by Boes and Hager [29] and Chanson [56] to the inequality (4.12) to ensure that the normal fluctuation is larger than the bubble rise velocity:

$$v'_y \geq |\boldsymbol{v}^r| \cos\left(\theta_s\right) \tag{4.14}$$

where θ_s is the slope of the chute. The disturbance radius R_s is moreover taken to the bubble diameter d^α. For Chanson [62, 65], self-aeration occurs when the shear stresses are larger than the surface tension force per unit area, leading to the criterion:

$$\left|\rho^\beta \overline{v'_x v'_y}\right| > \sigma_S \frac{\mathcal{P}_p}{\mathcal{S}_p} \tag{4.15}$$

where $\mathcal{P}_p$ and $\mathcal{S}_p$ are respectively the perimeter and the surface area of the disturbance. Noting that while the Reynolds stresses nearly vanish close to the fully developed free surface, an air super-layer does exist with a growing free surface roughness generating a velocity difference, this criterion was modified by Valero and Bung [355] to include contributions of this shear region due to the developing air flow that could explain early aeration (before the intersection of the

boundary layer with the free surface):

$$\left|\mu^{\alpha}\frac{\partial\overline{v_x}}{\partial y}+\left(\rho^{\alpha}+\rho^{\beta}\right)\overline{v'_x v'_y}\right|>\sigma_S\frac{\mathcal{P}_p}{\mathcal{S}_p} \tag{4.16}$$

As the ejected drops falling and capturing air bubbles when reaching surface were not a sufficient explanation for air entrainment in open channels, Wei et al. [381] made an energetic reasoning (when the kinetic energy of a turbulent eddy overcomes the surface tension energy) to derive a critical radius of deformation leading to air entrainment when exceeding the acceptable free surface deformation:

$$R_c=\sqrt{\frac{\rho^{\beta}L_T v'^2_y}{12\sigma_S}}\geq R_m=\frac{4\sigma_S}{\rho^{\beta}v'^2_y} \tag{4.17}$$

where L_T is the characteristic size of the turbulent eddy. The critical condition depends on the flow mean velocity and water depth through the closure of the fluctuation velocity. This 2D reasoning got good agreement with experimental results.

Hirt [164] and Souders and Hirt [336] gave few details about the air entrainment model implemented in the commercial software FLOW-3D®. The characteristic size of turbulent eddies:

$$L_T=C_{\mu}\sqrt{\frac{3}{2}}\frac{k^{3/2}}{\epsilon} \tag{4.18}$$

is used to describe the surface disturbances. An energetic reasoning similar to the one previously presented by Brocchini and Peregrine [40] is made. The volumic turbulent kinetic energy $P_T=\rho k$ and the volumic disturbance kinetic energy P_D associated with a fluid element raised to a height L_T with surface tension energy based on a curvature of L_T:

$$P_D=\rho\boldsymbol{g}\cdot\boldsymbol{n}L_T+K_h\sigma_S/L_T \tag{4.19}$$

are computed with $K_h=1$ (used as a calibration parameter in other studies). Turbulent disturbances shall be strong enough to overcome the stabilizing forces. If so, the volume of air entrained per unit time is computed as:

$$\delta V=C_{air}A_s\sqrt{2\frac{P_T-P_D}{\rho}} \tag{4.20}$$

where A_s is the surface area and C_{air} quantifies the portion of the raised disturbance volume occupied by air (less that unity, taken to 0.5 so that on average air will be trapped over about half the surface area).

Meireles et al. [249] tested the models (4.12), (4.14), (4.15) and (4.20) with experimental and numerical data for a smooth spillway and concluded that they predicted well the inception point, except for (4.15) (without the normal derivative) that predicted it too far, allegedly due to the lack of accuracy of the turbulence model employed. These criteria are physically related so that

it can explain their good agreement, as the bubble diameter considered for the disturbance (from experiments) gives more importance to the surface tension contribution.

Local aeration The mechanisms of air entrainment for local aeration are also complex and not completely understood today, as exemplified by the plunging jets that give a quite general view of local aeration (analogies can be made for hydraulic jumps [62]). The criterion for inception is not obvious for plunging jets, as it depends on the period of observation considered [93]. A primary event of entrainment in a clean pool can be used as a definition. Two main processes are at stake: the interaction of jet surface disturbances with the receiving pool as studied for individual bumps by Zhu et al. [403] and the generation of an elongated cavity between the jet and the receiving pool, breaking up into air pockets and bubbles. Bińi [24] indicated that the entrainment depends upon several parameters: the jet velocity at impact, the physical properties of fluid, the jet nozzle design, the length of free-falling jet and the jet turbulence. A classical empirical correlation between the onset velocity and turbulence intensity for planar and circular jets suggested by Chanson [62] indeed writes:

$$\frac{\mu^{\beta} V_e}{\sigma_S} = 0.0109 \left[1 + 3.502 \exp\left(-79.62 \mathrm{Tu}\right)\right] \tag{4.21}$$

In a schematic sketch of values found in the literature, with nevertheless some significant scatter, air entrainment appears for impact velocities around $V_e \approx 1$ m/s [59]. For velocities close to the onset velocity $V_x < 2$ m/s, individual bubbles or packets are entrained. Bińi [24] reported visual observations of air pockets generated by disturbances of the impinging jet the receiving pool could not adapt to. For higher velocities $V_x > 3$ to 8 m/s, a thin layer of air is generated below an induction trumpet between the impinging jet and the receiving pool and behaves as a ventilated cavity: the cavity pinches off and gusts are released intermittently due to a re-entrant jet [24].

The previously detailed model of Hirt [164] and Souders and Hirt [336] was also used for local aeration but required some adjustments. Due to discrepancies on plunging jet computations special treatment with restricted details is done: when there is an intersection of two fluid surfaces moving orthogonally, the surface turbulence level is increased and the turbulence length scale is modified by a length characteristic of the local entrainment.

Towards a generic criterion It appears that, to date, there is not an agreement for a generic air entrainment criterion for free surface water flows. The reason lies within the large range of processes occurring in interfacial and local aeration: propagation of different kinds of waves that may break, interaction of the turbulence with the free surface… The definition of the inception is not easy and some physical phenomena remain partly unexplained. A wide variety of criteria exist in the literature, many of them being therefore case-dependent. Some of them are intrinsically linked to the numerical resolution and will be detailed in Section 4.2.3. The model of Hirt [164] is quite generic and of practical use in CFD compared to the geometric criteria that require

a measure of the disturbance, either by the size of the eddies or the bubble diameter, but remains of limited validation for local aeration with adjustments related to the cases considered.

4.2.2.3 Air supply limit

While the air supply is unlimited for free surface flows, it can be restricted for confined flows and mitigate the air entrainment depending on the loss coefficient.

4.2.2.4 Transport capacity

Once entrained in the flowing water, the configuration becomes the one of a dispersed two-phase flow: flow velocity, depth and turbulence are considerably modified.

Bubble break-up The differential pressure force exerted by the tangential shear stresses, if strong enough compared to the capillary force, triggers the break-up of the captured air pockets [103]. The important parameter is therefore the Weber number. Chanson [62] suggested that bubbles are broken up by eddies of length scale similar to the bubble size: larger ones advect bubbles while smaller ones are not energetic enough to overcome the surface tension. One can find a review of the break-up mechanisms in [215]. As described by Hinze [162], in an equilibrium configuration, there exists a scale d_H, called the Hinze scale, at which turbulent fragmentation ceases. Following Deane and Stokes [103], it can be computed by:

$$d_H = \epsilon^{-2/5} \left(\frac{\sigma_S \mathrm{We}_c}{2\rho^\beta} \right)^{3/5} \tag{4.22}$$

where the critical Weber number We_c is taken to 4.7 (other values from the literature, closer to unity, are summarized in [59]). Chanson [59] proposed a different approach:

$$d_{\max} = \left(\frac{2\sigma_S \mathrm{We}_c}{\rho^\beta \left(\frac{\partial V_x}{\partial y} \right)^2} \right)^{1/3} \tag{4.23}$$

If such formulation proved to work reasonably well for gradually-varied flow, it is not valid for rapidly-varied flows as underlined by Chanson [59] due to the equilibrium assumption. Let us note that this could be used in computations as a time evolving bubble size, even though this diameter cannot be seen as a measure of mean diameter. The break-up of the air pockets generates a dispersed flow that encompasses therefore a wide range of bubble sizes as highlighted by Cummings and Chanson [91] for plunging jets or by Chanson and Toombes [70] for stepped spillways (three orders of magnitude).

Bubble transport The interfacial aeration results in droplets and bubbles spreading differently. Drops are projected at a distance depending mainly on their initial velocity. If the air flow is not too violent, gravity and drag limit the travel of drops. On the other hand, bubbles, due to their low inertia and limited rise velocity, are therefore drawn by the turbulent structure [40]. The transport capacity of the flow increases with turbulence intensity and velocity but decreases with air concentration. For high speed flows in open channels, it results of an equilibrium between the rising motion (due to buoyancy) and mixing (resulting for turbulent fluctuations). For confined flows, the orientation of the flow with respect to the gravity is an additional important parameter. When the transport capacity is exceeded, air detrainment occurs and leads to the formation of air pockets in the case of confined flow, possibly generating instabilities [188]. The dispersed phase advected by the flow can coalesce due to collisions. This process may not be significant in high velocity free surface flows, as long as the bubbles have not reached a region of lower shear stresses [59]. It counts three steps: the bubbles collide, the film between them is drained and finally is broken, generating a larger bubble. The Weber number is critical for this phase. Further details on the coalescence process can be found in [80].

A diffusion process According to Chanson [59] that performed considerable series of experiments and modeling of air-water flows, high-velocity shear flows mixing air and water behave as homogeneous mixtures. An advective diffusion process is well-suited to describe the evolution of the bubble swarm and analytical developments from the integration of the diffusion equation can lead to proper description of the volume fraction profiles, with little effect of the shear layer. The consequent air bubble diffusivity K_T is of the same order than the eddy viscosity, but generally larger. In the relation (1.101), $K_T = \frac{\nu_T^\beta}{\mathrm{Sc}_T}$ so that the previous remark would correspond to a turbulent Schmidt number smaller than one. The mean air-water velocity profiles resemble the single-phase ones while the air-water velocity distribution is only slightly modified by the interactions of bubbles with turbulence. Chanson and Toombes [69] considered the quasi-homogeneous air-water mixture with $\alpha < 90\%$ in a uniform equilibrium flow region to derive analytical expressions for the air concentration. In a steady quasi one-dimensional flow, for a small control volume, the air continuity equation writes:

$$\boldsymbol{\nabla} \cdot (\alpha \boldsymbol{v}) = \boldsymbol{\nabla} \cdot \left(K_T \boldsymbol{\nabla} \alpha - \alpha \boldsymbol{v}_{0,\mathrm{eff}} \right) \tag{4.24}$$

This relation is similar to (1.86) but in steady state and written with a mass-weighted mixture velocity. As one will see in Section 4.4.1.3, $\boldsymbol{v}_{0,\mathrm{eff}}$ corresponds to (3.36) but with a possible correction arising from the two-phase nature of the medium. Analytical resolutions by imposing a diffusivity profile are described by Chanson [65] in the four applications detailed on Figure 4.3: some of them are detailed in the Section 4.4. The assumption is generally a constant diffusivity, but more complex models are developed for the documented cases of the skimming flow over a stepped spillway and the flow downstream of a nappe impact. The fact that such an equation

can describe the mean air bubble behavior in the considered flows encourages to try the mixture model on such applications, even though one should note that the void fraction ranges from 0 to 100% so that the dynamics might be wrongly computed.

4.2.3 Numerical modeling

During the last two decades, noticeable efforts have been made in developing air entrainment models towards a generic free surface flow model. Let us underline that the complexity of the modeling is two-fold: one should be able to describe the entrainment phenomenon but also the transport and diffusion of the entrained air bubbles. A wide variety of numerical approaches have been developed in an Eulerian or Lagrangian (or coupled) framework, using the full set of equations or averaged formulations, resolving all scales or employing subgrid models for turbulence and/or air entrainment, in a one-way or two-way coupling (taking into account the action of the liquid phase on the gas phase only or including the gas phase effect on the liquid phase). One of the difficulties arises from the coexistence of separated and dispersed regimes in many of the air-water flows of interest for hydraulic applications. In the following, we shall not make a comprehensive review but rather try to highlight with some examples the prominent approaches and their features. The SPH literature related to air entrainment is addressed in the Section 4.3.1.

4.2.3.1 Costly DNS

The wide range of temporal and spatial scales involved for air entrainment prevents any resolution of the full set of Navier–Stokes equations at prototype scales, by several orders of computational capability [53]. A spherical droplet typically requires around 10 grid points for proper dynamic resolution [221]. If we consider schematic values with a dispersed phase size of 1 mm in a prototype domain of 10^3 m^3, one needs 10^{15} grid points (around five orders of magnitude higher than what can be handled today, and one should note that it is probably underestimated as the Kolmogorov scale can be smaller than the smallest bubbles). One has then to consider the time stepping restricted by a CFL condition: for a flow of 10 m/s with a physical time of 10 s, that would lead to at least a million steps. To give an idea of the computational cost of recent simulations for free surface air-water flows, DNS of air entrainment through vortical filament structures in a breaking wave was for example performed by Lubin and Glockner [227] using a VoF approach with 10^8 grid points allowing to catch bubbles down to 1 mm (bubbles larger than 1 mm are though subject to fragmentation according to [103]) in a periodic domain one-wavelength long (10 cm). One day of computations was required for 0.88 s of physical time. Wang et al. [378] focused on the small-scale interface structures of a breaking wave in air entrainment and spray formation processes with 10^{10} grid points using a minimum grid spacing of 0.065 mm and considering a wavelength of 27 cm. Mortazavi et al. [275] performed a DNS of an hydraulic jump with around eighty millions mesh points with reasonable agreement with experiments. It allowed to get further insights into the physics of the air entrainment, with identified periodicity

of the patches of bubbles entrained. Chanson [64] considered that a DNS would require 10^{10} grid points for a small plunging jet and 10^{17} for a large spillway flow. Adaptive mesh refinement or hybrid approaches (modeling part of the subscale physics) can be used to decrease the computational time but it appears unavoidable to model (or neglect) small-scale behaviors to allow for larger discretizations for a large scale computation. Regarding turbulence, a mid-way relies on LES: Lubin et al. [228] applied an Eulerian formulation with LES to the simulation of plunging breaking waves with a subgrid scale model less dissipative than the Smagorinsky approach. Still, this approach is expensive for industrial applications. DNS will probably remain restricted to study local phenomena related to air entrainment, providing some information to develop subgrid models [272]: for example Yu et al. [395] studied the air entrainment induced by a pair of horizontal vortex tubes and a vortex ring impinging the free surface.

4.2.3.2 Air entrainment as a source term

Facing the difficulty to model finely the air entrainment phenomenon with the available computational resources, a subgrid model for air entrainment appears as an enticing solution. As described by Moraga et al. [272], one can either impose a boundary condition (but the interfacial scales will not be solved) or set a volumetric source. The following references illustrate the wide variety of possible models available in the literature in view of the same applications, with fast-evolving formulations. The guiding idea is to get a model with few user inputs or calibration parameters regarding the air entrainment, able to compute automatically the quantity of air entrained, its location or even its distribution. These models generally still require case-dependent calibration and do not take into account the possibly limited resources of air.

Hirt's approach Hirt [164] and Souders and Hirt [336] model air entrainment through the introduction of a source term with the relations (4.19) and (4.20). A passive scalar approach can be used for small volume fractions. For stronger mixing, a RNG [1] turbulence model is used in a variable density single-fluid formulation. The mixture density allows for buoyancy effects and is used to compute the volume fraction through relation (E.1). The model was tested on 2D simulations of 3D cases with limited validation: on a plunging jet, a drop shaft, a hydraulic jump in a pipe and a smooth spillway. Validation is made by comparing with data available for the last three cases on the volume flow rate of air entrained with good precision for the drop shaft and the hydraulic jump, and with volume fraction values for the spillway.

Bombardelli et al. [31] makes a combined experimental-numerical study on stepped spillways with a focus on the non-aerated part. The numerical model relies on dilute mixture equations following [47] with a pseudo single phase flow model where the air is followed by a transport equation. The density in the momentum equation is a reference density that does not depend

[1] The Re-Normalization Group approach is a turbulence model similar to the $k-\epsilon$ model. The procedure described by Yakhot and Orszag [389] allows for the explicit computations of all the constants of the model.

on the air concentration. The air entrainment is introduced via Hirt's approach. Similar results are obtained for the RNG and standard $k-\epsilon$ approaches. A reasonable agreement is obtained for the fluid velocities, with often an underestimation of the velocities near the free surface, and boundary layer growth is well reproduced.

Hirt's model was tested and calibrated by Valero and García-Bartual [357] for a smooth spillway configuration with two parameters used as calibration, C_{air} and K_h of the relation (4.19), the references used for calibrating being the mean air concentration and the inception point location. The mixture model described in [38] together with a RNG model were employed. Limited agreement was obtained on the volume fraction profiles. The mean concentration values depending on the slope of the spillway fell within a 20% error and the results proved to be dependent on the cell size, allegedly due to the low convergence rate of the turbulent kinetic energy. It was also applied in a combined experimental-numerical study by Valero and Bung [354] on a 3D stepped chute spillway with a RANS model using VoF, observing a bending of the free surface before the inception exhibiting lateral steady waves that a 2D model cannot capture. The entrainment inception was not evenly distributed on the transverse direction, one or two steps distances being needed for an homogeneous distribution. Good agreement was obtained for the inception point position but too much air was entrained and discrepancies were noticed for the volume fraction and velocity profiles.

Moraga et al. and Ma et al.'s approach The air entrainment is critical for surface ships (drag reduction, stealth capability and design purposes [271]) with volume fractions exceeding 10% and a part of the air entrainment literature was therefore devoted to the numerical modeling of this phenomenon. A wide range of bubble sizes is usually observed so that Population Balance Equations (PBE) coupled to single or two-fluid models were frequently considered. Let us underline that PBEs introduce an additional order of magnitude of variables (number density and associated velocity resulting from a momentum balance for each class of bubbles). Air entrainment generally appears as a source term in those equations. Early models considered bubbles as only passive scalars. However, it was noted that the wave breaking involves strong two-way interactions between phases that need to be modeled. In the following references, the interfacial transfers account for mean pressure force on the mean bubble while the fluctuating interfacial term accounts for the drag, turbulent dispersion, virtual mass, lift and wall effects.

Carrica et al. [51] first developed a two-phase flow model with volume fraction and bubble number density equations under a monodisperse assumption. A focus was made on the RANS formulation including bubble effects on turbulence. The need to consider different sizes of bubbles drove those authors to then build a polydisperse model in [52] where entrained air was given as a boundary condition.

Moraga et al. [271, 272] then developed a physically-based subgrid model to detect the location in which air entrainment occurs to introduce bubbles as a volumetric term: a coarser resolution

than the one required to detail the interfacial process of entrainment can be used to capture the high void fraction region resulting from air entrainment. A two-fluid model handling polydisperse bubbles, two-way coupling and turbulence-induced bubble break-up near the free surface is then used for the transport of bubbles. Bubble size distribution following [103] and source intensity have to be prescribed (the latter being used to match the experimental data). They applied this model to surface ships at laboratory scales and obtained good agreement with experimental results. The location of air entrainment follows the criteria based on the averaged liquid velocity rather than turbulent quantities that could be more expensive and complex to compute:

$$\boldsymbol{v}^{\beta} \cdot \boldsymbol{g} > v_{ent} g \quad \text{and} \quad \boldsymbol{v}^{\beta} \cdot \boldsymbol{n} > v_{ent} \quad \text{and} \quad 0 < d_i < d_{ent} \tag{4.25}$$

where d_i is the distance to the interface, d_{ent} is the layer thickness over which the volume source is distributed and v_{ent} is the entrainment velocity limit fixed to 0.22 m/s as deduced from Figure 4.2. This choice is driven by a reasoning of Clanet and Lasheras [84]: the terminal velocity of bubbles displayed in Figure 4.2 is not a monotonic function of the bubble diameter and has a local minimum of $v_{ent} = 0.22$ m/s independently of the Morton number. If one considers a plunging jet, the bubbles will not be sorted by their diameter: still referring to Figure 4.2 and considering partially contaminated water, when the velocity of the bubbly plume decreases to this terminal velocity v_{ent}, all bubbles with a diameter higher than 1 mm will finally rise while smaller bubbles can still be entrained at further depths. One can see that bubbles with diameters of 1 mm and larger bubbles of 3 mm could reach this terminal depth. This induce an abrupt change in the volume fraction profile with depth. This behavior is therefore employed in [272] to locate the region of high volume fractions and define it as the source of bubbles in the transport equations. Turbulence is modeled through a blended $k - \omega$ model adapted for bubbly flows. A single-phase Level-Set method is used so that the equations are not solved in the air, as the flow is dominated by inertia. It provides an increased stability for high density ratio flow. The missing scales relevant for air entrainment are given by the subgrid model.

Shi et al. [325] used the double-averaged (ensemble average at bubble-to-bubble spacing and Reynolds average for turbulence scales larger than the inter-bubble distance) set of equations for dilute air-water mixtures of Buscaglia et al. [47]. This is therefore a single velocity model. Bubble population is computed with an advection-diffusion equation for different groups in which source terms are introduced to model air entrainment by relating the shear production at the air–water interface to the bubble number intensity through the bubble distribution described by Deane and Stokes [103] as references indicate a link between turbulence intensity and entrainment [17]. While good trends were obtained in wave breaking events, some discrepancies appear in quantitative comparisons, attributed to the single-phase approach and the air entrainment formulation.

Ma et al. [231] proposed a one-way coupled monodisperse RANS two-fluid model to simulate plunging jets. A PBE is used with a source term depending on a volumetric rate of air entrain-

ment derived with a phenomenological model (at low velocities, the air is entrained due to the roughness of the jet and the entrainment rate scales as V_1^3 while at higher velocities, an air cavity forms and breaks near the impact point and the rate scales with $V_1^{1.5}$, V_1 being the jet velocity at impact). Location of air entrainment follows [272] with $v_{ent} = 1$ m/s that is the entrainment velocity generally observed for turbulent jets. The numerical results matched closely experimental measurements.

In their RANS monodisperse one-way coupled two-fluid approach, Ma et al. [233] made a reasoning to approximate the quantity of air entrained at a disturbed surface. Using a disturbance amplitude of the form

$$a = cst \cdot \frac{k}{g} \tag{4.26}$$

they deduced the rate of entrainment which is per unit volume-time:

$$q = \frac{C_{ent}}{g d_{ent}} k \frac{\partial v_n}{\partial n} \tag{4.27}$$

where C_{ent} is a calibration coefficient for air entrainment and v_n is the inward component of the average liquid velocity on the interface. This gradient formulation prevents entrainment if the bubbles and the interface move with the same downwards velocity compared to [272] model. The constants of the model are however case-dependent. It is tested on a plunging jet for which reasonable agreement is obtained and a hydraulic jump with non-negligible discrepancies compared to experimental data in the roller region attributed to the RANS approach. This origin is confirmed by Ma et al. [232, 234] in which two turbulence models were tested on the hydraulic jump with the same model: the DES [2] proved to perform better than the RANS approach, as the latter failed at reproducing the entrainment in the upper roller region while both reproduced well the entrainment at the toe of the hydraulic jump.

Ma et al. [235] developed an Eulerian-Eulerian polydisperse two-fluid model with an entrainment model based on the turbulent dissipation rate at the interface exceeding a threshold. It follows from Baldy [17] that introduces the self-similarity of bubble entrainment related to small scale disturbances and therefore justifies its dependence on the turbulent dissipation rate. Two parameters are required: the entrainment efficiency (number of bubbles entrained) and the critical turbulence dissipation rate. Derakhti and Kirby [108] then extended the model of [235] to the LES framework with a dynamic Smagorinsky subgrid formulation, the dissipation being replaced by the shear-induced production rate of subgrid-scale kinetic energy. These works highlighted that the high void fractions occurring in these flows could lead to mitigate significantly the turbulence of breaking waves.

Ma et al. [236] further applied the model developed in the previous works to a two-way coupled simulation of a 3D plunging liquid jet. The polydisperse model is based on the distribution of

[2] The Detached Eddy Simulation is a hybrid turbulence model switching from RANS to LES in regions where large scale turbulence can be solved.

bubble sizes observed experimentally. A satisfactory agreement is obtained with volume fraction and bubble count rate profiles. The two-way coupling did not require to introduce turbulent dispersion, contrary to the one-way approach. A calibration was required for the model constant C_{ent}. The air entrainment location is consistently located within the free surface cusp around the plunging jet. It is underlined that models in which the volumetric source only depends on the dissipation rate are well-suited for configurations where turbulence is generated from two-phase interactions near the interface but will predict spurious entrainment in the presence of boundary layers near a solid boundary such as the hull of a ship.

Such air entrainment modeling is not restricted to PBEs: Lopes et al. [224, 225] introduced a volumetric source term for air entrainment similar to [233]. Variations of the surface disturbance estimation were made with expressions similar to (4.19). A VoF interface capturing model formulation was employed, but in [225] the dispersed air phase was followed with an extra advection-diffusion equation in the bulk of the fluid and an appropriate free surface detection formula was introduced. Lopes et al. [224] considered a 2D dam break and a 3D plunging jet while a stepped spillway structure was studied in [225] with a comprehensive testing of the parameters of the model: with an appropriate choice of these parameters, a good agreement with experimental results was obtained with satisfactory flow depths, air concentration profiles and velocity profiles only slightly modified by the presence of air for the stepped spillway. The above-described criteria of [272] were used for the location of the air entrainment region with $v_{ent} = 0.8$ m/s, with a threshold on turbulent kinetic energy adapted to stepped spillway cases to get an accurate transition between the non-aerated and aerated regions.

Hsiao et al. [168] presented a combined experimental-numerical approach in which they developed a one-way coupled Eulerian/Lagrangian approach using and extending the air entrainment subgrid model of [233] to model plunging jets. Once entrained, the bubbles are followed discretely in a Lagrangian way and can still be broken up by shear forces. Reasonable agreement was obtained on the frequency of flow structures but the stream-wise velocity was over-predicted.

Castro et al.'s approach Castro et al. [53] detailed a polydisperse two-fluid model and made an in-depth focus on the development of a closed air entrainment model splitting the phenomenon into separate fundamental processes and modeling them individually. A single air entrainment volumetric source is introduced in a number density equation and is deduced from the probabilities of occurrence of the different steps of air entrainment: bubble inception, drag within the fluid, interaction with vortices or other bubbles and pull by buoyancy. Entrainment size distribution is imposed as some physical processes might be missed for the smallest bubbles. RANS models neglecting free surface effects are pointed out by the authors: they proved to be important for breaking wave simulations. At the plunging point, high levels of turbulence are noticed but the blended $k - \omega/k - \epsilon$ failed at reproducing them due to the short time scales involved. A mixing length model is introduced and appears as a production term near the free surface. Promising results are obtained.

4.2.3.3 VoF, averaged two-phase models and coupling

A certain number of computations were performed with interface tracking, two-fluid or mixture models without going down to the discretizations required by the DNS. Regarding the averaged two-phase models, the entrainment occurrence relies on the fact that the interfacial momentum closure (that provides the relative velocity closure for the mixture model as shown in Chapter 1) gives the appropriate stresses at the interface to generate entrainment. To illustrate the diversity of these approaches and the resulting discrepancies in the results, we give a few references on different air entrainment cases.

In a combined experimental-numerical study, Qu et al. [300] employed a mixture model and a Level-Set approach combined with a $k-\epsilon$ model to simulate 2D axisymmetric plunging jets. In the notations of the present work, the relative velocity reads:

$$\boldsymbol{v}^r = \frac{\rho^\alpha - \rho}{\gamma}\left(\boldsymbol{g} - \frac{d\boldsymbol{v}}{dt}\right) \tag{4.28}$$

with the hindering power $n = 1$ in γ defined by (1.95). Compared to (1.101), there is no turbulent diffusion term but the acceleration is deducted from the gravity (for the set of Euler equations, that would give the pressure gradient). The Schiller and Naumann's expression as written by [85] is used. If both models give the appropriate order of penetration depth, the Level-Set approach gives better details on the flows at a more expensive computational cost.

Stepped spillways were studied extensively in numerous references. Cheng et al. [79] simulates flows over step-pool spillways using a mixture model with the RNG $k-\epsilon$ model. A very good quantitative agreement is obtained for the velocity and pressure profiles, while only a visual comparison is made for the volume fraction with good correspondence. Nikseresht et al. [281] performed such simulations with VoF and mixture models, and compared different turbulence models. In their case, a Reynolds stress model and the RNG $k-\epsilon$ model provided the best agreement with experimental results. The relative velocity followed an expression suggested by Manninen and Taivassalo [239]. Zhan et al. [397] applied and compared the results of three models, namely a VoF model, a mixture model and an Eulerian model, to a skimming flow over a stepped spillway with turbulence simulated by either LES or a RNG $k-\epsilon$ model. The mixture and VoF models combined with LES proved to give satisfactory results, while the Eulerian RANS approach failed at giving appropriate features of the flow. To assess different stepped spillway geometries, Li et al. [214] compared numerically the different configurations in terms of air concentration, interfacial velocities and dissipation using a mixture model and a realizable $k-\epsilon$ model [3]. The relative velocity followed (4.28) with an effective mixture viscosity and a modified expression of the drag coefficient for high Reynolds. Wan et al. [376] used the VoF approach with a realizable $k-\epsilon$ model to investigate the effect of the height of the steps over the inception point

[3] Variant of $k-\epsilon$ model built by Shih et al. [329] from the Explicit Algebraic Reynolds Stress Model (EARSM) such that it satisfies mathematical conditions on the Reynolds tensor of Cauchy–Schwarz type.

location for different step-pool spillways.

The realizable $k - \epsilon$ model was also used in the VoF approach by Witt et al. [384] to study the air entrainment in an hydraulic jump without subgrid air entrainment model. The 3D application proved to improve the prediction of entrained air and bubble size compared to the 2D computations.

One can see that these approaches are taken to their limits as separated or dispersed regimes can coexist for flows over hydraulic structures. As presented in Section 2.4.1, approaches coupling different formulations depending on the local configuration of the flow were developed. Regarding air entrainment applications, in the following of previous works as [351], Pereira [291] recently coupled VoF and two-fluid model approaches to model air entrainment over hydraulic structures such as a drop shaft or a stepped spillway. The transition between models relies on the volume fraction gradient. RANS formulations, DES and Very large eddy simulations (VLES), *i.e.* LES with an insufficient spatial resolution, were employed. The interest is two-fold compared to the source term approach of the last paragraph: conservation properties can be achieved as no artificial volume of air needs to be introduced and the associated calibration parameters can be avoided. However a fine resolution of the turbulent structures would theoretically be required to model accurately the entrainment. It was nevertheless noted that aeration could proceed from the numerical discretization in the case of local aeration while for self-aeration, sufficient numerical resolution was required to allow for the development of the air-entraining eddies. The approach is not free of parameters as the two-fluid model requires a bubble diameter that depends on the considered flow and the mesh (bubbles smaller that the ones resolved by the mesh) and can affect significantly the computations.

4.2.3.4 Validation

In the absence of prototype data, experimental data is pivotal for the calibration and validation of the numerical models: air concentration, velocity, turbulent intensity, distribution of bubble sizes [63] but also distribution of the turbulent integral length and time scales and microscopic configurations of clusters. Those data have intrinsic uncertainties, due to the complexity of metrology in those kinds of two-phase flows and the accuracy of the post-processing. One can find further details on the metrology in [59, 64, 73]. Once calibrated and validated, the numerical simulations can give further insights into the fields of the flow considered, and allow one to assess the impact of variations of flow conditions, help for the optimization of the design, etc. Using a combination of CFD and physical modeling appears as a powerful tool for studying multiphase flows [31, 300, 354]. The lack of validation and verification was however pointed out [64, 68].

4.2.3.5 Summary

Lopes et al. [224] sums up the stakes of the numerical air entrainment modeling as follows:

> "The accurate prediction of the air-entrainment process in a wide variety of air-water turbulent flows is a computationally challenging problem under current investigation. An ideal numerical model needs to be accurate and fast in the definition of a macroscopic interface and simultaneously precise enough to take into account the formation of bubbles through the free surface, their transport and their natural interactions: bubble-bubble and bubble-fluid."

One needs to define what are the quantities of interest for the engineering applications considered and design the consequent appropriate model.

We have underlined that turbulence is at the core of the air entrainment but only addressed its modeling transversely, as chosen models vary from one reference to another. Due to their computational efficiency, RANS models are of wide use. Viti et al. [372] made a state-of-the-art of the numerical simulation of hydraulic jumps, with Eulerian and Lagrangian approaches and the different existing turbulence models. They highlighted the satisfying accuracy of the RANS approaches for mean flow variables estimation, but the insights in aeration remain mostly limited to air concentration. However Ma et al. [234] highlighted the need of more complex turbulence models such as DES to get proper resolution of such flows. If one wants to focus on transient behaviors and the mechanisms of the air entrainment generation due to turbulent fluctuations, a larger resolution together with turbulence models more expensive computationally as DES or LES are required [291].

When the phases are not fully resolved, the quality of the air entrainment subgrid model is also critical. We have highlighted the wide variety of approaches developed in the literature, either by modeling the small-scale interfaces or introducing a source term. Mixture models appear as an efficient and simple way of simulating mean flow variables for stepped spillways while some discrepancies were noted on plunging jets. Coupling an interface tracking approach with a two-fluid formulation seems a promising approach.

The few attempts of air entrainment modeling in SPH, together with the model developed in the present work, are addressed in the following section.

4.3 Air entrainment modeling in SPH

Air entrainment was only recently addressed by the SPH community and only within the multifluid SPH framework. Several obstacles can indeed be identified: the difficulty to handle high density ratio two-phase flows, the computational resources required to handle discretizations able to reproduce accurately the air bubble entrainment and the turbulence modeling within the method. After a review of the SPH literature about air entrainment, the model developed in the present work is presented and application cases are considered.

4.3.1 Review of the literature

Recent work were performed for the simulation of air entrainment on hydraulic structures with SPH. We present here a review of the few references found in the literature. Let us underline that all these works were performed with multifluid SPH, *i.e.* without mixture model.

Dao et al. [100] aimed at simulating rogue waves following the model of Colagrossi and Landrini [86]. Qualitative agreement with experimental results underlined the interest of integrating the air phase in a nested domain near the breaking zone. They could observe the fragmentation of the entrapped air pockets that modified the dynamics of the breaking, what was not captured by single-phase simulations.

Meister and Rauch [250] implemented a multifluid model similar to Monaghan and Rafiee [268] with a small decrease of the repulsion force between phases in order to handle air entrainment cases. Sound speeds are computed following Colagrossi and Landrini [86] and the viscous force follows Adami et al. [4]. Kernel renormalization is employed. After validating the model on a 2D dam break and bubble rising, a two-dimensional homogeneous bubbly flow in water columns was computed based on the detailed multifluid simulation of the single bubble case and some experimental data (35 bubbles modeled as solid air particles with an assigned velocity from the experiment), in order to reach practical engineering configurations and focus on the air-induced mixing. As decribed in Section 2.3.2, bubble columns were also studied with the DEM-SPH approach by Torti and Sibilla [348].

Nakayama et al. [277] studied a dam break over an obstacle and the flow over one step of a stepped spillway under periodic conditions but without quantitative validation.

Wan et al. [374] used the model of Colagrossi and Landrini [86] (artificial viscosity, cohesive force, XSPH). An advection-diffusion equation on the dissolved oxygen is introduced with a source term depending on the specific surface area of bubbles computed thanks to the number of air particles in the kernel support. A reasonable agreement was obtained for the velocity profiles, except near the inception point, and the dissolved oxygen concentration was well reproduced.

Wan et al. [375] went further in the study of air entrainment. They included in the model of Colagrossi and Landrini [86] a drag force accounting for air-water interactions and used realistic viscosities by combining a molecular viscosity model with a sub-particle-scale turbulence model similarly to Lo and Shao [223] for the water phase and artificial viscosity for the air phase. Particle shifting with the correction of Mokos et al. [255] was used and as in [86] a cohesive force was set in the air phase. The drag force was written similarly to the closure (1.94) but with the drag coefficient computed following Tomiyama et al. [345]. The total drag force is computed as a sum over the neighboring particles. A cohesive force as in Colagrossi and Landrini [86] is applied. The air concentration is computed as the ratio of the volume of the air phase over the total volume within the support of the kernel of the current particle. The air concentration is therefore a consequence of the space arrangement of the air and water particles. The stepped

spillway of Chanson and Toombes [70] is tested and a satisfactory agreement is obtained for the concentration profiles at the different steps, except near the inception point. An hydraulic jump from Gualtieri and Chanson [153] is also considered with a good agreement of the concentration profiles at different distances from the impingement point.

Yang et al. [392] employed a mixed model with the δ–SPH continuity equation and an artificial viscosity in the momentum equation, complemented by a cohesive pressure term in the gas phase and XSPH shifting following Colagrossi and Landrini [86] to simulate air-water flows. The results obtained on a dam break and an hydraulic jump legitimated the use of a multifluid model compared to a single-fluid model to get results in quantitative agreement with the experimental data.

4.3.2 Present SPH air-water mixture model

We use the mixture model detailed in Chapter 3. The fluid features and relative velocity shall be specified. The previous section has shown that air-water flows are usually modeled in SPH with multifluid approaches where the SPH particles belong to assigned phases. To the author's knowledge, the present work is the first to use a mixture model within the SPH approach to model air-water flows.

4.3.2.1 Air and water characteristics

The air and water characteristics are detailed in Table 4.1 .

Table 4.1: Parameters for the air-water cases.

ρ^α	1.23	kg/m^3	ρ^β	1000	kg/m^3
ν^α	1.56 10^{-5}	m^2/s	ν^β	10^{-6}	m^2/s

4.3.2.2 Air-water relative velocity

Drag coefficient In this work, we have made the assumption that the dispersed phase consists of monodisperse spherical bubbles or drops. Clift et al. [85] following Schiller and Naumann [320] suggested to write the drag coefficient as:

$$C_D = \begin{cases} \dfrac{24}{Re^\alpha}\left(1 + 0.15\left(Re^\alpha\right)^{0.687}\right) & \text{if } Re^\alpha \leq 1000 \\ 0.44 & \text{if } Re^\alpha > 1000 \end{cases} \tag{4.29}$$

Tomiyama et al. [345] suggested to include effects of non-spherical air bubbles through the form of equation (4.7), with additional limits if the Reynolds number becomes too high in slightly

contaminated water and the shape is non-spherical, depending on the Eötvös number. However, on the considered cases regarding the assumptions made on the bubble diameter, this regime shall not be considered. The hindering coefficient was kept to $n = 1$.

Hydrostatic approximation Due to the very noisy nature of the pressure field in the SPH approach retained, despite of the volume diffusion and due to the strong density ratio, it did not appear numerically stable to use directly the pressure gradient in the relative velocity computation. An additional approximation was therefore made to use the hydrostatic value of the pressure gradient $\rho \boldsymbol{g}$. The dependence only on the gravity decouples the phase evolution from the dynamics generated by the momentum equation. In absence of diffusion, the only possible transfers occur in the gravity direction. It does not allow one to reproduce effects generated by a non-hydrostatic pressure gradient as described by [188]. It is expected that once the pressure field will be stabilized by either using a Riemann solver or implementing the multiphase δ–SPH approach, it will be possible to use the pressure gradient in the relative velocity computation and get better physically-based results.

Practical computation Because of the presence of $\boldsymbol{V}^r$ in the Reynolds number, the relative velocity definition is implicit and it would require some iterations to converge. To limit the computations, we make the following reasoning. Noting $R_\rho = \left(\rho^\alpha - \rho^\beta\right)/\rho^\beta$, we first define the Reynolds number function f_R:

$$f_R(\mathrm{Re}^\alpha) = \mathrm{Re}^\alpha \left(1 + 0.15 \left(\mathrm{Re}^\alpha\right)^{0.687}\right) = \frac{\left(d^\alpha\right)^3 \beta^n}{18 \left(\nu^\beta\right)^2} |R_\rho \boldsymbol{g}| \tag{4.30}$$

An approximation of f_R^{-1} over $\mathrm{Re}^\alpha \in [0; 1000]$ is:

$$\mathrm{Re}^\alpha = c_R \left(1 - \frac{1}{1 + \left(\frac{f_R(\mathrm{Re}^\alpha)}{b_R}\right)^{a_R}}\right) \tag{4.31}$$

where the coefficients $a_R = 0.6301226$, $b_R = 2124552$ and $c_R = 21037.87$ computed numerically. We propose the following scheme:

- Compute $f_R(\mathrm{Re}^\alpha)$ using (4.30)
- Deduce Re^α through (4.31)
- Then
  - If $\mathrm{Re}^\alpha < 1000$, we compute a first guess as

$$\boldsymbol{V}^r = \frac{4 \left(d^\alpha\right)^2 \beta^n}{3 \nu^\beta \mathrm{C_D} \left(\mathrm{Re}^\alpha\right) \mathrm{Re}^\alpha} R_\rho \boldsymbol{g} \tag{4.32}$$

– Else $\mathrm{C_D}\left(\mathrm{Re}^\alpha\right) = 0.44$ and the relative velocity is written explicitly

$$\boldsymbol{V}^r = \sqrt{\frac{4d^\alpha \beta^n}{3\mathrm{C_D}\rho^\beta |R_\rho \boldsymbol{g}|}} R_\rho \boldsymbol{g} \tag{4.33}$$

If $\mathrm{Re}^\alpha < 1000$, the first guess is already a good estimate generally. In the other case, the computation is explicit.

Modification of the diffusion term in the phase volume equation In the diffusion term of the new relative velocity closure, compared to the closure (3.42), the eddy viscosity now varies and $\boldsymbol{\nabla}\alpha$ is divided by $\alpha\beta$. The diffusion term detailed in (3.44) in the phase volume equation therefore requires an adaptation:

$$\begin{aligned}\frac{dV_a^\alpha}{dt} &= \alpha_a \frac{dV_a}{dt} - \sum_{b\in\mathcal{F}} \left(\alpha_a\beta_b \left[\boldsymbol{v}_{0,a|b}\cdot \boldsymbol{S}_{a|b}\right]^+ + \alpha_b\beta_a \left[\boldsymbol{v}_{0,a|b}\cdot \boldsymbol{S}_{ab}\right]^-\right) \\ &+ \sum_{b\in\mathcal{F}} \frac{\nu_{T,a}+\nu_{T,b}}{2\mathrm{Sc}_T} \frac{\alpha_a-\alpha_b}{r_{ab}} \frac{\boldsymbol{r}_{ab}\cdot \boldsymbol{S}_{a|b}}{r_{ab}}\end{aligned} \tag{4.34}$$

The condition for positiveness detailed in Section 3.2.6 is changed with a different relative velocity closure. One can find a derivation of an upper bound in Section C.2: a coarse limit amounts to replace K by $\nu_{T,\max}/\mathrm{Sc}_T$. To avoid a too strong limitation, we however made an approximation in (C.23), approximating the b neighboring values by the considered particle value a for the terminal velocity $\boldsymbol{v}_0$ and the turbulent viscosity ν_T, what led to the approximate condition:

$$\delta t \max\left(\eta_\alpha \frac{v_{0,a}}{\sigma_e} + \frac{\nu_{T,a}}{\mathrm{Sc}_T\sigma_e^2}\right) \leq \xi_\alpha \tag{4.35}$$

for which we used the same values of $(\xi_\alpha, \eta_\alpha)$ as in Section 3.2.6 due to the proximity of the formulations and a safety factor of 0.5 was set in front of this condition. Let us underline that in the turbulent flows considered in the following and consistently with the assumptions of the mixture model, the norm of the relative velocity is small compared to the flow velocity so that this condition will not be the strongest constraint on the time step.

Switch of dispersed phase We have assumed in the above-mentioned expressions that α was the dispersed phase. However, regarding the expected applications of this model, such as separation of two phases, both α and β can happen to be dispersed (i.e. bubbles of air in water or water droplets in air). When specified in the application cases, we try a switch of definition of dispersed quantity when α exceeds the threshold 0.5. Let us underline that physically the transition between dispersed and continuous configurations can coexist at such volume fraction. It is therefore an additional approximation of this model. Denoting the relative velocities where α or β is dispersed by respectively $\boldsymbol{v}^{r,\alpha}$ and $\boldsymbol{v}^{r,\beta}$, the smooth transition is done through the

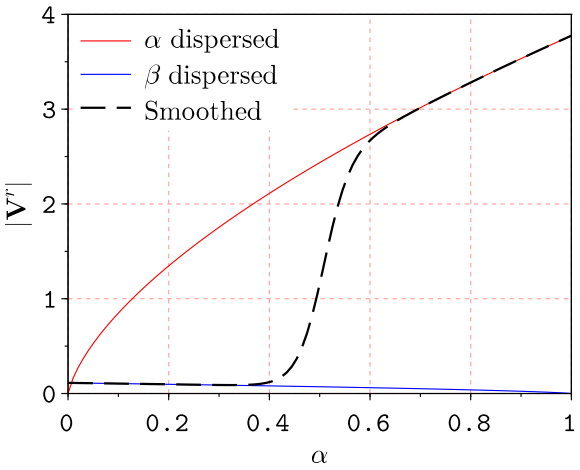

Figure 4.5: Relative velocity with a switch depending on the volume fraction for $d^{\alpha} = d^{\beta} = 1\,\text{mm}$ in the air-water case.

weighting:

$$w_t(\alpha) = \frac{1}{2}\left(1 + \tanh\left(20\left(\alpha - \frac{1}{2}\right)\right)\right) \tag{4.36}$$

so that the relative velocity writes:

$$\boldsymbol{v}^r = (1 - w_t(\alpha))\,\boldsymbol{v}^{r,\alpha} + w_t(\alpha)\,\boldsymbol{v}^{r,\beta} \tag{4.37}$$

The corresponding function is displayed on Figure 4.5.

4.3.2.3 Precaution at initialization and at open boundaries

At initialization and at open boundaries, the interface is diffused over a few particles using a hyperbolic tangent: this prevents the initial rearrangement of the particles, perturbed by the high density ratio, to lead to a crash of the simulations. The phases of particles of the bulk of the fluid are then separated progressively. One layer of particles of intermediate volume fraction can persist as the discretization may not allow phases to be perfectly separated with the available volumes.

4.4 Schematic two-dimensional air entrainment cases

In the light of Section 4.2.2.1, we considered two classical configurations of air entrainment: the interfacial aeration over a stepped spillway and the local aeration of a plunging jet. Regarding the complexity of those types of flows, we will focus on a steady state behavior. In the following 2D cases, the x variable will correspond to the longitudinal direction of the flow and the y

variable will refer to the orthogonal direction, along which the shear layer develops. The present SPH mixture model will give us insights into the void fraction α, the longitudinal air-water interfacial velocity V_x and the characteristic turbulent velocity v'. Additional schematic tests will be displayed in Section 4.4.3.

4.4.1 Stepped spillway

Spillways form a classical structure of hydraulic works and provide a controlled release of flows from dams. Several geometries can be considered from small-slope to steep chutes, from smooth to step-pool spillways. Self-aeration is a common process in such structures and leads to several effects, namely flow bulking, drag reduction, cavitation mitigation and air-water mass transfers [59]. While on steep chutes, it is generally admitted that the air entrainment occurs at the intersection of the free surface with the boundary layer developing from the bottom, experimental evidence has shown that the inception of air entrainment could happen before due to free surface instabilities, especially for small-slope structures. The ability of the mixture model to capture the air entrainment will then depend on its capacity to reproduce these instabilities while air entrainment will intrinsically be active when the boundary layer reaches the free surface due to the turbulent diffusion term of the relative velocity closure. Physical models of spillways are well-documented in the literature. In the following we focus on a stepped spillway described in Chanson [60] and Chanson and Toombes [69, 70].

4.4.1.1 Description

The stepped spillway has a simple design and is easy to build thanks to recent advances in the construction materials [28]. The interest of a staircase shape is two-fold: the high level of turbulence generated enhances the energy dissipation avoiding the need for a large basin downstream of the structure and the fast-growing boundary layer leads to an early aeration compared to a smooth spillway, mitigating cavitation hazards [59]. One can distinguish three regimes, depending on the incoming volume flow rate, ranked according to increasing values:

- A nappe flow: the flow takes the form of a succession of plunging jets and hydraulic jumps on each step [59, 126].
- A transition flow: this regime exhibits chaotic flow patterns as underlined by [60] that reported strong splashing and droplet ejection after the inception point and irregular generation of air cavities of variable sizes [60].
- A skimming regime: a coherent water stream flows over a pseudo-bottom formed by the edges of steps with in-between maintained recirculating vortices submitted to the shear forces of the main flow [59]. These step-induced macro-roughness causes a decrease of flow velocity involving a higher flow resistance and energy dissipation [44]. A turbulent

boundary layer develops from the first steps and it has been long considered that air entrainment occurs when it reaches the free surface [59].

In the last two regimes, the non-aerated region exhibits free surface oscillations in phase with the stepped profile. Free surface instabilities were also reported there and may play a role in the aeration. Valero and Bung [355] described different kinds of waves: while vanishing waves were generated by the inlet condition, others can develop all along the spillway such as capillary waves and the viscous Kelvin–Helmoltz instability with a decreased triggering velocity resulting from the viscosity ratio between air and water [140]. Downstream of the inception point, it becomes difficult to have a clear definition of the free surface. It is therefore defined as the iso-air concentration line $\alpha = 0.9$ (we will keep this definition in the aerated region from the numerical viewpoint following Lopes et al. [226]). According to [59], most of the mass and momentum fluxes occurs below the corresponding height Y_{90} and the air-water flow behaves as a quasi-homogeneous mixture where phases travel with an almost identical velocity. This experimental feedback supports the use of the model developed in this work for the application to such flows. The flow counts distinct regions:

- A bubbly flow for small air volume fractions ($\alpha < 0.3/0.4$) formed of single and clusters of irregular air bubbles and air packets;
- A highly aerated flow for intermediate air volume fractions ($0.3/0.4 < \alpha < 0.9$) formed by foam and air-water projections;
- Carosi and Chanson [49] distinguished a spray region for $\alpha > 0.7$.

Transition and skimming flow regimes are well-documented in the experimental results so that we will focus on those configurations. Moreover the nappe flow with its succession of plunging jets would require a fine resolution for a proper resolution step by step. In the skimming regime, three regions may be identified, depending on the size of the spillway and the flow conditions [386]:

- A non-aerated region of boundary layer growth
- A gradually-varied zone
- A uniform flow region

Those regions have been studied altogether, or sometimes individually in the literature. Strong levels of turbulence, higher than in single-phase flows [71], are reached in the skimming flows, in the region $0.3 < \alpha < 0.7$, sustained by the complexity of the two-phase flow in this region with strong deformations of the interfaces [49, 60]. According to the integral length and time scales, the energy is dissipated by large vortices and the turbulence is intensely generated in the stepped cavities [49]. A strong correlation is suggested between the turbulence intensity

and the interfacial area. Particle collisions and particle-turbulence interactions are allegedly the prominent features of this region [71]. As long as bubble chord distributions are concerned, in the bubbly flow region, Carosi and Chanson [49] found a log-normal law with a peak size between 0.5 and 1 mm. On the contrary the distribution of the droplet chord size in the spray region $\alpha > 0.7$ is flat. In both cases, a wide range of sizes from 0.3 to more than 15 mm was detected.

4.4.1.2 Dimensional analysis and quantities of interest

Let us consider a two-dimensional stepped spillway of invert slope θ_s with a step height h_{st} and an equivalent roughness height k_s with flowing water of discharge per unit width q^β. Following Chanson [64], one can perform a simplified dimensional analysis of this test case:

$$\alpha, \frac{V_x}{V_c}, \frac{v'}{V_c} = f\left(\frac{x}{d_c}, \frac{y}{d_c}, \frac{h_s}{d_c}, \frac{k_s}{d_c}, \theta_s, \mathsf{Fr} = \left(\frac{d_w}{d_c}\right)^{-\frac{3}{2}}, \mathsf{Re} = \frac{\sqrt{g d_c^3}}{\nu^\beta}, \mathsf{Mo}\right) \tag{4.38}$$

where the critical ($\mathsf{Fr}_c = 1$) flow depth d_c and associated velocity V_c for a rectangular channel write:

$$d_c = \sqrt[3]{\frac{(q^\beta)^2}{g}} \quad \text{and} \quad V_c = \sqrt[3]{g q^\beta} \tag{4.39}$$

d_w is the equivalent clear-water depth defined as:

$$d_w = \int_0^{Y_{90}} \beta(y) dy \tag{4.40}$$

V_{90} is the interfacial velocity at the height Y_{90}. We define U_W the clear-water flow velocity:

$$U_W = \frac{q^\beta}{d_w} \tag{4.41}$$

And C_{mean} the depth-averaged void fraction:

$$C_{\mathsf{mean}} = \frac{1}{Y_{90}} \int_0^{Y_{90}} \alpha(y) dy \tag{4.42}$$

Hence $d_w = Y_{90}\,(1 - C_{\mathsf{mean}})$. Some of these quantities are illustrated on Figure 4.6.

4.4.1.3 Semi-analytical model

The relation (4.24) projected along the normal to the flow writes:

$$\frac{\partial}{\partial y}\left(K_T \frac{\partial \alpha}{\partial y}\right) = (\boldsymbol{e}_g \cdot \boldsymbol{e}_y) \frac{\partial}{\partial y}\left(\alpha \sqrt{\beta} \boldsymbol{v}_0 \cdot \boldsymbol{e}_y\right) \tag{4.43}$$

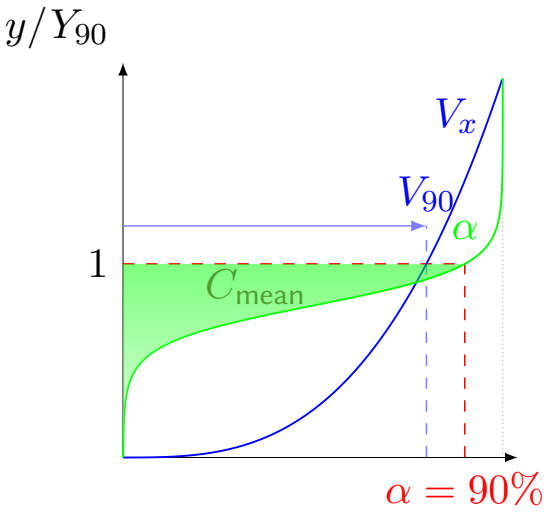

Figure 4.6: Quantities of interest to characterize air entrainment.

where K_T is the turbulent diffusivity of air bubbles, $\boldsymbol{e}_g$ is the unit vector directed along gravity and where the coefficient $\sqrt{\beta}$ in front of the bubble rising velocity $\boldsymbol{v}_0$ stems from the two-phase nature of the medium of density $\beta\rho^\beta$ following Chanson [57]. One can recover this relation using the volume fraction equation (1.86) for a steady configuration with the relative velocity (1.101), considering a unit turbulent Schmidt number and taking a hindering factor equal to $-\frac{1}{2}$. With the dimensionless position $y_\star = y/Y_{90}$, the first integration leads to:

$$\frac{\partial \alpha}{\partial y_\star} = \mathsf{Pe}\ \alpha\sqrt{\beta} \tag{4.44}$$

where the Péclet number is defined as $\mathsf{Pe} = (\boldsymbol{v}_0 \cdot \boldsymbol{e}_y)\,(\boldsymbol{e}_g \cdot \boldsymbol{e}_y)\,Y_{90}/K_T$. In case of homogeneous turbulence, *i.e.* constant K_T, a second integration leads to:

$$\alpha = 1 - \tanh^2\left(K_1 - \frac{y_\star}{2\mathsf{Pe}}\right) \tag{4.45}$$

where $K_1 = K_\star + 1/(2\mathsf{Pe})$ with $K_\star = \operatorname{argtanh}\left(\sqrt{0.1}\right)$. Pe can be deduced from the mean air concentration C_{mean} through:

$$C_{\text{mean}} = 2\mathsf{Pe}\left(\tanh\left(K_\star + \frac{1}{2\mathsf{Pe}}\right) - \tanh\left(K_\star\right)\right) \tag{4.46}$$

Different closures for the diffusivity can be considered, resulting in different formulations that are listed in Chanson and Toombes [69]. In applications, this formula is also used in the gradually-varied region, using local instead of uniform values [57]. The turbulent diffusivity K_T is of the same order of magnitude as the eddy viscosity ν_T. However, their ratio K_T/ν_T seemed to be larger in model experiments than in prototype data [57]. The characteristic transverse dimension

is Y_{90}. For transition flows, assuming a Péclet number of the form:

$$\mathsf{Pe} = \frac{\alpha\sqrt{\beta}}{K_3\left(K_2 - \alpha\right)} \tag{4.47}$$

with

$$\begin{aligned} K_2 &= \frac{0.9}{1 - \exp\left(-K_3\right)} \\ C_{\mathsf{mean}} &= K_2 - \frac{0.9}{K_3} \end{aligned} \tag{4.48}$$

Chanson [60] suggested the model:

$$\alpha = K_2\left[1 - \exp\left(-K_3 y_\star\right)\right] \tag{4.49}$$

For skimming and smooth-chute flows, assuming a Péclet number of the form:

$$\mathsf{Pe} = \frac{\mathsf{Pe}_0}{1 - 2\left(y_\star - \frac{1}{3}\right)^2} \tag{4.50}$$

The concentration profile reads:

$$\alpha = 1 - \tanh\left(K_4 - \frac{y_\star}{2\mathsf{Pe}_0} + \frac{\left(y_\star - \frac{1}{3}\right)^3}{3\mathsf{Pe}_0}\right) \tag{4.51}$$

with

$$\begin{aligned} K_4 &= K_\star + \frac{1}{2\mathsf{Pe}_0} - \frac{8}{81\mathsf{Pe}_0} \\ C_{\mathsf{mean}} &= 0.7622\left(1.0434 - \exp\left(-3.614\mathsf{Pe}_0\right)\right) \end{aligned} \tag{4.52}$$

For the velocity profile:

$$\begin{cases} v_\star = y_\star^{\frac{1}{n_v}} & \text{if } 0 \leq y_\star \leq 1 \\ v_\star = 1 & \text{if } 1 \leq y_\star \leq 2.5 \end{cases} \tag{4.53}$$

where $v_\star = V_x/V_{90}$. The n_v power is variable in the references, depending on the slope of the spillway [294, 354].

4.4.1.4 Numerical model

We considered for the numerical application the experiments of [69]. The geometry is described in Figure 4.7. The physical and numerical parameters are detailed in Table 4.2. The slope is equal to $\theta_s = 21.8°$. If not specified, the air phase is always considered as dispersed for the relative velocity computation. A volume diffusion coefficient $\Lambda = 0.3$ was used to smooth the pressure field (instabilities developed at the interface for smaller values). The $k - \epsilon$ model is employed

to model turbulence: it provides turbulent diffusion in the relative velocity expression. It is a high-speed flow so that the expected prominent turbulent contribution should come from water turbulence. The initial block of water reaches the level $h_s = 1.1$ m and falls down the steps before reaching the outlet boundary as a mixture.

Table 4.2: Parameters for the stepped spillway case.

ρ^α	1.23	kg/m^3	ρ^β	1000	kg/m^3
ν^α	$1.56\ 10^{-5}$	m^2/s	ν^β	10^{-6}	m^2/s
c^α	45	m/s	c^β	45	m/s
d^α	1	mm	d^β	1	mm
δr	5	mm	p_B	500	Pa

Focus on open boundaries The chosen open boundary formulation results from many tests on this stepped spillway test case. The target is an open boundary configuration allowing to impose a given flow rate at the inlet, letting the air-water mixture escape the domain after the steps and introducing the quantity of air needed to breed the air entrainment.

- Water inlet: as underlined in Section 3.5.5, some instabilities can develop near separated flow open boundaries probably due to the high density ratio between phases. To avoid issues at the inlet, the volume fraction profile imposed is smoothed over a few particles around the interface through an hyperbolic tangent function. Once introduced in the domain, the phases can be quickly separated by the relative velocity. Moreover only water is allowed to enter domain, through an imposed longitudinal velocity profile for a given volume flow rate computed as:

$$j_x = u_\star \left[\frac{1}{\kappa} \log\left(\frac{z u_\star}{\nu^\beta} \right) + C_\nu \right] \tag{4.54}$$

  where the friction velocity is deduced from iterations on the relation:

$$u_\star = \frac{\kappa q^\beta / h_{up}}{\log\left[\exp\left(\kappa C_\nu - 1 \right) h_{up} u_\star / \nu^\beta \right]} \tag{4.55}$$

  with h_{up} the upstream water level left to vary and computed on the fly. This velocity is multiplied by $\min(1, t)$ to have an initial ramp to reach the desired volume flow rate without destabilizing strongly the domain during the first iterations. A configuration using an air inlet with an imposed pressure above the water region was also tested but sometimes resulted in some spurious behaviors of the air particles close to water. No turbulence is introduced at the inlet. When we imposed a profile for the turbulent kinetic energy and

the dissipation linked to a channel formulation, those quantities propagated until the steps and generated air entrainment since the very first steps.

- Pressure conditions: the background pressure is imposed for air all over the upper limit of the domain (to decrease the computational time, we had also considered an upper limit following the slope of the steps to avoid to have too many air particles but the imposition of the pressure condition on a piece-wise wall was problematic). The outlet condition required some work. First an hydrostatic pressure for an air column was considered, what should bear some similarities with the classical null pressure condition of the single-fluid formulation that allows the fluid to leave the domain (here, we want to maintain the air layer so that we cannot let the associated particles escape). However, it led to a bulking of a fluid and some spurious back-flow gusts in the domain. It might be linked to the mixture pressure gradient in the bulk of the fluid trying to adapt to the weak pressure gradient of the air. Putting the outlet boundary further did not modify this issue. We then tried to impose a homogeneous Neumann condition on the pressure as usually done on outlets but it also resulted in unstable computations. To circumvent this issue, we impose the hydrostatic pressure of the incoming mixture following:

$$p(z) = p_B - \int_z^{H_d} \rho(z) g dz \tag{4.56}$$

where the mixture density $\rho(z)$ is computed thanks to an SPH interpolation on the neighbors of the boundary particle and where at $z = H_d$ the top height of the outlet, one has $p(H_d) = p_B$. This condition is only approximately enforced: to avoid too heavy computations and due to the complexity of identifying in this Lagrangian framework which particles form the column above a given boundary particle, an additional table was introduced storing the value of the integral of (4.56) for all the column of particles above. It is initialized with the value for the hydrostatic pressure of an air column. It needs some iterations to adapt if abrupt changes occur. However, this formulation should be convenient for the progressive arrival and growth of an air-water mixture layer. Such an approach improved the behavior near the outlet. Still, air penetrates through the right wall contrary to what we expect, *i.e.* air penetrating from the upper wall and being entrained by the flow. This work illustrates the complexity of imposing quantities at open boundaries: the exact solution we impose might not correspond exactly or even differ significantly from the behavior in the bulk of the fluid and trigger the development of instabilities, the computations trying to make the continuity between the upcoming and imposed quantities. When the pressure is imposed, the turbulent kinetic energy and dissipation are interpolated. A test made of imposing 10^{-6} for these quantities on pressure condition boundaries did not trigger significant discrepancies.

- Modification of the $k-\epsilon$ closure: an important issue we had is that turbulent kinetic tended

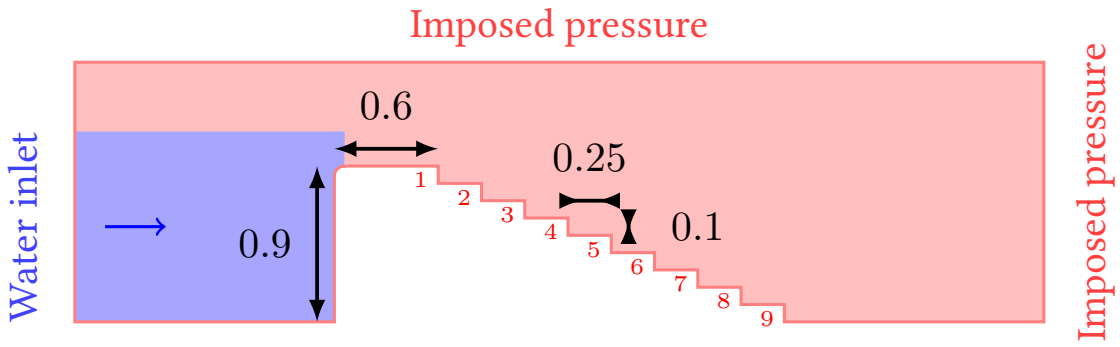

Figure 4.7: Stepped spillway: geometry (distances in m).

to accumulate and go back within the domain from the outlet boundary due to the shear between the out-going mixture and the in-going air. It was problematic as it triggered significant diffusion of air within water due to the relative velocity closure and prevented to reach a converged state. Hence, a correction was made in the turbulence model to prevent the production of turbulent kinetic energy in the air phase: the production term was multiplied by the volume fraction of water β in both the turbulent kinetic energy and dissipation equations:

$$\frac{\partial k}{\partial t} + \boldsymbol{j} \cdot \boldsymbol{\nabla} k = \frac{1}{\rho} \boldsymbol{\nabla} \cdot \left[\left(\mu + \frac{\mu_T}{\sigma_k} \right) \boldsymbol{\nabla} k \right] + \beta \mathbb{P}^j + \mathbb{G} - \epsilon \tag{4.57}$$

$$\frac{\partial \epsilon}{\partial t} + \boldsymbol{j} \cdot \boldsymbol{\nabla} \epsilon = \frac{1}{\rho} \boldsymbol{\nabla} \cdot \left[\left(\mu + \frac{\mu_T}{\sigma_\epsilon} \right) \boldsymbol{\nabla} \epsilon \right] + \frac{\epsilon}{k} \left(C_{\epsilon_1} \beta \mathbb{P}^j + C_{\epsilon_5} \mathbb{G} - C_{\epsilon_2} \epsilon \right) \tag{4.58}$$

Let us note that the correction also impacted the mixture regions as the factor β then takes intermediate values.

4.4.1.5 Results

Computations were performed with 400 000 particles during around 14 hours of computational time on one graphic card GeForce GTX Titan Black for 10 s of physical time[4]. To post-process the profiles along the y direction, a set of points spaced by δr were introduced along the normal to the slope starting at the edge. The variables of the nearest SPH particle were attributed to each of these points. In order to get smooth profiles for comparison with the time-averaged experimental results, we proceed to an average of the variables over ten equally-spaced time steps between 8 and 10 s to get the following results. This average is especially useful for transitional flows that exhibit variability.

[4]The code, still in development, is not optimized.

Basic configuration In our formulation, the transient of the flow going down the steps might not be accurate due to the assumptions of the formulation. We are more interested in the steady state obtained after a few seconds of physical time when the volume fraction and velocity profiles does not vary significantly anymore. We considered three volume flow rates tested by Chanson and Toombes [69] (the width of the spillway is $W_s = 1$ m so that the total volume flow rate has the same value as the one per unit length as $Q^\beta = q^\beta W_s$): two correspond to a skimming regime while the smaller one falls within the transitional regime. It is expected that the model performs better in the skimming regime where the variations of topology of the flow are confined to a smaller region. Figure 4.8 illustrates the steady states reached for the three configurations, plus a nappe flow regime computed to check the behavior of the model in this situation. These pictures allow one to identify the position of the inception point. We will address these different configurations in the following. The initial transient is presented in Figure 4.9.

For $q^\beta = 0.1819$ m^2/s, Figure 4.8d displays the volume fraction field over the steps: one can observe that air entrainment occurs just after the sixth step while it has started at this step in the experiments. One can check on Figure 4.10 that it corresponds to the region where the boundary layer is reaching the free surface (for the recall, it is defined here as the isoline $\alpha = 0.9$), activating the turbulent diffusion term in the relative velocity closure. The following graphs originate of a simulation with a more refined discretization of $\delta r = 2.5$ mm but are representative of the phenomena happening at the reference discretization of Table 4.2. The velocity field is plotted on Figures 4.11a and 4.11b. One can note a peak near the free surface. An air layer is entrained with the flow. An air back-flow enters the domain above the mixture as testified by Figure 4.12 where particles with $\alpha < 0.9999$ are displayed. The pressure field is plotted on Figure 4.13a. For the sake of legibility, the maximum values plotted have been diminished. One can indeed notice some peak positive and negative values near the step edges on Figure 4.13b. The pressure field is noisy with pressure waves developing from the step edges and some little voids forming after them in the low pressure region usually prone to cavitation in the absence of air. It is expected that the implementation of the δ–SPH approach might help to mitigate such behaviors. The background pressure does not appear to be sufficient to prevent the occurrence of those voids.

Recirculations can be observed at the steps, consistently with the patterns observed during experiments (please note that the experimental photographs were obtained for a different geometry and volume flow rate: aeration is indeed significant in these configurations so that bubbles are entrained in this region between steps and give a visualization of the recirculations), as shown on Figure 4.14. The velocity of the flow above the apparent bottom is far larger than the recirculation velocity, so that we focus on the space between the steps in Figure 4.14b to give further insights into the recirculation velocity field pattern.

Finally, the double refined simulation allows us to have an additional insight into the entrainment phenomenon as one can identify on Figure 4.15 small waves developing just before the boundary layer reaching the free surface. A rough assessment of the size of these waves is around 2.5 cm. It is in relative agreement with observations and computations of Valero and Bung [355] and the

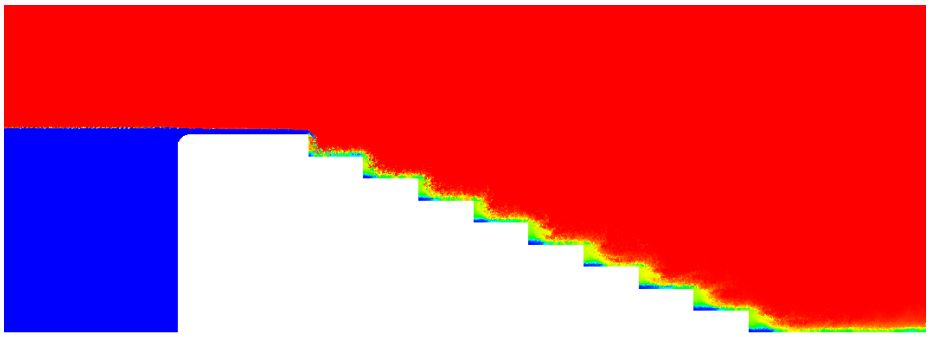

(a) Nappe regime – $q^{\beta} = 0.0020\ \mathrm{m}^2/\mathrm{s}$.

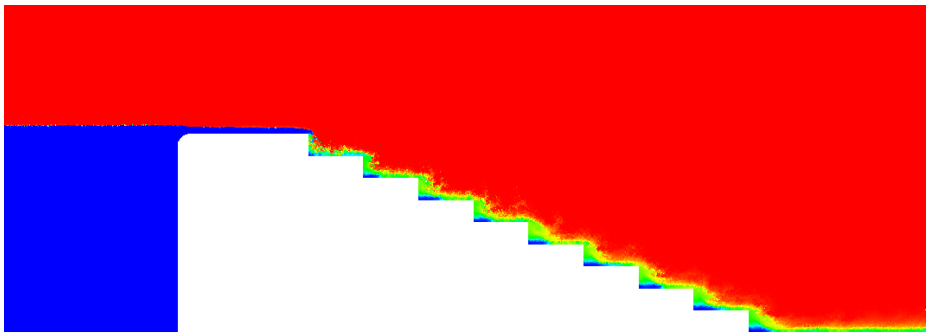

(b) Transition regime – $q^{\beta} = 0.0580\ \mathrm{m}^2/\mathrm{s}$.

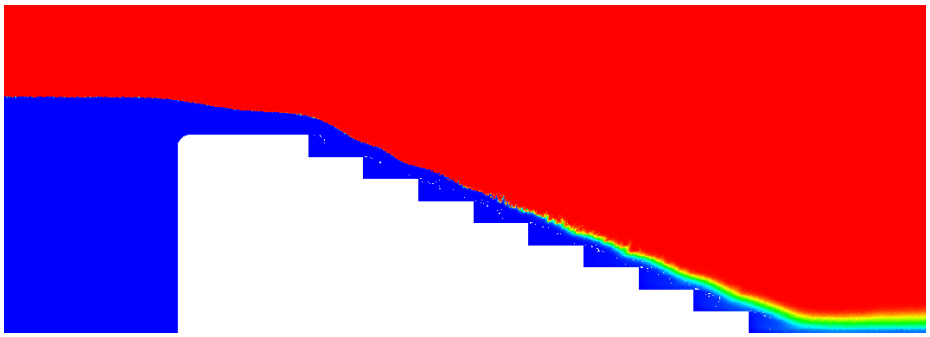

(c) Skimming regime – $q^{\beta} = 0.1142\ \mathrm{m}^2/\mathrm{s}$.

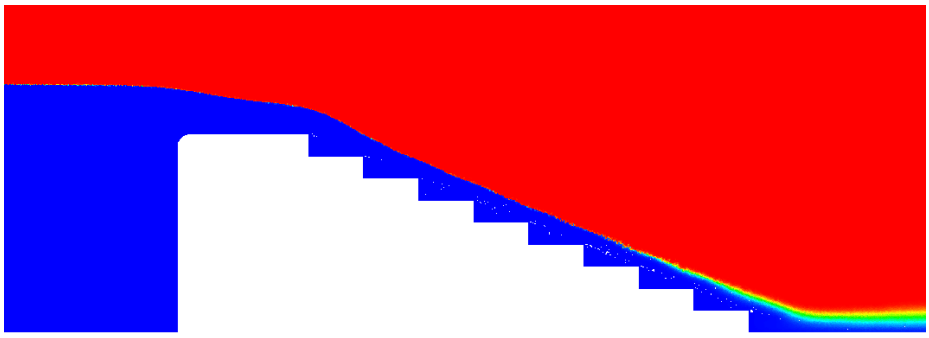

(d) Skimming regime – $q^{\beta} = 0.1819\ \mathrm{m}^2/\mathrm{s}$.

Figure 4.8: Stepped spillway: volume fraction field at steady state.

(a) Initial state.

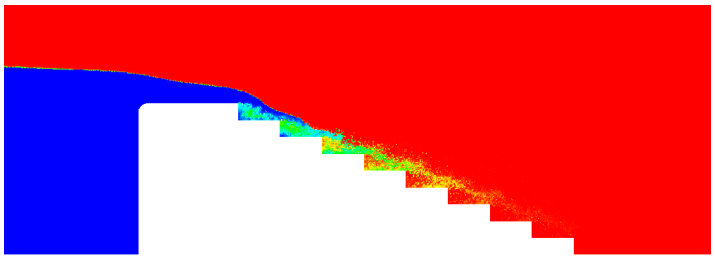

(b) t=1 s

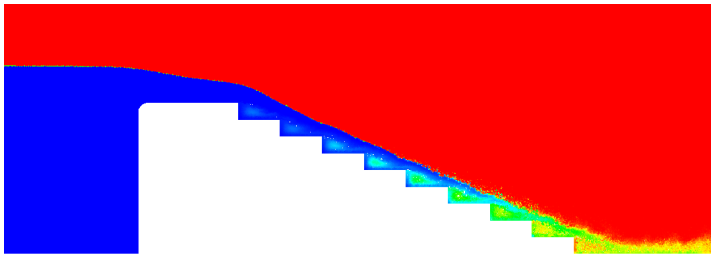

(c) t=2 s

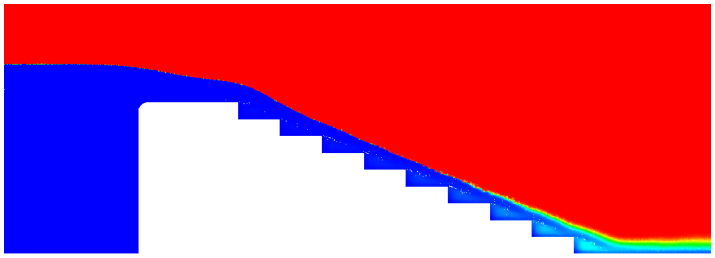

(d) t=3 s

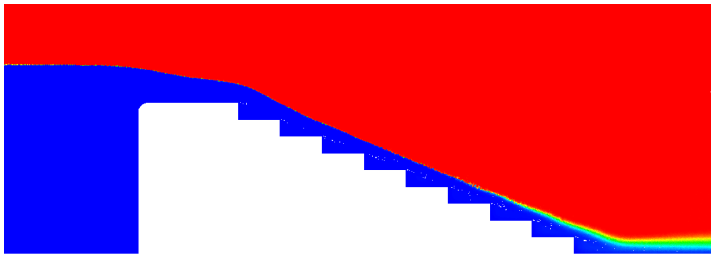

(e) t=4 s

Figure 4.9: Stepped spillway – $q^{\beta} = 0.1819$ m^2/s: volume fraction field during the initial transient.

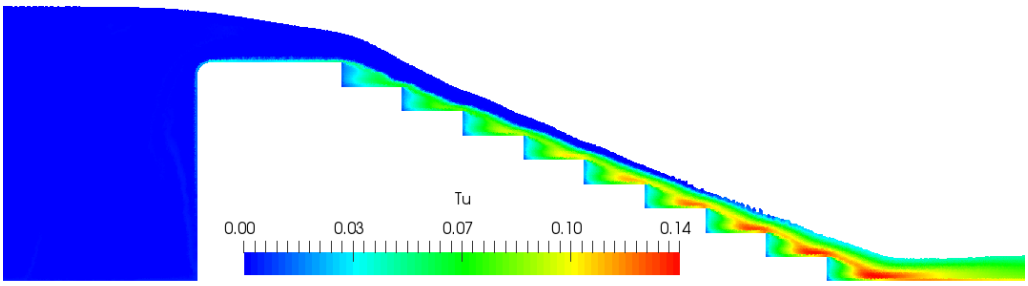

Figure 4.10: Stepped spillway – $q^{\beta} = 0.1819$ m^2/s: turbulent intensity Tu below the free surface. It is computed as Tu $= \sqrt{2k/3}/V_{\max}$ where $V_{\max}$ is the maximum mixture velocity magnitude.

Taylor lengthscale of (4.11) (obtained in an inviscid framework though). Those waves do not break as the interface is rapidly blurred by the diffusion of the phases due to the boundary layer reaching the free surface and activating the relative velocity diffusion term.

After this description of the flow, let us have quantitative insights into the reproduction of the skimming flow. The dispersion of the variables around the averaged values is limited as testified by Figure 4.17, except near the bottom and in the highly-aerated region. Volume fraction and interfacial air-water velocity profiles at the step edges are displayed on Figures 4.18 and 4.19. In the numerical model, this interfacial velocity is computed as:

$$V_x = \boldsymbol{v}_i \cdot \boldsymbol{e}_x \quad \text{where} \quad \boldsymbol{v}_i = \frac{\boldsymbol{v}^{\alpha} + \boldsymbol{v}^{\beta}}{2} = \boldsymbol{j} + \left(\frac{1}{2} - \alpha\right) \boldsymbol{v}^{r} \tag{4.59}$$

The correction linked to the relative velocity proved to be small compared to the mixture velocity. There are discrepancies of these profiles even though the good trends are reproduced. The mixing appears to occur too late and the velocities are overpredicted. Profiles are plotted along the direction perpendicular to the slope (coordinate named y), starting from the edge of each step as indicated on Figure 4.16. The uncertainties on the experimental measurements are not detailed for this experimental campaign, but the tools used correspond to the same instruments employed for the measurements of the planar plunging jet presented in the following section and for which they are detailed [23]:

$$\begin{cases} \frac{\Delta\alpha}{\alpha} < \frac{0.005}{\alpha} \text{ for } \alpha < 0.05 \\ \frac{\Delta\alpha}{\alpha} < 0.04 \text{ for } 0.05 < \alpha < 0.95 \\ \frac{\Delta\alpha}{\alpha} < \frac{0.002}{\beta} \text{ for } 0.95 < \alpha \end{cases} \quad \text{and} \quad \begin{cases} \frac{\Delta V_x}{V_x} < 0.1 \text{ for } 0.01 < \alpha < 0.05 \\ \frac{\Delta V_x}{V_x} < 0.05 \text{ for } 0.05 < \alpha < 0.95 \\ \frac{\Delta V_x}{V_x} < 0.1 \text{ for } 0.95 < \alpha < 0.99 \end{cases} \tag{4.60}$$

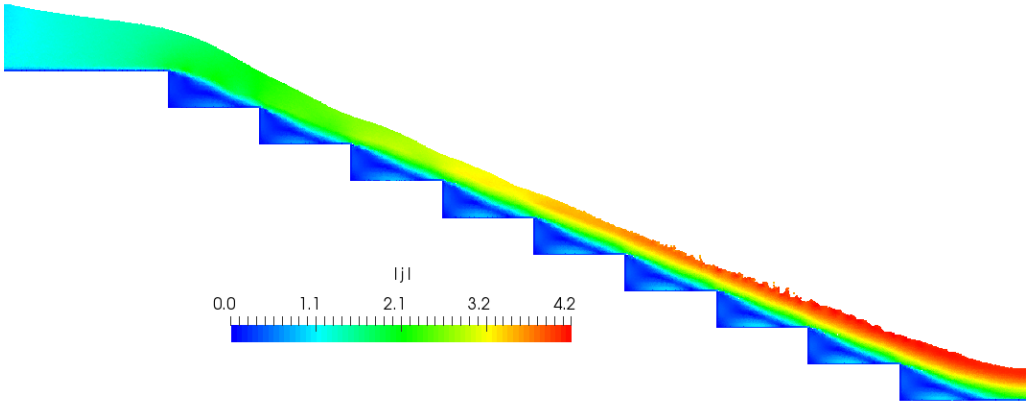

(a) Velocity magnitude below the free surface in m/s.

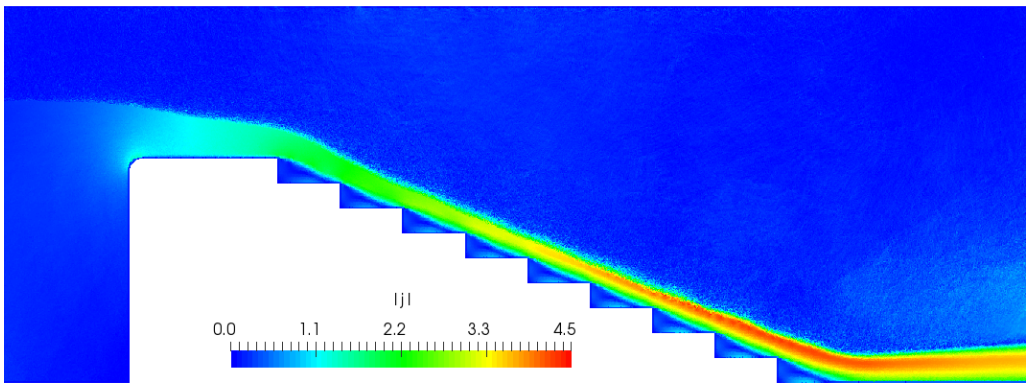

(b) Velocity magnitude in the whole domain in m/s.

Figure 4.11: Stepped spillway – $q^{\beta} = 0.1819$ m^2/s: velocity in m/s.

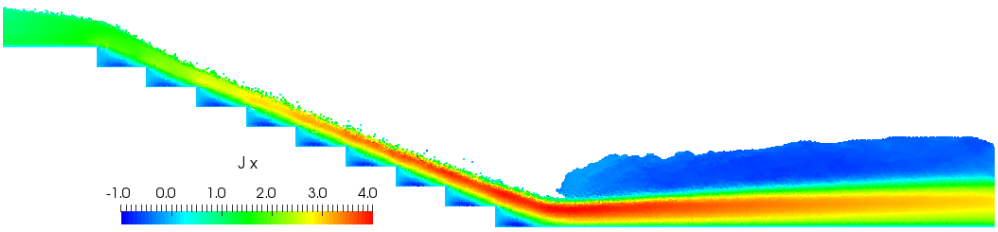

Figure 4.12: Stepped spillway – $q^\beta = 0.1819$ m^2/s: an air backflow.

Let us underline that these uncertainties might be case-dependent. Characteristic air entrainment quantities are displayed on Figure 4.20. Experimental results were obtained with single (SP) and double tip (DP) probes and one can note some discrepancies between the resulting values, highlighting the dispersion resulting from the unsteadiness and complex topology of the flow. There is a slight underestimation of Y_{90} and C_{mean} and a slight overestimation of the characteristic velocities. An interesting point is that it seems to have a one step delay in the profiles and characteristic values, what may point to an inception point appearing too late. Two main actions seem possible to improve the results: modify the size of the dispersed phase or introduce a roughness of the structure. These tests are addressed below.

For $q^\beta = 0.1142$ m^2/s, we are in the skimming flow regime. Characteristic air entrainment quantities are displayed on Figure 4.21. As in the experiment, the inception point is predicted around the fifth step. A reasonable agreement is obtained with the experimental values.

For $q^\beta = 0.058$ m^2/s, we are in the transition flow regime. Characteristic air entrainment quantities are displayed on Figure 4.22. We do not reproduce this regime in its transitional pattern, *i.e.* the distinct behavior at the sixth step in the experiments related to the appearance of a deflected nappe, as if the flow bypassed one step to reattach at the next downstream step [69]. The model with the chosen relative velocity closure generates a strong mixing that prevents the reappearance of mostly separated patterns. There are therefore big discrepancies for most of the characteristic values. The underestimated Y_{90} and overestimated C_{mean} trigger very large discrepancies on U_W. The volume fraction profile does not fit the semi-analytical profile derived for transition flows in Section 4.4.1.3 but still suits the one derived for skimming flows.

For $q^\beta = 0.002$ m^2/s, we are in the nappe flow regime. There is no comparison data on this test case. However in this regime one should observe a succession of falling nappes at each step. On the other hand, due to the strong mixing with the relative velocity closure, we have a continuous

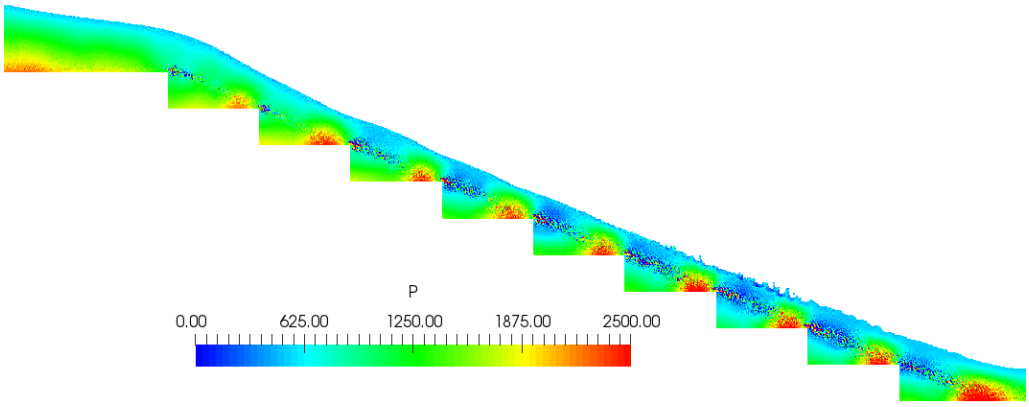

(a) Whole structure.

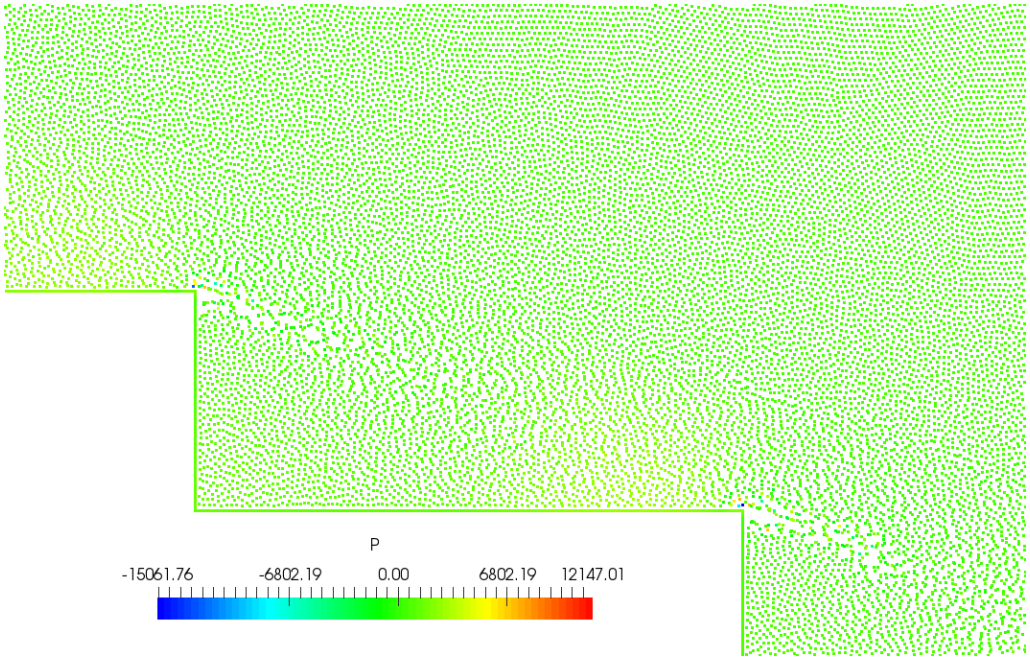

(b) Zoom on steps 6 and 7.

Figure 4.13: Stepped spillway – $q^{\beta} = 0.1819$ m^2/s: pressure field in Pa.

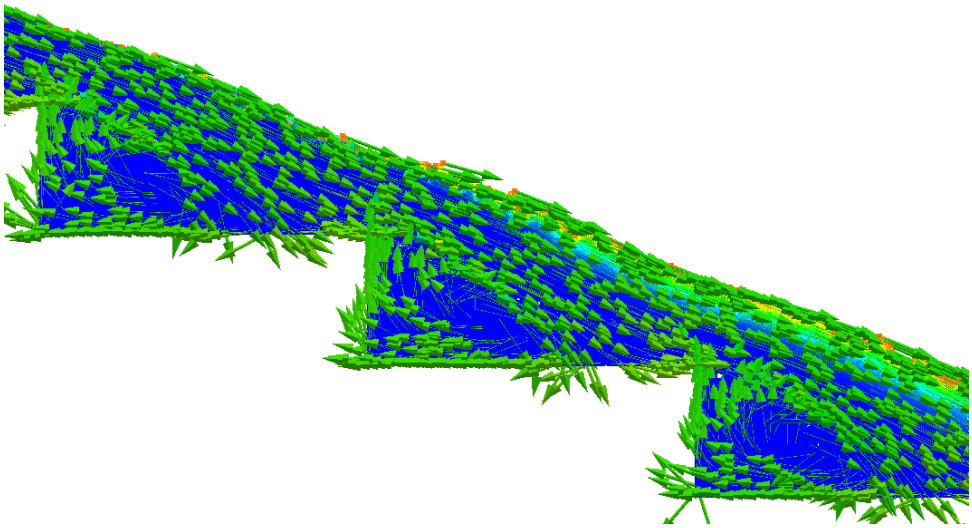

(a) Numerical model – $q^{\beta} = 0.1819\ \mathrm{m}^2/\mathrm{s}$: direction of the velocity vector field.

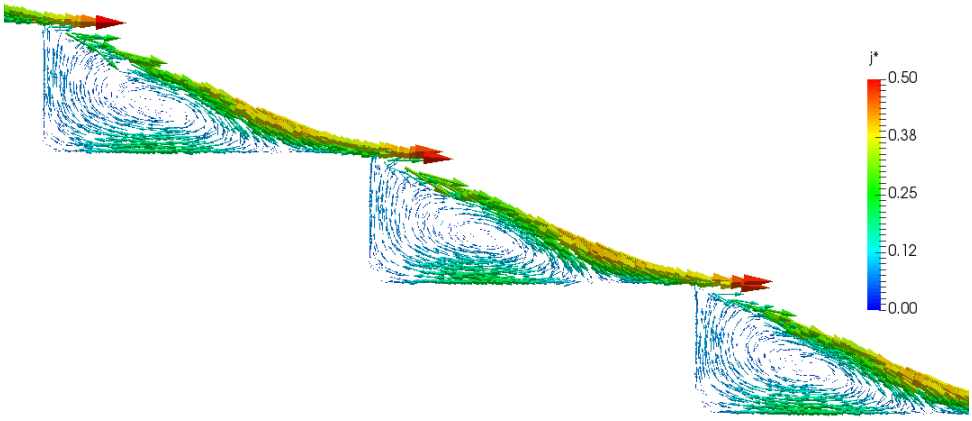

(b) Numerical model – $q^{\beta} = 0.1819\ \mathrm{m}^2/\mathrm{s}$: velocity vector field between the steps nondimensionalized by the maximum velocity in the whole flow.

(c) Experiment.

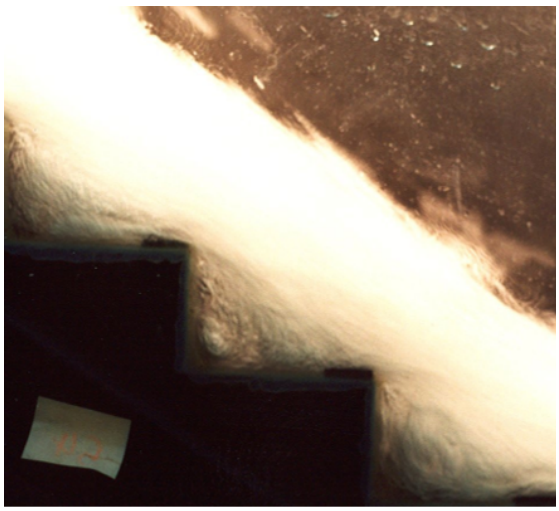

(d) Experiment.

Figure 4.14: Stepped spillway: focus on recirculations at the steps. The experimental photographs are HECE-ULiege property. A different geometry is used.

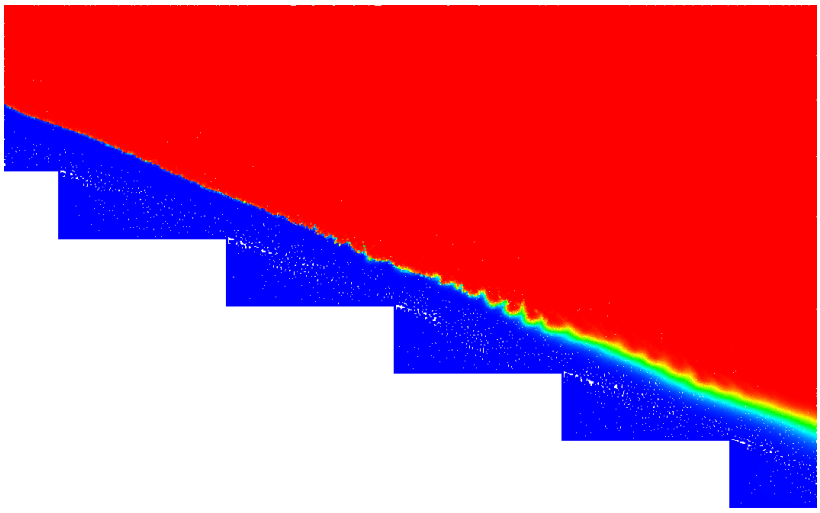

Figure 4.15: Stepped spillway – $q^{\beta} = 0.1819$ m^2/s: focus on the wavy free surface before entrainment.

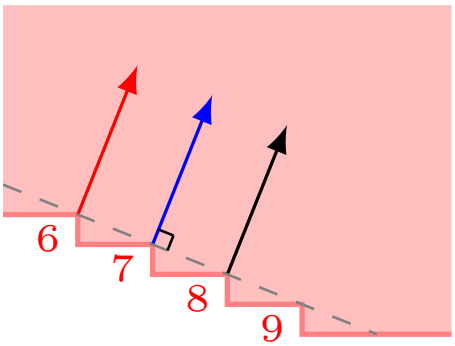

Figure 4.16: Stepped spillway: positions of the profiles.

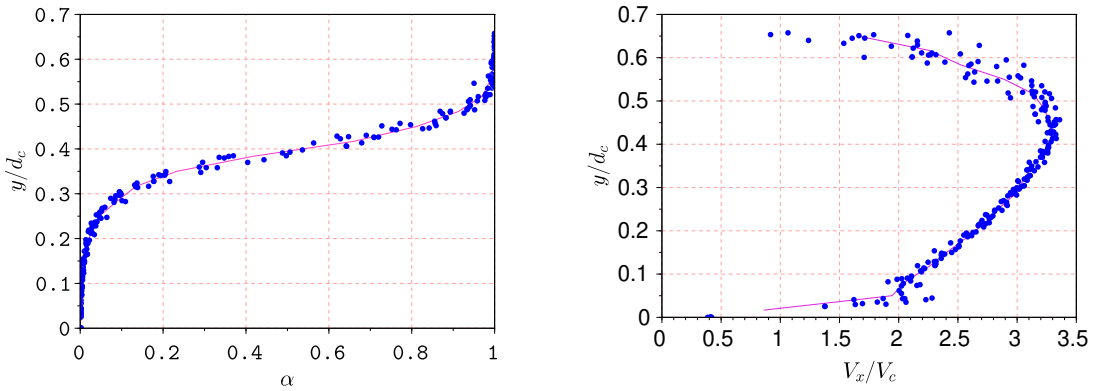

(a) Volume fraction.

(b) Longitudinal velocity.

Figure 4.17: Stepped spillway – $q^{\beta} = 0.1819$ m^2/s: variability of the profiles. Symbols: SPH particles used for the computations. Continuous line: resulting time-averaged value.

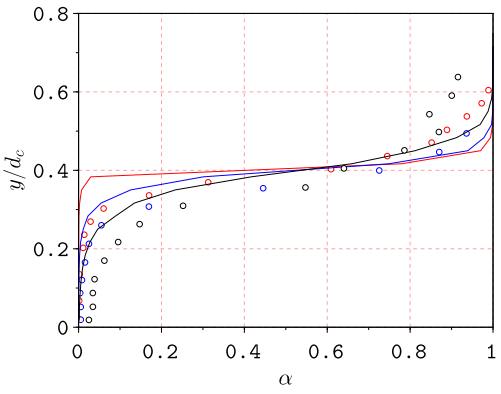

(a) Using critical values.

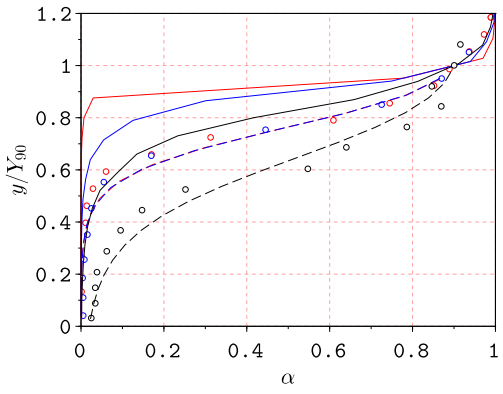

(b) Using 90% values.

Figure 4.18: Stepped spillway – $q^{\beta} = 0.1819\ \mathrm{m}^2/\mathrm{s}$: vertical distribution of the air volume fraction above the last three steps (steps 6, 7 and 8 in red, blue and black respectively). Symbols: experimental data by [60]. Continuous lines: present SPH simulation. Dashed lines: equation (4.51) based on C_{mean} values of [69]. The two snapshots show two different nondimensionalizations.

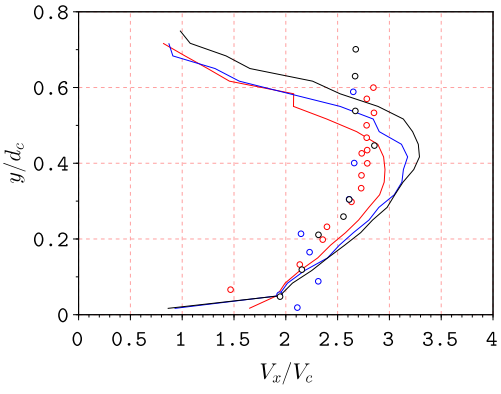

(a) Using critical values.

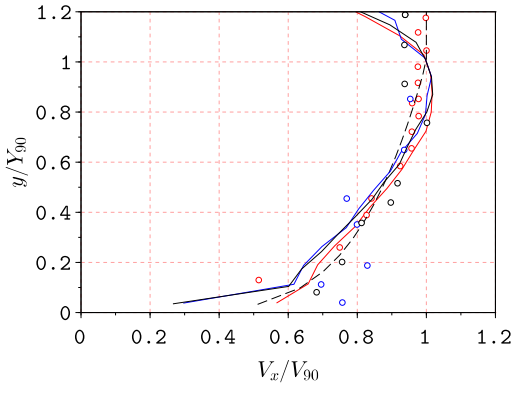

(b) Using 90% values.

Figure 4.19: Stepped spillway: vertical distribution of the longitudinal velocity for $q^{\beta} = 0.1819$ m^2/s above the last three steps (steps 6, 7 and 8 in red, blue and black respectively). Symbols: experimental data by [60]. Continuous lines: present SPH simulation. Dashed line: equation (4.53) (superimposed for the three steps, computed with the power $n_v = 5.1$ following [69]). The two snapshots show two different nondimensionalizations.

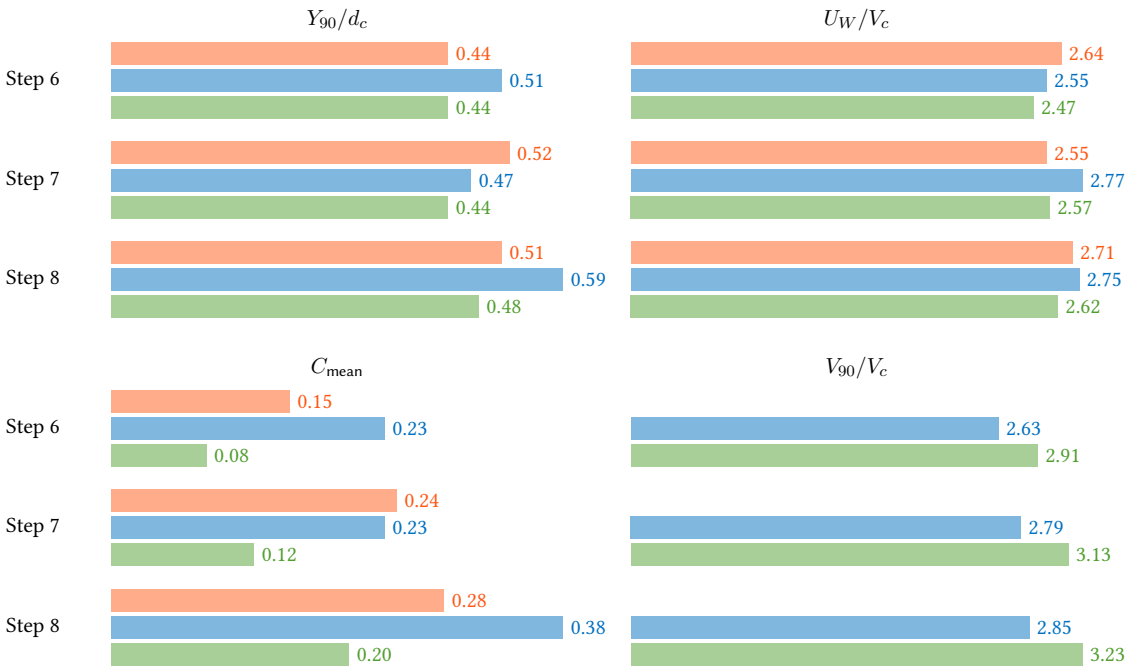

Figure 4.20: Stepped Spillway – $q^\beta = 0.1819$ m^2/s – Characteristic quantities. Present model results in green. Experimental results of Chanson and Toombes [69] with single tip probe in red and double tip probe in blue.

mixed flow with intermediate densities that streams over the steps after the first step.

Convergence We performed the simulation $q^\beta = 0.1819$ m^2/s with different particle discretizations, by multiplying and dividing by two the reference discretization. Averages were performed here between 7 and 9 s. The characteristic features of air entrainment are displayed for the different discretizations in Table 4.3. The computations of the characteristic features were performed on a grid relying on the coarser discretization, that does not allow for the most accurate assessment of the quantities for the refined computations. The variations between the two finest discretization remain limited.

Table 4.3: Stepped Spillway – $q^\beta = 0.1819$ m^2/s – Convergence of the characteristic quantities.

Step	Y_{90}/d_c			C_{mean}			U_W/V_c			V_{90}/V_c		
	$2\delta r$	δr	$\delta r/2$	$2\delta r$	δr	$\delta r/2$	$2\delta r$	δr	$\delta r/2$	$2\delta r$	δr	$\delta r/2$
6	0.50	0.43	0.43	0.13	0.07	0.08	2.31	2.51	2.54	2.64	2.98	2.78
7	0.55	0.44	0.43	0.25	0.12	0.09	2.40	2.58	2.57	2.84	3.12	2.90
8	0.57	0.48	0.46	0.27	0.23	0.19	2.43	2.67	2.70	3.01	3.20	3.23

Figure 4.21: Stepped Spillway – $q^{\beta} = 0.1142$ m^2/s – Characteristic quantities. Present model results in green. Experimental results of Chanson and Toombes [69] with single tip probe in red and double tip probe in blue.

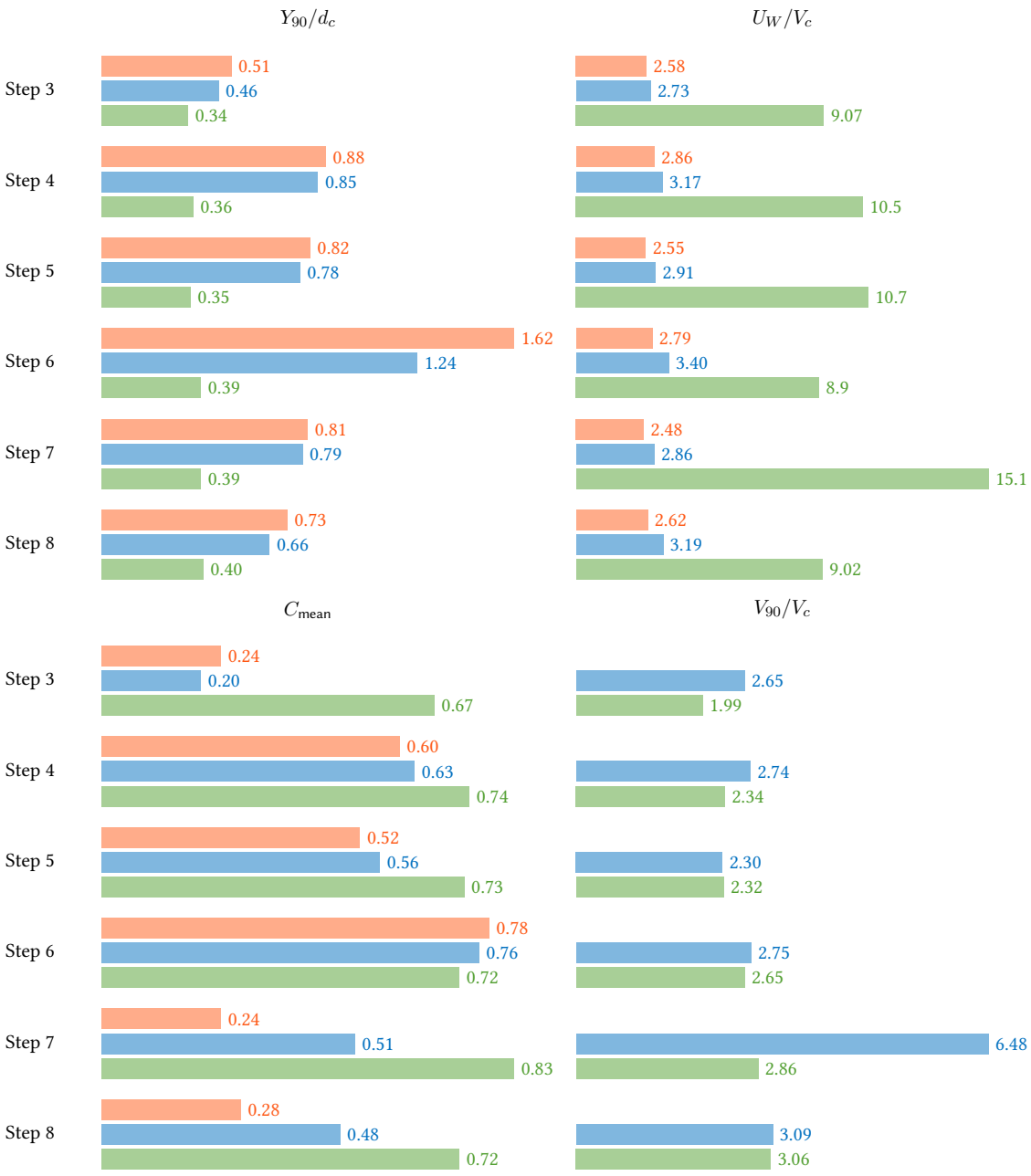

Figure 4.22: Stepped Spillway – $q^{\beta} = 0.058$ m^2/s – Characteristic quantities. Present model results in green. Experimental results of Chanson and Toombes [69] with single tip probe in red and double tip probe in blue.

Sensitivity to the dispersed phase diameter We performed the simulation $q^\beta = 0.1819$ m^2/s with different sizes of dispersed phase diameters. The characteristic features of air entrainment are displayed for those different sizes in Table 4.4. The influence of the dispersed phase diameter appears to be really limited and does not allow for a significant improvement of the results.

Table 4.4: Stepped Spillway – $q^\beta = 0.1819$ m^2/s – Sensitivity to dispersed phase diameter in mm.

	Y_{90}/d_c				C_{mean}			
Step \ d^α (mm)	2	1	0.5	0.1	2	1	0.5	0.1
6	0.44	0.43	0.44	0.44	0.08	0.07	0.07	0.08
7	0.44	0.44	0.45	0.45	0.12	0.13	0.13	0.13
8	0.48	0.48	0.48	0.48	0.19	0.20	0.21	0.21
	U_W/V_c				V_{90}/V_c			
Step \ d^α (mm)	2	1	0.5	0.1	2	1	0.5	0.1
6	2.46	2.49	2.43	2.46	2.87	2.96	2.84	2.89
7	2.58	2.60	2.57	2.58	3.13	3.12	3.05	3.07
8	2.59	2.61	2.64	2.63	3.23	3.23	3.23	3.23

Including the convective transfers The convective transfer term was lately introduced into the set of equations as it triggers some instabilities of the free surface. One should take with care the following results: indeed, if they are close to the experimental measurements and correspond to a more rigorous model, one should bear in mind that the agitation partly results from the numerics. In this test case, the flow should be initially perfectly separated, which is not the case because of the slight diffusion of the interface imposed at the initialization and at the open boundaries. For a perfectly separated state, the quantity $\alpha\beta\boldsymbol{v}^r$ is null, so that there should not be any contribution of this term in the momentum equation. However, in the simulation, one can see that the interface is quickly agitated before the entrainment occurs as shown on Figure 4.23: this enhances the entrainment phenomenon and triggers also an apparent diffusion for time-averaged value as the separated free surface is moving (this last point can however also happen in the experiments). The characteristic features of air entrainment are displayed in Figure 4.24. One can note that the unrest close to the free surface generates higher velocities in this region when the mixture layer is thin.

Rugosity The previous computations were made assuming smooth walls in the computations of the wall shear stresses. A roughness $k_s = 0.1$ mm seems reasonable according to the table of

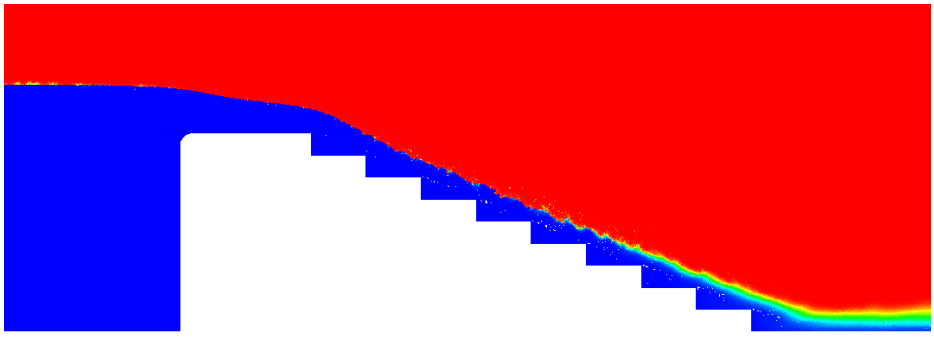

Figure 4.23: Stepped spillway – $q^{\beta} = 0.1819$ m^2/s: volume fraction field using the convective transfer term.

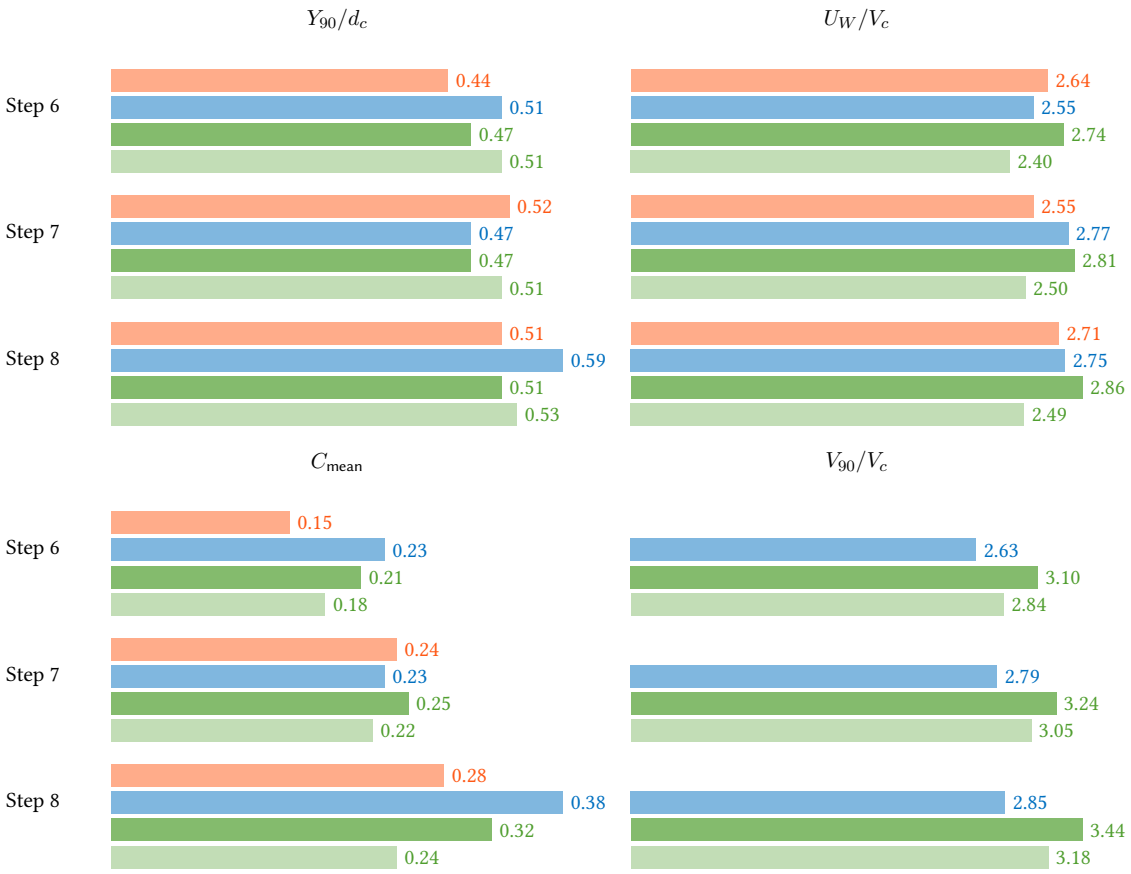

Figure 4.24: Stepped Spillway – $q^{\beta} = 0.1819$ m^2/s – Characteristic quantities. Present model results including convective transfers in dark green or using a relative velocity depending on the pressure gradient in light green. Experimental results of Chanson and Toombes [69] with single tip probe in red and double tip probe in blue.

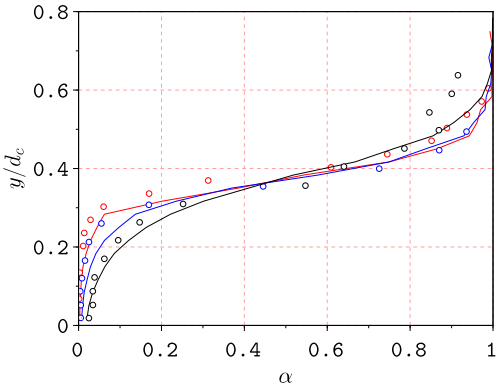

(a) Volume fraction.

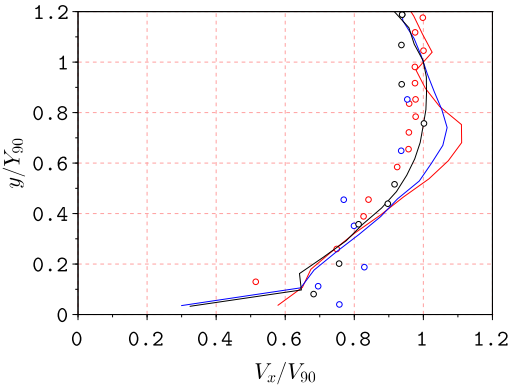

(b) Longitudinal velocity.

Figure 4.25: Stepped spillway – $q^\beta = 0.1819$ m^2/s: including the convective transfers term, vertical distribution above the last three steps (steps 6, 7 and 8 in red, blue and black respectively). Symbols: experimental data by [60]. Continuous lines: present SPH simulation.

[55]. Following [371], the friction velocity is deduced from the relation:

$$\frac{j_x}{u_\star} = \frac{1}{\kappa} \ln\left(\frac{y}{k_s}\right) + 8.5 \tag{4.61}$$

It modifies the turbulent wall shear stresses and should generate more turbulence, driving upstream the inception point. However, the two tested roughness heights, $k_s = 0.1$ mm and $k_s = 0.5$ mm, barely modified the profiles and the characteristic quantities.

Switch of dispersed phase We tested the model with a switch of dispersed phase definition in order to reproduce correctly both the limiting behaviors of droplets and bubbles. Indeed, due to the factor β in the relative velocity without switch, the relative velocity becomes arbitrarily small when β gets closer to 0, preventing complete separation. Following the formulation described in Section 4.3.2.2, we get the flow plotted on Figure 4.26. Y_{90} and U_W are only slightly altered while C_{mean} is decreased and V_{90} is increased. These evolutions therefore do not improve the results with respect to experimental data. The only positive evolution is that the separation between fluids is made clearer as droplets quickly fall back into the fluid.

Pressure gradient in the relative velocity We tested a relative velocity closure using the pressure gradient following (1.100) instead of the approximation by its hydrostatic value. This is a more physically-based expression that couples completely the system of equations. However, it is complex to handle due to the noisy pressure field encountered. We divided the safety factor of the CFL coefficient by ten to run this simulation as some instabilities developed since the first iterations with the usual criterion (the numerical stability of the formulation integrating

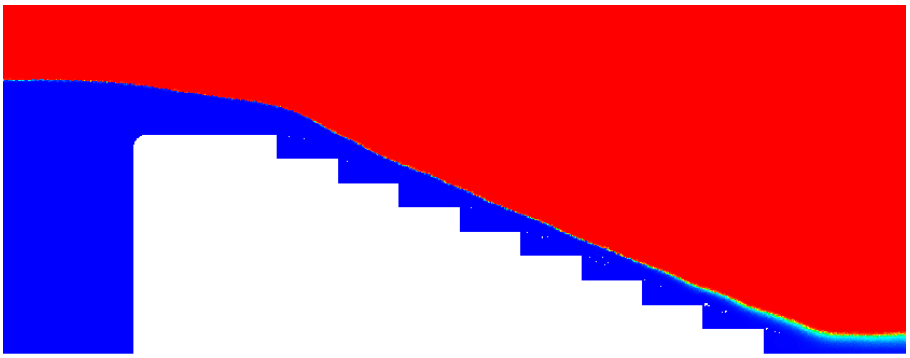

Figure 4.26: Stepped spillway – $q^\beta = 0.1819$ m^2/s: volume fraction field using a relative velocity with switch.

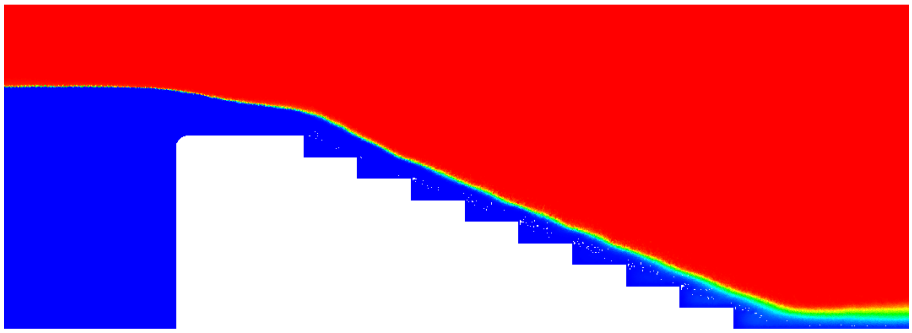

Figure 4.27: Stepped spillway – $q^\beta = 0.1819$ m^2/s: volume fraction field at $t = 6$ s using a relative velocity with switch.

the pressure gradient shall require further investigation). The characteristic features of air entrainment are displayed on Figure 4.24 and highlight a decrease of maximum velocities, getting closer to the experiments. While Y_{90} is accurately computed, the mean concentrations tend to be underestimated. One can notice on Figure 4.27 that the interface is always diffused over a few particles due to some pressure waves propagating along the interface as noted on the previous cases. Therefore it does not allow to identify an inception point. One can see a satisfactory agreement with the volume fraction, especially in the dispersed region close to the bottom, and longitudinal velocity profiles on Figure 4.28 highlighting that one should go towards that kind of closure once the pressure issues are solved. For an unknown reason the computations stopped so that these profiles might not be fully converged (profiles averaged between 5 and 6 s).

Buoyancy term in the $k-\epsilon$ model We tried to include the buoyancy term (1.102) into the turbulence model (the pressure gradient being approximated by its hydrostatic value) with the discrete form:

$$\mathbb{G}_a = \frac{\rho^\beta - \rho^\alpha}{\rho} \frac{\nu_{T,a}}{\mathrm{Sc}_T} \boldsymbol{G}_a^{-,1}\{\alpha_b\} \cdot \boldsymbol{g} \tag{4.62}$$

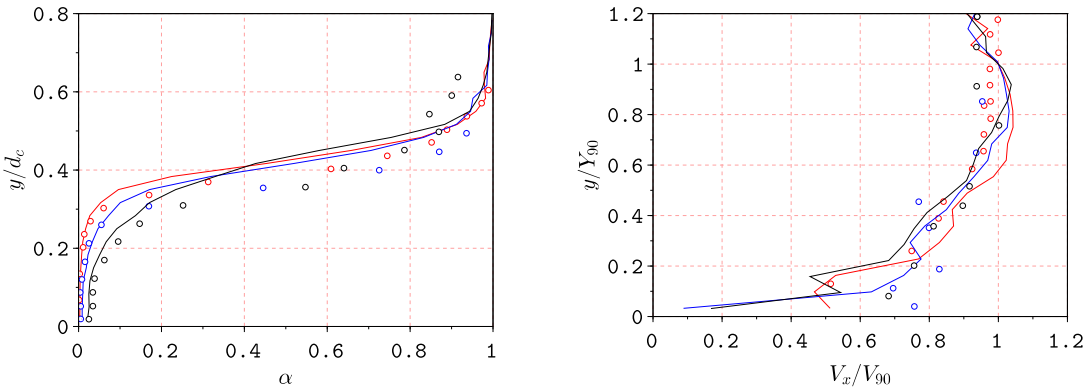

(a) Volume fraction.

(b) Longitudinal velocity.

Figure 4.28: Stepped spillway – $q^\beta = 0.1819$ m^2/s: with a relative velocity depending on the pressure gradient, vertical distribution above the last three steps (steps 6, 7 and 8 in red, blue and black respectively). Symbols: experimental data by [60]. Continuous lines: present SPH simulation.

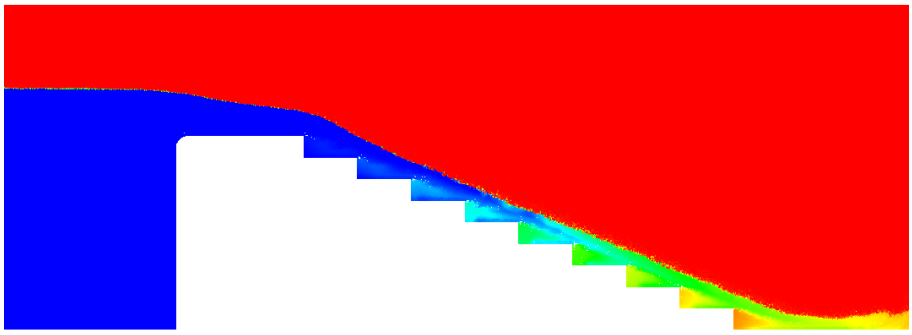

Figure 4.29: Stepped spillway – $q^\beta = 0.1819$ m^2/s: volume fraction field at $t = 2$ s with the buoyancy term introduced into the $k - \epsilon$ model.

The computation of this term is made semi-implicit by computing $\nu_{T,a}^n$ either as $C_\mu \left(k^n\right)^2 / \epsilon^n$ if $\boldsymbol{G}_a^{-,1}\{\alpha_b^n\} \cdot \boldsymbol{g} > 0$ or $C_\mu k^n k^{n+1} / \epsilon^{n+1}$ otherwise. One can see that the transient behavior is modified on Figure 4.29. However, at the outlet, some air enters the domain and generates big viscosities that block computations. This point will therefore require further investigations, on both the open boundary formulation and the buoyancy closure.

4.4.2 Planar plunging jet

Plunging jets are rapid flows impinging a slower liquid, as exemplified by vertical/supported plunging jets, hydraulic jumps or free jets impinging an inclined wall. Such flows fall within the local aeration framework, air being entrained at the intersection between the impinging flow and receiving waters under certain conditions to identify. A review of the literature and basic

processes of gas entrainment by plunging jets can be found in Bińk [24], Chanson [59], Kiger and Duncan [186]. In the following, focus is made on planar plunging jets of water entraining air (*i.e.* low-viscosity jets). We chose to work here on the case documented in [23, 35, 36, 57, 59, 66].

4.4.2.1 Description

We consider a planar plunging jet as described on Figure 4.30a with a zoom on the jet and its support slightly inclined with respect to the vertical on Figure 4.30b. This jet comes from a rectangular nozzle and discharges downwards into a receiving tank. Bertola et al. [23] presented a comprehensive view of this test case with focuses on the free falling jet, the pre-entrainment, the entrainment in the receiving pool, the mechanisms of break-up and coalescence, displaying concentrations, velocities, turbulent intensities, bubble count rates and chord lengths in many sections of the domain. Four mechanisms of air entrainment were described:

- Pre-entrainment in the supported free-falling jet at low velocities;
- Entrainment of individual bubbles and packets. This is the dominant mechanism at velocities close to the inception velocity;
- Formation of an elongated air cavity starting by an induction trumpet between the impinging jet and the receiving fluid of the tank. This cavity is stretched by turbulent shear and its lower tip breaks in air packets then broken up in smaller bubbles [73]. This is the dominant mechanism for higher velocities;
- Re-entrainment of bubbles that rose to the surface.

The inflow conditions are of prominent importance: as suggested by the relation (4.21), partially or fully developed conditions and consequent turbulence intensity together with possible pre-entrainment before impinging the receiving pool will affect the entrainment process [59]. Below the impingement point, Chanson [58] underlines that the dispersion of entrained bubbles gives birth to two regions:

- A diffusion cone: with significant entrainment, a bubble plume clearly appears visually testifying of a diffusion process [73]. The downwards flow generated by the plunging jet is characterized by a developing shear layer that triggers momentum transfers from the high-velocity jet core to the pool of water and a distinct air diffusion layer [92]. Indeed, for developing two-dimensional shear layers, the air bubble diffusion layer does not coincide with the momentum shear layer [59], with an air-bubble diffusivity higher than the eddy viscosity. It may suggest that the chosen closure for the relative velocity might not reproduce accurately the experimental results. However Cummings and Chanson [91] suggested that these layers interact: the momentum transfer between the core and surrounding fluid is modified and shifts away the shear layer from the support while the large

shear stresses trigger bubbles break-ups according to three different processes (explosion, stretching or small dejection mechanisms) described by Bertola et al. [23].

- A swarm of rising bubbles driven by buoyancy surrounding the cone: entrained bubbles undergo coalescence and break-up mechanisms but lose progressively momentum. According to Clanet and Lasheras [84], when their downwards velocity equals their terminal rising velocity, *i.e.* when the viscous drag of the downward entraining jet is exceeded by the buoyancy, they start to rise roughly vertically and reach nearly their terminal rising velocity [58].

Bertola et al. [23] described a wide range of bubble chord sizes from less than 0.5 mm to more than 20 mm. The distribution peaked for small bubbles between 0.5 and 1.5 mm, the largest bubbles disappearing at increasing depths due to detrainment and break-ups.

4.4.2.2 Dimensional analysis and quantities of interest

Let us consider a vertical two-dimensional plunging jet. Its characteristics at impingement, denoted by the index 1 are the distance to the nozzle x_1, the jet thickness d_1 at the impact, the jet impact velocity V_1 and the characteristic jet turbulent velocity v'_1. Following Chanson [64], one can perform a simplified dimensional analysis of this test case:

$$\alpha, \frac{V_x}{V_1}, \frac{v'}{V_1} = f\left(x_\star = \frac{x - x_1}{d_1}, y_\star = \frac{y}{d_1}, \frac{x_1}{d_1}, \mathsf{Fr} = \frac{V_1}{\sqrt{g d_1}}, \mathsf{Re} = \frac{V_1 d_1}{\nu^\beta}, \mathsf{Tu} = \frac{v'_1}{V_1}, \mathsf{Mo}\right) \tag{4.63}$$

According to Chanson [59], the onset velocity V_e is a function the Morton number (*i.e.* the fluid characteristics) and the impinging turbulent features. For turbulent intensities larger than 3%, the inception velocity is reported to be constant around 0.8-1 m/s.

4.4.2.3 Semi-analytical approach

In the case of a planar supported jet, Cummings and Chanson [92] and Chanson [65] formulated simplifying assumptions for an analytical development: a uniform velocity distribution; a diffusion coefficient independent of the transverse location; a small control volume; a bubble rise term negligible compared to the jet velocity. The air entrainment can then be described by a diffusion process:

$$\frac{\partial \alpha}{\partial x_\star} = \mathsf{Pe} \frac{\partial^2 \alpha}{\partial y_\star^2} \tag{4.64}$$

where $\mathrm{Pe} = K_T/(V_1 d_1)$. Considering a constant diffusivity K_T, the analytical solution detailed below reproduces correctly the void fraction observed experimentally[5]:

$$\alpha = \frac{q^\alpha}{q^\beta} \frac{1}{\sqrt{4\pi \mathrm{Pe} x_\star}} \left[\exp\left(-\frac{1}{4\mathrm{Pe}} \frac{(y_\star - 1)^2}{x_\star} \right) + \exp\left(-\frac{1}{4\mathrm{Pe}} \frac{(y_\star + 1)^2}{x_\star} \right) \right] \tag{4.65}$$

According to Cummings and Chanson [92], the diffusivity averages the effects of turbulent dispersion and streamwise velocity gradient, missing the nature of the turbulent shear layer and the vortical structures. The good agreement with experimental results suggests that the air bubble diffusion process is little affected by the turbulent shear flow. Velocity profiles get a shape similar to the analytical solution of monophase flows [6]:

$$\frac{V_x}{V_{x\,\max}} = \frac{1}{2} \left[1 - \mathrm{erf}\left(K_V \frac{y_\star - Y_{V50}/d_1}{x_\star} \right) \right] \tag{4.66}$$

where Y_{V50} is the location for which $V_x = V_{x\,\max}/2$ and the error function is defined as:

$$\mathrm{erf}\,(x) \frac{2}{\sqrt{\pi}} \int_0^x \exp\left(-u^2\right) du \tag{4.67}$$

The coefficient K_V is derived with an assumption of constant eddy viscosity and computed in the experiments of [23].

4.4.2.4 Numerical model

We considered for the numerical application the experiments of Bertola et al. [23] that are comprehensively documented. The geometry is described in Figure 4.30a with a zoom on the support structure in Figure 4.30b. One can notice a small angle of the support to the jet chosen to prevent jet detachment. The computational limits drove us to consider only the shaded region of Figure 4.30a. Walls have been placed on the lateral side with an outlet at the bottom of the right side to remove a volume of water equivalent to the one entering the domain at the nozzle inlet. The flow in the nozzle has not been modeled: a uniform velocity profile is directly imposed on the boundary of the domain to be consistent with the experimental measurements of Bertola et al. [23]. The shorter domain without the weir that allows the water (and potentially waves) to quit the domain will therefore cause some perturbations of the entrainment as the reflected waves can interact with the plunging jet. Measurements of air concentration, velocity and turbulence have been made near the support. The parameters of the model are detailed in Table 4.5. The computations were made without background pressure. When we introduced the same value as

[5] We used the measurements of [23] of Pe and q^α/q^β to compare with our numerical results. However one should note that in their work the distance for nondimensionalization of the coordinates and Pe is the location of the maximum concentration at a given section instead of d_1 used in [92].

[6] We used the measurements of [23] of K_V, Y_{V50} and $V_{\max}$ to compare with our numerical results. The sign in front of the error function was changed compared to [23].

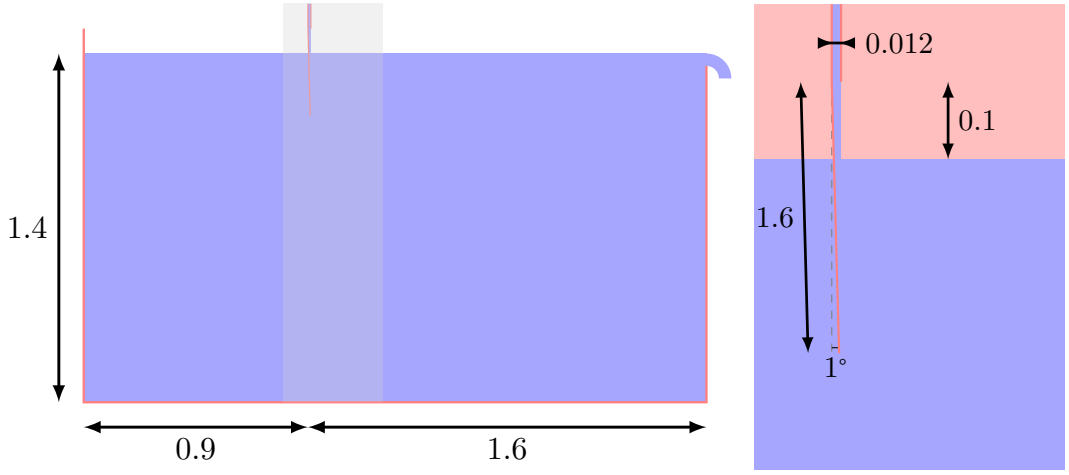

(a) Tank. (b) Support structure.

Figure 4.30: Planar plunging jet: geometry (distances in m). The shaded region corresponds to the numerical domain considered for the computations. The rectangular nozzle from which the jet is issued has the dimensions 0.269 m by 0.012 m.

in the stepped spillway case, *i.e.* $p_B = 500$ Pa, it did not allow one to prevent jet detachment nor to mitigate the appearance of voids within the flow. A volume diffusion coefficient $\Lambda = 0.1$ was used. The convective transfer term was not taken into account in the momentum equation.

Table 4.5: Parameters for the planar plunging jet case.

ρ^α	1.23	kg/m^3	ρ^β	1000	kg/m^3
ν^α	$1.56\ 10^{-5}$	m^2/s	ν^β	10^{-6}	m^2/s
c^α	45	m/s	c^β	45	m/s
d^α	1	mm	d^β	1	mm
δr	1	mm	p_B	0	Pa

4.4.2.5 Results

Computations were performed with 700 000 particles during around 2 days of computational time on one graphic card GeForce GTX Titan Black for 12 s of physical time. To compute the profiles along the y direction, a set of points spaced by δr were introduced along the horizontal direction starting at the jet support at the sections displayed on Figure 4.31. The variables of the nearest SPH particle were attributed to each of these points. In order to get smooth profiles for comparison with the time-averaged experimental results, we proceed to an average of the variables over ten equally-spaced time steps between 5 and 7 s to get the following results. Let us underline that due to the limited domain and strong mixing, together with the initial ramp

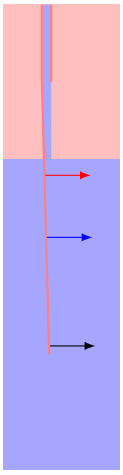

Figure 4.31: Planar plunging jet: zoom on the positions of the sections at which profiles are computed.

given to the velocity at the inlet, it is hard to identify a permanent regime. Further work will be required on this test case for proper treatment.

We tested the lowest value of volume flow rate $q^\beta = 0.0254$ m^2/s (corresponding to the value $Q^\beta = q^\beta W_s = 0.00683$ m^3/s with a width of the jet $W_s = 0.269$ m). We investigate in the following the numerical results and compare them to experimental data of Bertola et al. [23].

Global description The volume fraction field is plotted on Figure 4.32 and the velocity field on Figure 4.33. One can see that the interface close to the plunging jet is highly agitated. This unrest that certainly affects the air entrainment originates form two sources: the pre-entrainment occurring along the plunging jet that diffuses the interface and increases the region of impact of the jet and the reflected waves resulting from the shorter domain compared to the experiments. It is also expected that the two-dimensional framework may prevent some energy dissipation. Such observations were also made by Denèfle [106] on this test case using a finite volume approach with the NEPTUNE_CFD code. This unrest contributes to significant turbulent kinetic energy production and therefore diffusion of the interface when the $k-\epsilon$ model is used (without the corrective factor β in front of the production term as done for the stepped spillway in (4.57) and (4.58)). The bubble plume is smoothed and reaches a significantly shallower depth. One can also see that the level of particles has diminished compared to the initially filled domain: due to the high constraints exerted at high density ratios against the walls, some particles exited the domain. The velocity field in absence of turbulence model highlights some gusts of air packets within the tank with vortical structures. This behavior is smoothed out with the $k-\epsilon$ model with a distinct plunging region along the support and an upward flow region further from the support.

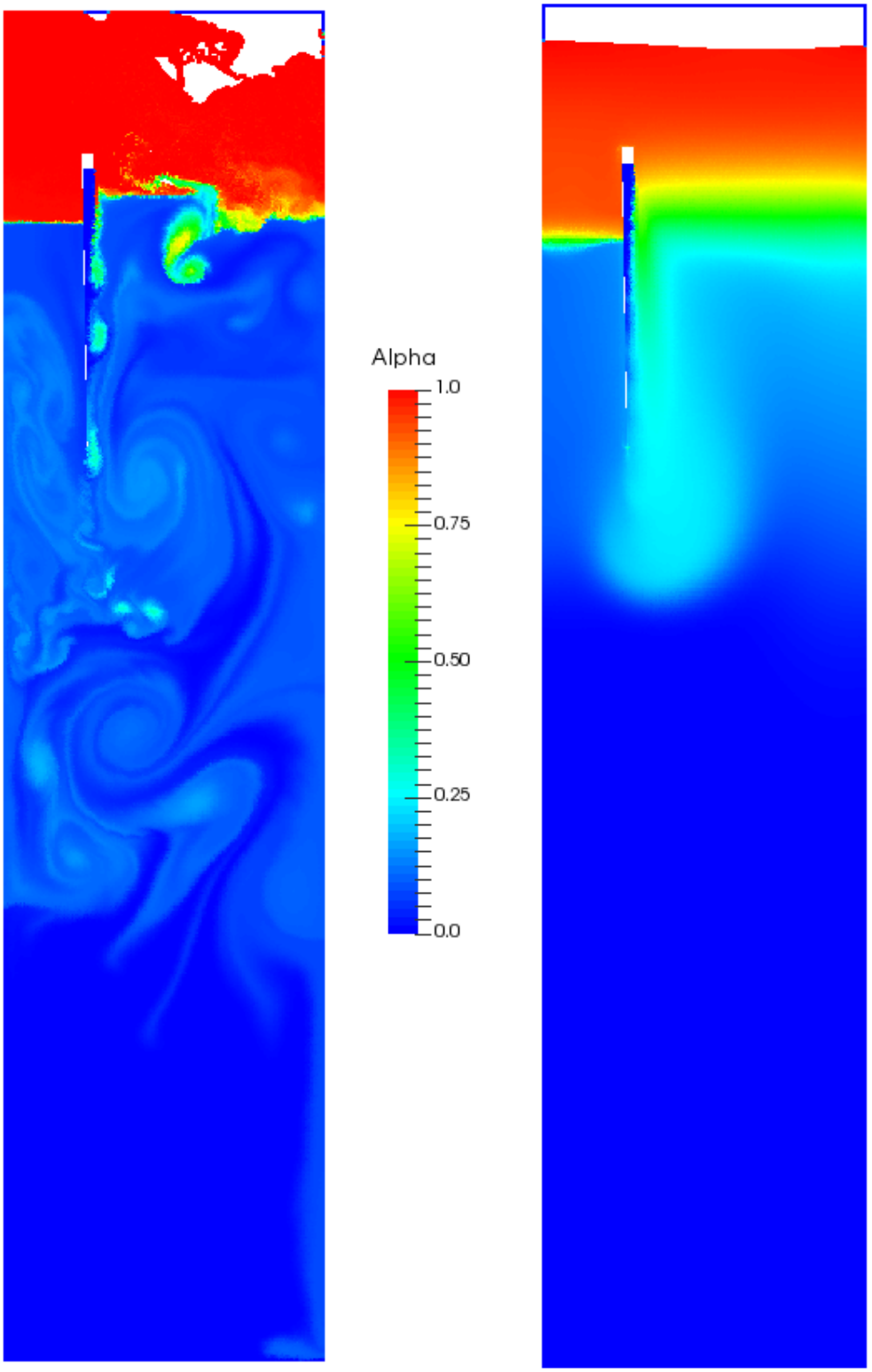

(a) No turbulence modeling.

(b) $k - \epsilon$.

Figure 4.32: Planar plunging jet: volume fraction field at $t = 9$ s.

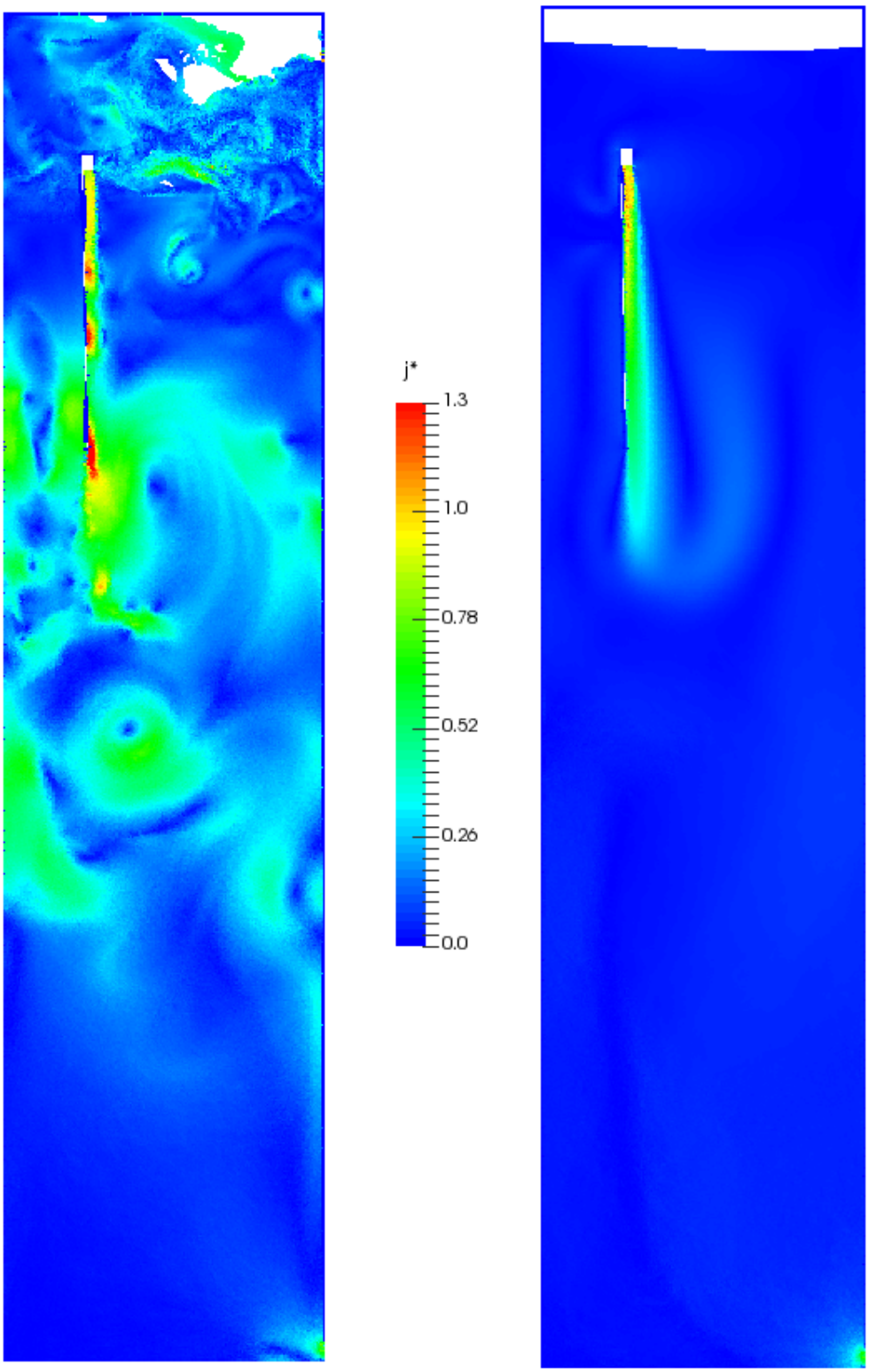

(a) No turbulence modeling.

(b) $k - \epsilon$.

Figure 4.33: Planar plunging jet: velocity magnitude field at $t = 9$ s nondimensionalized by impact velocity of the experiment $V_1 = 2.49$ m/s.

Bubble plume The void fraction profiles are compared to experimental results at the distances 2, 10 and 24 cm from the free surface along the support on Figure 4.34. The velocity profiles are displayed on Figure 4.35. Integrated and punctual quantities can also be computed and compared as displayed in Table 4.6. Without the turbulence model, while one can note a similar decrease in amplitude of the maximum concentration, the values predicted by the numerical model keeps higher than the experimental values. Moreover, far from the support, these values do not go below 0.06 while in the experiment they can decrease to zero. The displacement of the maximum volume fraction, as exemplified in Table 4.6, is missed by the model. The velocity profiles are quite different, with a lower decrease of the numerical interfacial velocity and stronger variations while getting further from the core compared to experimental results. It seems to point to an insufficient diffusion of the shear layer. With the $k-\epsilon$ model, due to a too strong diffusion of the phases resulting from the unrest of the interface in the restricted domain, the simulation of the $k-\epsilon$ model triggers a too strong mixing of phases so that the volume fraction profiles are shifted and altered. However the decrease in maximum velocity is captured, highlighting the influence of the turbulent viscosity in the momentum equation. One should however qualify this remark as the high volume fractions might also explain this change in the dynamics. To get a clearer insight, a simulation was computed without turbulence model, multiplying artificially by ten the water viscosity: the results shown on Figure 4.36 for the volume fraction profile now exhibit the drift of the maximum air concentration and the decrease in maximum velocity is also captured. One can see the significant improvement of the characteristics values on Table 4.7. The correct modeling of turbulence seems therefore critical.

Table 4.6: Planar plunging jet without turbulence model – Characteristic quantities. $\alpha_{\max}$ is the maximum concentration, $Y_{\alpha_{\max}}$ its associated distance from the support, $V_{x\max}$ is the maximum longitudinal interfacial velocity and Y_{V50} the distance from the support at which $V_x = V_{\max}/2$.

y (cm)	$\alpha_{\max}$		$Y_{\alpha_{\max}}$ (mm)		$V_{x\max}$ (m/s)		Y_{V50} (mm)	
	Exp	Num	Exp	Num	Exp	Num	Exp	Num
2	0.32	0.36	15	13	2.26	2.36	28	13
3	0.25	0.36	14	14	2.09	2.39	x	13
5	0.17	0.31	16	14	2.16	2.44	31	13
7	0.17	0.25	19	14	2.03	2.32	x	14
10	0.16	0.23	21	15	1.87	2.31	41	14
13	0.15	0.20	22	17	1.68	2.24	x	15
16	0.12	0.18	24	16	1.50	2.20	39	16
24	0.08	0.15	23	14	1.30	2.10	45	17

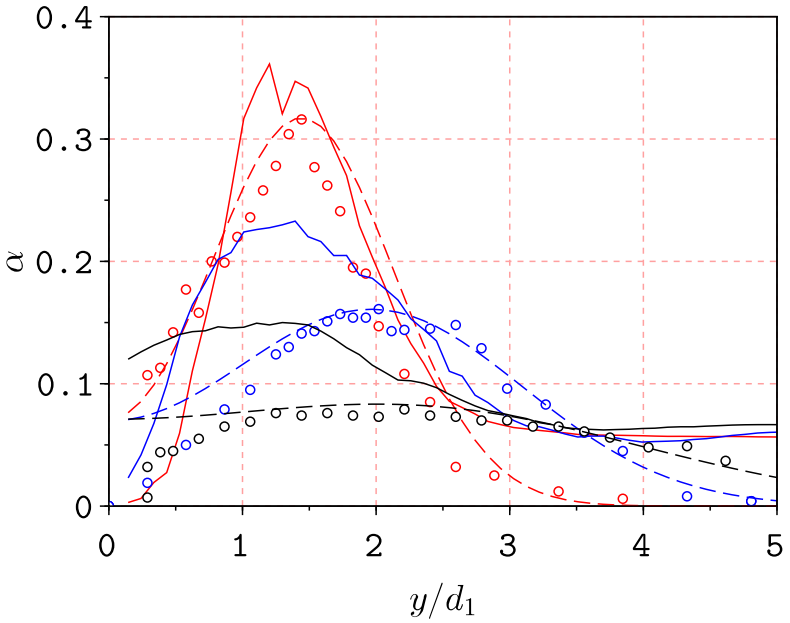

(a) No turbulence modeling.

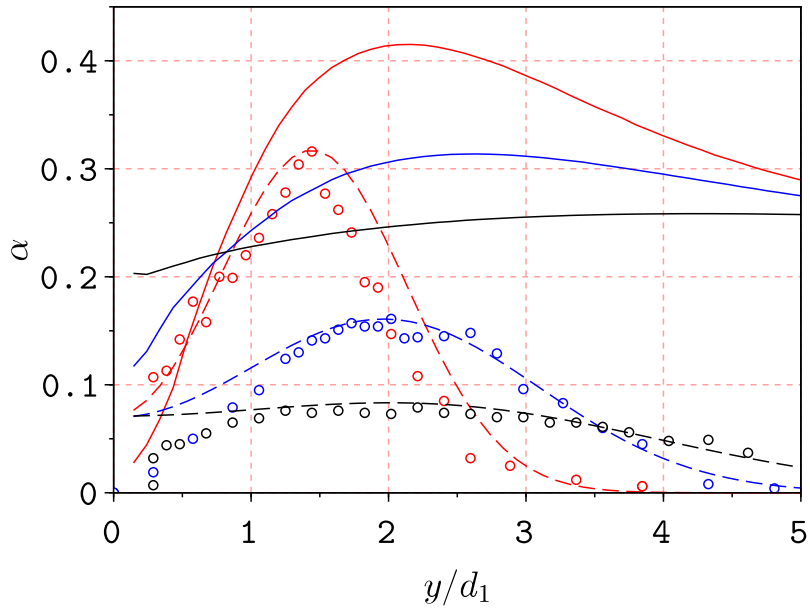

(b) $k-\epsilon$.

Figure 4.34: Planar plunging jet – bubble plume: volume fraction profiles at distances from the free surface $x - x_1 = 2$ cm in red, $x - x_1 = 10$ cm in blue and $x - x_1 = 24$ cm in black. Symbols: experimental values of [23]. Lines: numerical results. Dashed lines: equation (4.65) based on values of [23].

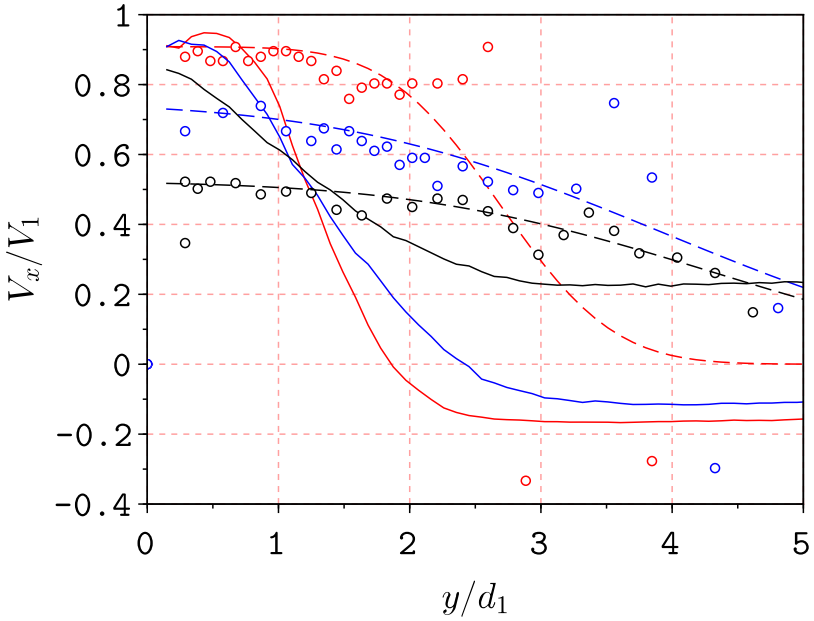

(a) No turbulence modeling.

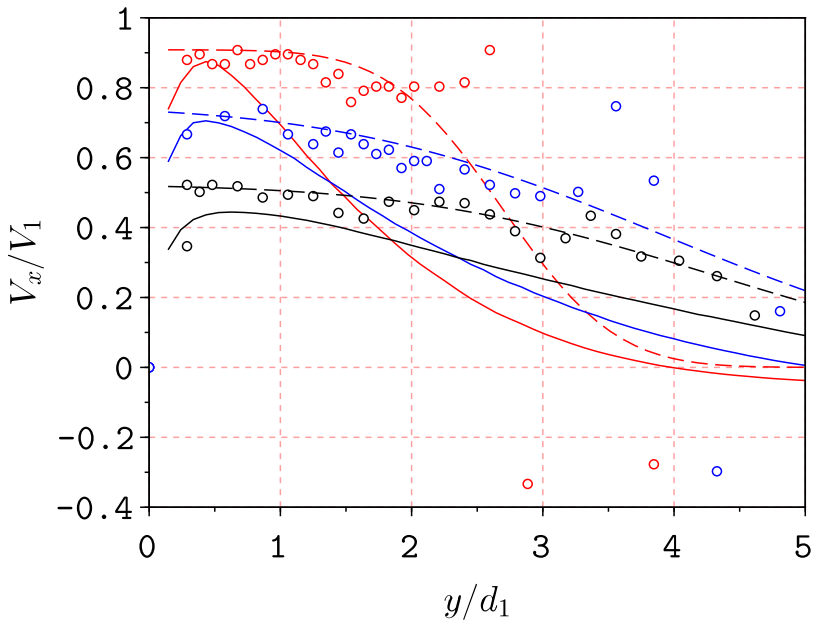

(b) $k-\epsilon$.

Figure 4.35: Planar plunging jet – bubble plume: interfacial velocity profiles at distances from the free surface $x - x_1 = 2$ cm in red, $x - x_1 = 10$ cm in blue and $x - x_1 = 24$ cm in black. Symbols: experimental values of [23]. Continuous lines: numerical results. Dashed lines: equation (4.66).

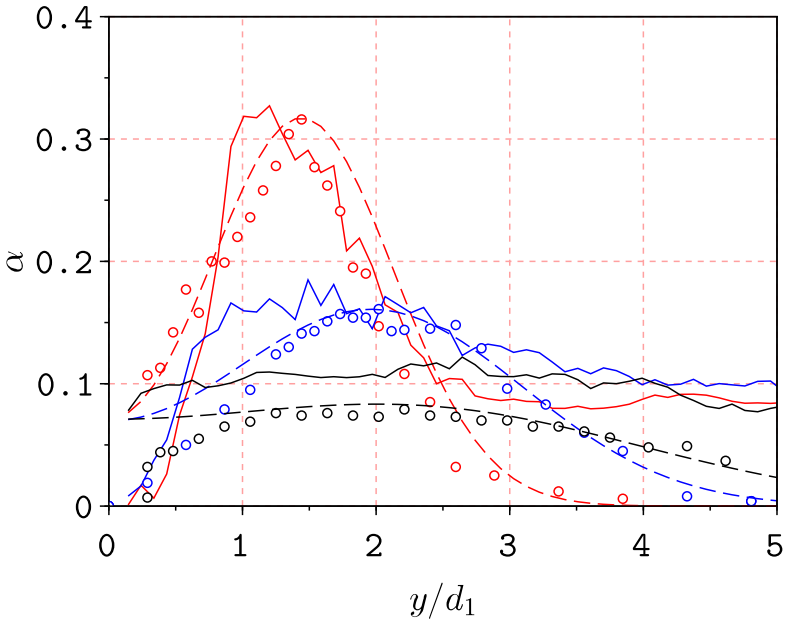

(a) Volume fraction.

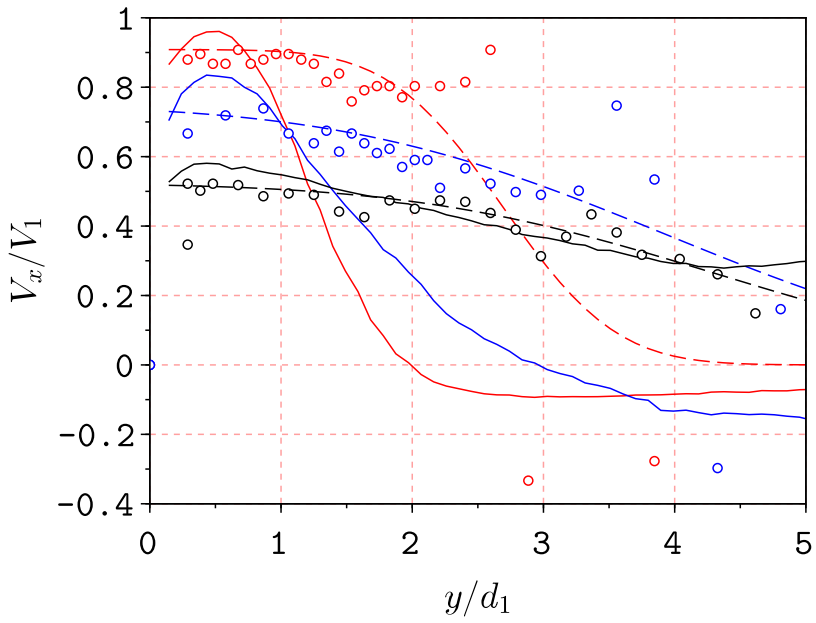

(b) Longitudinal velocity.

Figure 4.36: Planar plunging jet – bubble plume: without turbulence model and with a water viscosity multiplied by ten, profiles at distances from the free surface $x - x_1 = 2$ cm in red, $x - x_1 = 10$ cm in blue and $x - x_1 = 24$ cm in black. Symbols: experimental values of [23]. Lines: numerical results. Dashed lines: equations (4.65) and (4.66).

Table 4.7: Planar plunging jet with the water viscosity multiplied by ten – Characteristic quantities.

y (cm)	$\alpha_{\max}$		$Y_{\alpha_{\max}}$ (mm)		$V_{\max}$ (m/s)		Y_{V50} (mm)	
	Exp	Num	Exp	Num	Exp	Num	Exp	Num
2	0.32	0.33	15	13	2.26	2.39	28	13
3	0.25	0.27	14	16	2.09	2.42	x	13
5	0.17	0.29	16	14	2.16	2.48	31	13
7	0.17	0.26	19	14	2.03	2.33	x	14
10	0.16	0.18	21	16	1.87	2.08	41	17
13	0.15	0.17	22	27	1.68	1.99	x	18
16	0.12	0.16	24	30	1.50	1.67	39	22
24	0.08	0.12	23	28	1.30	1.45	45	43

Free-falling jet We can also investigate the reproduction of the free-falling jet that is pivotal to reproduce the conditions at the impact point. Void fraction profiles at 3 and 10 cm (impact zone) from the nozzle are displayed on Figure 4.37 while velocity profiles are shown on Figure 4.38. One can see that because of the waves, the volume fraction are no longer zero far from the support. Pre-entrainment can be noted also in the experiment. Moreover the increase in velocity is missed. These perturbations can therefore significantly affect the air entrainment. The presence of the $k-\epsilon$ model allows one to better capture the void fraction in the core of the jet.

Numerical pre-entrainment This test case highlights one limit of the resolution for volume fractions. Pre-entrainment is occurring in the free-falling jet. Though it is observed experimentally, we shall underline that the one observed in the computations results from the numerical discretization of the operators in the phase volume equation (3.20). Indeed, near the interface, the factor $(\alpha_a\beta_b + \alpha_b\beta_a)$ is never null: as the relative velocity is aligned with gravity, for a Cartesian arrangement of the particles, one could expect vertical contributions in the operator to cancel out. However, particles are disordered and the small errors accumulate and trigger the diffusion of the interface. One could note that a symmetric formulation of the form $(\alpha_a\beta_a + \alpha_b\beta_b)$ would not trigger diffusion: further investigations on a scheme inspired from slope limiters in the FV approach are therefore required. For our scheme, the idea could be to build a non linear convection scheme based on the ratio $r_{a|b}$ of local gradients of the volume fraction field:

$$r_{a|b} = \frac{[\boldsymbol{\nabla}\alpha]_d(\boldsymbol{r}_a)\cdot\boldsymbol{v}^r_{a|b}}{[\boldsymbol{\nabla}\alpha]_d(\boldsymbol{r}_b)\cdot\boldsymbol{v}^r_{a|b}} \tag{4.68}$$

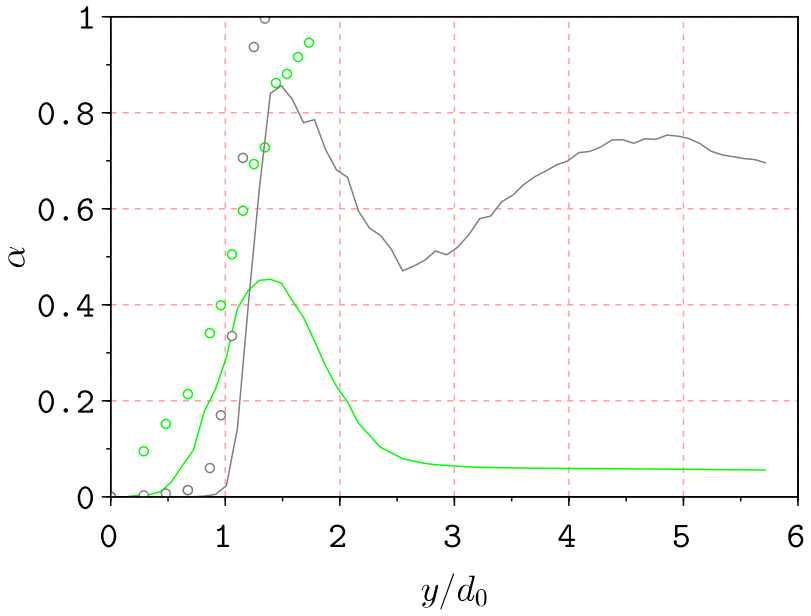

(a) No turbulence modeling.

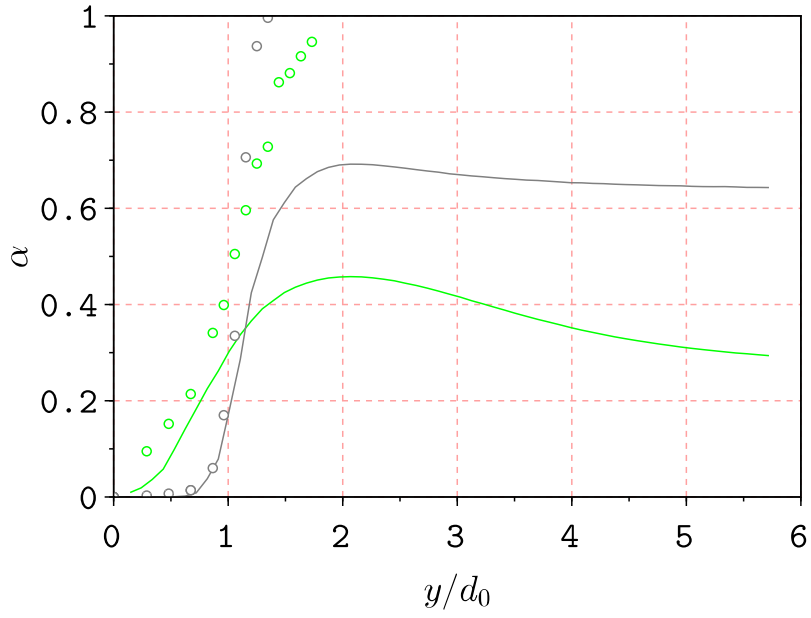

(b) $k - \epsilon$.

Figure 4.37: Planar plunging jet – free-falling jet: volume fraction profiles at distances from the nozzle $x = 3$ cm in grey and $x = 10$ cm in green. Symbols: experimental values of [23]. Continuous lines: numerical results.

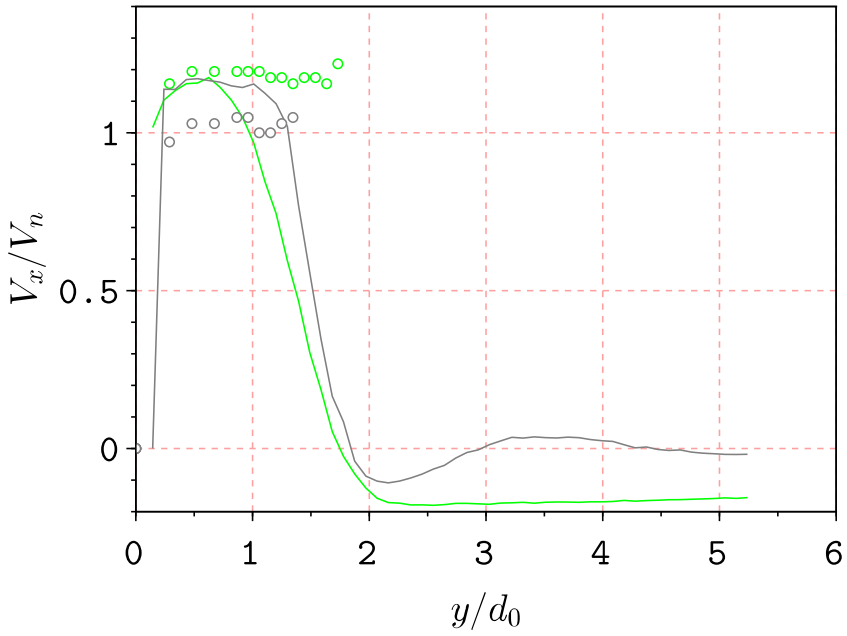

(a) No turbulence modeling.

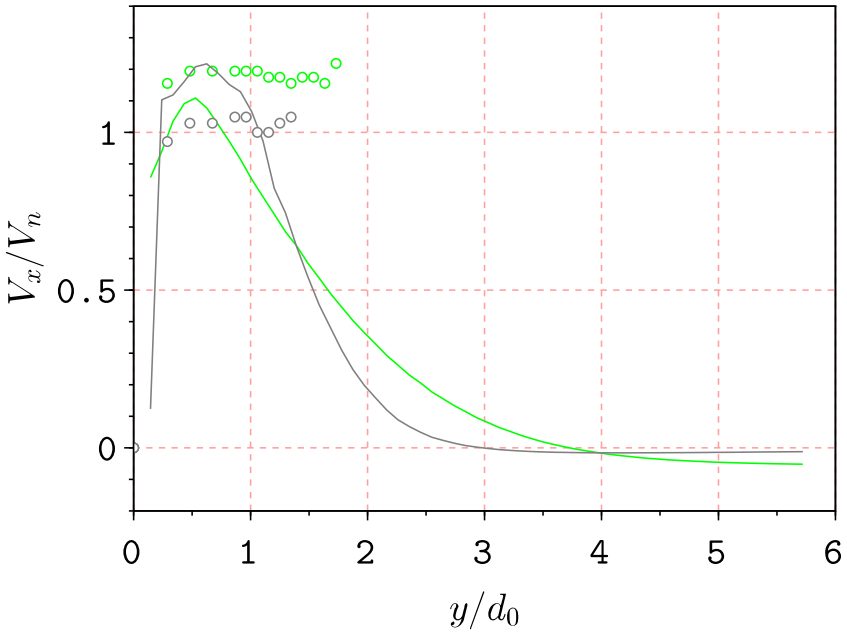

(b) $k-\epsilon$.

Figure 4.38: Planar plunging jet – free-falling jet: interfacial velocity profiles at distances from the nozzle $x = 3$ cm in grey and $x = 10$ cm in green. Symbols: experimental values of [23]. Continuous lines: numerical results.

The upwind and centered fluxes would write:

$$f^u_{a|b} = \alpha_a\beta_b \left[\boldsymbol{v}^r_{a|b}\cdot\boldsymbol{S}_{a|b}\right]^+ + \alpha_b\beta_a \left[\boldsymbol{v}^r_{a|b}\cdot\boldsymbol{S}_{a|b}\right]^- \quad \text{and} \quad f^c_{a|b} = (\alpha_a\beta_a + \alpha_b\beta_b)\left(\boldsymbol{v}^r_{a|b}\cdot\boldsymbol{S}_{a|b}\right) \tag{4.69}$$

The flux weighted by a limiter function ϕ^l would be:

$$f_{a|b} = f^u_{a|b} + \phi^l\left(r_{a|b}\right)\left(f^c_{a|b} - f^u_{a|b}\right) \tag{4.70}$$

with the limiters Minmod $\max\left(0, \min\left(1, r\right)\right)$ or Superbee $\max\left(0, \min\left(2r, 1\right), \min\left(r, 2\right)\right)$. It is of particular interest to see the behavior of that kind of approach in the SPH framework. Another idea is to introduce directly a limiter in the scheme, switching from a centered to an upwind approach, and compute an appropriate value to ensure the respect of physical boundaries.

$$\frac{\alpha_a^{n+1} - \alpha_a^n}{\delta t} = -\sum_{b\in\mathcal{F}} V_b\left[\phi^l_{a|b} f^c_{a|b} + \left(1 - \phi^l_{a|b}\right) f^u_{a|b}\right] \tag{4.71}$$

In the planar plunging jet test case, the importance of the inflow has been underlined experimentally so that one can expect a non-negligible influence on the results.

Larger domain To assess the influence of the reduced geometry, we considered a configuration with the full length of the domain on the right side, modeling also the weir allowing one to maintain the water level. The left-hand side of the domain behind the support remains shorter than in the experiment. To avoid too heavy computational times and remain below the maximum number of particles that can be handled, the height of the domain between the bottom and the nozzle has been divided by two, what may alter the bubble plume. 1.7 million SPH particles are used. This simulation was carried out without turbulence model. One can see on Figure 4.39 that the bubble plume, no longer restrained by lateral walls, can extend further in the domain. The unrest of the free surface is more limited but still apparent, as part of the waves escape the domain through the weir. One can see on Figure 4.40 an improved behavior, especially far from the support, compared to Figures 4.34a and 4.35a. These profiles were averaged on a larger period – from 5 to 11 s – compared to the previous cases as fewer numerical outputs were made due to the size of the files. A sufficiently large period was necessary to decrease the scatter of the resulting averaged profiles.

4.4.3 A wider variety of air-water flows

Air-water mixtures are encountered in a wide range of applications, many of them of interest for hydraulics such as hydraulic jumps, breaking waves… but also for chemical reactors, etc. The limited time did not allow us to apply our model to these other cases of interest. However, in order to highlight the variety of phenomena that this model can handle, we present here two examples of simulations without in-depth validation: the Boycott effect and the emptying of a

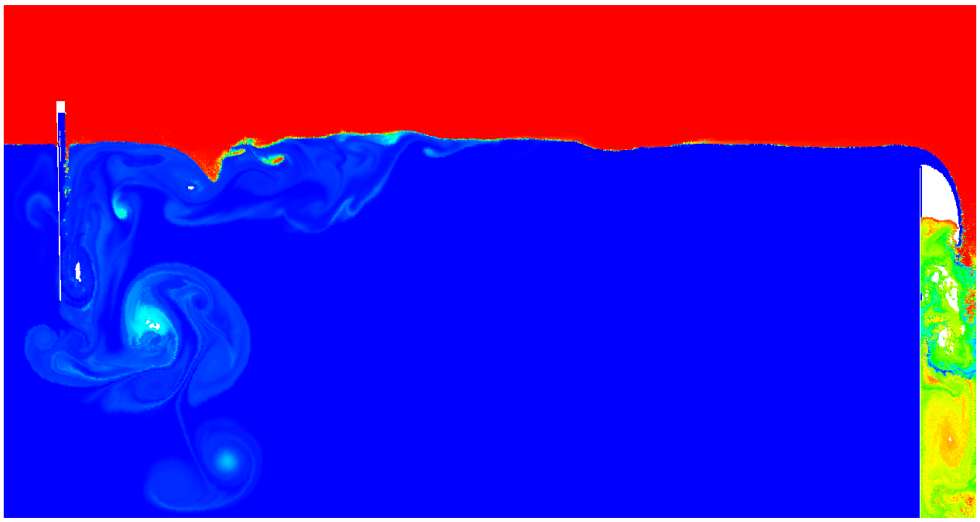

Figure 4.39: Planar plunging jet without turbulence model: volume fraction field in larger domain at $t = 4$ s.

bottle.

4.4.3.1 The Boycott effect

Named after Boycott [34] who studied red cells in blood and noticed their fast sedimentation near inclined walls, the Boycott effect also appears in aerated flows near an inclined wall when a dense clear-fluid film falls along the wall while the bubble-rich bulk rises, as described by Watamura et al. [379] for beer glasses. To proceed to a controlled series of experiments, a particle suspension of spherical glasses within tap water was used. Parameters used for the simulation are detailed in Table 4.8 with an artificial value of viscosity for the dispersed phase as its solid nature is not taken into account here. L is the bottom size and H the height of the initially filled glass. An initial volume $\alpha_0 = 0.08$ is set in the whole domain. The standard $k - \epsilon$ model is employed. The volume fraction and velocity magnitude are plotted in Figures 4.41 and 4.42 respectively. One can indeed note high volume fractions along the walls of the glass and a downward motion of the fluid in this region with some instabilities resembling the roll waves described in [379].

4.4.3.2 An emptying bottle

This application case reproduces in 2D the 3D case performed by Mer et al. [251] using a three-field numerical model. Numerical parameters are detailed in Table 4.9. Water is alternately released while gusts of air penetrate the bottle. The volume fraction evolution is displayed on Figure 4.43. The bottle diameter is denoted D and its height is H. The neck of the bottle has a di-

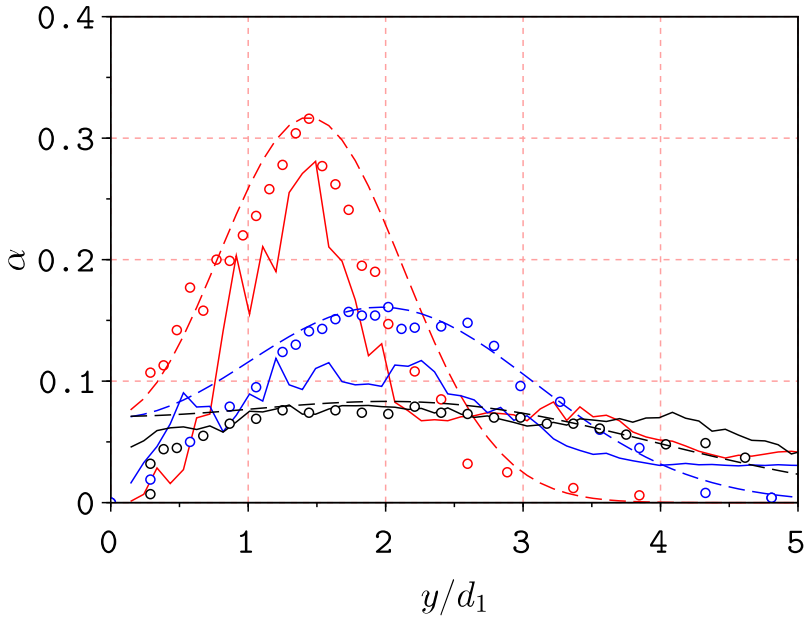

(a) Volume fraction.

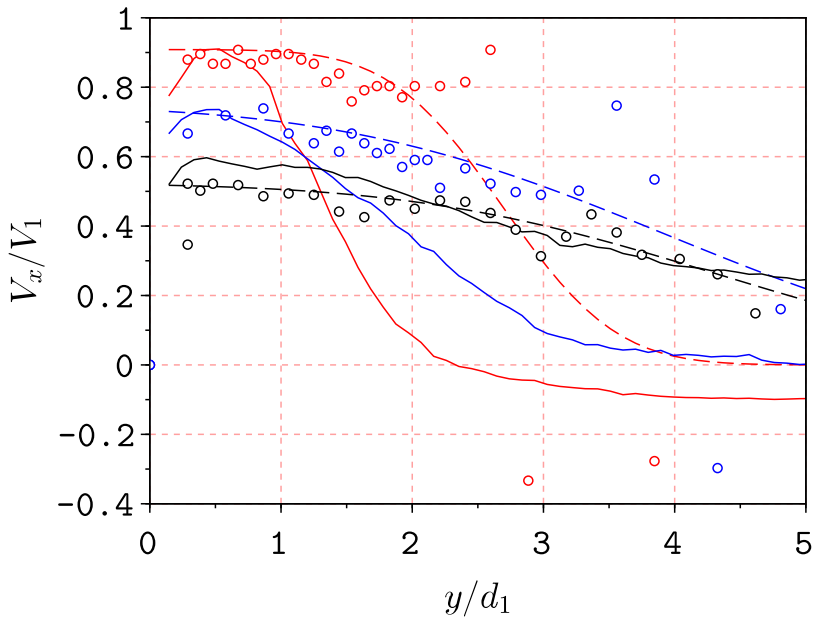

(b) Longitudinal velocity.

Figure 4.40: Planar plunging jet – bubble plume: without turbulence model, profiles at distances from the free surface $x - x_1 = 2$ cm in red, $x - x_1 = 10$ cm in blue and $x - x_1 = 24$ cm in black. Symbols: experimental values of [23]. Continuous lines: numerical results. Dashed lines: equations (4.65) and (4.66).

Table 4.8: Parameters for the Boycott effect computation.

L	60	mm	H	130	mm
ρ^α	140	kg/m^3	ρ^β	1006	kg/m^3
ν^α	1.56 10^{-5}	m^2/s	ν^β	9 10^{-7}	m^2/s
c^α	11.3	m/s	c^β	11.3	m/s
d^α	47	μm	d^β	47	μm
δr	0.5	mm	p_B	0	Pa

(a) $t = 0$ s (b) $t = 20$ s (c) $t = 40$ s (d) $t = 60$ s (e) $t = 80$ s (f) $t = 100$ s

Figure 4.41: Boycott effect: volume fraction evolution for particles with $\alpha \in [0; 0.1]$.

ameter d_n and a height d_h. The bottle is filled at 75% of its height by water. No turbulence model is used. One can notice Rayleigh-Taylor instabilities developing in the first moments of the computations. Some issues happen near the lower open boundary (imposed background pressure): the open boundary framework was not operational yet when this simulation was conducted. The air phase is probably not going up sufficiently fast, due to the mixture model approach that assumes a constant bubble diameter and maybe the terms neglected in the momentum equation. The mean pressure evolution within the upper air volume of the bottle is plotted on Figure 4.44 with a comparison with the numerical results of the compressible model and the experimental measurements of [251]. The pressure oscillations are going faster in the SPH model. Compressibility effects are at stake but were not the main points of this work. The values of the pressure peaks are however in reasonable agreement with the experimental results.

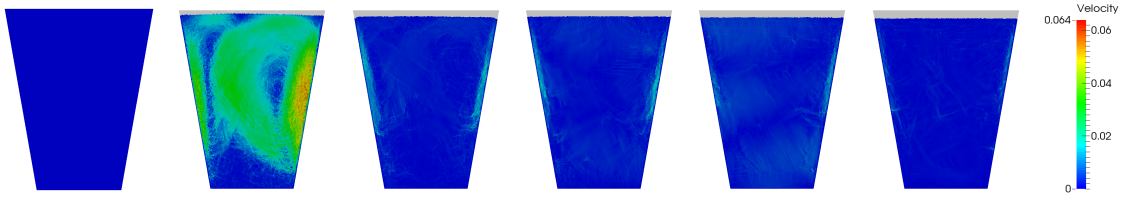

(a) $t = 0$ s (b) $t = 20$ s (c) $t = 40$ s (d) $t = 60$ s (e) $t = 80$ s (f) $t = 100$ s

Figure 4.42: Boycott effect: velocity magnitude evolution for particles with $\alpha \in [0; 0.1]$.

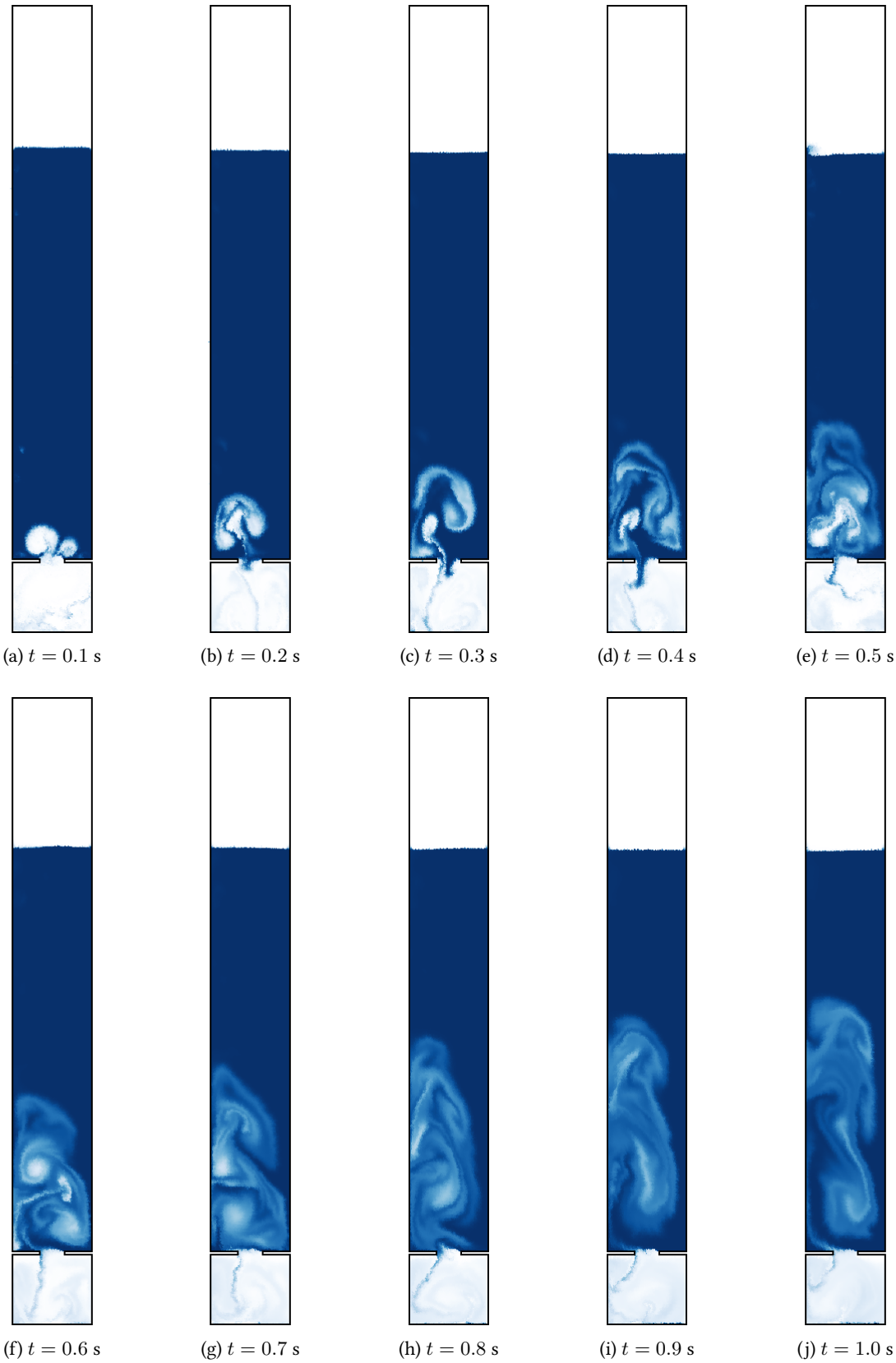

(a) $t = 0.1$ s (b) $t = 0.2$ s (c) $t = 0.3$ s (d) $t = 0.4$ s (e) $t = 0.5$ s

(f) $t = 0.6$ s (g) $t = 0.7$ s (h) $t = 0.8$ s (i) $t = 0.9$ s (j) $t = 1.0$ s

Figure 4.43: Emptying bottle: volume fraction evolution with air in white ($\alpha = 1$) and water in blue ($\alpha = 0$).

Table 4.9: Parameters for the emptying bottle computation.

D	114	mm	H	800	mm
d_n	35	mm	d_h	5	mm
ρ^α	1.23	kg/m^3	ρ^β	1000	kg/m^3
ν^α	10^{-5}	m^2/s	ν^β	10^{-6}	m^2/s
c^α	340	m/s	c^β	340	m/s
d^α	0.5	mm	d^β	0.5	mm
δr	1	mm	p_B	10000	Pa

4.5 A three-dimensional industrial application

We now aim at applying the SPH air-water mixture developed to a three-dimensional industrial test case: a hydraulic discharge-control structure. Single-fluid approach proved to fail at reproducing the dynamics of the flow. A two-phase approach appeared to be necessary. We aim at simulating the behaviour of the flow of the 1:8.33 scaled model described by Guyot and Rodriguez [155].

4.5.1 Description of the physics

As presented on the 3D geometry and a 2D projection on Figures 4.46 and 4.45, and described in [155], the structure consists of a drop region where half of the volume flow rate of water falls in the reception tank with vertical plunging jets and the other half flows along the cylinder surrounding this drop region. At the bottom end of this tank, the water exits through a pipe. A critical feature for the design of this structure is the air entrainment and then detrainment within the reception tank to avoid the propagation of air bubbles within the pipe. Such structures have already been studied in the literature as done by Kobus and Westrich [190] and illustrate the significant influence that the buoyancy of the entrained air can have on the flow field. The target is two-fold: dissipate a lot of energy thanks to maximized air entrainment in the drop section and remove the maximum of air before entering the pipeline in the detrainment section. Indeed, the formation of air packets within the pipeline could trigger some issues in pumps further down. As shown on Figure 4.46, depending on the water level in the tank (and therefore the amount of aeration due to the plunging jet), the flow can:

- Go directly to the bottom and reach the pipe without recirculating;
- Rise after the plunging region due to the vertical momentum given by the bubble swarm generated by a strong aeration, and flow along the surface with significant deaeration. Then, getting closer to the pipe outlet, it goes down again, hopefully with little or no

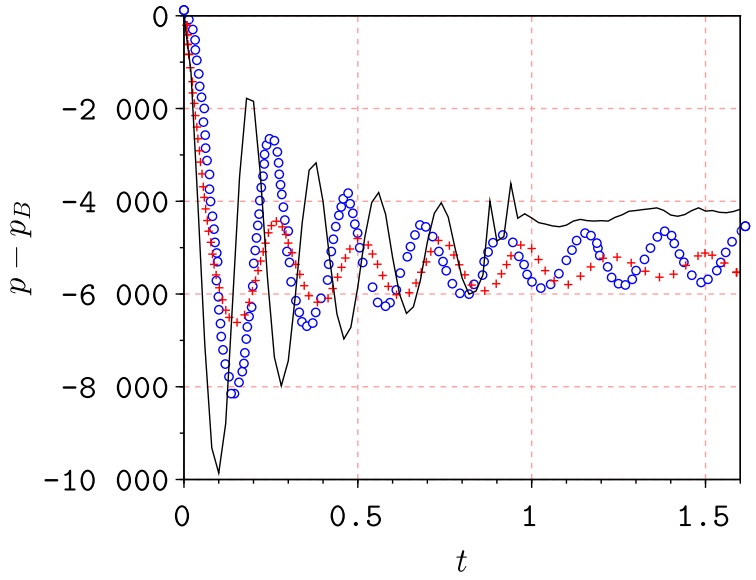

Figure 4.44: Emptying bottle: mean pressure evolution in the upper air volume in the bottle obtained with the present model in continuous black line and comparison with numerical and experimental results of [251] (time in s and pressure in Pa) in red and blue respectively.

aeration. As we will see, a single-phase simulation of this case would generate a flow without significant recirculations, looking like the first case.

An experimental campaign was carried out on this geometry by the Hydraulic Engineering Center of EDF so that some results are available to compare air concentration and velocity profiles.

4.5.2 Numerical model

The 3D .stl geometry displayed on Figure 4.45 was created by Agnès Leroy and we will compare our results to her single-fluid formulation computations in the following. The physical and numerical parameters are detailed in Table 4.10. The simulation counts around 2.76 million particles. One month of computation was required on one graphic card GeForce GTX Titan Black for 6.5 s of physical time. Let us recall that the code, still in development, is not optimized and such a case would gain to be run on multi-GPU. The air-water relative velocity closure developed in Chapter 4 is used without switch (the use of the switch did not improve the results on the stepped spillway test case). The $k - \epsilon$ model is used without buoyancy term (the buoyancy still requires further work as it triggered some peak viscosities that stopped the advances in the computations). The convective transfer term was not considered in the momentum equation due to numerical instabilities in its current implementation.

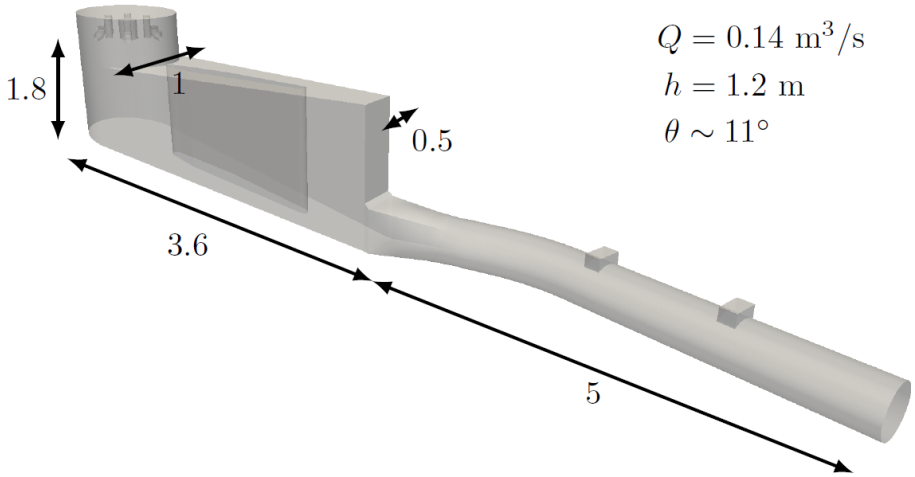

Figure 4.45: Discharge-control structure: geometry of the scaled model (distances in m). h is the free surface height relative to the bottom of the domain at the start of the exiting pipe and θ is the angle of the slope of the reservoir.

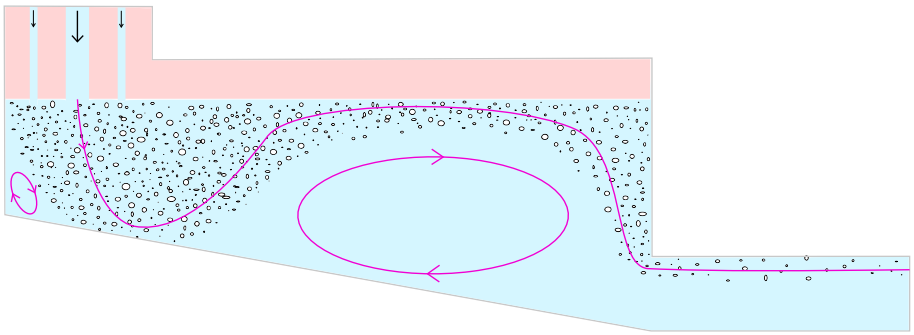

(a) Low tailwater level.

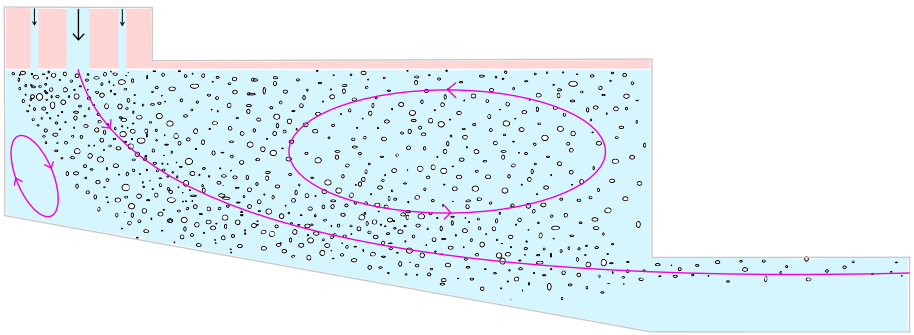

(b) High tailwater level.

Figure 4.46: Discharge-control structure: expected flow patterns.

Table 4.10: Parameters for the discharge-control structure.

ρ^α	1.23	kg/m^3	ρ^β	1000	kg/m^3
ν^α	1.56 10^{-5}	m^2/s	ν^β	10^{-6}	m^2/s
c^α	40	m/s	c^β	40	m/s
d^α	2	mm	d^β	2	mm
g	9.81	m/s^2	p_B	0	Pa

Initialization The domain is initially at rest, with the tank filled of water at the desired free surface height with an hydrostatic pressure profile. An air layer is put above, with a smooth transition in volume fractions with an hyperbolic tangent function. This air layer does not fill the whole domain due to the construction of the geometry that did not consider the potential presence of air around the inlet nozzles (absence of separating walls).

Open boundaries Only water is used at open boundaries and enters the domain at the inlet at the first iterations. Velocities are imposed with Poiseuille profiles at the inlet pipes visible on Figure 4.48. For the turbulent quantities, the initialization is done with:

$$k = \frac{u_\star^2}{\sqrt{C_\mu}} \quad \text{and} \quad \epsilon = \frac{u_\star^3}{\kappa r} \tag{4.72}$$

where r is the distance to the center of the pipe. An outlet pipe, further after the exit pipe one can observe on the right bottom corner of the Figure 4.48 allows for the flow to exit at the volume flow rate imposed at the inlet. A logarithmic velocity profile is imposed at the outlet with turbulent quantities but we do not go into further details as it is far from the domain of interest.

4.5.3 Results

The numerical results are plotted at t=6.5 s (actual time when this document was written; an update was introduced only for the comparisons of velocity profiles) for half the domain. This shall not be seen as a steady state. Velocity is nondimensionalized by its maximum value, that also serves for the normalization of the turbulent intensity: Tu $= \sqrt{2k/3}/V_{max}$. For the pressure, we use the maximum hydrostatic component. One can observe the bubble plume on Figure 4.47. Only small volume fractions reach the bottom. A region of intense mixing surrounds the inlet jets. Then a bubble swarm propagates with a wavy pattern towards the downstream wall of the tank. No air bubbles were found to be entrained deep enough to reach the outlet pipe at the time considered. Figures 4.48 and 4.49 highlight the velocity field: one can see that after the initial plunging region, the bubble cloud goes up and entrains water generating a general upward motion of the flow that then goes parallel to the free surface before plunging towards the outlet.

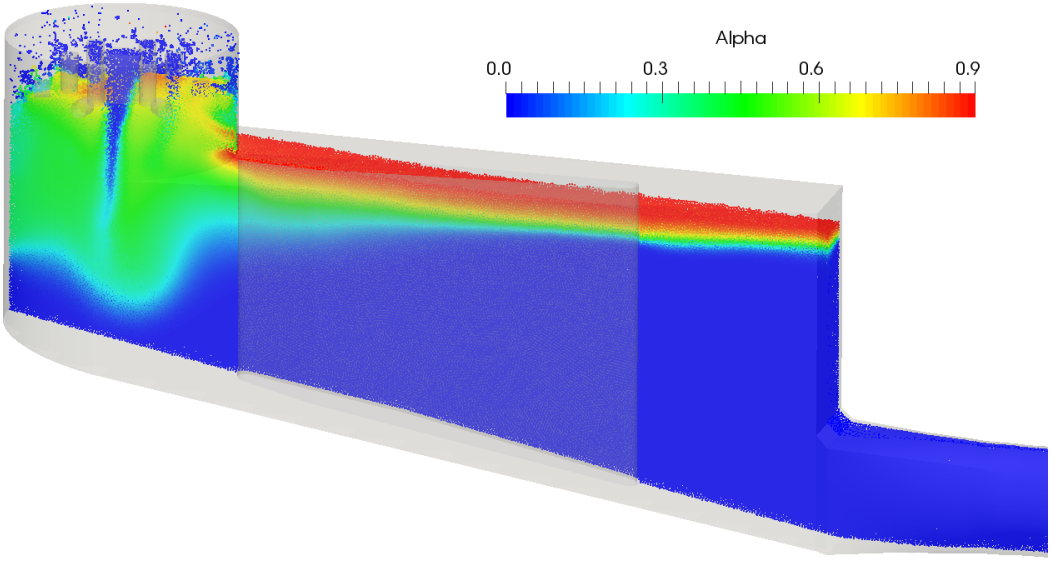

Figure 4.47: Discharge-control structure: volume fraction field.

A swirling behavior can be noticed in the drop region. The pressure profile in the tank is slightly altered compared to its initial hydrostatic pattern as shown on Figure 4.50. Peak pressures are punctually reached near the inlets. The turbulent intensity field plotted on Figure 4.51 shows the intense turbulent mixing in the plunging jet region and the propagation of the eddies in the rest of the domain, with a progressive dissipation.

A visual comparison of the bubble swarm indicates a satisfactory reproduction of its position and evolution in the basin, with a progressive reduction towards the downstream wall and some waves propagating along the blurred free surface. Figure 4.52b displays particles with a volume fraction smaller than 90%: above the free surface there is still some mixing due to the relative velocity closure that does not allow a complete separation of phases.

We compare in Figure 4.53 the longitudinal velocity profiles on two different planes detailed in Figure 4.53a. According to the numerical computations, these velocity profiles are computed in a poorly aerated region. One can see that we significantly underestimate the maximum values. However, the steady state is not reached and comparison with respect to former time steps shows a significant increase in velocities. The trend of maximum values at the top of the profiles is reproduced. One can note a significant improvement compared to the single-fluid simulations displayed on Figure 4.54. However, we miss the recirculation that is formed before the exit pipe and a longer simulation does not allow show any recirculation apperance. However, the significant turbulent kinetic energy in the domain might damp recirculations due to the increased

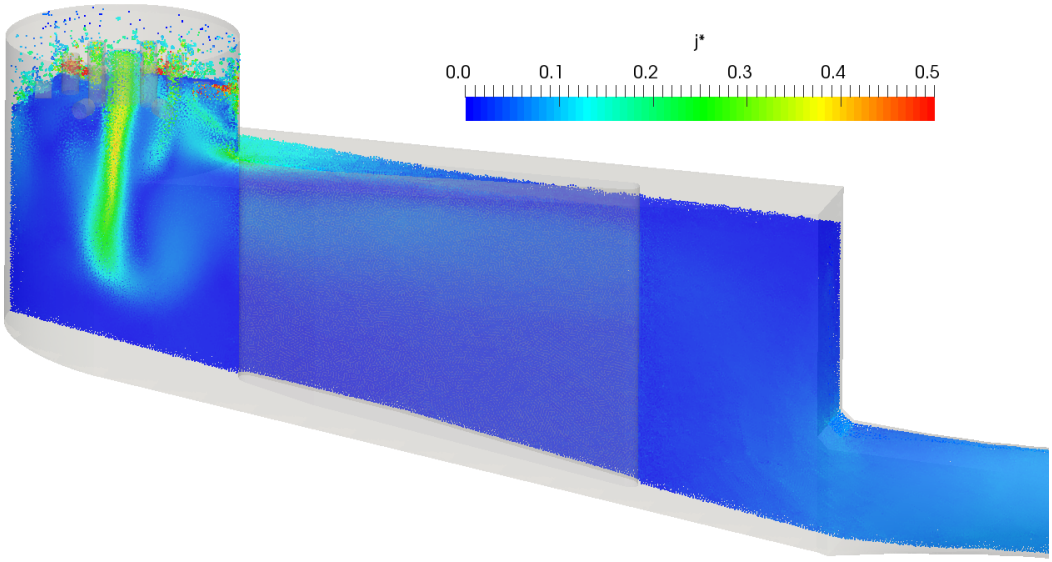

Figure 4.48: Discharge-control structure: dimensionless velocity magnitude field.

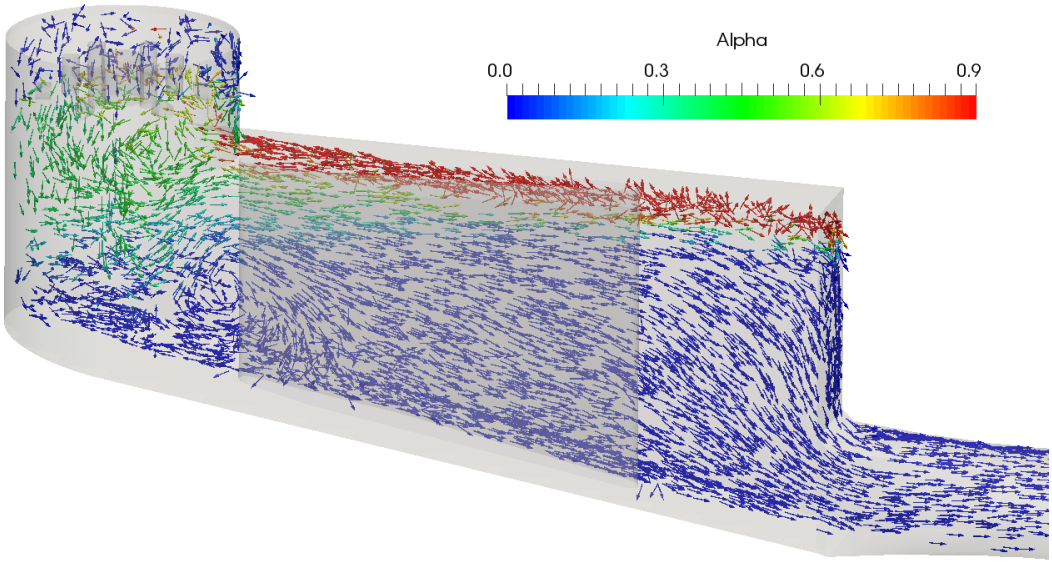

Figure 4.49: Discharge-control structure: direction of the velocity vector colored by α.

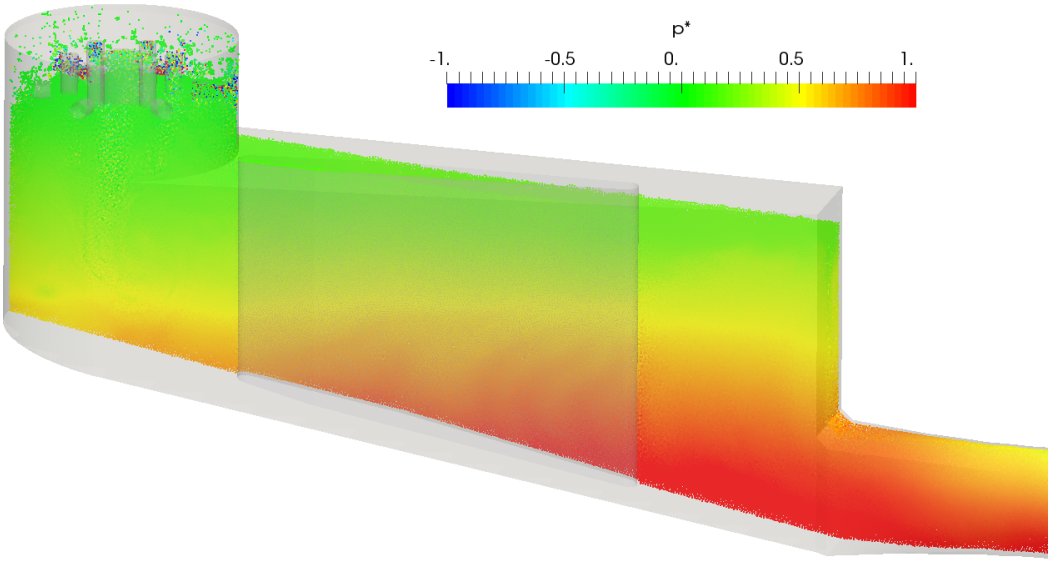

Figure 4.50: Discharge-control structure: dimensionless pressure field.

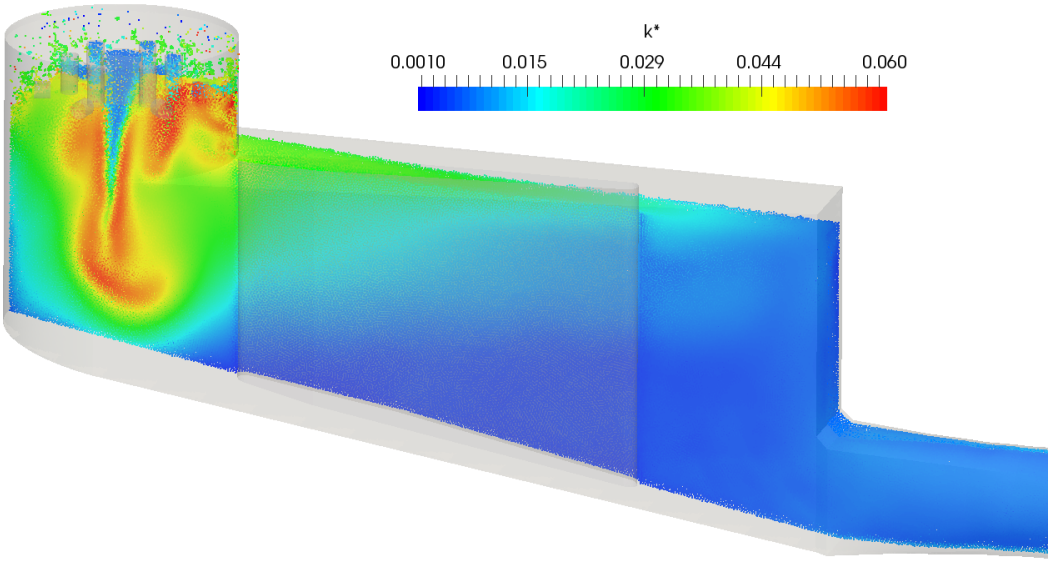

Figure 4.51: Discharge-control structure: turbulent intensity field.

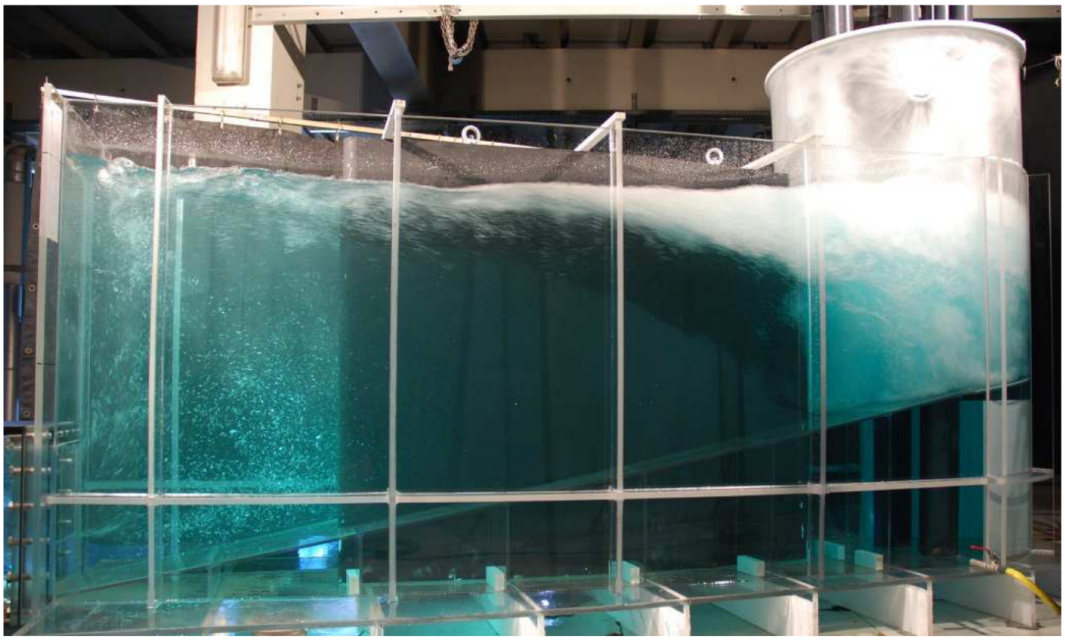

(a) Experiment performed by the Hydraulic Engineering Center (CIH, internal report).

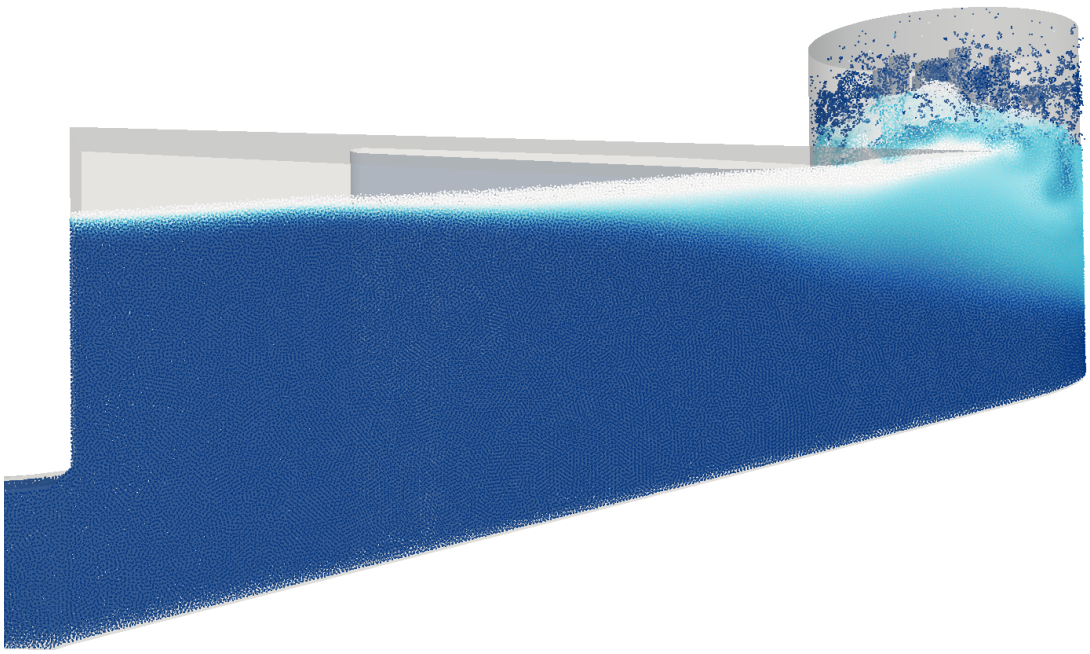

(b) Simulation colored by volume fraction (clip $\alpha < 0.9$).

Figure 4.52: Discharge-control structure: comparison of the bubble swarms.

viscosity. Computations without turbulence model [7] performed for the PhD defense confirmed it: the recirculation going upstream along the bottom of the structure appears, while the flow along the free surface is stronger and plunges more abruptly downwards when reaching the downstream wall. Some very small concentrations of bubbles ($alpha = 0.0001$) are entrained in the exiting pipe. The velocity profiles at the previously-considered sections averaged on 3 s are displayed on Figure 4.55 and highlight a better reproduction of the dynamics of the flow. Please note that these results cannot be considered as stationary as a longer simulation is required (and still running while writing this document).

We compare the velocity magnitude field obtained with our mixture model to the single-fluid formulation on Figure 4.56. With the mixture model, the jet is flapping a little while it falls straight with the single-fluid approach. The rising motion after the jet generated by the bubble swarm that was not caught by the single-fluid formulation is now modeled. One can see that without turbulence model, the dynamics are reproduced better, with the appearance of the recirculations in the reservoir.

4.6 Summary

4.6.1 A complex physical and numerical modeling

As illustrated in this chapter and recalled by Kiger and Duncan [186], air entrainment within water lies within a wide parametric space that led to a large range of empirical correlations and criterion definitions without reaching a comprehensive general formulation. The physical mechanisms overcoming the stabilizing forces of surface tension and/or gravity are varied. The scale of the physical system considered requires particular care in the modeling and gives rise to unavoidable scale effects. Turbulence together with the two-phase behavior of the entrained gas phase make air entrainment a full multi-scale problem. However, in view of high velocity shear flows of practical application for hydraulic works, common features have been identified and support the macroscopic view developed in this work.

4.6.2 Achievements and limits of the present approach

The present mixture model allowed for the simulation of air entrainment in schematic hydraulic structures. A reasonable agreement was obtained for the volume fraction profiles. However, the free surface hydraulic test cases drive the mixture model to is limits as some parts of the flow are highly mixed, so that the dispersed assumption is no longer verified.

Some discrepancies were found on the dynamics, that can be related to missing terms in the momentum equation to a certain extent (viscous terms generally disregarded and convective

[7] The planar plunging jet test case suggested that one could get better results for that kind of configuration without the turbulence model considered in this work for local aeration

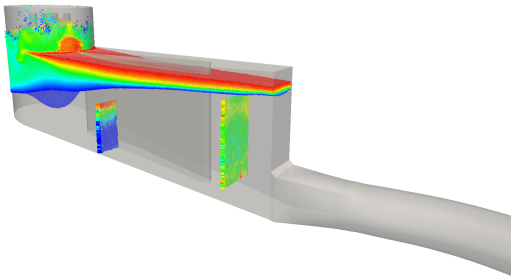

(a) Position of the sections for velocity profiles (the colored volume region corresponds to $0.1 < \alpha < 0.9$).

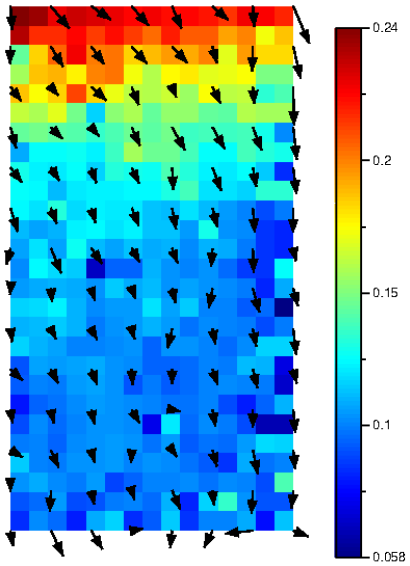

(b) Upstream section: simulation.

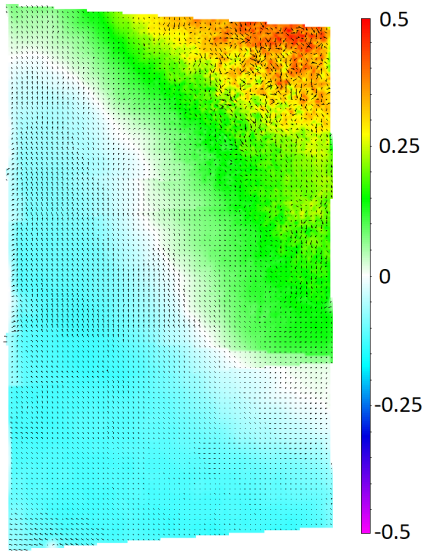

(c) Downstream section: experiment.

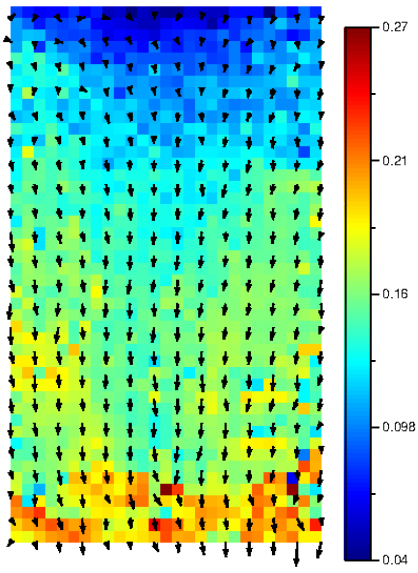

(d) Downstream section: simulation.

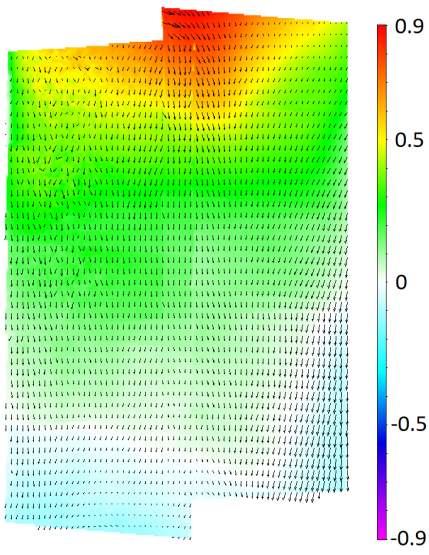

(e) Downstream section: experiment.

Figure 4.53: Discharge-control structure: comparison of the longitudinal velocity profiles at two sections at $t \approx 13$ s. Experiments carried out by the CIH (internal report).

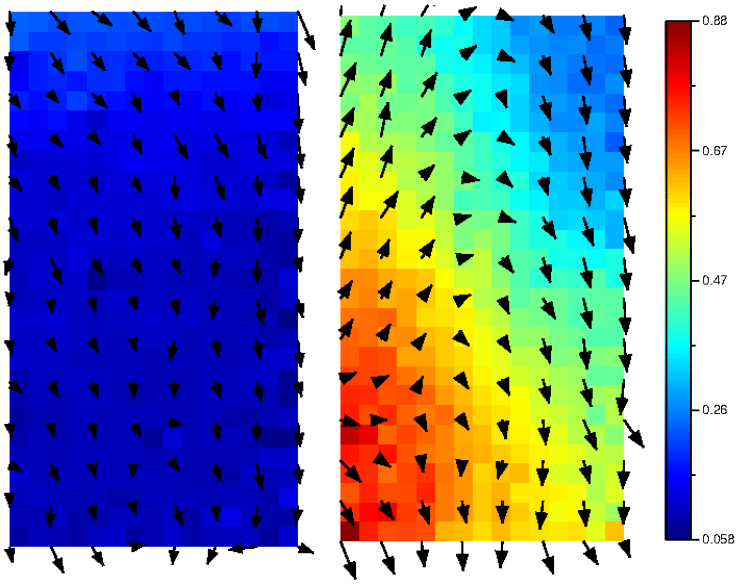

(a) Upstream section: present model simulation.

(b) Upstream section: single-fluid simulation.

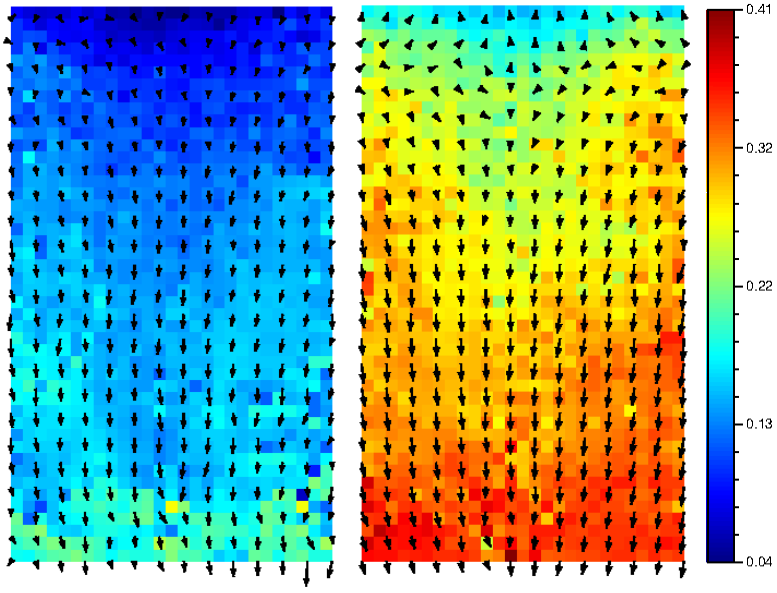

(c) Downstream section: present model simulation.

(d) Downstream section: single-fluid simulation.

Figure 4.54: Discharge-control structure: comparison of the longitudinal velocity profiles in m/s at two sections below the single-fluid formulation free surface height (the mixture velocity of the present model is compared to the water velocity with the single-fluid formulation). The arrows stand for the velocity field in the plane of the section.

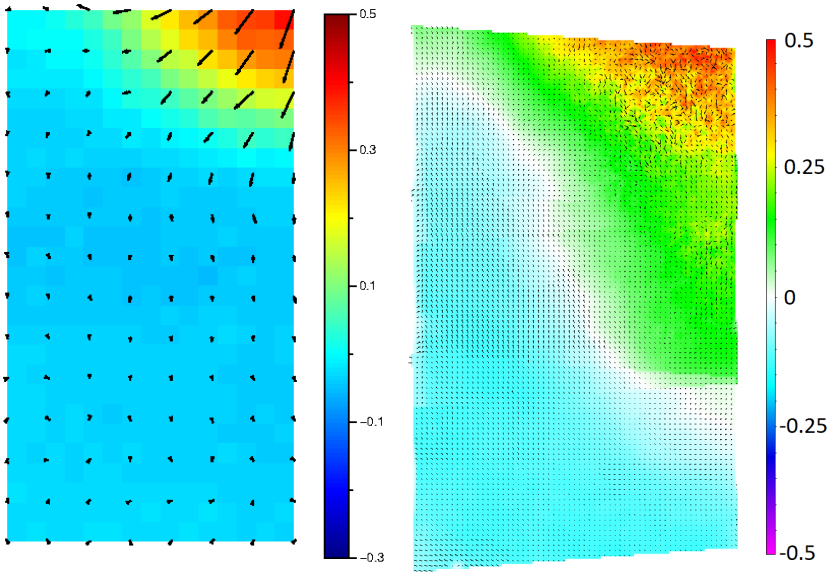

(a) Upstream section: simulation. (b) Downstream section: experiment.

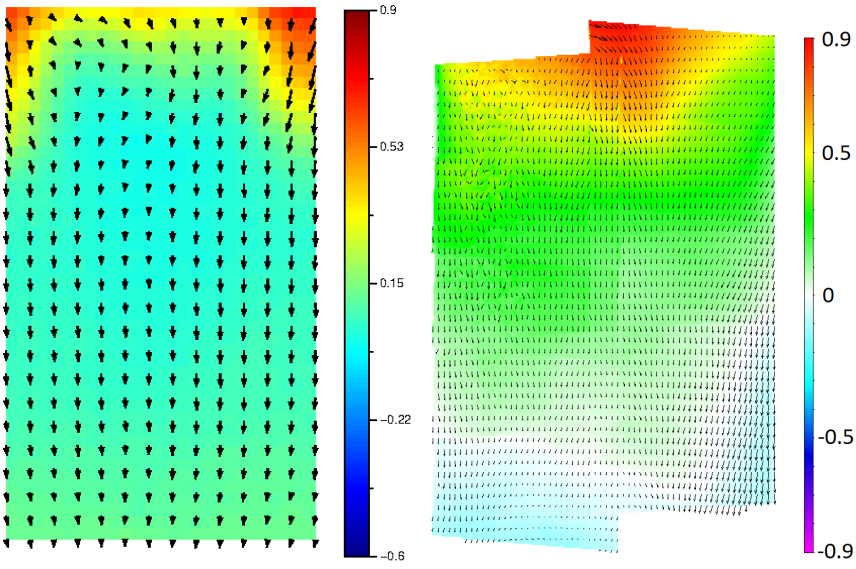

(c) Downstream section: simulation. (d) Downstream section: experiment.

Figure 4.55: Discharge-control structure: comparison of the avergared longitudinal velocity profiles at two sections at $t \approx 5$ s for the computation without turbulence model. Experiments carried out by the CIH (internal report).

(a) Single-fluid formulation (Agnès Leroy).

(b) Mixture model formulation (clip $\alpha < 0.9$).

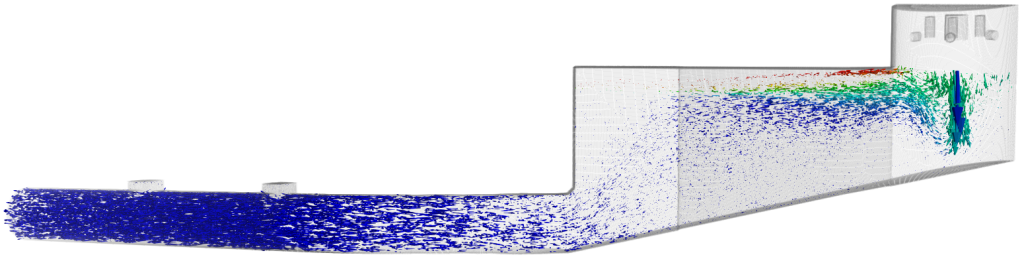

(c) Mixture model formulation with the $k - \epsilon$ turbulence model (clip $\alpha < 0.9$): velocity vector field colored by α.

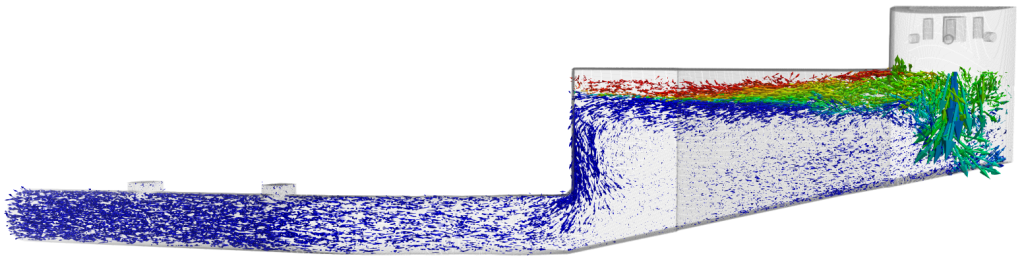

(d) Mixture model formulation without turbulence model (clip $\alpha < 0.9$): velocity vector field colored by α (instantaneous view).

Figure 4.56: Discharge-control structure: comparison of the velocity magnitude fields (the absolute velocities might be not comparable).

transfers), even though the two-phase nature influence was indicated to be limited according to experimental works. The inclusion of the convective transfer term still requires further work to limit the numerical effects and to highlight its contribution to the dynamics. The partial coupling between the volume fraction and the momentum equations can also explain some discrepancies through the relative velocity closure, as testified by the computations run with the pressure gradient replacing its hydrostatic approximation in the relative velocity closure that highlighted some improvements in the volume fraction and longitudinal velocity profiles. The robustness of the numerical model is at stake as the proper introduction of the convective transfers in the momentum equation and pressure gradient in the relative velocity closure will be possible only with a robust handling of high density ratio flows both within the domain and at boundaries.

The choice of a RANS mixture model does not allow for insights into the mesoscopic nature of those flows, regarding the bubble size distribution and fine representation of the turbulent structures that play a prominent role in the entrainment. Giving a fixed size to the dispersed phase can be an issue regarding the polydisperse nature of many environmental flows and be critical in some cases [103]. The results exhibited a small sensitivity to the variations of the size of the dispersed phase so that the choice was driven by the peak values observed in the experimental results. Computations were performed on two-dimensional cases but the integration in an optimized multi-GPU code is expected to improve the computational times and to allow for three-dimensional simulations in reasonable times.

Conclusions and prospects

Dans cette thèse, on propose un nouveau modèle de mélange diphasique SPH faiblement compressible adapté à de forts rapports de densité et incluant une vitesse relative entre les phases. Une attention particulière est portée à ses bonnes propriétés numériques en termes de respect des bornes physiques et de conservation. La simplicité et la polyvalence du modèle, permises par la fermeture de la vitesse relative par une relation dépendant de la physique considérée, va de pair avec les limitations du champ d'application du modèle : une phase est supposée dispersée et son comportement est fortement couplé à celui de la phase continue. La turbulence, centrale pour le phénomène d'entraînement d'air, est simulée via un modèle $k-\epsilon$ classique pouvant inclure un terme de flottabilité. Un formalisme SPH de frontières ouvertes pour un mélange est également développé en vue du cadre applicatif. Ce modèle est appliqué avec succès sur des cas simples de validation diphasiques. La phénoménologie de l'entraînement d'air permet de formuler une loi de fermeture de la vitesse relative incluant un terme de traînée et un terme de diffusion turbulente. Ce modèle conduit à de bons résultats de concentration en air sur un cas de coursier en escalier. La dynamique n'est toutefois pas précisément reproduite, de sorte qu'un travail sur l'inclusion de termes négligés dans l'équation de quantité de mouvement s'avère nécessaire. Par ailleurs, une amélioration de la formulation SPH semble requise pour obtenir un code robuste à même de représenter des écoulements à forts rapports de densité. Un cas de jet plongeant bidimensionnel est également considéré et présente des résultats prometteurs. Enfin, des résultats préliminaires sur une géométrie 3D industrielle sont présentés et illustre l'applicabilité de ce modèle à des cas d'entraînement d'air complexes. Parmi les perspectives de ce travail, on peut envisager l'extension du champ de validité du modèle par couplage avec d'autres approches ou l'inclusion d'un suivi plus précis des caractéristiques de la phase dispersée. Profitant de la versatilité du modèle, une multitude de cas d'application impliquant des physiques distinctes de celle de l'entraînement d'air peut être envisagée. Le modèle gagnerait en ce sens à être importé dans le logiciel GPUSPH afin de bénéficier de sa structure optimisée multi-GPU et de la possibilité de représenter des sédiments et des corps rigides mobiles.

Achievements of this work

The complexity of air entrainment numerical modeling is two-fold as one shall accurately model both the entrapment of the air bubbles and their transport by the turbulent flowing waters. It therefore structures the work in two main parts.

A new volume-weighted two-phase Weakly Compressible Smoothed Particle Hydrodynamics (WCSPH) mixture model suited to high density ratios and including a slip velocity between velocities is proposed. A careful derivation of the model from the general two-phase formulation allows us to draw the framework of application of this model: dispersed two-phase flow with strong coupling between phases. Due to the average approach retained, the interface between phases is no longer explicitly tracked when mixing occurs. Thanks to a finite volume-like reasoning, a realizable numerical scheme, conservative with respect to the relative velocity contribution, is derived to follow the phase exchanges between particles. The model relying on a specific volume formulation reduces to single-phase formulation for unit volume fraction. Turbulence is included through a $k - \epsilon$ model. This mixture model is first successfully validated on academic cases: a phase separation in a tank is considered to check that conservation and realizability are achieved, while the accuracy of the model is investigated with a two-phase mixture laminar Rouse flow for which an analytical solution was derived. A Rayleigh–Taylor instability case is also tested to check the reduction to single-fluid behavior. Open boundaries for mixtures are developed and tested on separated and mixed two-phase laminar Poiseuille case, but still require further investigations.

The phenomenology of air entrainment is then detailed and a specific closure including a drag and a turbulent diffusion terms is applied to the relative velocity to handle air-water cases. The only calibration parameter of this model is the size of the dispersed phase. Two schematic air entrainment cases were considered: the stepped spillway and the plunging jet. Then preliminary results on the three-dimensional industrial test case of a hydraulic discharge-control structure were presented. Looking back at the original questions we had in the introduction, one can see that the model:

- Gives reasonable results regarding the global and local quantities of entrained air as the volume fraction profiles in the high velocity turbulent flow considered generally result from an advection-diffusion process of bubbles.

- Provides partial information about the relative velocity behavior (that is algebraically closed compared to a two-fluid model) and accounts for the modification of the flow dynamics due to air presence. However this point still requires further investigation as some discrepancies were noticed on the test cases. Missing dissipative terms in the momentum equation, lack of coupling between volume fraction and momentum equations due to a simplified relative velocity closure together with an invalid dispersed assumption in some regions of the flow are possible explanations. Moreover, some instabilities due to the high den-

sity ratio still trigger a lack of robustness of this model. Finally, the turbulence modeling including buoyancy requires further work.

Other questions are left for further developments, regarding the bubble size distribution or the alteration of the water quality.

Publications

Oral communications and articles about the present work have been presented in conferences:

- *"An upwind scheme for conservative, realizable two-phase mixture SPH model with high density ratios"* presented during the 13th international SPHERIC workshop in Galway, Ireland and awarded the student Libersky Prize 2018 for the best presentation and article [135]. Consequent contribution in the 26th issue of the SPHERIC newsletter.
- *"A Lagrangian accurate numerical model for high-density ratio two-phase mixtures"* presented at the Dispersed Two-Phase Flows (DTPF) 2018 conference in Toulouse, France (no article).
- *"Air entrainment modelling using a Lagrangian accurate numerical model for high-density ratio two-phase mixtures"* presented at the 10th International Conference on Multiphase Flow (ICMF) 2019 in Rio de Janeiro, Brazil [137].
- *"A first air entrainment SPH model using a two-phase mixture formulation"* presented during the 14th international SPHERIC workshop in Exeter, United Kingdom and awarded the student Libersky Prize 2019 for the best presentation and article [138]. Consequent contribution in the 28th issue of the SPHERIC newsletter.

This work is described in two journal papers:

- *"Mixture model for two-phase flows with high density ratios: A conservative and realizable SPH formulation"* published in the International Journal of Multiphase Flow in February 2019 [136].
- *"Air entrainment modeling in the SPH method: a two-phase mixture formulation with open boundaries"* (to be submitted, selected in ICMF2019 for a special issue of Flow, Turbulence and Combustion)

Aside from the main topic of the PhD, the author made the following two contributions:

- The oral communication and article *"Numerical Modelling of the Undersluices of the Rance Tidal Power Station with SPH"* presented during the 12th international SPHERIC workshop

in Orense, Spain [134] describing the internship work of J. M. Lopez Asiain in the following of the author's work on numerical simulations with FLOW-3D® and SPH of the Rance tidal power station.

- The numerical validation of the paper *"Calculating the smoothing error in SPH"* published in Computer & Fluids in September 2019 [365].

Science popularization described in Appendix F was performed through the following competitions:

- *"Les bulles font leur cinéma"* in the competition "Ma thèse en 180 secondes 2019" [133] in Paris-Est University and "Pitch ta thèse 2019" in EDF R&D (two awards).
- *"3 ans en 3 minutes ou comment parler à tous de l'expérience de doctorat"* retained in the official selection of the competition "Je filme ma formation 2019" [132] in Paris.

Perspectives

Possible further developments and applications are now presented in order to improve the model, see how it performs on other test cases and extend its range of application.

Towards a broader validity for two-phase regimes

Two-fluid model and coupling The air-water flows can involve a wide range of regimes with possible transitions between them that are complex to model numerically. The disperse flow assumption of the mixture model developed is not always legitimate depending on the zone of the flow considered. It appeared as a necessary first step of development before going to a two-fluid model or more complex approaches able to deal with regime transition. Several numerical approaches are the object of active research in order to build model distinguishing short and long scale interfaces and adapting consequently the resolution. Three-field approaches with a continuous liquid phase and dispersed and continuous gas field were developed by Denèfle et al. [107], Mimouni et al. [253] and successfully applied to regime transition. An extended mixture model was developed by Damián [98], Damián and Nigro [99] to couple Volume of Fluid (VoF) and algebraic slip mixture models: the momentum equation includes surface tension effects in VoF while it uses drift stresses in the slip model. Whereas the relative velocity has a physical meaning for the mixture model, it can be used as an interface compression velocity for the VoF model. Such a model could be implemented in SPH by extending the writing of the geometrical or gradient criteria of the method to the SPH framework and would allow one to activate the mixture model only when needed, keeping the multifluid approach elsewhere (in order to preserve the interfaces). Another possible idea is to couple VoF and two-phase approach, as done and applied to air entrainment by Pereira [291].

A more complex description of the dispersed phase The model developed in this work is unable to give information about the bubble size distribution due to the monodisperse assumption and the absence of interfacial area density computation. These distributions are however of interest and can influence the dynamics. They are furthermore well documented on aerated flows. A possible evolution of the model can be to include population balance [79] or interfacial area density [114] equations to have a more precise idea of the topology and adapt consequently the computations.

Relative velocity expression The physics modeled could be enriched by including in the relative velocity more effects that has been neglected here, namely the added-mass and shear-induced lift forces acting on individual bubbles and wall effects.

Turbulence modeling A very simple model has been assumed for turbulence. Keeping a RANS approach, $k - \epsilon$ turbulence model for two-phase flows were developed [118] and could be tried. In the literature, realizable $k - \epsilon$ model is allegedly better to model flows over stepped spillways. As we are working with a macroscopic approach, using refined models requiring small discretizations seems to be out of scope. Indeed we are not reproducing the real deformation of the interface but model the entrainment through the relative velocity expression.

Applications

Other air entrainment test cases We have presented in this work two prominent air entrainment cases: the stepped spillway and the plunging jet. Further insights could be made by investigating three dimensional version of theses situations. Moreover, the air entrainment literature is rich of other schematic or industrial air entrainment configurations: the breaking wave that involves a large range of air packets and bubbles [53, 103, 233, 271], the wave slamming for which the entrained air modifies the impact phenomenology [109, 290], the hydraulic jump [63, 67, 232, 372], the drop shaft as studied in [291], the Piano Key Weir… It could improve the modeling of hydraulic structures such as ski jumps that were studied in the SPH method [148, 273] as the water depth were found to be smaller than expected, allegedly due to the air modeling missing in [273].

Enrich the model to follow other quantities of interest To assess the water quality or follow some chemical substances, which are common interests in engineering applications, this model could be enriched by an additional transport equation following the evolution of a scalar quantity that does not modify the dynamics.

Versatility By adapting the relative velocity closure (and possibly the viscous stress tensors), one can handle different types of flows as illustrated in this work with air-water and sediment-

water cases. Other physics could be considered: gas bubbles in oil of common occurrence in gearboxes [181], seepage in soils [43, 95, 185, 289] using Darcy's law, dispersion of contaminants in fractured media [341], fluidized bed reactors [387], but also problems of deposition, corrosion, combustion...

Deal with more than two phases Air-water-sediment cases happen in hydraulic and coastal engineering: introducing additional fields to handle several phases could allow one to model the sediments motion in the plunge pool described in the last chapter.

SPH formulation

A noisy pressure field A common issue in SPH is the noisy pressure field, that triggered problems in this work to compute a relative velocity depending directly on the pressure gradient, which is more physical and couples the momentum and volume fraction equations. Some approaches suggested in the literature could help in this prospect. Riemann solvers of now common use in SPH [82, 150] with SPH–ALE proved to give good results for violent air-water flows as shown by Rezavand et al. [307]. In this work, we solved Riemann problems only at the open boundaries but we might reach a consistent model by making a full Riemann resolution. The δ–SPH approach recently extended to the multifluid framework is also of interest to improve the pressure computations.

Accuracy of the volume fraction resolution The weak order of convergence of the volume fraction scheme together with the diffusion of the interface in situations where the physics should maintain a strict separation require to give a look at an evolution of the volume fraction scheme. The introduction of flux limiters of common use in the finite volume community as extensively classified by Waterson and Deconinck [380] could be an option.

Incompressible SPH (ISPH) The volume-weighted equations of the mixture model are generally chosen to take advantage of the divergence free condition for the volumetric flux [99]: it could be of interest to test this model within the ISPH framework.

Multi-GPU The developments described in this work were implemented in the in-house code Sphynx. However, they would gain to be included in the open-source code GPUSPH so as to run 3D simulations on multiple GPUs and benefit from its optimized structure. It would allow to meet the needs of the EDF Hydraulic Engineering Center for industrial applications such as hydraulic jumps and spillways. This would allow one to take advantage of the modules for interactions with moving bodies (one can imagine floating offshore structures submitted to breaking waves with the inclusion of air effects) and for work with sediments developed by Ghaïtanellis et al. [145].

Appendix A

Differential operators

A.1 Derivations of the multifluid operators

In this section, we will describe a possible derivation of the multifluid operators of Hu and Adams [170] adapted to the USAW boundary conditions in [145]. Let A be a scalar or vectorial field.

Divergence operator The continuous SPH interpolation of its divergence writes:

$$
\begin{aligned}
&\left[\boldsymbol{\nabla}\cdot\boldsymbol{A}\right]_c(\boldsymbol{r}) = \left[V^k\boldsymbol{\nabla}\cdot\left(\frac{\boldsymbol{A}}{V^k}\right) - V^k\boldsymbol{A}\cdot\boldsymbol{\nabla}\frac{1}{V^k}\right]_c(\boldsymbol{r}) \\
&\approx V^k(\boldsymbol{r})\left[\boldsymbol{\nabla}\cdot\left(\frac{\boldsymbol{A}}{V^k}\right)\right]_c(\boldsymbol{r}) - V^k\boldsymbol{A}(\boldsymbol{r})\cdot\left[\boldsymbol{\nabla}\frac{1}{V^k}\right]_c(\boldsymbol{r}) \\
&\approx \frac{1}{\gamma(\boldsymbol{r})}\int_{\Omega\cap\Omega_r}\left[V^k(\boldsymbol{r})\,\boldsymbol{\nabla}_{\boldsymbol{r}'}\cdot\left(\frac{\boldsymbol{A}}{V^k}\right)(\boldsymbol{r}') - V^k\boldsymbol{A}(\boldsymbol{r})\cdot\boldsymbol{\nabla}_{\boldsymbol{r}'}\frac{1}{V_k}(\boldsymbol{r}')\right]w(\boldsymbol{r}-\boldsymbol{r}')\,dV' \\
&\approx -\frac{1}{\gamma(\boldsymbol{r})}\int_{\Omega\cap\Omega_r}\left[V^k(\boldsymbol{r})\frac{\boldsymbol{A}}{V^k}(\boldsymbol{r}') - V^k\boldsymbol{A}(\boldsymbol{r})\,V^k(\boldsymbol{r}')\right]\cdot\boldsymbol{\nabla}_{\boldsymbol{r}'}w(\boldsymbol{r}-\boldsymbol{r}')\,dV' \\
&\quad+\frac{1}{\gamma(\boldsymbol{r})}\int_{\partial\Omega\cap\Omega_r}\left[V^k(\boldsymbol{r})\frac{\boldsymbol{A}}{V^k}(\boldsymbol{r}') - V^k\boldsymbol{A}(\boldsymbol{r})\frac{1}{V^k}(\boldsymbol{r}')\right]\cdot w(\boldsymbol{r}-\boldsymbol{r}')\,\boldsymbol{n}(\boldsymbol{r}')\,dS' \\
&\approx \frac{1}{\gamma(\boldsymbol{r})}\int_{\Omega\cap\Omega_r}\left[V^k(\boldsymbol{r})\frac{\boldsymbol{A}}{V^k}(\boldsymbol{r}') - V^k\boldsymbol{A}(\boldsymbol{r})\frac{1}{V^k}(\boldsymbol{r}')\right]\cdot\boldsymbol{\nabla}_{\boldsymbol{r}}w(\boldsymbol{r}-\boldsymbol{r}')\,dV' \\
&\quad+\frac{1}{\gamma(\boldsymbol{r})}\int_{\partial\Omega\cap\Omega_r}\left[V^k(\boldsymbol{r})\frac{\boldsymbol{A}}{V^k}(\boldsymbol{r}') - V^k\boldsymbol{A}(\boldsymbol{r})\frac{1}{V^k}(\boldsymbol{r}')\right]\cdot w(\boldsymbol{r}-\boldsymbol{r}')\,\boldsymbol{n}(\boldsymbol{r}')\,dS'
\end{aligned}
$$

where $\boldsymbol{n}(\boldsymbol{r}')$ is the unit vector normal to $\partial\Omega_{\boldsymbol{r}}$ at point $\boldsymbol{r}'$ and directed towards the outside (this will trigger a minus sign in the following for the boundary term, due to the definition of γ with an inward normal). One can then write the discrete approximation (let us underline that the

volume at stake are the reference volumes $\bar{V}$ except for the interpolation[1]):

$$\begin{aligned}
\left[\boldsymbol{\nabla}\cdot\boldsymbol{A}\right]_d(\boldsymbol{r}) &\approx \frac{1}{\gamma_a}\sum_{b\in\mathcal{P}} V_b\left[\bar{V}_a^k\frac{\boldsymbol{A}_b}{\bar{V}_b^k}-\bar{V}_a^k\boldsymbol{A}_a\frac{1}{\bar{V}_b^k}\right]\cdot\boldsymbol{\nabla}w_{ab}\\
&\quad-\frac{1}{\gamma_a}\sum_{s\in\mathcal{S}}\left[\bar{V}_a^k\frac{\boldsymbol{A}_s}{\bar{V}_s^k}-\bar{V}_a^k\boldsymbol{A}_a\frac{1}{\bar{V}_s^k}\right]\cdot\boldsymbol{\nabla}\gamma_{as}\\
&\approx -\frac{\bar{V}_a^k}{\gamma_a}\sum_{b\in\mathcal{P}} V_b\frac{1}{\bar{V}_b^k}\left(\boldsymbol{A}_a-\boldsymbol{A}_b\right)\cdot\boldsymbol{\nabla}w_{ab}+\frac{\bar{V}_a^k}{\gamma_a}\sum_{s\in\mathcal{S}}\frac{1}{\bar{V}_s^k}\left(\boldsymbol{A}_a-\boldsymbol{A}_s\right)\cdot\boldsymbol{\nabla}\gamma_{as}
\end{aligned}$$

Let us write $V_b=\theta_b\bar{V}_b$ where $\theta_b=1$ if the particle b is in the fluid. The previous equation becomes:

$$\begin{aligned}
\left[\boldsymbol{\nabla}\cdot\boldsymbol{A}\right]_d(\boldsymbol{r}) &\approx -\frac{V_a^k}{\gamma_a}\sum_{b\in\mathcal{P}} V_b\frac{1}{V_b^k}\left(\frac{\theta_b}{\theta_a}\right)^k\left(\boldsymbol{A}_a-\boldsymbol{A}_b\right)\cdot\boldsymbol{\nabla}w_{ab}\\
&\quad+\frac{V_a^k}{\gamma_a}\sum_{s\in\mathcal{S}}\frac{1}{V_s^k}\left(\frac{\theta_s}{\theta_a}\right)^k\left(\boldsymbol{A}_a-\boldsymbol{A}_s\right)\cdot\boldsymbol{\nabla}\gamma_{as}
\end{aligned}\tag{A.1}$$

For $k=1$, one gets:

$$\left[\boldsymbol{\nabla}\cdot\boldsymbol{A}\right]_d(\boldsymbol{r})\approx-\frac{V_a}{\gamma_a}\sum_{b\in\mathcal{P}}\frac{\theta_b}{\theta_a}\left(\boldsymbol{A}_a-\boldsymbol{A}_b\right)\cdot\boldsymbol{\nabla}w_{ab}+\frac{V_a}{\gamma_a}\sum_{s\in\mathcal{S}}\frac{\theta_s}{\theta_a}\frac{1}{V_s}\left(\boldsymbol{A}_a-\boldsymbol{A}_s\right)\cdot\boldsymbol{\nabla}\gamma_{as}\tag{A.2}$$

Gradient operator The continuous SPH interpolation of its gradient writes:

$$\begin{aligned}
&\left[\boldsymbol{\nabla}A\right]_c(\boldsymbol{r})=\left[\frac{1}{V^k}\boldsymbol{\nabla}\left(V^kA\right)+V^kA\boldsymbol{\nabla}\frac{1}{V^k}\right]_c(\boldsymbol{r})\\
&\approx \tfrac{1}{V^k}(\boldsymbol{r})\left[\boldsymbol{\nabla}\left(V^kA\right)\right]_c(\boldsymbol{r})+V^kA(\boldsymbol{r})\left[\boldsymbol{\nabla}\tfrac{1}{V^k}\right]_c(\boldsymbol{r})\\
&\approx\frac{1}{\gamma(\boldsymbol{r})}\int_{\Omega\cap\Omega_r}\left[\frac{1}{V^k}(\boldsymbol{r})\,\boldsymbol{\nabla}_{\boldsymbol{r}'}\left(V^kA\right)(\boldsymbol{r}')+V^kA(\boldsymbol{r})\,\boldsymbol{\nabla}_{\boldsymbol{r}'}\frac{1}{V^k}(\boldsymbol{r}')\right]w(\boldsymbol{r}-\boldsymbol{r}')\,dV'\\
&\approx-\frac{1}{\gamma(\boldsymbol{r})}\int_{\Omega\cap\Omega_r}\left[\frac{1}{V^k}(\boldsymbol{r})\,V^kA(\boldsymbol{r}')+V^kA(\boldsymbol{r})\,\frac{1}{V^k}(\boldsymbol{r}')\right]\boldsymbol{\nabla}_{\boldsymbol{r}'}w(\boldsymbol{r}-\boldsymbol{r}')\,dV'\\
&\quad+\frac{1}{\gamma(\boldsymbol{r})}\int_{\partial\Omega\cap\Omega_r}\left[\frac{1}{V^k}(\boldsymbol{r})\,V^kA(\boldsymbol{r}')+V^kA(\boldsymbol{r})\,\frac{1}{V^k}(\boldsymbol{r}')\right]w(\boldsymbol{r}-\boldsymbol{r}')\,\boldsymbol{n}(\boldsymbol{r}')\,dS'\\
&\approx\frac{1}{\gamma(\boldsymbol{r})}\int_{\Omega\cap\Omega_r}\left[\frac{1}{V^k}(\boldsymbol{r})\,V^kA(\boldsymbol{r}')+V^kA(\boldsymbol{r})\,\frac{1}{V^k}(\boldsymbol{r}')\right]\boldsymbol{\nabla}_{\boldsymbol{r}}w(\boldsymbol{r}-\boldsymbol{r}')\,dV'\\
&\quad+\frac{1}{\gamma(\boldsymbol{r})}\int_{\partial\Omega\cap\Omega_r}\left[\frac{1}{V^k}(\boldsymbol{r})\,V^kA(\boldsymbol{r}')+V^kA(\boldsymbol{r})\,\frac{1}{V^k}(\boldsymbol{r}')\right]w(\boldsymbol{r}-\boldsymbol{r}')\,\boldsymbol{n}(\boldsymbol{r}')\,dS'
\end{aligned}$$

[1]To convince yourself, consider the inteprolation of the volume $\left[\frac{1}{\bar{V}_a}\right]_d=\sum_b V_b\frac{1}{\bar{V}_b}w_{ab}=\sum_b\theta_b w_{ab}$

One can then write the discrete approximation:

$$\begin{aligned}
\left[\boldsymbol{\nabla} A\right]_d(\boldsymbol{r}) &\approx \frac{1}{\gamma_a}\sum_{b\in\mathcal{P}} V_b \left[\frac{1}{V_a^k} V_b^k A_b + V_a^k A_a \frac{1}{V_b^k}\right] \boldsymbol{\nabla} w_{ab} \\
&\quad - \frac{1}{\gamma_a}\sum_{s\in\mathcal{S}} \left[\frac{1}{V_a^k} V_s^k A_s + V_a^k A_a \frac{1}{V_s^k}\right] \boldsymbol{\nabla} \gamma_{as} \\
&\approx \frac{1}{\gamma_a}\sum_{b\in\mathcal{P}} V_b \left(\left(\frac{V_a}{V_b}\right)^k A_a + \left(\frac{V_b}{V_a}\right)^k A_b\right) \boldsymbol{\nabla} w_{ab} \\
&\quad - \frac{1}{\gamma_a}\sum_{s\in\mathcal{S}} \left(\left(\frac{V_a}{V_s}\right)^k A_a + \left(\frac{V_s}{V_a}\right)^k A_s\right) \boldsymbol{\nabla} \gamma_{as}
\end{aligned}$$

The previous equation becomes:

$$\begin{aligned}
\left[\boldsymbol{\nabla} A\right]_d(\boldsymbol{r}) &\approx \frac{1}{\gamma_a}\sum_{b\in\mathcal{P}} V_b \left(\left(\frac{V_a}{V_b}\right)^k \left(\frac{\theta_b}{\theta_a}\right)^k A_a + \left(\frac{V_b}{V_a}\right)^k \left(\frac{\theta_a}{\theta_b}\right)^k A_b\right) \boldsymbol{\nabla} w_{ab} \\
&\quad - \frac{1}{\gamma_a}\sum_{s\in\mathcal{S}} \left(\left(\frac{V_a}{V_s}\right)^k \left(\frac{\theta_s}{\theta_a}\right)^k A_a + \left(\frac{V_s}{V_a}\right)^k \left(\frac{\theta_a}{\theta_s}\right)^k A_s\right) \boldsymbol{\nabla} \gamma_{as}
\end{aligned} \tag{A.3}$$

And for $k = 1$, one gets:

$$\begin{aligned}
\left[\boldsymbol{\nabla} A\right]_d(\boldsymbol{r}) &\approx \frac{1}{\gamma_a}\sum_{b\in\mathcal{P}} V_b \left(\frac{V_a}{V_b}\frac{\theta_b}{\theta_a} A_a + \frac{V_b}{V_a}\frac{\theta_a}{\theta_b} A_b\right) \boldsymbol{\nabla} w_{ab} \\
&\quad - \frac{1}{\gamma_a}\sum_{s\in\mathcal{S}} \left(\frac{V_a}{V_s}\frac{\theta_s}{\theta_a} A_a + \frac{V_s}{V_a}\frac{\theta_a}{\theta_s} A_s\right) \boldsymbol{\nabla} \gamma_{as}
\end{aligned} \tag{A.4}$$

And finally:

$$\begin{aligned}
\left[\boldsymbol{\nabla} A\right]_d(\boldsymbol{r}) &\approx \frac{1}{\gamma_a V_a}\sum_{b\in\mathcal{P}} \left(V_a^2 \frac{\theta_b}{\theta_a} A_a + V_b^2 \frac{\theta_a}{\theta_b} A_b\right) \boldsymbol{\nabla} w_{ab} \\
&\quad - \frac{1}{\gamma_a V_a}\sum_{s\in\mathcal{S}} \frac{1}{V_s} \left(V_a^2 \frac{\theta_s}{\theta_a} A_a + V_s^2 \frac{\theta_a}{\theta_s} A_s\right) \boldsymbol{\nabla} \gamma_{as}
\end{aligned} \tag{A.5}$$

A.2 Hydrostatic test case

The aim of this section is to understand the behavior of the classical SPH formulation at high density ratios without considering mixtures.

Numerical issues Numerical issues encountered with the pressure gradient computations will be exemplified on the hydrostatic test case:

- Pressure oscillations usually take place in the beginning of simulations and take a long time to damp, especially for small viscosities. Periodic conditions allow for this phenomenon to last longer due to the absence of the side wall effects.
- For single fluid computations, spurious motions of the water phase along the lateral walls have been noted starting from a fluid at rest. It appears to be linked to the choice of gradient operator (the antisymmetric operator is not zeroth order consistent), together with the boundary condition (the antisymmetry property should not lead to momentum generation from a fluid at rest, so that the only possible defect in the antisymmetry property is on wall particles). The only mean that was found to keep a fluid quasi perfectly at rest was to consider a renormalized symmetric gradient (2.33) in a closed box. However it increases the computational time, cannot handle a free surface without correction and does not enforce momentum conservation so that this solution is not retained.
- Spurious behavior was observed near the air-water interface at high density ratios when considering two-phase computations, due to issues related to the discontinuity of the pressure gradient as explained in Sections 2.2.1.2 and 3.3.1.1. Pressure waves propagating along the interface have been noted.

Description of the case The computational domain is a rectangle of dimensions $L \times H$. The free surface is at half the height of the domain $h_s = 1$ m, separating the water phase from the air phase that can be modeled or not. Periodic conditions along the x axis are employed if specified. The fluid starts at rest. The numerical and physical parameters used for the single and two-phase computations of the hydrostatic case are detailed in Table A.1.

Table A.1: Parameters for the single and two-phase hydrostatic cases.

L	1	m	H	2	m
ρ^α	1.23	kg/m^3	ρ^β	1000	kg/m^3
ν^α	1.56 10^{-5}	m^2/s	ν^β	10^{-6}	m^2/s
c^α	32	m/s	c^β	32	m/s
ξ^α	1.4		ξ^β	7	
d^α	1	mm	d^β	1	mm
δr	20	mm	p_B	500	Pa

In single-fluid computations, the density-based SPH formulation is employed. For the two-phase cases, the multifluid formulation of Ghaïtanellis et al. [145] is employed. The state equation used is (1.10). Density diffusion with $\Lambda = 1$ is employed. Dimensionless variables used are the coordinates $x_\star = x/L$ and $z_\star = z/h_s$, the time $t_\star = t\sqrt{g/h_s}$, the pressure $p_\star = p/(\rho g h_s)$ and the velocity magnitude $v_\star = |\boldsymbol{v}|/\sqrt{g h_s}$.

A.2.1 Single-fluid case

We aim at understanding the single-fluid behavior before addressing the two-fluid computations.

Pressure oscillations We first consider a box domain. If one starts a simulation without initializing the pressure field, significant oscillations of this field can be observed. The time for their damping depends on the viscosity: with 0.03 m^2/s, the flow is stabilized in 5 s. With physical viscosities, observations are still observed after 20 s when Figure A.2a is displayed. The pressure field is therefore generally initialized with the incompressible linear hydrostatic profile. However oscillations can still be observed: with physical viscosities, the pressure field is still not stabilized after 500 s of physical time.

Checkerboard effects Without volume diffusion, stationary oscillations of the pressure field appear near the boundaries as shown on Figure A.2b for a viscosity of 0.03 m^2/s. For physical viscosities, instabilities develop and prevent convergence.

Weakly compressible *vs.* incompressible profiles Following Grenier [149], the pressure oscillations could result from the inconsistency between the incompressible pressure profile imposed and the weakly compressible solution of the resolved equations. For $\xi \neq 1$, the pressure profile can be computed by applying the state equation to the density solution:

$$\rho\left(z\right) = \rho_0 \left(1 + \frac{\left(1-\xi\right) g \left(h_s - z\right)}{c_0^2}\right)^{\frac{1}{\xi - 1}} \tag{A.6}$$

One can compare this solution to the linear solution in Figures A.1a and A.1b for respective sound speeds of 3 m/s and 32 m/s (the higher value being then considered in the following). Discrepancies are only visible for small sound speeds. For 32 m/s, the maximal discrepancy is below 0.5 % so that the incompressible pressure profile can be imposed. No difference was noted in the numerical tests.

Particle rearrangement During the first iterations, one can observe a settlement of the set of particles due to the compressibility: this rearrangement generates particle motions, density variations and therefore pressure oscillations. One can also always observe a reorganization of the first layers below the free surface, with a free surface denser in particles. They have a pressure of order $\rho_0 g \delta r$ (variations around 10-15% around this value). Near the walls, a small meniscus appear.

Let us consider a converged state and focus on the central column. Figure A.3a displays the vertical displacement of the particles with respect to their initial position. It varies continuously along the column with a maximum around $z_\star = 0.7$ and a noisy behavior close to the bottom and the free surface, highlighting the influence of boundary conditions. With periodic conditions

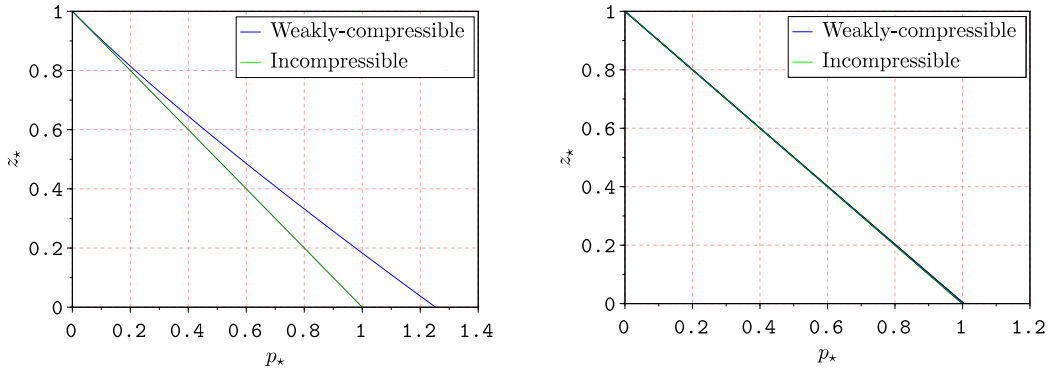

(a) Ma ≈ 1 (b) Ma ≈ 0.1

Figure A.1: Single-fluid hydrostatic case: dimensionless analytical pressure profile.

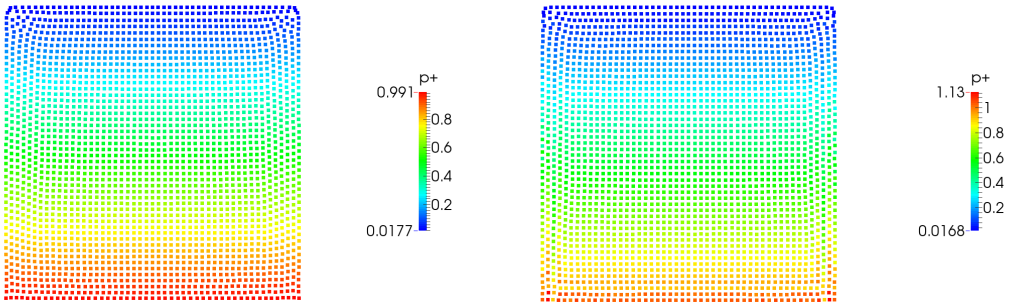

(a) With volume diffusion. (b) Without volume diffusion.

Figure A.2: Single-fluid hydrostatic case: dimensionless pressure at $t_\star = 62.6$.

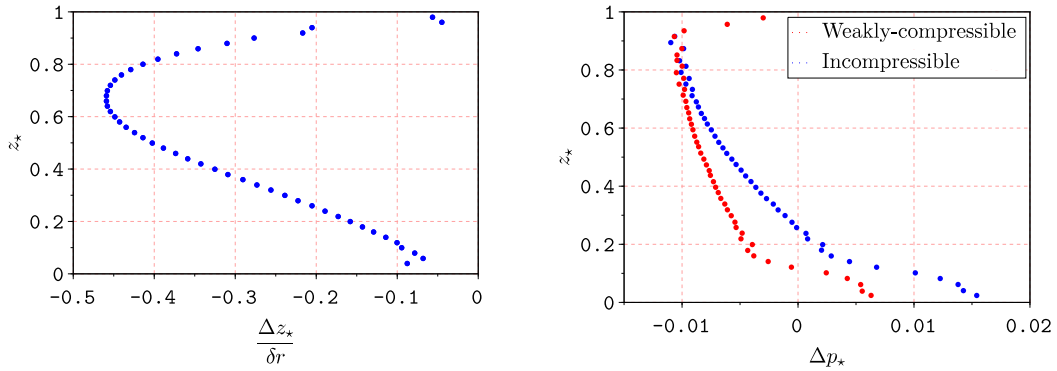

(a) Vertical displacement of the particles with respect to their initial position

(b) Pressure profile discrepancy depending on the initialization with the weakly-compressible or incompressible profile.

Figure A.3: Single-fluid hydrostatic case: particle rearrangement and pressure variations at $t_\star = 62.6$.

and an initialization with the analytical pressure profile, the oscillations last longer so that one should take a viscosity of 0.3 m^2/s to stabilize the flow in a few seconds. They are no longer damped by the presence of the walls. Fields are nevertheless more regular near the free surface and so does the vertical displacement of particles. Some instabilities were also noticed in long time simulation (100 s) with a rearrangement of particles, peak pressures, global motion and settlement of the free surface. Increasing the sound speed leads to a longer time for stabilization of the pressure field.

A.2.2 Two-fluid case

We now consider the two-phase version of the hydrostatic test case.

Analytical solution The analytical pressure profile can be deduced through the state equation applied to the density:

$$\left\{\begin{array}{rcl} \rho^\alpha &=& \rho_0^\alpha \left[\frac{(\xi^\alpha-1)g(H-z)}{(c_0^\alpha)^2}+1\right]^{\frac{1}{\xi^\alpha-1}} \\ \rho^\beta &=& \rho_0^\beta \left[\frac{\left(\xi^\beta-1\right)g(h_s-z)}{(c_0^\beta)^2}+\left(\frac{\xi^\beta\rho_0^\alpha(c_0^\alpha)^2}{\xi^\alpha\rho_0^\beta(c_0^\beta)^2}\left[\left(\frac{(\xi^\alpha-1)g(H-h_s)}{(c_0^\alpha)^2}+1\right)^{\frac{\xi^\alpha}{\xi^\alpha-1}}-1\right]\right. \\ && \left.+\frac{\xi^\beta}{\rho_0^\beta(c_0^\beta)^2}\left(p_B^\alpha-p_B^\beta\right)+1\right)^{\frac{\xi^\beta-1}{\xi^\beta}}\Bigg]^{\frac{1}{\xi^\beta-1}} \end{array}\right. \tag{A.7}$$

where it has been assumed that the polytropic indices were different from unity.

Issues The specific volume formulation [170] is indicated to be convenient for high density ratio flows. However it was noted that instabilities near the interface develop. An option can be to introduce a background pressure to decrease the gap appearing between the phases. However, background pressure shall remain small with respect to $\rho_0 c_0^2$. In presence of a high density ratio flow, this condition is complex to fulfill in the lighter phase, so that this phase becomes agitated and significant motions can develop in case of periodic lateral conditions until a crash of the simulations. As we use sufficiently high sound speeds, we initialize the pressure field with the linear incompressible profile.

With a viscosity of 0.03 m^2/s and periodic conditions, one obtains the results displayed on Figure A.4a. Compared to the single-phase case, oscillations seem to be damped more rapidly, probably thanks to the presence of the air phase. In this phase, a layer of particles separates from the others and gets denser in particles. The hydrostatic profile is respected in both phases. We obtain the same behavior in a box domain as displayed on Figure A.4b with no real influence of the walls, except at the first iterations. Looking closer to the first iterations of the computations, one can see that particles near the interface in the air phase get by pair as shown on Figure A.5.

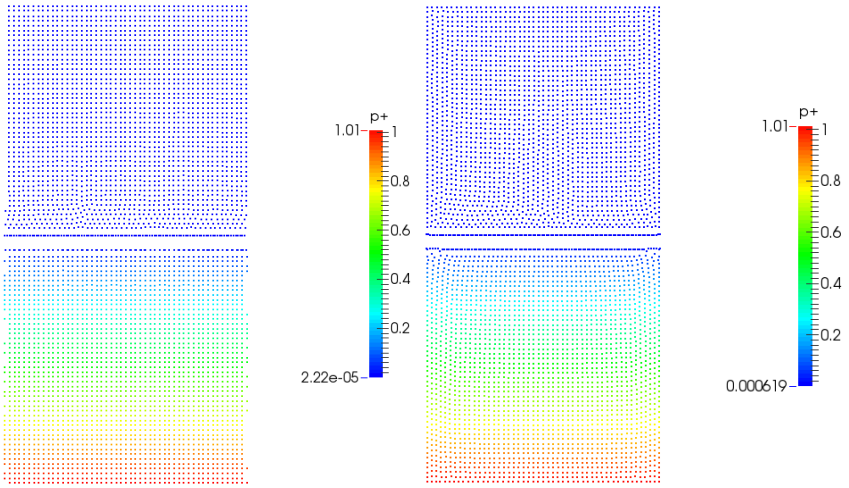

(a) Periodic (b) Box

Figure A.4: Air-water hydrostatic case: dimensionless pressure at $t_\star = 62.6$.

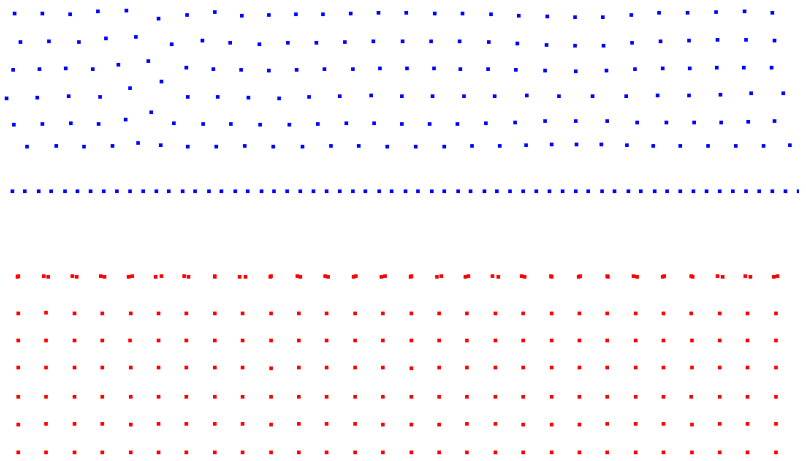

Figure A.5: Air-water hydrostatic case: focus on the air-water interface.

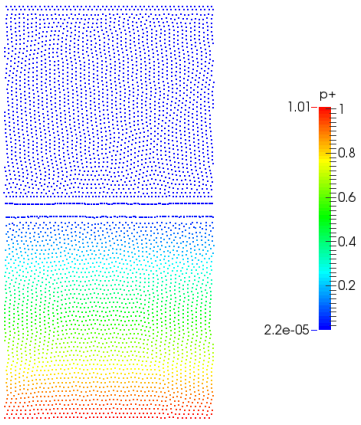

Figure A.6: Air-water hydrostatic case: dimensionless pressure at $t_\star = 62.6$ using physical viscosities.

With physical viscosities, the flow is more agitated in the air phase, with motions close to the interface (velocities of order $v_\star = 0.1 - 0.2$ diminishing progressively). The pressure field oscillations decrease with the time but maintain over the 20 s of physical time considered. A layer of water particles also separates as displayed on Figure A.6. By dividing by two the discretization, the gap is also divided by two: the gap has a size of around $3\delta r$. The clustering almost disappear as testified by Figure A.7.

Sound speeds Following the idea of Colagrossi and Landrini [86], we tried to modify the sound speed. With $c^\alpha = 32$ m/s and $c^\beta = 128$ m/s, the water phase gets agitated and the gap does not seem to be altered. The same can be told by exchanging c^α and c^β. However, we have not considered there a sound speed ratio of 13.5 as suggested by Colagrossi and Landrini [86]. Tests made on the case of stepped spillway detailed in Chapter 4 highlighted that the relation between sound speeds suggested by Colagrossi and Landrini in (2.110) cannot be the only answer in itself as spurious behaviors kept appearing.

Background pressure Introducing a background pressure (one need to close the domain in that case) allows for a reduction of the gap between phases as shown on Figure A.8 using $p_B^\alpha = p_B^\beta = 500$ Pa. Moreover, the clustering disappears for the water phase and fewer air particles form cluster. However, significant velocities are generated in the air phase, of order $\sqrt{gh_s}$, while working with physical viscosities as displayed on Figure A.9.

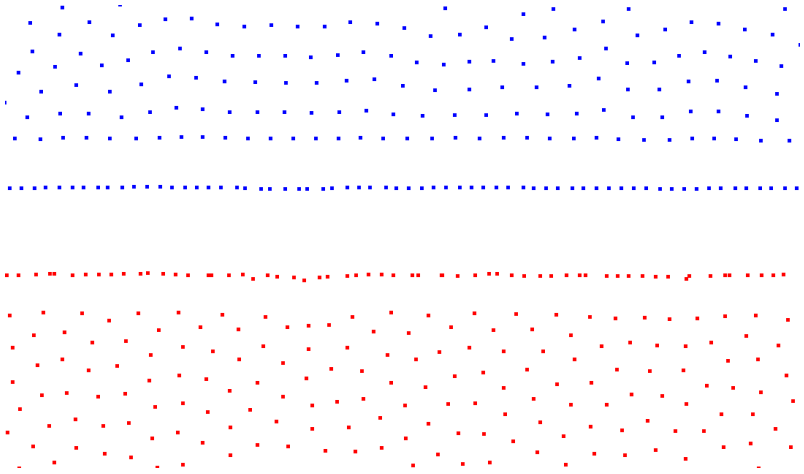

Figure A.7: Air-water hydrostatic case: focus on the air-water interface.

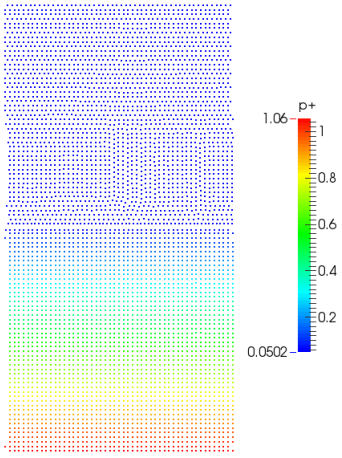

Figure A.8: Air-water hydrostatic case: dimensionless pressure at $t_\star = 62.6$ with background pressure.

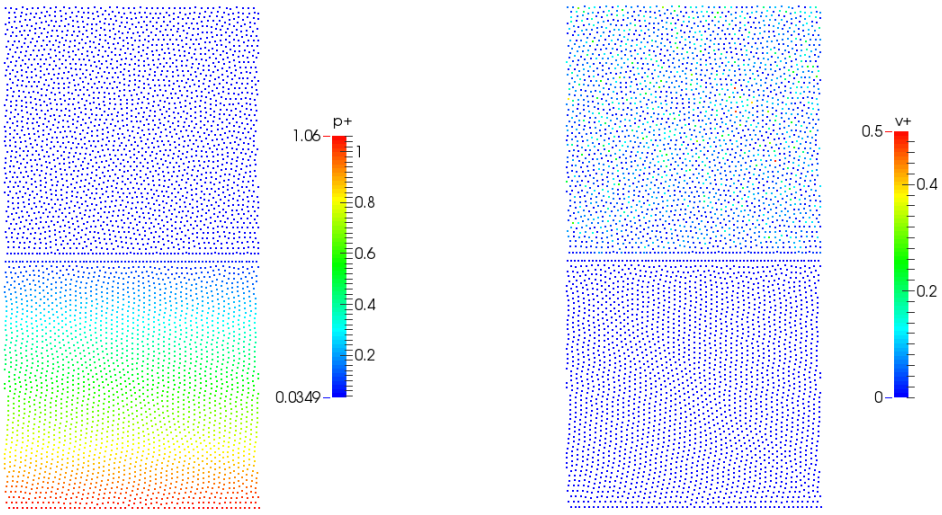

(a) Pressure

(b) Velocity magnitude

Figure A.9: Air-water hydrostatic case: flow at at $t_\star = 62.6$ with background pressure and physical viscosities.

A.2.3 Attempts of pressure gradient modifications

The pressure gradient computation is at the core of the nonphysical gap appearing at the air-water interface. We tried to test or develop some alternate formulations to improve this behavior. These attempts proved to be unsuccessful, but we detail here the main ideas.

Consistently with the derivation made in Section 2.2.1.2, numerical computations highlighted that the error on the pressure gradient close to the interface was effectively of the order of $|\boldsymbol{F}_{\beta\to\alpha}|$. This reasoning suggests a correction to apply to the pressure gradient to recover the expected pressure gradient in the hydrostatic case: $\boldsymbol{F}_{\beta\to\alpha}$ should be subtracted to the discrete pressure gradient. However, this correction led to significant nonphysical motion of the particles close to the interface and may not apply in non-hydrostatic cases.

To assess the behavior at the interface of alternate formulations, we follow the approach developed in Section 2.2.1.2 when possible to write explicitly the force generated by the continuous SPH interpolation of the pressure gradient at the interface, assuming an incompressible hydrostatic solution (compressibility effects might alter some conclusions at high density ratios). However, instead of replacing directly the pressure gradient by its analytical expression as in Section 2.2.1.2, we will work with the form obtained after the integration by parts (except for the approach computing the pressure gradient only on the associated phase) so that the derivative is applied to the kernel (pressure will be replaced by its linear incompressible solution profile).

This process makes appear a new variable linked to the position of the interface:

$$\boldsymbol{F}_{\beta\to\alpha}\left(\boldsymbol{r}\right)=\left(1-\frac{\rho^{\beta}}{\rho^{\alpha}}\right)\int_{\Omega_{\boldsymbol{r}}\cap\Omega^{\beta}}\left(\lambda\left(\boldsymbol{r},\boldsymbol{r}'\right)-1\right)\left[\left(\boldsymbol{r}-\boldsymbol{r}'\right)\cdot\boldsymbol{g}\right]\boldsymbol{\nabla}_{\boldsymbol{r}}w\left(\boldsymbol{r}-\boldsymbol{r}'\right)dV' \tag{A.8}$$

where $\lambda\left(\boldsymbol{r},\boldsymbol{r}'\right)$ is the ratio of the distance from $\boldsymbol{r}$ to the interface in the direction $\left(\boldsymbol{r}-\boldsymbol{r}'\right)$ to the distance $\left|\boldsymbol{r}-\boldsymbol{r}'\right|$, defined only if there is indeed an interface between $\boldsymbol{r}$ and $\boldsymbol{r}'$. Due to this new variable, it is harder to read the content of the integral but one can still see that the density ratio plays a prominent role and generates a strong force in the air phase. For the recall, in the ideal case, this force $\boldsymbol{F}_{\beta\to\alpha}$ should be null.

A.2.3.1 Developed models

Include the gravity term in the pressure gradient One can integrate directly the computation of the gravity within the pressure gradient:

$$\begin{aligned}
-\tfrac{1}{\rho}\boldsymbol{\nabla}p+\boldsymbol{g} &= -\tfrac{1}{\rho}\left(\boldsymbol{\nabla}p-\rho\boldsymbol{g}\right)\\
&= -\tfrac{1}{\rho}\left(\boldsymbol{\nabla}p-\rho\boldsymbol{g}\boldsymbol{\nabla}\cdot\boldsymbol{r}\right)\\
&= -\tfrac{1}{\rho}\left(\boldsymbol{\nabla}p-\boldsymbol{\nabla}\left[\rho\boldsymbol{g}\cdot\boldsymbol{r}\right]+\left[\boldsymbol{g}\cdot\boldsymbol{r}\right]\boldsymbol{\nabla}\rho\right)\\
&= -\tfrac{1}{\rho}\boldsymbol{\nabla}\left[p-\rho\boldsymbol{g}\cdot\boldsymbol{r}\right]-\left[\boldsymbol{g}\cdot\boldsymbol{r}\right]\tfrac{\boldsymbol{\nabla}\rho}{\rho}
\end{aligned}$$

To compute a local effect of the gravity on particle at position $\boldsymbol{r}_a$, one can subtract and add on the right-hand side the term $\frac{1}{\rho}\boldsymbol{\nabla}\left[\rho\boldsymbol{g}\cdot\boldsymbol{r}_a\right]$ and one gets finally:

$$-\frac{1}{\rho}\boldsymbol{\nabla}p+\boldsymbol{g}=-\frac{1}{\rho}\boldsymbol{\nabla}\left[p-\rho\boldsymbol{g}\cdot\left(\boldsymbol{r}-\boldsymbol{r}_a\right)\right]-\left[\boldsymbol{g}\cdot\left(\boldsymbol{r}-\boldsymbol{r}_a\right)\right]\frac{\boldsymbol{\nabla}\rho}{\rho} \tag{A.9}$$

The discrete SPH counterpart of this relation is at position $\boldsymbol{r}_a$:

$$\left[-\frac{1}{\rho}\boldsymbol{\nabla}p+\boldsymbol{g}\right]_a=-\frac{1}{\rho_a}\left[\boldsymbol{\nabla}\left(p-\rho\boldsymbol{g}\cdot\left(\boldsymbol{x}-\boldsymbol{x}_a\right)\right)\right]_a \tag{A.10}$$

However the simplification of the last term might not be legitimate in case of two-phase flow due to the indeterminacy of the term $\left[\boldsymbol{g}\cdot\left(\boldsymbol{x}-\boldsymbol{x}_a\right)\right]\frac{\boldsymbol{\nabla}\rho}{\rho}$ at the interface. In the multifluid formalism, it leads to the antisymmetric operator:

$$\left[-\frac{1}{\rho}\boldsymbol{\nabla}p+\boldsymbol{g}\right]_a=-\frac{1}{m_a\gamma_a}\sum_{b\in\mathcal{F}}\left(p_aV_a^2+\left(p_b+\rho_b\boldsymbol{g}\cdot\boldsymbol{r}_{ab}\right)V_b^2\right)\boldsymbol{\nabla}w_{ab} \tag{A.11}$$

The force generated by the continuous SPH interpolation in the air phase close to the interface writes:

$$\boldsymbol{F}_{\beta\to\alpha}\left(\boldsymbol{r}\right)=\int_{\Omega_{\boldsymbol{r}}\cap\Omega^{\beta}}\left[\left(1-\lambda\left(\boldsymbol{r},\boldsymbol{r}'\right)\right)+\lambda\left(\boldsymbol{r},\boldsymbol{r}'\right)\frac{\rho^{\beta}}{\rho^{\alpha}}\right]\left[\boldsymbol{g}\cdot\left(\boldsymbol{r}-\boldsymbol{r}'\right)\right]\boldsymbol{\nabla}_{\boldsymbol{r}}w\left(\boldsymbol{r}-\boldsymbol{r}'\right)dV' \tag{A.12}$$

One can see that there is still a dependence on the density ratio.

Compute the pressure gradient only on the associated phase The idea is to include contributions to the SPH gradient only from particles of the same phase, and to renormalize the result due to the missing support. In the air water hydrostatic case, we would recover approximately the same acceleration for both phases at the interface. This approach may lack of physical background, as the pressure of the other phase does not influence directly the one the phase considered. The force generated by the continuous SPH interpolation in the air phase close to the interface writes:

$$\boldsymbol{F}_{\beta\to\alpha}\left(\boldsymbol{r}\right)=-\boldsymbol{g}\int_{\Omega_{\boldsymbol{r}}\cap\Omega^{\alpha}}w\left(\boldsymbol{r}-\boldsymbol{r}'\right)dV' \tag{A.13}$$

For a perfectly plane interface, particles have the same acceleration at both sides, but the force, which no longer depends on the density ratio, is not null.

FV-like derivation In FV formulations, a common approach is to split the pressure between its hydrostatic and dynamical parts:

$$p_{a|b}=p_{a|b}^{h}+p'_{a|b} \tag{A.14}$$

Let us write $\boldsymbol{d}_{ab}$ the vector directed along $\boldsymbol{r}_{ab}$ whose norm equals the distance from a to the interface in the direction $\boldsymbol{r}_{ab}$. We will write $\boldsymbol{d}_{ab}=\lambda_{ab}\boldsymbol{r}_{ab}$ (λ_{ab} is the discrete version of the function λ introduced before). We then have two ways of writing the hydrostatic pressure at the interface $a|b$:

$$p_{a|b}^{h}=p_{a}^{h}+\left(\boldsymbol{r}_{a|b}-\boldsymbol{r}_{a}\right)\cdot\boldsymbol{\nabla}_{a}p^{h}=p_{a}^{h}-\boldsymbol{d}_{ab}\cdot\boldsymbol{\nabla}_{a}p^{h} \tag{A.15}$$

$$p_{a|b}^{h}=p_{b}^{h}+\left(\boldsymbol{r}_{a|b}-\boldsymbol{r}_{b}\right)\cdot\boldsymbol{\nabla}_{b}p^{h}=p_{b}^{h}+\left(\boldsymbol{r}_{ab}-\boldsymbol{d}_{ab}\right)\cdot\boldsymbol{\nabla}_{b}p^{h} \tag{A.16}$$

Using λ_{ab}, these expressions write:

$$p_{a|b}^{h}=p_{a}^{h}-\lambda_{ab}\boldsymbol{r}_{ab}\cdot\boldsymbol{\nabla}_{a}p^{h} \tag{A.17}$$

$$p_{a|b}^{h}=p_{b}^{h}+\left(1-\lambda_{ab}\right)\boldsymbol{r}_{ab}\cdot\boldsymbol{\nabla}_{b}p^{h} \tag{A.18}$$

Let us now write the dynamic part in an approximate way:

$$p_{a|b}^{d}=p_{a|b}-p_{a|b}^{h} \tag{A.19}$$

We use a weighting coefficient c_{ab} to approximate in the same manner both terms of the right-hand side:

$$p^d_{a|b} = (1 - c_{ab})p_a + c_{ab}p_b - (1 - c_{ab})p^h_a - c_{ab}p^h_b \tag{A.20}$$

Finally we compute the pressure at the interface, discretizing in two different ways the hydrostatic part:

$$p_{a|b} = p^h_{a|b} + p^d_{a|b} = (1 - c_{ab})p^h_{a|b} + c_{ab}p^h_{a|b} + p^d_{a|b} \tag{A.21}$$

$$\begin{aligned} p_{a|b} = (1 - c_{ab}) \left(p^h_a - \lambda_{ab}\boldsymbol{r}_{ab} \cdot \boldsymbol{\nabla}_a p^h\right) + c_{ab} \left(p^h_b + (1 - \lambda_{ab})\, \boldsymbol{r}_{ab} \cdot \boldsymbol{\nabla}_b p^h\right) \\ +(1 - c_{ab})p_a + c_{ab}p_b - (1 - c_{ab})p^h_a - c_{ab}p^h_b \end{aligned} \tag{A.22}$$

Simplifying:

$$p_{a|b} = -(1 - c_{ab})\lambda_{ab}\boldsymbol{r}_{ab} \cdot \boldsymbol{\nabla}_a p^h + c_{ab}\,(1 - \lambda_{ab})\,\boldsymbol{r}_{ab} \cdot \boldsymbol{\nabla}_b p^h + (1 - c_{ab})p_a + c_{ab}p_b \tag{A.23}$$

We now use the information we have on the hydrostatic pressure:

$$\boldsymbol{\nabla}_a p^h = \rho_a \boldsymbol{g} \tag{A.24}$$

To write the previous equation:

$$p_{a|b} = \left[c_{ab}\,(1 - \lambda_{ab})\,\rho_b - (1 - c_{ab})\lambda_{ab}\rho_a\right](\boldsymbol{r}_{ab} \cdot \boldsymbol{g}) + (1 - c_{ab})p_a + c_{ab}p_b \tag{A.25}$$

Taking $c_{ab} = \lambda_{ab}$:

$$p_{a|b} = (1 - \lambda_{ab})p_a + \lambda_{ab}p_b - \lambda_{ab}\,(1 - \lambda_{ab})\,(\rho_a - \rho_b)\,(\boldsymbol{r}_{ab} \cdot \boldsymbol{g}) \tag{A.26}$$

Finally, using the FV-SPH transformation as detailed in Section 3.2.1.2:

$$V_a \boldsymbol{G}_a\{p_b\} = \sum_b p_{a|b}\boldsymbol{S}_{a|b} \quad \text{with} \quad \boldsymbol{S}_{a|b} = 2V_a V_b \boldsymbol{\nabla} w_{ab} \tag{A.27}$$

We finally get:

$$\boldsymbol{G}_a\{p_b\} = 2\sum_{b\in\mathcal{F}} V_b \left[(1 - \lambda_{ab})p_a + \lambda_{ab}p_b - \lambda_{ab}\,(1 - \lambda_{ab})\,(\rho_a - \rho_b)\,(\boldsymbol{r}_{ab} \cdot \boldsymbol{g})\right] \boldsymbol{\nabla} w_{ab} \tag{A.28}$$

This approach suffers however a main drawback: one has to compute the distance to the interface, that needs to be well-defined. In absence of interface for the particle pair (a, b), one should take $\lambda = 1/2$. This issue does not appear in the FV framework as the cells are interacting only with their direct neighbors. It seems that this approach cannot therefore be of practical use in SPH. The force generated by the continuous SPH interpolation in the air phase close to the interface

writes:

$$\boldsymbol{F}_{\beta\to\alpha}\left(\boldsymbol{r}\right)=\int_{\Omega_{\boldsymbol{r}}\cap\Omega^{\beta}}\left(2\lambda\left(\boldsymbol{r},\boldsymbol{r}'\right)-1\right)\left[\boldsymbol{g}\cdot\left(\boldsymbol{r}-\boldsymbol{r}'\right)\right]\boldsymbol{\nabla}_{\boldsymbol{r}}w\left(\boldsymbol{r}-\boldsymbol{r}'\right)dV' \tag{A.29}$$

One can see that for $\lambda=1/2$, this term cancels out. However it happens only for particles at symmetrical position with respect to the interface so that we are still applying a force. The significant benefit is that this force does not depend on the density ratio.

A.2.3.2 Models of the literature

Several expressions of the pressure gradient have been used in the literature as shown in Chapter 2. The basic expressions usually fall within the reasoning presented in Section 2.2.1.2. We detail below two different approaches.

Adverse phase ghost particles As presented in Section 2.2.2.5, Zhou et al. [401] suggested to make a correction on neighboring pressures when evaluating the pressure gradient for air particles following (2.123) with a case dependent parameter c_p between 0 and 1 (depends on the deformation of the interface and the compressibility). For the hydrostatic case they used 0.995 but when we tested the approach it seemed better to take $c_p=1$ as illustrated on Figure A.10 to avoid any instability development. In this case one can see by detailing the numerical operator that it roughly amounts to replace the the pressure of the particles of the adverse phase by p_a. No gap appeared between phases and the fluid remains at rest after the damping of small oscillations of the velocity field within the whole domain. However, taking $c_p=1$ decouples the pressures of each phase.

Inter-particle pressure Hu and Adams [171] described an operator relying on the inter-particle pressure as shown in Section 2.2.2.6. One cannot perform the continuous SPH analysis made for the other cases, but the discrete SPH interpolation can be studied. The force generated in the air phase close to the interface writes approximately (volumes have been replaced by the reference volume to simplify the computations):

$$\begin{aligned}\boldsymbol{F}_{\beta\to\alpha}\left(\boldsymbol{r}_a\right) &= \frac{2p_a}{\rho^{\alpha}}\sum_{b\in\mathcal{F}}V_0\boldsymbol{\nabla}w_{ab}-\boldsymbol{g}-\sum_{b\in\mathcal{F}}V_0\boldsymbol{g}\cdot\boldsymbol{r}_{ab}\boldsymbol{\nabla}w_{ab}\\ &\quad+\mathsf{A}\sum_{b\in\mathcal{F}\cap\Omega^{\beta}}V_0\left(2\lambda_{ab}-1\right)\left(\boldsymbol{g}\cdot\boldsymbol{r}_{ab}\right)\boldsymbol{\nabla}w_{ab}\end{aligned}$$

where $\mathsf{A}=\frac{\rho^{\beta}-\rho^{\alpha}}{\rho^{\alpha}+\rho^{\beta}}$ is the Atwood number. From a continuous interpolation point of view, the right-hand side of the first line cancels out and only the second line remains. The force is different depending on the phase considered but the influence of the high density ratio is mitigated thanks to the presence of the Atwood number.

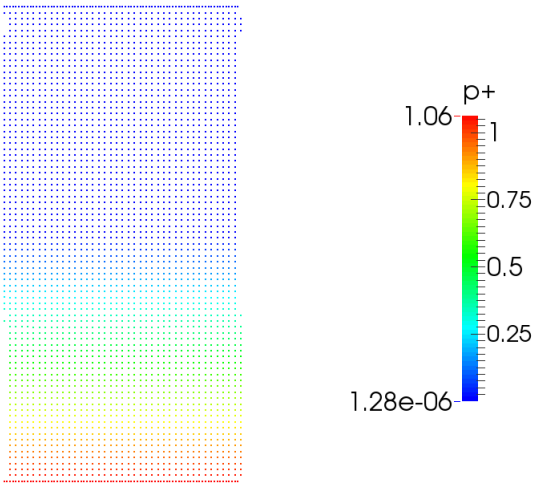

Figure A.10: Air-water hydrostatic pressure: simulation after 30 s with Zhou et al.'s approach.

A.2.4 Summary

We have highlighted in this section the numerical issues encountered due to the pressure gradient computations, in single-fluid and multifluid simulations involving a high density ratio between the phases. No completely satisfactory solution has been found in the literature nor in our developments. In order to limit the use of tuning parameters and keep antisymmetric forms in view of momentum conservation, we chose to use in the present work the specific volume formulation of Hu and Adams [170] followed by Ghaïtanellis et al. [145]. It generally requires to introduce a limited background pressure found by iterations: it should not destabilize too much the lighter phase while maintaining a reduced gap between the phases. We have to keep in mind that the solution for the pressure field is not free of noise nor oscillations. Considering different framework like δ–SPH as in Section 2.2.2.8 or Riemann solvers as in Section 2.2.2.9 might be an answer to the issues detailed here and will require further investigations.

Appendix B

The Riemann problem for open boundaries

In this appendix, we aim at writing a proper numerical framework for open boundaries adapted to the mixture model presented. Following the reasoning of Ferrand et al. [129], it consists in:

- Introducing additional terms in the continuity equation B.15 to avoid spurious density variations and nonphysical behavior near open boundaries;
- Deriving a numerical scheme to get compatible velocity and pressure fields at open boundaries through the resolution of a partial one-dimensional Riemann problem, as done in the SPH–ALE framework by [179].

We first focus on the single-fluid approach, remedying some approximations, and then extend it to the mixture model formulation.

B.1 Continuity equation and open boundaries

The following derivation follows faithfully [129], but replacing the density ρ by the inverse of the volume noted σ, making some adjustments when needed. The volume update relies on the interpolation of the inverse of the volume (2.113). From the continuity equation (B.15), one has:

$$\frac{d\sigma_a}{dt} = -\sigma_a D_a^\gamma\{\boldsymbol{j}\} \tag{B.1}$$

with:

$$D_a^\gamma\{\boldsymbol{j}\} = -\frac{1}{\gamma_a\sigma_a}\sum_{b\in(\mathcal{F}\cup\mathcal{V})}\theta_b\left(\boldsymbol{j}_a-\boldsymbol{j}_b\right)\cdot\boldsymbol{\nabla}w_{ab} + \frac{1}{\gamma_a\sigma_a}\sum_{s\in\mathcal{S}}\sigma_s\left(\boldsymbol{j}_a-\boldsymbol{j}_s\right)\cdot\boldsymbol{\nabla}\gamma_{as} \tag{B.2}$$

Let us make the distinction between the Eulerian fluid velocity $\boldsymbol{J}_b$ and the Lagrangian particle velocity $\boldsymbol{j}_b$. Additional terms then appear in the divergence operator computation and lead to:

$$\frac{d\sigma_a}{dt} = \frac{1}{\gamma_a} \sum_{b\in(\mathcal{F}\cup\mathcal{V})} \theta_b \left(\boldsymbol{j}_a - \boldsymbol{j}_b\right) \cdot \boldsymbol{\nabla} w_{ab} - \delta\sigma_a^{i/o} - \frac{1}{\gamma_a} \sum_s \sigma_s \left(\boldsymbol{j}_a - \boldsymbol{j}_s\right) \cdot \boldsymbol{\nabla}\gamma_{as} + \frac{\sigma_a}{\gamma_a}\delta\gamma_a^{i/o} \tag{B.3}$$

With the definitions:

$$\delta\sigma_a^{i/o} = \frac{1}{\gamma_a} \sum_{v\in\mathcal{V}^{I/O}} \theta_v \left(\boldsymbol{J}_v - \boldsymbol{j}_v\right) \cdot \boldsymbol{\nabla} w_{av} \tag{B.4}$$

$$\delta\gamma_a^{i/o} = \sum_{s\in\mathcal{S}^{I/O}} \frac{\sigma_s}{\sigma_a} \left(\boldsymbol{J}_s - \boldsymbol{j}_s\right) \cdot \boldsymbol{\nabla}\gamma_{as} \tag{B.5}$$

where $\mathcal{V}^{I/O}$ and $\mathcal{S}^{I/O}$ are respectively the sets of vertex particles and segments belonging to the open boundaries. In a Lagrangian frame, (1.93) leads to:

$$\frac{dw_{ab}}{dt} = \left(\boldsymbol{j}_a - \boldsymbol{j}_b\right) \cdot \boldsymbol{\nabla} w_{ab} \tag{B.6}$$

$$\frac{d\gamma_a}{dt} = \sum_{s\in\mathcal{S}} \left(\boldsymbol{j}_a - \boldsymbol{j}_s\right) \cdot \boldsymbol{\nabla}\gamma_{as} \tag{B.7}$$

If one makes the approximation:

$$\frac{d\gamma_a}{dt} \approx \sum_{s\in\mathcal{S}} \frac{\sigma_s}{\sigma_a} \left(\boldsymbol{j}_a - \boldsymbol{j}_s\right) \cdot \boldsymbol{\nabla}\gamma_{as} \tag{B.8}$$

as volume variations remain limited, (B.3) now writes:

$$\frac{d\sigma_a}{dt} = \frac{1}{\gamma_a}\frac{d}{dt}\left(\sum_{b\in(\mathcal{F}\cup\mathcal{V})} \theta_b w_{ab}\right) - \delta\sigma_a^{i/o} - \frac{\sigma_a}{\gamma_a}\frac{d\gamma_a}{dt} + \frac{\sigma_a}{\gamma_a}\delta\gamma_a^{i/o} \tag{B.9}$$

Hence:

$$\frac{d}{dt}\left(\gamma_a\sigma_a\right) = \gamma_a\frac{d\sigma_a}{dt} + \sigma_a\frac{d\gamma_a}{dt} = \frac{d}{dt}\left(\sum_{b\in(\mathcal{F}\cup\mathcal{V})} \theta_b w_{ab}\right) - \gamma_a\delta\sigma_a^{i/o} + \sigma_a\delta\gamma_a^{i/o} \tag{B.10}$$

The temporal integration of the continuity equation between t^n and t^{n+1} leads to:

$$\left(\gamma_a\sigma_a\right)^{n+1} - \left(\gamma_a\sigma_a\right)^n = \sum_{b\in(\mathcal{F}\cup\mathcal{V})} \left(\theta_b^{n+1} w_{ab}^{n+1} - \theta_b^n w_{ab}^n\right) - \int_{t^n}^{t^{n+1}} \gamma_a\delta\sigma_a^{i/o} + \int_{t^n}^{t^{n+1}} \sigma_a\delta\gamma_a^{i/o} \tag{B.11}$$

With the virtual displacement $\delta r_a^{i/o} = \delta t \left(\boldsymbol{J}_a^n - \boldsymbol{j}_a^n \right)$, the virtual variations terms write:

$$\int_{t^n}^{t^{n+1}} \gamma_a \delta \sigma_a^{i/o} = \sum_{v \in \mathcal{V}^{I/O}} \theta_v^n \left(w \left(\boldsymbol{r}_{av}^n + \delta \boldsymbol{r}_v^{i/o} \right) - w \left(\boldsymbol{r}_{av}^n \right) \right) \tag{B.12}$$

$$\int_{t^n}^{t^{n+1}} \sigma_a \delta \gamma_a^{i/o} = \frac{1}{2} \sum_{s \in \mathcal{S}^{I/O}} \sigma_s^n \left(\boldsymbol{\nabla} \gamma_{as} \left(\boldsymbol{r}_{as}^n + \delta \boldsymbol{r}_s^{i/o} \right) + \boldsymbol{\nabla} \gamma_{as} \left(\boldsymbol{r}_{as}^n \right) \right) \cdot \delta \boldsymbol{r}_s^{i/o} \tag{B.13}$$

where $\delta r_s^{i/o} = \delta t \left(\boldsymbol{J}_s^n - \boldsymbol{j}_s^n \right)$ and $\delta r_v^{i/o} = \delta t \left(\boldsymbol{J}_v^n - \boldsymbol{j}_v^n \right)$. In the present work, the factor σ_s^n was approximated by σ_a^n, consistently with the approximation (B.8). For an analytical computation of γ_a:

$$\int_{t^n}^{t^{n+1}} \sigma_a \delta \gamma_a^{i/o} = \sum_{s \in \mathcal{S}^{I/O}} \sigma_s^n \left(\gamma_{as} \left(\boldsymbol{r}_{as}^n + \delta \boldsymbol{r}_s^{i/o} \right) - \gamma_{as} \left(\boldsymbol{r}_{as}^n \right) \right) \tag{B.14}$$

B.2 Single-fluid approach

Compared to the usual framework in which such a derivation is made in finite volumes, *e.g.* [26], the WCSPH framework introduces two assumptions that simplify the resolution of the Riemann problem at boundaries. As discussed in 1.3.4, the flow is *barotropic*, hence pressure and density/volume are directly linked (*i.e.* an equality of pressures is tantamount to an equality of densities in the single-fluid configuration). Moreover, the flow is assumed to be *subsonic*, as the sound speed is chosen to be ten times the maximum velocity reached in the domain. However, it may punctually happen that particles get some spurious behaviors that put the simulation out of this theoretical framework.

B.2.1 Governing equations

In the bulk of the fluid, the following equations, written in non conservative form, are solved:

$$\frac{\partial \rho}{\partial t} + \boldsymbol{u} \cdot \boldsymbol{\nabla} \rho = -\rho \boldsymbol{\nabla} \cdot \boldsymbol{u} \tag{B.15}$$

$$\frac{\partial \boldsymbol{u}}{\partial t} + \boldsymbol{u} \cdot \boldsymbol{\nabla} \boldsymbol{u} = -\frac{1}{\rho} \boldsymbol{\nabla} p - \frac{1}{\rho} \boldsymbol{\nabla} \cdot (\mu \boldsymbol{\nabla} \boldsymbol{u}) + \boldsymbol{g} \tag{B.16}$$

From (1.106) and (1.11), one gets:

$$\boldsymbol{\nabla} p = c^2 \boldsymbol{\nabla} \rho \tag{B.17}$$

where $c = \sqrt{\dfrac{\partial p}{\partial \rho}} = c_0 \left(\frac{\rho}{\rho_0} \right)^{\frac{\xi - 1}{2}}$. For the resolution at the open boundary, we will neglect the viscous effects and the gravity to work with the hyperbolic system of Euler equations for which

theoretical results are available [335]. The system writes:

$$\frac{\partial \rho}{\partial t} + \boldsymbol{u} \cdot \boldsymbol{\nabla} \rho = -\rho \boldsymbol{\nabla} \cdot \boldsymbol{u} \tag{B.18}$$

$$\frac{\partial \boldsymbol{u}}{\partial t} + \boldsymbol{u} \cdot \boldsymbol{\nabla} \boldsymbol{u} = -\frac{c^2}{\rho} \boldsymbol{\nabla} \rho \tag{B.19}$$

B.2.2 1D Riemann problem formulation

We now project the governing equations (B.18) and (B.19) along the normal to the boundary oriented towards the domain (n denotes the normal component and τ the tangential component; $u_n = \boldsymbol{u} \cdot \boldsymbol{n}$ and $u_\tau = \boldsymbol{u} \cdot \boldsymbol{\tau}$) and neglect all the tangential derivatives:

$$\frac{\partial \rho}{\partial t} + u_n \frac{\partial \rho}{\partial n} + \rho \frac{\partial u_n}{\partial n} = 0 \tag{B.20}$$

$$\frac{\partial u_n}{\partial t} + u_n \frac{\partial u_n}{\partial n} + \frac{c^2}{\rho} \frac{\partial \rho}{\partial n} = 0 \tag{B.21}$$

$$\frac{\partial u_\tau}{\partial t} + u_n \frac{\partial u_\tau}{\partial n} = 0 \tag{B.22}$$

We can now put the non conservative system under the form:

$$\frac{\partial}{\partial t} \boldsymbol{W} + \boldsymbol{B}\left(\boldsymbol{W}\right) \frac{\partial \boldsymbol{W}}{\partial \boldsymbol{n}} = 0 \tag{B.23}$$

where:

$$\boldsymbol{W} = \begin{pmatrix} \rho \\ u_n \\ u_\tau \end{pmatrix} \text{ and } \boldsymbol{B}\left(\boldsymbol{W}\right) = \begin{pmatrix} u_n & \rho & 0 \\ \frac{c^2}{\rho} & u_n & 0 \\ 0 & 0 & u_n \end{pmatrix} \tag{B.24}$$

B.2.2.1 Eigenvalue problem

The matrix $\boldsymbol{B}$ has three distinct eigenvalues: $\lambda_{-1} = u_n - c$, $\lambda_0 = u_n$ and $\lambda_{+1} = u_n + c$. The corresponding right eigenvectors are:

$$\boldsymbol{r}_{-1} = \begin{pmatrix} -\rho \\ c \\ 0 \end{pmatrix} \text{ and } \boldsymbol{r}_0 = \begin{pmatrix} 0 \\ 0 \\ 1 \end{pmatrix} \text{ and } \boldsymbol{r}_{+1} = \begin{pmatrix} \rho \\ c \\ 0 \end{pmatrix} \tag{B.25}$$

B.2.2.2 Riemann invariants

Following Smoller [335], we consider the system of n_r equations:

$$\frac{\partial \boldsymbol{W}}{\partial t} + \boldsymbol{\nabla} \cdot \boldsymbol{f}_r(\boldsymbol{W}) = 0 \tag{B.26}$$

In our case $\boldsymbol{W} = (\rho, u_n, u_\tau)$. Let us consider N a neighborhood in $\mathbb{R}^{n_r}$ in which $\boldsymbol{f}_r(\boldsymbol{W})$ is smooth.

Definition B.2.1 *Riemann invariant. A k-Riemann invariant is a smooth function $w_r : N \to \mathbb{R}$ such that if $\boldsymbol{W} \in N$,*

$$\boldsymbol{r}_k(\boldsymbol{W}) \cdot \boldsymbol{\nabla} w_r(\boldsymbol{W}) = 0 \tag{B.27}$$

Proposition B.2.1 *There are $(n-1)$ k-Riemann invariants whose gradients are linearly independent in N.*

According to this proposition, we shall find two k-Riemann invariants for each of our three eigenvalues k.

- For λ_{-1}, the -1-Riemann invariants must satisfy $-\rho \dfrac{\partial w_r}{\partial \rho} + c \dfrac{\partial w_r}{\partial u_n} = 0$
- For λ_0, the 0-Riemann invariants must satisfy $\dfrac{\partial w_r}{\partial u_\tau} = 0$
- For λ_{+1}, the 1-Riemann invariants must satisfy $\rho \dfrac{\partial w_r}{\partial \rho} + c \dfrac{\partial w_r}{\partial u_n} = 0$

Those k-Riemann invariants will be conserved as one crosses the associated eigenvalue. We aim at finding linearly independent k-Riemann invariants.

Derivation of k-Riemann invariants We have initially the system:

$$\frac{\partial}{\partial t}\boldsymbol{W} + \boldsymbol{B}\left(\boldsymbol{W}\right)\frac{\partial \boldsymbol{W}}{\partial n} = 0 \tag{B.28}$$

The previous reasoning gave us the eigenvalues and eigenvectors that allow one to write:

$$\boldsymbol{B} = \boldsymbol{P}\boldsymbol{D}\boldsymbol{P}^{-1} \tag{B.29}$$

We can then write:

$$\boldsymbol{P}^{-1}\frac{\partial}{\partial t}\boldsymbol{W} + \boldsymbol{D}\boldsymbol{P}^{-1}\frac{\partial \boldsymbol{W}}{\partial n} = 0 \tag{B.30}$$

If we solve:

$$\boldsymbol{P}^{-1} d\boldsymbol{W} = d\boldsymbol{Z} \Longleftrightarrow \boldsymbol{Z} = \int \boldsymbol{P}^{-1}\left(\boldsymbol{W}\right) d\boldsymbol{W} \tag{B.31}$$

We can finally write:

$$\frac{\partial \boldsymbol{Z}}{\partial t} + \boldsymbol{D}\frac{\partial \boldsymbol{Z}}{\partial \boldsymbol{n}} = \boldsymbol{0} \tag{B.32}$$

Here we have:

$$\boldsymbol{W} = \begin{pmatrix} \rho \\ u_n \\ u_\tau \end{pmatrix} \quad \boldsymbol{D} = \begin{pmatrix} \lambda_{-1} & 0 & 0 \\ 0 & \lambda_{+1} & 0 \\ 0 & 0 & \lambda_0 \end{pmatrix} \quad \boldsymbol{P} = \begin{pmatrix} -\rho & \rho & 0 \\ c & c & 0 \\ 0 & 0 & 1 \end{pmatrix} \tag{B.33}$$

Let us compute the inverse of $\boldsymbol{P}$:

$$\det(\boldsymbol{P}) = -2\rho c \tag{B.34}$$

$${}^t\boldsymbol{P} = \begin{pmatrix} -\rho & c & 0 \\ \rho & c & 0 \\ 0 & 0 & 1 \end{pmatrix} \rightarrow \operatorname{adj}\left({}^t\boldsymbol{P}\right) = \begin{pmatrix} c & -\rho & 0 \\ -c & -\rho & 0 \\ 0 & 0 & -2\rho c \end{pmatrix} \tag{B.35}$$

Hence:

$$\boldsymbol{P}^{-1} = \frac{1}{\det(\boldsymbol{P})}\operatorname{adj}\left({}^t\boldsymbol{P}\right) = \frac{1}{2\rho c}\begin{pmatrix} -c & \rho & 0 \\ c & \rho & 0 \\ 0 & 0 & 2\rho c \end{pmatrix} \tag{B.36}$$

$$\boldsymbol{P}^{-1}d\boldsymbol{W} = \frac{1}{2\rho c}\begin{pmatrix} -c & \rho & 0 \\ c & \rho & 0 \\ 0 & 0 & 2\rho c \end{pmatrix}\begin{pmatrix} d\rho \\ du_n \\ du_\tau \end{pmatrix} = \frac{1}{2c}d\boldsymbol{Z} \tag{B.37}$$

The corresponding system is:

$$\begin{cases} -c\,d\rho + \rho\,du_n = \rho\,dz_1 \\ c\,d\rho + \rho\,du_n = \rho\,dz_2 \\ 2\rho c\,du_\tau = \rho\,dz_3 \end{cases} \rightarrow \begin{cases} -\frac{c}{\rho}d\rho + du_n = dz_1 \\ \frac{c}{\rho}d\rho + du_n = dz_2 \\ du_\tau = \frac{1}{2c}\,dz_3 \end{cases} \tag{B.38}$$

Table B.1: k-Riemann invariants for the single-fluid formulation.

	λ_{-1}	λ_{+1}	λ_0
u_τ	✓	✓	✗
$u_n + \psi_r(\rho)$	✓	✗	✓
$u_n - \psi_r(\rho)$	✗	✓	✓

If we work differently on each equation (dz_i remains unchanged for the first two equations, the third one is multiplied by $2c$), one gets:

$$\begin{cases} dz_1 = -\frac{c}{\rho} d\rho + du_n \\ dz_2 = \frac{c}{\rho} d\rho + du_n \\ dz_3 = du_\tau \end{cases} \tag{B.39}$$

We can now integrate these relations and assign the resulting invariants to their respective eigenvalues in Table B.1 where ψ_r is defined through its differential:

$$d\psi_r = \frac{c(\rho)}{\rho} d\rho \tag{B.40}$$

Depending on the polytropic index, it therefore writes:

$$\psi_r(\rho) = \frac{2c_0}{\xi - 1} \left(\frac{\rho}{\rho_0} \right)^{\frac{\xi-1}{2}} \text{ if } \xi > 1 \text{ and } \psi_r(\rho) = c_0 \ln \left(\frac{\rho}{\rho_0} \right) \text{ if } \xi = 1 \tag{B.41}$$

As expected, one has two invariants for each eigenvalue.

B.2.2.3 Rankine Hugoniot relations

Using the system in conservative form (B.43) and (B.44), one can identify a set of conservative variables:

$$\boldsymbol{Y} = \begin{pmatrix} \rho \\ \rho u_n \\ \rho u_\tau \end{pmatrix} \tag{B.42}$$

The conservative form of the set of equations used to find the Rankine-Hugoniot relations writes:

$$\frac{\partial \rho}{\partial t} + \boldsymbol{\nabla} \cdot (\rho \boldsymbol{u}) = 0 \tag{B.43}$$

$$\frac{\partial \rho \boldsymbol{u}}{\partial t} + \boldsymbol{\nabla} \cdot (p \boldsymbol{I} + \rho \boldsymbol{u} \otimes \boldsymbol{u}) = 0 \tag{B.44}$$

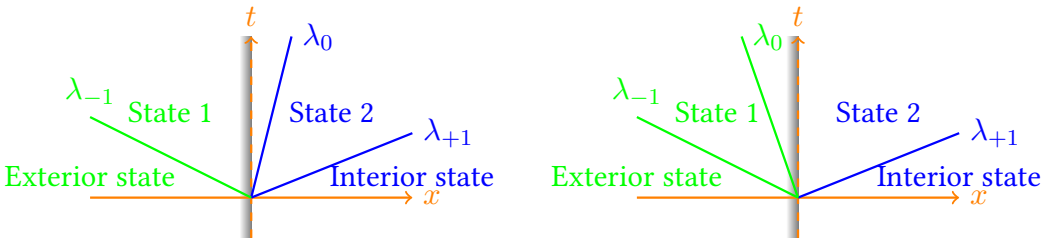

(a) Inlet (b) Outlet

Figure B.1: Riemann problems configurations [129].

In presence of a shock wave, one has therefore the jump conditions between left ℓ and right r sides of the shock:

$$S_c\left(\rho_\ell - \rho_r\right) = \rho_\ell u_{n,\ell} - \rho_r u_{n,r} \tag{B.45}$$

$$S_c\left(\rho_\ell u_{n,\ell} - \rho_r u_{n,r}\right) = p_\ell + \rho_\ell u_{n,\ell}^2 - p_r - \rho_r u_{n,r}^2 \tag{B.46}$$

$$S_c\left(\rho_\ell u_{\tau,\ell} - \rho_r u_{\tau,r}\right) = \rho_\ell u_{n,\ell} u_{\tau,\ell} - \rho_r u_{n,r} u_{\tau,r} \tag{B.47}$$

where S_c is the speed of the shock that is now taken into account compared to [129]. If $\rho_\ell \neq \rho_r$, one can write this system differently as:

$$S_c = \frac{\rho_\ell u_{n,\ell} - \rho_r u_{n,r}}{\rho_\ell - \rho_r} \tag{B.48}$$

$$\rho_\ell \rho_r \left(u_{n,\ell} - u_{n,r}\right)^2 = \left(\rho_\ell - \rho_r\right)\left(p_\ell - p_r\right) \tag{B.49}$$

If $u_{n,\ell} \neq u_{n,r}$, (B.47) can be simplified using (B.45) to get:

$$u_{\tau,\ell} = u_{\tau,r} \tag{B.50}$$

B.2.3 1D Riemann problem resolution

We are now equipped with all the tools to solve the 1D Riemann problem we are studying at the boundary and therefore define compatible pressure and velocity fields. We have shown that three characteristic waves $(\lambda_{-1}, \lambda_0, \lambda_{+1})$ model discontinuities between the exterior state (boundary condition to impose) and the interior state (deduced from bulk fields, by an SPH interpolation in our numerical framework) as illustrated on Figure B.1. Let us have a closer look at each of the characteristic waves:

- As the flow is subsonic, $\lambda_{-1} < 0$ so that the associated wave is outside the domain. We will consider it as a ghost wave so that the data of the exterior state $\boldsymbol{W}_{ext}$ are assumed equal to the data $\boldsymbol{W}_1$ of state 1.

- λ_0 is a contact discontinuity. From the associated Riemann invariants $u_n + \psi_r$ and $u_n - \psi_r$, we deduce that $u_{n,1} = u_{n,2}$ and $\rho_1 = \rho_2$ (equivalently $p_1 = p_2$ due to the barotropic assumption). There might be a jump of u_τ.

- As the flow is subsonic $\lambda_{+1} > 0$. This characteristic wave can belong to two kinds of discontinuity:

  - Expansion wave: characteristics are diverging, the states are connected through a smooth transition and the Riemann invariant holds across the characteristic wave:

$$u_{n,2} + c(\rho_2) < u_{n,int} + c(\rho_{int}) \tag{B.51}$$

$$u_{n,2} - \psi_r(\rho_2) = u_{n,int} - \psi_r(\rho_{int}) \tag{B.52}$$

  - Shock wave: characteristics are converging and the Rankine Hugoniot relations (B.48) and (B.49) apply:

$$u_{n,2} + c(\rho_2) > u_{n,int} + c(\rho_{int}) \tag{B.53}$$

$$\rho_2 \rho_{int} (u_{n,2} - u_{n,int})^2 = (\rho_2 - \rho_{int})(p_2 - p_{int}) \tag{B.54}$$

  For the three types of discontinuity, we have $u_{\tau,2} = u_{\tau,int}$ according to the previous developments (Riemann invariant for contact discontinuity or expansion wave, Rankine Hugoniot relation (B.50) for shock).

Depending on the sign of λ_0, positive or negative, the state at the boundary will be respectively state 1 or state 2 as shown on Figures B.1a and B.1b. However, under our set of assumptions, if we except the tangential discontinuity addressed further, the data of these two states are equivalent so that no distinction needs to be made. Moreover, we saw that considering λ_{-1} as a ghost wave, data of the states 1 and exterior are equal. Hence values at state 2 can be considered as values of the exterior state. In a nutshell, the interior state is known from SPH interpolation of the fields in the bulk of the fluid. According to what the user wants to impose at the boundary, either the external pressure/density or velocity is known and the above relations allow one to deduce the unknown quantity, velocity or pressure/density respectively. The choice of relation will depend on which of the relations (B.51) or (B.53) is fulfilled. For the tangential velocities, in the case of an inlet, they need to be defined by the user. In the case of an outlet, the tangential velocity is determined by the interior state.

B.2.4 Numerical resolution

For the shock case, according to (B.49), one can see that the velocity can easily be deduced from the imposed density (we recall that exterior states and state 2 are equal, except for the tangential

velocities) through:

$$u_{n,ext} = u_{n,int} + \sqrt{\frac{(p_{ext} - p_{int})(\rho_{ext} - \rho_{int})}{\rho_{ext}\rho_{int}}} \tag{B.55}$$

However, if the velocity is imposed, the relation on the unknown density is implicit and would require iterations to solve. We assume here that the density variation remains small (consistent with the weakly compressible framework in which we work) so that we linearize the relation through a small variation of the density around ρ_0 and deduce the corresponding density (let us recall that density and pressure are linked through the state law).

Derivation of a first guess Noting $r_{ext} = \rho_{ext}/\rho_0$ and $r_{int} = \rho_{int}/\rho_0$, the Rankine Hugoniot relation becomes:

$$r_{int}r_{ext}\rho_0 (u_{n,ext} - u_{n,int})^2 = (r_{ext} - r_{int})(p_{ext} - p_{int}) \tag{B.56}$$

$$p_{ext} = \frac{\rho_0 c_0^2}{\xi}\left(r_{ext}^{\xi} - 1\right) + p_B \tag{B.57}$$

As ρ_{int} is deduced from p_{int} through the inverse state law, we can also write:

$$p_{int} = \frac{\rho_0 c_0^2}{\xi}\left(r_{int}^{\xi} - 1\right) + p_B \tag{B.58}$$

Hence, noting $B_u = (u_{n,ext} - u_{n,int})^2 / c_0^2$:

$$\xi r_{int} r B_u = (r_{ext} - r_{int})\left(r_{ext}^{\xi} - r_{int}^{\xi}\right) \tag{B.59}$$

Noting $X = r_{ext}/r_{int} = \rho_{ext}/\rho_{int}$:

$$\xi B_u r_{int}^{1-\xi} X = (X - 1)\left(X^{\xi} - 1\right) \tag{B.60}$$

Let us approximate $X = 1 + \epsilon$ with $\epsilon \ll 1$ and write $K_r = B_u r_{int}^{1-\gamma}$:

$$\epsilon^2 - K_r\epsilon - K_r = 0 \tag{B.61}$$

$$\epsilon = \frac{K_r + \sqrt{K_r^2 + 4K_r}}{2} \tag{B.62}$$

Hence $\rho_{ext} = (1 + \frac{K_r + \sqrt{K_r^2 + 4K_r}}{2})\rho_{int}$. This solution is exact if $\xi = 1$.

Iterative approach The numerical tests showed that the first guess described above was already near the solution. One can iterate to get closer to the solution with the bisection or New-

ton's method. Let us define the function f_i such that:

$$f_i(X) = (X-1)\left(X^{\xi}-1\right) - \xi K_r X \tag{B.63}$$

$$f_i'(X) = (\xi+1)\,X^{\xi} - \xi X^{\xi-1} - \xi K_r - 1 \tag{B.64}$$

$$f_i''(X) = \xi X^{\xi-2}\left[(\xi+1)\,X - \xi + 1\right] \tag{B.65}$$

In the shock case, $X \geq 1$. $f_i''(X) > 0$ for $X \in [1, \infty[$. Hence f' is monotonically increasing for $X \geq 1$. $f'(1) = -\xi K_r < 0$ in the shock case. Hence f_i' is changing sign on the domain of interest: f is decreasing and then increasing. $f_i(1) = -\xi K_r < 0$ and $f_i(X) \underset{X\to+\infty}{\longrightarrow} +\infty$. Hence $f_i(X)$ has one solution in $[1, \infty[$.

B.2.4.1 Imposed pressure

if $p_{ext} \leq p_{int}$ **then**
  Expansion wave
  $u_{n,ext} = u_{n,int} + \psi_r\left(\rho_{ext}\right) - \psi_r\left(\rho_{int}\right)$
else
  Shock wave
  $u_{n,ext} = u_{n,int} + \sqrt{\left(p_{ext} - p_{int}\right)\left(\rho_{ext} - \rho_{int}\right) / \left(\rho_{ext}\rho_{int}\right)}$
end if

B.2.4.2 Imposed velocity

if $u_{n,ext} \leq u_{n,int}$ **then**
  Expansion wave
  $\psi_r\left(\rho_{ext}\right) = \psi_r\left(\rho_{int}\right) + u_{n,ext} - u_{n,int} \rightarrow \rho_{ext}$
else
  Shock wave
  $r_{int} = \rho_{int}/\rho_0$
  $B_u = \left(u_{n,ext} - u_{n,int}\right)^2 / c_0^2$
  $K_r = B_u r_{int}^{\gamma-1}$
  $\rho_{ext} = \left(1 + \left(K_r + \sqrt{K_r^2 + 4K_r}\right)/2\right)\rho_{int}$
end if

B.3 Mixture model approach

B.3.1 Governing equations

The numerical implementation described in Chapter 3 is tantamount to solving the following system, once gravity and viscosity effects are neglected:

$$\frac{\partial \sigma}{\partial t} + \boldsymbol{j} \cdot \boldsymbol{\nabla} \sigma = -\sigma \boldsymbol{\nabla} \cdot \boldsymbol{j} \tag{B.66}$$

$$\frac{\partial \alpha}{\partial t} + \boldsymbol{j} \cdot \boldsymbol{\nabla} \alpha = -\boldsymbol{\nabla} \cdot (\alpha \beta \boldsymbol{v}^r) \tag{B.67}$$

$$\frac{\partial \boldsymbol{j}}{\partial t} + \boldsymbol{j} \cdot \boldsymbol{\nabla} \boldsymbol{j} = -\frac{1}{\rho} \boldsymbol{\nabla} p - \boldsymbol{\nabla} \left(\alpha \beta \boldsymbol{v}^r \otimes \boldsymbol{v}^r \right) \tag{B.68}$$

We chose to work here with α that is the quantity we want to impose in practice (and that appears in the other equations, *e.g.* in the state equation), and not V^α. For the pressure gradient, we use the state equation (1.106) combined with the sound speed written following (1.105):

$$c = \sqrt{\frac{\alpha \rho^\alpha (c^\alpha)^2 + \beta \rho^\beta (c^\beta)^2}{\alpha \rho^\alpha + \beta \rho^\beta}} \tag{B.69}$$

Without restriction on the phase sound speeds[1], the gradient of pressure writes:

$$\boldsymbol{\nabla} p = \frac{\alpha \rho^\alpha \left(c^\alpha\right)^2 + \beta \rho^\beta (c^\beta)^2}{\sigma_0} \boldsymbol{\nabla} \sigma + \left(\rho^\alpha \left(c^\alpha\right)^2 - \rho^\beta (c^\beta)^2 \right) \left(\frac{\sigma}{\sigma_0} - 1 \right) \boldsymbol{\nabla} \alpha \tag{B.73}$$

With the definition of the local sound speed (1.107) and using the link between σ and ρ (3.35), the pressure force writes:

$$\frac{1}{\rho} \boldsymbol{\nabla} p = \frac{c^2}{\sigma} \boldsymbol{\nabla} \sigma + \frac{1}{\rho} \left(\rho^\alpha \left(c^\alpha\right)^2 - \rho^\beta (c^\beta)^2 \right) \left(\frac{\sigma}{\sigma_0} - 1 \right) \boldsymbol{\nabla} \alpha \tag{B.74}$$

[1] Let us underline that for multifluid computations, Colagrossi and Landrini [86] suggested to chose the sound speeds following:

$$\rho^\alpha \left(c^\alpha\right)^2 = \rho^\beta (c^\beta)^2 \tag{B.70}$$

Under this assumption, the equation of state simplifies (no more dependence on the volume fraction):

$$p = \rho^\alpha \left(c^\alpha\right)^2 \left(\frac{\sigma}{\sigma_0} - 1 \right) \tag{B.71}$$

Colagrossi's assumption deletes the dependence of the pressure with α. Under the constant speed of sound hypothesis, we rather get:

$$p = \rho_0 \left(c^\alpha\right)^2 \left(\frac{\sigma}{\sigma_0} - 1 \right) \tag{B.72}$$

B.3.2 1D Riemann problem formulation

We now project the governing equations (B.18) and (B.19) along the normal to the boundary oriented towards the domain (n denotes the normal component and τ the tangential component; $j_n = \boldsymbol{j}\cdot\boldsymbol{n}$ and $j_\tau = \boldsymbol{j}\cdot\boldsymbol{\tau}$; $v_n^r = \boldsymbol{v}^r\cdot\boldsymbol{n}$ and $v_\tau^r = \boldsymbol{v}^r\cdot\boldsymbol{\tau}$) and neglect all the tangential derivatives:

$$\frac{\partial\sigma}{\partial t} + j_n\frac{\partial\sigma}{\partial n} + \sigma\frac{\partial j_n}{\partial n} = 0 \tag{B.75}$$

$$\frac{\partial\alpha}{\partial t} + j_n\frac{\partial\alpha}{\partial n} = -\frac{\partial}{\partial n}\left(\alpha\beta\boldsymbol{v}^r\right) \tag{B.76}$$

$$\frac{\partial j_n}{\partial t} + j_n\frac{\partial j_n}{\partial n} + \frac{c^2}{\sigma}\frac{\partial\sigma}{\partial n} + \frac{1}{\rho}\left(\rho^\alpha\left(c^\alpha\right)^2 - \rho^\beta\left(c^\beta\right)^2\right)\left(\frac{\sigma}{\sigma_0}-1\right)\frac{\partial\alpha}{\partial n} = -\frac{\partial}{\partial n}\left(\alpha\beta v_n^r v_n^r\right) \tag{B.77}$$

$$\frac{\partial j_\tau}{\partial t} + j_n\frac{\partial j_\tau}{\partial n} = -\frac{\partial}{\partial n}\left(\alpha\beta v_n^r v_\tau^r\right) \tag{B.78}$$

We can now put the non conservative system under the form:

$$\frac{\partial}{\partial t}\boldsymbol{W} + \boldsymbol{B}\left(\boldsymbol{W}\right)\frac{\partial\boldsymbol{W}}{\partial\boldsymbol{n}} = 0 \tag{B.79}$$

where:

$$\boldsymbol{W} = \begin{pmatrix}\sigma\\ \alpha\\ j_n\\ j_\tau\end{pmatrix} \text{ and } \boldsymbol{B}\left(\boldsymbol{W}\right) = \begin{pmatrix} j_n & 0 & \sigma & 0\\ 0 & j_n + A_r & 0 & 0\\ \frac{c^2}{\sigma} & B_r + D_r & j_n & 0\\ 0 & E_r & 0 & j_n\end{pmatrix} \tag{B.80}$$

where:

$$A_r = \frac{\partial\left(\alpha\beta v_n^r\right)}{\partial\alpha} \quad B_r = \frac{\partial\left(\alpha\beta v_n^r v_n^r\right)}{\partial\alpha} \quad E_r = \frac{\partial}{\partial\alpha}\left(\alpha\beta v_n^r v_\tau^r\right)$$
$$D_r = \frac{1}{\rho}\left(\rho^\alpha\left(c^\alpha\right)^2 - \rho^\beta(c^\beta)^2\right)\left(\frac{\sigma}{\sigma_0}-1\right) \tag{B.81}$$

B.3.2.1 Eigenvalue problem

Let us search for the eigenvalues of this matrix.

$$\left|\boldsymbol{B}\left(\boldsymbol{W}\right) - \lambda_k\boldsymbol{I}\right| = \begin{vmatrix} j_n-\lambda_k & 0 & \sigma & 0\\ 0 & j_n + A_r - \lambda_k & 0 & 0\\ \frac{c^2}{\sigma} & B_r + D_r & j_n-\lambda_k & 0\\ 0 & E_r & 0 & j_n-\lambda_k\end{vmatrix} \tag{B.82}$$

This determinant writes:

$$|\boldsymbol{B}(\boldsymbol{W}) - \lambda_k \boldsymbol{I}| = (j_n - \lambda_k)(j_n + A_r - \lambda_k)(j_n - \lambda_k + c)(j_n - \lambda_k - c) \tag{B.83}$$

The eigenvalues are therefore j_n, $j_n \pm c$ and $j_n + A_r$. We will from now on focus on the homogeneous problem (*i.e.* without relative velocities: $A_r = B_r = E_r = 0$). The eigen problem becomes:

$$\boldsymbol{B}(\boldsymbol{W}) - \lambda_k \boldsymbol{I} = \begin{pmatrix} j_n - \lambda_k & 0 & \sigma & 0 \\ 0 & j_n - \lambda_k & 0 & 0 \\ \frac{c^2}{\sigma} & D_r & j_n - \lambda_k & 0 \\ 0 & 0 & 0 & j_n - \lambda_k \end{pmatrix} \tag{B.84}$$

There are three eigenvalues: $\lambda_0 = j_n$ (of multiplicity 2) and $\lambda_{\pm 1} = j_n \pm c$. Two right eigenvectors are then associated to λ_0:

$$\boldsymbol{r}_{0,1} = \begin{pmatrix} 0 \\ 0 \\ 0 \\ 1 \end{pmatrix} \text{ and } \boldsymbol{r}_{0,2} = \begin{pmatrix} -\sigma D_r \\ c^2 \\ 0 \\ 0 \end{pmatrix} \tag{B.85}$$

The right eigenvectors associated to $\lambda_{\pm 1}$ are:

$$\boldsymbol{r}_{+1} = \begin{pmatrix} \sigma \\ 0 \\ c \\ 0 \end{pmatrix} \text{ and } \boldsymbol{r}_{-1} = \begin{pmatrix} -\sigma \\ 0 \\ c \\ 0 \end{pmatrix} \tag{B.86}$$

B.3.2.2 Riemann invariants

Following [335], we shall find three k-Riemann invariants for each of the four eigenvalues k.

- For λ_{-1}, the -1-Riemann invariants must satisfy $-\sigma \dfrac{\partial w_r}{\partial \sigma} + c \dfrac{\partial w_r}{\partial j_n} = 0$
- For λ_0, the 0-Riemann invariants must satisfy $\dfrac{\partial w_r}{\partial j_\tau} = 0$ and $\dfrac{\partial w_r}{\partial \alpha} = 0$
- For λ_{+1}, the 1-Riemann invariants must satisfy $\sigma \dfrac{\partial w_r}{\partial \sigma} + c \dfrac{\partial w_r}{\partial j_n} = 0$

We aim at finding linearly independent Riemann invariants.

Derivation of Riemann invariants We have:

$$\boldsymbol{W} = \begin{pmatrix} \sigma \\ \alpha \\ j_n \\ j_\tau \end{pmatrix} \quad \boldsymbol{D} = \begin{pmatrix} \lambda_{-1} & 0 & 0 & 0 \\ 0 & \lambda_{+1} & 0 & 0 \\ 0 & 0 & \lambda_0 & 0 \\ 0 & 0 & 0 & \lambda_0 \end{pmatrix} \quad \boldsymbol{P} = \begin{pmatrix} -\sigma & \sigma & -\sigma D_r & 0 \\ 0 & 0 & c^2 & 0 \\ c & c & 0 & 0 \\ 0 & 0 & 0 & 1 \end{pmatrix} \tag{B.87}$$

Let us compute the inverse of $\boldsymbol{P}$:

$$\det(\boldsymbol{P}) = 2\sigma c^3 \tag{B.88}$$

$${}^t\boldsymbol{P} = \begin{pmatrix} -\sigma & 0 & c & 0 \\ \sigma & 0 & c & 0 \\ -\sigma D_r & c^2 & 0 & 0 \\ 0 & 0 & 0 & 1 \end{pmatrix} \rightarrow \operatorname{adj}\left({}^t\boldsymbol{P}\right) = \begin{pmatrix} -c^3 & -\sigma c D_r & \sigma c^2 & 0 \\ c^3 & \sigma c D_r & \sigma c^2 & 0 \\ 0 & 2\sigma c & 0 & 0 \\ 0 & 0 & 0 & 2\sigma c^3 \end{pmatrix} \tag{B.89}$$

$$\boldsymbol{P}^{-1} = \frac{1}{\det(\boldsymbol{P})} \operatorname{adj}\left({}^t\boldsymbol{P}\right) = \frac{1}{2\sigma c^2} \begin{pmatrix} -c^2 & -\sigma D_r & \sigma c & 0 \\ c^2 & \sigma D_r & \sigma c & 0 \\ 0 & 2\sigma & 0 & 0 \\ 0 & 0 & 0 & 2\sigma c^2 \end{pmatrix} \tag{B.90}$$

$$\boldsymbol{P}^{-1} d\boldsymbol{W} = \frac{1}{2\sigma c^2} \begin{pmatrix} -c^2 & -\sigma D_r & \sigma c & 0 \\ c^2 & \sigma D_r & \sigma c & 0 \\ 0 & 2\sigma & 0 & 0 \\ 0 & 0 & 0 & 2\sigma c^2 \end{pmatrix} \begin{pmatrix} d\sigma \\ d\alpha \\ dj_n \\ dj_t \end{pmatrix} = \frac{1}{2c} d\boldsymbol{Z} \tag{B.91}$$

The corresponding system is:

$$\left\{\begin{array}{l} -c\,d\sigma - \frac{\sigma D_r}{c}\,d\alpha + \sigma\,dj_n = \sigma\,dz_1 \\ c\,d\sigma + \frac{\sigma D_r}{c}\,d\alpha + \sigma\,dj_n = \sigma\,dz_2 \\ 2\frac{\sigma}{c}\,d\alpha = \sigma\,dz_3 \\ 2\sigma c\,dj_\tau = \sigma\,dz_4 \end{array}\right. \rightarrow \left\{\begin{array}{l} -\frac{c}{\sigma}d\sigma - \frac{D_r}{c}\,d\alpha + dj_n = dz_1 \\ \frac{c}{\sigma}d\sigma + \frac{D_r}{c}\,d\alpha + dj_n = dz_2 \\ d\alpha = \frac{c}{2}\,dz_3 \\ dj_\tau = \frac{1}{2c}\,dz_4 \end{array}\right. \tag{B.92}$$

If we work differently on each equation (dz_i remains unchanged for the first two equations, the third and the fourth one are multiplied by $2c$), one gets:

$$\left\{\begin{array}{l} dz_1 = -\frac{c}{\sigma}d\sigma - \frac{D_r}{c}\,d\alpha + dj_n \\ dz_2 = \frac{c}{\sigma}d\sigma + \frac{D_r}{c}\,d\alpha + dj_n \\ dz_3 = d\alpha \\ dz_4 = dj_\tau \end{array}\right. \tag{B.93}$$

We can now integrate these relations and assign the resulting invariants to their respective eigenvalues in Table B.2. As expected, one has three invariants for each eigenvalue. We have linearized the state equation so that we note:

$$\psi_r\left(\alpha,\sigma\right) = c\left(\alpha\right)\ln\left(\frac{\sigma}{\sigma_0}\right) \tag{B.94}$$

We also introduce the function ϕ_r defined through $d\phi_r = \frac{D_r}{c}d\alpha$ that can be integrated:

$$\phi_r\left(\alpha,\sigma\right) = c^\beta\sqrt{\frac{r_\rho}{r_c}}\,\mathrm{argcosh}\left(\left|\frac{2r_c r_\rho}{|r_c - r_\rho|}\alpha + \frac{r_c + r_\rho}{|r_c - r_\rho|}\right|\right) \tag{B.95}$$

if $r_\rho \neq r_c$ where $r_\rho = \frac{\rho^\alpha (c^\alpha)^2}{\rho^\beta (c^\beta)^2} - 1$ and $r_c = \frac{\rho^\alpha}{\rho^\beta} - 1$. We assumed that $r_c \neq 0$: we do not consider here the case of two fluids with the same density but different compressibility. If $r_\rho = r_c$, which is the framework retained in our numerical applications when using equal sound speeds, one gets by integrating:

$$\phi_r\left(\alpha,\sigma\right) = c^\beta\ln\left(|1 + r_c\alpha|\right)\left(1 - \frac{\sigma_0}{\sigma}\right) \tag{B.96}$$

The inclusion of this term still requires further investigation and was not included in the computations of the present work. For the sake of completeness, it however appears in the following developments. Under the Colagrossi and Landrini's assumption, one has $r_\rho = 0$ and ϕ_r cancels. One can make the following remarks:

- We recover the known Riemann invariants for the velocities, nevertheless a change oc-

Table B.2: k-Riemann invariants for the mixture formulation.

	λ_0	λ_{-1}	λ_{+1}
α	✗	✓	✓
j_τ	✗	✓	✓
$j_n + \psi_r(\alpha,\sigma) + \phi_r(\alpha,\sigma)$	✓	✓	✗
$j_n - \psi_r(\alpha,\sigma) - \phi_r(\alpha,\sigma)$	✓	✗	✓

curs: the celerity definition that depends on the volume fraction. The resulting Riemann invariants write:

$$R_{-1} = j_n + \psi_r(\alpha,\sigma) + \phi_r(\alpha,\sigma) \tag{B.97}$$

$$R_{+1} = j_n - \psi_r(\alpha,\sigma) - \phi_r(\alpha,\sigma) \tag{B.98}$$

- j_τ is a Riemann invariant.
- An additional invariant appears: the volume fraction α.

B.3.2.3 Rankine Hugoniot relations

In view of Rankine-Hugoniot relations, we can write the following set of conservation equations in absence of relative velocity:

$$\frac{\partial \sigma}{\partial t} + \boldsymbol{\nabla}\cdot(\sigma \boldsymbol{j}) = 0 \tag{B.99}$$

$$\frac{\partial \alpha\rho}{\partial t} + \boldsymbol{\nabla}\cdot(\alpha\rho \boldsymbol{j}) = 0 \tag{B.100}$$

$$\frac{\partial \rho\boldsymbol{j}}{\partial t} + \boldsymbol{\nabla}\cdot(p\boldsymbol{I} + \rho\boldsymbol{j}\otimes\boldsymbol{j}) = 0 \tag{B.101}$$

Indeed, using the relation (3.35), we have:

$$\frac{\partial \rho}{\partial t} + \boldsymbol{\nabla}\cdot(\rho\boldsymbol{j}) = \frac{\partial}{\partial t}\left(\rho_0\frac{\sigma}{\sigma_0}\right) + \boldsymbol{\nabla}\cdot\left(\rho_0\frac{\sigma}{\sigma_0}\boldsymbol{j}\right) = \frac{\sigma}{\sigma_0}\left[\frac{\partial \rho_0}{\partial t} + \boldsymbol{j}\cdot\boldsymbol{\nabla}\rho_0\right] + \frac{\rho_0}{\sigma_0}\left[\frac{\partial \sigma}{\partial t} + \boldsymbol{\nabla}\cdot(\sigma\boldsymbol{j})\right] \tag{B.102}$$

where:

$$\frac{\partial \rho_0}{\partial t} + \boldsymbol{j}\cdot\boldsymbol{\nabla}\rho_0 = \left(\rho^\alpha - \rho^\beta\right)\left[\frac{\partial \alpha}{\partial t} + \boldsymbol{j}\cdot\boldsymbol{\nabla}\alpha\right] = 0 \tag{B.103}$$

Hence, we get:

$$\frac{\partial \rho}{\partial t} + \boldsymbol{\nabla}\cdot(\rho\boldsymbol{j}) = 0 \tag{B.104}$$

For the momentum relation, using this result, we can write:

$$\frac{\partial \rho\boldsymbol{j}}{\partial t} + \boldsymbol{\nabla}\cdot(\rho\boldsymbol{j}\otimes\boldsymbol{j}) = \rho\left[\frac{\partial \boldsymbol{j}}{\partial t} + \boldsymbol{j}\cdot\boldsymbol{\nabla}\boldsymbol{j}\right] = -\boldsymbol{\nabla}p \tag{B.105}$$

For the volume fraction equation we have, the same reasoning gives:

$$\frac{\partial \rho\alpha}{\partial t} + \boldsymbol{\nabla}\cdot(\rho\alpha) = \rho\left[\frac{\partial \alpha}{\partial t} + \boldsymbol{j}\cdot\boldsymbol{\nabla}\alpha\right] = 0 \tag{B.106}$$

We can therefore use the same Rankine Hugoniot relations as before for the shock, assimilating $\boldsymbol{u}$ and $\boldsymbol{j}$ as relative velocity is neglected, with an additional transported quantity, the volume fraction, for which the relation writes as the tangential velocity:

$$\alpha_\ell = \alpha_r \tag{B.107}$$

B.3.3 1D Riemann problem resolution

We are now equipped with all the tools to solve the 1D Riemann problem at the boundary. As we are working with the homogeneous model, $u_n = j_n$. We have seen that three characteristic waves $(\lambda_{-1}, \lambda_0, \lambda_{+1})$ model discontinuities between the exterior state and the interior state as illustrated on Figure B.1. Let us have a closer look at each of the characteristic waves:

- As the flow is subsonic, $\lambda_{-1} < 0$ so that the associated wave is outside the domain. We will consider it as a ghost wave so that the data of the exterior state $\boldsymbol{W}_{ext}$ are assumed equal to the data $\boldsymbol{W}_1$ of state 1.
- λ_0 is a contact discontinuity. From the associated Riemann invariants $u_n + \psi_r + \phi_r$ and $u_n - \psi_r - \phi_r$, we deduce that:

$$u_{n,1} = u_{n,2} \text{ and } \psi_r(\alpha_1, \sigma_1) + \phi_r(\alpha_1, \sigma_1) = \psi_r(\alpha_2, \sigma_2) + \phi_r(\alpha_2, \sigma_2) \tag{B.108}$$

  There might be a jump of u_τ or α.

- As the flow is subsonic $\lambda_{+1} > 0$. This characteristic wave can belong to two kinds of discontinuity:
  - Expansion wave: characteristics are diverging, the states are connected through a smooth transition and the Riemann invariant holds across the characteristic wave:

$$u_{n,2} + c(\alpha_2) < u_{n,int} + c(\alpha_{int}) \tag{B.109}$$

$$u_{n,2} - \psi_r(\alpha_2, \sigma_2) - \phi_r(\alpha_2, \sigma_2) = u_{n,int} - \psi_r(\alpha_{int}, \sigma_{int}) - \phi_r(\alpha_{int}, \sigma_{int}) \tag{B.110}$$

  - Shock wave: characteristics are converging and the Rankine Hugoniot relations (B.45) and (B.46) apply:

$$u_{n,2} + c(\alpha_2) > u_{n,int} + c(\alpha_{int}) \tag{B.111}$$

$$\rho_2\rho_{int}(u_{n,2} - u_{n,int})^2 = (\rho_2 - \rho_{int})(p_2 - p_{int}) \tag{B.112}$$

For the three types of discontinuity, we have $u_{\tau,2} = u_{\tau,int}$ and $\alpha_2 = \alpha_{int}$ according to the previous developments (Riemann invariant for contact discontinuity or expansion wave, Rankine Hugoniot relation (B.50) and (B.107) for shock). This simplifies the above conditions as consequently $c(\alpha_2) = c(\alpha_{int})$.

Depending on the sign of $\lambda_0 = u_n$, the state at the boundary will be defined by state 1 or state 2. To sum up, we know the interior state from SPH interpolation of quantities in the bulk of the fluid. We know either the external volume fraction and pressure or velocity, and we can use the above relations to deduce the unknown quantity, velocity or pressure respectively. The choice of relation will depend on which of the relations (B.109) or (B.111) is fulfilled. The tangential velocity and the volume fraction need to be defined by the user at an inlet. At an outlet, they are determined by the interior state.

B.3.4 Numerical resolution

Shock case Using (B.112), the velocity can be easily deduced from the imposed pressure and the volume fraction through:

$$u_{n,ext} = u_{n,int} + \sqrt{\frac{(p_2 - p_{int})(\rho_2 - \rho_{int})}{\rho_2 \rho_{int}}} \tag{B.113}$$

where p_2 and ρ_2 are computed using (3.35) and (1.106) with $\alpha_2 = \alpha_{int}$, $\alpha_{ext} = \alpha_1$ and (B.108) from the contact wave (for constant sound speed and $\phi_r = 0$, one has $\sigma_2 = \sigma_{ext}$). On the other hand, if the velocity is imposed, we have to solve a second order polynomial in σ_2 (contrary to the single-fluid case, the relation is not implicit and can be solved explicitly as we have taken $\xi = 1$).

Derivation of the polynomial and solution We start from:

$$\rho_2 \rho_{int} (u_{n,ext} - u_{n,int})^2 = (\rho_2 - \rho_{int})(p_2 - p_{int}) \tag{B.114}$$

By replacing $\rho_2 = \rho_{0,2}\sigma_2/\sigma_0$ and $\rho_{int} = \rho_{0,int}\sigma_{int}/\sigma_0$ and noticing that $\rho_{0,2} = \rho_{0,int}$:

$$\frac{\sigma_2}{\sigma_0}\rho_{0,int}\frac{\sigma_{int}}{\sigma_0}(u_{n,ext} - u_{n,int})^2 = \left(\frac{\sigma_2}{\sigma_0} - \frac{\sigma_{int}}{\sigma_0}\right)(p_2 - p_{int}) \tag{B.115}$$

Noting $r_2 = \sigma_2/\sigma_0$ and $r_{int} = \sigma_{int}/\sigma_0$:

$$r_{int} r_2 \rho_{0,int} (u_{n,ext} - u_{n,int})^2 = (r_2 - r_{int})(p_2 - p_{int}) \tag{B.116}$$

The pressures write:

$$p_2 = \left(\alpha_{int}\rho^{\alpha}(c^{\alpha})^2 + \beta_{int}\rho^{\beta}(c^{\beta})^2\right)(r_2 - 1) \tag{B.117}$$

$$p_{int} = \left(\alpha_{int}\rho^{\alpha}\left(c^{\alpha}\right)^2 + \beta_{int}\rho^{\beta}(c^{\beta})^2\right)(r_{int} - 1) \tag{B.118}$$

Noting $B_u = \left(u_{n,ext} - u_{n,int}\right)^2 / c_{int}^2$ and replacing in the Rankine Hugoniot relation:

$$r_{int} r_2 B_u = \left(r_2 - r_{int}\right)^2 \tag{B.119}$$

Noting $X = r/r_{int} = \sigma_2/\sigma_{int}$, we obtain the second order polynomial:

$$X^2 - (B_u + 2)X + 1 = 0 \tag{B.120}$$

$$X = 1 + \frac{B_u + \sqrt{B_u^2 + 4B_u}}{2} \tag{B.121}$$

Finally, we compute $\sigma_2 = \left(1 + \frac{B+\sqrt{B^2+4B}}{2}\right)\sigma_{int}$. In the numerical implementation, we can work with renormalized quantities to limit the numerical errors.

Expansion case Using (B.110), the velocity can be easily deduced from the imposed pressure (and therefore the corresponding inverse volume) and the volume fraction. On the other hand, if the velocity is imposed, the relation is implicit due to the forms of ψ_r and ϕ_r, except if $\phi_r = 0$. As volumes does not vary significantly, one can use a linearized form of the relation (B.110) according to the volume variations. Splitting the functions $\psi_r(\alpha, \sigma) = c(\alpha)\psi_r^{\sigma}(\sigma)$ and $\phi_r(\alpha, \sigma) = \phi_r^{\alpha}(\alpha)\phi_r^{\sigma}(\sigma)$ and linearizing the σ parts $\psi_r^{\sigma}(\sigma) = \ln(\sigma/\sigma_0)$ and $\phi_r^{\sigma}(\sigma) = (1 - \sigma_0/\sigma)$ (ϕ_r^{α} can be deduced accordingly using (B.95) or (B.96)), one gets:

$$\psi_r(\alpha, \sigma) + \phi_r(\alpha, \sigma) \approx \left[c(\alpha) + \phi_r^{\alpha}(\alpha)\right]\left(\frac{\sigma}{\sigma_0} - 1\right) \tag{B.122}$$

So that one can deduce σ from the computed value of $\psi_r(\alpha, \sigma) + \phi_r(\alpha, \sigma)$.

B.3.4.1 Imposed pressure

if $p_{ext} \leq p_{int}$ **then**

Expansion wave

$p_{ext} \rightarrow \sigma_{ext} \rightarrow \sigma_2$

$u_{n,ext} = u_{n,int} + \psi_r(\alpha_{int}, \sigma_2) + \phi_r(\alpha_{int}, \sigma_2) - \psi_r(\alpha_{int}, \sigma_{int}) - \phi_r(\alpha_{int}, \sigma_{int})$

else

Shock wave

$u_{n,ext} = u_{n,int} + \sqrt{(p_2 - p_{int})(\rho_2 - \rho_{int})/(\rho_2\rho_{int})}$

end if

States to impose at the interface (denoted by index i)

if $u_{n,ext} \geq 0$ **then**

Inlet: boundary at state 1

$\alpha_i = \alpha_{ext}$

else

Outlet: boundary at state 2

$\alpha_i = \alpha_{int}$

end if

B.3.4.2 Imposed velocity

if $u_{n,ext} \leq u_{n,int}$ **then**

Expansion wave

$\psi_r\left(\alpha_{int}, \sigma_2\right) + \phi_r\left(\alpha_{int}, \sigma_2\right) = \psi_r\left(\alpha_{int}, \sigma_{int}\right) + \phi_r\left(\alpha_{int}, \sigma_{int}\right) + u_{n,ext} - u_{n,int} \rightarrow \sigma_2 \rightarrow \sigma_{ext}$

else

Shock wave

$B_u = \left(u_{n,ext} - u_{n,int}\right)^2 / c_{int}^2$

$\sigma_2 = \left(1 + \left(B_u + \sqrt{B_u^2 + 4B_u}\right)/2\right) \sigma_{int} \rightarrow \sigma_{ext}$

end if

States to impose at the interface (denoted by index i)

if $u_{n,ext} \geq 0$ **then**

Inlet: boundary at state 1

$\sigma_i = \sigma_{ext}$

$\alpha_i = \alpha_{ext}$

else

Outlet: boundary at state 2

$\sigma_i = \sigma_2$

$\alpha_i = \alpha_{int}$

end if

Appendix C

Developments for the phase volume equation

We address in this section the derivation of the volume diffusion term applied to the phase volume equations to avoid checker-board effects. We then write a condition of positiveness for the phase volume equation for a given closure of the relative velocity.

C.1 Volume diffusion

We follow the derivation of Brezzi and Pitkäranta [39], but apply it to the volume equation (3.1) instead of the density equation. Using the momentum equation (3.48), the discrete volume equation writes:

$$\begin{aligned}\frac{V_a^{n+1}-V_a^n}{\delta t} &= V_a^n D_a\{\boldsymbol{j}_b^{n+1}\} \\ &\approx V_a^n D_a\{\boldsymbol{j}_b^n - \frac{\delta t}{\rho_a^n}\boldsymbol{G}_a\{p_b^n\} + \frac{\delta t}{\rho_a^n}\rho_a^n \boldsymbol{g}\} \\ &\approx V_a^n D_a\{\boldsymbol{j}_b^n\} - V_a^n D_a\{\frac{\delta t}{\rho_a^n}\boldsymbol{G}_a\{p_b^n\} - \delta t \boldsymbol{G}_a\{\boldsymbol{g}\cdot\boldsymbol{r}_b^n\}\}\end{aligned} \tag{C.1}$$

where D_a and $\boldsymbol{G}_a$ stand for the discrete divergence and gradient operators and δt the time step. Using the Laplacian operator L_a, which is slightly different from the divergence of a gradient in SPH, the volume diffusion term $\mathcal{D}_a$ writes:

$$\mathcal{D}_a = V_a L_a\{\frac{\delta t}{\rho_b}, p_b\} - V_a L_a\{\delta t, \boldsymbol{g}\cdot\boldsymbol{r}_b\} \tag{C.2}$$

It is written discretely as:

$$\mathcal{D}_a^n = 2V_a\delta t\sum_{b\in\mathcal{F}} V_b \frac{1}{r_{ab}}\left(\frac{2}{\rho_a+\rho_b}\left(p_a-p_b\right)-\boldsymbol{g}\cdot\boldsymbol{r}_{ab}\right)\boldsymbol{\nabla}w_{ab} \tag{C.3}$$

The easiest approach is now to introduce the usual volume diffusion in both V^α and V^β equations, but weighted respectively by α and β. The new phase volumes computed by (3.20) and (3.21) being denoted $V^{\alpha,\star}, V^{\beta,\star}$, using a volume diffusion coefficient Λ (generally $\Lambda = 0.1$), we finally write at time $n+1$:

$$V_a^{\alpha,n+1} = V_a^{\alpha,\star} + \frac{\delta t}{\gamma_a}\Lambda\alpha_a^n\mathcal{D}_a^n \tag{C.4}$$

$$V_a^{\beta,n+1} = V_a^{\beta,\star} + \frac{\delta t}{\gamma_a}\Lambda\beta_a^n\mathcal{D}_a^n \tag{C.5}$$

Combining these relations, one can obtain the diffusion applied to the total volume:

$$V_a^{n+1} = V_a^{\star} + \frac{\delta t}{\gamma_a}\Lambda\mathcal{D}_a^n \tag{C.6}$$

C.2 Derivation of a condition for positiveness of phase volumes

Schematic relative velocity closure In the following, the particle a considered is far from boundaries (no boundary term) and we neglect the volume diffusion term. We search for a sufficient condition of realizability of the phase volume using equation (3.44) resulting of the relative velocity closure (3.44):

$$\begin{aligned}\frac{dV_a^\alpha}{dt} &= \alpha_a\frac{dV_a}{dt} - \sum_{b\in\mathcal{F}}\left(\alpha_a\beta_b\left[\boldsymbol{v}_{0,a|b}\cdot\boldsymbol{S}_{a|b}\right]^+ + \alpha_b\beta_a\left[\boldsymbol{v}_{0,a|b}\cdot\boldsymbol{S}_{a|b}\right]^-\right)\\ &+K\sum_{b\in\mathcal{F}}\frac{\beta_a+\beta_b}{2}\frac{\alpha_a-\alpha_b}{r_{ab}}\frac{\boldsymbol{r}_{ab}\cdot\boldsymbol{S}_{a|b}}{r_{ab}}\end{aligned} \tag{C.7}$$

Let us note

$$\varphi\left(r\right) = -2\frac{\boldsymbol{r}\cdot\boldsymbol{\nabla}w}{r^2} \text{ so that } \varphi_{ab} = -2\frac{\boldsymbol{r}_{ab}\cdot\boldsymbol{\nabla}w_{ab}}{r_{ab}^2} \geq 0 \tag{C.8}$$

Replacing α, β and $\boldsymbol{S}_{a|b}$ by their definitions:

$$\begin{aligned}\frac{dV_a^\alpha}{dt} &= \frac{V_a^\alpha}{V_a}\frac{dV_a}{dt} - 2\sum_{b\in\mathcal{F}}\left(V_a^\alpha V_b^\beta\left[\boldsymbol{v}_{0,a|b}\cdot\boldsymbol{\nabla}w_{ab}\right]^+ + V_b^\alpha V_a^\beta\left[\boldsymbol{v}_{0,a|b}\cdot\boldsymbol{\nabla}w_{ab}\right]^-\right)\\ &-\tfrac{1}{2}K\sum_{b\in\mathcal{F}}\left(V_bV_a^\beta + V_aV_b^\beta\right)\left(\frac{V_a^\alpha}{V_a}-\frac{V_b^\alpha}{V_b}\right)\varphi_{ab}\end{aligned} \tag{C.9}$$

Using $V^\beta = V - V^\alpha$:

$$\begin{aligned}\frac{dV_a^\alpha}{dt} &= \frac{V_a^\alpha}{V_a}\frac{dV_a}{dt} - 2\sum_{b\in\mathcal{F}}\left(V_a^\alpha V_b^\beta\left[\boldsymbol{v}_{0,a|b}\cdot\boldsymbol{\nabla}w_{ab}\right]^+ + V_b^\alpha V_a^\beta\left[\boldsymbol{v}_{0,a|b}\cdot\boldsymbol{\nabla}w_{ab}\right]^-\right)\\ &-K\sum_{b\in\mathcal{F}}\left(\left(1-\frac{\alpha_a}{2}\right)V_b V_a^\alpha - \left(1-\frac{\alpha_b}{2}\right)V_a V_b^\alpha\right)\varphi_{ab}\end{aligned} \tag{C.10}$$

Discretizing temporally (V_a^{n+1} is taken as an input here, computed separately before, its factor is explicit):

$$\begin{aligned}\frac{V_a^{\alpha,n+1}-V_a^{\alpha,n}}{\delta t} &= \frac{V_a^{\alpha,n}}{V_a^n}\frac{V_a^{n+1}-V_a^n}{\delta t}\\ -2\sum_{b\in\mathcal{F}}&\left(V_a^{\alpha,n}V_b^{\beta,n}\left[\boldsymbol{v}_{0,a|b}\cdot\boldsymbol{\nabla}w_{ab}^n\right]^+ + V_b^{\alpha,n}V_a^{\beta,n}\left[\boldsymbol{v}_{0,a|b}\cdot\boldsymbol{\nabla}w_{ab}^n\right]^-\right)\\ -K\sum_{b\in\mathcal{F}}&\left(\left(1-\frac{\alpha_a^n}{2}\right)V_b^n V_a^{\alpha,n} - \left(1-\frac{\alpha_b^n}{2}\right)V_a^n V_b^{\alpha,n}\right)\varphi_{ab}^n\end{aligned} \tag{C.11}$$

Rearranging and using $[x,0]^- = -[-x,0]^+$, we finally get:

$$\begin{aligned}V_a^{\alpha,n+1} &= V_a^{\alpha,n}\left[\frac{V_a^{n+1}}{V_a^n} - \delta t\sum_{b\in\mathcal{F}}V_b^n\left(\beta_b^n\left[2\boldsymbol{v}_{0,a|b}\cdot\boldsymbol{\nabla}w_{ab}^n\right]^+ + K\left(1-\frac{\alpha_a^n}{2}\right)\varphi_{ab}^n\right)\right]\\ &+\delta t\sum_{b\in\mathcal{F}}V_b^{\alpha,n}\left(V_a^{\beta,n}\left[-2\boldsymbol{v}_{0,a|b}\cdot\boldsymbol{\nabla}w_{ab}^n\right]^+ + K\left(1-\frac{\alpha_b^n}{2}\right)V_a^n\varphi_{ab}^n\right)\end{aligned} \tag{C.12}$$

If we assume $V^{\alpha,n} > 0$ and $V^{\beta,n} > 0$ for every particle (therefore $V^n > 0$), a sufficient condition to have $V^{\alpha,n+1} > 0$ (and symmetrically $V^{\beta,n+1} > 0$) is:

$$\delta t\sum_{b\in\mathcal{F}}V_b^n\left(\beta_b^n\left[2\boldsymbol{v}_{0,a|b}\cdot\boldsymbol{\nabla}w_{ab}^n\right]^+ + K\left(1-\frac{\alpha_a^n}{2}\right)\varphi_{ab}^n\right) \leq \frac{V_a^{n+1}}{V_a^n} \tag{C.13}$$

as the second term of the left-hand side of equation (C.12) is always positive. That relation can be used in the code to compute a local time step. One can then use the minimum of the time steps required by the whole set of particles. Let us try to identify a coarse upper bound of the left-hand side term of the inequality (C.13) so as to highlight the dependences to the problem parameters. One can first write:

$$\delta t\sum_{b\in\mathcal{F}}V_b^n\left(\left[2\boldsymbol{v}_{0,a|b}\cdot\boldsymbol{\nabla}w_{ab}^n\right]^+ + K\varphi_{ab}^n\right) \leq \frac{V_a^{n+1}}{V_a^n} \tag{C.14}$$

In the continuous interpolation framework, we have according to [367]:

$$\int_\Omega \varphi\left(r\right) d\boldsymbol{r} \sim \frac{2}{\sigma_e^2} \tag{C.15}$$

with the kernel standard deviation $\sigma_e = \sqrt{\frac{5}{18}}h$ for the $\mathcal{C}^2$ Wendland kernel in 2 dimensions. Noting $v_{0\,\max} = \max_{a\in\mathcal{F}}\left(|\boldsymbol{v}_{0,a}|\right)$, an upper bound can be written:

$$\delta t\left(\eta_\alpha \frac{v_{0\,\max}}{\sigma_e} + \frac{K}{\sigma_e^2}\right) \leq \xi_\alpha \frac{V_a^{n+1}}{V_a^n} \tag{C.16}$$

where η_α and ξ_α are unknown. Volumes do not vary a lot so that we may consider that the ratio V_a^{n+1}/V_a^n is close to 1. Noting the numerical Péclet number:

$$\mathsf{Pe}_\sigma = \frac{v_{0\,\max}\sigma_e}{K} \tag{C.17}$$

one can deduce an approximate upper bound C_α to the condition for positiveness of phase volume:

$$\mathsf{C}_\alpha = \frac{v_{0\,\max}\delta t}{\sigma_e} \leq \xi_\alpha\left(\eta_\alpha + \frac{1}{\mathsf{Pe}_\sigma}\right)^{-1} \tag{C.18}$$

We finally used this upper bound when associated to the relative velocity closure (3.44) in the numerical resolution of the present work but the relation (C.13) could be used to have a possibly less restrictive condition.

Air-water relative velocity closure We now search for a sufficient condition of realizability of the phase volume using equation (4.34) resulting of the relative velocity closure (1.101):

$$\begin{aligned}\frac{dV_a^\alpha}{dt} &= \alpha_a \frac{dV_a}{dt} - \sum_{b\in\mathcal{F}}\left(\alpha_a\beta_b\left[\boldsymbol{v}_{0,a|b}\cdot\boldsymbol{S}_{a|b}\right]^- + \alpha_b\beta_a\left[\boldsymbol{v}_{0,a|b}\cdot\boldsymbol{S}_{ab}\right]^+\right)\\ &+\sum_{b\in\mathcal{F}}\frac{\nu_{T,a}+\nu_{T,b}}{2\mathsf{Sc}_T}\frac{\alpha_a-\alpha_b}{r_{ab}}\frac{\boldsymbol{r}_{ab}\cdot\boldsymbol{S}_{a|b}}{r_{ab}}\end{aligned} \tag{C.19}$$

Replacing α, β and $\boldsymbol{S}_{a|b}$ by their definitions:

$$\begin{aligned}\frac{dV_a^\alpha}{dt} &= \frac{V_a^\alpha}{V_a}\frac{dV_a}{dt} - 2\sum_{b\in\mathcal{F}}\left(V_a^\alpha V_b^\beta\left[\boldsymbol{v}_{0,a|b}\cdot\boldsymbol{\nabla}w_{ab}\right]^+ + V_b^\alpha V_a^\beta\left[\boldsymbol{v}_{0,a|b}\cdot\boldsymbol{\nabla}w_{ab}\right]^-\right)\\ &-\sum_{b\in\mathcal{F}}\frac{\nu_{T,a}^n+\nu_{T,b}^n}{2\mathsf{Sc}_T}\left(V_bV_a^\alpha - V_aV_b^\alpha\right)\varphi_{ab}\end{aligned} \tag{C.20}$$

Discretizing temporally (V_a^{n+1} is taken as an input here, computed separately before, its factor is explicit):

$$\begin{aligned}
&\frac{V_a^{\alpha,n+1}-V_a^{\alpha,n}}{\delta t} = \frac{V_a^{\alpha,n}}{V_a^n}\frac{V_a^{n+1}-V_a^n}{\delta t} \\
&-2\sum_{b\in\mathcal{F}}\left(V_a^{\alpha,n}V_b^{\beta,n}\left[\boldsymbol{v}_{0,a|b}\cdot\boldsymbol{\nabla}w_{ab}^n\right]^+ + V_b^{\alpha,n}V_a^{\beta,n}\left[\boldsymbol{v}_{0,a|b}\cdot\boldsymbol{\nabla}w_{ab}^n\right]^-\right) \\
&-\sum_{b\in\mathcal{F}}\frac{\nu_{T,a}^n+\nu_{T,b}^n}{2\mathrm{Sc}_T}\left(V_b^nV_a^{\alpha,n}-V_a^nV_b^{\alpha,n}\right)\varphi_{ab}^n
\end{aligned} \tag{C.21}$$

Rearranging and using $[x,0]^- = -[-x,0]^+$, we finally get:

$$\begin{aligned}
V_a^{\alpha,n+1} = V_a^{\alpha,n}&\left[\frac{V_a^{n+1}}{V_a^n} - \delta t\sum_{b\in\mathcal{F}}V_b^n\left(\beta_b^n\left[2\boldsymbol{v}_{0,a|b}\cdot\boldsymbol{\nabla}w_{ab}^n\right]^+ + \frac{\nu_{T,a}^n+\nu_{T,b}^n}{2\mathrm{Sc}_T}\varphi_{ab}^n\right)\right] \\
+\delta t\sum_{b\in\mathcal{F}}V_b^{\alpha,n}&\left(V_a^{\beta,n}\left[-2\boldsymbol{v}_{0,a|b}\cdot\boldsymbol{\nabla}w_{ab}^n\right]^+ + \frac{\nu_{T,a}^n+\nu_{T,b}^n}{2\mathrm{Sc}_T}V_a^n\varphi_{ab}^n\right)
\end{aligned} \tag{C.22}$$

If we assume $V^{\alpha,n}>0$ and $V^{\beta,n}>0$ for every particle (therefore $V^n>0$), a sufficient condition to have $V^{\alpha,n+1}>0$ (and symmetrically $V^{\beta,n+1}>0$) is:

$$\delta t\sum_{b\in\mathcal{F}}V_b^n\left(\beta_b^n\left[2\boldsymbol{v}_{0,a|b}\cdot\boldsymbol{\nabla}w_{ab}^n\right]^+ + \frac{\nu_{T,a}^n+\nu_{T,b}^n}{2\mathrm{Sc}_T}\varphi_{ab}^n\right) \leq \frac{V_a^{n+1}}{V_a^n} \tag{C.23}$$

as the second term of the left-hand side of equation (C.12) is always positive.

We now search for an upper bound of the left-hand side term of the inequality (C.13). One can first write:

$$\delta t\sum_{b\in\mathcal{F}}V_b^n\left(\left[2\boldsymbol{v}_{0,a|b}\cdot\boldsymbol{\nabla}w_{ab}^n\right]^+ + \frac{\nu_{T,\max}}{\mathrm{Sc}_T}\varphi_{ab}^n\right) \leq \frac{V_a^{n+1}}{V_a^n} \tag{C.24}$$

where $\nu_{T,\max}=\max_{a\in\mathcal{F}}(\nu_T)$. And get, using the same terms as in the previous derivation:

$$\delta t\left(\eta_\alpha\frac{v_{0\,\max}}{\sigma_e} + \frac{\nu_{T,\max}}{\mathrm{Sc}_T\sigma_e^2}\right) \leq \xi_\alpha\frac{V_a^{n+1}}{V_a^n} \tag{C.25}$$

where η_α and ξ_α are unknown. Volumes do not vary a lot so that we may consider that the ratio V_a^{n+1}/V_a^n is close to 1. Noting the numerical Péclet number:

$$\mathrm{Pe}_\sigma = \frac{v_{0\,\max}\sigma_e\mathrm{Sc}_T}{\nu_{T,\max}} \tag{C.26}$$

one can deduce an approximate upper bound C_α to the condition for positiveness of phase volume:

$$\mathrm{C}_\alpha = \frac{v_{0\,\max}\delta t}{\sigma_e} \leq \xi_\alpha\left(\eta_\alpha + \frac{1}{\mathrm{Pe}_\sigma}\right)^{-1} \tag{C.27}$$

Appendix D

Analytical solution of the two-phase mixture Poiseuille flow

D.1 Description of the system to solve

At steady state, the volume fraction equation of (1.122) becomes:

$$\boldsymbol{\nabla} \cdot (\alpha\beta \boldsymbol{v}^r) = 0 \tag{D.1}$$

Under the longitudinal periodicity condition, it becomes:

$$\frac{d}{dz} (\alpha\beta \boldsymbol{v}^r \cdot \boldsymbol{e}_z) = 0 \tag{D.2}$$

The no-flux conditions at the upper and lower walls imply that at steady state the equation (D.2) becomes after integration:

$$\boldsymbol{v}^r \cdot \boldsymbol{e}_z = 0 \tag{D.3}$$

The volume fraction equation will therefore depend on the chosen closure on the relative velocity. Starting with the closure (3.42), the momentum equation of (1.122) becomes in this framework:

$$\begin{cases} \dfrac{dp}{dz} = -\rho g \\ \dfrac{d}{dz}\left(\rho\nu \dfrac{d}{dz}\boldsymbol{j} \cdot \boldsymbol{e}_x\right) + \rho \boldsymbol{F} \cdot \boldsymbol{e}_x = 0 \end{cases} \tag{D.4}$$

D.2 Linear combination of dynamic viscosities

In the simplified momentum equation (D.4), the dynamic viscosity defined by (1.89) is variable and depends on the volume fraction solution of equation (D.3). Let us nondimensionalize the

system using $z_\star = z/e$, $j_\star = \boldsymbol{j} \cdot \boldsymbol{e}_x / U_{m0}$ with $U_{m0} = \rho^\beta \left(\boldsymbol{F} \cdot \boldsymbol{e}_x\right) e^2 / \left(3\mu^\beta\right)$ (discharge for the usual single-fluid Poiseuille flow), $p_\star = p / \left(\rho^\beta g e\right)$ and introduce the Péclet number $\mathsf{Pe} = e|\boldsymbol{v}_0 \cdot \boldsymbol{e}_z|/K$ as the ratio of convective and diffusive transports. Noting the density ratio $R_\rho = \left(\rho^\alpha - \rho^\beta\right)/\rho^\beta$ and viscosity ratio $R_\mu = \left(\mu^\alpha - \mu^\beta\right)/\mu^\beta$, the system becomes:

$$\begin{cases} \dfrac{d\alpha}{dz_\star} = \mathsf{Pe}\ \alpha \\ \dfrac{dp_\star}{dz_\star} = -\left(1 + R_\rho \alpha\right) \\ \dfrac{d}{dz_\star}\left[\left(1 + R_\mu \alpha\right)\dfrac{dj_\star}{dz_\star}\right] = -3\left(1 + R_\rho \alpha\right) \end{cases} \tag{D.5}$$

Constant dynamic viscosity The nondimensionalized solution for a constant dynamic viscosity $\mu = \mu^\alpha = \mu^\beta$ writes:

- Volume fraction

$$\alpha\left(z_\star\right) = \alpha_1 \exp\left(\mathsf{Pe}\ z_\star\right) \tag{D.6}$$

- Longitudinal velocity

$$j_\star(z_\star) = \frac{3}{2}\left(1 - z_\star^2\right) + \frac{3\alpha_1 R_\rho}{\mathsf{Pe}^2}\left(\cosh\left(\mathsf{Pe}\right) + z_\star \sinh\left(\mathsf{Pe}\right) - \exp\left(\mathsf{Pe}\ z_\star\right)\right) \tag{D.7}$$

- Pressure profile

$$p_\star\left(z_\star\right) = p_{B\star} + 1 - z_\star + \alpha_1 R_\rho \frac{\exp\left(\mathsf{Pe}\right)}{\mathsf{Pe}}\left[1 - \exp\left(-\mathsf{Pe}\left(1 - z_\star\right)\right)\right] \tag{D.8}$$

  where $p_{B\star}$ is the background pressure nondimensionalized as the total pressure.

By integrating the velocity over the height, one can deduce the discharge:

$$U_m = U\left[1 + 3\frac{\alpha_1 R_\rho}{\mathsf{Pe}^2}\left(\cosh\left(\mathsf{Pe}\right) - \frac{\sinh\left(\mathsf{Pe}\right)}{\mathsf{Pe}}\right)\right] \tag{D.9}$$

α_1 is computed thanks to the conservation of volume (integrating over the height of the channel) for a given initial uniform profile of $\alpha\left(z\right) = \alpha_0$:

$$\frac{\alpha_1}{\alpha_0} = \frac{\mathsf{Pe}}{\sinh\left(\mathsf{Pe}\right)} \tag{D.10}$$

To avoid complete separation of phases, (D.6) gives a condition on α_1:

$$0 \leq \alpha_1 \leq \exp\left(-\mathsf{Pe}\right) \tag{D.11}$$

And therefore a condition on the initial uniform volume fraction α_0 using (D.10):

$$0 \leq \alpha_0 \leq \frac{1-\exp\left(-2\mathsf{Pe}\right)}{2\mathsf{Pe}} \tag{D.12}$$

Variable dynamic viscosity We consider that the dynamic viscosity is left to vary according to the volume fraction. Only the momentum equation resolution is modified and we find:

$$\begin{aligned} j_\star(z_\star) &= \frac{3}{2}\left(1-z_\star^2\right)+\frac{3}{\mathsf{Pe}^2}\left[\mathsf{Li}_{2,R}\left(z_\star\right)+\mathsf{Pe}\, z_\star \ln_R\left(z_\star\right)\right. \\ &\quad \left.-\frac{r}{R}\ln_R\left(z_\star\right)+C_1\left(\ln_R\left(z_\star\right)-\mathsf{Pe}\, z_\star\right)-C_2\right] \end{aligned} \tag{D.13}$$

where Li_2 is the dilogarithm function that writes $\mathsf{Li}_2(x) = -\int_0^x \ln(1-t)/t\, dt$ [3]. If $|x| \leq 1$, one can write a series expression $\mathsf{Li}_2(x) = \sum_n x^n/n^2$. We introduced the notations $\ln_R\left(z_\star\right) = \ln\left(1+\alpha_1 R_\mu \exp\left(\mathsf{Pe}\, z_\star\right)\right)$ and $\mathsf{Li}_{2,R}\left(z_\star\right) = \mathsf{Li}_2\left(-\alpha_1 R_\mu \exp\left(\mathsf{Pe}\, z_\star\right)\right)$. C_1 and C_2 are deduced from the no-slip condition at walls:

$$C_1 = \frac{\mathsf{Li}_{2,R}(1)-\mathsf{Li}_{2,R}(-1)+\mathsf{Pe}\left[\ln_R\left(1\right)+\ln_R\left(-1\right)\right]-R_\rho/R_\mu\left[\ln_R\left(1\right)-\ln_R\left(-1\right)\right]}{2\mathsf{Pe}-\ln_R\left(1\right)+\ln_R\left(-1\right)} \tag{D.14}$$

$$C_2 = \mathsf{Li}_{2,R}(1)+\mathsf{Pe}\ln_R(1)-\frac{R_\rho}{R_\mu}\ln_R(1)+C_1\left(\ln_R(1)-\mathsf{Pe}\right) \tag{D.15}$$

D.3 Physical relative velocity

The complete analytical resolution is not possible with the relative velocity (1.101). We note $K_T = \nu_T^\beta/\mathsf{Sc}_T$ and assume that K_T and γ are constant. The Péclet number writes $\mathsf{Pe} = \left(\rho^\alpha-\rho^\beta\right) ge/\left(\gamma K_T\right)$. The dimensionless volume fraction equation becomes:

$$\frac{d\alpha}{dz} = \mathsf{Pe}\,\alpha\beta^2 \tag{D.16}$$

The integration with the partial fraction decomposition method leads to:

$$\ln\left(\alpha\left(z_\star\right)\right)-\ln\left(1-\alpha\left(z_\star\right)\right)+\frac{1}{1-\alpha\left(z_*\right)} = \mathsf{Pe}\, z_\star + C_0 \tag{D.17}$$

that is an implicit relation in α, C_0 being linked to the initial volume of the α phase in the domain. The consequent computation of the velocity profile is not possible explicitly. For small α (*i.e.* dispersed phase), we recover a profile of the form (D.6) so that we can approximately expect the previous profiles for pressure and velocity. By considering the variable $\alpha/(1-\alpha)$ in (D.17), one obtains an equation for which a solution can be expressed through the Lambert W_0 function

[89], namely the principal branch of the reciprocal of the function $z \to z\exp(z)$:

$$\alpha(z_\star) = \frac{\mathrm{W}_0(\psi_e(z_\star))}{\psi_e(z_\star)\exp(\psi_e(z_\star)) + \mathrm{W}_0(\psi_e(z_\star))} \tag{D.18}$$

where $\psi_e(z_\star) = \exp(\mathsf{Pe} z_\star + C_1 - 1)$.

D.4 Linear combination of kinematic viscosities

In the initial formulation used for the convergence studies on the two-phase Poiseuille flow, we considered the viscosity $\nu = \alpha\nu^\alpha + \beta\nu^\beta$.

Constant kinematic viscosity The adimensionalized solution for a constant kinematic viscosity $\nu = \nu^\alpha = \nu^\beta$ writes:

- Volume fraction

$$\alpha(z_\star) = \alpha_1 \exp(\mathsf{Pe}\, z_\star) \tag{D.19}$$

- Longitudinal velocity

$$\begin{aligned} j_\star(z_\star) &= \frac{3}{2}\left(1 - z_\star^2\right) \\ &+ \frac{3}{\mathsf{Pe}^2}\left[\mathsf{Li}_{2,r}(z_\star) + \mathsf{Pe}\, z_\star \ln_r(z_\star) + C_1\left(\mathsf{Pe}^2 z_\star + \mathsf{Pe}\ln_r(z_\star)\right) + C_2\right] \end{aligned} \tag{D.20}$$

where we used the notations $\ln_r(z_\star) = \ln(1 + \alpha_1 R_\rho \exp(\mathsf{Pe}\, z_\star))$ and $\mathsf{Li}_{2,r}(z_*) = \mathsf{Li}_2(-\alpha_1 R_\rho \exp(\mathsf{Pe}\, z_\star))$. C_1 and C_2 are deduced from the no-slip condition at walls:

$$C_1 = \frac{-\mathsf{Li}_{2,r}(1) + \mathsf{Li}_{2,r}(-1) - \mathsf{Pe}\left(\ln_r(1) + \ln_r(-1)\right)}{2\mathsf{Pe}^2 + \mathsf{Pe}\left(\ln_r(1) - \ln_r(-1)\right)} \tag{D.21}$$

$$\begin{aligned} C_2 \;=\; & \frac{\left[\mathsf{Pe}\ \ln_r(1) + \mathsf{Li}_{2,r}(1)\right]\left[\ln_r(-1) - \mathsf{Pe}\right]}{2\mathsf{Pe} + \ln_r(1) - \ln_r(-1)} \\ & + \frac{\left[\mathsf{Pe}\ln_r(-1) - \mathsf{Li}_{2,r}(-1)\right]\left[\ln_r(1) + \mathsf{Pe}\right]}{2\mathsf{Pe} + \ln_r(1) - \ln_r(-1)} \end{aligned} \tag{D.22}$$

Variable kinematic viscosity Noting $R_\nu = \left(\nu^\alpha - \nu^\beta\right)/\nu^\beta$, only the longitudinal velocity profile is modified:

$$\begin{aligned} j_\star(z_\star) = \quad & \frac{3}{2}\left(1-z_\star^2\right) + \frac{3}{\left(R_\nu - R_\rho\right)\mathsf{Pe}^2}\left[\mathsf{Pe}\left(R_\nu \ln_R\left(z_\star\right) - R_\rho \ln_r\left(z_\star\right)\right) z_\star\right. \\ & + R_\nu \mathsf{Li}_{2,R}\left(z_\star\right) - R_\rho \mathsf{Li}_{2,r}\left(z_\star\right) - R_\rho \ln_R\left(z_\star\right) + R_\rho \ln_r\left(z_\star\right) \\ & \left. + C_1\left(\left(R_\nu - R_\rho\right)\mathsf{Pe}^2 z_\star - \mathsf{Pe}\left(R_\nu \ln_R\left(z_\star\right) + R_\rho \ln_r\left(z_\star\right)\right)\right) + C_2\right] \end{aligned} \tag{D.23}$$

C_1 and C_2 are deduced from the no-slip condition at walls:

$$\begin{aligned} C_1 = & \frac{-\left(R_\rho + \mathsf{Pe}R_\nu\right)\ln_R\left(-1\right) + R_\rho\left(\mathsf{Pe}+1\right)\ln_r\left(-1\right)}{2\left(R_\nu - R_\rho\right)\mathsf{Pe}^2 - \mathsf{Pe}\left(R_\nu\left(\ln_R\left(1\right) - \ln_R\left(-1\right)\right) + R_\rho\left(\ln_r\left(1\right) - \ln_r\left(-1\right)\right)\right)} \\ & + \frac{-R_\nu\left(\mathsf{Li}_{2,R}\left(1\right) - \mathsf{Li}_{2,R}\left(-1\right)\right) + R_\rho\left(\mathsf{Li}_{2,r}\left(1\right) - \mathsf{Li}_{2,r}\left(-1\right)\right)}{2\left(R_\nu - R_\rho\right)\mathsf{Pe}^2 - \mathsf{Pe}\left(R_\nu\left(\ln_R\left(1\right) - \ln_R\left(-1\right)\right) + R_\rho\left(\ln_r\left(1\right) - \ln_r\left(-1\right)\right)\right)} \\ & + \frac{\left(R_\rho - \mathsf{Pe}R_\nu\right)\ln_R\left(1\right) + R_\rho\left(\mathsf{Pe}-1\right)\ln_r\left(1\right)}{2\left(R_\nu - R_\rho\right)\mathsf{Pe}^2 - \mathsf{Pe}\left(R_\nu\left(\ln_R\left(1\right) - \ln_R\left(-1\right)\right) + R_\rho\left(\ln_r\left(1\right) - \ln_r\left(-1\right)\right)\right)} \end{aligned} \tag{D.24}$$

$$\begin{aligned} C_2 = & -C_1\left[\left(R-r\right)\mathsf{Pe}^2 - \mathsf{Pe}\left(R\ln_R\left(1\right) + r\ln_r\left(1\right)\right)\right] \\ & -\mathsf{Pe}\left[R\ln_R\left(1\right) - r\ln_r\left(1\right)\right] - R\mathsf{Li}_{2,R}\left(1\right) + r\mathsf{Li}_{2,r}\left(1\right) + r\ln_R\left(1\right) - r\ln_r\left(1\right) \end{aligned} \tag{D.25}$$

Appendix E

Volume-weighted mixture model

Practical relations for mixtures quantities are first given. Then, mixture model equations are derived for the two sets of variables: the classical triplet $(Y^\alpha, \boldsymbol{v}, \boldsymbol{u}^\alpha)$ and the set chosen in this work $(\alpha, \boldsymbol{j}, \boldsymbol{v}^r)$.

E.1 Practical relations for mixture models

E.1.1 Density

$$\rho = \frac{m}{V} = \frac{m^\alpha + m^\beta}{V} = \frac{\rho^\alpha V^\alpha + \rho^\beta V^\beta}{V} = \alpha\rho^\alpha + \beta\rho^\beta \tag{E.1}$$

E.1.2 Mass fraction

$$Y^\alpha = \frac{m^\alpha}{m} = \frac{\rho^\alpha V^\alpha}{\rho V} = \frac{\alpha\rho^\alpha}{\rho} \tag{E.2}$$

Using (1.20), we have a direct relation between Y_α and α:

$$Y^\alpha = \frac{\alpha\rho^\alpha}{\alpha\rho^\alpha + \beta\rho^\beta} = \frac{\alpha}{\left(1 - \dfrac{\rho^\beta}{\rho^\alpha}\right)\alpha + \dfrac{\rho^\beta}{\rho^\alpha}} \text{ or reciprocally } \alpha = \frac{Y^\alpha}{\left(1 - \dfrac{\rho^\alpha}{\rho^\beta}\right)Y^\alpha + \dfrac{\rho^\alpha}{\rho^\beta}} \tag{E.3}$$

One can also deduce a link between density and volume fraction:

$$\rho = \frac{\rho^\alpha\rho^\beta}{\rho^\alpha Y^\beta + \rho^\beta Y^\alpha} \tag{E.4}$$

E.2 Velocities

Let us relate the mixture velocity $\boldsymbol{v}$ and the volumetric flux $\boldsymbol{j}$:

$$\boldsymbol{v} - \boldsymbol{j} = \frac{\alpha\rho^\alpha \boldsymbol{v}^\alpha + \beta\rho^\beta \boldsymbol{v}^\beta}{\rho} - \alpha\boldsymbol{v}^\alpha - \beta\boldsymbol{v}^\beta = \frac{\rho\boldsymbol{v}^\alpha - \beta\rho^\beta \boldsymbol{v}^r}{\rho} - \alpha\boldsymbol{v}^\alpha - \beta\boldsymbol{v}^\beta = \beta\left(1 - \frac{\rho^\beta}{\rho}\right)\boldsymbol{v}^r$$

Hence:

$$\boldsymbol{v} - \boldsymbol{j} = \alpha\beta\frac{\rho^\alpha - \rho^\beta}{\rho}\boldsymbol{v}^r \tag{E.5}$$

Phase velocities can be written in the volume-weighted framework:

$$\boldsymbol{v}^\alpha = \boldsymbol{j} + \beta\boldsymbol{v}^r \quad \text{and} \quad \boldsymbol{v}^\beta = \boldsymbol{j} - \alpha\boldsymbol{v}^r \tag{E.6}$$

For diffusion velocities, we have by definition:

$$Y^\alpha \boldsymbol{u}^\alpha + Y^\beta \boldsymbol{u}^\beta = 0 \tag{E.7}$$

E.3 From mixture velocity to volumetric flux

E.3.1 Continuity equation

The continuity equations of the two fluid model write:

$$\frac{\partial \alpha\rho^\alpha}{\partial t} + \boldsymbol{\nabla}\cdot(\alpha\rho^\alpha\boldsymbol{v}^\alpha) = 0 \tag{E.8}$$

E.3.1.1 Mass-weighted formulation

By summing over the two phases using (E.1):

$$\frac{\partial \rho}{\partial t} + \boldsymbol{\nabla}\cdot(\rho\boldsymbol{v}) = 0 \tag{E.9}$$

E.3.1.2 Volume-weighted formulation

Using (E.5) in (E.9):

$$\frac{\partial \rho}{\partial t} + \boldsymbol{\nabla}\cdot(\rho\boldsymbol{j}) = -\boldsymbol{\nabla}\cdot\left[\alpha\beta\left(\rho^\alpha - \rho^\beta\right)\boldsymbol{v}^r\right] \tag{E.10}$$

Under the constant phase density hypothesis, (E.8) becomes:

$$\frac{\partial \alpha}{\partial t} + \boldsymbol{\nabla}\cdot(\alpha\boldsymbol{v}^\alpha) = 0 \tag{E.11}$$

Summing this equation on the two phases and using (1.20), one gets:

$$\boldsymbol{\nabla} \cdot \boldsymbol{j} = 0 \tag{E.12}$$

Therefore

$$\frac{\partial \rho}{\partial t} + \boldsymbol{j} \cdot \boldsymbol{\nabla} \rho = -\boldsymbol{\nabla} \cdot \left[\alpha\beta \left(\rho^{\alpha} - \rho^{\beta} \right) \boldsymbol{v}^{r} \right] \tag{E.13}$$

E.3.2 Momentum equation

The starting point corresponds to the momentum equations of the two-fluid model including turbulence and interfacial deformation effects under the assumptions of the Section 1.1.3:

$$\begin{aligned} \frac{\partial \alpha\rho^{\alpha}\boldsymbol{v}^{\alpha}}{\partial t} + \boldsymbol{\nabla} \cdot \left(\alpha\rho^{\alpha}\boldsymbol{v}^{\alpha} \otimes \boldsymbol{v}^{\alpha} \right) = -\boldsymbol{\nabla} \left(\alpha p^{\alpha} \right) + \boldsymbol{\nabla} \cdot \left[\alpha \left(\mu^{\alpha} + \mu_{T}^{\alpha} \right) \left(\boldsymbol{\nabla}\boldsymbol{v}^{\alpha} + {}^{t}\boldsymbol{\nabla}\boldsymbol{v}^{\alpha} \right) \right] + \alpha\rho^{\alpha}\boldsymbol{g} \\ + \boldsymbol{\nabla} \cdot \left(2\alpha\mu^{\alpha}\mathbb{D}^{\alpha} \right) - \boldsymbol{\nabla} \cdot \left(\tfrac{2}{3}\alpha\rho^{\alpha}k^{\alpha}\boldsymbol{I} \right) + \boldsymbol{M}^{\alpha} \end{aligned} \tag{E.14}$$

E.3.2.1 Mass-weighted formulation

By summing (E.14) over the two phases, one gets:

$$\begin{aligned} &\frac{\partial}{\partial t} \left(\rho\boldsymbol{v} \right) + \boldsymbol{\nabla} \left(\rho Y^{\alpha}\boldsymbol{v}^{\alpha} \otimes \boldsymbol{v}^{\alpha} \right) + \boldsymbol{\nabla} \left(\rho Y^{\beta}\boldsymbol{v}^{\beta} \otimes \boldsymbol{v}^{\beta} \right) = -\boldsymbol{\nabla} p + \rho\boldsymbol{g} \\ &+ \boldsymbol{\nabla} \cdot \left[\rho Y^{\alpha} \left(\nu^{\alpha} + \nu_{T}^{\alpha} \right) \left(\boldsymbol{\nabla}\boldsymbol{v}^{\alpha} + {}^{t}\boldsymbol{\nabla}\boldsymbol{v}^{\alpha} \right) + \rho Y^{\beta} \left(\nu^{\beta} + \nu_{T}^{\beta} \right) \left(\boldsymbol{\nabla}\boldsymbol{v}^{\beta} + {}^{t}\boldsymbol{\nabla}\boldsymbol{v}^{\beta} \right) \right] \\ &+ \boldsymbol{\nabla} \cdot \left[2\rho \left(Y^{\alpha}\nu^{\alpha}\mathbb{D}^{\alpha} + Y^{\beta}\nu^{\beta}\mathbb{D}^{\beta} \right) \right] - \boldsymbol{\nabla} \cdot \left(\tfrac{2}{3}\rho \left(Y^{\alpha}k^{\alpha} + Y^{\beta}k^{\beta} \right) \boldsymbol{I} \right) + \boldsymbol{M} \end{aligned} \tag{E.15}$$

where, as suggested in Ishii and Hibiki [177], the mixture quantities introduced are:

$$p = \alpha p^{\alpha} + \beta p^{\beta} \tag{E.16}$$

$$\boldsymbol{M} = \boldsymbol{M}^{\alpha} + \boldsymbol{M}^{\beta} \tag{E.17}$$

We also introduce a mixture turbulent kinetic energy:

$$k = Y^{\alpha}k^{\alpha} + Y^{\beta}k^{\beta} \tag{E.18}$$

Let us simplify this relation by using mixture quantities. Using (E.6) and (E.5) and (E.7):

$$\begin{aligned}
&\boldsymbol{\nabla}\left(\rho Y^\alpha \boldsymbol{v}^\alpha \otimes \boldsymbol{v}^\alpha\right) + \boldsymbol{\nabla}\left(\rho Y^\beta \boldsymbol{v}^\beta \otimes \boldsymbol{v}^\beta\right) \\
= \;& \boldsymbol{\nabla}\left(\rho Y^\alpha \left(\boldsymbol{v}+\boldsymbol{u}^\alpha\right) \otimes \left(\boldsymbol{v}+\boldsymbol{u}^\alpha\right)\right) + \boldsymbol{\nabla}\left(\rho Y^\beta \left(\boldsymbol{v}+\boldsymbol{u}^\beta\right) \otimes \left(\boldsymbol{v}+\boldsymbol{u}^\beta\right)\right) \\
= \;& \boldsymbol{\nabla}\cdot\left(\rho \boldsymbol{v} \otimes \boldsymbol{v}\right) \\
& + \boldsymbol{\nabla}\left(\rho Y^\alpha \boldsymbol{v} \otimes \boldsymbol{u}^\alpha\right) + \boldsymbol{\nabla}\left(\rho Y^\alpha \boldsymbol{u}^\alpha \otimes \boldsymbol{v}\right) + \boldsymbol{\nabla}\left(\rho Y^\alpha \boldsymbol{u}^\alpha \otimes \boldsymbol{u}^\alpha\right) \\
& + \boldsymbol{\nabla}\left(\rho Y^\beta \boldsymbol{v} \otimes \boldsymbol{u}^\beta\right) + \boldsymbol{\nabla}\left(\rho Y^\beta \boldsymbol{u}^\beta \otimes \boldsymbol{v}\right) + \boldsymbol{\nabla}\left(\rho Y^\beta \boldsymbol{u}^\beta \otimes \boldsymbol{u}^\beta\right) \\
= \;& \boldsymbol{\nabla}\cdot\left(\rho \boldsymbol{v} \otimes \boldsymbol{v}\right) - \boldsymbol{\nabla}\left(\rho \boldsymbol{u}^\alpha \otimes \boldsymbol{u}^\beta\right)
\end{aligned} \tag{E.19}$$

Regarding the viscous efforts, the linear combination becomes:

$$\begin{aligned}
&\rho\left[Y^\alpha \nu^\alpha \left(\boldsymbol{\nabla}\boldsymbol{v}^\alpha + {}^t\boldsymbol{\nabla}\boldsymbol{v}^\alpha\right) + Y^\beta \nu^\beta \left(\boldsymbol{\nabla}\boldsymbol{v}^\beta + {}^t\boldsymbol{\nabla}\boldsymbol{v}^\beta\right)\right] \\
&= \rho\left[\nu\left(\boldsymbol{\nabla}\boldsymbol{v} + {}^t\boldsymbol{\nabla}\boldsymbol{v}\right) + Y^\alpha \nu^\alpha \left(\boldsymbol{\nabla}\boldsymbol{u}^\alpha + {}^t\boldsymbol{\nabla}\boldsymbol{u}^\alpha\right) + Y^\beta \nu^\beta \left(\boldsymbol{\nabla}\boldsymbol{u}^\beta + {}^t\boldsymbol{\nabla}\boldsymbol{u}^\beta\right)\right]
\end{aligned} \tag{E.20}$$

where $\nu = Y^\alpha \nu^\alpha + Y^\beta \nu^\beta$ that is not the mixture viscosity: one can see that there are additional viscous terms. Hence, introducing those results in (E.15), we recover the mixture momentum equation directly derived from a general balance equation:

$$\begin{aligned}
&\frac{\partial}{\partial t}\left(\rho \boldsymbol{v}\right) + \boldsymbol{\nabla}\cdot\left(\rho \boldsymbol{v} \otimes \boldsymbol{v}\right) = -\boldsymbol{\nabla}\left(p + \frac{2}{3}\rho k \boldsymbol{I}\right) + \boldsymbol{\nabla}\cdot\left[\rho\left(\nu+\nu_T\right)\left(\boldsymbol{\nabla}\boldsymbol{v} + {}^t\boldsymbol{\nabla}\boldsymbol{v}\right)\right] + \rho \boldsymbol{g} \\
&+\boldsymbol{\nabla}\cdot\left(\rho\left[Y^\alpha\left(\nu^\alpha + \nu_T^\alpha\right)\left(\boldsymbol{\nabla}\boldsymbol{u}^\alpha + {}^t\boldsymbol{\nabla}\boldsymbol{u}^\alpha\right) + Y^\beta\left(\nu^\beta + \nu_T^\beta\right)\left(\boldsymbol{\nabla}\boldsymbol{u}^\beta + {}^t\boldsymbol{\nabla}\boldsymbol{u}^\beta\right)\right]\right) \\
&+\boldsymbol{\nabla}\cdot\left[2\rho\left(Y^\alpha \nu^\alpha \mathbb{D}^\alpha + Y^\beta \nu^\beta \mathbb{D}^\beta\right)\right] + \boldsymbol{\nabla}\cdot\left(\rho \boldsymbol{u}^\alpha \otimes \boldsymbol{u}^\beta\right) + \boldsymbol{M}
\end{aligned} \tag{E.21}$$

where $\nu_T = Y^\alpha \nu_T^\alpha + Y^\beta \nu_T^\beta$. One recognizes on the first line the classical momentum equation for a single-phase flow. The two additional lines introduced viscous efforts linked to the diffusion velocity and interfacial deformation, together with convective transfers and interfacial source term linked to surface tension.

E.3.2.2 Volume-weighted formulation

One can inject (E.5) in (E.21), to deduce a relation in the volume-weighted framework. However it triggers several additional temporal and spatial derivatives involving the relative velocity that prevent a practicable resolution of the system. Rather, we shall use the constant phase density

approximation and derive the momentum equation on $\boldsymbol{j}$ using the combination on both phases of (E.14) divided by ρ^α:

$$\frac{\partial \alpha \boldsymbol{v}^\alpha}{\partial t} + \boldsymbol{\nabla} \cdot (\alpha \boldsymbol{v}^\alpha \otimes \boldsymbol{v}^\alpha) = -\frac{1}{\rho^\alpha} \boldsymbol{\nabla} (\alpha p^\alpha) + \frac{1}{\rho^\alpha} \boldsymbol{\nabla} \cdot \left[\alpha \left(\mu^\alpha + \mu_T^\alpha \right) \left(\boldsymbol{\nabla} \boldsymbol{v}^\alpha + {}^t \boldsymbol{\nabla} \boldsymbol{v}^\alpha \right) \right] + \alpha \boldsymbol{g} + \frac{1}{\rho^\alpha} \boldsymbol{\nabla} \cdot (2\alpha \mu^\alpha \mathbb{D}^\alpha) - \frac{1}{\rho^\alpha} \boldsymbol{\nabla} \cdot \left(\frac{2}{3} \alpha \rho^\alpha k^\alpha \boldsymbol{I} \right) + \frac{1}{\rho^\alpha} \boldsymbol{M}^\alpha \tag{E.22}$$

Following similar computations as in previous part, adding this relation on both phases yields:

$$\begin{aligned} &\frac{\partial \boldsymbol{j}}{\partial t} + \boldsymbol{\nabla} \cdot (\boldsymbol{j} \otimes \boldsymbol{j}) = -\frac{1}{\rho^\alpha} \boldsymbol{\nabla} (\alpha p^\alpha) - \frac{1}{\rho^\beta} \boldsymbol{\nabla} \left(\beta p^\beta \right) + \boldsymbol{g} - \boldsymbol{\nabla} \cdot (\alpha \beta \boldsymbol{v}^r \otimes \boldsymbol{v}^r) \\ &+ \frac{1}{\rho^\alpha} \boldsymbol{\nabla} \cdot \left(\alpha \left(\mu^\alpha + \mu_T^\alpha \right) \left(\boldsymbol{\nabla} \boldsymbol{v}^\alpha + {}^t \boldsymbol{\nabla} \boldsymbol{v}^\alpha \right) \right) + \frac{1}{\rho^\beta} \boldsymbol{\nabla} \cdot \left(\beta \left(\mu^\beta + \mu_T^\beta \right) \left(\boldsymbol{\nabla} \boldsymbol{v}^\beta + {}^t \boldsymbol{\nabla} \boldsymbol{v}^\beta \right) \right) \\ &+ \frac{1}{\rho^\alpha} \boldsymbol{\nabla} \cdot (2\alpha \mu^\alpha \mathbb{D}^\alpha) + \frac{1}{\rho^\beta} \boldsymbol{\nabla} \cdot \left(2\beta \mu^\beta \mathbb{D}^\beta \right) - \frac{1}{\rho^\alpha} \boldsymbol{\nabla} \cdot \left(\frac{2}{3} \alpha \rho^\alpha k^\alpha \boldsymbol{I} \right) - \frac{1}{\rho^\beta} \boldsymbol{\nabla} \cdot \left(\frac{2}{3} \beta \rho^\beta k^\beta \boldsymbol{I} \right) \\ &+ \left(\frac{1}{\rho^\alpha} - \frac{1}{\rho^\beta} \right) \boldsymbol{M}^\alpha + \frac{1}{\rho^\beta} \boldsymbol{M} \end{aligned} \tag{E.23}$$

One can see that because of the division by the phase densities, some combinations are not as natural as in the mass-weighted approach. Especially, we need an expression of the interfacial momentum transfer term $\boldsymbol{M}^\alpha$. Before going any further in these combinations, we therefore need to derive this expression. In this prospect we derive from (E.8) and (E.14) an equation on the relative velocity (at the moment without constant phase density):

$$\frac{\partial \boldsymbol{v}^\alpha}{\partial t} + \boldsymbol{v}^\alpha \cdot \boldsymbol{\nabla} \boldsymbol{v}^\alpha = -\frac{1}{\alpha \rho^\alpha} \boldsymbol{\nabla} (\alpha p^\alpha) + \frac{1}{\alpha \rho^\alpha} \boldsymbol{\nabla} \cdot \left[\alpha \left(\mu^\alpha + \mu_T^\alpha \right) \left(\boldsymbol{\nabla} \boldsymbol{v}^\alpha + {}^t \boldsymbol{\nabla} \boldsymbol{v}^\alpha \right) \right] + \boldsymbol{g} + \frac{1}{\alpha \rho^\alpha} \boldsymbol{\nabla} \cdot (2\alpha \mu^\alpha \mathbb{D}^\alpha) - \frac{1}{\alpha \rho^\alpha} \boldsymbol{\nabla} \cdot \left(\frac{2}{3} \alpha \rho^\alpha k^\alpha \boldsymbol{I} \right) + \frac{1}{\alpha \rho^\alpha} \boldsymbol{M}^\alpha \tag{E.24}$$

Subtracting this relation from one phase to the other, one gets a relation on the relative velocity:

$$\begin{aligned} &\frac{\partial \boldsymbol{v}^r}{\partial t} + \boldsymbol{v}^\alpha \cdot \boldsymbol{\nabla} \boldsymbol{v}^\alpha - \boldsymbol{v}^\beta \cdot \boldsymbol{\nabla} \boldsymbol{v}^\beta = -\frac{1}{\alpha \rho^\alpha} \boldsymbol{\nabla} (\alpha p^\alpha) + \frac{1}{\beta \rho^\beta} \boldsymbol{\nabla} \left(\beta p^\beta \right) \\ &+ \frac{1}{\alpha \rho^\alpha} \boldsymbol{\nabla} \cdot \left[\alpha \left(\mu^\alpha + \mu_T^\alpha \right) \left(\boldsymbol{\nabla} \boldsymbol{v}^\alpha + {}^t \boldsymbol{\nabla} \boldsymbol{v}^\alpha \right) \right] - \frac{1}{\beta \rho^\beta} \boldsymbol{\nabla} \cdot \left[\beta \left(\mu^\beta + \mu_T^\beta \right) \left(\boldsymbol{\nabla} \boldsymbol{v}^\beta + {}^t \boldsymbol{\nabla} \boldsymbol{v}^\beta \right) \right] \\ &+ \frac{1}{\alpha \rho^\alpha} \boldsymbol{\nabla} \cdot (2\alpha \mu^\alpha \mathbb{D}^\alpha) - \frac{1}{\beta \rho^\beta} \boldsymbol{\nabla} \cdot \left(2\beta \mu^\beta \mathbb{D}^\beta \right) \\ &- \frac{1}{\alpha \rho^\alpha} \boldsymbol{\nabla} \cdot \left(\frac{2}{3} \alpha \rho^\alpha k^\alpha \boldsymbol{I} \right) + \frac{1}{\beta \rho^\beta} \boldsymbol{\nabla} \cdot \left(\frac{2}{3} \beta \rho^\beta k^\beta \boldsymbol{I} \right) + \left(\frac{1}{\alpha \rho^\alpha} + \frac{1}{\beta \rho^\beta} \right) \boldsymbol{M}^\alpha - \frac{1}{\beta \rho^\beta} \boldsymbol{M} \end{aligned} \tag{E.25}$$

Expressing the interfacial momentum transfer:

$$\begin{aligned}\boldsymbol{M}^\alpha = \rho Y^\alpha Y^\beta \left(\frac{\partial \boldsymbol{v}^r}{\partial t} + \boldsymbol{v}^\alpha \cdot \boldsymbol{\nabla}\boldsymbol{v}^\alpha - \boldsymbol{v}^\beta \cdot \boldsymbol{\nabla}\boldsymbol{v}^\beta\right) + Y^\beta \boldsymbol{\nabla}\left(\alpha p^\alpha\right) - Y^\alpha \boldsymbol{\nabla}\left(\beta p^\beta\right) \\ - Y^\beta \boldsymbol{\nabla}\cdot\left[\alpha\left(\mu^\alpha + \mu_T^\alpha\right)\left(\boldsymbol{\nabla}\boldsymbol{v}^\alpha +^t \boldsymbol{\nabla}\boldsymbol{v}^\alpha\right)\right] + Y^\alpha \boldsymbol{\nabla}\cdot\left[\beta\left(\mu^\beta + \mu_T^\beta\right)\left(\boldsymbol{\nabla}\boldsymbol{v}^\beta +^t \boldsymbol{\nabla}\boldsymbol{v}^\beta\right)\right] \\ - Y^\beta \boldsymbol{\nabla}\cdot\left(2\alpha\mu^\alpha \mathbb{D}^\alpha\right) + Y^\alpha \boldsymbol{\nabla}\cdot\left(2\beta\mu^\beta \mathbb{D}^\beta\right) \\ + Y^\beta \boldsymbol{\nabla}\cdot\left(\frac{2}{3}\alpha\rho^\alpha k^\alpha \boldsymbol{I}\right) - Y^\alpha \boldsymbol{\nabla}\cdot\left(\frac{2}{3}\beta\rho^\beta k^\beta \boldsymbol{I}\right) + Y^\alpha \boldsymbol{M}\end{aligned} \tag{E.26}$$

Introducing (E.26) in (E.23), simplifying density factors with (E.1), and using (E.12), one gets:

$$\begin{aligned}&\frac{\partial \boldsymbol{j}}{\partial t} + \boldsymbol{j}\cdot\boldsymbol{\nabla}\boldsymbol{j} = -\frac{1}{\rho}\boldsymbol{\nabla}\left(p + \frac{2}{3}\rho k \boldsymbol{I}\right) + \frac{1}{\rho}\boldsymbol{\nabla}\cdot\left[\left(\mu + \mu_T\right)\left(\boldsymbol{\nabla}\boldsymbol{j} +^t \boldsymbol{\nabla}\boldsymbol{j}\right)\right] + \boldsymbol{g} \\ &+\frac{1}{\rho}\boldsymbol{\nabla}\cdot\left(\alpha\left(\mu^\alpha + \mu_T^\alpha\right)\left(\boldsymbol{\nabla}\left(\beta\boldsymbol{v}^r\right) +^t \boldsymbol{\nabla}\left(\beta\boldsymbol{v}^r\right)\right) - \beta\left(\mu^\beta + \mu_T^\beta\right)\left(\boldsymbol{\nabla}\left(\alpha\boldsymbol{v}^r\right) +^t \boldsymbol{\nabla}\left(\alpha\boldsymbol{v}^r\right)\right)\right) \\ &+\frac{1}{\rho}\boldsymbol{\nabla}\cdot\left[2\left(\alpha\mu^\alpha\mathbb{D}^\alpha + \beta\mu^\beta\mathbb{D}^\beta\right)\right] - \boldsymbol{\nabla}\cdot\left(\alpha\beta\boldsymbol{v}^r\otimes\boldsymbol{v}^r\right) + \frac{1}{\rho}\boldsymbol{M} \\ &+\alpha\beta\frac{\rho^\alpha - \rho^\beta}{\rho}\left(\frac{\partial \boldsymbol{v}^r}{\partial t} + \boldsymbol{v}^\alpha\cdot\boldsymbol{\nabla}\boldsymbol{v}^\alpha - \boldsymbol{v}^\beta\cdot\boldsymbol{\nabla}\boldsymbol{v}^\beta\right)\end{aligned} \tag{E.27}$$

At this point, compared to the previous section result on mass-weighted formulation, the only approximation we made was that phase densities are constant. Due to the choice of variables, we see that an additional term arose in the fourth line. This relation is simplified in the Section 1.3.2 regarding the physics considered and in order to have a practical way of solving this equation. For an homogeneous approach, $\boldsymbol{v}^r = \boldsymbol{0}$ and $\boldsymbol{j} = \boldsymbol{v}$ according to (E.5) so that we recover the common momentum equation:

$$\frac{\partial \boldsymbol{j}}{\partial t} + \boldsymbol{j}\cdot\boldsymbol{\nabla}\boldsymbol{j} = -\frac{1}{\rho}\boldsymbol{\nabla}\left(p + \frac{2}{3}\rho k \boldsymbol{I}\right) + \frac{1}{\rho}\boldsymbol{\nabla}\cdot\left[\left(\mu + \mu_T\right)\left(\boldsymbol{\nabla}\boldsymbol{j} +^t \boldsymbol{\nabla}\boldsymbol{j}\right)\right] + \boldsymbol{g} \tag{E.28}$$

If α is dispersed within the continuous phase β, so that one can use the closures (1.41) and (1.42), one can write more compactly the viscous strains. Let us focus on the additional viscous tensors without transpose parts nor turbulent viscosities (*i.e.* $\mathbb{T}_+^j = \mathbb{T}^j - \mu\boldsymbol{\nabla}\boldsymbol{j}$ if we ignore the transpose parts):

$$\mathbb{T}_+^j = \alpha\mu^\alpha\boldsymbol{\nabla}\left(\beta\boldsymbol{v}^r\right) - \beta\mu^\beta\boldsymbol{\nabla}\left(\alpha\boldsymbol{v}^r\right) + 2\alpha\mu^\alpha\mathbb{D}^\alpha + 2\beta\mu^\beta\mathbb{D}^\beta$$

$$\mathbb{D}^\alpha = \boldsymbol{0} \text{ and } \mathbb{D}^\beta = -\frac{1}{2\beta}\boldsymbol{\nabla}\beta\otimes\boldsymbol{v}^r$$

It yields:

$$\begin{aligned}
\mathbb{T}_{+}^{j} &= \alpha\mu^{\alpha}\boldsymbol{\nabla}\left(\beta\boldsymbol{v}^{r}\right)-\beta\mu^{\beta}\boldsymbol{\nabla}\left(\alpha\boldsymbol{v}^{r}\right)-\mu^{\beta}\boldsymbol{\nabla}\beta\otimes\boldsymbol{v}^{r} \\
&= \alpha\mu^{\alpha}\boldsymbol{\nabla}\left(\beta\boldsymbol{v}^{r}\right)-\mu^{\beta}\left(\beta\boldsymbol{\nabla}\left(\alpha\boldsymbol{v}^{r}\right)+\boldsymbol{\nabla}\beta\otimes\boldsymbol{v}^{r}\right) \\
&= \alpha\mu^{\alpha}\boldsymbol{\nabla}\left(\beta\boldsymbol{v}^{r}\right)-\mu^{\beta}\left[\beta\left(\boldsymbol{\nabla}\boldsymbol{v}^{r}-\boldsymbol{\nabla}\left(\beta\boldsymbol{v}^{r}\right)\right)+\boldsymbol{\nabla}\left(\beta\boldsymbol{v}^{r}\right)-\beta\boldsymbol{\nabla}\boldsymbol{v}^{r}\right] \\
&= \alpha\left(\mu^{\alpha}-\mu^{\beta}\right)\boldsymbol{\nabla}\left(\beta\boldsymbol{v}^{r}\right)
\end{aligned}$$

Appendix F

Pitch

This work has been presented in EDF R&D for the competition "Pitch ta thèse" (Prix du jury - Originalité, Prix du public), in the competition Ma thèse en 180 secondes (French equivalent to the "Three Minutes Thesis" initiated by the University of Queensland in 2008) at the final of Université Paris Est ("Les bulles font leur cinéma" available at [133]), and formed part of a making-of video for the competition Je filme ma formation ("3 ans en 3 minutes ou comment parler à tous de l'expérience de doctorat" available at [132]).

T. Fonty: Bonjour. Je suis thésard, et cela va peut-être vous surprendre... je prends parfois des vacances ! Mais même en vacances, je continue à penser à ma thèse. Tenez, l'été dernier. Séjour au Pays Basque. Ma planche de surf sous le bras, je longe un torrent jusqu'à la plage. Je me lance vite dans les rouleaux pour une session de surf plutôt musclée. Après l'effort, le réconfort : je partage un verre avec mes compagnons de fortune. Cet après-midi là, mon sujet de thèse m'est revenu trois fois à l'esprit ! Le torrent et ses eaux blanchies par les bulles d'air, la mousse des vagues qui déferlent, les bulles entraînées dans mon verre en me servant. Chaque fois, un même phénomène : l'entraînement d'air. Alors, qu'est ce qui se passe ? L'eau en mouvement vient capturer des bulles d'air au niveau d'une zone de discontinuité : quand le jet vient transpercer la surface de mon verre d'eau, quand la vague se referme et capture des poches d'air ou quand les tourbillons à la surface de l'eau, générés par la turbulence du fluide, emportent avec eux des bulles. Alors vous vous demandez sans doute pourquoi EDF, l'entreprise qui finance ma thèse, s'intéresse à ce phénomène ? Tout simplement parce qu'on le retrouve à grandes échelles sur ses infrastructures. Que ce soit le déversement d'une nappe d'eau au-dessus d'un barrage, le déferlement d'une vague sur une digue protégeant une centrale… toutes ces situations mettent en jeu des flots, des mélanges complexes d'eau et d'air, qu'il est important de représenter pour des questions tant de sécurité que de bon fonctionnement des ouvrages. Le but de mon travail de thèse est de simuler ces écoulements sur ordinateur. Pour cela, je fais appel à une méthode numérique particulière : la méthode SPH, pour Smoothed Particle Hydrodynamics. Hydrodynamique des particules lissées. Vous voilà bien avancés ! En fait, vous la connaissez sans doute un peu sans le savoir cette méthode. Vous vous rappelez dans le Seigneur des Anneaux, lorsque Gollum tombe et se fait engloutir par les laves de la fournaise du mont Destin. Eh bien, cette roche en fusion qui avale et consume le dernier porteur de l'anneau est simulée avec la méthode SPH. Elle consiste à voir le fluide, dans le film la lave, dans mon cas un mélange d'eau et d'air, comme plein de petits volumes, de petites billes, qui se déplacent et interagissent les unes avec les autres. Alors, certes dans l'animation on l'utilise pour rendre crédibles visuellement des écoulements très déformés, montrer des vagues réalistes mettant à mal l'esquif du héros ou un énorme tsunami ravageant la ville. Dans ma thèse, le logiciel de simulation que je développe sera amené à traiter des cas industriels. Il est donc important d'avoir une description fidèle de la réalité. Mais, comment vérifier la qualité, la justesse de mes simulations ? Pour cela, je peux les confronter à des résultats mathématiques pour des cas simples comme la remontée d'une bulle, ou des expériences réalisées en laboratoire pour des situations plus complexes comme le déferlement d'une vague. Alors, pendant vos prochaines vacances en bord de mer, ou votre prochaine séance ciné devant un film catastrophe, vous penserez peut-être à moi et *(imitant la voix de Gollum)* **mes précieuses billes** !

Bibliography

[1] GPUSPH official website. www.gpusph.org. Accessed: 2019-03-17.

[2] SPHERIC official website. spheric-sph.org/grand-challenges. Accessed: 2019-04-22.

[3] M. Abramowitz and I. Stegun. *Handbook of Mathematical Functions with Formulas, Graphs, and Mathematical Tables*. 1964.

[4] S. Adami, X. Y. Hu, and N. A. Adams. A conservative SPH method for surfactant dynamics. *Journal of Computational Physics*, 229:1909–1926, March 2010. doi: 10.1016/j.jcp.2009.11.015.

[5] S. Adami, X. Y. Hu, and N. A. Adams. A new surface-tension formulation for multi-phase SPH using a reproducing divergence approximation. *Journal of Computational Physics*, 229:5011–5021, July 2010. doi: 10.1016/j.jcp.2010.03.022.

[6] S. Adami, X. Hu, and N. A. Adams. A transport-velocity formulation for smoothed particle hydrodynamics. *Journal of Computational Physics*, 241:292–307, May 2013. doi: 10.1016/j.jcp.2013.01.043.

[7] R. Alihan and J. F. Sleath. Sediment Transport in Oscillatory Flow Over Flat Beds. *Journal of Hydraulic Engineering*, 113(3):308–321, 1987. doi: 10.1061/(ASCE)0733-9429(1987)113:3(308).

[8] C. E. Alvarado-Rodríguez, J. Klapp, L. Di G. Sigalotti, J. M. Domínguez, and E. de la Cruz Sánchez. Nonreflecting outlet boundary conditions for incompressible flows using SPH. *Computers & Fluids*, 159:177–188, December 2017. doi: 10.1016/j.compfluid.2017.09.020.

[9] A. Amicarelli, J.-C. Marongiu, F. Leboeuf, J. Leduc, and J. Caro. SPH truncation error in estimating a 3D function. *Computers & Fluids*, 44:279–296, May 2011. doi: 10.1016/j.compfluid.2011.01.018.

[10] T. B. Anderson and R. Jackson. Fluid Mechanical Description of Fluidized Beds. Equations of Motion. *Industrial & Engineering Chemistry Fundamentals*, 6:527–539, November 1967. doi: 10.1021/i160024a007.

[11] M. Antuono, A. Colagrossi, S. Marrone, and D. Molteni. Free-surface flows solved by means of SPH schemes with numerical diffusive terms. *Computer Physics Communications*, 181 (3):532–549, December 2010. doi: 10.1016/j.cpc.2009.11.002.

[12] R. Aris. *Vectors, Tensors and the Basic Equations of Fluid Mechanics*, chapter 9. Dover Publications, 1962. ISBN 978-04866611008.

[13] F. Aristodemo, S. Marrone, and I. Federico. SPH modelling of plane jets into water bodies through an inflow/outflow algorithm. *Ocean Engineering*, 105:160–175, September 2015. doi: 10.1016/j.oceaneng.2015.06.018.

[14] M. Assirelli, W. Bujalski, A. Eaglesham, and A. W. Nienow. Macro- and micromixing studies in an unbaffled vessel agitated by a Rushton turbine. *Chemical Engineering Science*, 63 (1):35–46, January 2008,. doi: 10.1016/j.ces.2007.07.074.

[15] D. Avesani, M. Dumbser, and A. Bellin. A new class of Moving-Least-Squares WENO–SPH schemes. *Journal of Computational Physics*, 270:278–299, August 2014. doi: 10.1016/j.jcp.2014.03.041.

[16] M. R. Baer and J. W. Nunziato. A Two-phase Mixture Theory for the Deflagration-to-Detonation Transition (DDT) in Reactive Granular Materials. *Journal of Multiphase Flows*, 12:861–889, 1986. doi: 10.1016/0301-9322(86)90033-9.

[17] S. Baldy. A generation-dispersion model of ambient and transient bubbles in the close vicinity of breaking waves. *Journal of Multiphase Flows*, 98(C10):18277–18293, October 1993. doi: 10.1029/93JC01627.

[18] L. Barrière-Fouchet, J.-F. Gonzalez, J. R. Murray, R. J. Humble, and S. T. Maddison. Dust distribution in protoplanetary disks - Vertical settling and radial migration. *Astronomy & Astrophysics*, 443(1):185–194, November 2005. doi: 10.1051/0004-6361:20042249.

[19] A. Behzadi, R. I. Issa, and H. Rusche. Modelling of dispersed bubble and droplet flow at high phase fractions. *Chemical Engineering Science*, 59(4):759–770, February 2004. doi: 10.1016/j.ces.2003.11.018.

[20] E. Bertevas, T. Tran-Duc, B. C. Khoo, and N. Phan-Thien. Smoothed Particle Hydrodynamics (SPH) Applications in Some Sediment Dispersion Problems. In *Proceedings of the 7th International Conference on Computational Methods (ICCM2016)*, Berkeley, California, United States, 2016.

[21] E. Bertevas, T. Tran-Duc, K. Le-Cao, B. C. Khoo, and N. Phan-Thien. A smoothed particle hydrodynamics (SPH) formulation of a two-phase mixture model and its application to turbulent sediment transport. *Physics of Fluids*, 31:103303, November 2019. doi: 10.1063/1.5122671.

[22] M. Lopez De Bertodano, R. T. Lahey, and O. C. Jones. Development of a $k - \epsilon$ Model for Bubbly Two-Phase Flow. *Journal of Fluids Engineering*, 116(1):128–134, March 1994. doi: 10.1115/1.2910220.

[23] N. J. Bertola, H. Wang, and H. Chanson. Air bubble entrainment at vertical plunging jets: a large-scale experimental study. Technical report, School of Civil Engineering, The University of Queensland, 2017. Hydraulic Model Report CH, 104/17.

[24] A. Biń. Gas entrainment by plunging liquid jets. *Chemical Engineering Science*, 48(21): 3585–3630, November 1993. doi: 10.1016/0009-2509(93)81019-R.

[25] F. Bischof, M. Höfken, and F. Durst. Design and construction of aeration systems for optimum operation of large wastewater treatment plants. *Water Science and Technology*, 33(12):189–198, 1996. doi: 10.1016/0273-1223(96)00473-8.

[26] F. Blondel, B. Audebert, T. Pasutto, and M. Stanciu. Condensation models and boundary conditions for non-equilibrium wet steam flows. *International Journal on Finite Volumes*, 10, 2013.

[27] F. G. Blottner. Accurate Navier-Stokes Results for the Hypersonic Flow over a Spherical Nosetip. *Journal of Spacecraft and Rockets*, 27(2):113–122, March 1990. doi: 10.2514/3.26115.

[28] R. Boes and W. Hager. Hydraulic Design of Stepped Spillways. *Journal of Hydraulic Engineering*, 129(9):671–679, September 2003. doi: 10.1061/(ASCE)0733-9429(2003)129:9(671).

[29] R. Boes and W. Hager. Two-Phase Flow Characteristics of Stepped Spillways. *Journal of Hydraulic Engineering*, 129(9):661–670, September 2003. doi: 10.1061/(ASCE)0733-9429(2003)129:9(661).

[30] P. Bohorquez. Finite volume method for falling liquid films carrying monodisperse spheres in Newtonian regime. *AIChE Journal*, 58(8):2601–2616, June 2012. doi: 10.1002/aic.13863.

[31] F. A. Bombardelli, I. Meireles, and J. Matos. Laboratory measurements and multi-block numerical simulations of the mean flow and turbulence in the non-aerated flow region of steep stepped spillways. *Environmental Fluid Mechanics*, 11(3):263–288, June 2011. doi: 10.1007/s10652-010-9188-6.

[32] J. Bonet and T. S. L. Lok. Variational and momentum preservation aspects of smoothed particle hydrodynamics formulations. *Computer Methods in Applied Mechanics and Engineering*, 180:97–115, 1999. doi: 10.1016/S0045-7825(99)00051-1.

[33] J. Boussinesq. Essai sur la théorie des eaux courantes. *Mémoires présentés par divers savants à l'Académie des Sciences*, 23(1):1–680, 1877.

[34] A. E. Boycott. Sedimentation of Blood Corpuscles. *Nature*, 104:532, January 1920. doi: 10.1038/104532b0.

[35] T. Brattberg and H. Chanson. Air entrapment and air bubble dispersion at two-dimensional plunging water jets. *Chemical Engineering Science*, 53(24):4113–4127, December 1998. doi: 10.1016/S0009-2509(98)80004-3.

[36] T. Brattberg, H. Chanson, and L. Toombes. Experimental Investigations of Free-Surface Aeration in the Developing Flow of Two-Dimensional Water Jets. *Journal of Fluids Engineering*, 120(4):738–744, December 1998. doi: 10.1115/1.2820731.

[37] T. Breinlinger, A. Wonisch, and T. Kraft. Simulation of particulate flows using coupled SPH and DEM simulations. In *Proceedings of the 6th International SPHERIC Workshop*, Hamburg, Germany, 2011.

[38] J. M. Brethour and C. W. Hirt. Drift model for two-component flows. Technical report, Flow Science, Inc., 2009. Technical note FSI-09-TN83Rev.

[39] F. Brezzi and J. Pitkäranta. On the stabilization of finite element approximations of the Stokes equations. *Efficient Solutions of Elliptic Systems, Notes on Numerical Fluid Mechanics*, 10:11–19, 1984. doi: 10.1007/978-3-663-14169-3_2.

[40] M. Brocchini and D. H. Peregrine. The dynamics of strong turbulence at free surfaces. Part 1. Description. *Journal of Fluid Mechanics*, 449(3):225–254, December 2001. doi: 10.1017/S0022112001006012.

[41] E. Buckingham. On Physically Similar Systems; Illustrations of the Use of Dimensional Equations. *Physical Review*, 4(4):345–376, October 1914. doi: 10.1103/PhysRev.4.345.

[42] J. Bühler and D. A. Papantoniou. On the motion of suspension thermals and particle swarms. *Journal of Hydraulic Research*, 39(6):643–653, 2001. doi: 10.1080/00221686.2001.9628293.

[43] H. H. Bui and G. D. Nguyen. A coupled fluid-solid SPH approach to modelling flow through deformable porous media. *International Journal of Solids and Structures*, 125:244–264, October 2017. doi: 10.1016/j.ijsolstr.2017.06.022.

[44] D. B. Bung. Developing flow in skimming flow regime on embankment stepped spillways. *Journal of Hydraulic Research*, 49(5):639–648, August 2011. doi: 10.1080/00221686.2011.584372.

[45] B. Bunner and G. Tryggvason. Dynamics of homogeneous bubbly flows Part 1. Rise velocity and microstructure of the bubbles. *Journal of Fluid Mechanics*, 466:17–52, September 2002. doi: 10.1017/S0022112002001179.

[46] A. D. Burns, T. Frank, I. Hamill, and J.-M. Shi. The Favre Averaged Drag Model for Turbulent Dispersion in Eulerian Multi-Phase Flows. In *Proceedings of the 5th International Conference on Multiphase Flow, ICMF'04*, Yokohama, Japan, 2004.

[47] G. C. Buscaglia, F. A. Bombardelli, and M. H. García. Numerical modeling of large-scale bubble plumes accounting for mass transfer effects. *International Journal of Multiphase Flow*, 28(11):1763–1785, November 2002. doi: 10.1016/S0301-9322(02)00075-7.

[48] J. C. Cano-Lozano, C. Martínez-Bazán, J. Magnaudet, and J. Tchoufag. Paths and wakes of deformable nearly spheroidal rising bubbles close to the transition to path instability. *Physical Review Fluids*, 1(5):053604, September 2016. doi: 10.1103/PhysRevFluids.1.053604.

[49] G. Carosi and H. Chanson. Turbulence characteristics in skimming flows on stepped spillways. *Canadian Journal of Civil Engineering*, 35(9):865–880, 2008. doi: 10.1139/L08-030.

[50] F. Felis Carrasco. *Atomisation et dispersion d'un jet liquide: approches numérique et expérimentale*. PhD thesis, Ecole Centrale de Marseille, 2017. Available at tel.archives-ouvertes.fr/tel-01558141.

[51] P. M. Carrica, F. J. Bonetto, D. A. Drew, and R. T. Lahey Jr. The interaction of background ocean air bubbles with a surface ship. *International Journal for Numerical Methods in Fluids*, 28(4):571–600, September 1998. doi: 10.1002/(SICI)1097-0363(19980930)28:4<571::AID-FLD731>3.0.CO;2-E.

[52] P. M. Carrica, D. A. Drew, F. J. Bonetto, and R. T. Lahey Jr. A polydisperse model for bubbly two-phase flow around a surface ship. *International Journal of Multiphase Flow*, 25 (2):257–305, March 1999. doi: 10.1016/S0301-9322(98)00047-0.

[53] A. M. Castro, J. Li, and P. M. Carrica. A mechanistic model of bubble entrainment in turbulent free surface flows. *International Journal of Multiphase Flow*, 86:35–55, November 2016. doi: 10.1016/j.ijmultiphaseflow.2016.07.005.

[54] H. Chanson. Etude des phénomènes d'entraînement d'air. Application aux évacuateurs de crue. *La Houille Blanche*, 6:443–462, 1992. doi: 10.1051/lhb/1989045.

[55] H. Chanson. Entraînement d'air dans les écoulements à surface libre : application aux évacuateurs de crues de barrage. *La Houille Blanche*, 4:277–285, 1992. doi: 10.1051/lhb/1992027.

[56] H. Chanson. Self-aerated flows on chutes and spillways. *Journal of Hydraulic Engineering*, 119(2):220–243, February 1993. doi: 10.1061/(ASCE)0733-9429(1993)119:2(220).

[57] H. Chanson. Air Bubble Diffusion in Supercritical Open Channel Flows. In *Proceedings of the 12th Australasian Fluid Mechanics Conference*, Sydney, Australia, 1995.

[58] H. Chanson. Air entrainment in two-dimensional turbulent shear flows with partially developed inflow conditions. *International Journal of Multiphase Flow*, 21(6):1107–1121, November 1995. doi: 10.1016/0301-9322(95)00048-3.

[59] H. Chanson. *Air Bubble Entrainment in Free-Surface Turbulent Shear Flows*. Academic Press, 1996. ISBN 978-0-12-168110-4. doi: 10.1016/B978-0-12-168110-4.X5000-0.

[60] H. Chanson. Caractéristiques diphasiques des écoulements sur les coursiers en marches d'escalier. *La Houille Blanche*, 8:16–28, December 2001. doi: 10.1051/lhb/2001084.

[61] H. Chanson. Drag reduction in skimming flow on stepped spillways by aeration. *Journal of Hydraulic Research*, 42(3):316–322, 2004. doi: 10.1080/00221686.2004.9641200.

[62] H. Chanson. Turbulent air-water flows in hydraulic structures: dynamic similarity and scale effects. *Environmental Fluid Mechanics*, 9(2):125–142, April 2009. doi: 10.1007/s10652-008-9078-3.

[63] H. Chanson. Convective transport of air bubbles in strong hydraulic jumps. *International Journal of Multiphase Flow*, 36(10):798–814, October 2010. doi: 10.1016/j.ijmultiphaseflow.2010.05.006.

[64] H. Chanson. Hydraulics of aerated flows: qui pro quo? *Journal of Hydraulic Research*, 51:223–243, 2013. doi: 10.1080/00221686.2013.795917.

[65] H. Chanson. Advective Diffusion of Air Bubbles in Turbulent Water Flows. In *Fluid Mechanics of Environmental Interfaces - 2nd Edition*. Taylor & Francis, 2013. ISBN 9780415621564.

[66] H. Chanson and T. Brattberg. Air entrainment by two-dimensional plunging jets: the impingement region and the very-near flow field. In *Proceedings of the 1998 ASME Fluids Engineering Division Summer Meeting*, Washington DC, United States, 1998.

[67] H. Chanson and G. Carosi. Turbulent time and length scale measurements in high-velocity open channel flows. *Experiments in Fluids*, 42(3):385–401, March 2007. doi: 10.1007/s00348-006-0246-2.

[68] H. Chanson and P. Lubin. Discussion of "Verification and validation of a computational fluid dynamics (CFD) model for air entrainment at spillway aerators". *Canadian Journal of Civil Engineering*, 37(1):135–138, September 2010. doi: 10.1139/L09-133.

[69] H. Chanson and L. Toombes. Experimental Investigations of Air Entrainment in Transition and Skimming Flows down a Stepped Chute. Application to Embankment Overflow Stepped Spillways. Technical Report CE158, Department of Civil Engineering, The University of Queensland, Brisbane, Australia, July 2001.

[70] H. Chanson and L. Toombes. Air-water flows down stepped chutes: turbulence and flow structure observations. *International Journal of Multiphase Flows*, 28(11):1737–1761, November 2002. doi: 10.1016/S0301-9322(02)00089-7.

[71] H. Chanson and L. Toombes. Strong interactions between free-surface aeration and turbulence in an open channel flow. *Experimental Thermal and Fluid Science*, 27(5):525–535, May 2003. doi: 10.1016/S0894-1777(02)00266-2.

[72] H. Chanson, S.-I. Aoki, and M. Maruyama. Unsteady air bubble entrainment and detrainment at a plunging breaker: dominant time scales and similarity of water level variations. *Coastal Engineering*, 46(2):139–157, July 2002. doi: 10.1016/S0378-3839(02)00069-8.

[73] H. Chanson, S. Aoki, and A. Hoque. Physical modelling and similitude of air bubble entrainment at vertical circular plunging jets. *Chemical Engineering Science*, 59(4):747–758, February 2004. doi: 10.1016/j.ces.2003.11.016.

[74] H. Chanson, S. Aoki, and A. Hoque. Bubble Entrainment and Dispersion in Plunging Jet Flows: Freshwater *vs.* Seawater. *Journal of Coastal Research*, 22(3):664–677, May 2006. doi: 10.2112/03-0112.1.

[75] G. Chanteperdrix. *Modélisation et simulation numérique d'écoulements diphasiques à interface libre. Application à l'étude des mouvements de liquides dans les réservoirs de véhicules spatiaux*. PhD thesis, École Nationale Supérieure de l'Aéronautique et de l'Espace, Toulouse, Centre National d'Études Spatiales, 2004. 39–42.

[76] P. Chassaing, R. A. Antonia, F. Anselmet, L. Joly, and S. Sarkar. *Variable Density Fluid Turbulence*. Springer, 2002. ISBN 978-1-4020-0671-5. doi: 10.1007/978-94-017-0075-7.

[77] K.-C. Chen and Y.-C. Tai. Volume-weighted mixture theory for granular materials. *Continuum Mechanics and Thermodynamics*, 19:457–474, February 2007. doi: 10.1007/s00161-007-0064-7.

[78] Z. Chen, Z. Zong, M. B. Liu, L. Zou, H. T. Li, and C. Shu. An SPH model for multiphase flows with complex interfaces and large density differences. *Journal of Computational Physics*, 283:169–188, February 2015. doi: 10.1016/j.jcp.2014.11.037.

[79] X. Cheng, Y. Chen, and L. Luo. Numerical simulation of air-water two-phase flow over stepped spillways. *Science in China Series E: Technological Sciences*, 49:674–684, December 2006. doi: 10.1007/s10288-006-2029-2.

[80] A. K. Chesters. The modelling of coalescence processes in fluid-liquid dispersions: a review of current understanding. *Chemical Engineering Research and Design*, 69:259–270, 1991.

[81] L. Chiron. *Couplage et améliorations de la méthode SPH pour traiter des écoulements à multi-échelles temporelles et spatiales*. PhD thesis, École Centrale de Nantes, 2017. Available at tel.archives-ouvertes.fr/tel-01529282.

[82] L. Chiron, M. de Leffe, G. Oger, and D. Le Touzé. Fast and accurate SPH modelling of 3D complex wall boundaries in viscous and non viscous flows. *Computer Physics Communications*, 234:93–111, January 2019. doi: 10.1016/j.cpc.2018.08.001.

[83] A. J. Chorin. Numerical Solution of the Navier-Stokes Equations. *Mathematics of Computation*, 22(104):745–762, October 1968. doi: 10.1016/j.cpc.2018.08.001.

[84] C. Clanet and J. C. Lasheras. Depth of penetration of bubbles entrained by a plunging water jet. *Physics of Fluids*, 9(7):1864–1866, July 1997. doi: 10.1063/1.869336.

[85] R. Clift, J. R. Grace, and M. E. Weber. *Bubbles, Drops and Particles*. Dover, 1978. ISBN 0486445801.

[86] A. Colagrossi and M. Landrini. Numerical simulation of interfacial flows by smoothed particle hydrodynamics. *Journal of Computational Physics*, 191:448–475, 2003. doi: 10.1016/S0021-9991(03)00324-3.

[87] A. Colagrossi, M. Antuono, A. Souto-Iglesias, and D. Le Touzé. Theoretical analysis and numerical verification of the consistency of viscous smoothed-particle-hydrodynamics formulations in simulating free-surface flows. *Physical Review E*, 84, 2011. doi: 10.1103/PhysRevE.84.026705.

[88] R. H. Cole. *Underwater explosions*, chapter 2. Princeton University Press, 1948.

[89] R. M. Corless, G. H. Gonnet, D. E. G. Hare, D. J. Jeffrey, and D. E. Knuth. On the Lambert W function. *Advances in Computational Mathematics*, 5:329–359, December 1996. doi: 10.1007/BF02124750.

[90] P. V. Cueille. *Modélisation par Smoothed Particle Hydrodynamic des phénomènes de diffusion présents dans un écoulement*. PhD thesis, INSA de Toulouse, 2005. Available at core.ac.uk/download/pdf/35285308.pdf.

[91] P. D. Cummings and H. Chanson. Air Entrainment in the Developing Flow Region of Plunging Jets – Part 2: Experimental. *Journal of Fluids Engineering*, 119(3):597–602, September 1997. doi: 10.1115/1.2819286.

[92] P. D. Cummings and H. Chanson. Air Entrainment in the Developing Flow Region of Plunging Jets – Part 1: Theoretical Development. *Journal of Fluids Engineering*, 119(3):603–608, September 1997. doi: 10.1115/1.2819287.

[93] P. D. Cummings and H. Chanson. An Experimental Study of Individual Air Bubble Entrainment at a Planar Plunging Jet. *Chemical Engineering Research and Design*, 77(2):159–164, March 1999. doi: 10.1205/026387699525918.

[94] S. J. Cummins and M. Rudman. An SPH projection method. *Journal of Computational Physics*, 152:584–607, 1999. doi: 10.1006/jcph.1999.6246.

[95] L. M. Dakssa and I. S. H. Harahap. Investigating rainfall-induced unsaturated soil slope instability: A meshfree numerical approach. *WIT Transactions on Engineering Sciences*, 73: 231–242, May 2012. doi: 10.2495/DEB120201.

[96] R. A. Dalrymple and O. Knio. SPH modelling of water waves. In *Proceedings of the 4th Conference on Coastal Dynamics*, pages 779–787, Lund, Sweden, 2001. doi: 10.1061/40566(260)8004.

[97] S. Dalziel. Toy models for Rayleigh Taylor instability. In *8th International Workshop on the Physics of Compressible Turbulent Mixing*, Lawrence Livermore National Laboratory, 2001.

[98] S. Márquez Damián. *An extended mixture model for the simultaneous treatment of small-scale and large-scale interfaces.* PhD thesis, Santiago, 2013. Available at http://bibliotecavirtual.unl.edu.ar:8080/tesis/handle/11185/489.

[99] S. Márquez Damián and N. M. Nigro. An extended mixture model for the simultaneous treatment of small-scale and large-scale interfaces. *International Journal for Numerical Methods in Fluids*, 75:547–574, July 2014. doi: 10.1002/fld.3906.

[100] M. H. Dao, H. Xu, E. S. Chan, and P. Tkalich. Numerical modelling of extreme waves by Smoothed Particle Hydrodynamics. *Natural Hazards and Earth System Sciences*, 11(2): 419–429, February 2011. doi: 10.5194/nhess-11-419-2011.

[101] R. M. Davies and G. I. Taylor. The mechanics of large bubbles rising through extended liquids and through liquids in tubes. *Proceedings of the Royal Society A*, 200:375–390, 1950. doi: 10.1098/rspa.1950.0023.

[102] M. de Leffe, D. Le Touzé, and B. Alessandrini. Normal flux method at the boundary for SPH. In *Proceedings of the 4th International SPHERIC Workshop*, Nantes, France, 2009.

[103] G. B. Deane and M. D. Stokes. Scale dependence of bubble creation mechanisms in breaking waves. *Nature*, 418(6900):839–844, August 2002. doi: 10.1038/nature00967.

[104] W. Dehnen and H. Aly. Improving convergence in smoothed particle hydrodynamics simulations without pairing instability. *Monthly Notices of the Royal Astronomical Society*, 425: 1068–1082, 2012. doi: 10.1111/j.1365-2966.2012.21439.x.

[105] J.M. Delhaye. Les divers modèles d'écoulements diphasiques gaz-liquide. *La Houille Blanche*, 3-4:179–192, 1984. doi: 10.1051/lhb/1984009.

[106] R. Denèfle. *Modélisation locale diphasique eau-vapeur des écoulements dans les générateurs de vapeur.* PhD thesis, Université Bordeaux 1, 2013. Available at ori-oai.u-bordeaux1.fr/pdf/2013/DENEFLE_ROMAIN_2013.pdf.

[107] R. Denèfle, S. Mimouni, J.-P. Caltagirone, and S. Vincent. Multifield hybrid approach for two-phase flow modeling - Part 1: Adiabatic flows. *Computers & Fluids*, 113:106–111, May 2015. doi: 10.1016/j.compfluid.2014.07.018.

[108] M. Derakhti and J. T. Kirby. Bubble entrainment and liquid–bubble interaction under unsteady breaking waves. *Computers & Fluids*, 761:464–506, December 2014. doi: 10.1017/jfm.2014.637.

[109] F. Dias, D. Dutykh, and J.-M. Ghidaglia. A two-fluid model for violent aerated flows. *Computers & Fluids*, 39(2):283–293, February 2010. doi: 10.1016/j.compfluid.2009.09.005.

[110] T. Douillet-Grellier, F. De Vuyst, H. Calandra, and P. Ricoux. Simulations of intermittent two-phase flows in pipes using smoothed particle hydrodynamics. *Computers & Fluids*, 177:101–122, November 2018. doi: 10.1016/j.compfluid.2018.10.004.

[111] D. A. Drew. Mathematical modeling of two-phase flow. *Annual Review of Fluid Mechanics*, 15(1):261–291, 1983. doi: 10.1146/annurev.fl.15.010183.001401.

[112] D. A. Drew and R. T. Lahey Jr. Application of general constitutive principles to the derivation of multidimensional two-phase flow equations. *International Journal of Multiphase Flow*, 5:243–264, August 1979. doi: 10.1016/0301-9322(79)90024-7.

[113] D. A. Drew and R. T. Lahey. *Particulate Two-Phase Flow*. Butterworth Heinemann, 1993. ISBN 978-0-750-69275-5.

[114] D. A. Drew and S. L. Passman. *Theory of Multicomponent Fluids*. Springer, 1999. ISBN 978-0-387-22637-8. doi: 10.1007/978-0-387-22637-8.

[115] F. Dubois. Partial Riemann problem, boundary conditions, and gas dynamics. *Absorbing Boundaries and Layers, Domain Decomposition Methods: Applications to Large Scale Computations*, pages 16–77, 2001.

[116] C. T. Dyka and R. P. Ingel. An approach for tension instability in smoothed particle hydrodynamics (SPH). *Computers & Structures*, 57(4):573–580, November 1995. doi: 10.1016/0045-7949(95)00059-P.

[117] R. Ehrenberger. Wasserbewegung in steilen Rinnen (Schusstennen) mit besonderer Berücksichtigung der Selbstbelüftung (Flow of Water in Steep Chutes with Special Reference to Self-Aeration). *Zeitschrift des Österreichischen Ingenieur und Architektenvereins*, 15/16, 17/18, 1926.

[118] S. E. Elghobashi and T. W. Abou-Arab. A two-equation turbulence model for two-phase flows. *The Physics of Fluids*, 26(931):101–122, May 1983. doi: 10.1063/1.864243.

[119] S. Erpicum, M. Lodomez, J. Savatier, P. Archambeau, B. J. Dewals, and M. Pirotton. Physical Modeling of an Aerating Stepped Spillway. In *Proceedings of the 6th International Symposium on Hydraulic Structures*, Portland, Oregon, USA, 2016. doi: 10.15142/T368062816085.

[120] D. A. Ervine and H. T. Falvey. Behaviour of turbulent water jets in the atmosphere and in plunge pools. *Proceedings of the Institution of Civil Engineers*, 83(1):295–314, March 1987. doi: 10.1680/iicep.1987.353.

[121] P. Español and M. Revenga. Smoothed dissipative particle dynamics. *Physical Review E*, 67, 2003. doi: 10.1103/PhysRevE.67.026705.

[122] H. T. Falvey. *Air-Water Flow in Hydraulic Structures.* A water resources technical publication. Engineering Monograph No. 41, 1980.

[123] R. Fatehi and M. T. Manzari. A remedy for numerical oscillations in weakly compressible smoothed particle hydrodynamics. *International Journal for Numerical Methods in Fluids*, 67(9):1100–1114, November 2011. doi: 10.1002/fld.2406.

[124] A. Favre. Equations statistiques de fluides turbulents compressibles. In *Proceedings of the 5th Carad. Congress of Applied Mechanics*, pages G3–G34, 1975.

[125] S. Felder and H. Chanson. Turbulence, dynamic similarity and scale effects in high-velocity free-surface above a stepped chute. *Experiments in Fluids*, 47(1):1–18, July 2009. doi: 10.1007/s00348-009-0628-3.

[126] S. Felder, M. Geuzaine, B. Dewals, and S. Erpicum. Nappe flows on a stepped chute with prototype-scale steps height: Observations of flow patterns, air-water flow properties, energy dissipation and dissolved oxygen. *Journal of Hydro-environment Research*, 2019. doi: 10.1016/j.jher.2019.07.004.

[127] J. Feldman and J. Bonet. Dynamic refinement and boundary contact forces in SPH with applications in fluid flow problems. *International Journal for Numerical Methods in Engineering*, 72(3):295–324, October 2007. doi: 10.1002/nme.2010.

[128] M. Ferrand, D. R. Laurence, B. D. Rogers, D. Violeau, and C. Kassiotis. Unified semi-analytical wall boundary conditions for inviscid, laminar or turbulent flows in the meshless SPH method. *International Journal for Numerical Methods in Fluids*, 71:446–472, 2013. doi: 10.1002/fld.3666.

[129] M. Ferrand, A. Joly, C. Kassiotis, D. Violeau, A. Leroy, F.-X. Morel, and B. D. Rogers. Unsteady open boundaries for SPH using semi-analytical conditions and Riemann solver in 2D. *Computer Physics Communications*, 210:29–44, 2017. doi: 10.1016/j.cpc.2016.09.009.

[130] A. Ferrari, M. Dumbser, E. F. Toro, and A. Armanini. A new 3D parallel SPH scheme for free surface flows. *Computers & Fluids*, 38(6):1203–1217, June 2009. doi: 10.1016/j.compfluid.2008.11.012.

[131] O. Flores, J. J. Riley, and A. R. Horner-Devine. On the dynamics of turbulence near a free surface. *Journal of Fluid Mechanics*, 821:248–265, June 2017. doi: 10.1017/jfm.2017.209.

[132] T. Fonty. 3 ans en 3 minutes ou comment parler à tous de l'expérience de doctorat, 2019. URL www.parcoursmetiers.tv/video-formation/6759-3-ans-en-3-minutes-ou-comment-parler-a-tous-de-lexperience-du-doctorat.

[133] T. Fonty. Les bulles font leur cinéma, 2019. URL https://youtu.be/ncXDB9AKDfA.

[134] T. Fonty, J. M. Lopez Asiain, A. Leroy, G. Guyot, D. Violeau, and A. Joly. Numerical Modelling of the Undersluices of the Rance Tidal Power Station with SPH. In *Proceedings of 12th international SPHERIC workshop*, Orense, Spain, 2017.

[135] T. Fonty, M. Ferrand, A. Leroy, A. Joly, and D. Violeau. An upwind scheme for conservative, realizable two-phase mixture SPH model with high density ratios. In *Proceedings of 13th international SPHERIC workshop*, Galway, Ireland, 2018.

[136] T. Fonty, M. Ferrand, A. Leroy, A. Joly, and D. Violeau. Mixture model for two-phase flows with high density ratios: a conservative and realizable SPH formulation. *International Journal of Multiphase Flow*, 111:158–174, February 2019. doi: 10.1016/j.ijmultiphaseflow.2018.11.007.

[137] T. Fonty, M. Ferrand, A. Leroy, and D. Violeau. Air entrainment modelling using a Lagrangian accurate numerical model for high-density ratio two-phase mixtures. In *Proceedings of the 10th International Conference on Multiphase Flow*, Rio de Janeiro, Brazil, 2019.

[138] T. Fonty, M. Ferrand, A. Leroy, and D. Violeau. A first air entrainment SPH model using a two-phase mixture formulation. In *Proceedings of the 14th International SPHERIC Workshop*, Exeter, United Kingdom, 2019.

[139] C. J. Freitas. Perspective: Selected Benchmarks from Commercial CFD Codes. *Transactions of the ASME*, 117:208–218, 1995. doi: 10.1115/1.2817132.

[140] T. Funada and D. D. Joseph. Viscous potential flow analysis of Kelvin–Helmholtz instability in a channel. *Journal of Fluid Mechanics*, 445:263–283, October 2001. doi: 10.1017/S0022112001005572.

[141] D. Gao and J. A. Herbst. Alternative ways of coupling particle behaviour with fluid dynamics in mineral processing. *International Journal of Computational Fluid Dynamics*, 23: 109–118, April 2009. doi: 10.1080/10618560902754932.

[142] L. Gastaldo, R. Herbin, and J.-C. Latché. A discretization of the phase mass balance in fractional step algorithms for the drift-flux model. *IMA Journal of Numerical Analysis*, 31 (1):116–146, January 2011. doi: 10.1093/imanum/drp006.

[143] A. Ghaïtanellis. *Modélisation du charriage sédimentaire par une approche granulaire avec SPH*. PhD thesis, Université Paris Est, 2017.

[144] A. Ghaïtanellis, D. Violeau, A. Leroy, and A. Joly. Application of the unified semi-analytical wall boundary conditions to multi-phase SPH. In *Proceedings of the 10th international SPHERIC workshop*, pages 333–340, Parma, Italy, 2015.

[145] A. Ghaïtanellis, D. Violeau, M. Ferrand, K. El Kadi Abderrezzak, A. Leroy, and A. Joly. A SPH elastic-viscoplastic model for granular flows and bed-load transport. *Advances in Water Resources*, 111:156–173, January 2018. doi: 10.1016/j.advwatres.2017.11.007.

[146] R. A. Gingold and J. J. Monaghan. Smoothed particle hydrodynamics: theory and application to non-spherical stars. *Monthly Notices of the Royal Astronomical Society*, 181:375–389, 1977. doi: 10.1093/mnras/181.3.375.

[147] K. Gong, S. Shao, H. Liu, B. Wang, and S.-K. Tan. Two-phase SPH simulation of fluid-structure interactions. *Journal of Fluids and Structures*, 65:155–179, August 2016. doi: 10.1016/j.jfluidstructs.2016.05.012.

[148] J. González-Cao, O. García-Feal, J. M. Domínguez, A. J. C. Crespo, and M. Gómez-Gesteira. Numerical analysis of Ski Jumps using DualSPHysics. In *Proceedings of the 14th International SPHERIC Workshop*, Exeter, United Kingdom, 2019.

[149] N. Grenier. *Modélisation numérique par la méthode SPH de la séparation eau-huile dans les séparateurs gravitaires*. PhD thesis, École Centrale de Nantes, 2009. Available at tel.archives-ouvertes.fr/tel-00664668v2.

[150] N. Grenier, M. Antuono, A. Colagrossi, D. Le Touzé, and B. Alessandrini. An Hamiltonian interface SPH formulation for multi-fluid and free surface flows. *Journal of Computational Physics*, 228(22):8380–8393, 2009. doi: 10.1016/j.jcp.2009.08.009.

[151] N. Grenier, D. Le Touzé, A. Colagrossi, G. Colicchio, and M. Antuono. SPH multiphase simulation of bubbly flows. Towards oil and water separation. In *Proceedings of the ASME 2013 32nd International Conference on Ocean, Offshore and Arctic Engineering OMAE 2013*, volume 7, Nantes, France, June 9-14, 2013. doi: 10.1115/OMAE2013-11610.

[152] HR Wallingford Steering Group. Air problems in pipelines – A design manual. Technical report, HR Wallingford, 2005.

[153] C. Gualtieri and H. Chanson. Experimental analysis of Froude number effect on air entrainment in the hydraulic jump. *Environmental Fluid Mechanics*, 7(3):217–238, 2007. doi: 10.1007/s10652-006-9016-1.

[154] V. Guimet and D. Laurence. A linearised turbulent production in the $k - \epsilon$ model for engineering applications. In *Proceedings of the Vth International Symposium on Engineering Turbulence Modelling and Measurements*, pages 157–166, Majorca, Spain, 2002. doi: 10.1016/B978-008044114-6/50014-4.

[155] G. Guyot and M. Rodriguez. La Coche Pelton enhancement project scale model. In *Proceedings of the 37th IAHR World Congress*, Kuala Lumpur, Malaysia, 2017.

[156] W. L. Haberman and R. K. Morton. An experimental investigation of the drag and shape of air bubbles rising in various liquids. Technical Report 802, Armed Services Technical Information Agency – Navy Department, Washington, September 1953.

[157] J. S. Hadamard. Mouvement permanent lent d'une sphère liquide et visqueuse dans un liquide visqueux. *Comptes rendus hebdomadaires des séances de l'Académie des sciences*, 152:1735–1738, 1911.

[158] I. Hammani, G. Oger, D. Le Touzé, A. Colagrossi, and S. Marrone. How to derive the multifluid delta-SPH model. In *Proceedings of the 13th International SPHERIC Workshop*, Galway, Ireland, 2018.

[159] T. J. Hanratty, T. Theofanous, J.-M. Delhaye, J. Eaton, J. McLaughlin, A. Prosperetti, S. Sundaresan, and G. Tryggvason. Workshop Findings. *International Journal of Multiphase Flow*, 29(7):1047–1059, July 2003. doi: 10.1016/S0301-9322(03)00068-5.

[160] Y. He, A. E. Bayly, A. Hassanpour, F. Muller, K. Wu, and D. Yang. A GPU-based coupled SPH-DEM method for particle-fluid flow with free surfaces. *Powder Technology*, 338:548–562, October 2018. doi: 10.1016/j.powtec.2018.07.043.

[161] V. Heller. Scale effects in physical hydraulic engineering models. *Journal of Hydraulic Research*, 49(3):293–306, 2011. doi: 10.1080/00221686.2011.578914.

[162] J. O. Hinze. Fundamentals of the hydrodynamic mechanism of splitting in dispersion processes. *AIChE Journal*, 1(3):289–295, September 1955. doi: 10.1002/aic.690010303.

[163] M. Hirschler, P. Kunz, M. Huber, F. Hahn, and U. Nieken. Open boundary conditions for ISPH and their application to micro-flow. *Journal of Computational Physics*, 307:614–633, February 2016. doi: 10.1016/j.jcp.2015.12.024.

[164] C. W. Hirt. Modeling turbulent air entrainment of air at a free surface. Technical report, Flow Science, Inc, 2003.

[165] C. W. Hirt and B. D. Nichols. Volume of Fluid (VOF) method for the dynamics of free boundaries. *Journal of Computational Physics*, 39(1):201–225, 1981. doi: 10.1016/0021-9991(81)90145-5.

[166] Wm. G. Hoover. Isomorphism linking smooth particles and embedded atoms. *Physica A: Statistical Mechanics and its Applications*, 260(3–4):244–254, November 1998. doi: 10.1016/S0378-4371(98)00357-4.

[167] S. M. Hosseini and J. J. Feng. Pressure boundary conditions for computing incompressible flows with SPH. *Journal of Computational Physics*, 230(19):7473–7487, August 2011. doi: 10.1016/j.jcp.2011.06.013.

[168] C.-T. Hsiao, X. Wu, J. Ma, and G. L. Chahine. Numerical and experimental study of bubble entrainment due to a horizontal plunging jet. In *Papers from the 29th Symposium on Naval Hydrodynamics*, Gothenburg, Sweden, 2012.

[169] T.-J. Hsu, J. T. Jenkins, and P. L.-F. Liu. On two-phase sediment transport: Dilute flow. *Journal of Geophysical Research: Oceans*, 108(C3):3057, March 2003. doi: 10.1029/2001JC001276.

[170] X. Y. Hu and N. A. Adams. A multi-phase SPH method for macroscopic and mesoscopic flows. *Journal of Computational Physics*, 213:844–861, 2006. doi: 10.1016/j.jcp.2005.09.001.

[171] X. Y. Hu and N. A. Adams. An incompressible multi-phase SPH method. *Journal of Computational Physics*, 227:264–278, 2007. doi: 10.1016/j.jcp.2007.07.013.

[172] X. Y. Hu and N. A. Adams. A constant-density approach for incompressible multi-phase SPH. *Journal of Computational Physics*, 228:2082–2091, April 2009. doi: 10.1016/j.jcp.2008.11.027.

[173] J. C. R. Hunt and J. M. R. Graham. Free-stream turbulence near plane boundaries. *Journal of Fluid Mechanics*, 84:209–235, January 1978. doi: 10.1017/S0022112078000130.

[174] M. Ihmsen, J. Bader, G. Akinci, and M. Teschner. Animation of air bubbles with SPH. *Proceedings of the International Conference on Computer Graphics Theory and Applications*, Volume 1: GRAPP, (VISIGRAPP 2011):225–234, 2011. doi: 10.5220/0003322902250234.

[175] S. Inutsuka. Godunov-type SPH. *Memorie della Società Astronomia Italiana*, 65:1027, 1994.

[176] M. Ishii. *Thermo-fluid dynamics theory of two-phase flow*, volume 22. Eyrolles, 1975.

[177] M. Ishii and T. Hibiki. *Thermo-fluid dynamics of two-phase flow – Second Edition.* Springer, 2011. ISBN 978-1-4419-7985-8.

[178] R. Issa, D. Violeau, E.-S. Lee, and H. Flament. *Modelling nonlinear water waves with RANS and LES SPH models*, chapter 14, pages 497–537. Advances in Coastal and Ocean Engineering | Advances in Numerical Simulation of Nonlinear Water Waves. World Scientific, 2010. doi: 10.1142/9789812836502_0014.

[179] Y. Jang, J.-C. Marongiu, E. Parkinson, N. Gervais, and H. Garcin. Riemann solvers and efficient boundary treatments: an hybrid SPH-finite volume numerical method. In *Proceedings of 3rd international SPHERIC workshop*, Lausanne, Switzerland, 2008.

[180] S. A. K. Jeelani and S. Hartland. Effect of dispersion properties on the separation of batch liquid-liquid dispersions. *Industrial & Engineering Chemistry Research*, 37(2):547–554, 1998. doi: 10.1021/ie970545a.

[181] Z. Ji, M. Stanic, E. A. Hartono, and V. Chernoray. Numerical simulations of oil flow inside a gearbox by Smoothed Particle Hydrodynamics (SPH) method. *Tribology International*, 127:47–58, November 2018. doi: 10.1016/j.triboint.2018.05.034.

[182] G. R. Johnson, R. A. Stryk, and H. Flament. Sph for high velocity impact computations. *Computer methods in applied mechanics and engineering*, 139:347–373, 1996. doi: 10.1016/S0045-7825(96)01089-4.

[183] D. J. Joseph. Rise velocity of a spherical cap bubble. *Journal of Fluid Mechanics*, 488:213–223, July 2003. doi: 10.1017/S0022112003004968.

[184] I. Kataoka, A. Serizawa, and D. C. Besnard. Prediction of turbulence suppression and turbulence modeling in bubbly two-phase flow. *Nuclear Engineering and Design*, 141(1–2):145–158, June 1993. doi: 10.1016/0029-5493(93)90099-U.

[185] A. Khayyer, H. Gotoh, Y. Shimizu, K. Gotoh, H. Falahaty, and S. Shao. Development of a projection-based SPH method for numerical wave flume with porous media of variable porosity. *Coastal Engineering*, 140(06):1–22, October 2018. doi: 10.1016/j.coastaleng.2018.05.003.

[186] K. Kiger and J. H. Duncan. Air-Entrainment Mechanisms in Plunging Jets and Breaking Waves. *Annual Review of Fluid Mechanics* , 44(06):563–596, January 2012. doi: 10.1146/annurev-fluid-122109-160724.

[187] J. R. C. King and S. J. Lind. A partitioned approach for multiphase flows using ISPH. In *Proceedings of the 14th International SPHERIC Workshop*, Exeter, United Kingdom, 2019.

[188] H. Kobus. Local air entrainment and detrainment. In *Symposium on Scale Effects in Modelling Hydraulic Structures*, Stuttgart, Germany, 1984. doi: 10.18419/opus-559.

[189] H. Kobus. *An introduction to air-water flows*. Hydraulic structures design manual, 1985. ISBN 3-921694-61-2. doi: 10.18419/opus-604.

[190] H. Kobus and B. Westrich. An example of a combined disharge-control and aeration structure. In *Proceedings of the 20th Congress of the IAHR*, Moscow, USSR, 1983.

[191] A. N. Kolmogorov. The Local Structure of Turbulence in Incompressible Viscous Fluid for Very Large Reynolds. *Mathematical and Physical Sciences*, 434(1890):9–13, July 1991. doi: 10.1098/rspa.1991.0075.

[192] A. Krimi, M. Rezoug, S. Khelladi, X. Nogueira, M. Deligant, and L. Ramírez. Smoothed Particle Hydrodynamics: A consistent model for interfacial multiphase fluid flow simulations. *Journal of Computational Physics*, 358:53–87, April 2018. doi: 10.1016/j.jcp.2017.12.006.

[193] A. C. H. Kruisbrink, F. R. Pearce, T. Yue, and H. P. Morvan. An SPH multi-fluid model based on quasi buoyancy for interface stabilization up to high density ratios and realistic wave speed ratios. *Numerical Methods in Fluids*, 87(10):487–507, August 2018. doi: 10.1002/fld.4498.

[194] S. Kulasegaram, J. Bonet, R. W. Lewis, and M. Profit. A variational formulation based contact algorithm for rigid boundaries in two-dimensional SPH applications. *Computational Mechanics*, 33(4):316–325, March 2004. doi: 10.1007/s00466-003-0534-0.

[195] I. Kumagai, Y. Takahashi, and Y. Murai. Power-saving device for air bubble generation using a hydrofoil to reduce ship drag: Theory, experiments, and application to ships. *Ocean Engineering*, 95:183–194, February 2015. doi: 10.1016/j.oceaneng.2014.11.019.

[196] P. Kunz, M. Hirschler, M. Huber, and U. Nieken. Inflow/outflow with Dirichlet boundary conditions for pressure in ISPH. *Journal of Computational Physics*, 326:171–187, December 2016. doi: 10.1016/j.jcp.2016.08.046.

[197] J. Kwon. Smoothed particle hydrodynamics model for simulating miscible multi-fluid flow. *Journal of Computational Physics*, 384:114–133, 2019. doi: 10.1016/j.jcp.2018.12.007.

[198] J. Kwon and J. J. Monaghan. Sedimentation in homogeneous and inhomogeneous fluids using SPH. *International Journal of Multiphase Flow*, 72:155–164, 2015. doi: 10.1016/j.ijmultiphaseflow.2015.02.004.

[199] J. Kwon and J. J. Monaghan. A novel SPH method for simulating sedimentation in a turbulent tank. *Journal of Computational Physics*, 300:520–532, November 2015. doi: 10.1016/j.jcp.2015.06.040.

[200] M. Labois. *Modélisation des déséquilibres mécaniques dans les écoulements diphasiques : approches par relaxation et par modèle réduit.* PhD thesis, Université de Provence, Marseille, 2008. pp. 24–27. Available at tel.archives-ouvertes.fr/tel-00338818.

[201] R. T. Lahey Jr. The simulation of multidimensional multiphase flows. *Nuclear Engineering and Design*, 235:1043–1060, May 2005. doi: 10.1016/j.nucengdes.2005.02.020.

[202] L. D. Landau and E. M. Lifshitz. Section 163: The impossibility of the existence of phases in one-dimensional systems. In *Statistical Physics: Volume 5 of Course of Theoretical Physics*. Robert Maxwell, M. C., 1980. ISBN 0750633727.

[203] E. W. Lane. Recent Studies of Flow Conditions in Steep Chutes. *Engineering news - Record*, pages 5–7, January 1936.

[204] A. E. Larreteguy, L. F. Barceló, and P. A. Caron. A bounded upwind-downwind semi-discrete scheme for finite volume methods for phase separation problems. *Applied Mathematical Modelling*, 50:118–134, 2017. doi: 10.1016/j.apm.2017.05.003.

[205] M. Lastiwka, M. Basa, and N. J. Quinlan. Permeable and non-reflecting boundary conditions in SPH. *International Journal for Numerical Methods in Fluids*, 61(7):709–724, November 2009. doi: 10.1002/fld.1971.

[206] B. Launder and D. B. Spalding. The Numerical Computation of Turbulent Flow. *Computer Methods in Applied Mechanics and Engineering*, 3(2):269–289, March 1974. doi: 10.1016/0045-7825(74)90029-2.

[207] D. Layzer. On the Instability of Superposed Fluids in a Gravitational Field. *Astrophysical Journal*, 122:1, July 1955. doi: 10.1086/146048.

[208] J. Leduc, J.-C. Marongiu, F. Leboeuf, M. Lance, and E. Parkinson. Multiphase SPH: A new model based on acoustic Riemann solver. In *Proceedings of 4th international SPHERIC workshop*, Nantes, France, 2009.

[209] J. Leduc, F. Leboeuf, M. Lance, E. Parkinson, and J. C. Marongiu. Improvement of multiphase model using preconditioned Riemann solvers. In *Proceedings of the 5th International SPHERIC Workshop*, Manchested, United Kingdom, 2010.

[210] B. Van Leer. Towards the ultimate conservative difference scheme. V. A second-order sequel to Godunov's method. *Journal of Computational Physics*, 32(1):101–136, July 1979. doi: 10.1016/0021-9991(79)90145-1.

[211] T. G. Leighton, M. F. Schneider, and P. R. White. Study of bubble fragmentation using optical and acoustic techniques. In *Sea Surface Sound*, 1994.

[212] A. Leroy. *Un nouveau modèle SPH incompressible : vers l'application à des cas industriels*. PhD thesis, Université Paris Est, 2014. Available at pastel.archives-ouvertes.fr/tel-01126905.

[213] A. Leroy, D. Violeau, M. Ferrand, and C. Kassiotis. Unified semi-analytical wall boundary conditions applied to 2-d incompressible SPH. *Journal of Computational Physics*, 261:106–129, 2014. doi: 10.1016/j.jcp.2013.12.035.

[214] S. Li, J. Zhang, and W. Xu. Numerical investigation of air-water flow properties over steep float and pooled stepped spillways. *Journal of Hydraulic Research*, 56(1):1–14, April 2018. doi: 10.1080/00221686.2017.1286393.

[215] Y. Liao and D. Lucas. A literature review of theoretical models for drop and bubble breakup in turbulent dispersions. *Chemical Engineering Science*, 64(15):3389–3406, August 2009. doi: 10.1016/j.ces.2009.04.026.

[216] L. D. Libersky and A. G. Petschek. Smooth particle hydrodynamics with strength of materials. *Advances in the free-Lagrange method including contributions on adaptive gridding and the smooth particle hydrodynamics method*, pages 248–257, 1991. doi: 10.1007/3-540-54960-9_58.

[217] L. D. Libersky, A. G. Petschek, T. C. Carney, J. R. Hipp, and F. A. Allahdadi. High Strain Lagrangian Hydrodynamics: A Three-Dimensional SPH Code for Dynamic Material Response. *Journal of Computational Physics*, 109(1):67–75, November 1993. doi: 10.1006/jcph.1993.1199.

[218] S. J. Lind, P. K. Stansby, and B. D. Rogers. Incompressible smoothed particle hydrodynamics for free-surface flows: A generalised diffusion-based algorithm for stability and validations for impulsive flows and propagating waves. *Journal of Computational Physics*, 231(4):1499–1523, February 2012. doi: 10.1016/j.jcp.2011.10.027.

[219] S. J. Lind, P. K. Stansby, B. D. Rogers, and P. M. Lloyd. Numerical predictions of water-air wave slap using incompressible-compressible smoothed particle hydrodynamics. *Applied Ocean Research*, 49:57–71, January 2015. doi: 10.1016/j.apor.2014.11.001.

[220] S. J. Lind, P. K. Stansby, B. D. Rogers, and P. M. Lloyd. Incompressible-compressible flows with a transient discontinuous interface using smoothed particle hydrodynamics (SPH). *Journal of Computational Physics*, 309:129–147, March 2016. doi: 10.1016/j.jcp.2015.12.005.

[221] Y. Ling, S. Zaleski, and R. Scardovelli. Multiscale simulation of atomization with small droplets represented by a Lagrangian point-particle model. *International Journal of Multiphase Flow*, 76:122–143, November 2015. doi: 10.1016/j.ijmultiphaseflow.2015.07.002.

[222] S. Liu, Q. Liu, and Q. Peng. Realistic simulation of mixing fluids. *The Visual Computer*, 27: 241–248, March 2011. doi: 10.1145/2645703.

[223] E. Y. M. Lo and S. Shao. Simulation of near-shore solitary wave mechanics by an incompressible SPH method. *Applied Ocean Research*, 24:275–286, October 2002. doi: 10.1016/S0141-1187(03)00002-6.

[224] P. Lopes, G. Tabor, R. F. Carvalho, and J. Leandro. Explicit calculation of natural aeration using a Volume-of-Fluid model. *Applied Mathematical Modelling*, 40:7504–7515, April 2016. doi: 10.1016/j.apm.2016.03.033.

[225] P. Lopes, J. Leandro, and R. F. Carvalho. Self-Aeration Modelling Using a Sub-Grid Volume-Of-Fluid Model. *International Journal of Nonlinear Sciences and Numerical Simulation*, 18: 241–248, October 2017. doi: 10.1515/ijnsns-2017-0015.

[226] P. Lopes, J. Leandro, and R. F. Carvalho. Numerical procedure for free-sruface detection using a Volume-of-Fluid model. *Journal of Hydro-environment Research*, 21:43–51, October 2018. doi: 10.1016/j.jher.2018.07.002.

[227] P. Lubin and S. Glockner. Numerical simulations of three-dimensional plunging breaking waves: generation and evolution of aerated vortex filaments. *Journal of Fluid Mechanics*, 767:364–393, March 2015. doi: 10.1017/jfm.2015.62.

[228] P. Lubin, S. Vincent, S. Abadie, and J.-P. Caltagirone. Three-dimensional Large Eddy Simulation of air entrainment under plunging breaking waves. *Coastal Engineering*, 53(8): 631–655, June 2006. doi: 10.1016/j.coastaleng.2006.01.001.

[229] M. De Luca, A. Vallet, and R. Borghi. Pesticide atomization modeling for hollow-cone nozzle. *Atomization and Sprays*, 19(8):741–753, January 2009. doi: 10.1615/AtomizSpr.v19.i8.30.

[230] L. B. Lucy. A numerical approach to the testing of the fission hypothesis. *Astronomical Journal*, 82:1013–1024, 1977. doi: 10.1086/112164.

[231] J. Ma, A. A. Oberai, D. A. Drew, R. T. Lahey Jr, and F. J. Moraga. A quantitative sub-grid air entrainment model for bubbly flows - plunging jets. *Computers & Fluids*, 39(1):77–86, January 2010. doi: 10.1016/j.compfluid.2009.07.004.

[232] J. Ma, A. A. Oberai, and R. L. Lahey Jr. The simulation of air entrainment in a hydraulic jump using two-fluid DES and RANS models. In *Proceedings of the 7th International Conference on Multiphase Flow, ICMF 2010*, Tampa, Florida, 2010.

[233] J. Ma, A. A. Oberai, D. A. Drew, R. T. Lahey Jr, and M. C. Hyman. A Comprehensive Sub-Grid Air Entrainment Model for RANS Modeling of Free-Surface Bubbly Flows. *The Journal of Computational Multiphase Flows*, 3(1):41–56, March 2011. doi: 10.1260/1757-482X.3.1.41.

[234] J. Ma, A. A. Oberai, R. T. Lahey Jr, and D. A. Drew. Modeling air entrainment and transport in a hydraulic jump using two-fluid RANS and DES turbulence models. *Heat and Mass Transfer*, 47(911):C05010, August 2011. doi: 10.1007/s00231-011-0867-8.

[235] J. Ma, F. Shi, and J. T. Kirby. A polydisperse two-fluid model for surf zone bubble simulation. *Journal of Geophysical Research*, 116(C5):C05010, May 2011. doi: 10.1029/2010JC006667.

[236] J. Ma, A. A. Oberai, D. A. Drew, R. T. Lahey Jr, and M. C. Hyman. A Two-way Coupled Polydispersed Two-Fluid Model for the Simulation of Air Entrainment Beneath a Plunging

Liquid Jet. *Journal of Fluids Engineering*, 134(10):101304, October 2012. doi: 10.1115/1.4007335.

[237] H. Madarame and T. Chiba. Gas entrainment inception at the border of a flow-swollen liquid surface. *Nuclear Engineering and Design*, 120(2–3):193–201, June 1990. doi: 10.1016/0029-5493(90)90372-5.

[238] S. T. Maddison. *Gravitational Instabilities in Protostellar Disks*. PhD thesis, Monash University, 1998. Abstract at http://astronomy.swin.edu.au/~smaddiso/research/pubs/thesisabs.html.

[239] M. Manninen and V. Taivassalo. *On the mixture model for multiphase flow*, volume 288. Technical Research Center of Finland, 1996. ISBN 9513849465.

[240] J.-C. Marongiu. *Méthode numérique lagrangienne pour la simulation d'écoulements à surface libre : application aux turbines Pelton*. PhD thesis, École Centrale de Lyon, 2007.

[241] J.-C. Marongiu, J. Caro F. Leboeuf, and E. Parkinson. Free surface flows simulations in Pelton turbines using an hybrid SPH-ALE method. *Journal of Hydraulic Research*, 48:40–49, 2010. doi: 10.1080/00221686.2010.9641244.

[242] S. Marrone, M. Antuono, A. Colagrossi, and G. Graziani. δ-SPH model for simulating violent impact flows. *Computer Methods in Applied Mechanics and Engineering*, 200:1526–1542, 2011. doi: 10.1016/j.cma.2010.12.016.

[243] A. Di Mascio, M. Antuono, A. Colagrossi, and S. Marrone. Smoothed Particle Hydrodynamics method from a Large Eddy Simulation perspective. *Physics of Fluids*, 29:035102, March 2017. doi: 10.1063/1.4978274.

[244] R. W. P. May and I. R. Willoughby. Impact pressures in plunge basins due to vertical plunging jets. Technical report, HR Wallingford, 1991. SR242.

[245] A. Mayrhofer, B. D. Rogers, D. Violeau, and M. Ferrand. Investigation of wall bounded flows using SPH and the unified semi-analytical wall boundary conditions. *Computer Physics Communications*, 184(11):2515–2527, 2013. doi: j.cpc.2013.07.004.

[246] A. Mayrhofer, B. D. Rogers, D. Violeau, D. Laurence, and M. Ferrand. Direct numerical simulation of 3-D turbulent wall bounded flows with SPH. In *Proceedings of the 8th International SPHERIC Workshop*, Trondheim, Norway, 2019.

[247] D. F. McTigue. Mixture Theory for Suspended Sediment Transport. *Journal of the Hydraulics Division*, 107:659–673, January 1981. doi: 10.1016/j.nucengdes.2016.12.009.

[248] I. Meireles, F. Renna, J. Matos, and F. Bombardelli. Skimming, Nonaerated Flow on Stepped Spillways over Roller Compacted Concrete Dams. *Journal of Hydraulic Engineering*, 138:870–877, October 2012. doi: 10.1061/(ASCE)HY.1943-7900.0000591.

[249] I. Meireles, F. Bombardelli, and J. Matos. Air entrainment onset in skimming flows on steep stepped spillways: an analysis. *Journal of Hydraulic Research*, 52:375–385, 2014. doi: 10.1080/00221686.2013.878401.

[250] M. Meister and W. Rauch. Modelling aerated flows with smoothed particle hydrodynamics. *Journal of Hydroinformatics*, 17:493–504, July 2015. doi: 10.2166/hydro.2015.132.

[251] S. Mer, O. Praud, H. Neau, N. Merigoux, J. Magnaudet, and V. Roig. The emptying of a bottle as a test case for assessing interfacial momentum exchange models for Euler–Euler simulations of multi-scale gas-liquid flows. *International Journal of Multiphase Flow*, 106: 109–124, September 2018. doi: 10.1016/j.ijmultiphaseflow.2018.05.002.

[252] D. D. Meringolo, S. Marrone, A. Colagrossi, and Y. Liu. A dynamic delta-SPH model: how to get rid of diffusive parameter tuning. *Computers & Fluids*, 106:334–355, January 2019. doi: 10.1016/j.compfluid.2018.11.012.

[253] S. Mimouni, S. Fleau, and S. Vincent. CFD calculations of flow pattern maps and LES of multiphase flows. *Nuclear Engineering and Design*, 321:118–131, September 2017. doi: 10.1016/j.nucengdes.2016.12.009.

[254] A. Mokos, B. D. Rogers, P. K. Stansby, and J. M. Domínguez. Multi-phase SPH modelling of violent hydrodynamics on GPUs. *Computer Physics Communications*, 196:304–316, November 2015. doi: 10.1016/j.cpc.2015.06.020.

[255] A. Mokos, B. D. Rogers, and P. K. Stansby. A multi-phase particle shifting algorithm for SPH simulations of violent hydrodynamics with a large number of particles. *Journal of Hydraulic Research*, 55:143–162, 2017. doi: 10.1080/00221686.2016.1212944.

[256] G. Möller, M. Detert, and R. M. Boes. Vortex-Induced Air Entrainment Rates at Intakes. *Journal of Hydraulic Engineering*, 141(11):04015026, November 2015. doi: 10.1061/(ASCE) HY.1943-7900.0001036.

[257] D. Molteni and C. Bilello. Riemann solver in SPH. *Memorie della Società Astronomica Italiana Supplement*, 1:36, 2003.

[258] D. Molteni and A. Colagrossi. A simple procedure to improve the pressure evaluation in hydrodynamic context using the SPH. *Computer Physics Communications*, 180(6):861–872, June 2009. doi: 10.1016/j.cpc.2008.12.004.

[259] A. Di Monaco, S. Manenti, M. Gallati, S. Sibilla, and G. Agate. SPH Modeling of Solid Boundaries Through a Semi-Analytic Approach. *Engineering Applications of Computational Fluid Mechanics*, 5:1–15, 2011. doi: 10.1080/19942060.2011.11015348.

[260] J. J. Monaghan. On the problem of penetration in particle methods. *Journal of Computational Physics*, 82(1):1–15, May 1989. doi: 10.1016/0021-9991(89)90032-6.

[261] J. J. Monaghan. Smoothed Particle Hydrodynamics. *Annual Review of Astronomy and Astrophysics*, 30:543–574, 1992. doi: 10.1146/annurev.aa.30.090192.002551.

[262] J. J. Monaghan. Simulating free surface flows with SPH. *Journal of Computational Physics*, 110:399–406, 1994. doi: 10.1006/jcph.1994.1034.

[263] J. J. Monaghan. Implicit SPH drag and dusty gas dynamics. *Journal of Computational Physics*, 138:801–820, 1997. doi: 10.1006/jcph.1997.5846.

[264] J. J. Monaghan. SPH without a Tensile Instability. *Journal of Computational Physics*, 159 (2):290–311, April 2000. doi: 10.1006/jcph.2000.6439.

[265] J. J. Monaghan. Smoothed particle hydrodynamics. *Reports on Progress in Physics*, 68: 1703–1759, 2005. doi: 10.1088/0034-4885/68/8/R01.

[266] J. J. Monaghan and A. Kocharyan. SPH simulation of multi-phase flow. *Computer Physics Communications*, 87:225–235, 1995. doi: 10.1016/0010-4655(94)00174-Z.

[267] J. J. Monaghan and A. Kos. Solitary Waves on a Cretan Beach. *Journal of Waterway, Port, Coastal, and Ocean Engineering*, 125(3):145–154, May 1999. doi: 10.1061/(ASCE)0733-950X(1999)125:3(145).

[268] J. J. Monaghan and A. Rafiee. A simple SPH algorithm for multi-fluid flow with high density ratio. *International Journal for Numerical Methods in Fluids*, 71:537–561, February 2013. doi: 10.1002/fld.3671.

[269] A. Monteleone, M. Monteforte, and E. Napoli. Inflow/outflow pressure boundary conditions for smoothed particle hydrodynamics simulations of incompressible flows. *Computers & Fluids*, 159:9–22, December 2017. doi: 10.1016/j.compfluid.2017.09.011.

[270] D. W. Moore. The boundary layer on a spherical gas bubble. *Journal of Fluid Mechanics*, 16:161–176, 1963. doi: 10.1017/S0022112063000665.

[271] F. J. Moraga, P. M. Carrica, D. A. Drew, and R. T. Lahey Jr. The modeling of air entrainment processes for surface ships. *Mecánica Computacional 2005 - VIII Congreso Argentino de Mecánica Computacional*, 24:2549–2571, 2005.

[272] F. J. Moraga, P. M. Carrica, D. A. Drew, and R. T. Lahey Jr. A sub-grid air entrainment model for breaking bow waves and naval surface ships. *Computers & Fluids*, 37(3):281–298, March 2008. doi: 10.1016/j.compfluid.2007.06.003.

[273] A. Moreira, A. Leroy, D. Violeau, and F. Taveira-Pinto. Dam spillways and the SPH method: two case studies in Portugal. *Journal of Applied Water Engineering and Research*, 2019. doi: 10.1080/23249676.2019.1611496.

[274] J. P. Morris, P. J. Fow, and Y. Zhu. Modeling low Reynolds number incompressible flows using SPH. *Journal of Computational Physics*, 136(1):214–226, 1997. doi: 10.1006/jcph.1997.5776.

[275] M. Mortazavi, V. Le Chenadec, P. Moin, and A. Mani. Direct numerical simulation of a turbulent hydraulic jump: turbulence statistics and air entrainment. *Journal of Fluid Mechanics*, 797:60–94, June 2016. doi: 10.1017/jfm.2016.230.

[276] K. Nakasuji, M. Tamai, and A. Murota. Dynamic behaviour of sand clouds in water. *Proceedings of the International conference on Physics: Modeling of Transport and Dispersion, Massachusetts Institute of Technology*, Boston, United States, 1990.

[277] A. Nakayama, L. Y. Leong, and W. S. Kong. Development of Smoothed Particle Hydrodynamics Method for Analysis of High-Speed Two-Phase Flows in Hydropower Spillways. *AIP Conference Proceedings*, 1828(1):020027, April 2017. doi: 110.1063/1.4979398.

[278] M. Neuhauser. *Development of a coupled SPH-ALE/Finite Volume method for the simulation of transient flows in hydraulic machines.* PhD thesis, École Centrale de Lyon, 2015. 58–60.

[279] D. H. Nguyen, F. Levy, D. Pham Van Bang, S. Guillou, K. D. Nguyen, and J. Chauchat. Simulation of dredged sediment releases into homogeneous water using a two-phase model. *Advances in Water Resources*, 48:102–112, 2012. doi: 10.1016/j.advwatres.2012.03.009.

[280] M. S. Nigam. Numerical simulation of buoyant mixture flows. *International Journal of Multiphase Flows*, 29(6):983–1015, June 2003. doi: 10.1016/S0301-9322(03)00042-9.

[281] A. H. Nikseresht, N. Talebbeydokhti, and M. J. Rezaei. Numerical simulation of two-phase flow on step-pool spillways. *Scientia Iranica*, 20(2):222–230, April 2013. doi: 10.1016/j.scient.2012.11.013.

[282] S. Nugent and H. A. Posch. Liquid drops and surface tension with smoothed particle applied mechanics. *Physical Review E*, 62(4):222–230, October 2000. doi: 1063-651X/2000/62(4)/4968(8).

[283] G. Oger. *Aspects théoriques de la méthode SPH et applications à l'hydrodynamique à surface libre.* PhD thesis, École Centrale de Nantes, 2006. Available at docplayer.fr/54160459-Aspects-theoriques-de-la-methode-sph-et-applications-a-l-hydrodynamique-a-surface-libre-guillaume-oger.html.

[284] H. N. Oğuz, A. Prosperetti, and A. M. Lezzi. Examples of air-entraining flows. *Physics of Fluids A: Fluid Dynamics*, 4:649–651, November 1992. doi: 10.1063/1.858281.

[285] S. Osher and J. A. Sethian. Fronts propagating with curvature-dependent speed: Algorithms based on Hamilton-Jacobi formulations. *Journal of Computational Physics*, 79(1): 12–49, November 1988. doi: 10.1016/0021-9991(88)90002-2.

[286] W. Pan, J. Bao, and A. M. Tartakovsky. Smoothed particle hydrodynamics continuous boundary force method for Navier Stokes equations subject to a Robin boundary condition. *Journal of Computational Physics*, 259:242–259, 2014. doi: 10.1016/j.jcp.2013.12.014.

[287] A. N. Parshikov, S. A. Medin, I. I. Loukashenko, and V. A. Milekhin. Improvements in SPH method by means of interparticle contact algorithm and analysis of perforation tests at moderate projectile velocities. *International Journal of Impact Engineering*, 24(8):779–796, September 2000. doi: 10.1016/S0734-743X(99)00168-2.

[288] A. W. Patwardhan, R. G. Mali, S. B. Jadhao, K. D. Bhor, G. Padmakumar, and G. Vaidyanathanb. Argon entrainment into liquid sodium in fast breeder reactor. *Nuclear Engineering and Design*, 249:204–211, August 2012. doi: 10.1016/j.nucengdes.2011.07.046.

[289] C. Peng, G. Xu, W. Wu, H.-S. Yu, and C. Wang. Multiphase SPH modeling of free surface flow in porous media with variable porosity. *Computers and Geotechnics*, 81:239–248, January 2017. doi: 10.1016/j.compgeo.2016.08.022.

[290] D. H. Peregrine and L. Thais. The effect of entrained air in violent water wave impacts. *Journal of Fluid Mechanics*, 325:377–397, October 1996. doi: 10.1017/S0022112096008166.

[291] G. Pereira. *Modélisation numérique d'écoulements turbulents avec entraînement d'air au sein d'ouvrages hydrauliques*. PhD thesis, Université de Strasbourg, 2019.

[292] J. A. Perkins and E. Whitehead. Impact pressures in falling-jet energy dissipators - Literature review and preliminary experiments. Technical report, HR Wallingford, 1987. SR124.

[293] A. J. Peterka. The effect of entrained air on cavitation pitting. In *Proceedings of the 5th IAHR Congress*, Minneapolis, Minnesota, United States, 1953.

[294] M. Pfister and W. H. Hager. Self-entrainment of air on stepped spillways. *International Journal of Multiphase Flow*, 37(2):99–107, March 2011. doi: 10.1016/j.ijmultiphaseflow.2010.10.007.

[295] M. Politano, P. Carrica, and L. Weber. A multiphase model for the hydrodynamics and total dissolved gas in tailraces. *International Journal of Multiphase Flow*, 35(11):1036–1050, November 2009. doi: 10.1016/j.ijmultiphaseflow.2009.06.009.

[296] D. Price. Smoothed particle hydrodynamics and magnetohydrodynamics. *Journal of Computational Physics*, 231(3):759–794, February 2012. doi: 10.1016/j.jcp.2010.12.011.

[297] D. Price and G. Laibe. Two-phase mixtures in SPH – A new approach. *Proceedings of 10th international SPHERIC workshop, Parma, Italy*, pages 68–75, June 2015.

[298] D. J. Price and G. Laibe. A fast and explicit algorithm for simulating the dynamics of small dust grains with smoothed particle hydrodynamics. *Monthly Notices of the Royal Astronomical Society*, pages 1–15, September 2015. doi: 10.1093/mnras/stv996.

[299] A. Prosperetti and H. N. Oğuz. The Impact of Drops on Liquid Surfaces and the Underwater Noise of Rain. *Annual Review of Fluid Mechanics*, 25:577–602, September 1993. doi: 10.1146/annurev.fl.25.010193.003045.

[300] X. L. Qu, L. Khezzar, D. Danciu, M. Labois, and D. Lakehal. Characterization of plunging liquid jets: a combined experimental and numerical investigation. *International Journal of Multiphase Flow*, 37(7):722–731, September 2011. doi: 10.1016/j.ijmultiphaseflow.2011.02.006.

[301] N. J. Quinlan, M. Basa, and M. Lastiwka. Truncation error in mesh-free particle methods. *International Journal of Numerical Methods in Engineering*, 66(13):2064–2085, June 2006. doi: 10.1002/nme.1617.

[302] A. Rafiee, S. Cummins, M. Rudman, and K. Thiagarajan. Comparative study on the accuracy and stability of SPH schemes in simulating energetic free-surface flows. *European Journal of Mechanics - B/Fluids*, 36:1–16, November–December 2012. doi: 10.1016/j.euromechflu.2012.05.001.

[303] A. Rafiee, D. Dutykh, and F. Dias. Numerical simulation of wave impact on a rigid wall using two-phase compressible SPH method. *Procedia IUTAM*, 139:123–137, 2015. doi: 10.1016/j.piutam.2015.11.013.

[304] M. Rein. Phenomena of liquid drop impact on solid and liquid surfaces. *Fluid Dynamics Research*, 12(2):61–93, August 1993. doi: 10.1016/0169-5983(93)90106-K.

[305] B. Ren, C. Li, X. Yan, M. C. Ling, J. Bonet, and S.-M. Hu. Multiple-fluid SPH simulation using a mixture model. *ACM Transactions on Graphics*, 33:171:1–171:11, 2014. doi: 10.1145/2645703.

[306] M. Rezavand, M. Taeibi-Rahni, and W. Rauch. An ISPH scheme for numerical simulation of multiphase flows with complex interfaces and high density ratios. *Computers & Mathematics with Applications*, 75:2658–2677, April 2018. doi: 10.1016/j.camwa.2017.12.034.

[307] M. Rezavand, C. Zhang, and X. Hu. Multi-phase simulation of highly violent flows using an SPH method based on a Riemann solver. In *Proceedings of the 14th International SPHERIC Workshop*, Exeter, United Kingdom, 2019.

[308] C. M. Rhie and W. L. Chow. Numerical study of the turbulent flow past an airfoil with trailing edge separation. *AIAA Journal*, 21(11):1525–1532, 1983. doi: 10.2514/3.8284.

[309] R. G. Rice. Analytical solutions for film thinning dynamics in bubble coalescence. *AIChE Journal*, 52(4):1621–1622, April 2006. doi: 10.1002/aic.10742.

[310] W. K. M. Rice, G. Lodato, J. E. Pringle, P. J. Armitage, and I. A. Bonnell. Accelerated planetesimal growth in self-gravitating protoplanetary discs. *Monthly Notices of the Royal Astronomical Society*, 355(2):543–552, 2004. doi: 10.1111/j.1365-2966.2004.08339.x.

[311] J. F. Richardson and W. N. Zaki. Sedimentation and fluidisation: Part I. *Chemical Engineering Research and Design*, 75(Supplement):S82–S100, 1997. doi: 10.1016/S0263-8762(97)80006-8.

[312] M. Robinson and M. Ramaioli. Mesoscale fluid-particle interaction using two-way coupled SPH and the Discrete Element Method. In *Proceedings of the 6th International SPHERIC Workshop*, Hamburg, Germany, 2011.

[313] B. D. Rogers and R. A. Dalrymple. SPH modelling of breaking waves. *Coastal Engineering*, pages 415–427, 2004. doi: 10.1142/9789812701916_0032.

[314] H. Rouse. Modern conceptions of the mechanics of turbulence. *Transactions of the American Society of Civil Engineers*, 102(1):463–505, 1937.

[315] C. P. Ruggles and D. G. Murray. A review of fish response to spillways. Technical Report 1172, Canadian Technical Report of Fisheries and Aquatic Sciences, Halifax, Nova Scotia, 1983.

[316] H. Rusche. *Computational fluid dynamics of dispersed two-phase flows at high phase fractions*. PhD thesis, Imperial College, London, 2002. 115–120.

[317] E. M. Ryan, A. M. Tartakovsky, and C. Amon. A novel method for modeling Neumann and Robin boundary conditions in smoothed particle hydrodynamics. *Computer Physics Communications*, 181:2008–2023, 2010. doi: 10.1016/j.cpc.2010.08.022.

[318] W. Rybczynski. Über die fortschreitende Bewegung einer flüssigen Kugel in einem zähen Medium. *Bulletin international de l'Académie des sciences de Cracovie*, pages 40–46, 1911.

[319] J. Sauter. *Die Groössenbestimmung der im Gemischnebel von Verbrennungskraftmaschinen vorhandenen Brennstoffteilchen*. 1926.

[320] L. Schiller and Z. Naumann. A Drag Coefficient Correlation. *Zeitschrift des Vereins Deutscher Ingenieure Zeitung*, 77:318–320, March 1935.

[321] H. Sdiq, D. I. Graham, and J. Hughes. Smoothed Particle Hydrodynamics Modelling of a Flat Plate Impact on Aerated Water. In *Proceedings of the 14th International SPHERIC Workshop*, Exeter, United Kingdom, 2019.

[322] M. S. Shadloo, A. Zainali, M. Yildiz, and A. Suleman. A robust weakly compressible SPH method and its comparison with an incompressible SPH. *International Journal for Numerical Methods in Engineering*, 89(8):939–956, February 2012. doi: 10.1002/nme.3267.

[323] S. Shao. Incompressible smoothed particle hydrodynamics simulation of multifluid flows. *International Journal for Numerical Methods in Fluids*, 69(11):1715–1735, August 2012. doi: 10.1002/fld.2660.

[324] D. Shepard. A two-dimensional interpolation function for irregularly-spaced data. In *ACM '68 Proceedings of the 1968 23rd ACM national conference*, New York, NY, USA, 1968.

[325] F. Shi, J. T. Kirby, and G. Ma. Modeling quiescent phase transport of air bubbles induced by breaking waves. *Ocean Modelling*, 35(1–2):105–117, July 2010. doi: 10.1016/j.ocemod.2010.07.002.

[326] H. Shi and X. Yu. A two-phase SPH model for sediment transport in free surface flows. In *Proceedings of the SPHERIC Beijing 2017*, Beijing, China, 2017.

[327] H. Shi, X. Yu, and R. A. Dalrymple. Development of a two-phase SPH model for sediment laden flows. *Computer Physics Communications*, 221:259–272, 2017. doi: 10.1016/j.cpc.2017.08.024.

[328] H. Shi, P. Si, P. Dong, and X. Yu. A two-phase SPH model for massive sediment motion in free surface flows. *Advances in Water Resources*, 129:80–98, July 2019. doi: 10.1016/j.advwatres.2019.05.006.

[329] T.-H. Shih, W. W. Liou, A. Shabbir, Z. Yang, and J. Zhu. A new $k-\epsilon$ eddy-viscosity model for high Reynolds number turbulent flows-model development and validation. *Computers & Fluids*, 24(3):227–238, March 1995. doi: 10.1016/0045-7930(94)00032-T.

[330] Y. Shimizu, A. Khayyer, and H. Gotoh. Development of Enhanced ISPH method for accurate and consistent computational modeling of fluid flow interactions with saturated/unsaturated porous media of spatially variable porosity. In *Proceedings of the 14th International SPHERIC Workshop*, Exeter, United Kingdom, 2019.

[331] M. A. Esmaili Sikarudi and A. H. Nikseresht. Neumann and Robin boundary conditions for heat conduction modeling using smoothed particle hydrodynamics. *Computer Physics Communications*, 198:1—-11, 2016. doi: 10.1016/j.cpc.2015.07.004.

[332] O. Simonin. Prediction of the dispersed phase turbulence in particle-laden jets. *ASME FED*, 121:197–206, January 1994.

[333] A. Skillen, S. Lind, P. K. Stansby, and B. D. Rogers. Incompressible smoothed particle hydrodynamics (SPH) with reduced temporal noise and generalised Fickian smoothing applied to body–water slam and efficient wave–body interaction. *Computer Methods in*

Applied Mechanics and Engineering, 265:163–173, October 2013. doi: 10.1016/j.cma.2013.05.017.

[334] J. Smagorinsky. General Circulation Experiments with the Primitive Equation I the Basic Experiment. *Monthly Weather Review*, 91:99–164, 1963. doi: 10.1175/1520-0493(1963)091<0099:GCEWTP>2.3.CO;2.

[335] J. Smoller. *Shock waves and reaction-diffusion equations. Second edition.* Springer Verlag, 1994. ISBN 978-1-4612-0873-0.

[336] D. T. Souders and C. W. Hirt. Modeling Entrainment of Air at Turbulent Free Surfaces. In *World Water and Environmental Resources Congress 2004*, Salt Lake City, Utah, United States, 2004.

[337] P. N. Sun, A. Colagrossi, S. Marrone, and A. M. Zhang. Detection of Lagrangian Coherent Structures in the SPH framework. *Computer Methods in Applied Mechanics and Engineering*, 305:849–868, June 2016. doi: 10.1016/j.cma.2016.03.027.

[338] P. N. Sun, A. Colagrossi, S. Marrone, M. Antuono, and A.-M. Zhang. A consistent approach to particle shifting in the δ-Plus-SPH model. *Computer Methods in Applied Mechanics and Engineering*, 348:912–934, May 2019. doi: 10.1016/j.cma.2019.01.045.

[339] X. Sun, M. Sakai, and Y. Yamada. Three-dimensional simulation of a solid–liquid flow by the DEM–SPH method. *Journal of Computational Physics*, 248:147–176, September 2013. doi: 10.1016/j.jcp.2013.04.019.

[340] A. Tafuni, J. M. Domínguez, R. Vacondio, and A. J. C. Crespo. A versatile algorithm for the treatment of open boundary conditions in Smoothed particle hydrodynamics GPU models. *Computer Methods in Applied Mechanics and Engineering*, 342:604–624, December 2018. doi: 10.1016/j.cma.2018.08.004.

[341] A. M. Tartakovsky and P. Meakin. A smoothed particle hydrodynamics model for miscible flow in three-dimensional fractures and the two-dimensional Rayleigh–Taylor instability. *Journal of Computational Physics*, 207:610–624, August 2005. doi: 10.1016/j.jcp.2005.02.001.

[342] A. M. Tartakovsky, K. F. Ferris, and P. Meakin. Lagrangian particle model for multiphase flows. *Computer Physics Communications*, 180:1874–1881, October 2009. doi: 10.1016/j.cpc.2009.06.002.

[343] M. A. C. Teixera and S. E. Belcher. Dissipation of shear-free turbulence near boundaries. *Journal of Fluid Mechanics*, 422:167–191, November 2000. doi: 10.1017/S002211200000149X.

[344] S. Temkin. Sound propagation in bubbly liquids: A review. Technical report, Memorandum Report, Naval Research Lab., Washington, DC. Acoustic Systems Branch, 1989.

[345] A. Tomiyama, I. Kataoka, I. Zun, and T. Sakaguchi. Drag coefficients of single bubbles under normal and micro gravity conditions. *JSME International Journal Series B*, 41(2): 472–479, October 1998. doi: 10.1299/jsmed.41.472.

[346] A. Tomiyama, G. P. Celata, S. Hosokawa, and S. Yoshida. Terminal velocity of single bubbles in surface tension force dominant regime. *International Journal of Multiphase Flow*, 28(9):1497–1519, September 2002. doi: 10.1016/S0301-9322(02)00032-0.

[347] L. Toombes and H. Chanson. Air–Water Mass Transfer on a Stepped Waterway. *Journal of Environmental Engineering*, 131(10):1377–1386, October 2005. doi: 10.1061/(ASCE)0733-9372(2005)131:10(1377).

[348] E. Torti and S. Sibilla. SPH modelling of two-phase bubbly flows. In *7th International SPHERIC Workshop*, pages 1–6, Monash University Prato Centre, Italy, 2012.

[349] T. Tran-Duc, N. Phan-Thien, and B. Cheong Khoo. A smoothed particle hydrodynamics (SPH) study of sediment dispersion on the seafloor. *Physics of Fluids*, 29(8):083302, August 2017. doi: 10.1063/1.4993474.

[350] A. A. Troshko and Y. A. Hassan. A two-equation turbulence model of turbulent bubbly flows. *International Journal of Multiphase Flow*, 27(11):1965–2000, November 2001. doi: 10.1016/S0301-9322(01)00043-X.

[351] G. Černe, S. Petelin, and I. Tiselj. Coupling of the interface tracking and the two-fluid models for the simulation of incompressible two-phase flow. *Journal of Computational Physics*, 171(2):776–804, August 2001. doi: 10.1006/jcph.2001.6810.

[352] S. O. Unverdi and G. Tryggvason. A front-tracking method for viscous, incompressible, multi-fluid flows. *Journal of Computational Physics*, 100(1):25–37, May 1992. doi: 10.1016/0021-9991(92)90307-K.

[353] R. Vacondio, B. D. Rogers, P. K. Stansby, and P. Mignosa. SPH modelling of shallow flow with open boundaries for practical flood simulation. *Journal of Hydraulic Engineering*, 138 (6):530–541, June 2012. doi: 10.1061/(ASCE)HY.1943-7900.0000543.

[354] D. Valero and D. B. Bung. Hybrid Investigation of Air Transport Processes in Moderately Slopped Stepped Spillway Flows. In *E-proceedings of the 36th IAHR World Congres*, The Hague, Netherlands, 2015.

[355] D. Valero and D. B. Bung. Development of the interfacial air layer in the non-aerated region of high-velocity spillway flows. Instabilities growth, entrapped air and influence on the self-aeration onset. *International Journal of Multiphase Flow*, 84:66–74, September 2016. doi: 10.1016/j.ijmultiphaseflow.2016.04.012.

[356] D. Valero and D. B. Bung. Reformulating self-aeration in hydraulic structures: Turbulent growth of free surface perturbations leading to air entrainment. *International Journal of Multiphase Flow*, 100:127–142, March 2018. doi: 10.1016/j.ijmultiphaseflow.2017.12.011.

[357] D. Valero and R. García-Bartual. Calibration of an Air Entrainment Model for CFD Spillway Applications. *Advances in Hydroinformatics*, 84:571–582, January 2016. doi: 10.1007/978-981-287-615-7_38.

[358] A. Vallet, A. A. Burluka, and R. Borghi. Development of a Eulerian model for the "atomization" of a liquid jet. *Atomization and Sprays*, 11(6):741–753, November 2001. doi: 10.1615/AtomizSpr.v11.i6.20.

[359] A. Vergnaud, G. Oger, and D. Le Touzé. A higher order SPH scheme based on WENO reconstructions for two-dimensional problems. In *Proceedings of the 14th International SPHERIC Workshop*, Exeter, United Kingdom, 2019.

[360] J. P. Vila. On particle weighted methods and Smoothed Particle Hydrodynamics. *Mathematical Models and Methods in Applied Sciences*, 09:161–209, 1999. doi: 10.1142/S0218202599000117.

[361] L. Da Vinci. Della schiuma dell'acqua. In *Trattato della Pittura – Parte terza - De' vari accidenti e movimenti dell'uomo e proporzione di membra*. 1651.

[362] L. Da Vinci. Del moto e misura dell'acqua. In *Raccolta d'autori italiani che trattano del moto dell'acque. Vol. 10*. Francesco Cardinali, 1821-1826.

[363] D. Violeau. Dissipative forces for Lagrangian models in computational fluid dynamics and application to smoothed-particle hydrodynamics. *Physical Review E*, 80, 2009. doi: 10.1103/PhysRevE.80.036705.

[364] D. Violeau. *Fluid mechanics and the SPH method: theory and applications*. Oxford University Press, 2012. ISBN 978-0-19-965552-6. doi: 10.1093/acprof:oso/9780199655526.001.0001.

[365] D. Violeau and T. Fonty. Calculating the smoothing error in SPH. *Computers & Fluids*, 191: 104240, September 2019. doi: 10.1016/j.compfluid.2019.104240.

[366] D. Violeau and R. Issa. Numerical modelling of complex turbulent free-surface flows with the SPH method: an overview. *International Journal for Numerical Methods in Fluids*, 53 (2):277–304, January 2007. doi: 10.1002/fld.1292.

[367] D. Violeau and A. Leroy. On the maximum time step in weakly compressible SPH. *Journal of Computational Physics*, 256:388–415, 2014. doi: 10.1016/j.jcp.2013.09.001.

[368] D. Violeau, C. Buvat, K. Abed-Meraim, and E. de Nanteuil. Numerical modelling of boom and oil spill with SPH. *Coastal Engineering*, 54(12):895–913, December 2007. doi: 10.1016/j.coastaleng.2007.06.001.

[369] D. Violeau, A. Leroy, and A. Mayrhofer. Exact computation of SPH wall renormalising integrals in 3-D. In *Proceedings of the 9th International SPHERIC Workshop*, Nantes, France, 2014.

[370] P. L. Viollet and O. Simonin. Modelling Dispersed Two-Phase Flows: Closure, Validation and Software Development. *Applied Mechanics Reviews*, 47(6S):S80–S84, June 1994. doi: 10.1115/1.3124445.

[371] P.-L. Viollet, J.-P. Chabard, P. Esposito, and D. Laurence. *Mécanique des fluides appliquée. Écoulements incompressibles dans les circuits, canaux et rivières, autour des structures et dans l'environnement.* Presses de l'École Nationale des Ponts et Chaussées, 1999. ISBN 2859783016.

[372] N. Viti, D. Valero, and C. Gualtieri. Numerical simulation of hydraulic jumps. Part 2: recent results and future outlook. *Water*, 11(1):28, January 2019. doi: 10.3390/w11010028.

[373] G. B. Wallis. Some hydrodynamics aspects of two-phase flow. In *International Developments in Heat Transfer*, ASME 319–340, 1963.

[374] H. Wan, C. Gualtieri, H. Yang, and J. Feng. Numerical Simulation of Hydrodynamics and Reaeration over a Stepped Spillway by the SPH Method. *Water*, 9(8):565, August 2017. doi: 10.3390/w9080565.

[375] H. Wan, R. Li, X. Pu, H. Zhang, and J. Feng. Numerical Simulation for the air entrainment of aerated flow with an improved multiphase SPH model. *International Journal of Computational Fluid Dynamics*, 31(10):435–449, January 2017. doi: 10.1080/10618562.2017.1420175.

[376] W. Wan, A. Raza, and X. Chen. Effect of Height and Geometry of Stepped Spillway on Inception Point Location. *Applied Science*, 9(10):2091, May 2019. doi: 10.3390/app9102091.

[377] C. Wang, Y. Wang, C. Peng, and X. Meng. Smoothed particle hydrodynamics simulation of water-soil mixture flows. *Journal of Hydraulic Engineering*, 142:1–16, 2016. doi: 10.1061/(ASCE)HY.1943-7900.0001163.

[378] Z. Wang, J. Yang, and F. Stern. High-fidelity simulations of bubble, droplet and spray formation in breaking waves. *Journal of Fluid Mechanics*, 792:307–327, April 2016. doi: 10.1017/jfm.2016.87.

[379] T. Watamura, F. Iwatsubo, K. Sugiyama, K. Yamamoto, Y. Yotsumoto, and T. Shiono. Bubble cascade in Guinness beer is caused by gravity current instability. *Scientific Reports*, 9(5718), April 2019. doi: 10.1038/s41598-019-42094-0.

[380] N. P. Waterson and H. Deconinck. Design principles for bounded higher-order convection schemes – a unified approach. *Journal of Computational Physics*, 224(1):182–207, May 2007. doi: 10.1016/j.jcp.2007.01.021.

[381] W. Wei, W. Xu, J. Deng, Z. Tian, and F. Zhang. Free-surface air entrainment in open-channel flows. *Science China Technological Sciences*, 60(6):893–901, June 2017. doi: 10.1007/s11431-016-0220-1.

[382] H. Wendland. Piecewise polynomial, positive definite and compactly supported radial functions of minimal degree. *Advances in Computational Mathematics*, 4(1):389–396, 1995. doi: 10.1007/BF02123482.

[383] S. Whitaker. *The Method of Volume Averaging*. Kluwer Academic Publishers, 1999. ISBN 0-7923-5486-9. doi: 10.1007/978-94-017-3389-2.

[384] A. Witt, J. S. Gulliver, and L. Shen. Simulating air entrainment and vortex dynamics in a hydraulic jump. *International Journal of Multiphase Flow*, 72:165–180, 2015. doi: 10.1016/j.ijmultiphaseflow.2015.02.012.

[385] A. B. Wood. *A Textbook of Sound*, pages 361–363. Bell and Sons, 1941.

[386] I. R. Wood. Uniform region of self-aerated flow. *Journal of Hydraulic Engineering*, 109(3):447–461, January 1983. doi: 10.1061/(ASCE)0733-9429(1983)109:3(447).

[387] Q. Xiong, L. Deng, W. Wang, and W. Ge. SPH method for two-fluid modeling of particle–fluid fluidization. *Chemical Engineering Science*, 66(9):1859–1865, May 2011. doi: 10.1016/j.ces.2011.01.033.

[388] R. Xu, P. Stansby, and D. Laurence. Accuracy and stability in incompressible SPH (ISPH) based on the projection method and a new approach. *Journal of Computational Physics*, 228(18):6703–6725, October 2009. doi: 10.1016/j.jcp.2009.05.032.

[389] V. Yakhot and S. A. Orszag. Renormalization group analysis of turbulence. I. Basic theory. *Journal of Scientific Computing*, 1(1):3–51, 1986. doi: 10.1007/BF01061452.

[390] K. Yamagiwa, Y. Ohmae, M. H. Dahlan, and A. Ohkawa. Activated sludge treatment of small-scale wastewater by a plunging liquid jet bioreactor with cross-flow filtration. *Bioresource Technology*, 37(3):215–222, 1991. doi: 10.1016/0960-8524(91)90186-N.

[391] X. Yan, Y.-T. Jiang, C.-F. Li, R. R. Martin, and S.-M. Hu. Multiphase SPH simulation for interactive fluids and solids. *ACM Transactions on Graphics*, 35(4), July 2016. doi: 10.1145/2897824.2925897.

[392] H. Yang, R. Li, P. Lin, H. Wan, and J. Feng. Two-phase smooth particle hydrodynamics modeling of air-water interface in aerated flows. *Science China Technological Sciences*, 60 (3):479–490, March 2017. doi: 10.1007/s11431-016-0586-5.

[393] T. Yang, J. Chang, B. Ren, M. C. Lin, J. J. Zhang, and S.-M. Hu. Development of turbulence models for shear flows by a double expansion technique. *ACM Transactions on Graphics*, 34(6):201:1–201:11, November 2015. doi: 10.1145/2816795.2818117.

[394] C. J. Yap. *Turbulent heat and momentum transfer in recirculating and impinging flows*. PhD thesis, University of Manchester, Manchester, UK, 1987. 115–120.

[395] S. Yu, D. K. P. Yue, L. Wang, and X. Yu. Direct Numerical Simulations of Air Entrainment Induced by Vortex Structures. In *Proceedings of the 28th International Ocean and Polar Engineering Conference*, Sapporo, Japan, 2018.

[396] A. Zainali, N. Tofighi, M. S. Shadloo, and M. Yildiz. Numerical investigation of Newtonian and non-Newtonian multiphase flows using ISPH method. *Computer Methods in Applied Mechanics and Engineering*, 254:99–113, February 2013. doi: 10.1016/j.cma.2012.10.005.

[397] J. Zhan, J. Zhang, and Y. Gong. Numerical investigation of air-entrainment in skimming flow over stepped spillways. *Theoretical and Applied Mechanics Letters*, 6(3):139–142, May 2016. doi: 10.1016/j.taml.2016.03.003.

[398] C. Zhang, X. Y. Hu, and N. A. Adams. A weakly compressible SPH method based on a low-dissipation Riemann solver. *Journal of Computational Physics*, 335:605–620, April 2017. doi: 10.1016/j.jcp.2017.01.027.

[399] L. Zhang and B. G. Thomas. State of the Art in Evaluation and Control of Steel Cleanliness. *ISIJ International*, 43(3):271–291, April 2003. doi: 10.2355/isijinternational.43.271.

[400] B. X. Zheng and Z. Chen. A multiphase smoothed particle hydrodynamics model with lower numerical diffusion. *Journal of Computational Physics*, 382:177–201, April 2019. doi: 10.1016/j.jcp.2019.01.012.

[401] L. Zhou, Z. W. Cai, Z. Zong, and Z. Chen. An SPH pressure correction algorithm for multiphase flows with large density ratio. *International Journal for Numerical Methods in Fluids*, 81(12):765–788, August 2016. doi: 10.1002/fld.4207.

[402] G. X. Zhu, L. Zou, Z. Chen, A. M. Wang, and M. B. Liu. An improved SPH model for multiphase flows with large density ratios. *International Journal for Numerical Methods in Fluids*, 86(2):167–184, January 2018. doi: 10.1002/fld.4412.

[403] Y. Zhu, H. N. Oğuz, and A. Prosperetti. On the mechanism of air entrainment by liquid jets at a free surface. *Journal of Fluid Mechanics*, 404:151–177, February 2000. doi: 10.1017/S0022112099007090.

[404] N. Zuber and J. A. Findlay. Average Volumetric Concentration in Two-Phase Flow Systems. *Journal of Heat Transfer*, 87(4):453–468, November 1963. doi: 10.1115/1.3689137.